



Università degli Studi di Ferrara

DOTTORATO DI RICERCA IN

SCIENZE DELLA TERRA

CICLO XXV

COORDINATORE Prof. Luigi Beccaluva

Evaluation of natural and present subsidence in the
northeastern coast of the Caspian Sea

Settore Scientifico Disciplinare GEO/04

Tutore Interno

Prof. Simeoni Umberto

Dottorando

Dott. Magagnini Luca

Tutori Esterni

PhD. Ulazzi Elisa

Prof. Teatini Pietro



Università degli Studi di Ferrara

DOTTORATO DI RICERCA IN
SCIENZE DELLA TERRA

CICLO XXV

COORDINATORE Prof. Luigi Beccaluva

Evaluation of natural and present subsidence in the
northeastern coast of the Caspian Sea

Settore Scientifico Disciplinare GEO/04

Tutore Interno

Prof. Simeoni Umberto

Dottorando

Dott. Magagnini Luca

Tutori Esterni

PhD. Ulazzi Elisa

Prof. Teatini Pietro

Anni 2010/2012

TABLE OF CONTENT

1.	ABSTRACT	1
2.	GOAL, OBJECTIVES, METHODOLOGY AND LIMITATIONS	7
3.	GEO-HYDROGEOLOGICAL RECONSTRUCTION.....	17
3.1	Geology, Tectonic And Seismicity.....	17
3.1.1	<i>Brief description of main geological features in the Caspian area</i>	<i>17</i>
3.1.2	<i>The North Caspian Basin Structure</i>	<i>23</i>
3.1.3	<i>The North Ustyurt Basin Structure.....</i>	<i>68</i>
3.2	Stratigraphy	75
3.2.1	<i>North and West Basin Margin.....</i>	<i>77</i>
3.2.2	<i>East-Southeast Basin Margin</i>	<i>79</i>
3.2.3	<i>South Basin Margin</i>	<i>81</i>
3.2.4	<i>Details on Zones B and C.....</i>	<i>85</i>
3.3	Details About Salt Dome Structures.....	88
3.3.1	<i>Permian Deposition, Salt Formation, and Movements.....</i>	<i>90</i>
3.3.2	<i>Triassic Deposition and Salt Movements.....</i>	<i>91</i>
3.3.3	<i>Jurassic Deposition and Salt Movements (Mainly Extrusion and Overhangs).....</i>	<i>94</i>
3.3.4	<i>Jurassic–Paleogene Deposition and Polygonal Faults</i>	<i>98</i>
3.3.5	<i>Cenozoic Deposition.....</i>	<i>103</i>
3.4	Soils Distribution And Characterisation	107
3.4.1	<i>Spatial distribution of soil features in Zone B (Northern Area, from Atyrau City to the Emba River valley)</i>	<i>109</i>
3.4.2	<i>Spatial distribution of soil features in Zone C (North – Eastern Area, from the basin of the Emba River to the Mertvy Kultuk Bay).....</i>	<i>114</i>
3.4.3	<i>Spatial distribution of soil features in Zone D (Southern Area, Northern Shoreline of Buzachi Peninsula).....</i>	<i>118</i>
3.5	Hydrogeological Setting.....	124
3.5.1	<i>Spatial distribution of hydrogeological features in Zone B (from Atyrau City to the Emba River valley)</i>	<i>125</i>

3.5.2	<i>Spatial distribution of hydrogeological features in Zone C (from the basin of the Emba River to the Mertvy Kultuk Bay)</i>	128
3.5.3	<i>Spatial distribution of hydrogeological features in Zone D (Northern Shoreline of Buzachi Peninsula)</i>	130
3.5.4	<i>Hydrogeology of the Tyub-Karagan Peninsula</i>	133
3.5.5	<i>Future Use of the Underground Waters</i>	133
3.6	Oil&Gas Resources	138
3.6.1	<i>Description of the Precaspian basin petroleum system</i>	138
3.6.2	<i>Oil&Gas Resources of the North Ustyurt Basin</i>	143
4.	EVALUATION OF NATURAL AND PRESENT SUBSIDENCE	147
4.1	Rock Compressibility	147
4.1.1	<i>Definitions</i>	147
4.1.2	<i>Measurements of rock compressibility</i>	151
4.1.3	<i>Pore compressibility calculated by traveltime log</i>	156
4.2	Natural Susidence Calculation Through Numerical Modeling	165
4.2.1	<i>Preliminary Analysis Of Natural Subsidence Numerical Models</i>	165
4.2.2	<i>Synthetic overview of existing models</i>	166
4.2.3	<i>The Natsub code</i>	172
4.2.4	<i>The Basin code</i>	189
4.2.5	<i>Models application and results</i>	200
4.2.6	<i>General discussion of NATSUB and BASIN output</i>	255
4.3	Evaluation Of Present Subsidence By Sar Interferometry	257
4.3.1	<i>Principles of Interferometric SAR technique</i>	257
4.3.2	<i>SAR resolution: cell projection on the ground</i>	262
4.3.3	<i>Applications and limits</i>	265
4.3.4	<i>Innovative aspects of InSAR application to the study area</i>	277
4.3.5	<i>Analysis and interpretation of SBAS results</i>	304
4.3.6	<i>Preliminary application of IPTA</i>	325
4.3.7	<i>Comparison of achieved results with the northern Adriatic coastland case study</i>	335
5.	CALCULATED AND MEASURED RESULTS COMPARISON AND CONCLUSION	347
6.	SWOT ANALYSIS	349
7.	FUTURE SCENARIO ESTIMATION	351
8.	MONITORING PLAN	353
8.1	Spatial and temporal distribution of radar images acquisition for SBAS monitoring analysis within frames Z1, Z2 and Z3.....	353

8.2	Integration of monitoring plan with artificial Persistent Scatters and fix GPS stations.....	353
8.3	Best solution for fix GPS installation	357
9.	PROPOSED NEXT ACTIVITIES.....	361
9.1	Present subsidence monitoring along the whole Kazakh coastal area	361
9.2	Creation of a Digital Elevation Model	363
9.3	InSAR analysis on production islands.....	366
10.	REFERENCES	367
11.	ACKNOWLEDGEMENT	376

LIST OF FIGURES

Figure 1: Landscapes within Frame Z1, along the Ural river vegetated belt and Eskene area.....	10
Figure 2: Landscapes within Frame Z3, Buzachi peninsula.....	11
Figure 3: Study area subdivision.....	11
Figure 4: Links between the geo-hydrogeological reconstruction and activities carried out during the analysis of present subsidence.....	13
Figure 5: Tectonic scheme of the North Caspian Region, after “A. P. Afanasenkov et al., 2008”.....	19
Figure 6: Petroleum system and assessment units of North Caspian Basin. After G. F. Ulmishek, 2003”.....	23
Figure 7: Structural map of the North Caspian Basin, after “G. F. Ulmishek, 2003”.....	26
Figure 8: Isobathic maps of Precaspian Basin at the level of main reflectors, isolines in km, after “Yu.A. Volozh et al., 2003”.....	28
Figure 9: Geological –geophysical crustal section Volgograd –Chelkar, after “Volozh et al., 2003”.....	29
Figure 10: Palinspastic reconstruction along a profile on the east Precaspian margin, line Ural River –Izembet (Urals), after “Volozh et al., 2003”.....	30
Figure 11: Reconstruction of evolution of the Precaspian Basin along a N–S line after “Brunet et al., 1999”. Layers are reconstituted without the movements of salt.....	31
Figure 12: Palaeogeological reconstruction across profile Karaton–Tengiz–Yuzhnaya, southeast Precaspian margin, after “Volozh et al., 2003”.....	32
Figure 13: Geodynamic reconstructions of Riphean–Vendian history, after “Volozh et al., 2003”.....	34
Figure 14: Riphean– Early Palaeozoic geodynamic reconstruction along an East–West section demonstrating eclogites emplacement, after “Volozh et al., 2003”.....	35
Figure 15: Map of the crustal thickness without HVL (a) and thickness of the HVL (b), after “Brunet et al., 1999”.....	38
Figure 16: Subsidence curves in the centre of the Precaspian Basin, after “Brunet et al., 1999”.....	42
Figure 17: Stratigraphical site of seismic reflector P3, by Akhmetshina et al., 1993 modified by Volozh et al. 2003.....	44

Figure 18: North– south section on the southwest Astrakhan margin of the Precaspian Basin, after “Volozh et al. 2003”.....	45
Figure 19: Structural and tectonic map showing consolidated crust in the Caspian region, after “Volozh et al., 2009”.....	48
Figure 20: Geologic-geophysical section across the South Emba uplift (b) and a fragment of time section (a) showing the morphology of tectonic dislocations within the South Emba regional fault, after “Volozh et al., 1999”.....	49
Figure 21: Gross depositional environment map of the Ordovician, after “Volozh and Parasyina, 2008”.....	50
Figure 22: Geologic section through the Tsimlyansk line across the Karpinskiy Range, after “Volozh et al., 1999”.....	51
Figure 23: Paleotectonic reconstructions across the Tsimlyansk line illustrating the major tectonic events that result in the development of the Sarmat–Turkry rift system, after “Volozh et al., 2009”.....	52
Figure 24: Palinspastic reconstruction of consolidated crust of the Paleozoic East European continent at the beginning of the Kungurian, after “Volozh and Parasyina, 2008”.....	53
Figure 25: Relationship between structural geometry of different sequences of the sedimentary cover, North Caspian salt dome region,after “Volozh et al., 2009”.....	55
Figure 26: Cross-section across the Ural foredeep, after “Volozh et al., 2009”.....	56
Figure 27: Fragment of time section through a regional line across junction zone between the Ural foredeep and East Orenburg arch, after “Volozh et al., 2009”.....	56
Figure 28: Paleozoic (presalt) petroleum potential, after “Volozh et al., 2009”.....	59
Figure 29: Diagram of amplitudes of recent tectonic movements in the Caspian and Turanskaya Platform regions, after “KDCP, 2002”.....	62
Figure 30: Diagram of recent (active) faults in the Caspian and Turanskaya Platform regions, after KDCP, 2002.....	65
Figure 31: Earthquakes of the North Caspian Region, after “Granherne, 2006”.....	67
Figure 32: Petroleum system and assessment units of the North Ustyurt basin, after “Ulmishek, 2003”.....	69
Figure 33: Principal structural unit of the North Ustyurt basin, after “Ulmishek, 2003”.....	70
Figure 34: Generalized structure of Buzachi arch and adjacent areas, after “G.F. Ulmishek, 2003”.....	72
Figure 35: Cross-section through north basin margin. Located in the westernmost portion of the northern margin. After “Ulmishek, 2003” and Cross section through Karachaganak carbonate build-up, after “Ulmishek, 2003”.....	78
Figure 36: Cross section through east basin margin, after “Ulmishek, 2003”.....	80
Figure 37: Carbonate build-ups of northern Caspian Sea. Scale approximate. After “Ulmishek, 2003”.....	81
Figure 38: Cross section of Karaton-Tengiz zone, after “Ulmishek, 2003”.....	83

Figure 39: Cross section of Astrakhan arch, after “Ulmishek, 2003”.....	84
Figure 40: Well section stratigraphic correlation in Caspian Sea and coastal zones, after “GAS, 2007”.....	85
Figure 41: Synthetic column in the centre of the Precaspian basin, showing the thickness of sediments, paleo water depths, ages and main seismic horizons, with velocities and density.	86
Figure 42: Schematic cross-section NW-SE across Tengiz-Karaton Platform, after “Max Petroleum, 2010”.....	87
Figure 43: Summary of the typical stratigraphy in Zone C.....	87
Figure 44: Historical map of salt domes in Southern Precaspian Basin, after “Sanders, 1939”.	88
Figure 45: Historical dome cross-section, after “Sanders, 1939”.....	89
Figure 46: Salt structures in the Precaspian basin from the Triassic to the Early Jurassic, after “Volozh et al., 2003”.....	91
Figure 47: Map of Precaspian basin showing current shapes of salt structures, after “Volozh et al., 2003”.....	92
Figure 48: Seismic profile (located in Emba River Valley) and restoration to stated times. Dotted line along right-hand end of restored profiles indicates changing profile length by area balancing.	94
Figure 49: Summary of sedimentation and halokinesis in the Precaspian basin. Regions a1–b5 are identified in Figure 47.....	97
Figure 50: The sheet of allochthonous Kungurian salt at Kum (Kazakh area of the Volga mouth) was extruded in the Late Jurassic and began to upbuild during the Paleogene, after “Volozh et al., 2003”.	98
Figure 51: The Kotyrtas North oil field (located on North Emba River Valley) is trapped above a sheet of allochthonous Kungurian salt extruded in the Middle Triassic, after “Volozh et al., 2003”.....	101
Figure 52: A sheet of allochthonous Kungurian (±Kazanian salt) extruded in the Middle to Late Triassic trapped the Novobogatinsk oil field (located near Atyrau), after “Volozh et al., 2003”.....	102
Figure 53: Maps of part of the southern Precaspian basin showing normal faults offsetting base Cretaceous, after “Volozh et al., 2003”.....	103
Figure 54: Structural map of the Precaspian basin in Pliocene times illustrating incisions and canyons eroded through Cretaceous platform sediments by the paleo-Volga and paleo-Amu-Dariya rivers draining into the South Caspian lake having a surface about 1 km below ocean level, after “Volozh et al., 2003”.....	105
Figure 55: Map of soils distribution between Atyrau City and Emba River Valley, after “Mo Energy and Mineral resources et al., 2001”.....	112
Figure 56: Map of soils distribution between Emba River basin and Mertvyv Kultuk Bay, after “Mo Energy and Mineral resources et al., 2001”.....	116
Figure 57: Map of soils distribution in the Northern shoreline of the Buzachi Peninsula, after “Mo Energy and Mineral resources et al., 2001”.....	121

Figure 58: Groundwater depths in Zone B	126
Figure 59: Groundwater depths in Zone C	129
Figure 60: Groundwater depths in Zone D	132
Figure 61: Mineral and iodine-bromine underground waters in the study area (green circles)	135
Figure 62: Events chart of North Caspian Total Petroleum System, after “Ulmishek, 2003”	140
Figure 63: Sketch of an extensometric apparatus using a string of solid pipes.....	153
Figure 64: Radioactive marker technique for measuring the compaction of deep formations.....	154
Figure 65: Evaluation of bottom velocity and land subsidence over the last three centuries, projected until 2100 in the Emilia-Romagna coast, using NATSUB, after “Gambolati et al., 1999.”	167
Figure 66: Three main conceptual blocks of the Galo model, after (Makhous et al, 1997).	169
Figure 67: DeCompactionTool work flow, after “Holzel et al., 2008”	170
Figure 68: Print-screen of TerraMod software.....	171
Figure 69: The sediment column has height $l(t)$ at time t after inception of the accretion process and rests on an impermeable basement at $z=0$. Seawater elevation is L	175
Figure 70: Typical compression profile of a cohesive soil vs. the effective intergranular stress: a) arithmetic plot and b) semilogarithmic plot.....	180
Figure 71: Log-log graphic of the whole compressibility dataset.	207
Figure 72: Porosity n vs. depth z at Test 1 well, for different compressional trends.	211
Figure 73: Porosity n vs. depth z at Test 2 well, for different compressional trends.	212
Figure 74: Porosity n vs. depth z at Test 3 well, for different compressional trends.	212
Figure 75: Porosity n vs. depth z at Test 4 well, for different compressional trends.	213
Figure 76: Porosity n vs. depth z at Test 5 well, for different compressional trends.	213
Figure 77: Sedimentation rate (Sed.rate) and settling velocity (Bott.vel.) vs. geological time (high trend).....	229
Figure 78: Sedimentation rate (Sed.rate) and settling velocity (Bott.vel.) vs. geological time (mean trend).	229
Figure 79: Sedimentation rate (Sed.rate) and settling velocity (Bott.vel.) vs. geological time (low trend).....	229
Figure 80: AK1 Sedimentary column depths comparison, at selected time steps (high, mean and low trends).....	229
Figure 81: Sedimentary column compaction vs. time.....	229
Figure 82: Pore pressure vs. depth.....	229
Figure 83: Pore pressure vs. time.....	229
Figure 84: Sedimentation rate (Sed. rate) and settling velocity (Bott.vel.) vs. geological time (high trend).....	231

Figure 85: Sedimentation rate (Sed. rate) and settling velocity (Bott.vel.) vs. geological time (mean trend).....	231
Figure 86: Sedimentation rate (Sed. rate) and settling velocity (Bott.vel.) vs. geological time (low trend).....	231
Figure 87: Sedimentary column depths comparison, at selected time steps.	231
Figure 88: Sedimentary column compaction vs. time.....	231
Figure 89: Pore pressure vs. depth.....	231
Figure 90: Pore pressure vs. time	231
Figure 91: Sedimentation rate (Sed.rate) and settling velocity (Bott.vel.) vs. geological time (high trend).....	233
Figure 92: Sedimentation rate (Sed.rate) and settling velocity (Bott.vel.) vs. geological time (mean trend).....	233
Figure 93: Sedimentation rate (Sed.rate) and settling velocity (Bott.vel.) vs. geological time (low trend).....	233
Figure 94: Sedimentary column depths comparison, at selected time steps.	233
Figure 95: Sedimentary column compaction vs. time.....	233
Figure 96: Pore pressure vs. depth.....	233
Figure 97: Pore pressure vs. time.....	233
Figure 98: Sedimentation rate (Sed.rate) and settling velocity (Bott.vel.) vs. geological time (high trend).....	235
Figure 99: Sedimentation rate (Sed.rate) and settling velocity (Bott.vel.) vs. geological time (mean trend).....	235
Figure 100: Sedimentation rate (Sed.rate) and settling velocity (Bott.vel.) vs. geological time (low trend).....	235
Figure 101: Sedimentary column depths comparison, at selected time steps.	235
Figure 102: Sedimentary column compaction vs. time.....	235
Figure 103: Pore pressure vs. depth.....	235
Figure 104: Pore pressure vs. time.....	235
Figure 105: Sedimentation rate (Sed.rate) and settling velocity (Bott.vel.) vs. geological time (high trend).....	237
Figure 106: Sedimentation rate (Sed.rate) and settling velocity (Bott.vel.) vs. geological time (mean trend).....	237
Figure 107: Sedimentation rate (Sed.rate) and settling velocity (Bott.vel.) vs. geological time (low trend).....	237
Figure 108: Sedimentary column depths comparison, at selected time steps.	237
Figure 109: Sedimentary column compaction vs. time.....	237
Figure 110: Pore pressure vs. depth.....	237
Figure 111: Pore pressure vs. time.....	237
Figure 112: Position of numerical simulation 2D section.....	240
Figure 113: Chronostratigraphy simulated through BASIN model (Simulation 1) and comparison with schematic cross-section elaborated by Max Petroleum (2008).	244

Figure 114:Simulation’s mesh at different time steps (Late Devonian, Serpukhovian-Bashkirian boundary, Triassic-Jurassic boundary, Early Cretaceous) (Simulation 1).	245
Figure 115:Porosity at different time steps (Late Devonian, Serpukhovian-Bashkirian boundary, Triassic-Jurassic boundary, Early Cretaceous) (Simulation 1).....	246
Figure 116:Specific storage at different time steps (Late Devonian, Serpukhovian-Bashkirian boundary, Triassic-Jurassic boundary, Early Cretaceous) (Simulation 1).	247
Figure 117: Hydraulic conductivity at different time steps (Late Devonian, Serpukhovian-Bashkirian boundary, Triassic-Jurassic boundary, Early Cretaceous) (Simulation 1).	248
Figure 118:Consolidational settling rate at different time steps (Late Devonian, Serpukhovian-Bashkirian boundary, Triassic-Jurassic boundary, Early Cretaceous) (Simulation 1).	249
Figure 119:Simulation’s mesh at different time steps (Late Devonian, Serpukhovian-Bashkirian boundary, Triassic-Jurassic boundary, Early Cretaceous) (Simulation 2).	250
Figure 120:Porosity at different time steps (Late Devonian, Serpukhovian-Bashkirian boundary, Triassic-Jurassic boundary, Early Cretaceous) (Simulation 2).....	251
Figure 121:Specific storage at different time steps (Late Devonian, Serpukhovian-Bashkirian boundary, Triassic-Jurassic boundary, Early Cretaceous) (Simulation 2).	252
Figure 122:Hydraulic conductivity at different time steps (Late Devonian, Serpukhovian-Bashkirian boundary, Triassic-Jurassic boundary, Early Cretaceous) (Simulation 2).	253
Figure 123:Consolidational settling rate at different time steps (Late Devonian, Serpukhovian-Bashkirian boundary, Triassic-Jurassic boundary, Early Cretaceous) (Simulation 2).	254
Figure 124:SAR system from a satellite (Ferretti et al., 2007).	259
Figure 125:Sinusoidal function $\sin \varphi$ is periodic with a 2π radian period.....	261
Figure 126:Effect of terrain on the SAR image.....	263
Figure 127:Layover and shadow effects.	264
Figure 128:ENVISAT resolution cell dimension in ground range as a function of the terrain slope. The vertical dotted line indicates the incidence angle relative to a flat horizontal terrain (23°) (Ferretti et al., 2007).....	265
Figure 129:Geometry of a satellite interferometric SAR system.	266
Figure 130:Geometric parameters of a satellite interferometric SAR system (Ferretti et al., 2007).....	267
Figure 131:Interferometric phase dispersion (degrees) as a function of the coherence for varying numbers of looks (NL) (Ferretti et al., 2007).	272
Figure 132:Interferometric phase dispersion exact values (blue curves) and approximated ones (red curves) (Ferretti et al., 2007).....	272
Figure 133:SBAS algorithm block diagram (Casu et al., 2006).	275

Figure 134: Frames of SBAS application in the area of interest.	279
Figure 135: Images focused on Frame Z1.	282
Figure 136: Images focused on Frame Z2.	283
Figure 137: Images focused on Frame Z3.	284
Figure 138: Topographic reference of the study area based on SRTM.	285
Figure 139: Temporal and spatial baseline of frame Z1.	286
Figure 140: Temporal and spatial baseline of frame Z2.	287
Figure 141: Temporal and spatial baseline of frame Z3.	287
Figure 142: Possible interferograms with baselines shorter than 200 m in frame Z1.....	288
Figure 143: Possible interferograms with baselines shorter than 200 m in frame Z2.....	289
Figure 144: Possible interferograms with baselines shorter than 200 m in frame Z3.....	290
Figure 145: Location of the reference point (green triangle) in each frame.....	291
Figure 146: Interferograms considered after phase unwrapping in frame Z1.....	299
Figure 147: Interferograms considered after phase unwrapping in frame Z2.....	300
Figure 148: Interferograms considered after phase unwrapping in frame Z3.....	301
Figure 149: Interferograms considered after multi-baseline interferometry analysis in frame Z1.	302
Figure 150: Interferograms considered after multi-baseline interferometry analysis in frame Z2.	302
Figure 151: Interferograms considered after multi-baseline interferometry analysis in frame Z3.	303
Figure 152: Results of SBAS analysis in frame Z1.....	305
Figure 153: Detail of SBAS analysis within frame Z1.	307
Figure 154: Results of SBAS analysis in frame Z2.....	313
Figure 155: Uplifts along the coastal area.....	314
Figure 156: Results of SBAS analysis in frame Z3.....	320
Figure 157: Identification of candidate persistent scatterers in frame Z1.....	326
Figure 158: Identification of candidate persistent scatterers in frame Z2.....	327
Figure 159: Identification of candidate persistent scatterers in frame Z3.....	328
Figure 160: Results of IPTA before outliers filtering.	329
Figure 161: Example of local displacements in a zone of Atyrau (light blue dots: rates value between ± 2 mm/y; yellow dots: rates value between -2 and -8 mm/y).	330
Figure 162: Location of the persistent scatterers removed from the regional investigation.....	331
Figure 163: Displacement map for the frame Z1 obtained by IPTA after filtering out the measurements affected by a site-specific displacement trend.....	332
Figure 164: Comparison between IPTA (left) and SBAS (right) on the whole frame Z1 and in correspondence to Atyrau.	333
Figure 165: Differences between IPTA and SBAS analysis.	334
Figure 166: Digital elevation model (DEM) of the northern Adriatic region obtained from SRTM data.....	336

Figure 167:Relative sea level rise (RSLR) at Venice and Ravenna over the period 1896–2007.....	336
Figure 168:Recent natural land subsidence in the northern Adriatic coastal area (after Gambolati and Teatini 1998).....	337
Figure 169:Vertical displacement rates (mm/year) in the Venetian region obtained by the SIMS over the decade 1992–2002.....	340
Figure 170:Vertical displacement rates (mm/year) in the Venetian coastland obtained by IPTA of ENVISAT scenes acquired between 2003 and 2007.	341
Figure 171:Map of the cumulative displacements (cm) occurring from 1992 to 2007 in the Venetian coastland as obtained by the integration of ERS-1/2 and ENVISAT IPTA results. Green dots position of the IGM34 (IRMA54) leveling benchmarks used for the validation of the IPTA outcomes.....	342
Figure 172:Comparison between leveling and IPTA results along the IGM34 (IRMA54) line.....	342
Figure 173:Parallelisms between two different study areas.....	344
Figure 174:Reached detail of SAR based measured at Venice (Teatini et al., 2007).	345
Figure 175:Example of sedimentation rate and settling velocity during future scenario, well Test 3.	351
Figure 176:Example of depth (or thickness) of the sedimentary column during future scenario, well Test 3.....	352
Figure 177:Identified PT in frame Z1.....	354
Figure 178:Identified PT in frame Z2.....	354
Figure 179:Identified PT in frame Z3.....	355
Figure 180:Integration between natural and artificial PTs	356
Figure 181:Location of the GPS stations in international GPS networks around the Caspian Sea (after SOPAC archives, http://sopac.ucsd.edu/sites/).....	357
Figure 182:Possible GPS location (red circle) within frame Z1.....	358
Figure 183:Possible GPS location (red circle) within frame Z2.....	358
Figure 184:Possible GPS location (red circle) within frame Z3.....	359
Figure 185: Snapshot of ESA imagery catalogue.....	361
Figure 186:RADARSAT-1 tracks covering the north-eastern Caspian. The red "squares" represent the three frames selected from the ENVISAT-ASAR archive.....	362
Figure 187:Preliminary selection of RADARSAT-1 frames (in blue) for the DInSAR analysis.	362
Figure 188:DEM generation in the eastern part of the Volga Delta: step of elaboration.	365
Figure 189:Distances between artificial islands at Kashagan area.....	366
Figure 190:InSAR technique applied to the artificial Island of Palm Jumeirah, Dubai.....	366

LIST OF TABLES

Table 1:	Advantages and disadvantages of applied methodologies.....	13
Table 2:	Geodynamic events linked to sedimentary environment in the PCB, after "Volozh et al., 2003".....	37
Table 3:	Regional quaternary stratigraphy.....	107
Table 4:	Preliminary evaluation of Numerical models.....	166
Table 5:	Main logs used for this study.....	200
Table 6:	Mean values of e_0 vs. z_0 founded in geotechnical reports and values assumed during the model application for $z_0=20$ m.....	210
Table 7:	Depth of available sonic logs.....	216
Table 8:	Present thickness of the layering sequence at Test 1 as compared to the uncompacted thickness b_i	217
Table 9:	Present thickness of the layering sequence at Test 2 as compared to the uncompacted thickness b_i	219
Table 10:	Present thickness of the layering sequence at Test 3 as compared to the uncompacted thickness b_i	221
Table 11:	Present thickness of the layering sequence at Test 4 as compared to the uncompacted thickness b_i	223
Table 12:	Present thickness of the layering sequence at Test 5 as compared to the uncompacted thickness b_i	225
Table 13:	Comparison between present total thicknesses and uncompacted ones.....	227
Table 14:	Results sheet description.....	228
Table 15:	Dates and orbits of acquisition.....	279
Table 16:	List of interferograms considered after phase unwrapping.....	292
Table 17:	Displacements versus time for a few sites selected within the Z1 frame.....	308
Table 18:	Displacements versus time for a few sites selected within the frame Z2.....	316
Table 19:	Displacements versus time for a few sites selected within the frame Z3.....	322
Table 20:	Natural and present SWOT analysis.....	349
Table 21:	Summary of SRTM performance. All quantities represent 90% errors in meters.....	363

ACRONYMS

ATM:	Atmospheric (referred to DInSAR analysis);
BH:	Borehole;
BoD:	Basis of Design;
BTOE:	Billion Tons of Oil Equivalent;
CAL:	Caliper
CMB:	Crust/Mantle Boundary;
CPD:	Central Precaspian Depression;
CPT:	Cone Penetration Testing;
DEM:	Digital Elevation Model;
DInSAR:	Differential Interferometric Synthetic Aperture Radar;
ESA:	European Space Agency;
GDB:	Geodatabase;
GIS:	Geographic Information System;
GOR:	Gas Oil Ratio;
GPS:	Global Positioning System;
ICZM:	Integrated Coastal Zone Management;
InSAR:	Interferometric Synthetic Aperture Radar;
IPTA:	Interferometric Point Target Analysis;
LAS:	Log Ascii Standard
LOS:	Line of Sight;
LS:	Last square solution;
MD:	Measured Depth referenced from well elevation;

NCB: North Caspian Basin;
NPHI: Neutron porosity;
NL: Number of looks;
PSI: Persistent Scatterer Interferometry;
PCB: Precaspian Basin;
RHOB: Bulk density;
SAR: Synthetic Aperture Radar;
SBAS: Small Baseline Subset
TPF: Temporal Phase Filtered
TPS: Total Petroleum System;

1. ABSTRACT

The main goal of the study is to test different methodologies helpful for the definition of natural and present subsidence along coastal area. Specifically, tests were carried out on the Kazakh coastal area (northeastern part of the Caspian Sea coast).

Specific objectives include:

- the reconstruction of the geological assets of the projects area;
- the definition of processes that influence the subsidence under specific geological conditions;
- the calculation, through numerical models application (both 1D – NATUB and 2D - BASIN), of natural subsidence;
- the detection of present ground vertical movements through Synthetic Aperture Radar Interferometry (InSAR), from 2003 to 2009.

Collected data was derived from international literature (especially for the basin-scale) and from O&G companies reports and surveys, and considering several geological disciplines (stratigraphy, geodynamics, hydrogeology *etc.*).

Integration of data and the reconstruction of the geological framework of the area have been developed at different scales:

- basin-scale: regional geology and geodynamic evolution of the Precaspian Basin and the North Ustyurt Basin;
- local scale: four subareas of the northern part of the Caspian Sea have been identified. For each subarea, when data is available the study focuses on the complexity and variability of the area; the stratigraphic complexity is determined by several kilometres of clastic and carbonatic sediments interrupted by 4 km salt layer, a distribution of soil features (with geotechnical properties) linked to the interaction of fluvial and marine dynamics, prevalence of saline waters in a multistage aquifer system, and the presence of oil and gas reservoirs.

The realization of a datasets (stratigraphy, geochronology, compressibility of different sedimentary layers, *etc.*) required by activities foreseen during the analysis of natural subsidence has been exhaustively fulfilled.

This data has been used as input during the mono- and bi- dimensional numerical simulation of natural subsidence on 5 different locations.

Collected data provided also information required for the interpretation of the present subsidence detected by InSAR analysis; the application of two different InSAR techniques ((Small BAseline Substet and Interferometric Poin Target Analysis), never tested in coastal environments similar to this one, allowed to measure vertical land movements at local scale; sometimes lack of data on top on that linked to salt dome characteristics does not permit a detailed correlation between vertical movements detected and their geological causes.

NATSUB and BASIN models outputs underline the stable behaviour of the area and the absence of clear subsidential phenomena.

In the southern margin of the Precaspian basin, the limited depth of elder drilled strata (carbonates of Devonian period) reveals that the basin was filled with very low rates of sedimentation and NATSUB shows that consolidational processes were coeval with sedimentational ones. Therefore, subsidential processes do not affect the deep and ancient rocks, and BASIN application shows that the consolidation involves only shallow sedimentary layers.

DInSAR analysis, applied on three 100x100 km frames and based on ENVISAT images acquired between 2003 and 2009, confirms the calculated trend. Recorded movements for the most of the area investigated are negligible, with values comprise between ± 1 mm/y.

This technique identified areas of particular interest (with values up to -6 and +5), in which movements are probably linked to salt diapirs (uplifts in correspondence to the top of the salt domes, and lowerings more marked within intra-domes areas) or coastal processes.

Results coming from two different methodologies are compared and confirm that the study area considered in present study is a stable one, with very low values of subsidence caused by sediments' compaction.

It is important to underline that InSAR technique is suitable for detecting both wide and localised displacement linked to human activities, and during natural-present subsidence analysis some signals which would deserve further interest have been revealed also in in-land areas, even if not fully presented for confidentiality agreement.

In order to fully understand the behaviour of the sedimentary column involved in anthropic processes, deeper analysis in these area through the acquisition of newest and updated radar images could be of interest for other operators . Moreover, both achieved and new results must be linked and interpreted with information related to ongoing processes.

A monitoring plan is given, considering both applied methodologies and new solutions for results improvement.

To take advantage of applied methodologies under different point of view, a set of possible future studies linked to reservoirs development are provided.

L'obiettivo principale del presente studio è la sperimentazione di differenti metodologie utili alla definizione della subsidenza naturale e presente in zone costiere. Nello specifico, viene presa in esame la costa Kazaka (porzione nordorientale del Mar Caspio).

Obiettivi specifici dello studio includono:

- la ricostruzione degli assetti geologici locali;*
- la definizione dei processi che inducono la subsidenza in condizioni specifiche;*
- il calcolo, attraverso l'applicazione di modelli numerici (sia 1D – NATSUB che 2D – BASIN) della subsidenza naturale;*
- la misura dei movimenti verticali del terreno tramite la tecnologia del Radar ad Apertura Sintetica (InSAR) per il periodo temporale 2003-2009.*

I dati raccolti, provenienti sia da letteratura scientifica internazionale (specialmente quelli interessanti l'intero bacino sedimentario) che da rapporti ed indagini di differenti compagnie petrolifere operanti nell'area, riguardano diverse discipline specifiche della geologia (stratigrafia, geodinamica, idrogeologia ecc).

L'integrazione dei dati raccolti e la ricostruzione del contesto geologico dell'area sono stati sviluppati a scale di indagine differenti:

- a scala di bacino: è stata considerata la geologia regionale e l'evoluzione geodinamica dei bacini sedimentari coinvolti nello studio (Precaspian e North Ustyurt);*
- a scala locale: sono state dettagliate, nel tratto costiero a nordest del Mar Caspio, quattro sotto aree. Per ciascuna di esse, lo studio approfondisce le complessità e variabilità dell'area; complessità determinata dalla presenza di sequenze chilometriche di sedimenti clastici e carbonatici interrotte da uno strato evaporitico dello spessore di circa quattro chilometri, dalla distribuzione di suoli (e conseguenti proprietà geotecniche) influenzati dall'interazione delle dinamiche sia fluviali che costiere, dalla prevalenza di acquiferi multistrato contenenti acque con elevato tenore salino e dalla presenza di importanti giacimenti di petrolio e gas.*

La realizzazione del set di dati richiesti dalle attività previste durante l'analisi della subsidenza (stratigrafia, geocronologia, compressibilità dei differenti strati) è stato completato in maniera esaustiva. Questi hanno rappresentato i dati di input durante il calcolo, tramite simulazione numerica monodimensionale e bidimensionale, della subsidenza naturale in 5 differenti posizioni. I dati raccolti hanno consentito inoltre di interpretare i valori di subsidenza presente, misurati tramite l'analisi interferometrica; l'applicazione di due differenti tecniche InSAR (Small BAseline Substet and Interferometric Poin Target Analysis), fino ad ora mai testate in ambienti costieri con caratteristiche paragonabili alla presente area di studio, hanno consentito di registrare movimenti verticali del terreno ad un livello locale, ma in alcuni casi la mancanza di

alcune informazioni (legate soprattutto al diapirismo) non ha premesso una precisa correlazione tra i tassi di spostamento misurati dall'interferometria e le relative cause geologiche.

I risultati della modellistica numerica hanno sottolineato il comportamento stabile dell'area e l'assenza di chiari fenomeni subsidenziali. Nel margine sud del bacino Precaspico, la limitata profondità degli strati più antichi perforati (carbonati del periodo Devoniano) rivela che il bacino sedimentario venne interessato da bassissimi tassi di sedimentazione e il modello monodimensionale NATSUB evidenzia che i processi di consolidazione avvengono in concomitanza con la sedimentazione. Inoltre i processi subsidenziali non coinvolgono gli strati più antichi e profondi; l'applicazione del modello bidimensionale BASIN dimostra infatti che i processi di consolidazione interessano solamente gli strati più superficiali.

L'interferometria differenziale DInSAR, applicata in tre aree della dimensione di 100x100 km sulla base di immagini ENVISAT acquisite tra il 2003 ed il 2009, conferma gli abbassamenti calcolati. I movimenti verticali del terreno misurati sono infatti per la maggior parte delle aree investigate di entità trascurabile, con valori compresi tra ± 1 mm/anno. L'applicazione di questa tecnica identifica tuttavia aree di particolare interesse (con valori compresi tra i -6 ed i +5 mm/anno), nelle quali i movimenti sono probabilmente legati a fenomeni di diapirismo (innalzamenti in corrispondenza del culmine del domo salini ed abbassamenti più marcati nelle aree infra-domo) o dinamiche costiere.

I risultati provenienti dalle due differenti metodologie sono stati comparati e confermano che l'area studio considerata nella presente tesi è sostanzialmente stabile, con bassissimi valori di subsidenza causati dalla compattazione sedimentaria.

E' importante sottolineare che la tecnica InSAR è adeguata per l'individuazione sia di abbassamenti estesi che di movimenti verticali localizzati e collegati ad attività antropiche, e durante l'analisi alcune situazioni locali di particolare interesse sono state individuate, anche se non presentate nella loro forma integrale per accordi di confidenzialità. Al fine di comprendere a pieno il comportamento della colonna sedimentaria in presenza di attività antropiche, si suggerisce l'approfondimento mirato delle analisi in queste aree attraverso l'acquisizione di nuove immagini radar. Inoltre, i risultati ottenuti dovrebbero essere collegati ed interpretati con informazioni inerenti i processi antropici in corso.

In funzione dei risultati è stato impostato un piano di monitoraggio, considerando sia le metodologie già applicate che nuove soluzioni tecniche potenzialmente idonee all'area di indagine.

Vengono fornite infine una serie di possibili studi in relazione anche allo sfruttamento dei giacimenti petroliferi presenti.

2. GOAL, OBJECTIVES, METHODOLOGY AND LIMITATIONS

Land subsidence is one of the major environmental problem affecting flat coastal areas. The cumulative land displacements affecting a certain portion of a costal territory where urban areas are located and anthropogenic actions take place is usually the superposition of short-term local-scale and long-term basin-scale components. The former are caused by human activities (e.g., mining, fluid withdrawals from the subsurface, land reclamation, excavation, conversion of rural in urban areas, etc), the latter by the geo-dynamic processes such as tectonics and compaction of sedimentary basin.

This study aims to assess natural and present subsidence characterizing the area, both focusing on natural development of the territory through the application of numerical models and trying to understand present displacements recorded through radar images, sometimes potentially linked to human activities. It is an important aspect of coastal zone management, as subsidence can cause inundation and other problems in urban and sensitive environmental areas. Establishing a baseline of natural and current subsidence is important in establishing the baseline of environmental conditions.

Rock compressibility is the key parameter in land subsidence problem; it is used in geomechanics, to quantify the ability of a soil or rock to reduce in volume due to a pressure variation. The void space can be full of liquid or gas. Geologic materials reduce in volume primarily when the void spaces are reduced, yielding that the liquid or gas must be expelled from the voids. This process occurs over a certain period of time, resulting in a settlement of the ground surface. In wide uninhabited areas, as the study area, it is fundamental to understand the natural volume reduction of a sedimentary column.

The study is carried out following two different methodologies.

- The natural component of subsidence is investigated through numerical models, by using information from geodynamic studies and researches available in the documentation provided by O&G companies and in the international literature. Specifically, key documents are related to deep wells located in the northern Caspian Sea.

In addition to detailed stratigraphies and chronostratigraphies of the southern part of the Precaspian basin (coming from end of well reports), wireline logs are available. These

ones, processed as shown in detail in the following paragraphs, allow to estimate the soil compressibility for the investigated sedimentary columns. This kind of information, combined with sedimentological characteristics and shallow geotechnical data, permits the characterisation of the long-term evolution of the Precaspian basin in terms of tectonics, sedimentation rates and consolidation and the application of 1D and 2D numerical models.

The first applied model is NATSUB. It is a one-dimensional finite element model that simulates the natural compaction driven by unsteady groundwater flow in an accreting isothermal sedimentary basin. The model assumes a process of time-varying sedimentation and makes use of a 1-D model of flow where water flow obeys the relative Darcy's law in a porous medium, which undergoes a progressive compaction under the effect of an increasing load of the overburden. Soil porosity, permeability, and compressibility may vary with the effective intergranular stress according to empirically based constitutive relationship. The model correctly assumes the geometric nonlinearity that arises from the consideration of large solid grain movements.

The equations are solved using both the Eulerian and the Lagrangian approaches. With this latter approach, the model uses a dynamic mesh made of fine elements, which deforms in time and increases in number as deposition occurs and the soil column compacts (Gambolati et al., 1998; Gambolati and Teatini, 1998).

The outcome of the model consists in the behaviour of time and of the length of the column and the velocity of its top and bottom, with the evolution over time of the pore pressure in excess of the hydrostatic value along the length of the column (Gambolati et al., 1999). Considering the availability of data, the model has been applied only in offshore location.

Starting from data used in 1-D medullisation, the BASIN 2-D model has been applied. BASIN is a finite-element program that simulates the filling of a sedimentary basin and includes transport, erosion and consolidation of sediment, tectonic processes such as isostatic compensation, consolidational fluid flow, topography driven fluid flow, and heat flow including advection and solute transport. BASIN incorporates a physically consistent compaction model based on the equation of the state of porosity.

The bidimensional model is applied in the southern part of the Precaspian basin, from offshore area (quantitative data available) to the centre of the sedimentary basin (where data is exclusively qualitative). The different level of detail of the input data allows a simplified application of the BASIN.

It has to be highlighted that both these approaches (in particular 2-D numerical models application), even if chosen as adequate to the study's aims, have some limitations linked to the geological complexity of the area, the approximations required for the techniques' application and the data availability, and their implications must be considered during the results' analysis. Models' application always implies a simplification of the real asset, and is not realistic try to simulate numerically the real behaviour of sediment especially in a complex and ancient geological environment; so results' interpretation has to be performed with care. Main advantages and disadvantages for both the applied model are listed in Table 1.

- Present vertical displacement at the local scale (three frames 100x100 km) is investigated by using Synthetic Aperture Radar (SAR)-based techniques on satellite acquisitions.

Accurate assessment of present land subsidence occurred in the area of interest over the last decade has been carried out using a SAR-based investigation. Due to the lack of traditional geodetic surveys and the paucity of GPS measurements, SAR-based interferometry represents the unique methodology that can be used to investigate the recent/present ground displacements.

Due to scope of the research, that is to provide a general understanding of the subsidence occurring along the coastland of the northern Caspian Sea, we have elected to use the DInSAR (Differential Interferometric Synthetic Aperture Radar) methodology to process the SAR images (Strozzi et al., 2001).

In DInSAR, a pair of SAR images (or more) acquired from slightly different orbit configurations and at different times is combined to exploit the phase difference of the signals (Bamler and Hartl, 1998). Measurement of the radar phase change is made on a pixel-resolution basis. The interferometric phase is sensitive to both surface topography and coherent displacement along the look vector occurring between the acquisitions of the interferometric image pair, with inhomogeneous propagation delay, so-called atmospheric artifacts, and phase noise introducing the main error sources.

With respect to PSI (Persistent Scatterer Interferometry)-type investigation, DInSAR is particularly suitable for detecting average ground movements over large areas (Teatini et al., 2005). Conversely, PSI is more useful when the time-behaviour of the displacements are needed for some specific areas. However, a partial PSI application has been carried out with the main aim at evaluating its capability in this type of landscape.

Considering the general aim of the study, it has been carried out the InSAR analysis on three 100 km × 100 km frames, one for each of the inland zone identified within the geological characterization (Zone B, Zone C, and Zone D)(Figure 134).

The evaluation of existing land subsidence have been performed firstly focusing on the effects along the coast excluding internal in-land areas which in some cases could be interested by different oil and gas extraction activities.

Anyway, for formal correctness and scientific soundness of the approaches followed, the processing described above has been applied on three frames, covering the whole surface investigated.

In some cases (and for limited areas), strong atmospheric disturbs or vegetational cycles causes a loss of data coherence, and results are not available.

The DInSAR technique in wide uninhabited areas, even if already tested in environment similar to the Kazakh coast of the Caspian Sea, did not ensure high data coherence and a complete coverage of the area. The “experimental” application established that the terrain response to radar technique is suitable in this coastal zone, also in geomorphologically different areas (Frame Z3 has different characteristics if compared to Frames Z1 and Z2, as shown in Figure 1 and Figure 2).

Hence, the frames cover the all three "sides" of the coastland of the north-eastern Caspian and suffice to map the possible evolution of the present land subsidence acting in the study area.



Figure 1: Landscapes within Frame Z1, along the Ural river vegetated belt and Eskene area.



Figure 2: Landscapes within Frame Z3, Buzachi peninsula.

Looking within the available SAR archives, the most useful satellites to be used were ENVISAT-ASAR of the European Space Agency (ESA) and RADARSAT-1 of the Canadian Space Agency. Their acquisitions span the period from 2003-2004 to 2009. Unfortunately, ERS-1/2 satellites did not acquire over the north Caspian and therefore any analysis can be carried out during the 1990s. Since significantly more cheaper than RADARSAT-1 scenes, the ENVISAT-ASAR images have been used.



Figure 3: Study area subdivision

Applied methodologies are described in detail in following paragraphs. Models' results have been compared with data recorded through DInSAR technique, considering especially

uninhabited areas in which vertical displacements recorded are referred exclusively to natural sediments' compaction. A brief discussion of the topic is given in 5.

The conceptual diagram below (Figure 4) shows the relevance of the geo-hydrogeological reconstruction during the development of this scientific research. It is a key step both for the interpretation of DInSAR interferometry results and for the implementation (choice - data input – results' interpretation) of the models.

It has been outlined at different scales:

➤ **Basin-scale:**

At the basin-scale, three main geological provinces of the study area include:

- 1) **Precaspian Basin**
- 2) **North Ustyurt Basin**

➤ **Local scale:**

Four subareas of the northern part of the Caspian Sea have been identified. The subdivision has been identified according to the geologic asset of the area and the spatial distribution of InSAR interferometry analysis, which foresees the technical application in three 100x100 km frames (one for each onshore zone). The 4 selected zones include:

- Zone (A)** Transitional and offshore northern area;
- Zone (B)** Northern onshore area, from the Atyrau region to the Emba River valley;
- Zone (C)** Eastern portion, from the Emba River valley to Mertviy Kultuk Bay;
- Zone (D)** Central portion of the Mangystau region, included in the North Ustyurt Basin.

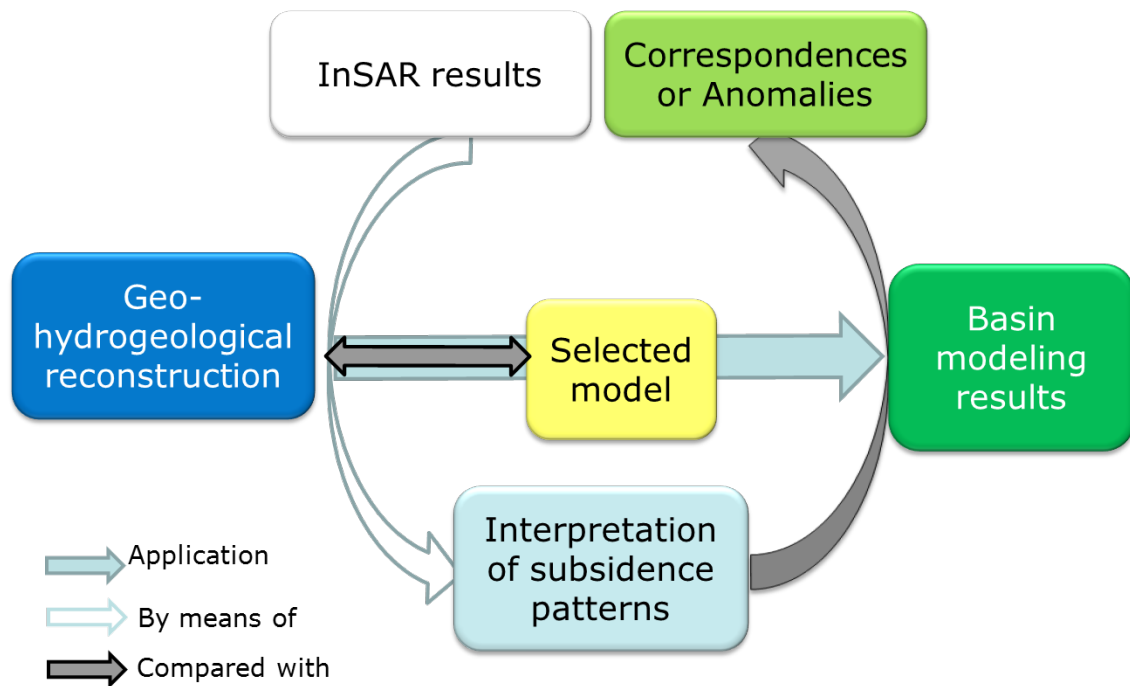


Figure 4: Links between the geo-hydrogeological reconstruction and activities carried out during the analysis of present subsidence.

Main advantages and disadvantages, for every applied methodology, are listed below.

Table 1: Advantages and disadvantages of applied methodologies.

Methodology of investigation	Advantages	Disadvantages
Investigation of natural subsidence through 1D numerical model (NATSUB)	<ul style="list-style-type: none"> • High manageability of the code; • Previous successfully applications in similar contexts (e.g., Northern Adriatic Sea); • Since the model considers only one dimension, no lateral approximations are required; • Very accurate stratigraphical information of the whole sedimentary column is available as input data; 	<ul style="list-style-type: none"> • The model cannot consider dynamics related to salt diapirs; • Assessment of compressibility calculated from logs is not as reliable as laboratory tests, so the model's results are "semi-quantitative". • As highlighted during Gap Analysis, required information is localised in offshore area, and model's

Methodology of investigation	Advantages	Disadvantages
	<ul style="list-style-type: none"> • Availability of wireline logs, needed for compressibility calculation; • Model's application at 5 different locations, with 3 different compressibility trends; • High local variability of shallow sediments' geotechnical properties (up to 30 m) doesn't cause strong variations in final results. 	<p>applications in onshore area of study are not allowed.</p>
Investigation of natural subsidence through 2D numerical model (BASIN)	<ul style="list-style-type: none"> • The model provides a wide range of different results; • The model considers different sedimentation rates from the southern border to the centre of the Precaspian basin. 	<ul style="list-style-type: none"> • Heavy later approximations and simplifications are required during the implementation; • Stratigraphic and chronostratigraphic information required is not detailed outstanding the offshore area.
Present vertical displacement investigation through DInSAR methodology	<ul style="list-style-type: none"> • It is the only way to perform analysis over past time interval (from 2003); • Results confirm that it is ideal for subsidence assessment in wide and inaccessible onshore areas; • Do not require field surveys; • Best rate between cost and surface monitored; • Its vertical movement resolution is about 2 	<ul style="list-style-type: none"> • Vertical resolution (about 2 mm/y) is comparable to value of natural subsidence of the study area; • Lack of permanent GPS stations that are required for the calibration of measurements; • Adequate presence of point targets only within frame Z1; • Insufficient information about salt diapirs location and

Methodology of investigation	Advantages	Disadvantages
	mm/year; <ul style="list-style-type: none"> • Planar resolution is 40X40 meters; • Its area of analysis (frame) is up to 100X100 km; • Some areas present natural point targets. 	dynamic; <ul style="list-style-type: none"> • Insufficient information about ongoing human activities in the study area that can cause the lowering (or the uplift) of the terrain recorded by DInSAR application.

Obtained results allow to foresee possible vertical movements in the next future (trends projected till 2013) and to plan possible monitoring activities, with techniques already applied during this phase of study (e.g. acquisition of new SAR images) coupled with new ones (best potential solution for installation of fix GPS and best potential improvement of IPTA application through the installation of artificial Point Target).

The versatility of some of the techniques applied in this work allows us to hypothesize other activities that could be applied in the area of study in the future, as the study and monitoring of wider areas (at the moment not covered by the analysis), the use of other satellites in order to improve the SAR results in areas of particular interest, the creation of a Digital Elevation Model (DEM) from SAR images and an experimental application of InSAR analysis on the production islands to investigate possible differential displacements, potentially caused by the weight of the island and the expected anthropogenic land subsidence due to oil production.

3. GEO-HYDROGEOLOGICAL RECONSTRUCTION

3.1 GEOLOGY, TECTONIC AND SEISMICITY

3.1.1 Brief description of main geological features in the Caspian area

3.1.1.1 *North and Middle area*

According to Afanasev et. al. (2008), the following structures are identified within the study region (Figure 5):

1. North Caspian Basin with a Central Depression and a Southern System of relative elevations of the Astrakhan–Aktyubinsk Zone;
2. Karakul–Smushkovskii Foredeep;
3. South Emba Foredeep;
4. Karpinsky Range Fold Zone;
5. Mangyshlak–Central Ustyurt Fold Zone;
6. South Emba Suture;
7. North Ustyurt Massif;
8. Prikumsk (Kuma) Block of Cis-Caucasus;
9. Agrakhan Zone;
10. Central Caspian Massif;
11. Alpine Orogen of the Greater Caucasus.

THE NORTH CASPIAN BASIN

The North Caspian Basin is filled with several sedimentary successions that was extensively examined from seismic data. The lower region fills a rift basin with strongly thinned continental or oceanic crust, and can be interpreted as a sinrifting basin. This succession has not been penetrated by bore holes and its age is, therefore, disputable: (1) Ordovician and (2) Middle Devonian. The former option is based on discoveries of Ordovician faunal complexes at the northern margin of the North Caspian Basin, where sediments that need to be studied fill graben-like troughs of Ordovician age at the opening of the Paleo-Ural Ocean, which could have a branch-like extension into the North Caspian Region. The second option is based on the wide distribution of Devonian rifting in the East European Platform with the presence of

Devonian normal faults on the western slope of the North Caspian Basin *e.g.*, within the Don–Medveditsa Basin. A deepwater basin similar to that of the Red Sea could have originated during accumulation of the lower succession.

The second succession consists of sediments overlying the rifting complex (a post-rifting succession). The age of its base is debatable (either Silurian or Middle Devonian). Its upper boundary is conventional, traced to the beginning of the formation of a foreland basin at the Ural and Karpinsky Range orogens. A deepwater basin existed in the middle of this basin, bordered by passive continental margins and shelf basins. Conditions for originating carbonate edifices were favourable at the margins of the shelves.

The third succession was an orogenic complex filling the deepwater basin with clastic material from erosion of mountain ranges in the Uralian and Scythian orogens. The lower limit of the complex was Middle or Upper Carboniferous and the upper boundary was Triassic. The rise of the Ural Orogen commenced in the Middle Carboniferous, becoming the principal event by the beginning of the Permian. Under these conditions, supply of great amounts of clastic material began into the previously formed deepwater basins from the orogens associated with the Caspian Basin. The residual basin was filled with clastic material due to this avalanche-like sedimentation. A thick evaporite succession accumulated in the basin due to its nearly complete isolation from the World Ocean during the Kungurian Age.

The fourth succession is the Triassic post-rifting complex, which accumulated owing to thermal subsidence of the zone of the Paleozoic rift. The fifth succession is the Jurassic–Cenozoic platform cover overlying a considerable portion of the East-European Platform. The Astrakhan–Aktyubinsk uplift zone crowned with numerous Late Paleozoic carbonate edifices is traceable along the southern margin of the basin. According to gravity and magnetic data, the carbonate edifices may be underlain by Lower Paleozoic or Early – Middle Triassic volcanics (Segalovich et al., 2007).

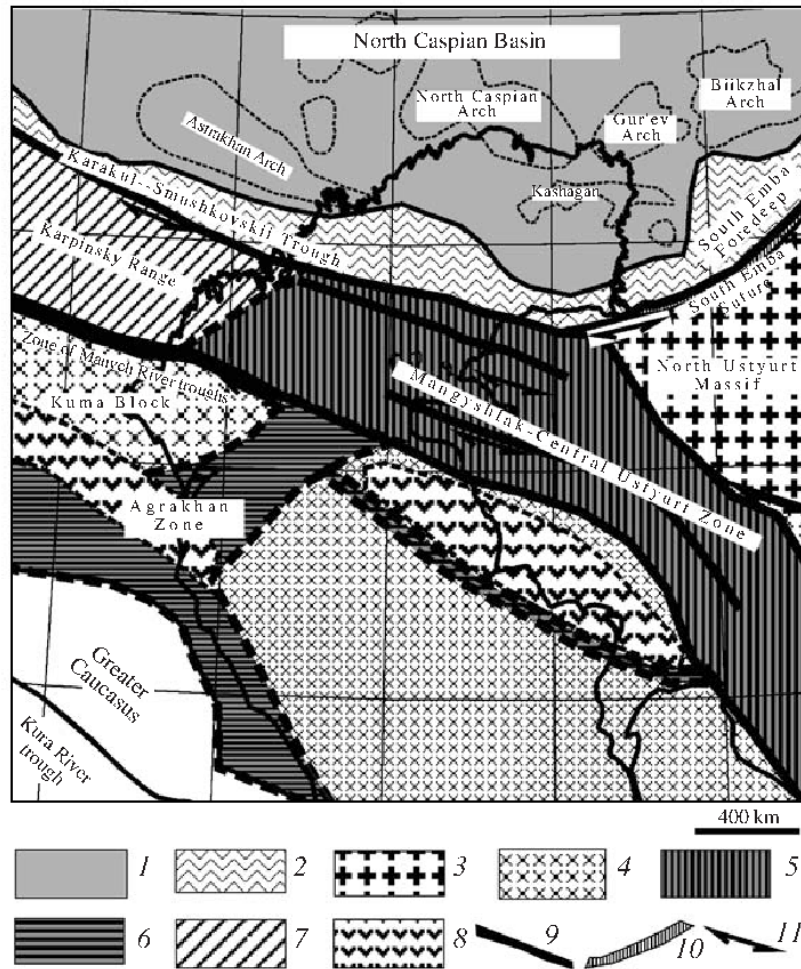


Figure 5: Tectonic scheme of the North Caspian Region, after “A. P. Afanasenkov et al., 2008”

1, North Caspian Basin; 2, Late Paleozoic Foredeep; 3, Precambrian terrane; 4, Paleozoic and Precambrian terranes; 5, Paleozoic zones with Triassic rift and pre-Jurassic inversion; 6, Paleozoic zones with Triassic sediments of various facies and pre-Jurassic inversion; 7, Karpinsky Range Zone of Early Permian Orogeny and pre-Jurassic inversion; 8, Triassic volcanic belts; 9, zone of Manych River troughs with pre-Jurassic inversion; 10, South Emba Late Paleozoic Suture with pre-Jurassic transpression; 11, strike-slip faults of unclear kinematics.

KARAKUL–SMUSHKOVSKII FOREDEEP

The Karakul-Smushkovskii Foredeep is traceable along the northern margin of the Karpinsky Range. This zone was a shelf margin during the Late Devonian and Early–Middle Carboniferous, where carbonate edifices originated. Beginning in the Moscovian Age, the basin was filled with clastic material supplied from the Karpinsky Range and Scythian Orogen, that is, the shelf basin began transforming into a foredeep. The maximum fill-up of the basin with clastic material of a flysch–molasse succession was during the Asselian Age. The foredeep was transformed into a fold-nappe zone prior to the Kungurian Age (possibly during the Sakmarian Age).

SOUTH EMBA FOREDEEP (INCLUDING THE MYNSUALMAZ FOLD ZONE)

South Emba Foredeep is formally a continuation of the Karakul–Smushkovskii Zone. The principal difference between the two lies in the fact that the subsidence of this basin as a foredeep took place during the Devonian and Visean ages. Its clastic material included fragments of mafic and intermediate volcanics, jasper, limestone, serpentinite, and tuffs; this implies that these sediments originated due to erosion of the orogenic rock complex with fragments of ophiolites and island-arc rock associations. The South Emba is interpreted as a suture that collided with the North Caspian Basin and North Ustyurt terrain, subsequently transformed into a pre-Sinemurian strike-slip zone.

KARPINSKY RANGE FOLD ZONE

The Karpinsky Range Fold Zone mostly consists of Carboniferous schists and interlayered siltstones more than 10 km thick. This succession is strongly deformed, with overthrusts and duplexes playing an important role in its structure. The rock complex of the Karpinsky Range was thrust northward over the Karakul–Smushkovskii Zone in Early Permian (most likely during the Sakmarian Age). The Karpinsky Range lies on a continuation of the Devonian Rift in the Donets Basin, and there is the possibility that the basin within the Karpinsky Range was a rift trough (possibly, a backarc basin) during the Devonian. During the Early–Middle Triassic, rift basins formed within the Karpinsky Range region. These were strongly deformed, and inversion took place at approximately the Triassic–Jurassic boundary; therefore, Triassic basins within secondary (after deformations and erosion) contours can be traced. Since the Jurassic, the Karpinsky Range became a portion of the sedimentary basin of the East European Platform.

MANGYSHLAK–CENTRAL USTYURT FOLD ZONE

The Mangyshlak–Central Ustyurt Fold Zone shows a complex structure vaguely understood due to its overlain basement virtually everywhere by thick cover. The following tectono-stratigraphic units have been recognized within its folded complex: Lower Paleozoic; Devonian–Middle Carboniferous; Upper Carboniferous–Lower Permian; and Upper Permian–Triassic. The Lower Paleozoic unit is hypothetical and may represent metamorphic complexes. The Middle Devonian–Carboniferous succession encloses ophiolites and deep-water sediments (Tuarkyr Rise) definitely originated under conditions of an oceanic basin and its closing. The Upper Carboniferous–Lower Permian succession includes carbonates of different facies, clastic rocks, and subduction-related volcanics. All these rocks originated during the collision stage of the orogen evolution. A complex orogen formed in the Mangyshlak–Central Ustyurt Zone by the Middle Permian time (in the Early Permian), though its structure is not known in detail. The orogen extended southward from the South Emba Suture and completely embraced the southern part of the contemporary Turan Platform. The Hercynian orogen

collapsed during the Kungurian Age and the Late Permian Epoch (that is, a system of fault-bounded orogenic extension troughs formed in its place), and molasse-filled basins were widespread in this region.

Rifting was very common throughout the whole region during the Early Triassic, which was accompanied by formation of deep (up to 3–5 km) rifting basins. One such rift is currently under the Kulaly Swell. The Triassic rifts are located north of the Early–Middle Triassic volcanic belt and, hence, backarc extension is the most probable cause of the rifting.

Strong compression of the region took place at approximately the Triassic–Jurassic boundary. Most rift basins experienced inversion there accompanied by folding and overthrusting deformations. Strike-slip displacements of individual blocks considerably complicated the deformations. The presence of strike-slip faults is noted, but there is zero possibility of reconstructing the motion kinematics along the zone where displacements could reach hundreds of kilometres. Since the Jurassic, the Mangyshlak–Central Ustyurt Zone became a portion of a vast platform-type sedimentary basin.

NORTH USTYURT MASSIF

This massif with Precambrian metamorphic basement is viewed as a terrain of continental crust that collided in the Late Devonian–Visean with a margin of the North Caspian Basin, which was probably a part of the Late Paleozoic Turanian Orogen.

PRIKUMSK (KUMA) BLOCK

This block within the Cis-Caucasian region is a terrain in the Late Paleozoic Orogen with Mesozoic–Cenozoic sedimentary cover.

AGRAKHAN BLOCK

Afanasenkov, et. al. (2007) recognized the Agrakhan Block conditionally as a fragment of the Hercynian Orogen overlain both by sediments and volcanics. The block is poorly studied thus far.

CENTRAL CASPIAN MASSIF

This is a massif resultant from the Hercynian Ustyurt Orogen.

3.1.1.2 **Southern area**

The South Caspian is located over a high-velocity ($V_p = 7$ km/s) thin (10–18 km) basement has often interpreted as an oceanic basin filled with ~20 km of sediments (e.g., Allen et al., 2002). However, the sedimentary thickness is about twice that needed to fill a basin upon oceanic crust as thick as that in the South Caspian. Maintaining consolidated crust at a depth of 20 km requires 20–25 km of eclogites, denser than mantle peridotites, to occur under the

Moho. According to its chemistry, eclogites belong to the crust but have typical mantle seismic velocities, and are thus placed beneath the Moho in many seismic models.

The Moho in the South Caspian basin is overlain by high-grade felsic and intermediate rocks with P velocities up to 7 km/s. Its high density is due to metamorphism with the formation of garnet at $T \geq 400$ °C. With eclogites lying under the Moho, the basin basement totals a thickness of 40–50 km, which corresponds to a continental crust.

Crustal subsidence in the South Caspian was induced by a phase change of gabbro into denser eclogites. Subsidence occurred at rapidly increased rates at least twice, at the Eocene/Oligocene boundary and during the Pliocene-Pleistocene time.

The first episode of rapid subsidence produced (or deepened) a marine basin and a subsequent episode was associated with a deposition of a 10 km thick sedimentary succession in 5 Myr. The increased subsidence rates may have been due to the effect of active fluids that catalyzed the gabbro-eclogite transition. Rapid subsidence as occurs in the South Caspian is impossible upon oceanic crust. Rapid and major crustal subsidence was found typical of hydrocarbon basins (Artyushkov and Yegorkin, 2005). The reliability of this criterion as a diagnostic for the discovery of hydrocarbon reservoirs elsewhere was confirmed by the evidence of rapid subsidence in the large petroleum province of South Caspian.

The rapid Pliocene-Pleistocene subsidence in the South Caspian with a deposition of 10 km-thick sediments was explained in terms of a flexural basin developing in front of a subduction zone in the south or in the north (Allen et al., 2002; Axen et al., 2001; Knapp et al., 2004). However, even though it existed, the flexure could be located within a wide zone of a few kilometres along the Apsheron-Balkhan sill that caused no influence on subsidence outside that strip. Judging by the presence of steep basement flexures up to 10–12 km deep, the lithosphere of the South Caspian apparently experienced strong softening as a result of fluid infiltration during the recent rapid subsidence.

Relatively large historic earthquakes ($M = 5-6$) located at depths of ≥ 30 km beneath the Apsheron-Balkhan sill and north within a ~ 100 km wide zone were interpreted as an indication of northward subduction. The consolidated lithosphere as in the South Caspian basin, with its density higher than the asthenosphere due to phase change, could in principle be involved in subduction with delamination of the overlying lighter sediments on condition of strong lateral compression and softening. Had subduction occurred in the South Caspian, the subduction plate would have been ~ 100 km long, and the delaminated sediments would have experienced shortening of the same magnitude. Yet, judging by very shallow fold dips in the area, shortening was no more than 5–10 km. Therefore, hardly any subduction occurred.

Furthermore, slopes of oceanic trenches on active margins are normally dominated by compression but most earthquakes in the northern South Caspian show extension mechanisms. The earthquakes originate mostly in the crust (at 30 to 50 km) and show no alignment like a Benioff zone. Therefore, the basin with its thick sedimentary fill lies over continental crust, and the extension focal mechanisms may record normal faulting associated with ongoing consolidation of mafic rocks by eclogitization (Artyushkov, 2007).

3.1.2 The North Caspian Basin Structure

The North Caspian Basin province occupies the northern part of the Caspian Sea and a large plain to the north (Figure 6) and covers some 500,000 km².

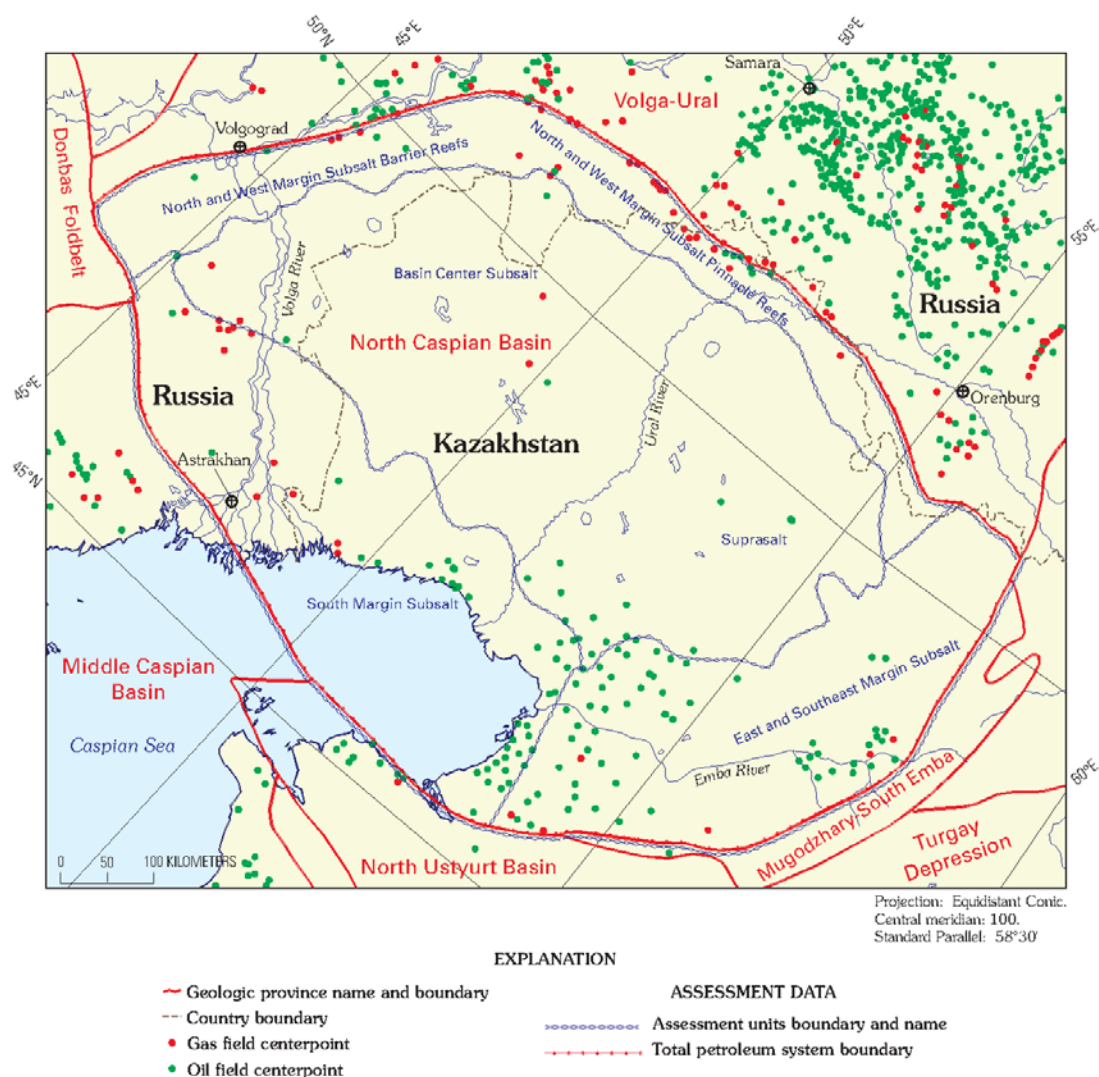


Figure 6: Petroleum system and assessment units of North Caspian Basin. After G. F. Ulmishek, 2003”.

The basin is bounded to the east by the Ural foldbelt and the Mugodzhary zone, the latter a southern continuation of the Urals that is partially buried beneath a thin section of Mesozoic rocks. Hercynian deformation in the foldbelt began in Late Carboniferous time after collision of the Russian (East European) craton with the Kazakhstan continent. The Paleozoic South Emba high (Figure 6) borders the basin to the southeast. This high is covered by flat lying Mesozoic sediments, its geology poorly understood. The crest of the high is marked by large gravity and magnetic anomalies and is probably composed of Lower and Middle Devonian volcanics (Kan and Tropp, 1996). Younger Paleozoic sedimentary rocks form the northwestern flank. The high is structurally expressed as an uplift of upper Paleozoic strata but is underlain by a deep trough in the basement surface. Possibly, the Devonian volcanics formed an oceanic volcanic arc that was accreted on the craton margin in pre-Late Devonian time. The South Emba high plunges southwestward, and the gravity and magnetic anomalies gradually diminish and disappear east of the Caspian Sea.

The southwestern basin boundary is the Karpinsky foldbelt, known in Russian literature as the Karpinsky Ridge (Figure 7). The foldbelt is composed of deformed Carboniferous fine clastics, which reach a thickness of 15 km as interpreted from seismic data. The rocks were deposited in postrift sag above the Devonian rift that extended northwest into the Donets coal basin of Ukraine (Ulmishek et al., 1994). In middle Early Permian (Artinskian) time, the Devonian rift basin was structurally inverted, folded, and thrust onto the North Caspian basin margin. The foldbelt extends into the Caspian Sea where it becomes poorly defined. The 1,500 km long north and west margins of the basin separate the North Caspian basin from the Volga-Ural petroleum province. The boundary is defined by a sedimentary escarpment in subsalt Paleozoic rocks. Across the escarpment, thick shallow-water carbonate rocks of the Volga-Ural province pass into much thinner deep-water black-shale facies of the North Caspian basin. The top of the escarpment is formed by a Lower Permian barrier reef.

More than three-quarters of the North Caspian basin lies in Kazakhstan with the remaining portion in Russia. The area has a semi-arid continental climate with hot summers and cold windy winters. The northern Caspian Sea is characterized by shallow water; the water depth does not exceed 200m and is less than 5m in about 70 percent of the offshore area.

3.1.2.1 ***Tectono-Stratigraphic Development***

The North Caspian basin is one of the deepest basins in the world, containing sedimentary strata more than 20 km thick (Figure 7). Deep seismic sounding data indicate that oceanic or thinned continental crust underlies the central basin areas (Kleshchev et al., 1995). Most geologists believe that the basin originated as a rift, but the time of rifting is disputable. Three

models have been proposed with rifting time in the Riphean (Middle–Late Proterozoic, 1,650 to 650 million years old), in the Middle Devonian (Malushin, 1985; Zonenshain and others, 1990; Volchegursky and others, 1995), or alternatively in Early Ordovician time contemporaneously with rifting in the Urals that resulted in opening of the Uralian ocean (Ulmishek G.F., 2003). A partially inverted Ordovician graben filled with a 5 km thick sequence of coarse to fine clastics is present north of the northeast basin margin where it underlies the supergiant Orenburg gas field (Figure 7; Yakhimovich, 1996).

Probably, original rifting and formation of grabens occurred in both areas at the same time, but subsequent spreading that started in the North Caspian graben resulted in cessation of rifting and following compression and structural inversion in the Orenburg graben. As a result of spreading in the North Caspian basin, cratonic blocks that presently form a series of arches along the south and east basin margins (Astrakhan- Aktyubinsk system of highs in Figure 7) moved away from the Russian craton and opened the oceanic crust. Tectonic development during Devonian, Carboniferous, and much of Early Permian time (rocks older than Middle Devonian have not been reached by drill) was characterized by continuous subsidence of the basin and deposition of carbonate and clastic formations on its margins. Basinward, these strata grade into deep-water black shales and turbidites that presently occur at great depths and are only locally penetrated by wells in areas close to the basin margins. Hercynian deformation started in the Late Carboniferous in the Ural foldbelt and in the Early Permian (Sakmarian-Artinskian) in the Karpinsky foldbelt and South Emba high. Thick Upper Carboniferous–Lower Permian orogenic molasse clastics are present on the east and south basin margins. Continental collisions along the basin margins separated the North Caspian small deep-water oceanic basin from the Tethys Ocean. Consequently, the basin was filled by a Kungurian (latest Early Permian) evaporite sequence, which is dominantly composed of salt and has an estimated original depositional thickness of 4–5 km (Volchegursky et al., 1995).

Orogeny in the Urals, rapid subsidence of the basin, and deposition of thick sedimentary sequences continued during Late Permian and Triassic time. Sediments of this age were mostly continental orogenic clastics, but some Upper Permian (Kazanian Stage) carbonates and evaporites and Lower and Middle Triassic marine shales and marls are present in the western areas. Active deformation of Kungurian salt began soon after its deposition, and Upper Permian–Lower Triassic sediments are several kilometres thick in depressions between salt domes. Intense tectonic subsidence of the basin floor terminated by Jurassic time. Various narrow (commonly one stage) stratigraphic intervals of the Jurassic through Tertiary section attain large (to 3km) thickness only locally, in depressions near domes that experienced active growth during corresponding time. Deformation of salt continues at present and some salt domes are exposed on the surface.

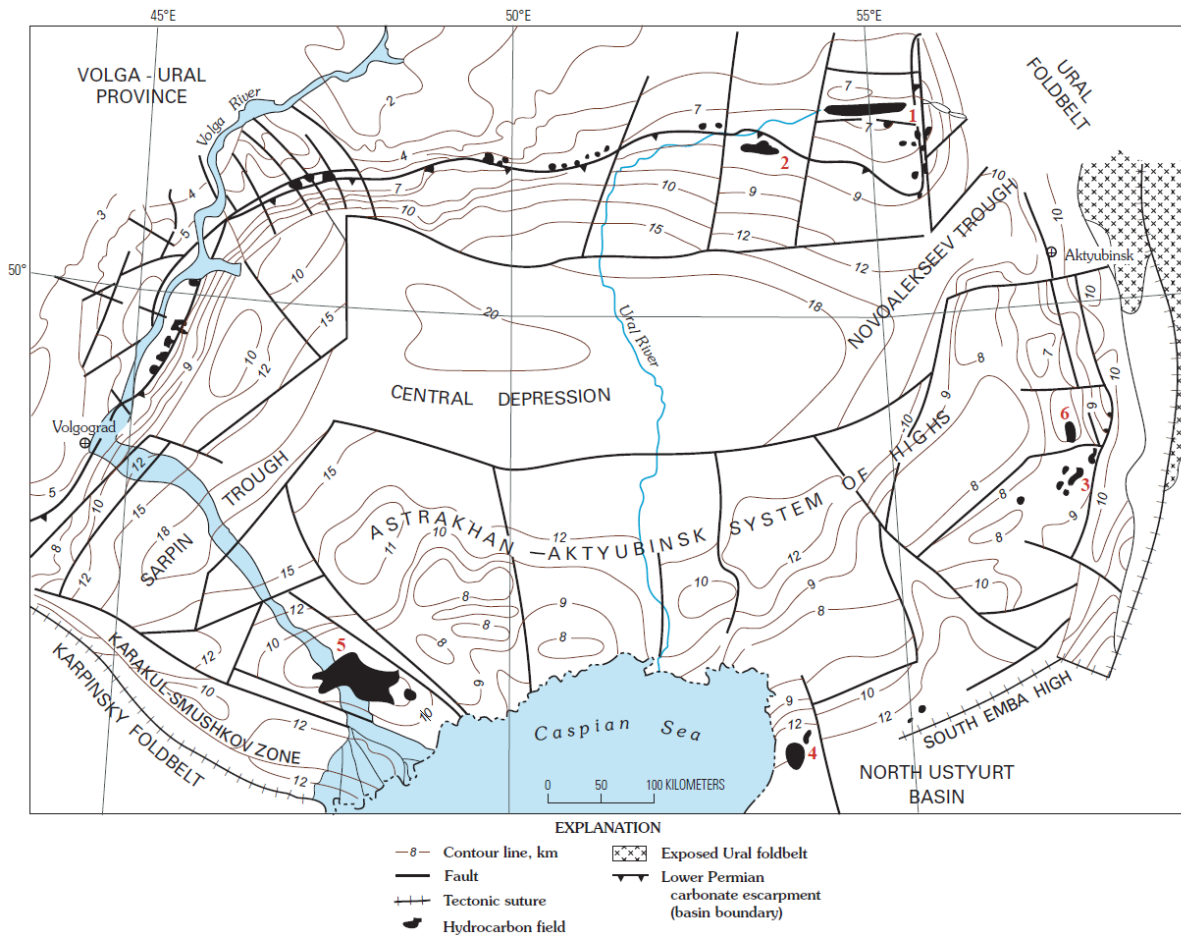


Figure 7: Structural map of the North Caspian Basin, after “G. F. Ulmishek, 2003”.
 Contours are on top of basement. Hydrocarbon fields shown by red numbers; 1, Oremburg; 2, Karachaganak; 3, Zhanazhol; 4, Tengiz; 5, Astrakhan; 6, Kenkiyak.

3.1.2.2 Historical evolution of the basin

The sedimentary cover of the Central Precaspian depression exceeding 20 km (Figure 8 and Figure 9) contains:

- Riphean terrigenous-carbonate (4 km),
- Lower Palaeozoic (Vendian to Middle Ordovician) terrigenous (2 km),
- Upper Ordovician to Silurian carbonate (2 km),
- Devonian to Lower Permian terrigenous (4 km),
- Kungurian to Kazanian salt (4 km),
- Upper Permian to Triassic red bed (2 km), and
- Jurassic, Cretaceous, and Cainozoic carbonate-terrigenous deposits (2.5 km) (Volozh et al., 2003).

The Central Precaspian depression experienced the highest subsidence rate in the basin, as indicated by the sedimentary infill of distal and deep-marine deposits that can be observed on the following sections through the basin.

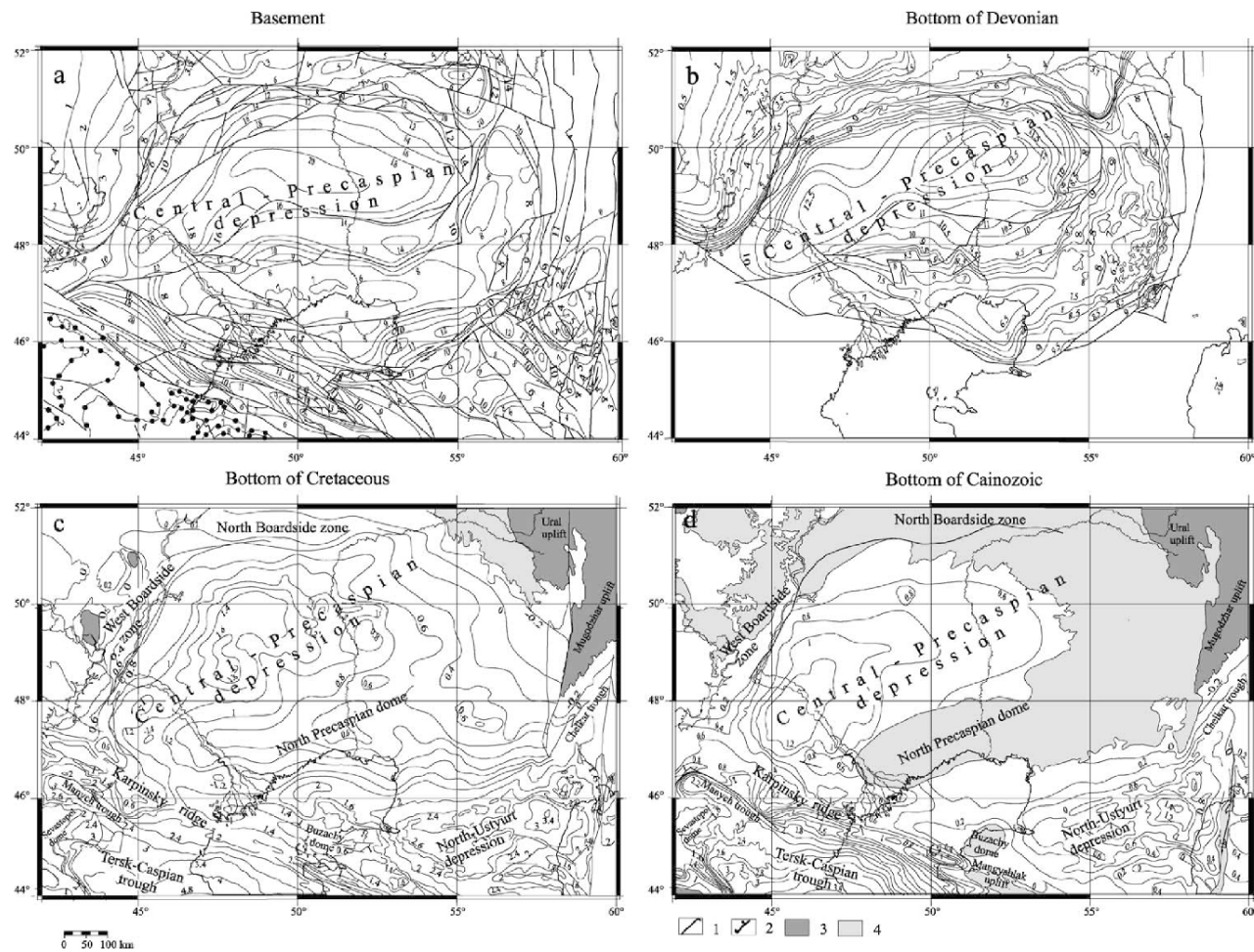


Figure 8: Isobathic maps of Precaspian Basin at the level of main reflectors, isolines in km, after “Yu.A. Volozh et al., 2003”.
 (a) basement (grey lines with points: isolines at depth base of Palaeozoic); (b) base of Devonian; (c) base of Cretaceous; (d) base of Cainozoic. 1: Faults; 2: contour of the area where Cretaceous sediments lay on pre-Jurassic rock complex; 3– 4: outcrops of pre-Cretaceous (c) or pre-Palaeogene (d) rock complexes, 3: basement, 4: sedimentary cover.

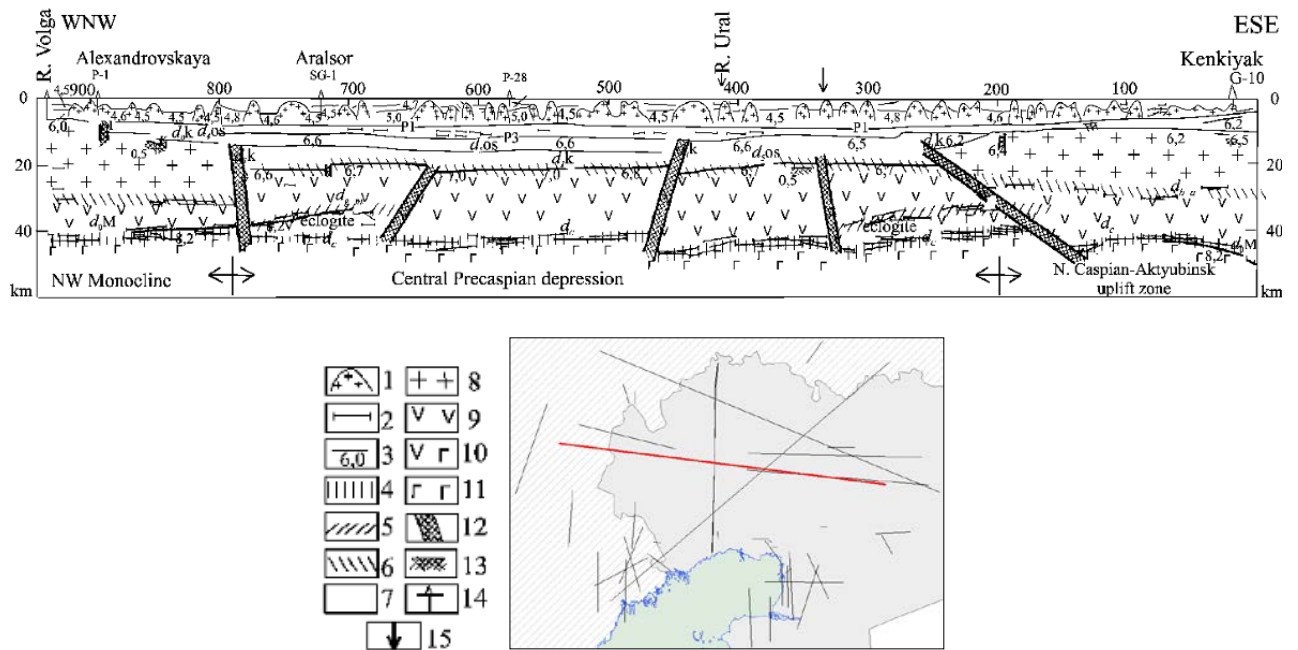


Figure 9: Geological –geophysical crustal section Volgograd –Chelkar, after “Volozh et al., 2003”.

(1) Salt domes; (2) reflectors: P1—top of subsalt sediments, P3—base of Devonian; dba—boundary upper/lower crust, dgm—surface of abnormal gravity maximum, dc—bottom of crust; (3) refraction events with velocity km/s: d4OS—first subsalt, d5OS —second subsalt, d0k—surface of upper crust, d1k—top of lower crust, d0M—Moho; (4) base of crust; (5) top of abnormal layer; (6) top of lower crust; crustal complexes: (7) sediments, (8) upper crust, (9) lower crust, (10) abnormal gravity maximum (eclogites), (11) upper mantle; (12) tectonic faults; (13) upper part of magnetic bodies; (14) deep boreholes; (15) point of sections crossing.

A deep-water intercontinental basin existed within the Central Precaspian depression from Carboniferous to Permian. Its creation and evolution is illustrated along a selection of palinspastic reconstructions transecting the basin and showing the evolution of its margins (Figure 10, Figure 11 and Figure 12).

Figure 10 demonstrates the relations between the northeastern part of the Precaspian Basin and the southern pre-Uralian foredeep. The latter was mainly affected by an Early Permian phase of thrusting representing a stage of E–W Uralian compression (Giese et al., 1999).

Figure 11 is a general cross-section of the basin perpendicularly to its main W–E direction, and Figure 12 presents some carbonate build-ups on the southeastern margin.

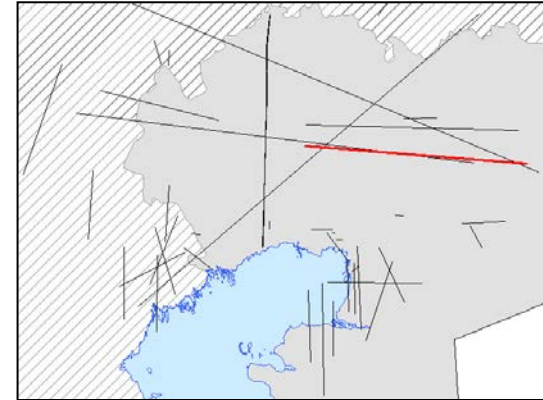
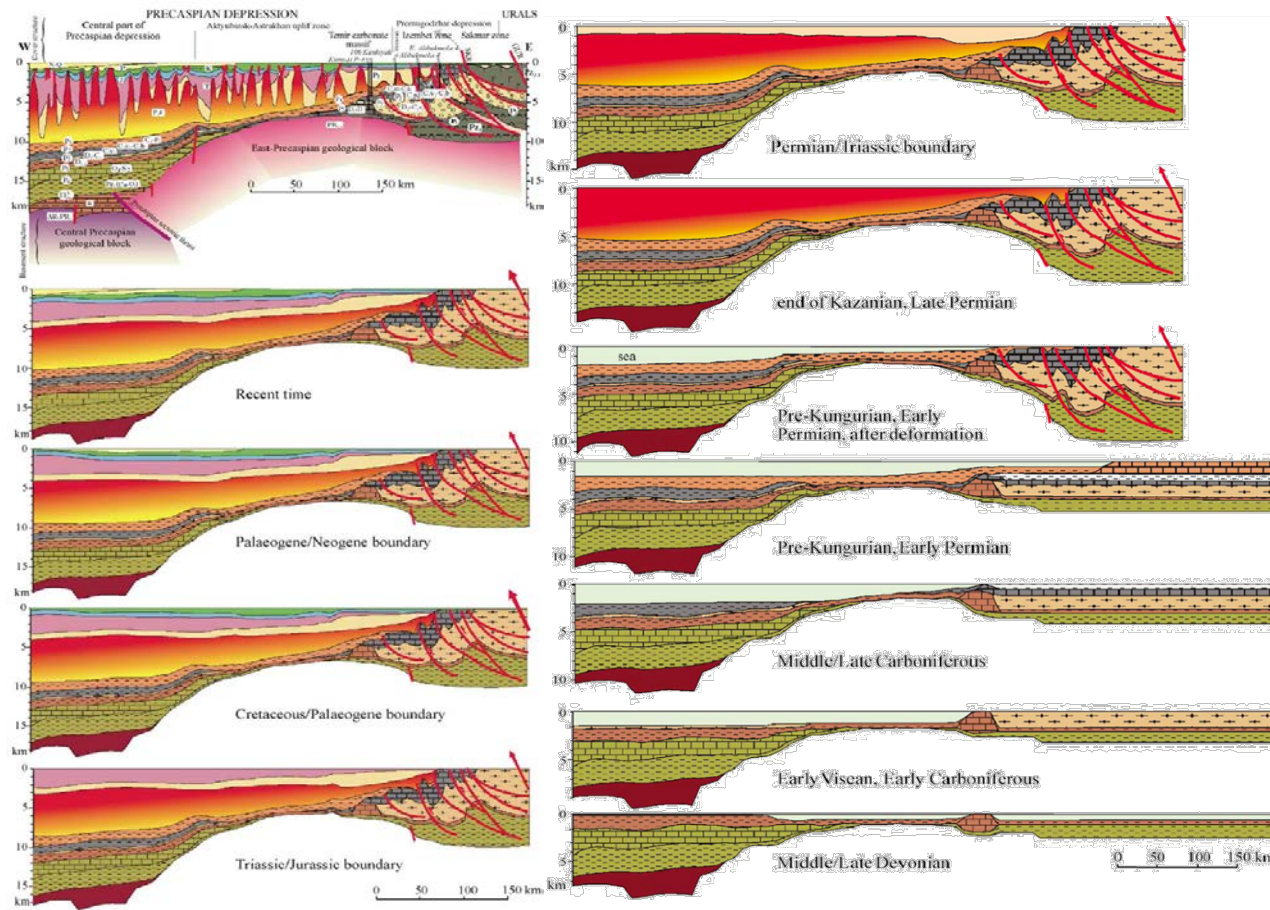


Figure 10: Palinspastic reconstruction along a profile on the east Precaspian margin, line Ural River –Izembet (Urals), after “Volozh et al., 2003”.

Some levels are grouped during the evolution but detailed with different colours on the real section. First section is the Present real section; the following are reconstituted without movements of salt. Index circled, reflectors: P1—top of subsalt sediments, P2, P2', P3—base of Devonian, P4, d5os Stratigraphic levels: N– Q, Neogene– Quaternary; P, Palaeogene; K, Cretaceous; J, Jurassic; T, Triassic; P, Permian; P2k, Kungurian; C, Carboniferous, C3k, Kasimovian; C2m, Moscovian; C2b, Bashkirian; C1v, Viséan; D, Devonian; S, Silurian; O, Ordovician; Ca, Cambrian; Pz, Palaeozoic; R, Riphean; AR– PR, Archaean–Proterozoic; SKR; Sakmaro– Kokpeptyn Fault; GUR, Main Urals Fault.

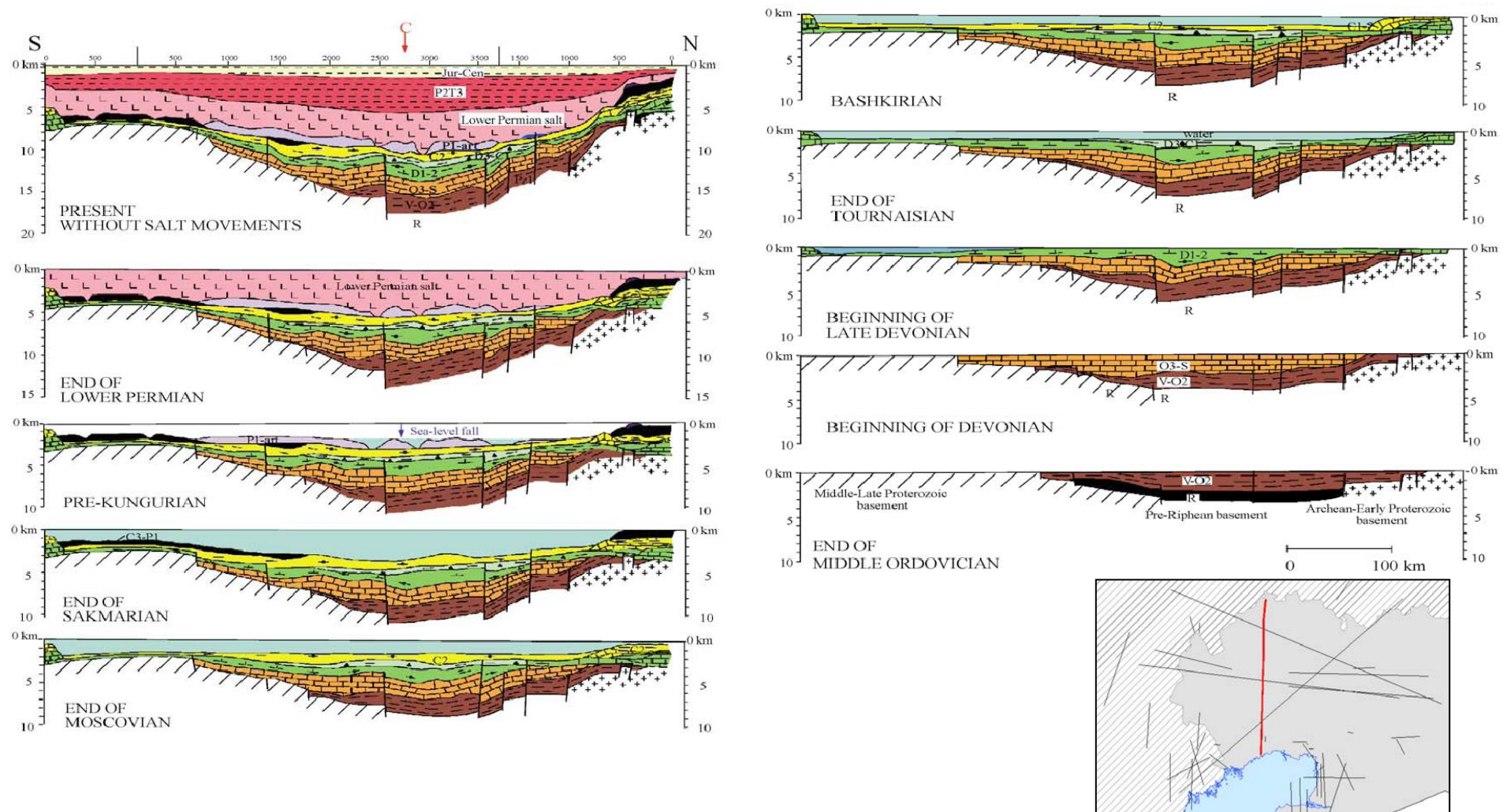
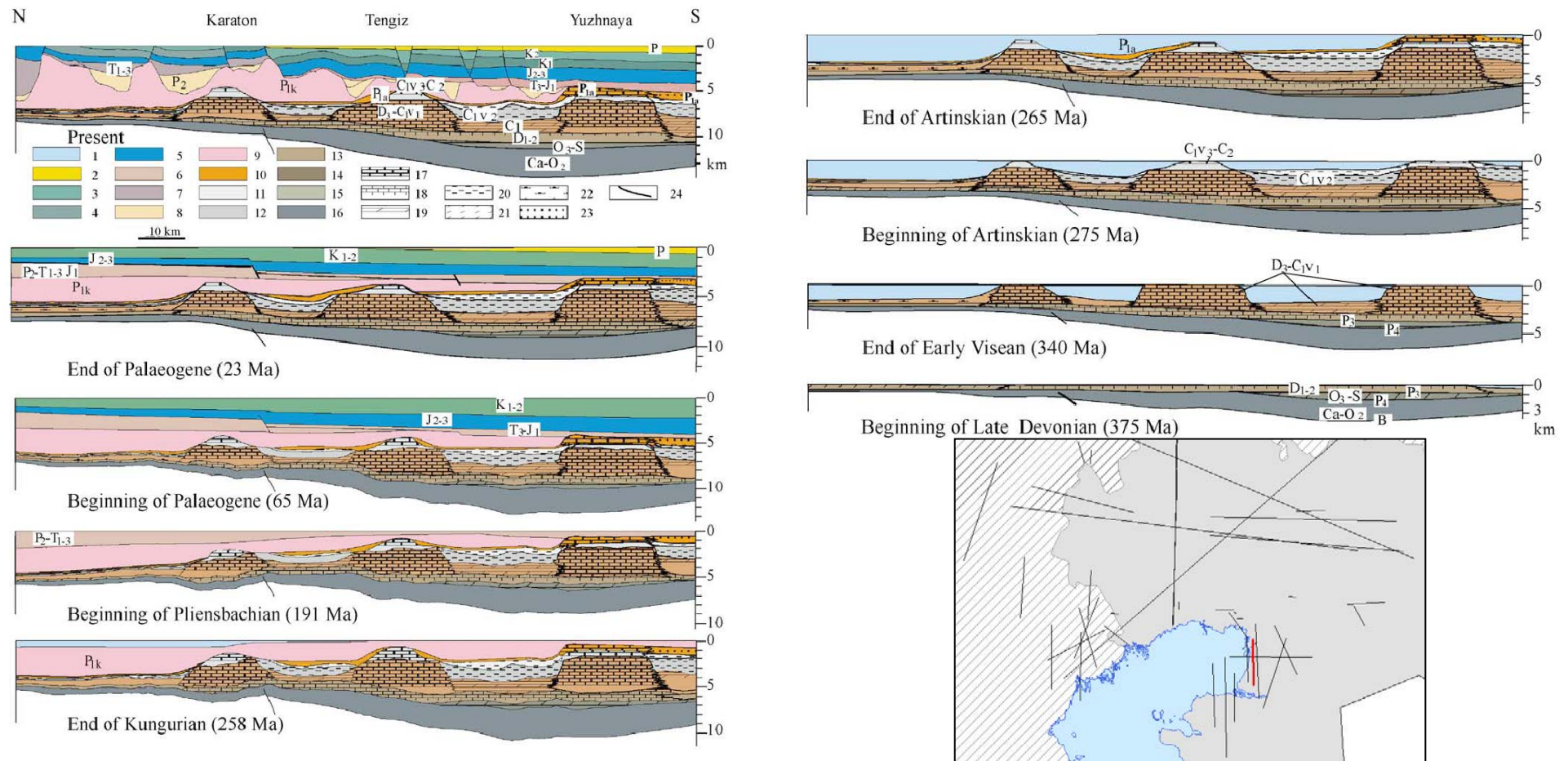


Figure 11: Reconstruction of evolution of the Precaspian Basin along a N–S line after “Brunet et al., 1999”. Layers are reconstituted without the movements of salt.



Before and during Devonian, the area of the Precaspian Basin was in a shallow water environment.

Then the palaeo waterdepth considerably increased (more than 1.5 km) during the Carboniferous. Palaeodepths were determined, mainly during Carboniferous, by the heights of the sediment scarps of the carbonate platform, located to the north of the basin (Figure 11), and also by the heights of intercontinental carbonate build-ups (Karaton, Tengiz, Yuzhnaya) on the southern slope of the North Caspian– Aktyubinsk uplift zone (Figure 12). The basin was filled during the Permian. From Triassic to Present, several additional kilometres of sediments were deposited in shallow marine or continental conditions.

The post-salt sedimentary cover is mainly affected by salt-flow creating numerous salt diapirs. Rim-syncline infill is predominantly composed of Mesozoic sediments.

The palinspastic profiles (Figure 10, Figure 11 and Figure 12), have been tentatively restored to show initial thicknesses of uniform layers of salt and post-salt sediments deposited on the whole basin surface. These thicknesses were derived by integrating the salt volumes in all the salt domes and sediments volumes in the rim-synclines through all the seismic profiles. A numerical approach has also been attempted on this type of reconstruction (Ismail-Zadeh et al., 2001).

PROPOSED EARLY HISTORY OF THE BASIN

The Precaspian salt basin became an individual basin only at the end of Permian, when the orogenic Urals belt arose along its eastern margins and inversion uplift occurred in the Donbass–Tuarkey rift system (Volozh et al., 1997, 1999). Before these events, parts of the depression were incorporated in various sedimentary basins and the Precaspian Basin did not yet exist in its present configuration.

The regional geodynamical evolution before the Precaspian Basin Permian origin is exposed in the following paragraph. It should be noted that very different other reconstructions exist in the literature. They vary according to timing of terranes collision in the south and east and also on the history of oceans opening and closing between these terranes and the East European platform.

In the Middle Proterozoic, the Central Precaspian depression was included into the structure of the Baltica continental passive margin (Figure 13). At this period, a shelf basin opened towards a deep-water oceanic basin in the east. At Late Riphean–Early Vendian, a foredeep basin was created in front of the Proto-Urals, within the domain of the Central Precaspian depression limited to the south and southeast by an orogenic structure (currently corresponding to the North Caspian– Aktyubinsk block as remnant of a larger structure).

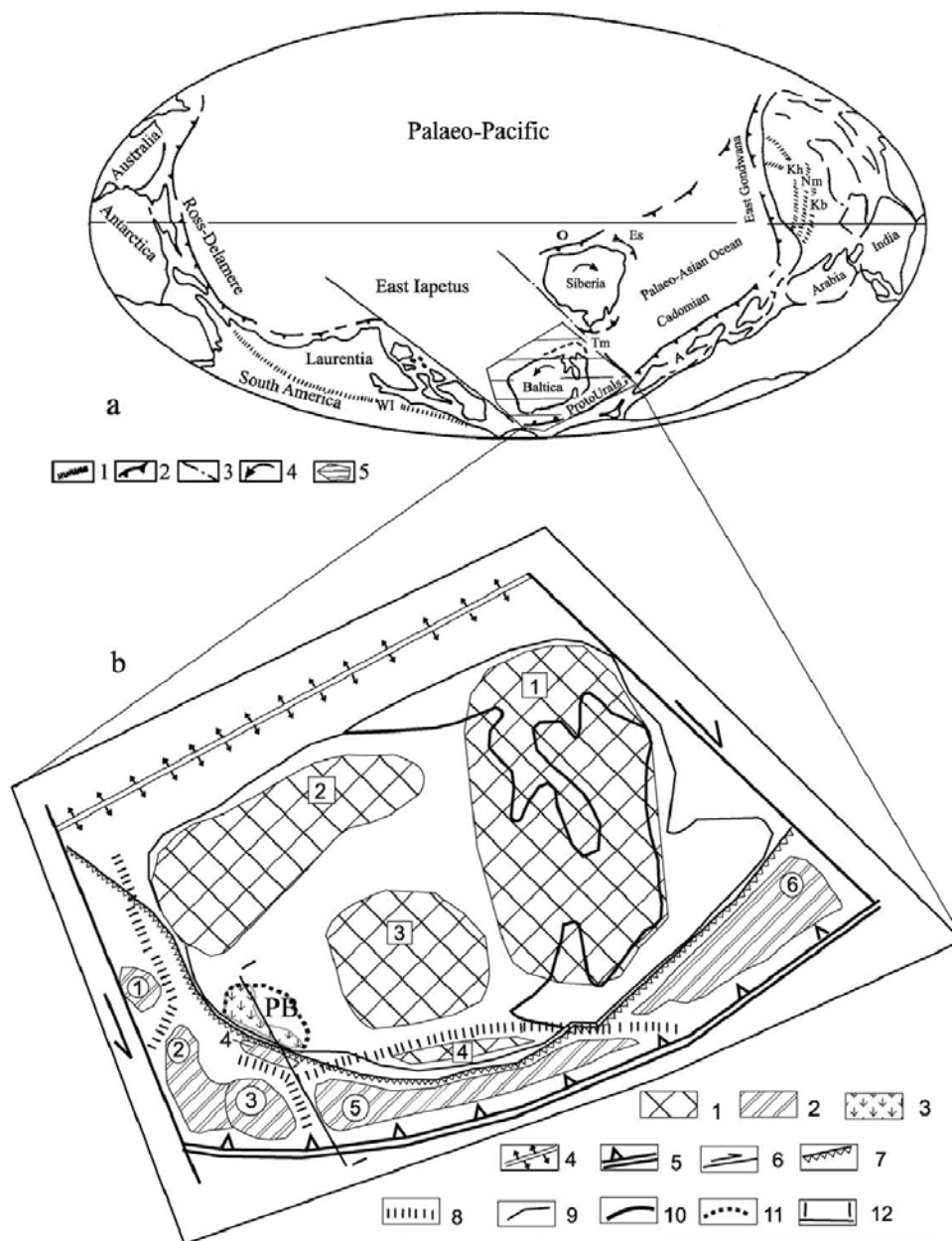


Figure 13: Geodynamic reconstructions of Riphean–Vendian history, after “Volozh et al., 2003”.

(a) Reconstruction of continents in Riphean–Vendian (after Mossakovsky et al., 1998, modified for the vergence of the subduction in area of (b)). 1—Vendian rift, 2—suture, 3—transform fault, 4—direction of rotation, 5—block shown on (b). A: Avalonian, ES: East Sajans, Kb: Karatau–Bajkonur, Kh: Khantajshir, Nm: Nej-Mongolian, O: Omolon, Tm: Tajmyr, WI: West Iapetus. (b) Detail for Proto-Urals ocean 1–2—different blocks: 1—Baltica (number within square: (1) Baltic dome, (2) Sarmatian dome, (3) Volga–Urals dome, (4) Uraltau block); 2 Proto-Urals Ocean: (number within circle: (1) Moesian, (2) Scythian [pre-Caucasus and Karabogaz domes], (3) Turan [North Ustyurt, Karakum, Central Turkmenia, Zeravshan], (4) East Precaspian block, (5) Turgaj–Syrdarya, (6) Pechora–Barentz Sea); 3—Eclogites; 4–6—East European lithosphere plate boundaries: 4—divergent, 5—convergent, 6—transform, 7—main overthrust Urals folded belt; 8—rifts; 9–11—boundaries: 9—continents, 10—recent continent (shoreline), 11—Precaspian Basin PB; 12—line of profile 11.

At the end of Proterozoic, collision of Baltica and Gondwana continents led to the formation of the supercontinent Rodinia. The Proto-Urals Ocean closed after subduction dipping towards the west. It formed the accretionary Proto-Urals folded belt in the Late Vendian (Figure 14).

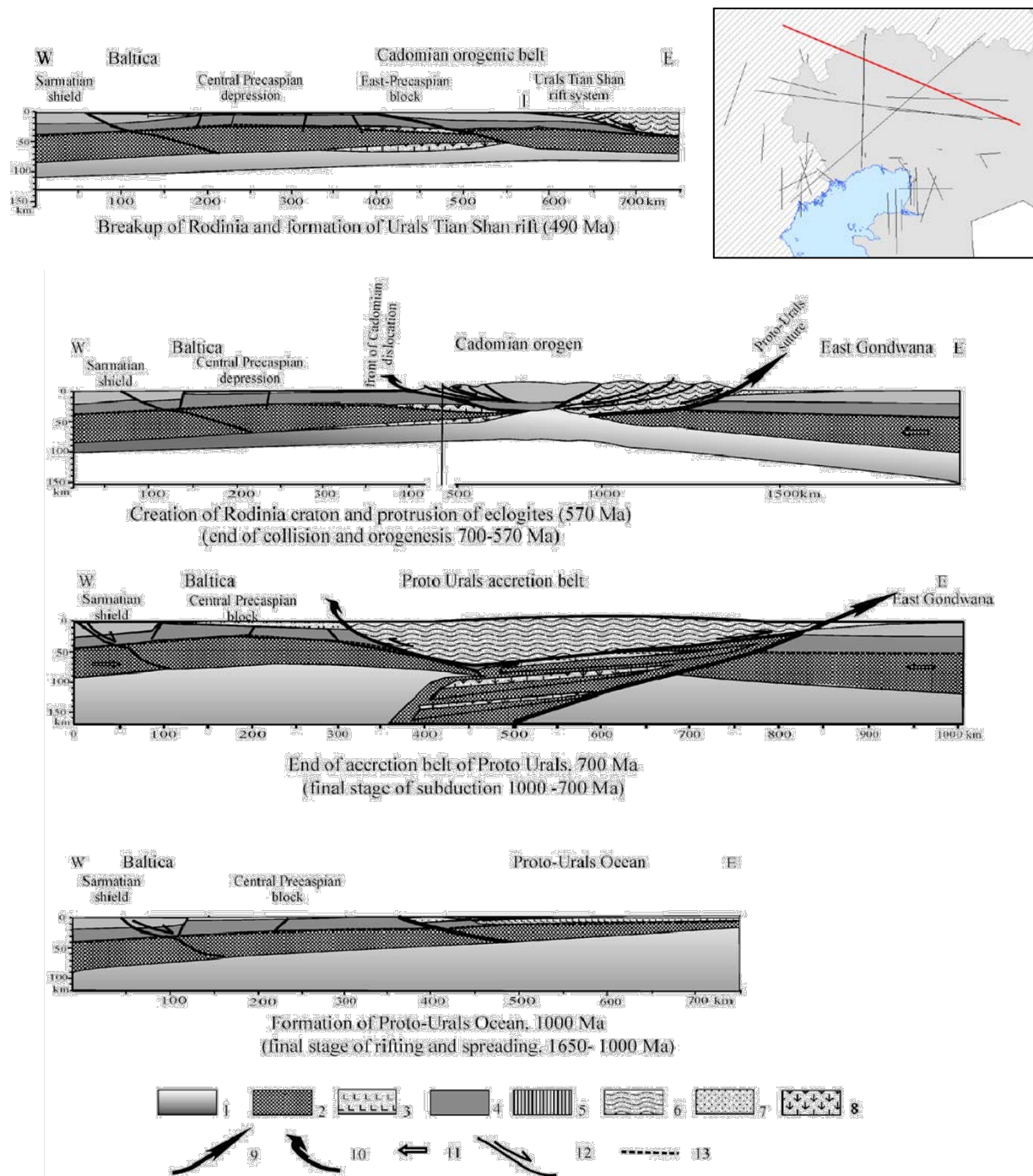


Figure 14: Riphean– Early Palaeozoic geodynamic reconstruction along an East–West section demonstrating eclogites emplacement, after “Volozh et al., 2003”.

1—Asthenosphere, 2—upper mantle, 3—oceanic crust, 4—lower continental crust, 5—upper continental crust, 6—accretion-collided and subduction-accretion fold belts, 7—sedimentary cover, 8—lenses of eclogites and mantle, 9– 10: main faults: 9—suture, 10— front of dislocation, 11—tectonic stress direction, 12—faults with moving direction, 13—Moho boundary.

At the end of Vendian–Early Cambrian, the Proto-Urals orogen was dismantled in connection with break-up of Rodinia (Volozh et al., 2003). Rift basins were created here by the collapse of the orogen. Later, they evolved into the Urals Ocean in the east and into the South Emba intercontinental rift in the south. At the end of Ordovician, the North Caspian– Aktyubinsk uplift zone was involved in the subsiding area, as a result of the Urals Ocean opening (Burtman et al., 2000). It lasted till Middle Devonian and rifting occurred within the South Emba trough. This resulted in an expansion of the epicontinental basin and its connection with the oceans surrounding the East European platform (Urals and Palaeo-Tethys). The whole Precaspian territory was included in sea shelf basin at Late Ordovician–Silurian. In the south, it was part of the back-arc basin system of the Palaeo-Tethys Ocean. At the end of Silurian, collision processes started on the northern periphery of the Palaeo-Tethys. These processes have resulted in the formation of a collided belt in the southern framework of the Precaspian Basin. In the Early Devonian, the border between the Precaspian Basin and the Caledonian orogenic belt foredeep basin was created within the South Emba trough. This basin accumulated terrigenous material, transported from the orogenic belt. It predetermined the formation of a basin, not compensated by sedimentation, within the Central Precaspian shelf depression. In the Middle Devonian, an important stage in the evolution of the Precaspian region, major structural changes occurred as well within the basin as on its periphery. The onset of the Uralian deformation is dated from the Mid-Late Devonian. It is based on the radiometric ages of HP metamorphism and beginning of the Zilair flysch sedimentation in southwest Urals. During this period, distension was active in the Precaspian Basin. Subduction occurred on the Kazakh active margin, then collision between the East European and Kazakhstan plates, as the arrival of the Ustyurt micro-continent in the South Emba area (Zonenshain et al., 1990). This resulted in the final structural configuration of the Central Precaspian depression as an isolated deep-water intercontinental basin.

Folded belts or uplifts created southern and eastern barriers around the Precaspian Basin. They periodically cut the communications with the open ocean leading to the formation of thick (several kilometres) Permian salt layers (Snyder et al., 1994).

Thus, the western half of the depression was incorporated in a sedimentary basin that continuously developed since Late Riphean, while the southeastern half belonged to a large orogenic area up to the beginning of Devonian. During Devonian through Early Carboniferous, sedimentation took place all over the entire region of the depression, which represented the shelf of the deep-sea marginal basin (Zholtayev, 1989). The latter was located in front of the subduction zone, which separated the East European continent from the Urals Ocean. The

Precaspian Basin, in its present shape and size, appeared during Permian when it was isolated from the southern and eastern areas.

Table 2: Geodynamic events linked to sedimentary environment in the PCB, after “Volozh et al., 2003”.

time Ma	Sedimentary environment within Precaspian basin				Geodynamical events within East European lithosphere plate		
	Central Precaspian block	East-Precaspian block	Duration, Ma	Main geological times(main seismic reflectors)	continent	Continental margins	
					Old East-European platform	PalaeoAsia sector	Palaeo-Tethys sector
680					destruction, break up of supercontinent Rodinia	subduction	opening of palaeoTethys
540	foredeep basin	orogen	90	Camb-O ₂	extension and subsidence	active margins destruction and formation of triple rift system (Urals, Tian-Shan and Tugarakhtan) towards east Central Precaspian basin	passive margin formation
450	epicontinental basin	passive margin basin	42	O ₃ -S	stabilisation	opening of Urals-Turkestan ocean and	accretion of microcontinents and islands arcs
408	shelf basin	shelf basin	18	D ₁ -D ₃ cm	uplift, erosion	formation of the passive margin	accretive fold belt formation
390	outer-shelf basin	inner shelf basin	15	D ₂ -D ₃ f	rifting	formation of accretive fold belt along Urals margin within East European continent	Sarmatian-Tuarkyr transcontinental shear zone formation
375	deep sea basin formation	Donbass- Tuarkyr rift (DTR) basin in SW margin	30	D ₃ -C ₁ v ₁			collision of East-European with Kazakh continents
312	filling the deep basin	folding within DTR	13	C ₁ v ₂ -C ₂ h	uplift { stabilisation uplift	formation of Urals-Tian Shan orogen	formation of active Eurasian continent margin along palaeoTethys boundary; and formation of volcano-pluton belt
270	epicontinental basin	PreUrals molasse basin	34	C ₂ -P ₁ a			formation of Urals-General transcontinental shear zone
255		epicontinental basin	10	P ₁ k-P ₂ t	extension	mobile platform	orogen
203	Precaspian-Scythian-Turan intra-continental basin		45	T	uplift		formation of Donbass-Tuarkyr intraplate fold system
	cutting (erosion)		30	J			
175							

DEEP STRUCTURE OF THE BASIN

Geophysical data (gravitational, magnetic, and seismic) can illustrate a distinct expression of the Central Precaspian depression in the structure of the mantle, basement, and sedimentary cover (Volozh et al., 1975; Brunet et al., 1999).

A distinct regional negative magnetic anomaly corresponds to the Central Precaspian depression on the magnetic field map and the most intense Khobda and Aralsor gravitational maximums (about 40 mgal) coincide with the depression on the gravity map (Brunet et al., 1999). These maximums show a regional level of the gravitational field higher than that of the uplifted structures of the Russian plate. The basement of the Central Precaspian depression is characterised by abnormally high velocities.

Boundary velocities vary from 6.7 to 7 km/s (Figure 9); layer velocities (in the upper part of the crust) show a stable velocity of more than 6.5 km/s (Volozh et al., 1975), to a maximum of 6.9 km/s in the Khobda area (Kostyuchenko et al., 1999). Thus, the characteristic lower crust velocity of 7–7.2 km/s, observed on the margins, is not present below most of the Central Precaspian depression. Besides velocities, other characteristics of crust and mantle are anomalous. In contrast to other areas, the crust of the Central Precaspian depression is 12–15 km thick.

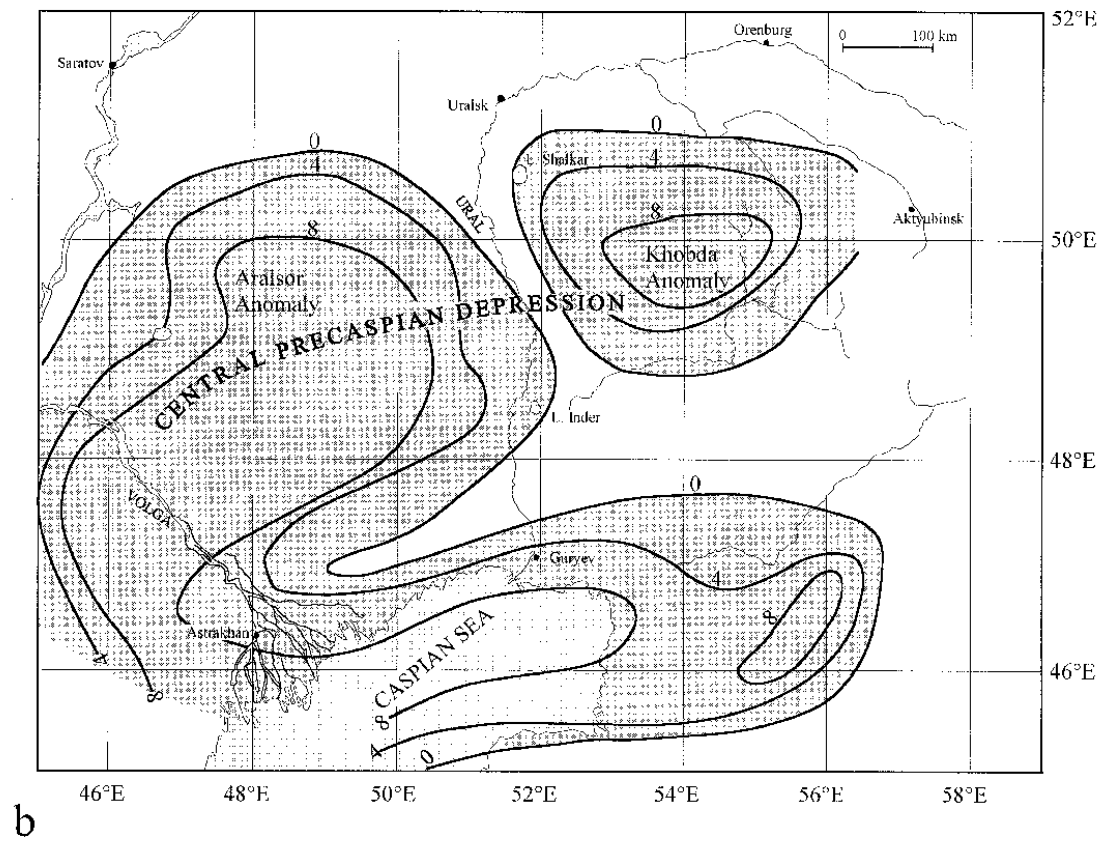
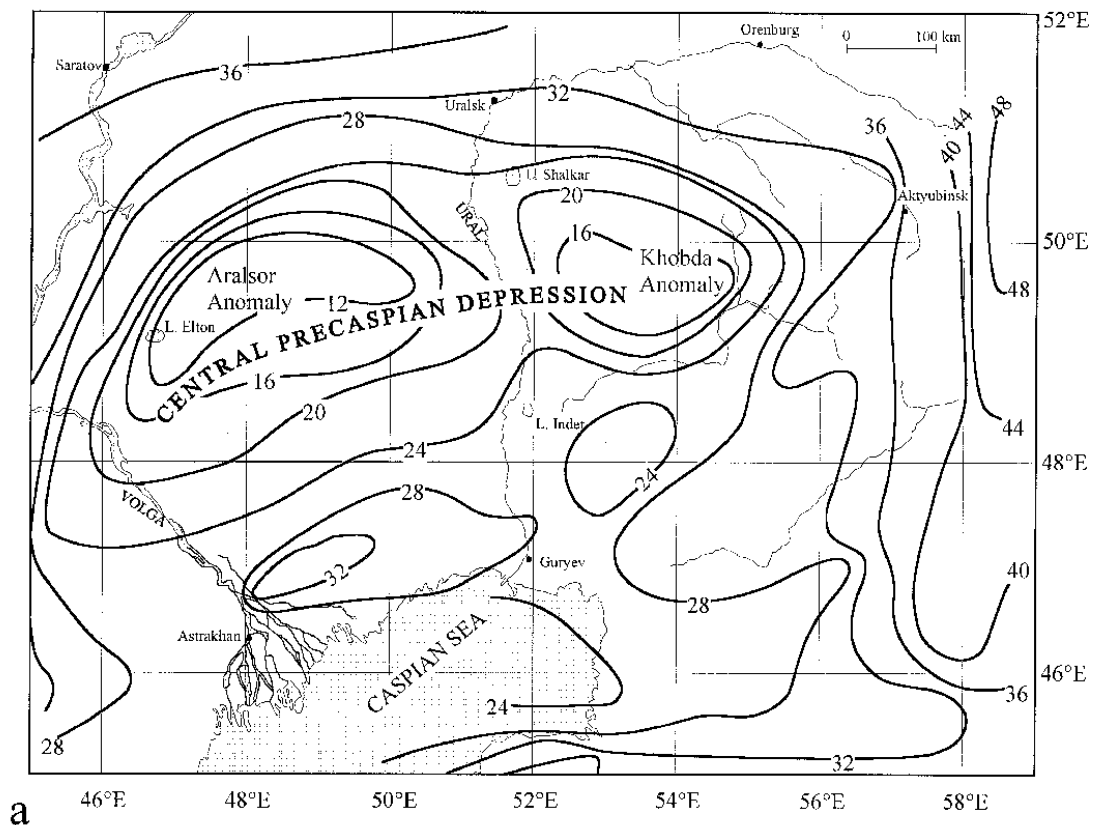


Figure 15: Map of the crustal thickness without HVL (a) and thickness of the HVL (b), after “Brunet et al., 1999”.

Two prominent seismic reflectors at the lower levels of the crust are recognised, at the depths of 32 and 42 km. A refracting horizon with $V_b = 8.0\text{--}8.1$ km/s identified as the Moho-surface coincides with the upper reflector. A reflecting horizon, about 42 km in depth, corresponds to the Moho on the margins (where reflecting and refracting horizons are merged), and then extends towards the centre of the basin almost flatly. In the centre of the basin, it is separated from the Moho, which is uplifted, by an 8- to 10 km layer. Analysis of the structure, gravitational field, analysis of density contrast between the different layers and composition of the crust indicates (Volozh et al., 1975; Volozh, 1990) that the layer between the two described reflectors (32 and 42 km) may be interpreted as eclogites. The presence of these eclogites was a key factor in the development of the very deep and particular Precaspian Basin. The lower reflector is situated near the upper boundary of an anomaly layer (8.6–8.7 km/s) which was identified by other studies between 45- and 60-km depth (Kostyuchenko et al., 1999).

If the HVL is composed of eclogites, the problem is to know how they can exist at the observed depth and when they were formed. Artyushkov (2007) proposed that the sole mechanism responsible for rapid subsidence of the PCB was the eclogitisation¹ of basaltic rocks in the lower crust. However, he did not take into account the observed thickness of the present crust, which also contributes to the subsidence of the basin, and the likelihood that eclogites cannot be formed at this depth where pressures are far too low. One way around the latter objection is to suppose that the eclogites were initially formed at greater depths/higher pressures in a different tectonic setting, such as a plate convergent one and, subsequently, were transported to their present depth. This kind of mechanism could occur as a result of rapid uplift and denudation related to post-orogenic extensional collapse events or by transport of the high-pressure metamorphic rocks to shallower levels by buoyancy forces combined with retro-thrusting.

If the eclogites inferred to lie beneath the PCB were formed as a result of collisional tectonics followed by exhumation, then there are two possible times at which the eclogitisation may have occurred. There are two main collisional phases during the history of the PCB.

The first is at the end of Riphean–Vendian collision with exhumation taking place during the subsequent rifting phase. Although the timing of this phase of rifting is not well known because

¹ *Eclogites are plagioclase-free metamorphic rocks composed of ≥ 75 vol.% of garnet and omphacite (IUGS Subcommission on the Systematics of Metamorphic Rocks). They generally have basaltic bulk compositions and recrystallized at high to ultrahigh pressures during subduction. Trace element and isotopic data of eclogites can be used to identify the geologic settings in which the eclogite precursors formed. In addition, trace element data of eclogites and eclogite minerals are important for assessing recycling processes in subduction zones.*

of the scarcity of data, most of the consequent subsidence would have occurred in Cambrian–Ordovician times and not later as observed. Nevertheless, the geometrical arguments used to support this possibility are as follows. The inferred eclogitic lenses are roughly limited to the southeast by a deeply penetrating fault bordering the CPD (Elton–Inder fault; Figure 9). This structure dips to the southeast and is sealed by lower Palaeozoic sediments and is thought to be the base of the NCAZ overthrust onto the CPD, possibly representing an end of Riphean–early Vendian ‘suture’ marking the closure of the Pre-Ural Ocean. The area of the present PCB would have been situated at this time on the continental margin of the Pre-Ural Ocean, adjacent to the oceanic crust subducted during the collision. The model supposes that subducted oceanic crust transformed into eclogites at depths of more than 60 km but was subsequently transported to a position beneath the present CPD and, in so doing, inducing an important component of its subsidence (Garagash et al., 1997). The mechanism transporting the eclogitic lens, involving a displacement of at least 300 km from the inferred suture, is not clear.

The second possibility is that eclogites formed during the Uralian collision; indeed, it could be suggested that they are related to Middle Devonian eclogites observed in the Urals (380 Ma). In this case, an excessively thick Devonian crust should have been subsequently affected by an important crustal thinning. But the presence of thick older sediments, not extended, seems to contradict this hypothesis, unless the formation of eclogites can be explained by other mechanisms.

Other explanations for eclogitisation, not involving collisional tectonics, have also been suggested. Lobkovsky et al. (1996) and Ismail-Zadeh (1998), for example, proposed that eclogites can form in the uppermost mantle as a result of mantle flow and explained the middle Frasnian–Famennian and post- Devonian subsidence phase of the PCB in such a manner.

There may also be models whereby the HVL is not composed of eclogites; for example, it could comprise ultramafic mantle rocks emplaced near or at the bottom of the crust. However, the same question as discussed in the previous paragraphs about eclogitisation arises about the timing of the emplacement of the HVL.

The lack of a confident identification of the true base of the crust and its relationship with the HVL is a significant problem hampering a better understanding of basin forming mechanisms. Estimations of crustal thickness in the basin vary; they depend greatly on the chosen interpretations of the HVL. If the HVL is considered to be part of the upper mantle or if eclogitic lenses have been brought to the base of the crust (but are not part of it), then the Moho depth, in the central PCB, is a depth of 32– 36 km. With a reference crustal thickness of 40 km (and taking into account the sedimentary layer), the crustal thinning factor in such a case is 3.3. However, if the HVL is interpreted to be an eclogitic part of the lower crust transformed in situ

by a process to be defined, the depth of the Moho below the central basin would be 40–44 km and the thinning factor would not exceed 2.

These values of the thinning factor will be used in the subsequent modelling analysis. Another possibility that is considered is that the PCB crust is either oceanic beneath the whole CPD or that it comprises two separate oceanic sub-basins in the areas of the Aralsor and Khobda anomalies.

3.1.2.3 *Tectonic subsidence evolution in the Precaspian basin*

The characteristics of the Central Precaspian depression predetermine the special features of the entire Precaspian Basin. These are: (1) the sedimentary cover (important thickness, significant stratigraphic volume, and completeness of the section), (2) the crust (small thickness and absence of low-velocity layer), (3) the mantle (low depth of the Moho surface, presence of another seismic boundary beneath the Moho surface), (4) geophysical fields (high gravitational and very low magnetic fields). That is why all geodynamic hypotheses and formation mechanisms of the Precaspian Basin primarily have to explain the structure and evolution of the Central Precaspian depression.

Numerous models have been proposed to explain the nature of this depression. The first group includes models that focus on both the small thickness and high-velocity composition of the crust of the Central Precaspian depression, considering it as an oceanic crust. According to these models, the thin crust of the depression represents the remnant of a marginal oceanic crust which was formed in either pre-Urals or Urals Ocean. In the first case, the crust is Riphean in age (Nevolin, 1978), and in the second, the crust is Riphean to Early Palaeozoic in age, or even Middle Devonian.

The models of the second group suppose that rifting is the leading mechanism with a thinning of the continental crust during several rifting phases from Riphean to Devonian (Volozh et al., 2003).

To explain the subsidence of the Precaspian depression, models of the third group examine the processes and phenomena related to a metamorphic alteration of the crust.

It is notable that none of the depicted models has been supported by numerical calculations based on real geological–geophysical data.

This led to more realistic models of the Central Precaspian depression (Brunet, 1995). The existing geological data on structure and composition of the sedimentary cover and crust give constraints that must be taken into account. For example, an oceanic crust of Riphean age is too old to explain the Palaeozoic Devonian to Permian subsidence of the basin.

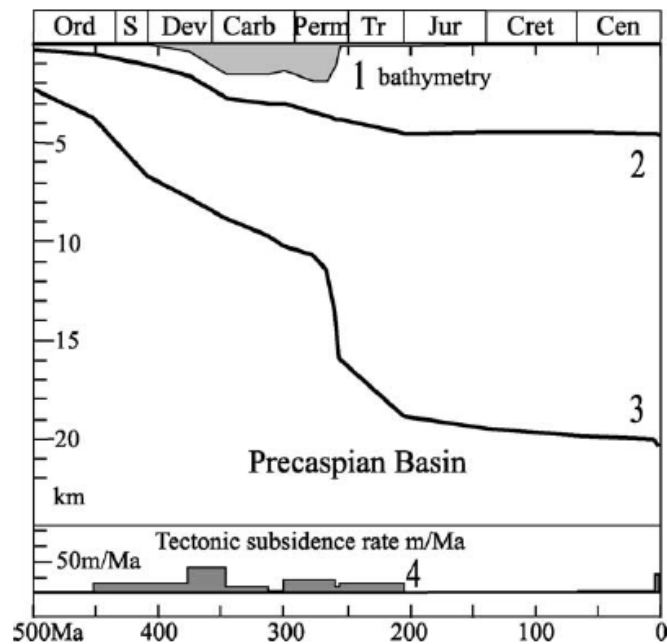


Figure 16: Subsidence curves in the centre of the Precaspian Basin, after “Brunet et al., 1999”.

1: Tectonic air-loaded subsidence curve, 2: total subsidence of the basement with sediments, 3: paleo-water depth, 4: tectonic subsidence rate. Location: centre of the depression.

AGE OF THE OLDEST SEDIMENTS

The large age discrepancy for the basin origin results from the uncertainty on the age of the first sediments deposited in the central part of the Precaspian Basin. It should be noted that the base of the sedimentary cover within the areas surrounding the Central Precaspian depression consists of Devonian terrigenous-carbonate. It is the same lithology as that found in the base of the sedimentary pile of the central part of the basin. This similarity of lithology has led to different hypotheses on the age of origin of the basin: either an older Riphean age is proposed or the same Devonian age is attributed to the sediments in the centre of the basin and on its periphery.

But some stratigraphic data exist on the deep horizon (P3) in the subsalt section. These data seem to exclude all groups of models that explain the formation of the Central Precaspian Basin as a result of Devonian rifting and consequent spreading of oceanic crust. The authors of these models proceeded from the assumption that the deepest main horizon P3 is restricted to the top of Devonian deposits. They consider also that the thick sedimentary complex (more than 8 km), comprised between this horizon and the basement, is not older than Devonian in age.

The drilling data obtained from some areas in the east and southeast of the Precaspian depression (east Akjar, Kumsai, Baktygaryn, etc.) (Akhmetshina et al., 1993), strongly support the stratigraphic position of the main reflector P3 as close to the base of Lower Devonian. This reflector was penetrated by hole G-5 (east Akjar), at a significant distance from the slope of the depression, in the zone of the Aktyubinsk uplift. Within this area, two holes G-1 (Baktygaryn) and G-4 (Kumsai) penetrated thick Devonian carbonate deposits. Logging (Geophysical interpretation of wells) data determine the stratigraphic position of boundaries. The drilling was stopped at 300 (G1)– 500 (G4) m above horizon P3. Devonian deposits, which are evenly cored in G4, are known in the depth interval of 4830–6007 m. The drilled section contains numerous organic remnants that permit to definitely determine the age of hosting carbonate rocks. The presence of Conodonts species *Ozarkodina remscheidenis remscheidenis* Ziegler in carbonates from hole G-5 (intervals 5738–5745 and 5745–5751 m) is indicative of the lowermost portion of the Lower Devonian Lochkovian stage. The presence of Foraminifers *Tubeporina tenue* Sabirov in Hole G-1 (interval 6204–6212 m) determines the time interval as the Lower Devonian Pragian stage. The fragment of the time-scale seismic section in the vicinity of hole G-5 (Figure 17) shows that the main reflector P3 is restricted to the base of the Lower Devonian (Lower Lochkovian) carbonate deposits.

As shown in the available substantial volume of seismic data, main horizon P3 is well expressed in the whole region. It is traced from margin towards centre of basin along almost all seismic profiles. For example, Figure 18 shows the correlation of P3 horizon between the southwest Astrakhan margin and the basin.

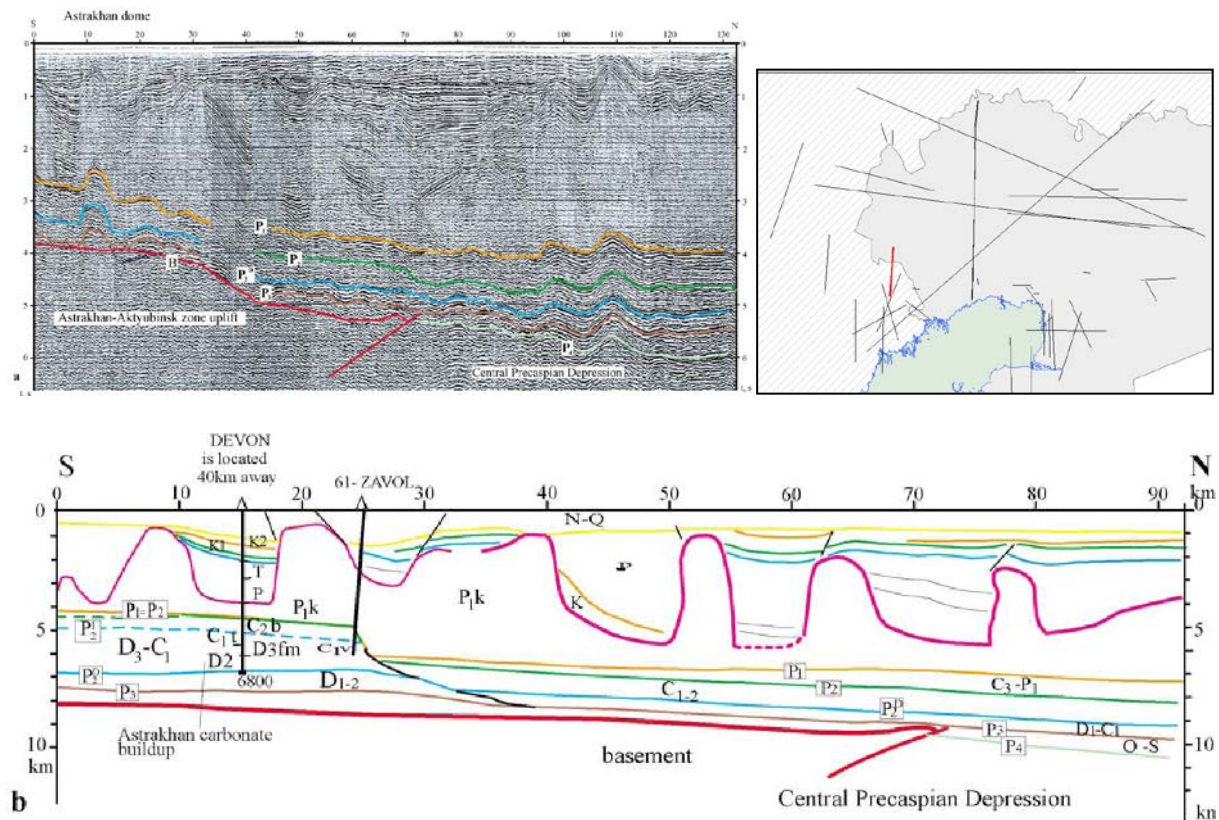


Figure 18: North– south section on the southwest Astrakhan margin of the Precaspian Basin, after “Volozh et al. 2003”.
(a) Seismic profile; (b) depth converted section of a part of the profile (a).

Seismo–stratigraphic and structural constraints along P3 horizon within the Precaspian Basin, permit to depict gentle and rounded structures of secondary order (Aktyubinsk uplift, Central Precaspian depression, etc.). In the most subsided part of the Central Precaspian depression, the base of the Lower Devonian deposits is situated at a depth of almost 14 km (Figure 8) shown by the deepening of the seismic horizon P3. Hence, a thick (more than 6–8 km) unit of pre-Devonian carbonate and terrigenous rocks is present between the top of the basement and the base of Devonian (seismic horizon P3) to Lower Permian series.

Data constraining precisely the initial age of the sedimentary unit existing below the P3 Lower Devonian horizon are not available. Below P3, there exist other seismic horizons (Figure 9 and Figure 10) P4, P5 or D_{50S} that were never drilled, and the basement.

Sediment deposition began during Riphean, by comparison, for example, with Pachelma rift and Pre-Uralian foredeep where thick Riphean deposits are known. Velocity data and wave images of Riphean deposits were correlated with information from Bashkirian region where seismic records have been carried out and have been published (Scripij et al., 1990). Some data on Lower Palaeozoic sediments provided by boreholes on the margins of the basin are available (Jatskevich, 1996). Some boreholes in the northwest Precaspian (3—Ershov; 11, 14—Krasnokut; 1, 2— Vostochno— Kudinov; 300—Zhirnov; 10—Petroval'sk) penetrated: Ordovician–Silurian terrigenous and carbonate sediments (about 100 m) containing Brachiopods, Trilobites, Corals and Crinoids. In the northeast Precaspian, boreholes (85—Berdiansk; 110—Predurals) drilled Cambrian–Ordovician terrigenous and carbonate sediments (about 200–300 m) with Graptolites, Algae and Ostracods. Jatskevich (1996) wrote that Upper Proterozoic sediments were covered by thick (1000–2000 m) post-Vendian deposits (Cambrian, Silurian and Ordovician) in Riasano–Saratov basin (in the former situation of the Pachelma Riphean Basin and in prolongation of the Precaspian Basin). These Lower Palaeozoic sediments were eroded during pre-Devonian time. Thus, the thickness of Lower Palaeozoic terrigenous sediments is 100–300 m and carbonate sediments 100–200 m as well in northwest as in northeast.

Paleo-reconstructions show that Lower Palaeozoic sediment thickness increased towards the basin up to 3.5–4 km and that older layers appear below these deposits.

Even if the age of first sediments is still partly undefined, the existing data do not support a Middle Devonian spreading, since older sediments cannot cover a Devonian oceanic crust.

3.1.2.4 *Details about regional geology*

The basement of the southeastern Caspian basin and Scythian plate is thought to have consolidated in the pre-Paleozoic Baikalian (Cadomian). Blocks of the Cadomides formed a single Scythian–Turanian terrain which joined to the Archean–Late Proterozoic continent Baltia in Late Precambrian time to form the vast European continent. Through all of Paleozoic and Early Mesozoic (Triassic) time the southeastern part of the European continent with the Cadomian-consolidated crust was an active continental margin where thick terrigenous and volcanic sequences accumulated (Figure 19).

The boundary between the Scythian and Turanian young (Mesozoic–Cenozoic) plates was defined. The proposed boundary between these plates was drawn along the northeastern margin of the Donbass–Tuarkyr folded area, following the line demarcating differences in stratigraphic age between “preplate” and “folded” complexes of the sedimentary cover (Figure 19). The “folded” complex of sedimentary cover in the Turanian plate is no younger than the

Artinskian of Early Permian, whereas in the Scythian plate it extends into the Upper Permian. Thus, the “preplate” complex of the Turanian and Scythian plates begins with Kungurian and Triassic deposits, respectively. Within these outlines, each plate has a specific structure typical of “folded” or “preplate” complex of the sedimentary cover, distinct structural constraints as well as specific seismic properties of the petroleum potential.

Transregional post-collision strike-slip faults were first recognized as large structural displacements in the lithosphere developed at the end of a collision stage of the formation of large volumes of continental crust, and thought to have been the main structure-forming elements during the preplate evolution of the region (Volozh et al., 2005). Large inversion and fold-and-thrust intraplate structures are associated with these strike-slip faults. Motion along them continued at the plate stage as well; and most of these faults are still active today. There have been five strike-slip faults revealed (with different degree of certainty) within the Caspian region: Ural–Gerirud, South Emba, Aksu–Kenderli, Donbass–Zeravshan and Caucasus–Kopet Dag (Figure 19). These faults are subparallel to the Tethyan or Uralian margins of the East European continent. Major strike-slip motions along faults occurred during late Triassic– early Jurassic (Ural–Gerirud, South Emba, Aksu–Kenderli), Paleogene (Donbass–Zeravshan), Pliocene–Quaternary (Caucasus– Kopet Dag). The amplitude of the faults is a few hundred kilometres. This resulted in the formation of the Aral–Kyzylkum arch along the Ural–Gerirud N–S strike-slip fault, South Emba uplift along the South Emba fault. The Mangyshlak–Central Ustyurt uplift system and Karpinsky Range are associated with the Donbass–Zeravshan fault. For the Tien Shan structures of the South Aral region a northward displacement on the Ural–Gerirud dextral strike-slip fault reaches 400–500 km, where they extend into E–W trending Hercynides of the Northwestern Aral region. The above faults remained active after the main phase of their lifetime, which is reflected in their structure as well as in facies and thickness variability within the sedimentary cover. Structural traps are expected to exist along faults, most of which may contain large amount of hydrocarbon reserves (Zhetybai–Uzen’ step and others).

New conceptual understanding of the nature of the South Emba uplift as a southeastern marginal structure of the North Caspian salt dome region is given in Volozh et al. (1999), and Segalovich et al. (2007). The South Emba uplift is located in the eastern part of the Tugarakchan rift, a large buried structure. However, they are not genetically related to each other. The Tugarakchan rift extends from the Urals in the east across the North Caspian offshore to the Astrakhan uplift in the west, where it is truncated by the Sarmat–Tuarkyr rift structures formed in the Devonian. The Tugarakchan rift initiated during the Late Cambrian–Early Ordovician and ceased development in the late Silurian. It appears as the third branch of landward divergent extensional structures, which developed above the hot spots (two other

branches initiated the Ural and Turkistan Ocean spreading axes) (Figure 20). The South Emba uplift probably resulted from strike-slip movements along a large transcontinental postcollision fault (South Emba) associated with a Hercynian orogeny event, which took place on eastern collision margin of the Paleozoic European continent (Figure 21).

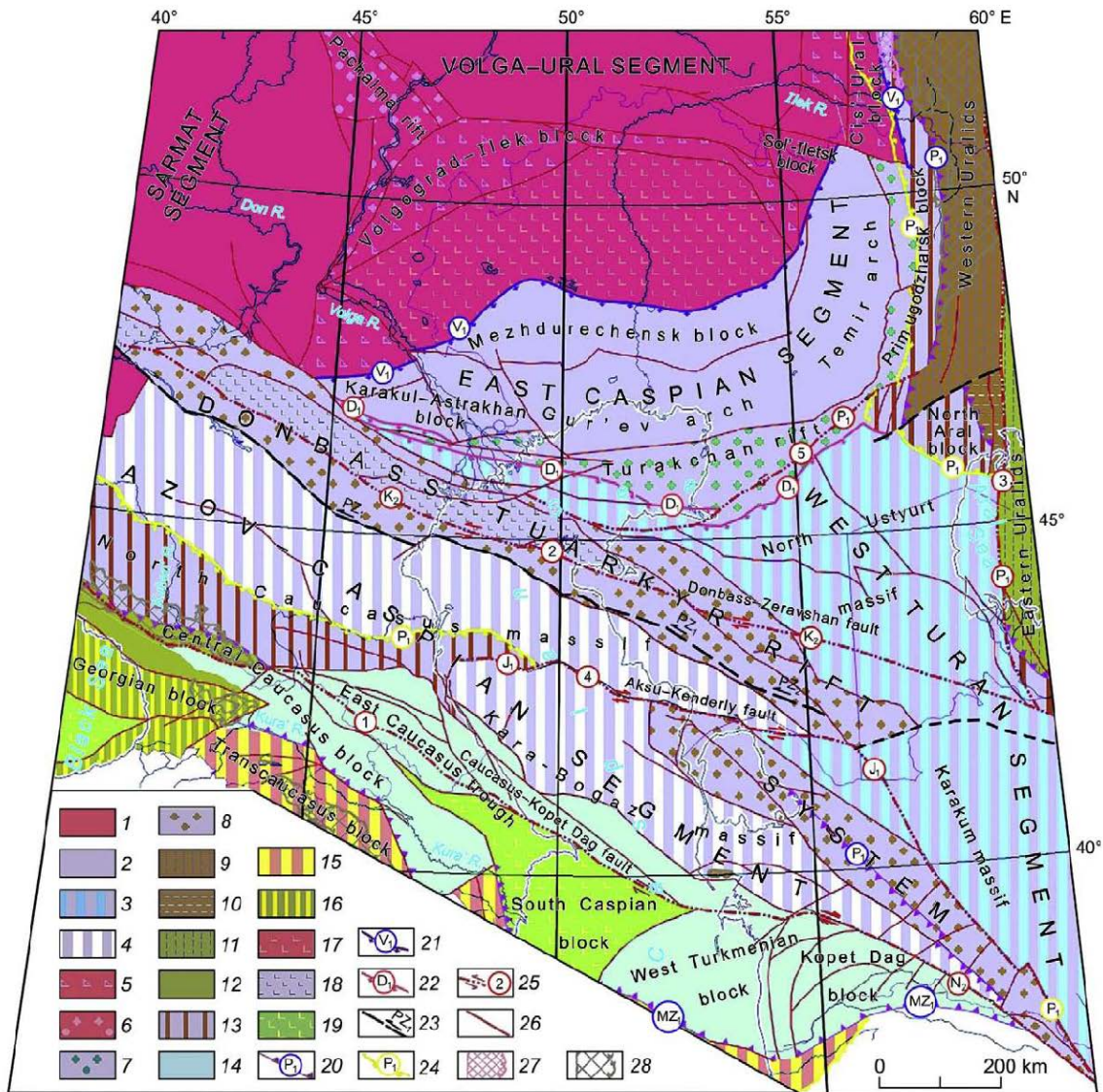


Figure 19: Structural and tectonic map showing consolidated crust in the Caspian region, after “Volozh et al., 2009”.

1–4. Basement segments and blocks of the East European Paleozoic continent: 1, basement blocks of pre-Riphean consolidation; 2, blocks of pre-Paleozoic (Cadomian) consolidation; 3, blocks of pre-Paleozoic (Cadomian) consolidation reworked in the Early Paleozoic (Cambrian–Silurian), basement of the western Turanian plate; 4, blocks of pre-Paleozoic (Cadomian) consolidation reworked in the Late Paleozoic (Late Devonian–Early Carboniferous), basement of the Scythian plate. 5. Basement of passive continental margins with thinned Riphean crust. 6, 7. Basement of intracontinental rifts: 6, Riphean; 7, Early Paleozoic. 8. Basement. 9–11. Basement of Paleozoic consolidation of the Ural–Tien Shan collision belt: 9, Western Uralids; 10, Tien Shanides; 11, Eastern Uralids. 12–16. Basement blocks of the Paleozoic continent active margin (northern margin of the Paleo-Tethys Ocean) and Alpine collision belt: 12, undifferentiated crust of the Late Paleozoic consolidation; 13, pre-Paleozoic reworked in the Late Paleozoic; 14, of the Early Mesozoic consolidation; 15, of the Early Mesozoic consolidation reworked in the Alpine time; 16, undifferentiated crust of the Late Alpine consolidation. 17–19. Areas with the thinned consolidated crust of:

17, central North Caspian block; 18, Donbass–Tuarkyr folded system; 19, South Caspian and East Black Sea blocks. 20–24. Suture structures: 20, ophiolitic sutures (age is designated as indices); 21, boundary of the back crust deformations within the collision-related Cadomides foldbelt; 22, boundary of the back crust deformations within the subduction-related Cadomides foldbelt; 23, transform faults; 24, crown of transform folds (age is designated as indices). 25. Transcontinental post-collision strike-slip faults (numbers in circle: 1, Caucasus–Kopet Dag; 2, Donbass–Zeravshan; 3, Ural–Gerirud; 4, Aksu–Kenderli. 5. South Emba (age of motion is designated as indices). 26. Other regional tectonic dislocations. 27, 28. Basement outcrops: 27, pre-Riphean; 28, Paleozoic.

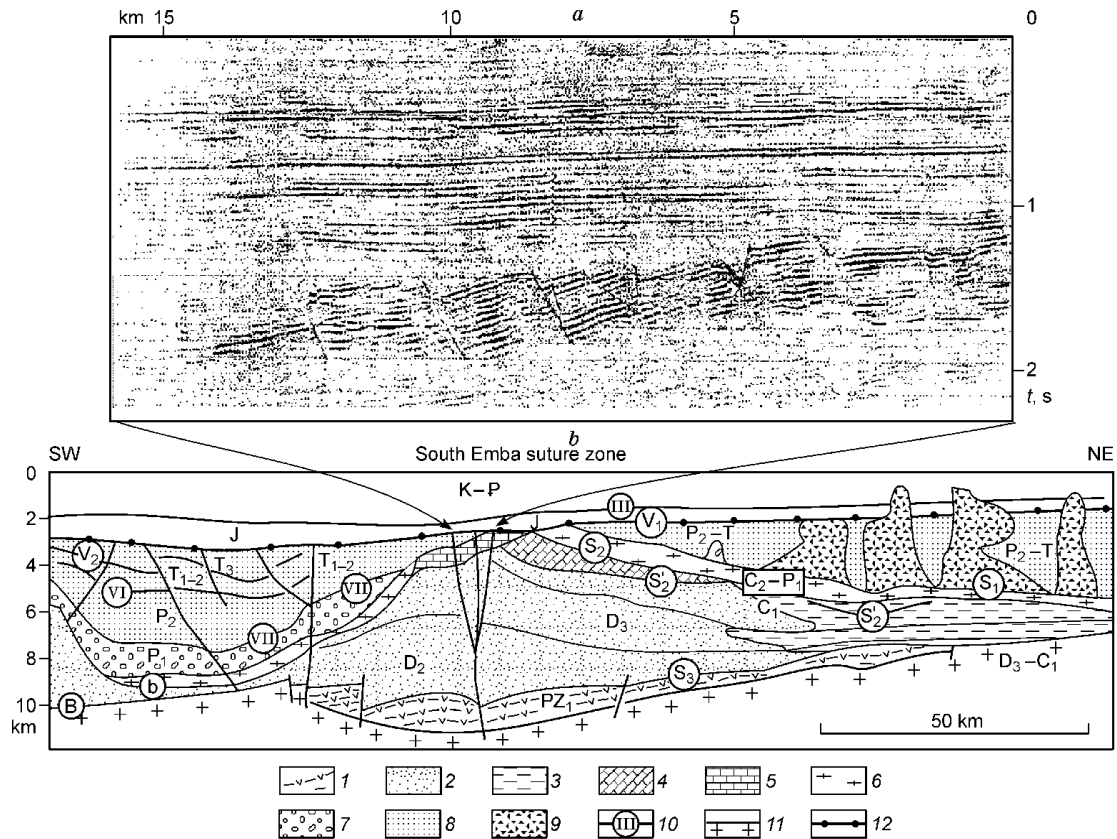
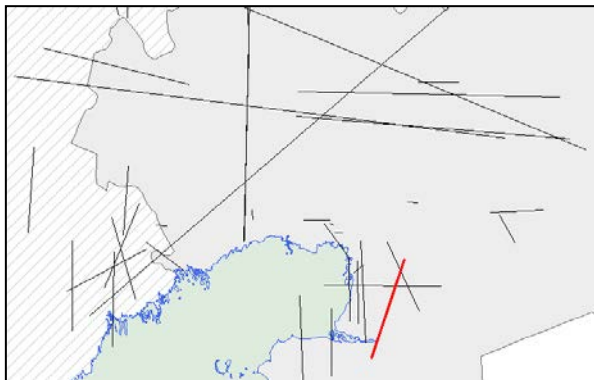


Figure 20: Geologic-geophysical section across the South Emba uplift (b) and a fragment of time section (a) showing the morphology of tectonic dislocations within the South Emba regional fault, after “Volozh et al., 1999”.



1, Lower Paleozoic volcano-sedimentary strata. 2, 3. Middle Devonian–Lower Carboniferous deposits: 2, Carbonate-terrigenous; 3, Terrigenous. 4. Middle Carboniferous carbonates. 5, 6. Middle Carboniferous–Lower Permian deposits: 5, carbonate; 6, terrigenous. 7. Lower Permian terrigenous deposits. 8. Upper Permian–Triassic terrigenous deposits. 9. Kungurian salts. 10. Key reflectors and their indices. 11. Basement surface. 12. Pre-Jurassic unconformity surface. III, VI, VII, S₁, S₂, S₂′, S₃. Key reflectors. B. Basement.

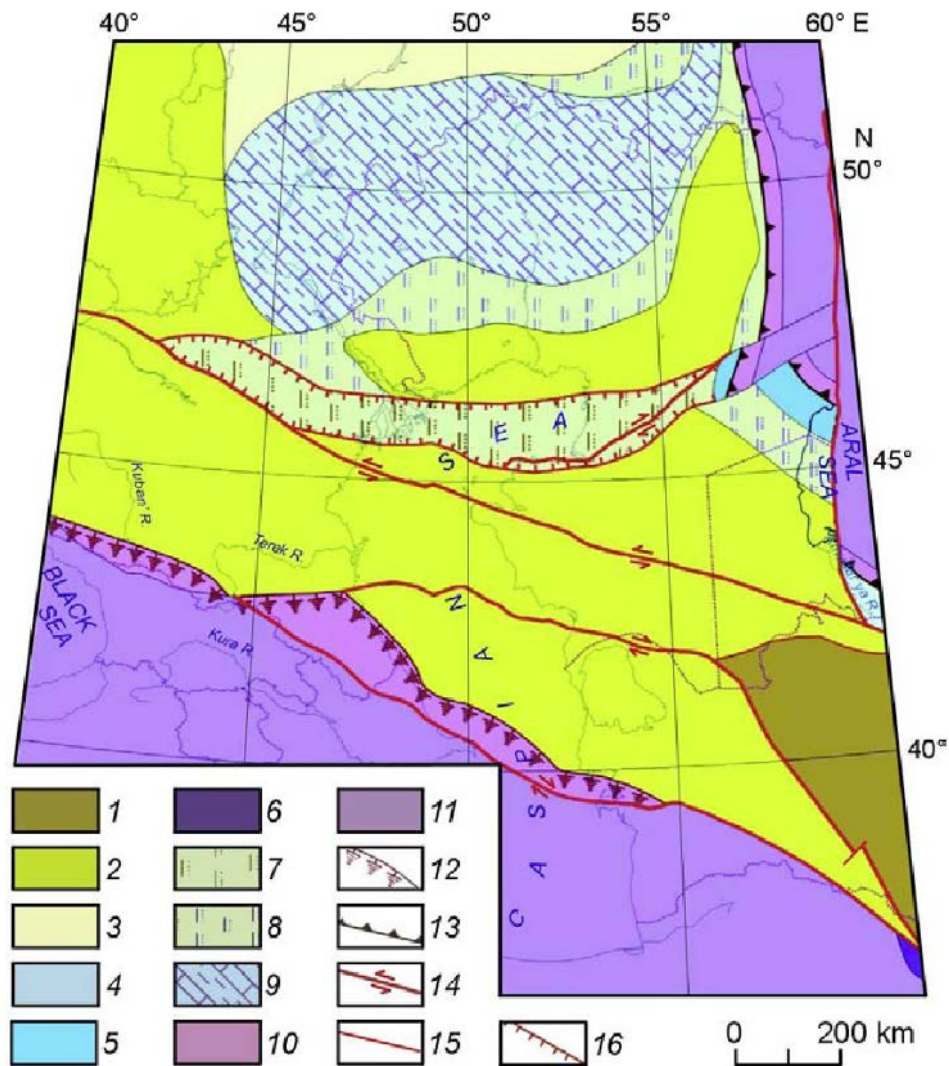


Figure 21: Gross depositional environment map of the Ordovician, after “Volozh and Parasyna, 2008”.

1. High and mid-sized mountains.
2. Peneplains and gentle hilly plain plateaus.
3. Fluvialacustrine plains.
4. Inner shelves, shallow marine areas.
5. Outer deep shelves.
6. Bathyal zone of deep inland and marginal seas.
7. Shallow shelf with terrigenous sedimentation setting.
8. Fluvialacustrine plains with terrigenous sedimentation setting and clinoform structure.
9. Fluvialacustrine plains with terrigenous sedimentation setting and clinoform structure.
10. Continental slopes and rises.
11. Ocean and inland-sea basins.
12. Active accretionary margin break.
13. Passive margin shelf break.
14. Thrusts.
15. Actual and inferred faults of unknown nature.

Structural history of the Karpinsky Range has been studied in Volozh et al. (1999). It has been shown that the range is part of the Donbass–Tuarkyr intra-continental folded zone, which was formed during the development of a more extensive Paleozoic Sarmat–Tuarkyr rift system. In addition to the above folded zone, the latter comprises the Devonian– Carboniferous Dnieper–Donets and Pripyat’ aulacogens (Figure 22 and Figure 23). As shown by Volozh et al. (1997), the Sarmat–Tuarkyr rift system initiated in the mid Devonian and ceased development in Late Triassic–Early Jurassic time. The South Emba or Central Ustyurt uplifts by many researchers are thought to be extensions of the Karpinsky Range.

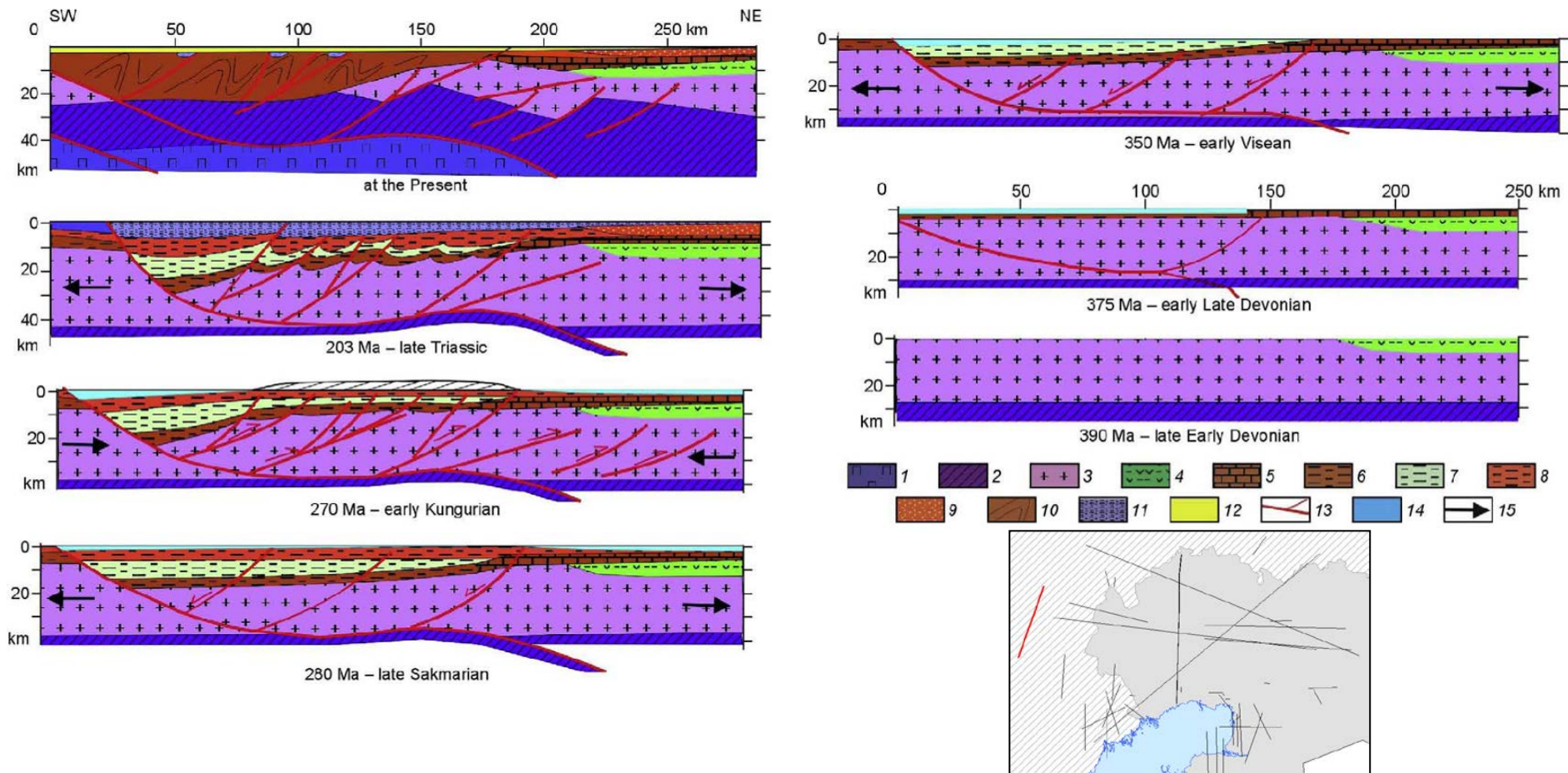


Figure 23: Paleotectonic reconstructions across the Tsimlyansk line illustrating the major tectonic events that result in the development of the Sarmat–Turkyr rift system, after “Volozh et al., 2009”.

1. Upper mantle. 2. Lower crust. 3. Upper crust. 4. Lower Paleozoic volcano-sedimentary strata. 5. Devonian carbonates. 6. Devonian terrigenous deposits. 7. Carboniferous terrigenous deposits. 8. Permian terrigenous deposits. 9. Kungurian salt-bearing deposits. 10. Paleozoic fold complexes. 11. Triassic deposits. 12. Mesozoic–Cenozoic strata. 13. Fractures. 14. Sea. 15. Direction of tectonic movements.

Palinspastic reconstructions were first made for the southeastern margin of the Paleozoic European continent to estimate offsets on transcontinental post-collision strike-slip faults and define the palinspastic position of the Permian salt basin in the North Caspian region relative to tectonic units of the basement and sedimentary cover and their relationship with different paleomorphologic elements of Caspian region structure.

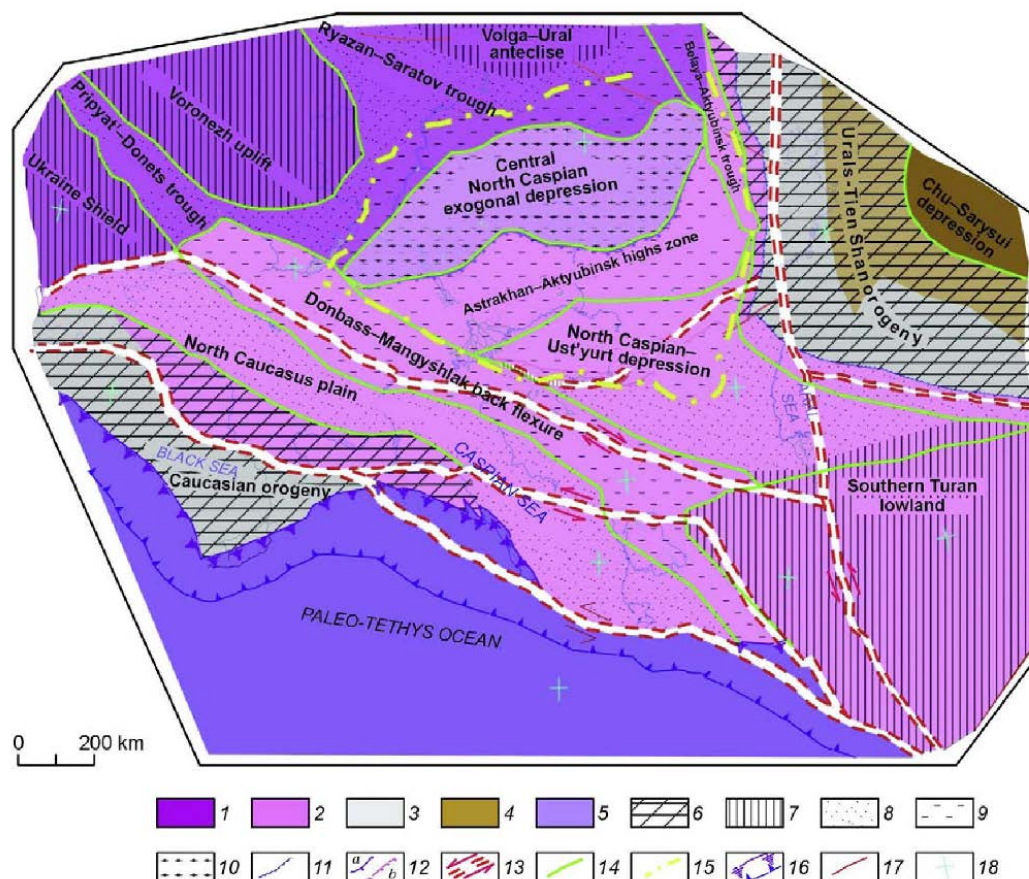


Figure 24: Palinspastic reconstruction of consolidated crust of the Paleozoic East European continent at the beginning of the Kungurian, after “Volozh and Parasyna, 2008”.

1–4. Blocks of consolidated crust: 1, pre-Riphean; 2, Precambrian (Cadomian); 3, Early Paleozoic; 4, Late Paleozoic. 5. Paleo-Tethys ocean. 6, 7. Erosion zones: 6, orogens; 7, denudation plains and uplands. 8–10. Sedimentation areas: 8, coastal accumulation plains and shallow shelves; 9, submerged shelf and slope; 10, deep-water basins. 11. Ophiolitic sutures. 12. Deformation fronts: a, Riphean; b, Early Paleozoic. 13. Transcontinental strike-slip faults, lines of palinspastic reconstructions. 14. Boundaries of the main continental structural elements. 15. Boundary of the Caspian salt-bearing basin. 16. Eurasia active margin. 17. Faults. 18. Orientation of present-day geographic coordinates.

The tectono-depositional framework of the North Caspian intra-continental (Kungurian) basin was determined (Volozh et al., 1999). Hypsometry for salt deposition shows a disharmony with overlying and underlying beds owing to a specific combination of tectonic movements and a rate of deposition, which persisted during a large time span (Late Devonian–Early Permian) in areas including five large tectonic structures with different geodynamic regimes: (a) Volga–

Ural anticline; (b) Central–North Caspian exogonous depression; (c) North Caspian– Ustyurt syncline; (d) Karpinsky Range; (e) Belaya–Aktyubinsk depression (basin) of the Ural foredeep. Each of these structures correlates with a specific type of sedimentary basins: Volga–Ural anticline—shelf epicontinental basin; (b) Central–North Caspian exogonous depression—Riphean– Paleozoic pericratonic basin; (c) North Caspian–Ustyurt syncline—Early Paleozoic intracontinental rift and Late Paleozoic epicontinental basin; (d) Karpinsky Range—Late Devonian rift and Upper Paleozoic back-arc basin; (e) Belaya- Aktyubinsk depression of the Ural foredeep—Late Paleozoic foredeep basin. This conclusion is supported by a set of structural maps based on key seismic reflectors and 2D and 3D backstripping reconstructions. Comparison between present day and restored (flattened) seismic profiles (with stripped off salt tectonics) confined to the base of pre-Jurassic, pre-Cretaceous and pre-Paleogene complexes shows that they are conformal and follow (when flattened) structural configuration of the basement surface and pre-Devonian complex, whereas the internal horizons (pre-Kungurian and pre-Moscovian) are disharmonious with overlying and underlying boundaries (Figure 25).

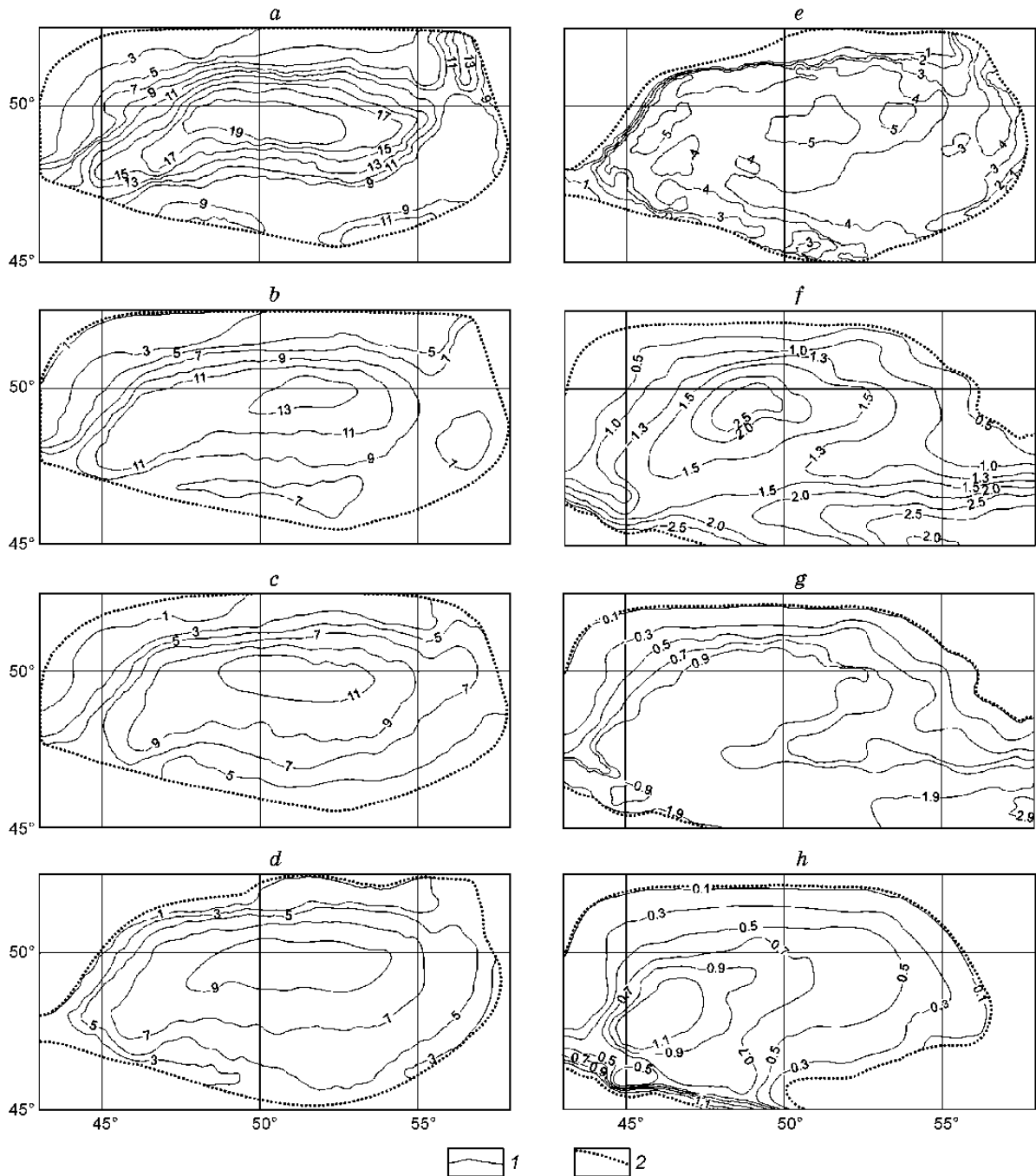


Figure 25: Relationship between structural geometry of different sequences of the sedimentary cover, North Caspian salt dome region, after “Volozh et al., 2009”.
a. Basement surface. b. Pre-Devonian unconformity surface (reflector S3). c. Pre-Moscovian surface (reflector S2). d. Pre-Kungurian surface (reflector S1). e. Flat surface of the Kungurian salt-bearing sequence. f. Pre-Jurassic unconformity surface (reflector V). g. Pre-Cretaceous surface (reflector III). h. Pre-Paleogene surface (reflector I). e–h. Present-day geometry of the marker beds with stripped off salt tectonic. 1. Contour lines, km. 2. North Caspian basin boundary.

Revised seismo-stratigraphic subdivision was suggested for the lower (pre-Frasnian) part of the sedimentary cover in the northern Belaya–Aktyubinsk syncline of the Ural depression (Yuryuzan–Sylvinsk depression). A Lower Riphean carbonate stratum (Kaltasin Series) identified there was recognized to be Lower Paleozoic. The key question is how accurate is

traditional assignment of pre-Frasnian section of the sedimentary cover to Lower Riphean within the part of profile that enters outlines of the Ural depression (Figure 26).

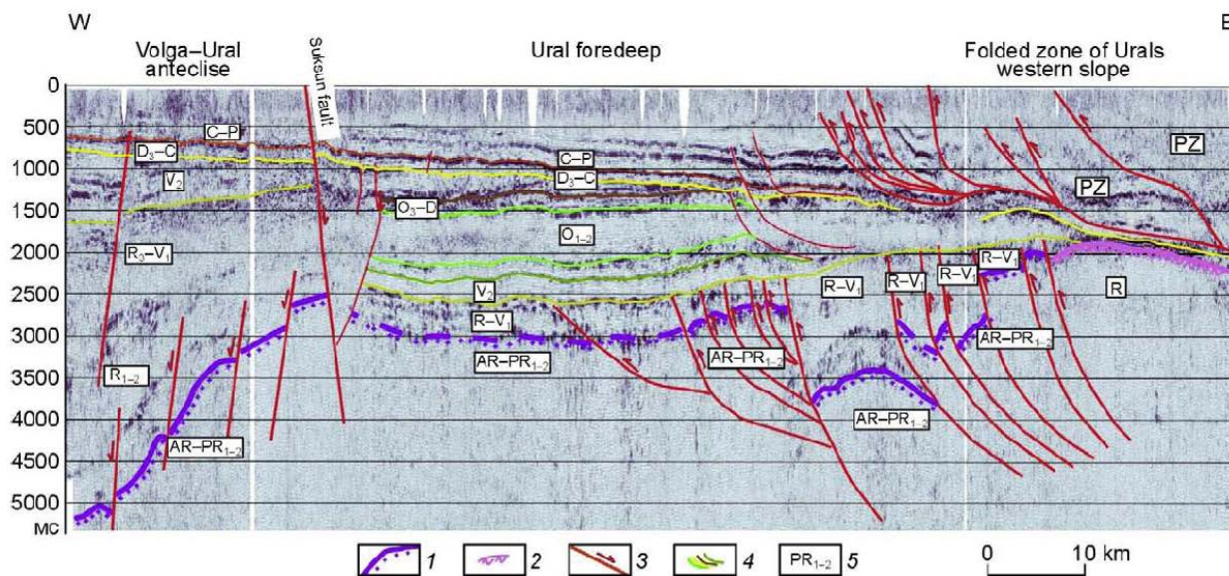


Figure 26: Cross-section across the Ural foredeep, after “Volozh et al., 2009”.
 1, 2. Top of consolidated Archean–Proterozoic (1) and Riphean (Cadomian) (2) crust. 3. Faults. 4. Reflectors. 5. Seismic sequence indices.

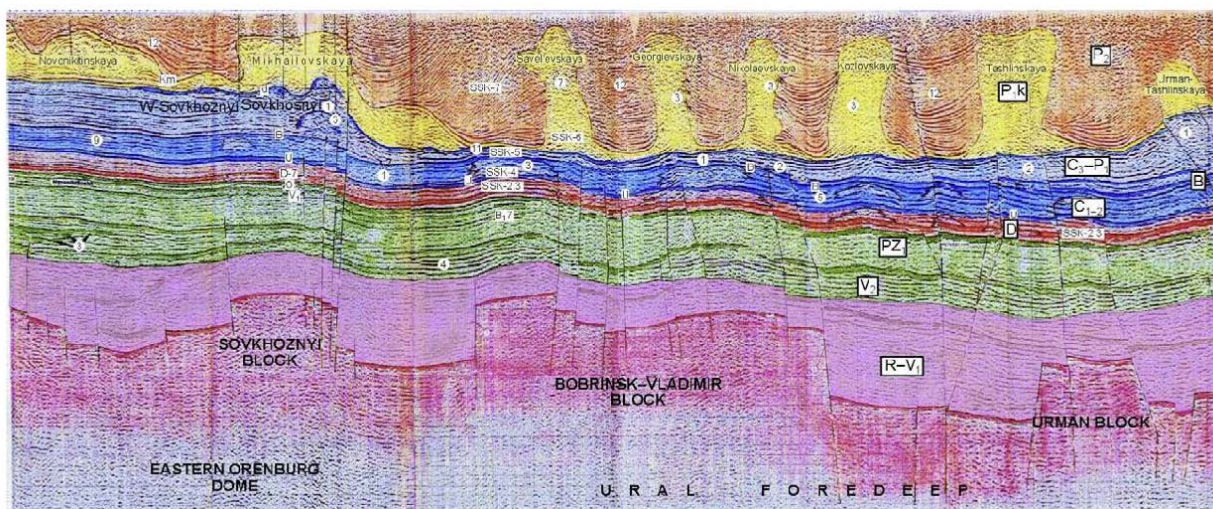


Figure 27: Fragment of time section through a regional line across junction zone between the Ural foredeep and East Orenburg arch, after “Volozh et al., 2009”.

In the work carried out by Belokon' et al., 2001 Lower Riphean age of the stratum overlain by Frasnian deposits was confirmed from boreholes (Bukharovskaya 10 and Manchazh 5 boreholes) drilled to the north of a seismic line. At the same time, the age of this stratum was determined from indirect evidence (no direct paleontological data) on the basis of correlation with sections in the Arlan and Oryebash wells drilled in the Kama–Belaya trough, East

European platform. Such correlation seems to be unacceptable because of boreholes located within areas with different geo-seismic characteristics. In this case, the seismo-stratigraphic approach should be used preferably for age determination. It is plainly seen on the Mikhailovsky seismic profile that reflection patterns of the pre-Frasnian section vary considerably on different sides of the Suksun fault which separates the Riphean Kama–Belaya trough of East European platform from the Paleozoic Ural foredeep. The angular unconformity between the Riphean and Upper Vendian successions is locally evident in the eastern part of the profile and disappears east of the Suksun fault. Thus, the pre-Frasnian succession of considerable thickness appears to be conformable with the overlying Devonian–Carboniferous deposits to make up a single seismic sequence. These structural relationships testify to a Paleozoic age of deposits from pre-Frasnian succession within the study interval. It is likely identical in its age and composition to Lower Paleozoic deposits of the Belaya shelf zone, which are widely developed on the western slope of the Urals and to the south, in the Orenburg Region. After data given by Puchkov (2000) it's assumed the presence of Lower Paleozoic–Lower Devonian sediments in this area. In addition, there are some indications for the presence of Upper Ordovician deposits in the Uralian foredeep. According to A.V. Yaroshenko, a borehole drilled westward of the Baskirian anticlinorium has penetrated Upper Ordovician section of limestones with trilobite finds. Lower Devonian facies on the eastern margin of the East European platform within the Uralian foredeep are found in the Central Urals (Us'va River), Southern Urals (Kaga River—sandstones and limestones) (Volozh et al., 2009).

In the seismic profile 370505 located further south a similar in its structural position, thick, unfossiliferous sequence has been identified. Several carbonate build-ups have been recognized on seismic records within its uppermost part (Figure 27) referred to as Upper Ordovician–Lower Devonian based on borehole data. If the study carbonate rock sequence is known to be of Lower Paleozoic (Upper Cambrian–Lower Devonian) rather than Riphean age, it has, by analogy with the Timan–Pechora basin, higher prospectively as compared to the Riphean sequences.

Hydrocarbon geological zoning was made for the Caspian region on the basis of the ranked fluid-bearing geo-systems. These are age subdivisions of the sedimentary cover (structural-tectonic or lithostratigraphic units *etc.*) separated by seals of a respective rank: transregional, regional or zonal. The extent of first-rank seals is defined by the limits of petroleum provinces (petroleum basins, petroleum regions for the second-rank seals, and petroleum zone for the third-rank seals. A petroleum region within the Mesozoic–Cenozoic sequence formed at the last stage of Alpine tectonics corresponds to a sedimentary basin or adequately ranked

platform type tectonic structure. A petroleum province encompasses several adjacent tectonic structures or sedimentary basins that are related in terms of common transregional seal.

Understanding of geodynamic, tectonic and depositional processes in the Caspian region allowed the recognition of four first-ranked fluid-bearing (petroleum) geo-systems within the sedimentary cover: pre-Kungurian, Upper Permian–Triassic, Jurassic–Miocene, and Pliocene–Quaternary. Accordingly, there have been distinguished four transregional seals and four petroleum provinces: Volga–Ural, North Caspian, Caucasian–South Mangyshlak, South Caspian, and North Ustyurt (as part of West Turanian province). The recognized transregional seals include the Kungurian salt for the North Caspian province, Maikopian shale for the Caucasian-South Mangyshlak province, Akchagyl–Apsheronian sand and shale for the South Caspian, and Upper Jurassic carbonate and shale for the West Turanian province.

This approach has significantly altered the traditionally recognized boundary between the North Caspian and Volga–Ural petroleum provinces and, to a less extent, the boundary between the North Caspian and Caucasian–South Mangyshlak provinces. The North Caspian province thus encompasses the Belaya–Aktyubinsk depression of the Uralian foredeep, Sol'-Iletsk salient, Volgograd and Saratov areas of Trans-Volga region, Buzachinsk dome and northwestern part of the Karpinsky Range (Figure 28).

3.1.2.5 *Present-Day Structure*

The basement surface of the North Caspian basin occurs at depths reaching more than 20km in the Central depression. The depression is about 450 km long from west to east. Two narrow troughs extend from the depression to the southwest and northeast; these troughs were probably deep straits that connected the North Caspian oceanic basin with the Tethys and Uralian oceans. The north and west basin margins are narrow and steep. In contrast, the south margin is wide, being formed by a series of structural arches in which the basement lies at depths of 7–8km. From the crests of the arches, the basement dips both toward the Central depression and toward the marginal troughs in front of the Hercynian foldbelts. At the top of subsalt rocks the Central depression is a gentle structure with a maximum depth of about 10 km. The marginal troughs are absent and the top of subsalt rocks dips away from the margins toward the basin centre. Carbonate platforms and organic build-ups are expressed as structural highs. The regional structural pattern of Upper Permian and younger strata is dominated by salt tectonics. More than 1,000 salt domes have been identified in the basin. In marginal areas, the domes are arranged in salt ridges that are generally parallel to the basin margins (Ulmishek, 2003).

RECENT TECTONIC MOVEMENT

As shown by an analysis of data on recent tectonic movements, they differ in direction and intensity in different regions of the study area (Figure 29).

The most intense uplifts during the Middle Miocene - Quaternary period are noted in the Central - Mangyshlak-Ustyurt dislocation zone, where the base of the Middle Miocene formations, or its corresponding erosion-denudation level, is raised to a height of 556m (at Besshoky). Considering that in the adjoining South-Buzachi depression to the north this level lies at an elevation of minus 50-100m, the amplitude of displacement across the Central-Mangyshlak-Ustyurt fault reaches 600-700m. It is precisely in this area where rock types associated with the consolidated foundation emerge at the daylight surface. In the south-east direction, the intensity of the uplift lessens but this zone is nonetheless reflected in submeridional rampart-like uplifts and gentle depressions in the relief, generally reflecting new deformations.

The North-Ustyurt Plateau, formed as a result of moderate uplift of the area (50-100 m) is to be found to the north of the Central-Mangyshlak-Ustyurt intense uplift zone. On the whole, the Ustyurt Plateau appears to have an emphasised tectonic character. As a result of exposure to exogenic processes, all elements of the tectonics (anticlinal and synclinal zones, local uplifts)

are directly expressed in the relief, with a certain exaggeration of amplitudes compared with the amplitudes of the structural forms (Aristarkhova et al., 1970).

In neo-tectonic terms, the North-Caspian plain is associated with a region of intense modern settling events, reaching 300-700 m in amplitude. In the modern relief, this region is characterised by significant levels below world ocean level. The recent structural forms are associated with salt-dome tectonics, which is indirectly reflected in the lineaments (Azgirsky, Zholdybai) traced by different investigators.

Thus, the direction of recent tectonic movements is reflected in the morphological structure of the region, in that it is to a large extent determined by the stages of its development. This is particularly true of the regional features of the modern structure of the area under investigation. At the same time, a similarly clear direct and indirect relationship is found between the basic morphological structures of the region and its deep tectonic plan, which has influenced the nature of the deformations in regions with a different regime of recent movements.

Insofar as deformations of the sedimentary strata are the reflection of the dynamics and kinematics of tectonic movements, they are the structural diagnostic criteria of mobile zones in the Earth's crust. As shown by analysis of the available data, several unequal regions or zones can be identified in relation to the way in which folding deformations are manifested in the platform mantle.

The most extensive region – the Pre-Caspian Trough – is characterised by extensive development of salt tectonics and related deformations of the over salt complex of sediments, including the most recent. As a result of the growth of salt massifs, gently sloping dome-shaped uplifts are formed with a 2-5° dip of the rock on the limbs, accompanied by pinching out of individual interlayer towards the crown of the domes, in some cases omitting entire Pliocene and Quaternary series from the profile.

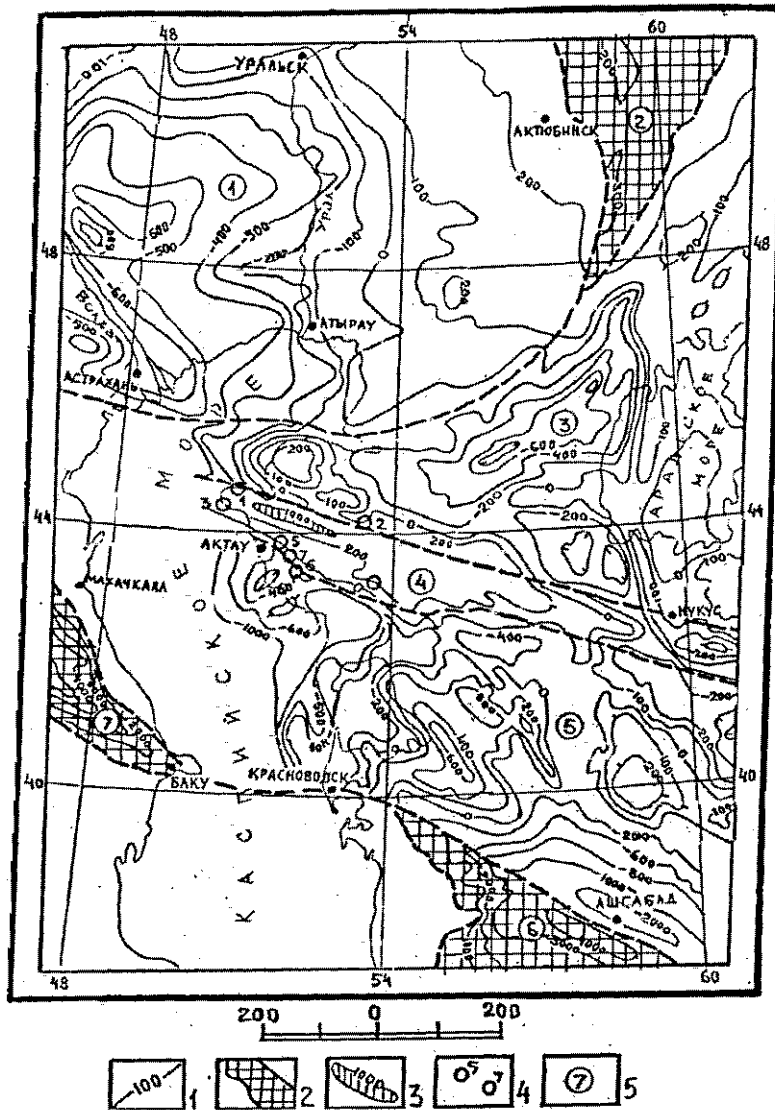


Figure 29: Diagram of amplitudes of recent tectonic movements in the Caspian and Turanskaya Platform regions, after "KDCP, 2002".

1 - Isolines of amplitudes of vertical neotectonic movements (at the base of the Middle Miocene); 2 - montane uplifts; 3 - low montane intra-platform massifs; 4 - areas of occurrence of Cenozoic dislocations (1 - North-Tyubkaragansky, 2 - Sai- Utessky, 3 - Fort-Shevchenko, 4 - Tumgachinsky, 5 - Uzunbassky, 6 - Tarlinsky, 7 - Ushkonursky); 5 - structural zones (1 - Pre-Caspian, 2 - Uralskaya, 3 - North-Ustyurt, 4 - Central-Mangyshlak-Ustyurt, 5 - South-Mangyshlak-Ustyurt, 6 - Uralskaya, 7 - Kopetdag'skaya, 8 - Kavkaz'skaya).

In the Holocene, the growth of domes is also fairly clearly identifiable in the relief, and the most active domes correspond to large topographic highs (Inder). The morphological types of the salt domes are highly varied - arch, brachyantichinal, monoclinial, double-limb, triple-limb. Careful geomorphological analysis has shown that all of these dislocations are not linked to major tectonic disturbances in the consolidated foundation, but are attributable to the dynamics of post-sedimentational re-forming of the salt bearing strata.

With the North-Ustyurt zone, the character of deformations of the platform mantle differs from that in the Pre-Caspian Trough. Here, in the upper structural stages of the sedimentary mantle, there is a development of small-amplitude brachyanticlinal folds replaced at greater depth by more complex overthrust type structures. An important feature of these structures is their overlapping stepwise conformation whereby the crest of each successive anticlinal fold is up thrown with horizontal displacement amplitude up to 300m, and the dip angles of the displacers in the frontal zone are 45-70°, sloping more gently with increasing depth with a transition to sub horizontal breaks.

In this connection it is noteworthy that the articulation zone of the Pre-Caspian Trough and Turanskaya Platform has an overthrust character, confirmed by the structure of the Kalamkas anticline in the northern part of the Buzachi Peninsula. Overall, the spatial position of folding overthrust dislocations in the North-Ustyurt zone suggests that they were formed under the effects of submeridional horizontal compressive forces (KDPC, 2002).

RECENT ACTIVE FAULTS

One of the most important structural features of the area under investigation is the continuous cover of very thick platform mantle formations, which calls for a specific approach to the investigation of fault dislocations. In these conditions, geophysical and geomorphological methods of identifying and tracing faults are of particular value. Based on the experience of various investigators (Aristarkhova, 1971, 1981), the following diagnostic signs of faults have been established: 1 – magnetometric signs - local maxima of ΔT_a in the form of chains and extended zones, bunching of ΔT_a isolines, abrupt change of sign and character of anomalous magnetic field, abrupt change in course of magnetic anomalies; 2 - gravimetric signs - sequences of intense gravity peaks, abrupt change in course of anomalous zones, abrupt changes in character of the gravity field, shifts in the line of gravity peaks; 3 - geomorphological signs - linear segments of modern and ancient river valleys and drainage hollows, regional benches, steep slopes and bends at levels of similar age, linearly oriented chains of certain topographical forms (relict uplands, solonchak sinks), clear rectilinear boundaries between relief types (of different genesis, morphology and age). Dislocations showing activity during the most recent stage can normally be readily traced on the satellite imagery. Based on these criteria, a number of dislocations activated during the Neogene-Quaternary stage and traced by various techniques have been identified in the region under investigation (Figure 30). The Precaspian Trough is described below; information about faults in the North Ustyurt Basin is described in relative chapter.

To the southeast of the Pre-Caspian Trough, the edge fault formed by the South-Emba lineament is a well known feature. It divides the Precambrian Russian platform and the epi-

Paleozoic Turanskaya Platform, and is part of a disjunctive zone bounding the East-European Platform to the east and south-east. The fault is clearly evident in the foundation and displaces layers of the earth's crust vertically for several kilometres. It is linked to the formation of the South-Emba aulacogen, and in the early and middle Paleozoic it already delineated the carbonaceous and greywacke formations of the Devonian - Early Carboniferous. In the magnetic field, the fault is marked by an abrupt change in course of magnetic anomalies, and in the gravimetric field - by linear zones of intense gravity peaks. On the satellite images, it is traced by intermittent lineaments dividing the region of moderate uplifts of the Poduralsky denudation plateau from the North-Ustyurt plains composed of a Middle Miocene - Quaternary sediment complex.

Among the diagonal southeast lineaments, the Azgirsky and Zholdybai linear morpho-structures are evident, running across the Pre-Caspian Trough within the area under investigation.

The Azgirsky linear morpho-structure corresponds to the fault of the same name identified by V.S. Zhuravlev and Yu.Ya. Kuzmin (1960). This fault is probably deep and ancient, as it coincides with the division between dissimilar magnetic fields (slightly anomalous to the north and fairly intense banded anomalies to the south of the fault). It is traced less reliably with reference to geomorphological criteria. The Azgirsky lineament zone has a concentration of active salt domes, which may indicate an extremely intense redistribution of salt strata at the present time. The modern rate of growth of the domes has been measured and observations of special reference marks have shown that the surface of mount B.Bogdo is rising by 1mm a year, and the bottom of lake Baskunchak is settling by the same amount (KDCP, 2002).

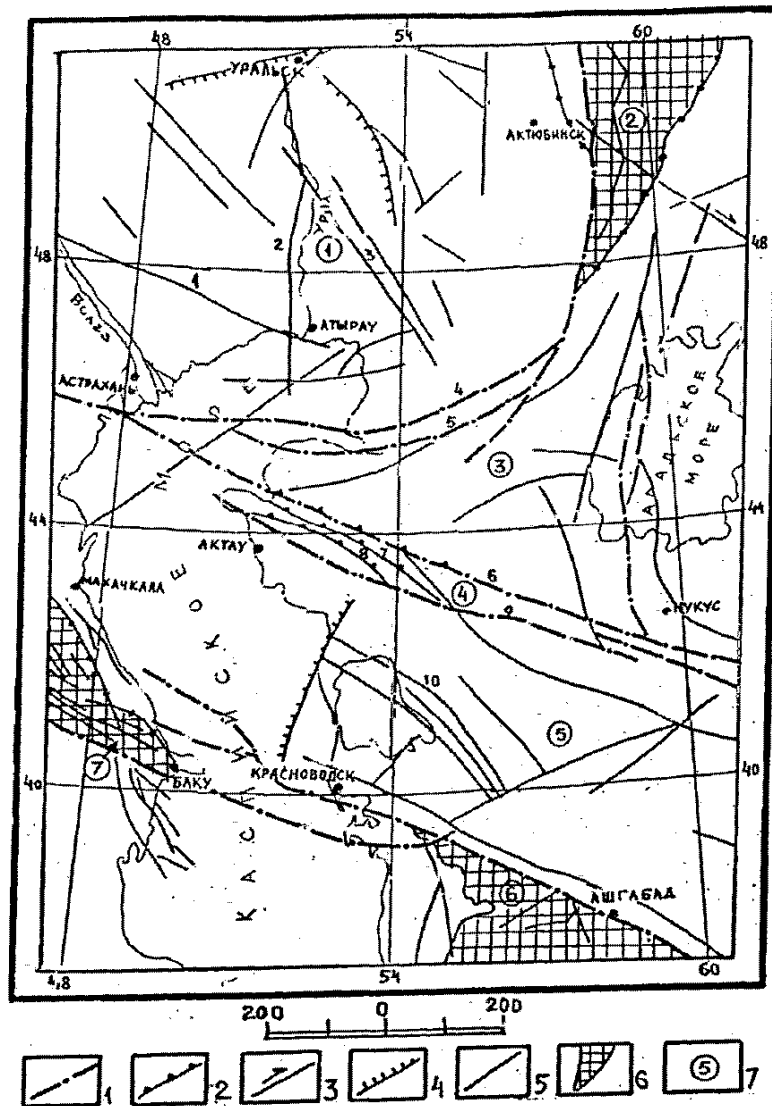


Figure 30: Diagram of recent (active) faults in the Caspian and Turanskaya Platform regions, after KDCP, 2002.

1 - Deep fault zones without division into kinematic types; 2 - up throw and up throw-overthrust faults; 3 - displacements; 4 - flexures; 5 - other faults; 6 - montane uplifts; 7 - structural zones (1 - Pre-Caspian, 2 - Uralskaya, 3 - North-Ustyurt, 4 - Central-Mangyshlak-Ustyurt, 5 - South-Mangyshlak-Ustyurt, 6 - Kopetdag, 7 - Kavkazskaya) Names of principal faults (numbers next to lines): 1 - Azgirsky, 2 - Uralsky, 3 - Zholdybai, 4 - South-Emben, 5 - North- Ustyurt, 6 - Central-Mangyshlak-Ustyurt, 7 - South-Karatau, 8 - Karatau-Tumgach, 9 - South-Bekebashkuduk- Shakhnaktinsky, 10 - North-Karabogaz.

The Zholdybai linear morpho-structure is also traced by its association with local troughs, depressions in the relief and salt domes, the occurrence of which is attributed to the active redistribution of salt strata in recent times. The Zholdybai lineament is not reliably confirmed on the geophysical traces. Its south-east flank is marked by the boundary between the moderate uplift region of the Poduralsky Plateau and the Prikaspiisky Plains which subsided in the Quaternary period.

The Uralsky lineament is traced along the Ural River valley from Atyrau to Uralsk (Eventov and Pronichev, 1967). Over its full extent, it is characterised by a high density of linear relief and

hydrological features, forming a unified zone. In addition, the elevation difference of the Khvalynsky terrace on the left and right hand banks of the Ural River is clearly evident over the full extent of the valley within Kazakhstan. The surface of the Khvalynsky terrace is 2-3m higher on the left bank than the surface of the same terrace on the right bank. It follows from this that the Ural River valley is associated with a fault zone, where the land to the east of the valley is a raised block, with a lowered block to the west. An example of the modern activity of this zone is the horizontal displacement of the dry bed of the Ural River 10m to the southeast in the vicinity of Topoli village.

At the same time, the southeast edge underwent a rising movement, producing head pressure and leading to the formation of a new bed following the line of the fault to the south-west. Modern displacements of this kind can also occur in areas of active salt tectonics.

3.1.2.6 ***Seismicity***

The Northeast Caspian is a stable zone in terms of seismic activity. Earthquake activity of the Caspian region is concentrated around the perimeter of the southern Caspian Sea and along a northwest-southeast trend across the central Caspian Sea extending from Azerbaijan to Turkmenistan. The seismic trend across the Caspian Sea (Figure 31) is actually comprised of two parallel belts based on mapped structural trends and deep crustal faults that have been mapped or inferred across the Caspian Sea.

The southernmost belt has relatively fewer earthquakes and coincides with the Apsheron Sill, which is a broad thrust-faulted fold. Higher seismicity is apparent in the northern belt that includes the possible sub-sea extension of the Greater Caucasus geologic structures, (Granherne, 2006).

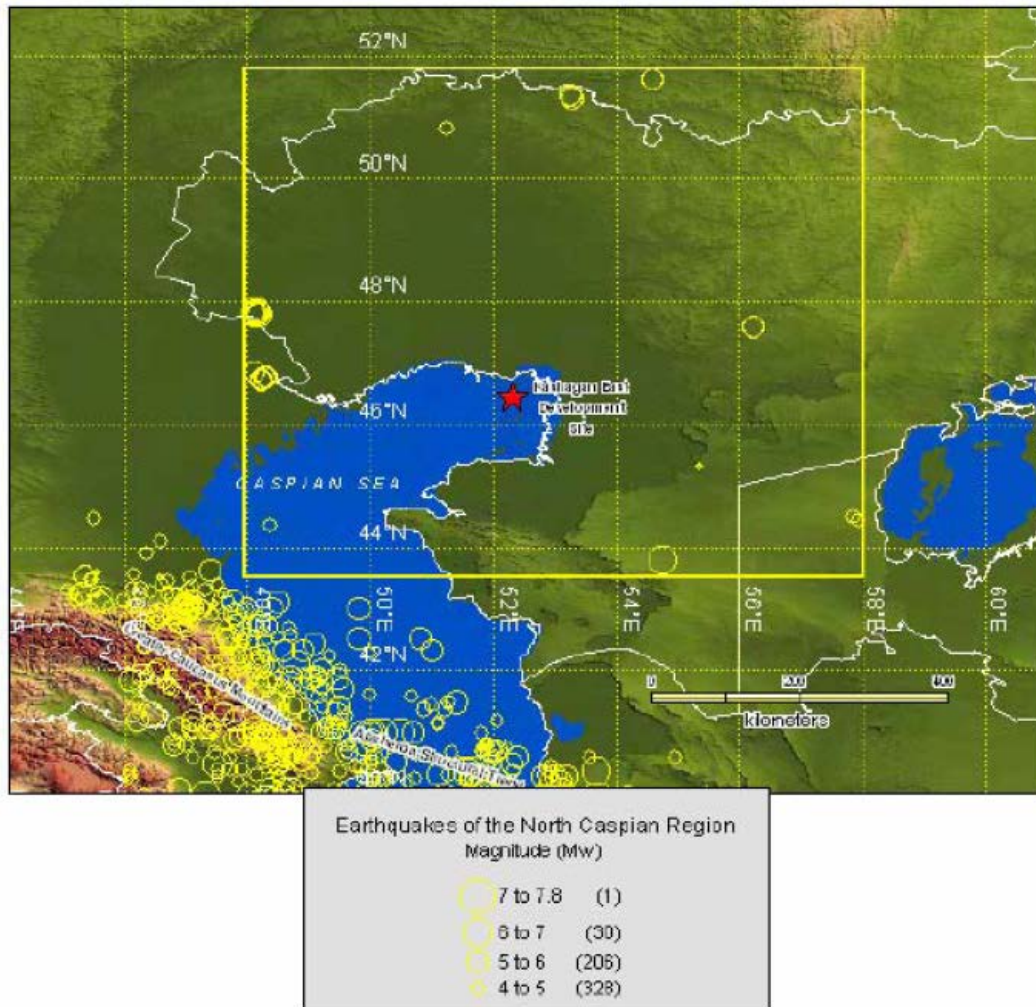


Figure 31: Earthquakes of the North Caspian Region, after “Granherne, 2006”.

The 1895 Krasnovodsk earthquake (Magnitude 7.5 - 8.0) occurred in the northern trans-Caspian seismic belt on the Krasnovodsk Peninsula in western Turkmenistan. This earthquake is the largest reported in the area of the eastern Caspian Sea and occurred on July 8, 1895. Strong shaking occurred on the Krasnovodsk Peninsula in Turkmenistan. The MSK intensity of this earthquake has been estimated to be 10 by Bune and Gorshkor (1970). This earthquake was located more than 650-km south of the Kashagan development in a distinct seismotectonic province. Therefore it is likely that the earthquake exhibited very low seismic effects at the development site. Earthquakes that have occurred north of the trans-Caspian seismic trends are very sparsely distributed (Figure 31).

The northern Caspian Sea is part of a tectonically stable region comprised of the East European and Turan platforms (Zoneshain et al., 1990). This region is characterised by a lack of significant tectonism and, consequently, a very low frequency of earthquake occurrence. These stable platform regions, as the name implies, are some of the Earth’s least active areas

with regard to earthquake activity. These areas constitute the oldest areas of continental crust where the most active geologic processes are erosion and deposition.

3.1.3 The North Ustyurt Basin Structure

The triangular-shaped North Ustyurt basin occupies the northern part of the Ustyurt Plateau in Kazakhstan and Uzbekistan and adjacent lowland areas. The basin area is approximately 250,000 km², most of which is onshore. Only small parts of the basin are in the Caspian Sea and Aral Lake (Figure 32).

The northwestern basin boundary is concealed by thin Mesozoic and Tertiary sediments; it is drawn along the southern flank of the Paleozoic South Emba high (Figure 33). The high is marked by large positive gravity and magnetic anomalies that probably are related to the presence of Middle Devonian and previous volcanics (Kan and Tropp, 1996). Thick Upper Devonian–Visean deformed greywacke clastics occur between the volcanics and thin (500–600 m) Mesozoic sediments in the central zone of the high. The South Emba high plunges southwestward and the geophysical anomalies disappear in near shore and offshore areas of the Caspian Sea, where the boundary between the North Ustyurt and North Caspian basins is poorly defined. This boundary is drawn conditionally along the pinch-out zone of Kungurian (Lower Permian) salt. The exact location of the pinch-out zone is difficult to determine from seismic sections; some geologists have suggested that the salt extends into the marginal areas of the North Ustyurt basin. The southern basin boundary extends along the Central Mangyshlak and Central Ustyurt uplifts (Figure 33). The central Mangyshlak uplift is a structurally inverted and deformed Late Permian–Triassic rift. In the present-day structure, it is a foldbelt composed of a series of thrust anticlines. Sinrifting clastics are exposed in cores of the structurally highest anticlines. The Central Ustyurt uplift is a Hercynian suture that is covered by thin Jurassic-Cretaceous sediments. Below these sediments, several wells penetrated middle Paleozoic partially metamorphosed clastic, carbonate, and volcanic rocks (Letavin, 1980). The western continuation of the suture is unknown; probably it is buried beneath the younger Central Mangyshlak rift.

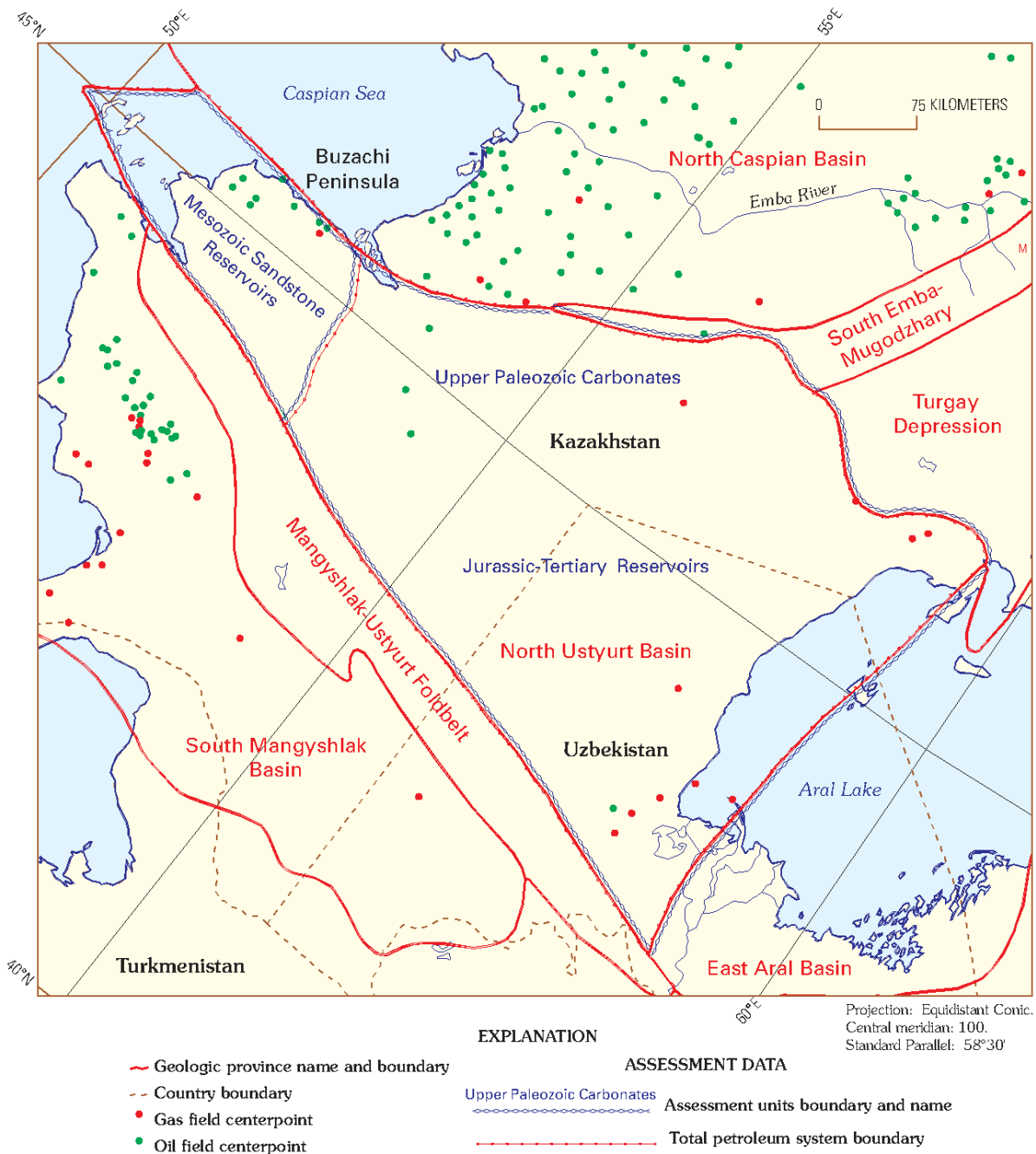


Figure 32: Petroleum system and assessment units of the North Ustyurt basin, after “Ulmishek, 2003”.

The eastern basin boundary has not been drilled; most of it is offshore in the Aral Lake. On the basis of seismic data, the basin is bounded by the north-trending Aral-Kizylkum uplift (Figure 33). Across this uplift, upper Paleozoic platform formations of the North Ustyurt basin are in contact with contemporaneous deformed and metamorphosed basement rocks of the East Aral basin, whereas Jurassic and younger formations are continuous between the basins.

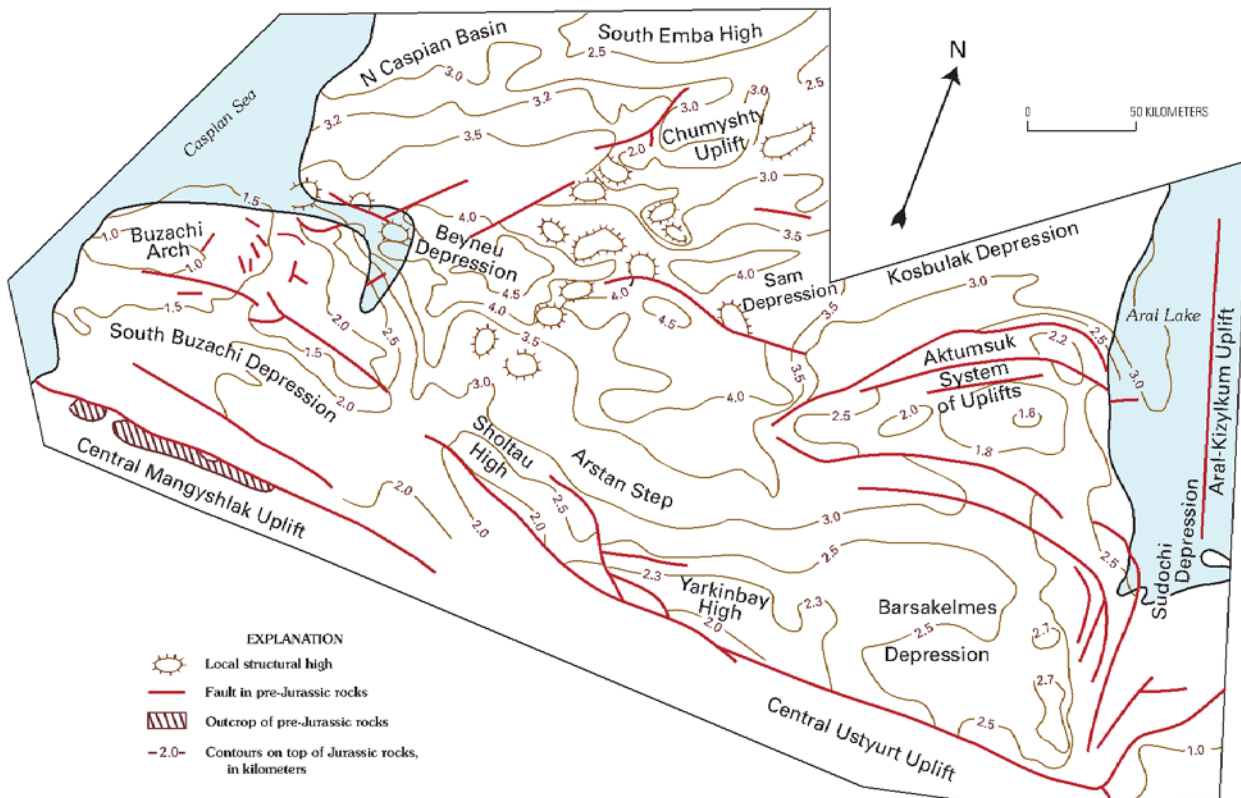


Figure 33: Principal structural unit of the North Ustyurt basin, after “Ulmishek, 2003”.

3.1.3.1 *Tectono-Stratigraphic Development*

The North Ustyurt basin is a simple, deep, Jurassic-Tertiary sag that unconformably overlies more complex and poorly known pre-Jurassic structures. The age of the basement is not known; age estimates include Early Proterozoic, similar to the age of basement of the Russian craton (Khain, 1977), Late Proterozoic (Milanovsky, 1987), or late Paleozoic Hercynian (Letavin, 1980). Seismic and limited drilling data indicate that the basement of the basin probably is not a homogeneous block. The southern zone of relative uplifts, where the basement is at depths of 5.5–8 km (Sholtau and Yarkinbay highs, Arstan step, and Barsakelmes depression in Figure 33), forms a stable block of granite crust of possible Precambrian age. The northern zone of deep (9–11 km) basement (Beyneu, Sam, and Kosbulak depressions in Figure 33) possibly has oceanic or thinned transitional crust.

Limited drilling and seismic data indicate that the basement of the Sudochi depression is Caledonian in age. It is composed of thick, lower Paleozoic, slightly metamorphosed, deep-water shales and small blocks of Precambrian crust. These rocks were deformed in the Early Devonian; they were overlain by Early– Middle Devonian orogenic molasse clastics and were intruded by granites. This basement composition is similar to that of the Central Kazakhstan

high (Paleozoic Kazakhstan continent), indicating a possible genetic affinity of this high with the North Ustyurt block.

During Late Devonian through Early Permian time, the North Ustyurt basin developed as a cratonic block. Rocks of that age are platform-type carbonates and clastics that unconformably overlie various older deposits. Seismic data show development of a relatively deep water Carboniferous basin in the Sudochi depression and offshore in the southern Aral Lake (Pilipenko, 1990). The collision time of the North Ustyurt block with the Russian craton margin along the South Emba suture is poorly defined. Judging from the geology of the northwest slope of the South Emba high in the North Caspian basin, the time of collision probably was pre-late Visean; alternatively it may have been Early Permian (Artinskian). Collision along the southern basin suture occurred in Early Permian time. The eastern boundary suture also is Hercynian (Late Carboniferous– Early Permian); it was formed by collision of the Kazakhstan continent and the Russian craton. Hercynian deformations in the North Ustyurt basin are deeply buried and poorly known. Significant uplifts may be deduced from the presence of thick Artinskian clastic clinoforms north of the South Emba high (Sapozhnikov et al., 1986). The clastic material was derived from the North Ustyurt block.

Late Permian–Triassic rifting in the area of the present Central Mangyshlak uplift along the southern border of the North Ustyurt block indicates post-collisional relaxation and north-south extension. However, thick continental clastic sediments of the same age were derived from the Hercynian terrane on the east, where orogeny apparently continued. The next and most important stage of deformation in the basin took place in latest Triassic or earliest Jurassic time; it was related to closing of paleo-Tethys in the south and collision of the Iran and other continental blocks with the Eurasian Tethyan margin. The Central Mangyshlak rift was compressed, inverted, and deformed, and thrusting occurred in some areas of the North Ustyurt block. Especially intense thrusting took place on the Buzachi Peninsula and offshore (Figure 34); however, reverse faults and thrusts in Triassic rocks also are known from seismic surveys in more eastern basin areas. Since Jurassic time, the North Ustyurt basin developed as a gentle sag, in which sediments as thick as 5 km were deposited. Only mild deformations, some of which were rejuvenated movements along Triassic thrusts, are known.

Uplift and formation of the present-day Ustyurt Plateau took place in post-Sarmatian time. Dense Sarmatian (upper Miocene) limestones and sandstones armour the surface of the plateau and prevent it from erosion.

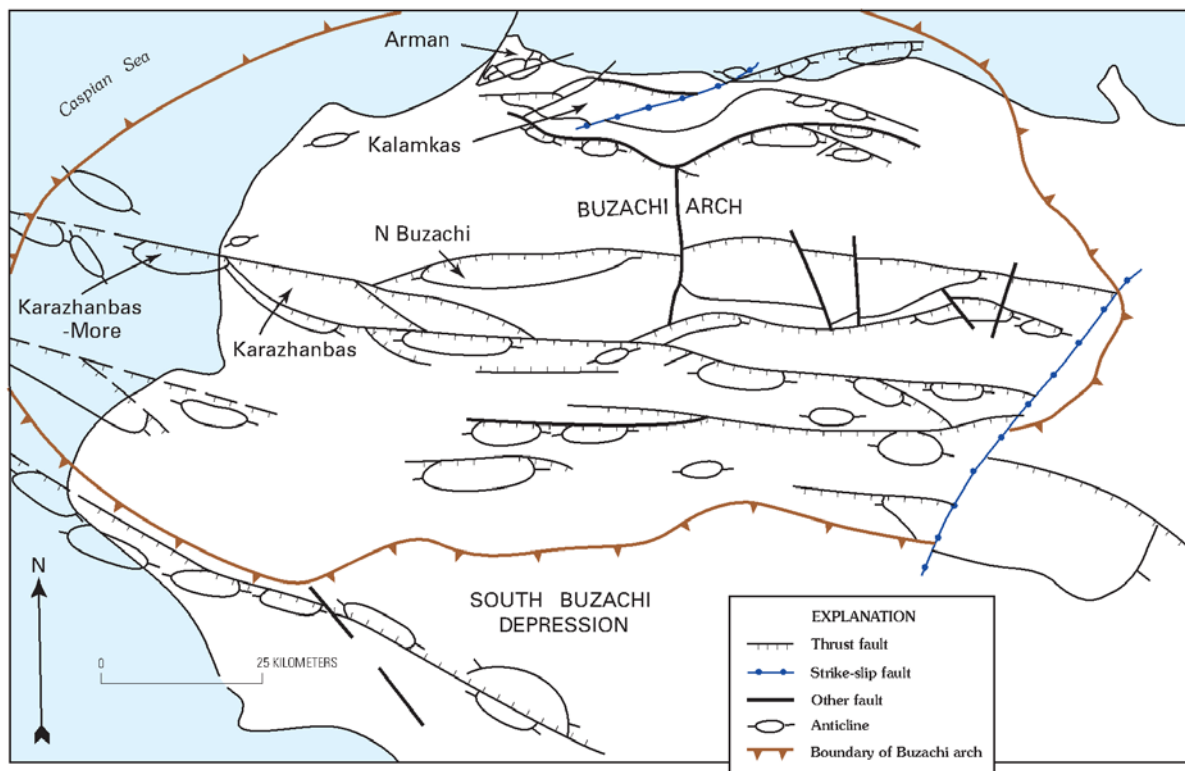


Figure 34: Generalized structure of Buzachi arch and adjacent areas, after “G.F. Ulmishek, 2003”.

3.1.3.2 *Present-Day Structure*

The main features of regional structure of the Jurassic-Tertiary sedimentary cover are shown in Figure 33. The southern and central zones of the basin are relatively uplifted. In these zones, the surface of Jurassic rocks gently dips northward from depths of 2–2.5 km in the south to 3–3.5 km in the north. Farther north, the uplifted zones are bordered by a system of depressions, in which the Jurassic surface lies at depths of 4–4.5 km and the base of the Jurassic is at 5 km and deeper. The system includes the Beyneu, Sam, and Kosbulak depressions (Figure 33). Still farther to the north, the depressions grade to the gentle southern slope of the South Emba high.

Post-Triassic structure of the Buzachi Peninsula has been mapped in detail because this area contains most of the discovered petroleum reserves of the North Ustyurt basin. The core of the structure is the Buzachi arch (Figure 34), with closure of about 3 km. On the crest of the arch, the base of Jurassic rocks is at a depth of less than 1 km, and Cretaceous rocks crop out. The arch dips northward abruptly into the Beyneu depression and its offshore continuation and dips gently southward into the South Buzachi depression. Both the arch and the South Buzachi depression contain several zones of linear asymmetric anticlines that are expressed in Jurassic and younger strata (Figure 34). The anticlinal zones are underlain by blind thrusts in

Triassic rocks and extend offshore. The structural framework of older parts of the sedimentary cover is virtually unknown because the thickness of Upper Permian–Triassic red beds is great (2.5–3 km) and older rocks have been penetrated by only a few wells (Ulmishek, 2003).

3.1.3.3 *Recent active faults*

For the region as a whole, the predominant direction of strike is north-west (290-300°) and north north east (20-40°), although the pattern of the fault network within the Precambrian and epi-Paleozoic parts of the platform is somewhat different. The former is characterised by sub latitudinal and north-north-east orientation of faults, and northwest orientation at the boundary with the Pre-Caspian Trough. For the Mangyshlak-Ustyurt region, the predominant direction of strike is west north west (290-310°) and north northeast (20-40°). The faults of northwest orientation coincide with the strike of the principal structural zones of the Mangyshlak foundation, were formed in the concluding period of the geo-synclinal development stage, and by their nature are compression structures. The most important faults are briefly described, in terms of structural significance, with reference to marginal sutures or inter-block sutures.

The marginal sutures dividing the ancient East-European and young Turanskaya platforms include the North-Ustyurt fault located to the south of the South-Emba fault and forming a marginal boundary zone in conjunction with the latter. The boundary between these platforms of differing ages has a overthrust character, and the young platform structures are thrust over to the north. The overthrust character of the articulation is confirmed by seismic survey data on the Buzachi Peninsula and North Caspian (Ismagilov, Popkov et al., 1990). In addition, deep drilling and seismic profiling have demonstrated overthrusting of the Paleozoic folded structures with an amplitude of horizontal overlap of 40-50km. The North-Ustyurt fault is traced at the surface by a series of lineaments with different orientations visible on the satellite imagery.

An important role in forming the modern structure of the Mangyshlak-Ustyurt system of dislocations is played by the Central-Mangyshlak-Ustyurt fault that marks the boundary between the North-Ustyurt and Mangyshlak-South-Ustyurt blocks of the Turanskaya Platform. This fault forms part of a planetary-scale band of deep faults along the southern edge of platform plains extending over 4000 km from the Belorussian massif to the Tien-Shan. The Central-Mangyshlak-Ustyurt fault consists of several imbricated dislocations of northwest strike accompanied by numerous marginal ruptures of sub latitudinal orientation branching off the main displacer at acute angles. The fault is clearly traced in the foundation by the 18 abrupt changes in sign of the geomagnetic field, and divides regions of dissimilar crustal types. To the north of the fault, the crust is characterised by reduced thickness (2-7 km) of the upper sialic

complex and increased thickness (up to 15 km) of the lower basitic complex, and to the south – by increased thickness (20 km) of the upper sialic complex and reduced thickness (<15 km) of the lower basitic complex. It should be noted that the Central-Mangyshlak-Ustyurt fault divides regions of different Hercynic development – eu-geo-synclinal in the south and mio-geo-synclinal in the north. In the late Paleozoic and early Mesozoic, grabens (Mangyshlak aulacogen) and horsts (Central-Ustyurt) formed in the fault zone. In the late Mesozoic and Cenozoic, folding-overthrust dislocations occurred extensively in the fault zone under conditions of submeridional horizontal compression. Finally, significant gradients of recent movements are observed in the area of this fault, attributable both to their differing intensity on either side of the suture, and to the differing directionality of these movements.

3.2 STRATIGRAPHY

In the sedimentary cover sequence, a subsalt, salt and suprasalt complexes are distinguished. Almost the entire section (over 90%) is composed of marine deposits, about one quarter of which is carbonate rocks.

Subsalt complex is subdivided into two parts: lower, pre-Eifelian sandy-shale sequence with participation of effusive sedimentary rocks and upper, Eifelian-Artinskian with terrigenous, carbonate terrigenous and carbonate sulphate types of sequences. In the younger, upper part of the complex, on the basis of major unconformities and other characteristic features, the certain structural stages are recorded: Devonian-Tournaisian, Viséan-Gzhelian, subsalt Lower Permian (Artinskian). In subsalt deposits of the Caspian Depression, 38 oil, oil-gas condensate and gas fields were discovered (mostly, of massive type with abnormally high formational pressures).

Salt-bearing complex is composed of rock salt with interbeds of anhydrites, dolomites, potash magnesium salts as well as terrigenous rocks. Initially, salts occurred as sheets; however, with accumulation of suprasalt sequences, large local accumulations of salt rocks started forming; between them, the thickness of salts decreases abruptly to complete omission from the section. Generally, salts form a common mass, within which diapirs of different height are separated by local depressions. Height of salt domes within the Tengiz-Karaton uplifts reaches 4 km; then the occurrence depth of dome arches decreases to 1-2 km.

Suprasalt complex is composed of shallow and lagoonal-continental deposits from the Upper Permian to the Quaternary inclusive. Thickness of deposits varies markedly through area and is directly related to the arrangement and configuration of salt structures. In certain intradome zones vertical thickness of the suprasalt complex reaches 5 km. Above the dome arches, thickness is reduced. Contacts of suprasalt deposits with salt are commonly unconformable and transgressive. Discontinuous contacts are frequent, particularly pronounced on broken domes. In the study area, four openly broken-through salt domes are known within the modern Ural River delta. A synthetic description of the whole stratigraphic column is given.

Deposits of the subsalt complex in the study area are represented with Upper Devonian-Lower Carboniferous terrigenous carbonate rocks, Middle Carboniferous limestones and dolomites as well as clayey and carbonate-sulphate sandy Lower Permian rocks.

Salt-bearing complex belongs to the lower series of Permian system, more precisely – to the Kungurian stage. Under it, boreholes penetrate the Artinskian deposits characterized by fauna; resting directly on salt are gypsified clays, marls and sandstones of the Ufimian stage (upper

series of the Permian), which complete the salt accumulation stage in the Caspian Depression. Section of the suprasalt complex starts with thick Upper Permian clayey-sandy sequence. Triassic is composed of sand-pebble and sand-clayey sequences. Lower Jurassic deposits are mainly coarsegrained, terrigenous with pebble interbeds. Thickness is 80-140 m. Characteristic Middle Jurassic deposits are composed of sandy-clayey rocks. Thickness is up to 360 m. Upper Jurassic sequence is composed in the lower part of clayey rocks with sandstone interbeds; in the upper part, limestones, clayey limestones and marls prevail. Thickness is 550-630 m.

Cretaceous deposits are represented by all stages of the stratigraphic chart starting with Valanginian and ending with Danian. Lower series is composed of clays, siltstones, sands and sandstones with total thickness of about 1,000 m. Upper series, except for the terrigenous Cenomanian, is made up of marls, chalk, limestone to 500 m thick.

Paleogene formations make up a uniform clayey-marly sequence with opoka-like clays and calcareous siltstones in the lower part and carbonate clays above. Deposits of the Neogene system are mainly composed of clay-marly and sandy rocks of the Apsheronian and Akchagylian stages (Pliocene). Total thickness of Paleogene and Neogene ranges within 130-320 m (Abdulin A.A., 1981).

Quaternary section typical of the study area is 30-35 m thick and is stratified as follows on the basis of drilling evidence:

- Lower Quaternary Baku Horizon is penetrated at a depth of 15-28 m. Thickness is 5-10 m. It is composed of dense grey and fat brown calcareous clays; in places, sandy and ferruginated.
- Khazarian (Middle Quaternary) Horizon has a continuous occurrence at a depth of 10-18 m. Brown gypsified clays, interbeds and lenses of fine-grained sands and siltstones. Above, coquina interbeds of 0.5-1.0 m are recorded.
- Khvalynian (Upper Quaternary) Horizon. Thickness 5-7 m. Dense structureless brown clays and loams with interbeds of light calcareous sandy loams and fine-grained sands. Upper Khvalynian deposits are exposed at absolute elevations above 22 m.
- Novocaspian (Holocene) Horizon. Fine-grained and dust-like sands, sandy loams, loams, sandy silts and clays, coquina. Thickness to 7 m. Deposits are associated with the last Caspian Sea transgression, its maximum reaching minus 22 m.

Modern Caspian deposits are distinguished (Upper Novocaspian); on the coast, they are recorded to elevations of -26 m. The latter, besides the listed forms, also contain *Mytilaster lineatus* Gmel (Stratigraphic Glossary of the USSR, 1982), which penetrated to the Caspian Sea at the beginning of the XX century.

Continental Quaternary deposits comprise alluvial loams, sandy loams and sands of the modern Ural and Emba river deltas to 10 m thick, alluvial deposits of their floodplains and riverbeds as well as inequi-granular sands and sandy loams in narrow valleys of modern streams. Deposits of sors are composed of brown-grey salinized sandy loams, sands, loams and clays 1-2 m thick. Aeolian sands 2-4m thick occur now and then.

The oldest rocks that have been drilled in the North Caspian basin are of Early and Middle Devonian age. Lower Eifelian shallow-shelf carbonates overlain by upper Eifelian– Givetian deep-water organic-rich calcareous black shales were penetrated in the Karachaganak field on the north basin margin (Konyukhova, 1998). Undivided Lower Devonian–Eifelian and Givetian shallow-shelf carbonate rocks were also encountered in several wells on the east basin margin at depths of 5–6 km (Akhmetshina et al., 1993). Distribution of pre-Upper Devonian rocks and paleo-geographic conditions of their deposition in the North Caspian basin are virtually unknown. The stratigraphy of younger, upper Paleozoic (Upper Devonian– Lower Permian) subsalt rocks is known much better; this stratigraphy is complex and varies significantly on different basin margins.

3.2.1 North and West Basin Margin

The narrow north and west margin is characterized by the presence of three thick carbonate formations in the Upper Devonian– Lower Permian interval. These formations are separated by lower-middle Visean and lower Moscovian (Verey Horizon) clastic sections. Each carbonate formation forms a barrier reef trend and grades basinward into thin deep-water black-shale facies (Grachevsky et al., 1976). The clastic formations form clinoforms (clastic wedges) on the paleo-slope. Both basinward progradation of the formations and back-stepping of younger barrier reefs toward the outer shelves are known in different parts of the margin. Only a few local carbonate build-ups (atolls, pinnacles) have been discovered basinward from the barrier reefs, one of which contains the giant Karachaganak field (Figure 35). Several carbonate banks with possible pinnacle development are inferred at depths of 6–7 km along the margin, but only two such banks have been penetrated by several wells. Therefore, the extent as well as the presence of some of the banks remains speculative (Solovyev et al., 1992).

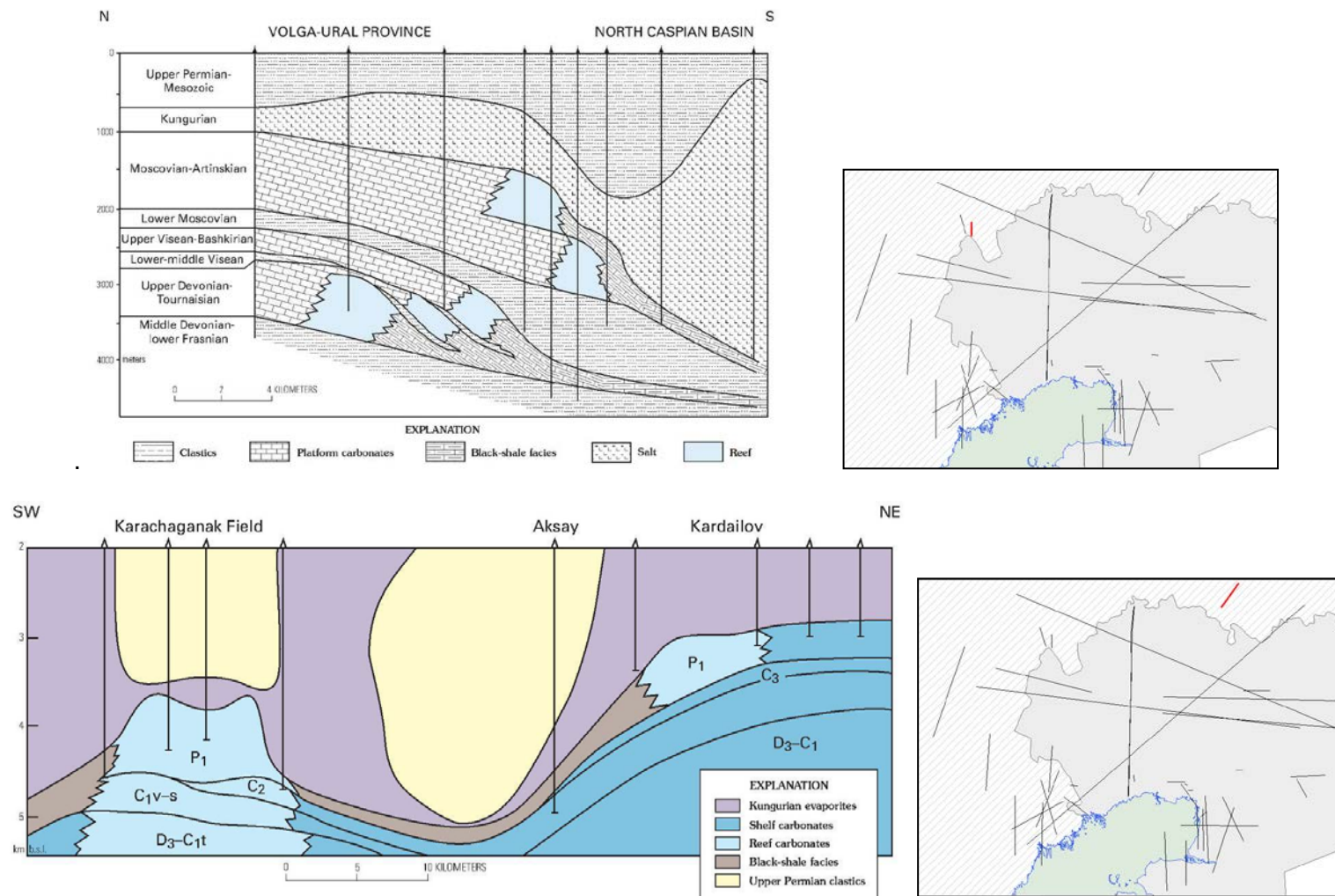


Figure 35: Cross-section through north basin margin. Located in the westernmost portion of the northern margin. After “Ulmishek, 2003” and Cross section through Karachaganak carbonate build-up, after “Ulmishek, 2003”.
D3, Upper Devonian; C1, C2, and C3, Lower, Middle, and Upper Carboniferous; P1, Lower Permian (Asselian-Artinskian); C1t, Tournaisian; C1v-s, Visean-Serpukhovian

3.2.2 East-Southeast Basin Margin

The main carbonate section of the east-southeast basin margin is of late Viséan–Late Carboniferous (in places as young as Early Permian) age. The section is separated into two parts, informally called KT-I (upper) and KT-II (lower) in Russian literature (KT stands for carbonate formation in Russian), by a shale interval in the middle Moscovian (Podol Horizon). Basinward, both carbonate formations grade into organic-rich black shales (radioactive shale beds of local nomenclature). The lower formation extends farther west and north compared to the upper one. Barrier reefs are present along basinal edges of both formations, but they are not as well developed as on the north and west margin (Figure 36).

The carbonate section of the east-southeast margin is underlain by the greywacke clastic Izembet (Zilair) Formation of Late Devonian–Early Carboniferous (Famennian-Viséan) age (Bakirov et al., 1991). Seismic data indicate that from the crests of basement arches of the Astrakhan-Aktyubinsk system toward the Urals and toward the South Emba high, the formation thickens from about 500 m to as much as 7,500 m. Clastic material was derived from the Mugodzhary microcontinent and Silurian volcanic arc (both presently incorporated into the Ural foldbelt), which were accreted to the craton in Middle Devonian–Frasnian time (Arabadzhi et al., 1993). Fine clastic material dominates the lower part of the Izembet Formation, which also contains some detrital carbonates; these rocks were probably deposited in a deep-water basin. Upward in the section, clastic material coarsens, and beds of conglomerates and thin coal seams appear. Apparently, clastic sediments from the Mugodzhary provenance did not reach the north half of the east basin margin. There, rocks correlative to the Izembet Formation are thin deep-water black shales overlying Frasnian limestones. Several wells have reached the bottom of the greywacke formation; they penetrated Lower Devonian and Frasnian carbonates (Akhmetshina et al., 1993). However, because of the great burial depths, the distribution of Devonian carbonate rocks remains poorly known.

The Middle–Upper Carboniferous carbonate formation is overlain by a thick section of Lower Permian orogenic clastics that form fans descending from the Urals and the South Emba high. Along the Urals, the clastic rocks are deformed into several lines of long, narrow anticlines probably associated with thrusts.

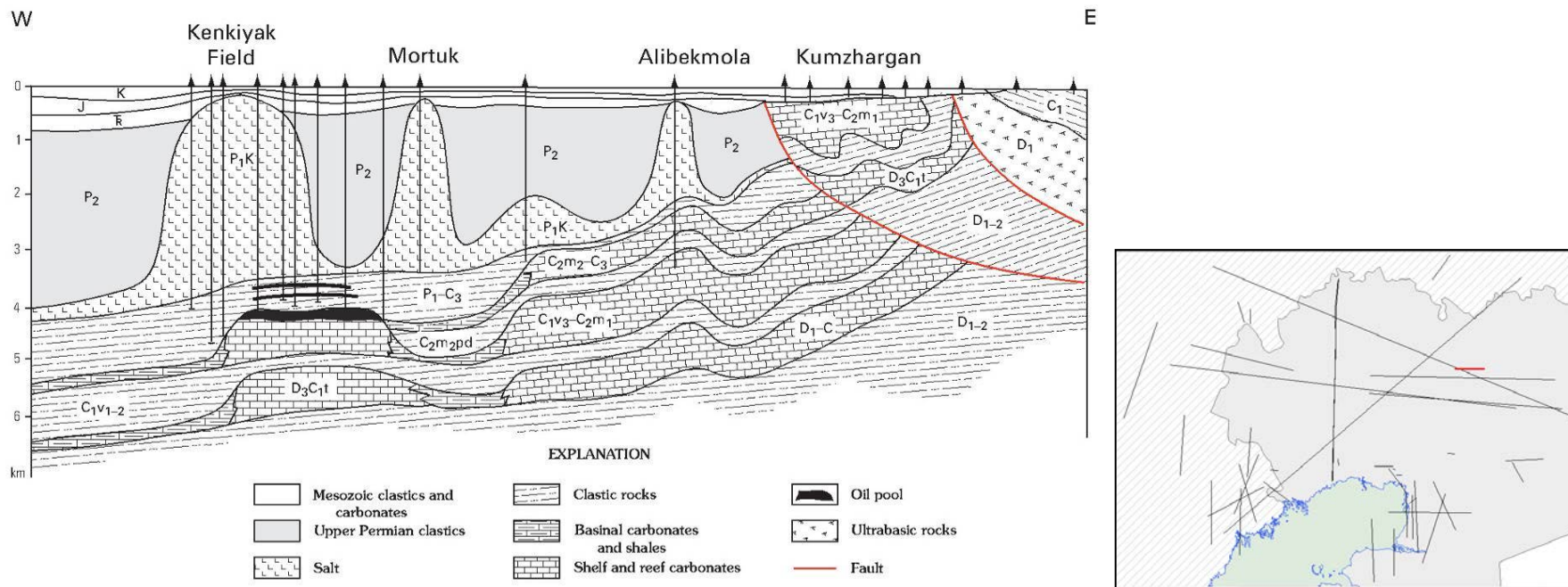


Figure 36: Cross section through east basin margin, after “Ulmishek, 2003”.

Suprasalt oil fields are not shown. Subscripts 1, 2, and 3 denote lower, middle, and upper subunits. D, Devonian; C, Carboniferous; P, Permian; t, Tournaisian; v, Visean; m, Moscovian; pd, Podol Horizon; P_{1k}, Kungurian; Tr, Triassic; J, Jurassic; K, Cretaceous.

3.2.3 South Basin Margin

Pre-Permian clastic rocks have not been encountered in wells on the carbonate platforms of the south basin margin; however, indirect evidence suggests that they may be present in the Middle Devonian of the Astrakhan arch. A few meters of clastic rocks recently penetrated at the bottom of a deep well at a depth of almost 6 km may lie at the top of the Middle Devonian (Orlov and Voronin, 1999). The Karaton-Tengiz zone in the eastern part of the south basin margin is composed of Upper Devonian through Bashkirian (Middle Carboniferous) carbonates that form large atolls many hundreds of meters high (Figure 37 and Figure 38).

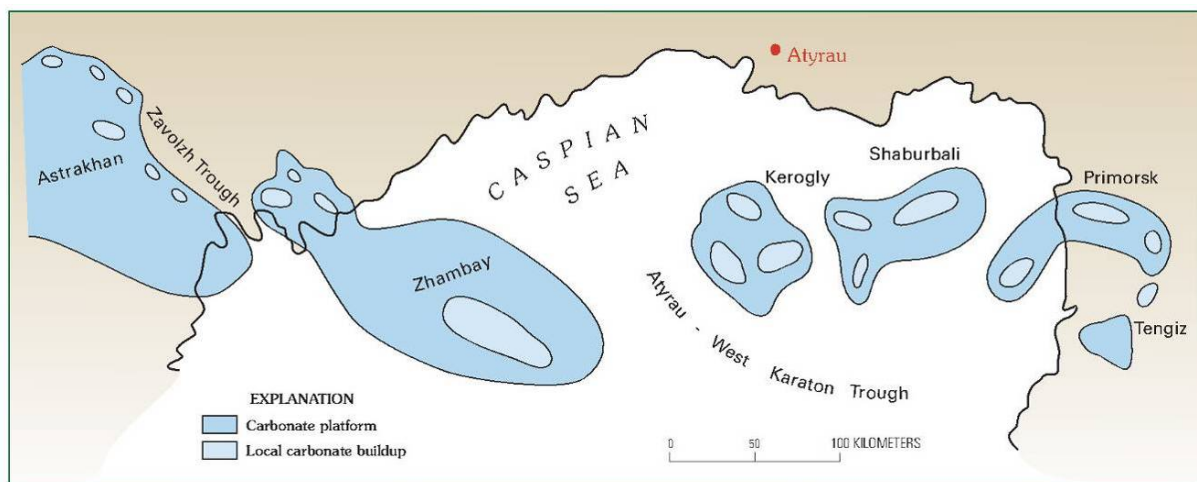


Figure 37: Carbonate build-ups of northern Caspian Sea. Scale approximate. After “Ulmishek, 2003”.

Outside the atolls, the carbonate rocks grade into a deep-water basinal facies. The tops of atolls are unconformably overlain by thin Lower Permian (mainly Artinskian) anoxic black shale that was deposited on submerged uplifts below the depth of organic carbonate sedimentation. The shale thickens rapidly on slopes of the atolls. The zone extends into the Caspian Sea, where several carbonate build-ups have been mapped by seismic surveys (Murzagaliev, 1995).

The Astrakhan platform west of the Caspian Sea is also composed of Upper Devonian to Bashkirian carbonate rocks. However, unlike in the Karaton-Tengiz zone, the platform is actually a flat carbonate bank slightly deformed into a gentle regional arch above the basement high (Figure 39). The giant Astrakhan gas field is located on the crest of the arch. Barrier reefs are developed along edges of the carbonate platform. The top of the platform is unconformably overlain by thin Lower Permian deep-water shales. Seismic data suggest the presence of a similar platform in the western area of the Caspian shelf (Figure 37).

South and west of the Astrakhan carbonate platform, the south basin margin is formed by a thrust belt north of the Hercynian Karpinsky foldbelt. In this thrust belt, known as the Karakul-Smushkov zone of deformation, Lower Carboniferous to Bashkirian carbonates are the oldest rocks penetrated by drilling. The carbonates underlie the Middle Carboniferous– Lower Permian clastic section that thickens to the north and is truncated by a pre-Jurassic unconformity to the south. The upper part of the section is composed of Artinskian orogenic clastic rocks as much as 1,000 m thick.

Throughout most of the basin, the Devonian–Lower Permian sequence is overlain by the Kungurian (uppermost Lower Permian) evaporite sequence, which is primarily composed of salt but includes some clastic and anhydrite beds. The evaporites are absent only in an extreme marginal zone adjacent to the Urals and along the south basin boundary where they are truncated by pre-Late Permian or pre-Jurassic unconformities (Figure 38).

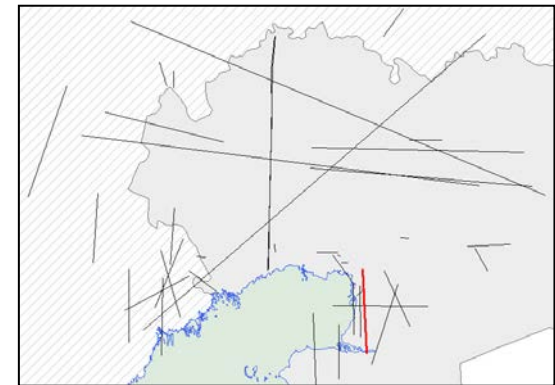
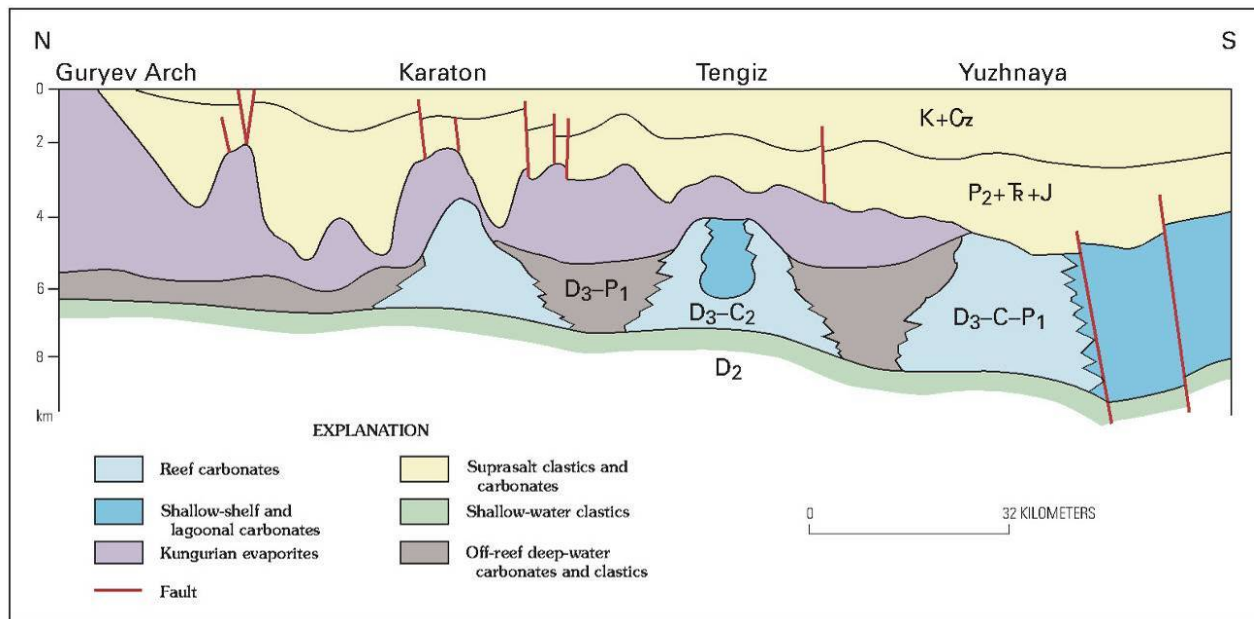


Figure 38: Cross section of Karaton-Tengiz zone, after “Ulmishek, 2003”.
D2 and D3, Middle and Upper Devonian; C2, Middle Carboniferous; P1 and P2, Lower and Upper Permian; Tr, Triassic; K, Cretaceous; Cz, Cenozoic.

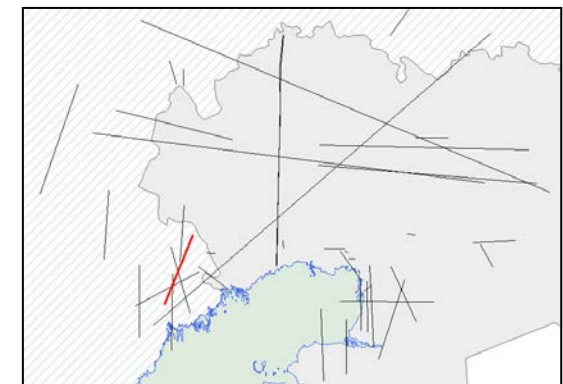
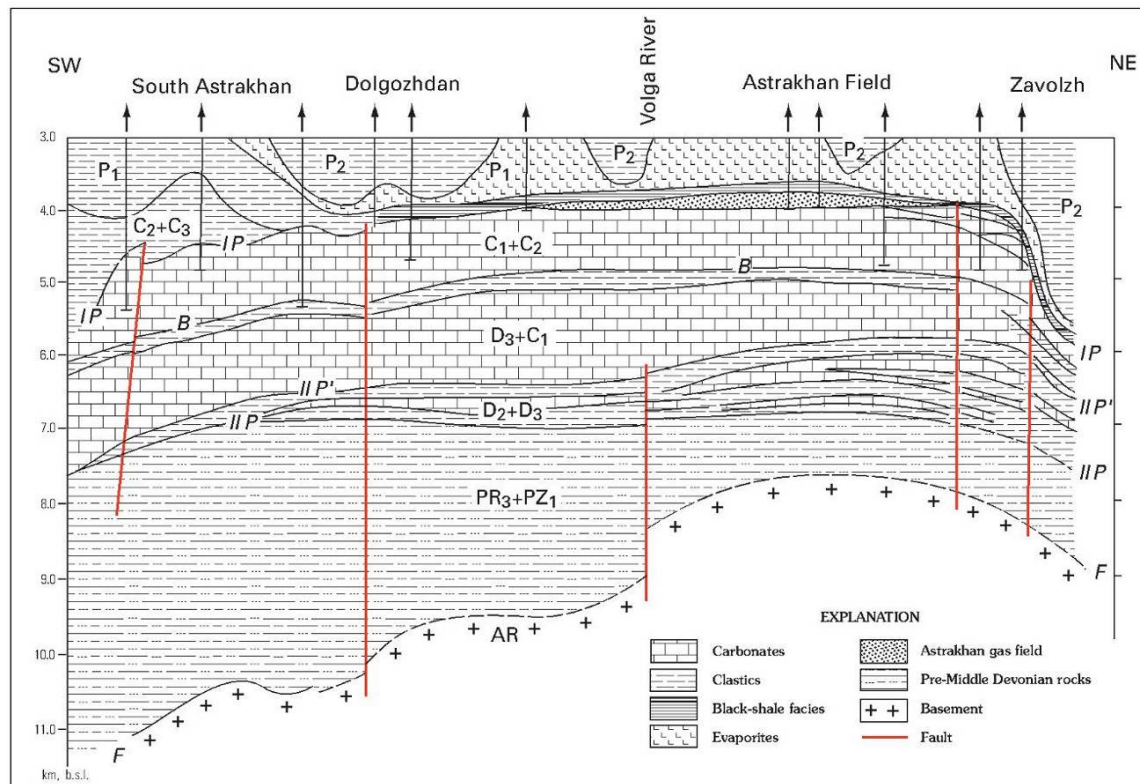


Figure 39: Cross section of Astrakhan arch, after "Ulmishek, 2003".

The arch constitutes westernmost segment of Astrakhan-Aktyubinsk system of highs. Scale is not available. Total length of section is about 60 km. AR, Archean; PR, Proterozoic; PZ, Paleozoic; D, Devonian; C, Carboniferous; P, Permian. Subscripts 1, 2, and 3 denote lower, middle, and upper subunits. Symbols B, I P, II P, II P' and F are referred to seismic reflector

3.2.4 Details on Zones B and C

The structure of the post-salt sequence consists of the Upper Permian to Neogene deposits inclusive, overlapped by Quaternary depositary cover. Upper Permian deposits occurring in the intradome zones and found in some places are the most ancient lithologic and stratigraphic divisions in this series. The overlying Triassic deposits are universally developed and involved in the structure of practically all intradome zones except young Jurassic-Cretaceous and Neogene compensatory intradome zones. Stratigraphic description is given on the basis of the sections penetrated by the wells drilled at the studied territory. Post salt section down to Kungurian deposits is penetrated by drilled wells in the crests of the domes (GAS, 2007; Figure 40).

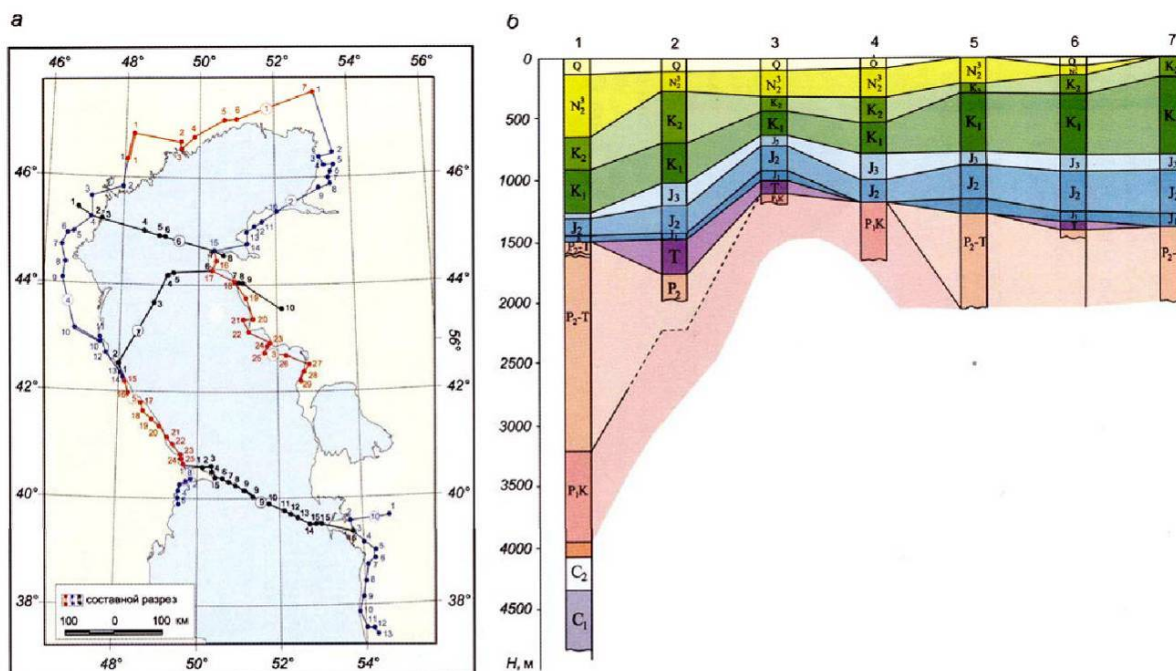


Figure 40: Well section stratigraphic correlation in Caspian Sea and coastal zones, after “GAS, 2007”.

a – location of well and correlation line, b – well section correlation on lines 1 (Astrakhan – Dossor), Well: 1 – Astrakhan -4 and composite section of Paleozoic deposits of Astrakhan anticline; 2 – Zhambay-22; 3 – Zhambay G-1; 4 – Oktyabrskaya G-2; 5 – Zhanatalap G-5; 6 – Martyshi G-3; 7 – Dossor G-518.

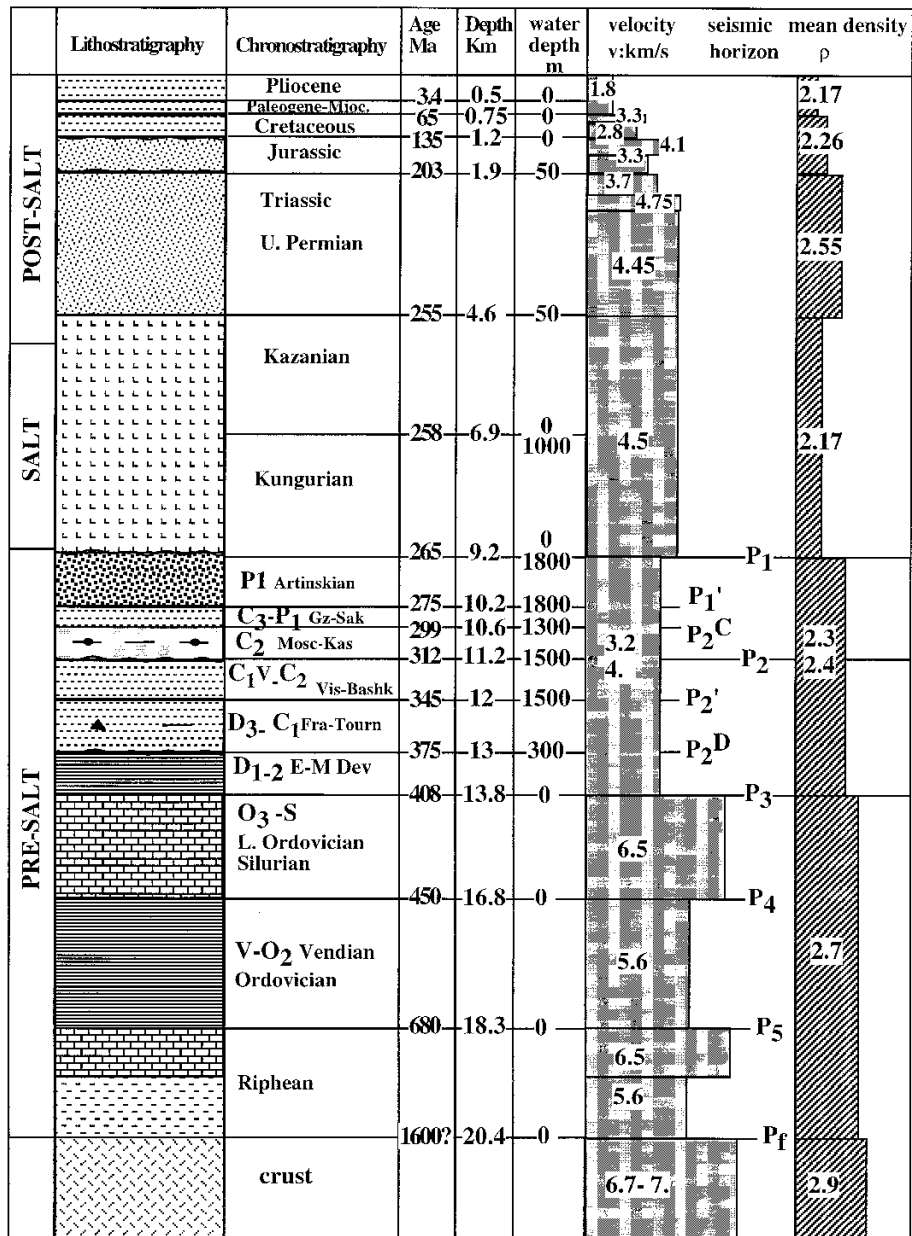


Figure 41: Synthetic column in the centre of the Precaspian basin, showing the thickness of sediments, paleo water depths, ages and main seismic horizons, with velocities and density.

Zone C is well studied because of the presence of Tengiz reservoir. In particular, works carried out by Harris P.M. clearly define the stratigraphical asset of the zone. However, these studies are focalized on the carbonatic body and the description of the post-salt sequence is not discussed in detail.

For better understand the stratigraphical asset of the area, some cross-sections are observable in the following pages (

Figure 42, and Figure 43).

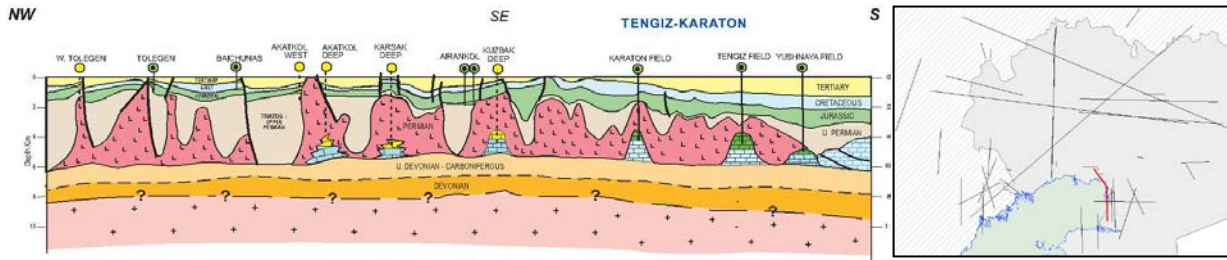
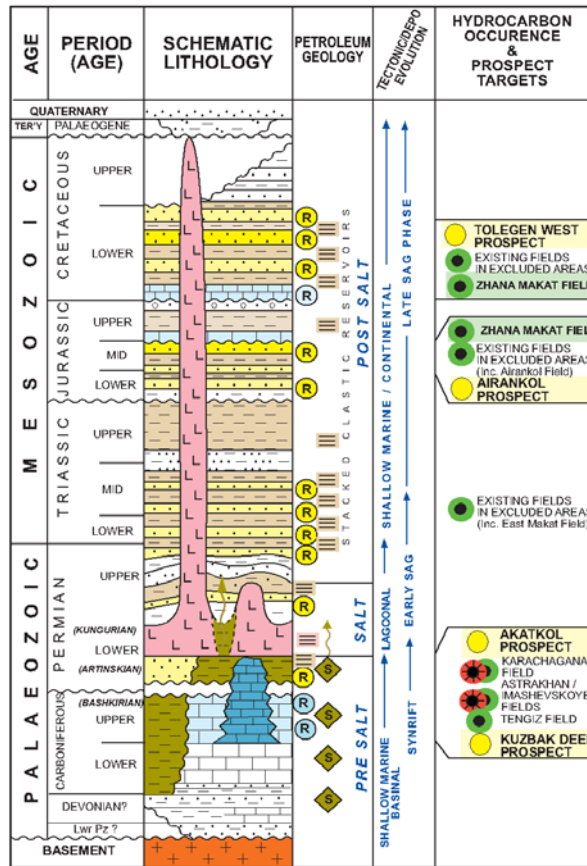


Figure 42: Schematic cross-section NW-SE across Tengiz-Karaton Platform, after “Max Petroleum, 2010”.

SUMMARY OF THE PETROLEUM GEOLOGY OF THE SOUTHERN PART OF THE PRE-CASPIAN BASIN



LEGEND:

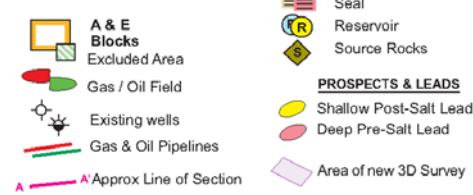


Figure 43: Summary of the typical stratigraphy in Zone C.

3.3 DETAILS ABOUT SALT DOME STRUCTURES

Considering the relevance of the Kungurian salt layer in the area (about 1800 structures in the Precaspian basin are attributed to movements of Permian salt (Ismail-Zadeh et al., 2004), a dedicated chapter has been written. The complexity of this topic is discussed above. It has been to note that salt in this area was matter of study from the beginning of the XX century. Oil in the Emba area has been produced from salt diapir structures since 1908, when a test at Karatchungul flowed at rate of 135 barrel of oil per day, and different others reservoirs started their production between the 1920 and 1930. A study of Sanders (1939) discusses in great detail (obviously, in relation with surveys techniques and knowledge available at that time); some examples elaborated in the '30s (map of salt domes in Southern Precaspian Basin and a dome section) are visible in Figure 44 and Figure 45.

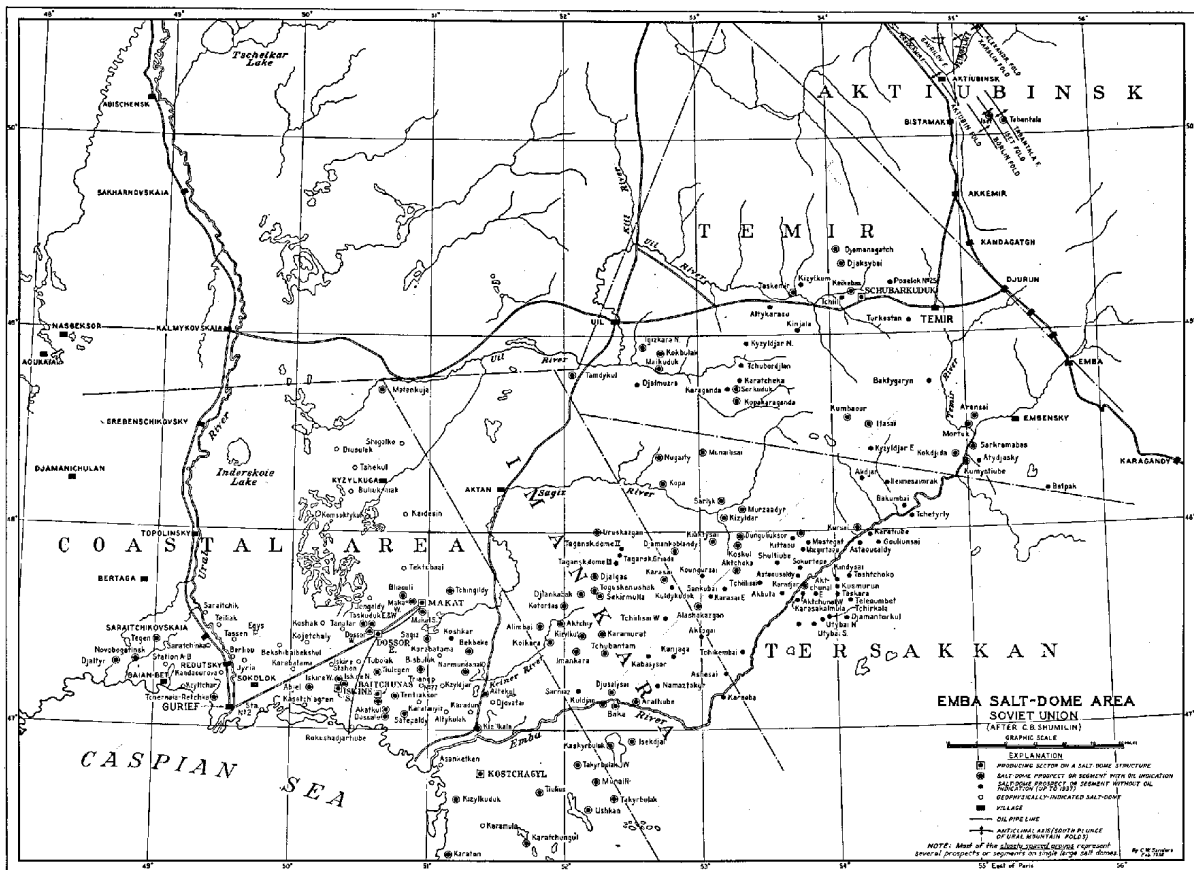


Figure 44: Historical map of salt domes in Southern Precaspian Basin, after “Sanders, 1939”.

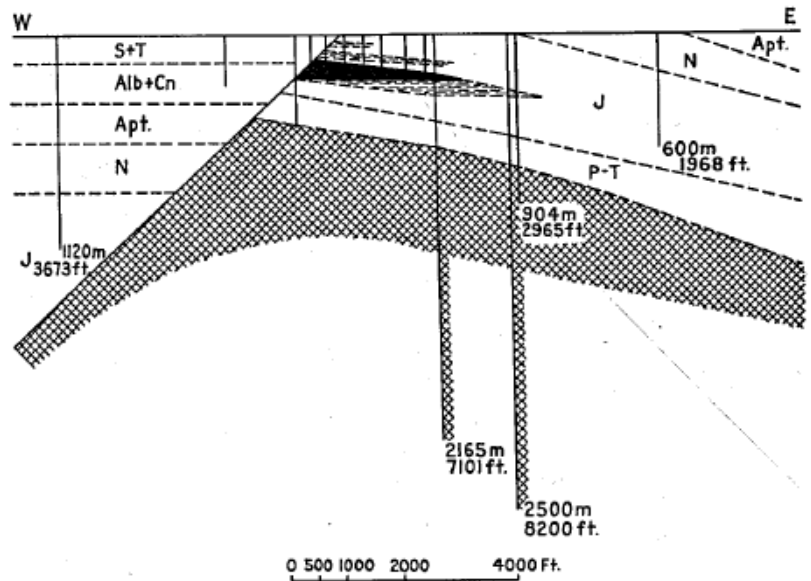


Figure 45: Historical dome cross-section, after “Sanders, 1939”.

Evaporitic caprocks in halogenic basins have regional significance. They play a crucial role in the formation of hydrocarbon fields. The base of evaporitic sections generally includes sulphate–carbonate rocks overlain by rock salt. In the process of lithogenesis, the residual brine is squeezed out into the underlying sulphate–carbonate sediments. Thus, their screening properties are upgraded and dense (virtually massive) evaporitic rocks are formed. The role of sulphate–carbonate rocks as caprocks is particularly important, because highly plastic halogenic rocks are squeezed out into salt domes. They are absent in intradome depressions, where the suprasalt rocks overlie basal layers of the evaporitic sequence. In such cases, the role of evaporitic caprock is played exclusively by sulphate–carbonate rocks, which are not as plastic as halogenic rocks and actually do not participate in the structure of salt domes. Isolating properties of evaporitic rocks are upgraded with increase in their grain size and depth of occurrence.

At shallow depths, they generally do not serve as caprocks (Kalinko, 1970). Evaporitic caprocks with a thickness of up to 20 m provide the reliable conservation of hydrocarbon pools. They are characterized by the following petrophysical parameters (density and velocity of longitudinal waves, respectively): gypsum 2.10 to 2.50 g/cm³, 1.5–4.6 km/s; anhydrite 2.40–2.90 g/cm³, 1.5–6.0 km/s; and rock salt 2.15–2.30 g/cm³, 4.5–5.5 km/s.

Carbonate and, particularly, evaporitic rocks can include the so-called “false” caprocks. In general, they are composed of anhydrites with primary or secondary fracturing and weak permeability. Hydrocarbon gases (and oil as well in some places) squeeze out into the false caprocks to the real caprocks. Based on seismic data, structural traps are frequently recorded at the base of the false caprock. Therefore, the filling of such traps turns out to be incomplete.

The value of underfilling of the trap is defined by the thickness of the false caprock (Ovkharenko et al.,2007).

3.3.1 Permian Deposition, Salt Formation, and Movements

During the late Artinskian to early Kungurian (≈ 268 – 265 Ma, Early Permian), thick deepwater clastic fans were deposited, the sediment being derived from erosion of a continent to the southeast. In Kungurian time (263–258 Ma), the supply of clastic sediments ceased, the climate became arid, and a sequence of thick beds of clean, uniform, marine halite interbedded with thin black shales rapidly buried the fans. This sequence accumulated to a thickness of 2–2.5 km throughout a basin bounded by clastic shore facies to the south and east and 0.5–1-km-thick beds of carbonate and sulfate sediments on shelves to the north and west.

In Kazanian time (258–253 Ma, Late Permian), a cyclic succession of thin halite beds interbedded with shales accumulated until the total evaporite succession reached a thickness of about 4.5 km in the center of the basin. Because the basin still had a marine connection to the southwest, the interbeds are black marine shales in the west, whereas time-equivalent strata in the east are red as a result of terrigenous input from the Urals.

Erosion of the north south–trending Ural Mountains to the east profoundly influenced Permian to Triassic sedimentation and consequent salt tectonics in the east of the Precaspian basin. Thus, while Kazanian salt was still accumulating in the centre and western part of the basin, clastic sediments sourced from the Ural Mountains were prograding westward into the basin. Loading of the salt by these prograding sediments had down-built several rows of inclined walls of Kungurian salt basinward from the eastern margin of the basin by the end of the Permian. Meanwhile, a series of salt rollers having steeply dipping basinward flanks developed beneath the footwalls of down-to-basin, normal, syn-depositional faults. The faults define the half graben along the southeastern margin of the Precaspian basin as their overburden glided down-slope (zone D1, Figure 46). At the same time, more symmetrical salt walls hundreds of kilometres long developed in thicker salt beneath the slope along the northern and western flanks of the basin (in zone D2, Figure 46). The reliefs of these salt walls increase progressively from 3 to 5 km basinward, reflecting both basinward thickening of the salt and thin-skinned lateral compression near the toe of the slope. Most of the salt sequence on the northern and western shelves remained essentially passive, but some underwent Late Permian through Triassic down-to-the basin faulting and block rotation, where the slope instability propagated backward (zone D2, Figure 46).

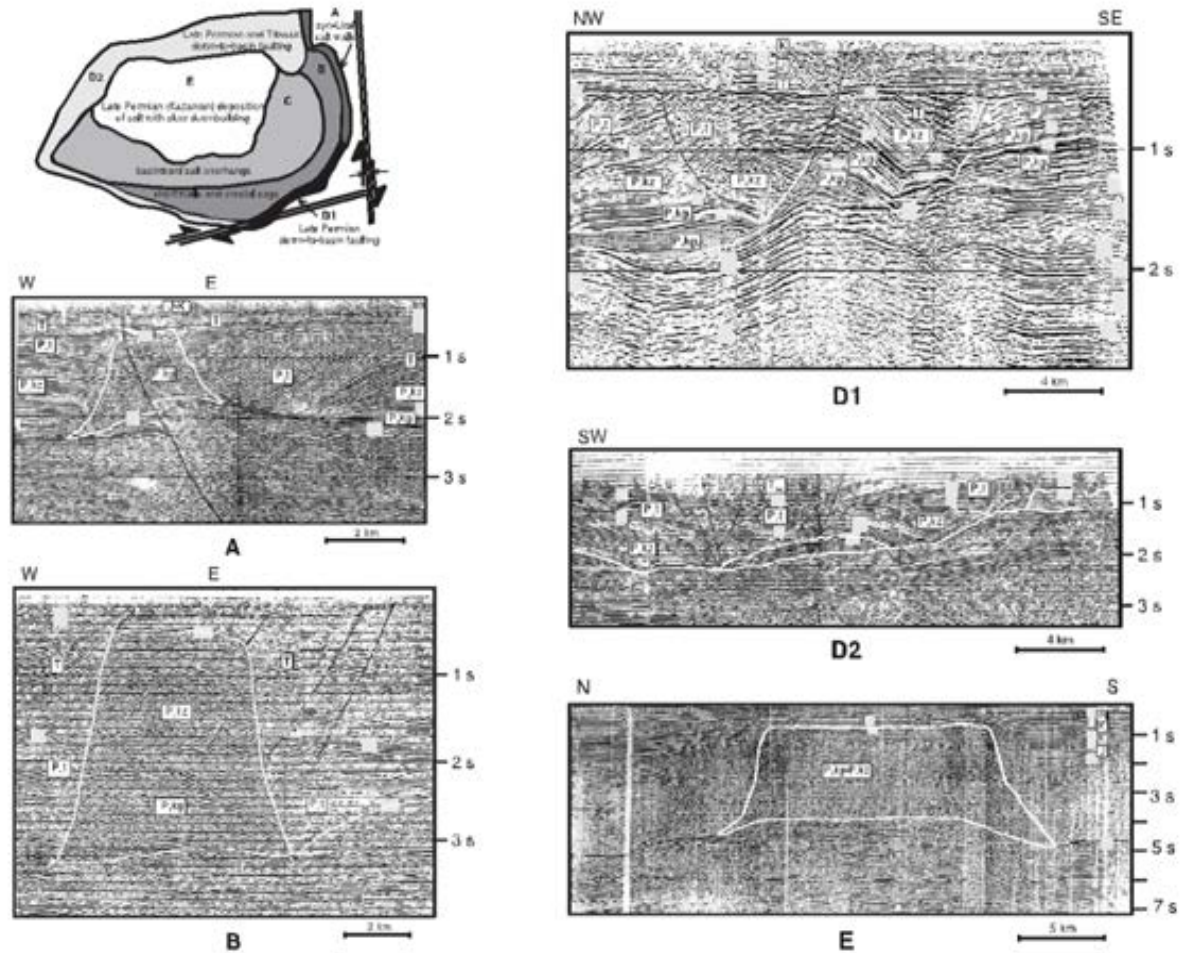


Figure 46: Salt structures in the Precaspian basin from the Triassic to the Early Jurassic, after “Volozh et al., 2003”.

Upper panel: Sketch map of zones (A–E) having different styles of salt structures. Transpression was transmitted into zone A from the Ural Mountains across a strike-slip shear having about 700 km of dextral displacement. Panels A, B, D1, D2, and E present seismic profiles showing structures in salt across zones indicated. Seismic profiles illustrating structures in salt across zone C are shown in Figures 7, 12, and 13. P1 = Lower Permian; P1kg = Kungurian; P1kg1 = lower Kungurian; P1kg2 = upper Kungurian; P2 = Upper Permian; P2kz = Kazanian; P2t = Tatarian; T = Triassic; T12 = Lower to Middle Triassic; J = Jurassic; J–K = Jurassic to Cretaceous; K1 = Lower Cretaceous; K2 = Upper Cretaceous; Pl = Paleogene.

3.3.2 Triassic Deposition and Salt Movements

By the end of the Permian, transpression in the Ural Mountains had localized to the Urals-Kopet Dagh strike-slip shear zone (Figure 46 key map) that had accumulated about 700 km of dextral displacement along the mutual border between the Urals and the Precaspian basin (Khramov, 1991). During the Triassic, the South Emba shear zone trended west-southwest–east-northeast along the southeastern margin of the Precaspian basin and now sinistrally offsets by about 60 km both a pre-Jurassic deformation front in the west and folds along the western margin of the Urals in the east (Figure 46, Volozh et al., 1999).

The source of terrigenous sediments prograding an arcuate depositional shelf into the basin migrated from the east to the southeast from Late Permian through the Triassic (Volozh et al.,

1996). Existing salt structures increased in relief as slope progradation rapidly down-built zones of successively younger salt structures basinward, first across zones A to C and then across zone D1 to C (Figure 46). The zones in Figure 46 emphasize how the structures propagated basinward, whereas those in Figure 47 emphasize their present shape. Many of the oldest Late Permian structures in zone A reached high reliefs before they became starved and inactive as the Kungurian salt supplying them closed to primary welds after the Early Triassic. Some deep turtleback structures survive where the primary welds around adjoining salt structures did not meet. Platform sediments showing no sign of salt movement began to bury the crests of starved diapirs in a zone that widened basinward, first from the eastern, and then from the southeastern margins. Reverse faults associated with thick-skinned Ural transpression propagated upward from beneath salt walls that were already inactive and alongside asymmetric salt walls that were still growing during sedimentation along the western side of zone A (Figure 46).

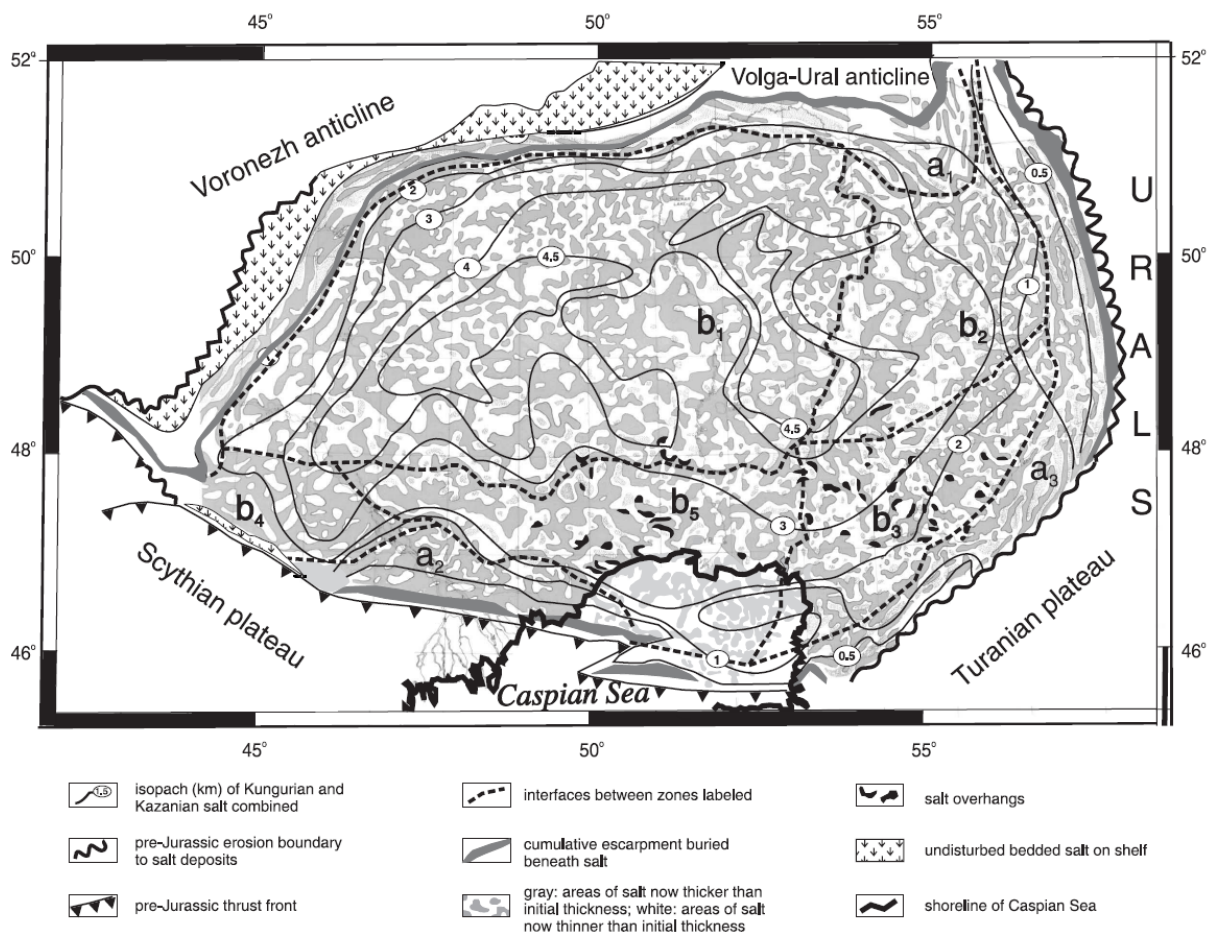


Figure 47: Map of Precaspian basin showing current shapes of salt structures, after “Volozh et al., 2003”.

Zones having various shapes of salt structure: a1 and a2 = equi-dimensional and wall-like pillows of Kungurian salt; a3 = rollers, anticlines, and turtlebacks of Kungurian salt; b = walls and domes where b1 = halokinesis involved both Kungurian and Kazanian salt; b2–b5 = halokinesis involved only Kungurian salt; b2 = diapiric by the end of the Permian; b3 = diapiric by the end of the Triassic; b4 = diapiric by the end of the Jurassic; b5 = not yet diapiric, but some have surfaced and extruded or been recycled.

In zone B (Figure 46), the crests of some of the salt stocks and short salt walls developed Triassic sag basins that were elongated north–south (Figure 48). Crestal sag basins between salt cusps suggest lateral extension. Although sedimentation in some of the sag basins in zone B appears to be contemporaneous with the last of the transpressional reverse growth faults beneath the shelf in zone A (see Figure 46), crestal sag basin formation is interpreted as contemporaneous with down-to-the-basin normal growth faulting further basinward in zone C (Figure 46). As in zone B, continued basinward migration of the depotrough through zone C down-built a succession of huge asymmetric salt stocks.

In contrast to the vigorous sediment progradation from the eastern and southeastern margins of the Precaspian basin, the northern and western margins remained comparatively starved of clastic sediment and were bordered by carbonate and/or sulphate shelves until Kazanian time (zone D2). Salt and overlying strata are characteristically flat lying and undeformed shelfward of a marginal zone of (mainly) down-to-the basin faults (zone D1).

In the basin centre beyond the slowly encroaching shelf (zone E), slow, essentially continuous sedimentation that kept pace with basin subsidence from the Early Triassic through the Cretaceous down-built huge salt massifs. These have reliefs ranging from 3 to 8 km and horizontal dimensions of about 100 km without any significant overhangs having been recognized (zone E in Figure 46, zone b1 in Figure 48). The earliest and largest of these salt massifs developed above the early Kungurian clastic fans beneath the salt. Slightly smaller and younger structures commonly surrounded larger massifs.

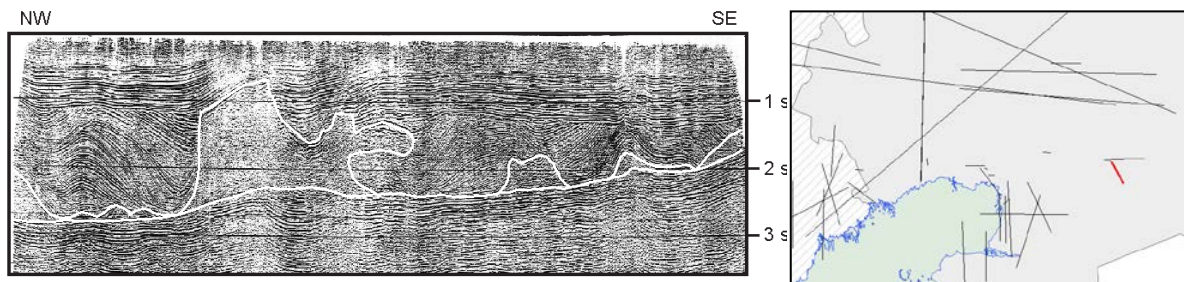
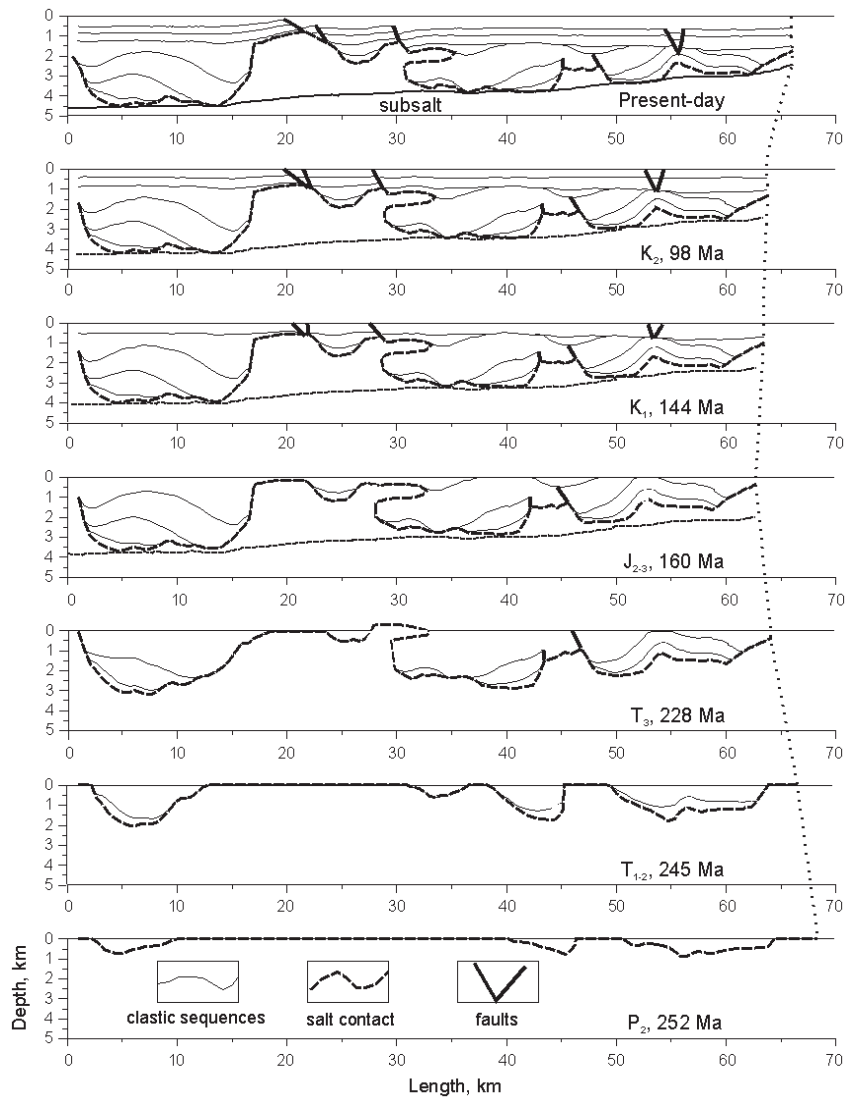


Figure 48: Seismic profile (located in Emba River Valley) and restoration to stated times. Dotted line along right-hand end of restored profiles indicates changing profile length by area balancing.

3.3.3 Jurassic Deposition and Salt Movements (Mainly Extrusion and Overhangs)

During the Early Jurassic (Hettangian and Sinemurian, ≈208–198 Ma), another wave of salt diapirism migrated into the basin, now from the southern boundary (zones D2 to C in Figure 46 key map, from a2 to b4 in Figure 47). Initiation of this wave is attributed to down-building by clastic sediments prograding from the active Donbass-Tuarkyr fold belt beyond the southern

boundary of the basin, but it continued to propagate northward during the Middle Jurassic in response to lateral shortening.

This folding and the more general Early Jurassic (Cimmerian) uplift attributed to the closure of paleo - Tethys and the resulting Cimmerian convergence (Alexander et al., 2000) led to an approximately 35-my hiatus (Figure 49). This hiatus is generally represented as an Upper Triassic–Middle Jurassic disconformity but is expressed as an angular unconformity in the vicinities of still-active salt structures. Some Late Permian to Early Triassic pillows of Kungurian salt deflated to drive diapirs that surfaced in association with Jurassic growth faults. Many of the diapirs in Zone C (Figure 46 key map) have significant overhangs interpreted as sheets of allochthonous (Kungurian) salt that extruded over the surface, likely accompanied by some recycling by dissolution and recrystallization.

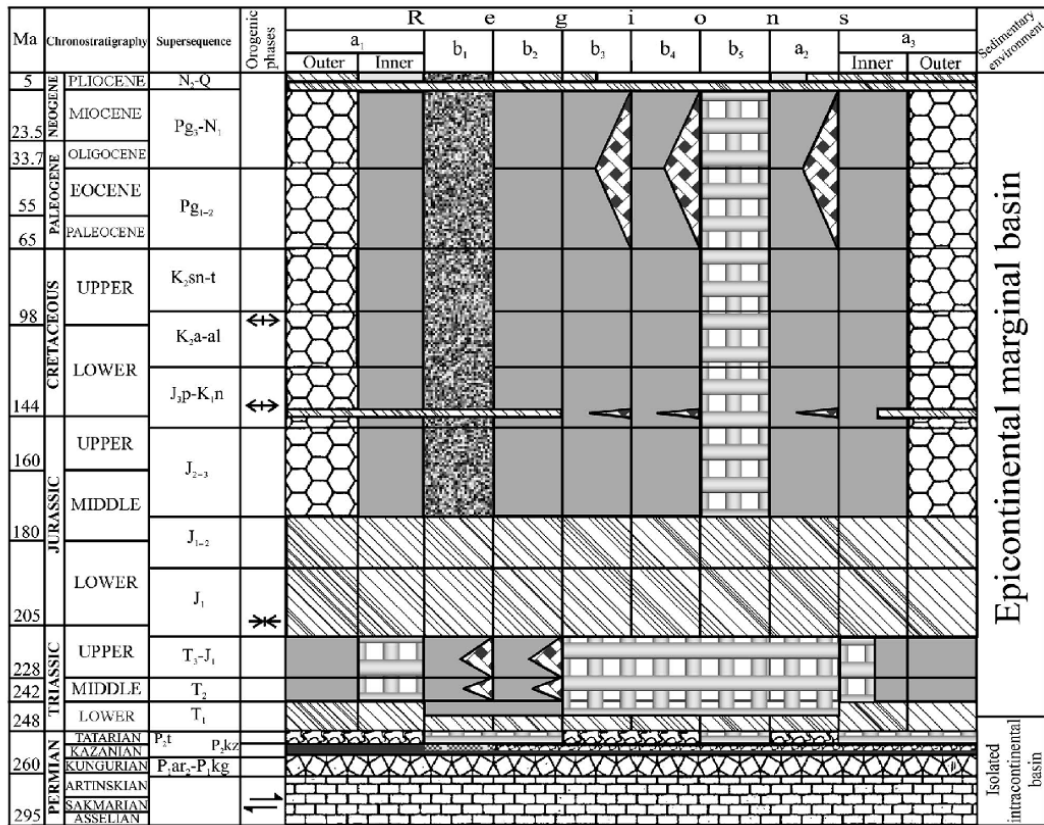
Backstripping of profiles of salt structures indicates that many were not only at the surface in and after the Late Permian but extruding above it, particularly during the Late Triassic–Middle Jurassic depositional hiatus, and that some were still extruding until the Late Jurassic. One of the youngest sheets of allochthonous salt so far recognized in the Precaspian basin was also the longest, that at Kum (Figure 50). This salt formed a pillow from Middle Permian through Triassic times after the salt structure immediately to the west had already surfaced. The crest of the Kum salt diapir appears to have been at, or close to, the surface from the Late Permian to the Late Jurassic (Figure 50). The column of Permian to Upper Jurassic strata (density = 2600 kg m^{-3}) loading the salt source (density = 2200 kg m^{-3}) was only 1.6 km high. Balancing forces (density of salt x gravitational acceleration x height of salt column = density of overburden x gravitational acceleration x height of column of overburden) implies that gravity alone could have supported a salt column with a level of neutral buoyancy only 0.3 km above the surface. Studies of salt extrusions at different stages of development in Iran indicate that where salt extrudes faster than it dissolves and where deposition of overburden is slow (or negative), extruding salt rises to its level of neutral buoyancy in an extrusive dome that then spreads into a sheet of allochthonous salt (Talbot, 1998). By the Late Jurassic, progressive squeezing of autochthonous salt from depth (Figure 50) had extruded a sheet of allochthonous salt at Kum that reached a thickness approaching 1 km and an east–west length of 14 km; it is not clear whether this extrusion was submarine or sub-aerial, and there is no known associated oil (Volozh et al., 1994). Rapid deposition of Upper Jurassic to Lower Cretaceous non-kinematic strata buried the extruded salt sheet at Kum, but subsequent deposition reactivated and upbuilt the diapir feeding it and also led to the allochthonous salt sheet upbuilding a salt pillow (Figure 50).

As extrusion starved increasing numbers of diapirs, the zone of starved salt structures in zones B and C (Figure 46) widened behind a basinward-migrating zone of salt structures that

were still active. Many of these active structures in zone C (Figure 46) extruded from deeper levels than Kum (e.g., Figure 48). Consequently, these could have risen much higher than 0.3 km and rivaled the currently active salt fountains of Iran, which rise to as much as 1 km above their bedrock orifices (Talbot, 1998). Numerical models tuned to the dimensions and measured velocities of extrusion of one of the largest Zagros salt fountains suggest that the salt of this fountain has been extruding from its bedrock orifice at rates near 1 m/yr for approximately 56,000 yr, the time estimated to exhaust its local source layer. The Iranian salt fountains are considered to be modern analogs of many salt structures in the Precaspian basin from the Late Permian to Middle Jurassic.

None of the salt overhangs in the Precaspian basin approach the dimensions of the large salt nappes in the Gulf of Mexico (e.g., Worrall and Snelson, 1989). It's attributed this to basin configuration. In the Gulf of Mexico, rapid sedimentary progradation results in salt nappes that spread downslope by gravity toward an open ocean basin. By contrast, the Precaspian basin was always closed, and salt extrusions there had no open continental slope toward which they could gravitate.

The current geometry of the approximately 1800 salt structures known in the Precaspian basin is summarized in map form in Figure 47 and in table form in Figure 49. Salt structures form an unusually high proportion of the area of the Precaspian basin, particularly at the Jurassic subcrop, which is generally less than 2 km deep.



- transension
- transpression
- strike-slip
- subsalt sediments
- hiatus
- Kungurian salt
- Kazanian salt
- prekinematic sediments
- synpillow sediments
- syndome sediments
- syndiapir sediments
- postkinematic sediments
- nonkinematic sediments
- allochthonous salt sheets rooted to structures of Kazanian salt

Figure 49: Summary of sedimentation and halokinesis in the Precaspian basin. Regions a1–b5 are identified in Figure 47.

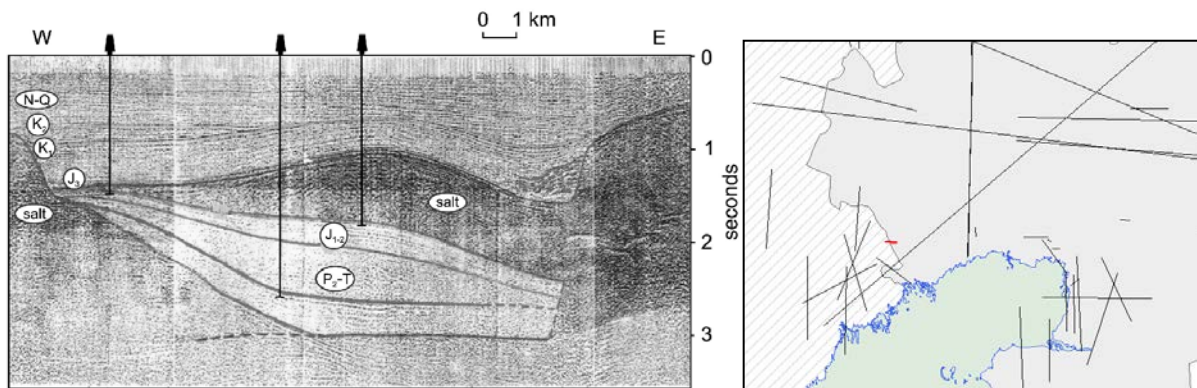
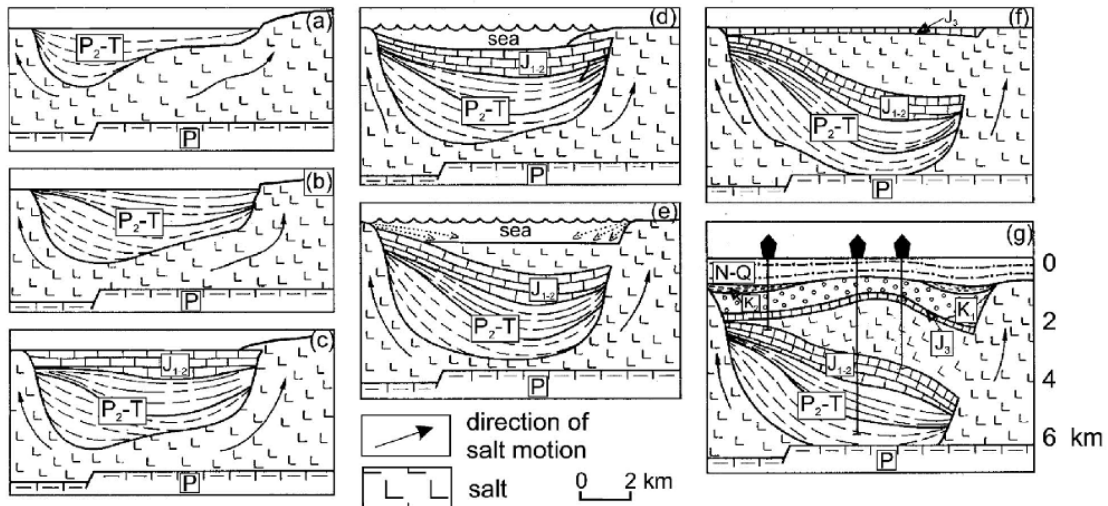


Figure 50: The sheet of allochthonous Kungurian salt at Kum (Kazakh area of the Volga mouth) was extruded in the Late Jurassic and began to upbuild during the Paleogene, after “Volozh et al., 2003”.

Upper panel: seismic profile showing the Kum overhang. Bottom panel: evolution sketches of the Kum overhang (a–g). P = pre-Kungurian substrate; P2–T = Middle Permian to Triassic; J1–2 = Lower to Middle Jurassic; J3 = Upper Jurassic; K1 = Lower Cretaceous; K2 = Upper Cretaceous; N–Q = Neogene to Quaternary.

3.3.4 Jurassic–Paleogene Deposition and Polygonal Faults

A pattern of polygonal grabens and half grabens connects pre-existing salt structures throughout most of the basin (Figure 53) and is interpreted here as having initiated during the Early Jurassic (Cimmerian) uplift and the extrusion of large volumes of salt withdrawn from depth during the consequent hiatus. When subsidence resumed, deposition throughout the basin was of shallow-water Jurassic to Paleogene argillites, sandstones, and thin carbonate beds. A minor discontinuity near the Jurassic- Cretaceous boundary (Figure 49) might be associated with localized uplift because of collisional events along the southern margin of Eurasia (Alexander et al., 2000).

Jurassic to Paleogene sediments that buried starved salt structures are post-kinematic and flat lying with a uniform thickness between 2.1 and 2.5 km. Contemporaneous sediments

deposited over potent diapirs are syn-kinematic and deformed by narrow asymmetric salt walls or stocks, most in the hanging walls of normal growth faults. It's inferred that the faults weakened and thinned any overburden that had overlapped exposed stillpotent Permian–Triassic salt structures. These structures reacted by actively up-building back to the depositional surface and resuming down-building. Diapiric salt walls and stocks that were down-built throughout the Jurassic to Paleogene are symmetric in profile and surrounded by overburdens with uniform thickness.

The faults in the laterally isotropic polygonal network display a wide range of orientations and degrees of connectivity (Figure 53). Complex polyhedral defined by faults are typically 5–20 km across and involve strata having regional dips of less than 1° and thicknesses between 2.1 and 2.5 km. Line balancing along profiles having a wide range of orientations indicates that lateral extension across the faults averages approximately 5% in all horizontal directions. The faults are curved in plan (Figure 53) and more or less listric in section. Fault pairs defining a graben are seldom symmetric. Some converge downward to intersect near the base of the Jurassic (which can be thrown by as much as 0.6 km).

More converge at the crests of potent Permian–Triassic structures of Permian salt that reactivated and grew from Jurassic to at least Paleocene; some are still active. As in other documented polygonal fault systems (e.g. Walsh et al., 2000), most fault traces in the Precaspian basin follow the axes of polygonal anticlines (Figure 53), are confined to a few stratigraphic intervals of post-“rift” basin infills, and include growth faults that reach the depositional surface. Polygonal systems of normal faults point to isotropic lateral extension. No independent evidence for either lateral extension of the Precaspian region or uplift of the magnitude that could account for the calculated 5% isotropic extension exists. Even an uplift of 2 km would result in only 0.0314% lateral extension.

Most polygonal fault patterns have been attributed to a gravity-driven mechanism instead of lateral tectonic forces (e.g., Ismail-Zadeh et al., 2002). Most of the above references invoke density inversions at the base of the faulted system, but Cartwright and Lonegran (1996) cited volumetric contraction during compactional dewatering of mud-dominated intervals. Compactional dewatering is not likely to have been particularly significant in the Precaspian basin, where the polygonal fault system developed in sediments that were not dominated by argillites. Instead, most faults rooting to the crests of reactivating structures of low-density salt implicate gravitational forces. The only part of the Precaspian basin missing polygonal faults is along the eastern margin (Figure 53), where salt structures had been starved by the end of the Triassic, and fluids beneath the deep Kungurian salt layer lost their usual overpressures along Ural-related thrusts (Figure 46, zone A).

It's attributed the polygonal fault system in the Precaspian basin to gravity having reactivated large salt structures that still had the potential for growth in smaller structures when they were buried further. Although it involves apparently brittle faults, the polygonal pattern is like the shallow levels of spoke patterns of gravity overturn modelled in ductile materials by Ismail-Zadeh et al. (2000). This comparison implies that the estimated 5% lateral extension might be confined to above polygonal salt uplifts and compensated on a basin scale by equivalent isotropic shortening across the intervening salt-withdrawal basins. Despite involving brittle faults in the top 2.5 km, the pattern involved withdrawal of salt from an autochthonous source layer about 5–10 km deep. The brittle deformation pattern at shallow levels in the Precaspian basin is therefore attributed to ductile flow of salt and overburden deeper in the unstable section.

In every other documented example of the polygonal fault system, polygonal normal faults near the top boundary directly overlie polygonal uplifts near the bottom boundary. This implies simple prismatic polygonal movement cells, very different from the complex spokes movement patterns modelled in very unstable sections by Talbot et al. (1991), in which polygons near the top boundary are offset half a wavelength from those near the bottom boundary. By analogy with thermal convection (Talbot et al., 1991), gravity drives stronger density instabilities in movement patterns that are more complex than the simpler movement patterns driven by weaker density instabilities. The generally simpler Jurassic to Paleogene movement cells obvious in the Precaspian basin were smaller in scale and complicated by inheriting aspects of the more complex and larger scale Permian–Triassic gravity structures.

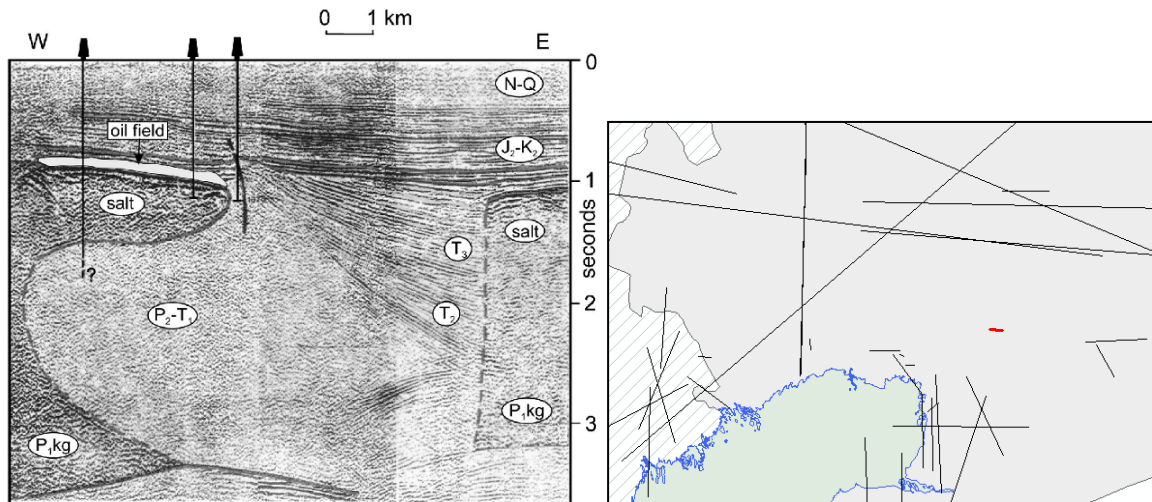
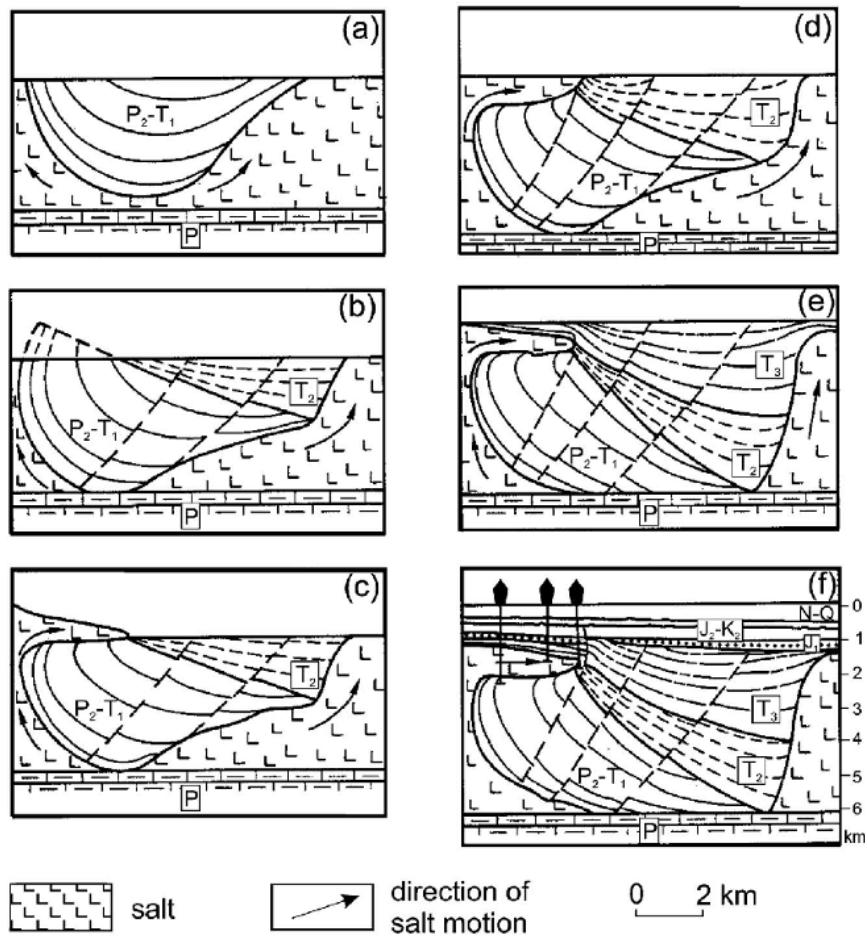


Figure 51: The Kotyrtas North oil field (located on North Emba River Valley) is trapped above a sheet of allochthonous Kungurian salt extruded in the Middle Triassic, after “Volozh et al., 2003”.

Upper panel: seismic profile showing the Kotyrtas North overhang. Bottom panel: evolution sketches of the Kotyrtas North overhang (a–f). P = pre-Kungurian substratum; P1kg = Lower Permian (Kungurian); P2–T1 = Middle Permian to Lower Triassic; T2 = Middle Triassic; T3 = Upper Triassic; J2–K2 = Middle Jurassic to Upper Cretaceous; N–Q = Neogene to Quaternary.

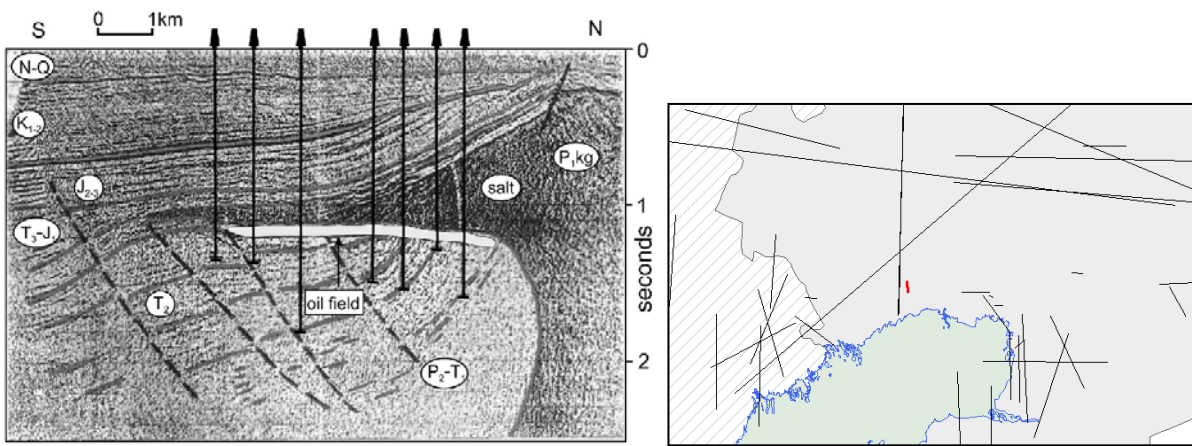
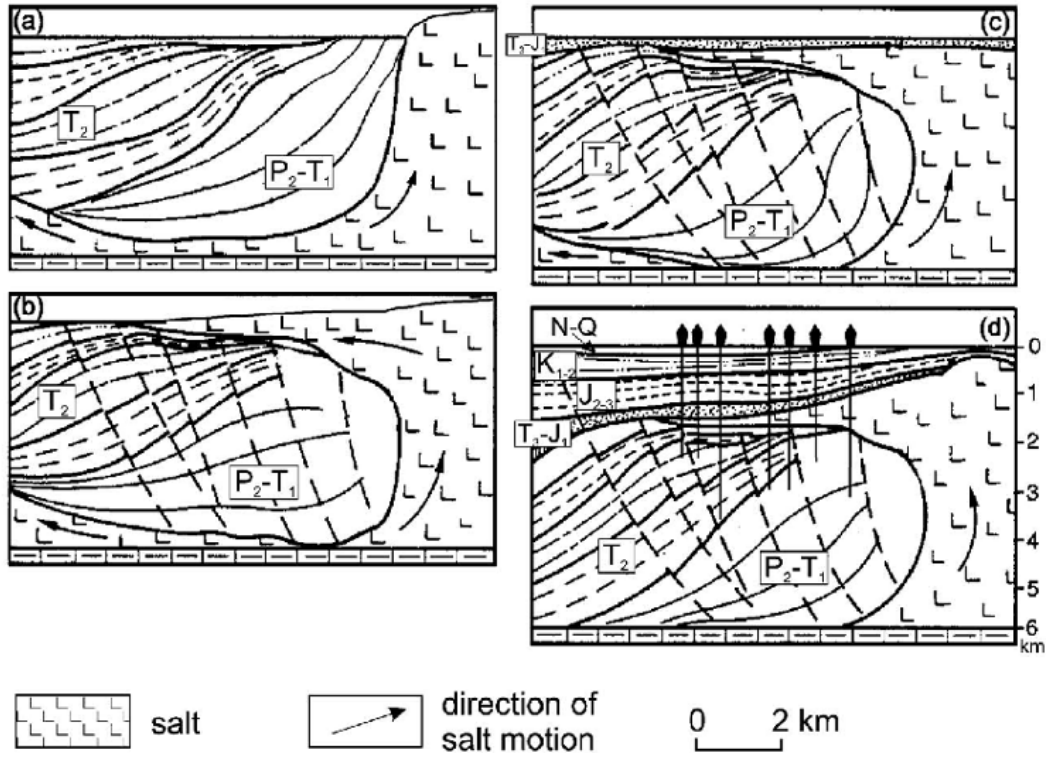


Figure 52: A sheet of allochthonous Kungurian (\pm Kazanian salt) extruded in the Middle to Late Triassic trapped the Novobogatinsk oil field (located near Atyrau), after “Volozh et al., 2003”.

Upper panel: seismic profile showing the Novobogatinsk overhang. Bottom panel: evolution sketches of the Novobogatinsk overhang (a–d). T3–J1 = Upper Triassic to Lower Jurassic; J2–3 = Middle to Upper Jurassic; K1–2 = Lower to Upper Cretaceous.

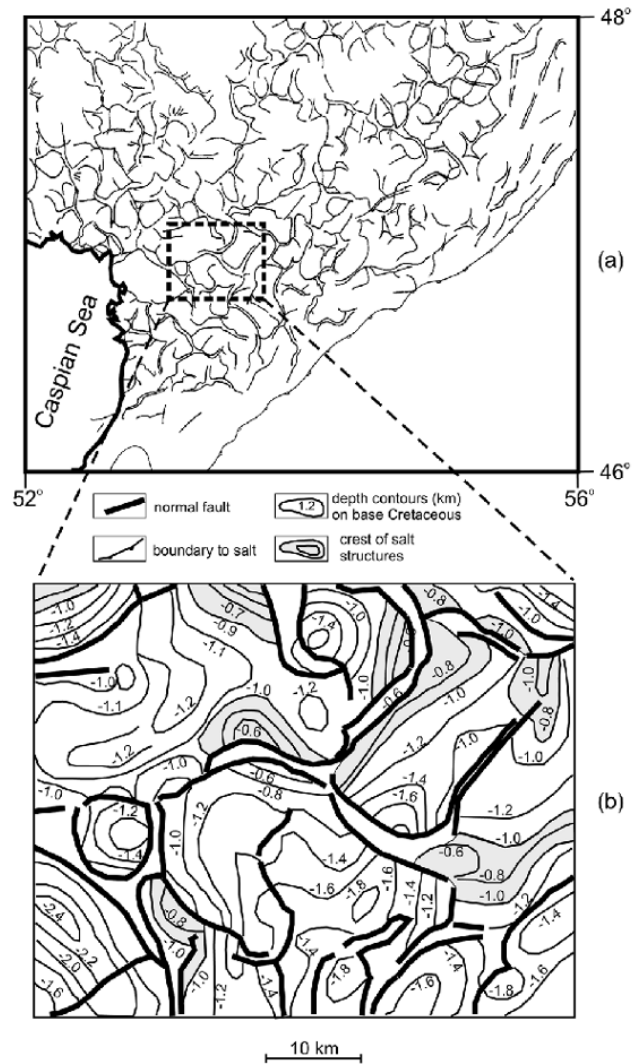


Figure 53: Maps of part of the southern Precaspian basin showing normal faults off-setting base Cretaceous, after “Volozh et al., 2003”.

3.3.5 Cenozoic Deposition

Sedimentation was slow in the intra-continental Precaspian basin during the Late Cretaceous but increased during renewed Paleogene subsidence. Many of both the potent Permian–Triassic salt structures and their narrower Jurassic to Paleogene upward extensions reactivated in Neogene times so that they up-built and lifted local overburden (Figure 48 and Figure 50).

During the Neogene, decreasing numbers of salt withdrawal basins localized to the margins of still-potent salt structures. Most such basins tend to be deep and aligned (e.g., 20 x 5 km) along northeast–southwest faults in the basement that reactivated beneath the margins of salt massifs in a central region now characterized by low relief and saline lakes. Some of the sheets of allochthonous salt emplaced in the Triassic and Jurassic in zone C (Figure 46 key

map and Figure 47, zones b3 and b4) upbuilt short-wavelength pillows in the Late Cretaceous and/or Neogene (e.g., Figure 50).

The geography of the Precaspian basin changed dramatically during the Pliocene, as a deep basin developed in the area of the South Caspian Sea (Figure 54) (Devlin et al., 1999). Subsidence kept pace with the rapid accumulation of 5–8 km of Pliocene sediments (which serve now as the main hydrocarbon reservoir rocks in the basin), so that the South Caspian Sea remained shallow. Sediments in the eastern half of the basin were red-brown terrigenous clastics supplied from the paleo-Amu-Darya river in the east (Figure 54). Those in the western South Caspian basin were gray organic-rich clastic rocks supplied from the paleo-Volga river (Figure 54). Early Pliocene sedimentation bypassed the former Precaspian basin through southward-trending canyons incised to depths of 0.7 km in Cretaceous platform strata. The paleo-Volga river draining to the base level provided by the South Caspian lake having a surface about 1 km below ocean level eroded these structures (Antipov et al., 1996). The bases of these early Pliocene canyons truncated the tops of the shallowest salt diapirs. Coarse clastic sediments filled the canyons as the lake level rose and transgressed north of the former Caspian basin by the end of the Messinian, about 3.8 Ma (Antipov et al., 1996).

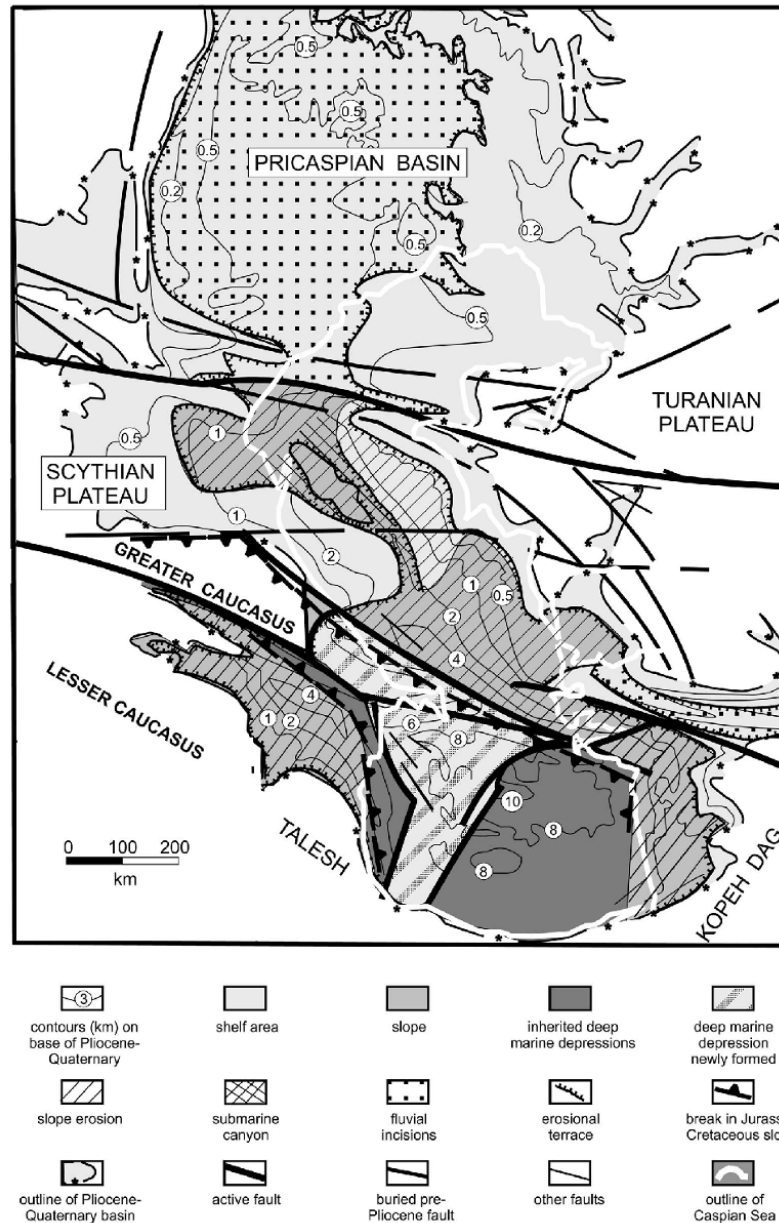


Figure 54: Structural map of the Precaspian basin in Pliocene times illustrating incisions and canyons eroded through Cretaceous platform sediments by the paleo-Volga and paleo-Amu-Dariya rivers draining into the South Caspian lake having a surface about 1 km below ocean level, after “Volozh et al., 2003”.

Ismail-Zadeh, et al. (2004) proposed a 3D numerical approach to investigate the evolution of salt structures in the Precaspian Basin. This approach is used to restore the evolution of salt structures through successive earlier stages. The numerical methodology is applied to study several model examples: (i) salt diapirs evolved from an initially random perturbation of the interface between salt and its overburden and a restoration of the salt diapirs to its initial stages; (ii) a salt wall; (iii) a salt extrusion with a gravity current over the depositional surface; (iv) secondary diapirism; and (v) a salt diapir subject to horizontal forces. The applicability of

the results of the models to the evolution of Late Permian salt structures in the Pricaspian basin is discussed. Given the complexity and specificity of the work, for further information see the publication (Ismail-Zadeh et al., 2001 and Ismail-Zadeh et al., 2004).

3.4 SOILS DISTRIBUTION AND CHARACTERISATION

Soils in the coastal zone are in close relation to the oscillations of the current sea level. With decreasing water level in the sea, the evolution of soil from primary bottom sediments through a solonchak stage to desert takyr-like soils occurs. With increasing level, the processes change towards increased hydromorphism, soil desalination in a narrow coastal band and salinization in the zone of capillar impact of groundwater. Serious corrections to the soil formation process are introduced by the wind surges of seawater determining flooding of significant coastal areas. The role of surges is especially pronounced at low coasts by absolute marks. The positive relief features are often washed and desalinized while stagnation of water and its subsequent evaporation in the negative components leads to a significant surface enrichment with salts. That is the reason why soil formations have a very high degree of salinization.

Another feature of soil genesis on maritime plains is their formation on marine deposits. Marine deposits including young current ones contain a large number of residual salts of sea origin. These salts as a result of geochemical transformations and migration constantly supplement the salt supply of soils.

In addition, the Caspian waters supply salts to soils, especially in the coastal band and in the shallow water bays and kultuks. The groundwater level at the seashore is usually below the water level in it due to intense evaporation under the hot desert climate conditions. That is why, the ground flow in many places is directed onshore.

During the various transgressive and regressive phases marine and continental deposit alternated. A summary of Quaternary strata described in the North Caspian region is listed in Table 3.

Table 3: Regional quaternary stratigraphy.

Age	Marine deposit	Continental deposit
Novocaspian	Coastal deposits of calcareous sands, shelly sands, shell beds and calcareous silts, grey to greenish gray. Black oolites. General increase of fine-grained deposits toward the base. Increase in finer-grained material also in Ural furrow, with intense chemogenic carbonate precipitation.	
Mangyshlakian		Alluvial, proluvial, eolian deposits of grayish-brownish slightly calcareous

Age	Marine deposit	Continental deposit
		aleurite clayey silts
Late Khvalynian	Clay and sand deposits, shells; Brown clayey silts, grayish/brownish aleurite clayey silts; Compared to Novocaspian: brownish colours, coarser grained, reduced amount of carbonate and organic carbon. Dagestan horizon: fine-grained, slightly calcareous grayish-brown and brownish clays. Locally carbonate gravel.	
Early Khvalynian	Light brown to chocolate brown clay and sand deposits, shells	
Atelian		Loess-like loams, alluvial sands and proluvial deposits
Late Khazarian	Clay and sand deposits, shells	
Inter Khazarian		Red-brown loams (Astrakhanian)
Early Khazarian	Sand and clay, plant remains (singilian); coarse gravel, sands and clayey sands, shells; grey silts, sands, coarse gravel and conglomerates	
Late Bakuvian	Sand and coarse gravel, shells; thin, coarse coastal facies, shell assemblages; sand and coarse gravel.	
Early Bakuvian	Clay, clayey sands, shells; stratified brown clays and silts with very thin interlayers of ochreous sands	

The soil cover over the entire study area is heterogeneous. Its formation and structure are closely related to the succession of the territory becoming free of seawater and the age of continental regime of drained surface as well as the specific relief conditions, character of moistening of the territory and composition of soil-forming rocks. A regularly alternating change of soil belts from a primary sea beach in the coastal zone of the current marine plain to zonal soils that have undergone a long automorphic development stage is observed in the soil cover structure.

3.4.1 Spatial distribution of soil features in Zone B (Northern Area, from Atyrau City to the Emba River valley)

The territory within the Zone B is confined to the southern part of the Precaspian lowland that is a low gently dipping to the Caspian Sea plain with the absolute marks from minus 8.3 m to minus 27.2 m. The absolute mark minus 27.2 m (Baltic Height System) determines the location of the coastline of the Caspian Sea (sea line) at status for January 2001. This accurate description is provided by Mo Energy and Mineral resources et al. (2001).

The modern geomorphologic appearance of the territory is closely related with the history of its geological development and is defined by repeated transgressions and regressions of the Caspian Sea in the Quaternary (Pleistocene) time: Bakinian and Kazanian in Early and Middle Pleistocene (Q1bk and Q2hz), Khvalynian in the Upper Pleistocene (Q3hv), and Novocaspian ingression in Holocene (Q4nk) (Figure 55). As a result of the influence of complexes of geological and natural exogenous factors the modern geomorphologic appearance of the Precaspian lowland has formed. The main feature of the lowland relief is the clearly identified gradation conditioned by the presence of the accumulative marine terraces of the Pleistocene-Holocene age.

Thus, the geomorphologic appearance of the territory under study is closely related to the history of its geological development and is defined by the surfaces of accumulative terraces of marine and continental genesis:

- Modern Accumulative Marine Terrace;
- Novocaspian Accumulative Marine Terrace;
- Khvalynian Accumulative Marine Terrace;
- Alluvial-marine Erosion-accumulative Terrace (spread area of the Baer knolls, a morphological structure in the Zone B);
- Alluvial Accumulative Terrace (valley of the Ural River and valley of the Emba River).

The description of the mentioned terraces is listed below (top-down):

THE MODERN ACCUMULATIVE MARINE TERRACE

The Modern Accumulative Marine Terrace is confined to the coastal part of the territory under study and extends in all directions. The northern border of the terrace corresponds to the level of the Caspian Sea for 1929 – 1930 and hypsometrically identified by the absolute mark minus 26.0m and is fixed by the clearly identified relics of the beach ridges with the height up to 1.0 - 1.2 m. In a number of cases the relics of beach ridges having a form of bars and tombolos with the height 1 - 2 m built up with the whole and fragment shells *Cardium Edule* with sand and sand – clay filler.

The southern border of the terrace is determined by the position of the Caspian Sea level and is changeable. At the present time it is at the hypsometrical level minus 27.2 m. The relief of the region is slightly sloping, sometimes almost flat, and is complicated with the shallow dry beds and sinks.

At the coastal part a waterlogged strip is identified which is practically impassable for any transport. The width of the waterlogged strip is not the same in different places and in some cases in the lower regions it penetrates deeper into the territory (to the north).

The surface of the terrace is permanently located in the zone of surge phenomenon influence from the Caspian Sea and in the period of the rise observed during the last years it has been considerably flooded with the seawater. The terrace surface is indented with the net of irrigation channels of the both main and distributive character.

NOVOCASPIAN ACCUMULATIVE MARINE TERRACE

Novocaspian Accumulative Marine Terrace is tracked within the whole territory under study and corresponds to the time when the Novocaspian ingression of the Caspian Sea occurred. The northern border of the terrace is quite clearly tracked as the slightly sloping beach ridge or as the slope crown with the height up to 1.8 m. The northern border of the terrace is hypsometrically identified with the absolute mark minus 22.0 m. The southern border of the terrace hypsometrically corresponds to the absolute mark minus 26.0 m.

The relicts of the Novobogatinskaya phase of the Ural River delta development in the Novocaspian time are confined to the terrace surface and presented by the buried and semi-buried channels, branches, eriks *etc.* The hollow and rarely ridging forms of the relief are characteristic for the terrace surface. They are mainly developed in the northern regions within the intensive show of deflation accumulative processes forming narrow sandy ridges usually sub meridian oriented. The sandy ridges rise over the surrounding area to the height of 0.7 – 1.2 m. Within the terrace surface a network of main and distributive irrigation systems is developed. Their accurate description is provided by (Mo Energy and Mineral resources et al., 2001)

KHVALYNIAN ACCUMULATIVE TERRACE

Khvalynian Accumulative Terrace is traced in the central and southeastern part of the Zone B. The northern border of the terrace in some cases exceeding the borders of the territory under study is identified with a quite clear though denuded coastline of the upper Khvalynian marine basin and on the region it is identified with a well-traced slightly sloping bench of 2.6 m height. The northern border of the terrace is hypsometrically fixed by the zero isohypse. The southern border of the terrace is determined with the absolute mark minus 22.0 m that respectively defines the northern border of the Novocaspian Marine Terrace.

The more divided relief is typical for the surface of the Khvalynian accumulative marine terrace: where the undulating ridgy forms of relief mainly predominate, with its subordinated development of the hollow and ridging forms. The vast hills and ridges with the absolute marks of top from minus 12.6 m – minus 16.6 m on the north up to minus 17.7 m – 18.8 m on the south alternate with quite big elongated hollows of oval form that are sub meridian oriented with the absolute marks of thalwegs from minus 20.8 m to minus 21.4 m reaching in some cases the absolute marks minus 23.3 m – minus 24.8 m. The more lowered regions are occupied with the wet sors and bitter-salt lakes with lake-salt (Tenizbay, Otarylytuz, Akkyz and others).

Within the terrace the semi-opened and buried delta channels end their existence that are tied to the Kushumsk phase of the development of the ancient delta of the Ural River. The terrace surface is influenced with deflation accumulative processes.

THE ALLUVIAL-MARINE EROSION-ACCUMULATIVE TERRACE

The Alluvial-marine Erosion-accumulative Terrace is developed in the northeastern part of the territory and is known in the special literature under the name of Baer knolls named after K. Baer, Academician, one of the first researchers interested in these formations. The terrace surface is presented as the worked out wavy ridgyhollow plain where the imbricate-linear ridges (knolls) with different length are located and the hollows that divide them are definitely sub-latitudinal oriented. The Baer knolls are gently slopping contours of ridge, rarely – the elongated knolls with the relative height from several meters to 10 and more meters. The length of these ridges varies from hundred meters to several kilometres. The intervals between the tops of neighbouring ridges are measured from 100-200 m to 1 km with declination to one or the other side. The ridges extend as parallel rows in the latitudinal direction. The hollows located between the ridges are usually closed. The position of the hollows in the plan indicates regular alteration of ridges and falls dividing them, which provides a corrugated picture. The ridges in socle are piled up with dense brown loams, rarely with clays of Khvalynian age. The hollows between the knolls are built with Novocaspian alluvial-marine sediments; these are the regions for floodwaters from the Sagiz River that make the system of wet sors, sometimes estuaries, rarely takyrs (dry lakes with clay bed) with the general name Tentekso tract. In some falls between the knolls and also on the knolls themselves blowing-out depressions can be observed.

The absolute marks of the region in the limits of the terrace are from 24.5 m (in hollows) to minus 16.3 m (the top of knolls).

ALLUVIAL ACCUMULATIVE TERRACE

The western portion of the territory from north to south is divided by the thick erosion cut-in of the lower (estuarine) current of the Ural River with its numerous active right and left deltoid channels. The depth of the erosion cut-in of the main bed of the Ural River counting from the low water level of the river reaches 4 to 6 m with the depth of the river at some parts from 4 to 9 m.

The absolute absence of the estuaries and super-flood land terraces is the characteristic feature of the Ural River valley: the valley of the river consists of the riverbed of the left and right flood-lands, the surface of which as moving away from the bed is imperceptibly joined with the surface of the accumulative marine terraces of Upper Pleistocene and Holocene age. The area in the limits of the Ural River flood-lands filled with floodwaters for 1% of provision determines the contour of the alluvial accumulative terrace. The fragments of the alluvial accumulative terrace are evident in the southeastern portion of the territory under study within the Emba River valley (Mo Energy and Mineral resources et al., 2001).

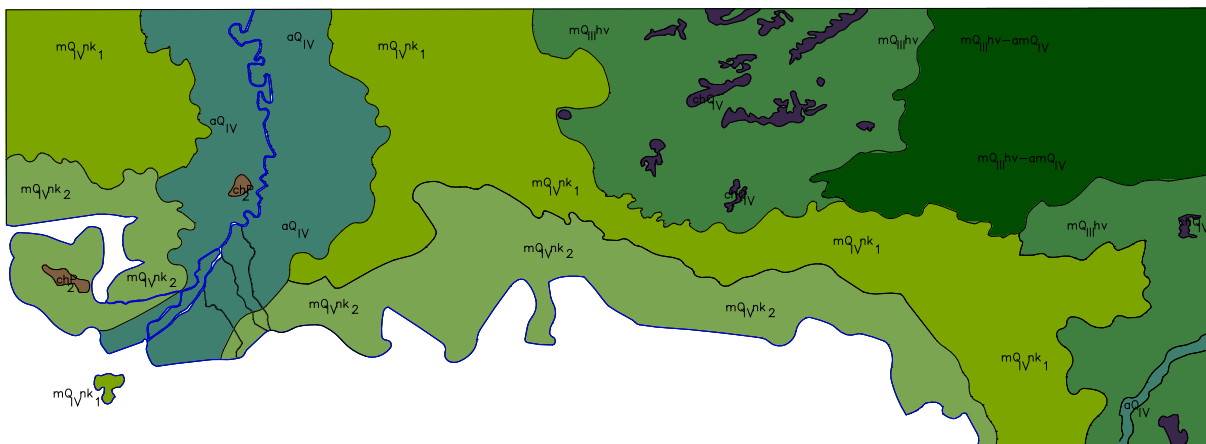


Figure 55: Map of soils distribution between Atyrau City and Emba River Valley, after “Mo Energy and Mineral resources et al., 2001”.

Taking into account the peculiarities of genesis and expansion, the conditions of deposits and content of non-lithified Quaternary sediments within the surveyed area include two main engineering geological complexes of rocks: marine sediments of Early and Middle Pliocene and sediments of Upper Pliocene and Holocene. Their distribution is shown in Figure 55.

➤ **Non-lithified Marine Sediments of Early and Middle Pliocene**

Non – lithified marine sediments of Early and Middle Pliocene are presented with marine sediments of Bakinian (mQ1b) and Khazarian (mQ2hz) stages of Quaternary system. They are laid in thin-layer clay, sometimes loam with sand streaks. The thickness of

sediments is 50-200 m. Within the area under the survey their roof is bedded at least 50 m deep from the surface. Since these sediments are embedded at a relatively significant depth and not impacted by the engineering facilities, the description is brief.

➤ Non-lithified Marine Sediments of Upper Pliocene and Holocene

Upper Pliocene (Q3) and Holocene (Q4) non-lithified sediments within surveyed area include marine, alluvial-marine, and continental sediments that form the surface of the Precaspian lowland area and serve as the foundation for all constructed engineering facilities. These sediments are divided into 5 stratigraphic-genetic complexes. The description of these complexes from top to bottom is given below .

- Complex 1: Halogen sediments (chQ4) are the bottom of major subsidence and bitter-salt lakes within Khvalynian accumulative marine terrace and represented by the layer of native salt with thickness 0.2 m-0.6 m. The layer of native salt underlies a horizon of liquid mass (mud) that consists of a mixture of black silt, organic substances, and a complex of halogen salts. The mud has valuable medical properties; the thickness of the horizon is 1m.
- Complex 2: Non-lithified alluvial sediments of Holocene age (aQ4) are spread within the alluvial terrace of the Ural River and the Emba River. These are represented by sandy loam and dusty sand, with low thickness formations of clay on the top ranging in colour from dark-grey to black with an admixture of silt and organic substances, and fine sand with gravel and pebbles in the valley of the Emba River. The ground is poorly salted. The thickness is 3-5 m.
- Complex 3: Non-lithified sediments of Novocaspian age of marine genesis (mQ4nk1-2) are spread across the Novocaspian accumulative marine terrace. This is represented by a light sandy clay brown, brown-grey color with thin streaks and galls of sandy loam, and an admixture at the top of silt and organic substances; with additives of shell and spots of ferrugination; the clay is salted and has swelling properties. The sandy loam is underlying with colours from brown-grey to green-grey and with clay streaks and additives of shells. Sandy loam is salted. There are islands in the near shore area. These are relics of onshore banks, bars and bay bars made of marine shells consisting of intact shells and shell fragments of *Cardium Edule* with sand inside; in the upper layer shells are mixed with clay loam and sandy loam; the ground is poorly salted. The thickness of the clay and sandy loams range from 3-12 m, and the thickness of shells up to 5 m.
- Complex 4: Non-lithified sediments of upper Pliocene – Holocene age of alluvial-marine and marine genesis (mQ3hv-amQ4). Spread within alluvial-marine erosion accumulative terrace. Spread out with marine sediments of upper Khvalynian

stage (mQ3hv) and upper quaternary alluvial-marine sediments (amQ4). Marine sediments create Baer knoll and are represented by the heavy dusty loam of a brown, red-brown colour, ferruginated with streaks of clay of a brown colour with the original texture of clay material consisting of tiny grains and smaller pellets and clay dust; during the wet seasons clay grains are fixed and create clay crusts. The ground is salted and has an ability of lowering a class; the thickness is 7-12 m. The erosion down cutting between Baer knolls is filled in with the sediments of alluvial-marine genesis, represented by interbanded layers of loam and sandy loam (dusty sand loam) with an insignificant inclusion of gravel-pebble material; the colour of this layer is brown, yellow-brown; the ground is salted; the thickness is 3-6 m.

- **Complex 5:** non-lithified sediments of upper Pliocene (Khvalynian) age of marine genesis (mQ3hv) are spread out from the development of the Khvalynian accumulative marine terrace. This is represented by an interbanded layer of light dusty brown clay, heavy dusty parti-coloured loam, brown sand loam with fauna *Didacna proetogonoides*. The grounds are salted. The loam has lowing facilities and clay swelling properties. Thickness of the layer 5- 10 m.

3.4.2 Spatial distribution of soil features in Zone C (North – Eastern Area, from the basin of the Emba River to the Mertvy Kultuk Bay)

The territory under consideration is located in the south-eastern part of the Precaspian basin and represents an accumulative marine plain with relative heights of 3-5 m, flat sloping from north to south. Absolute surface points (in regional aspect) respectively decrease from 50-80 m till minus 28 m. Rare isolated hilly range uplifts – salt domes rise over the plain. Their accurate description is given in the study carried out by Mo Energy and Mineral resources et al., (2001).

A substantial portion of the territory to the south of the zero contour line is occupied by a semi-stable range, and rarely winnowed sands with a hilly and sloping relief of 5-10 m height.

Numerous transgressions of the Caspian in the Quaternary period determined the modern geomorphological view of the studied territory: Bakinskaya and Khazarskaya in Early and Middle Pleistocene, Khvalynian and Novocaspian in Upper Pleistocene and Holocene. The geomorphology of the Precaspian basin was formed under the impact of geological and natural factors in serial form of accumulative marine terraces: Bakinian, Khazarian, Khvalynian and Novocaspian, where a modern accumulative marine terrace is distinguished.

The geomorphology of the territory under consideration is closely related with the history of its geological development and is determined by the surfaces of Khvalynian, Novocaspian and modern accumulative marine terraces.

KHVALYNIAN ACCUMULATIVE MARINE TERRACE

Khvalynian Accumulative Marine Terrace is traced in the northeastern and southeastern portions of the territory. The lower hypsometric terrace line is traced at point minus 22 m. raising above the Novocaspian terrace as a flat bench with a height of 1.5-3 m. Beach ridge is graded by denudation processes and is merely traced. At the bottom ridgy plain relief, absolute points of location are within the range of minus 22 m - minus 18 m (within the territory shown on the map of engineering and geological zoning). In the eastern portion, the ridgy plain terrace relief becomes more complicated due to the presence of sloping relief forms, with a height of 5-10 m, represented by stable and semi-stable sandland formed as a result of aeolian processes of sand and sandy-argillaceous Khvalynian sediments processing.

NOVOCASPIAN ACCUMULATIVE MARINE TERRACE

Novocaspian Accumulative Marine Terrace occupies the central portion of the territory under consideration. The lower hypsometric terrace line is traced at point minus 26 m that corresponds to the Caspian level of 1929-1930. The lower edge of the terrace is fixed by a relatively clear beach ridge with relics presented in a kind of a range of fixed sandland, raising above the area from 2 to 5 m and stretched out in a meridian direction. As a rule, sandland is edged by sor; narrow lowerings with a shape resembling canals and dry beds stretched in a latitudinal direction, an origin of mainly tectonic character is observed.

The plain with sloping forms is peculiar for the surface of Novocaspian terrace. Absolute points of the area range from minus 26 m to minus 22 m. The central portion of the terrace surface is slightly lowered and is within the points of minus 23.9 m to minus 25.4 m and is characterized by the presence of sor lowering (Mo Energy and Mineral resources et al., 2001).

MODERN ACCUMULATIVE MARINE TERRACE

Modern Accumulative Marine Terrace includes the territory released from the water basin of the Caspian Sea during the 30s and lying within the absolute points from minus 26 m to minus 27.2 m, which corresponds with the absolute point of the Caspian Sea level as of January 2001.

The islands located in the coastal portion of the Caspian water basin belong to this terrace as well. The surface of the terrace is a flat plain slightly sloped to sea direction. As a rule, the coastal portion and islands are swamped and practically impassable for all types of transport. The width of the swamped area differs and sometimes in low lying areas goes deep into the territory (eastward) creating an advanced hazard for area flooding by surge (e.g., Terenozek

Oilfield). The presence of a great quantity of whole and shell fragments of marine shellfish (*Cardium Edule*) from the surface is typical for the modern terrace territory. The surface of the modern accumulative marine terrace is a zone of constant surges affected by the Caspian Sea.

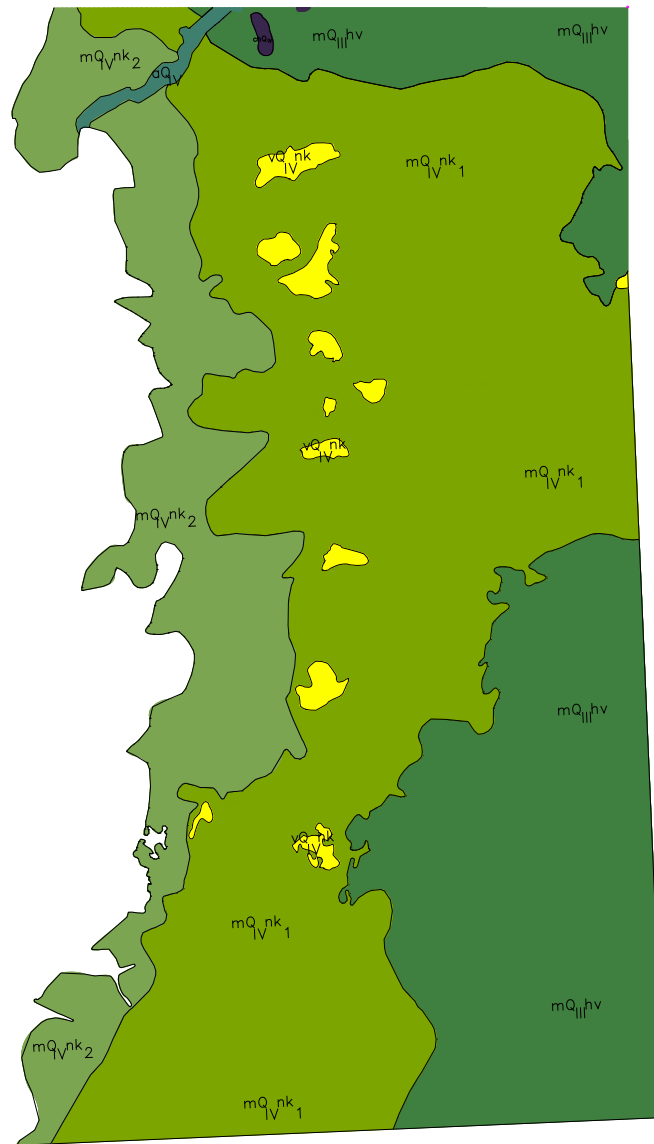


Figure 56: Map of soils distribution between Emba River basin and Mervyy Kultuk Bay, after “Mo Energy and Mineral resources et al., 2001”.

Taking into account the spreading features, bedding conditions, and composition of non-lithified deposits of the Quaternaries, the main engineering geological rock complexes distinguished among them include marine sediments of Early and Middle Pleistocene and Holocene (Figure 56).

➤ Non-lithified Marine Sediments of Early and Middle Pleistocene

Represented by marine sediments of Bakinian (mQ1b) and Khazarian (mQ2hz) layers of Quaternary System, these consist of thin clay layers, sandy clay, and a rare loam with sand alterations. The thickness of sediments is 50-200 m with an embedded roof at a depth of at least 50 m from the ground surface. As these sediments lie relatively deep and are not involved in the area of engineering facilities, the description is brief.

➤ Non-lithified Sediments of Upper Pleistocene and Holocene

Upper Pleistocene (Khvalynian layer Q3hv) and Holocene (Novocaspian layer Q4nk) non-lithified sediments, where marine sediments were primarily developed within the studied territory, and constitute the whole territory of the Precaspian basin from the surface, these serve as the foundation for all erected facilities in this area. Therefore, the description is given in more detail.

The sediments of Khvalynian and Novocaspian layers are divided into seven stratigraphical-genetic complexes, where the third, fifth and seventh complexes are of marine origin; the fourth and sixth complexes are of deflectionary-accumulative (Aeolian) origin; the second complex is of alluvial origin; and, the first complex is of chemogenic origin. A description of each stratigraphical-genetic complex (from top to bottom) follows.

- Complex 1: Halogenic sediments (chQ4) form the bottom of the immense lowering and salt lakes within the Khvalynian accumulative marine terrace. This is presented by the thickness of lake-salt from 0.2 - 0.6 m. The lake-salt is followed by a formation of liquid soil (mud), consisting of black sludge, organic substances, and a complex of Halogenic salt, which has healing properties; the layer thickness is up to 1m.
- Complex 2: Non-lithified alluvial sediments of Holocene (aQ4) are spread within the alluvial terrace of the Emba River and are represented by a sandy loam and fine sand. The roof has a thin clay formation varying from taupe to black with sludge and organic substance inclusions; the sand contains gravel and pebbles. Poorly-salted soil. The thickness is from 3-5 m.
- Complex 3: Non-lithified Holocene sediments of marine origin (Novocaspian layer, upper section (mQ4nk2) are spread within a modern accumulative marine terrace. Represented by a sludge sandy loam of a gray, taupe colour with seams and lenses of loam, clay and sludge with whole and shell fragments *Cardium Edule*, the soil is salted with a thickness from 2-6 m.
- Complex 4: Non-lithified sediments of Novocaspian accumulative marine terrace (Novocaspian layer, Aeolian origin (vQ4nk) is deposited by deflation processes.

Constitute relics of beach ridge determine the lower border of the Novocaspian Terrace. Represented by fine and dusty sand of brownish-gray color with whole and shell fragments of marine shellfish; salted soil has subsidence; thickness 2-5 m.

- **Complex 5:** Non-lithified Holocene sediments of marine origin (Novocaspian layer, lower section mQ4nk1) are mainly presented by a sandy loam of brownish gray colour with dependent formations and lenses of loam, sludge, and thin sand seams, with salted soil at a thickness from 5-12 m.
- **Complex 6:** Non-lithified sediments are formed by the deflation processes at the Khvalynian accumulative marine terrace (Khvalynian layer, upper section vQ3hv). These are observed in the extreme northwestern corner of the territory under consideration in the form of a small tongue and is represented by dusty sand with alterations and lenses of brownish-yellow fine sand; salted soil has subsidence; thickness 3-12 m.
- **Complex 7:** Non-lithified sediments of marine origin lie at the Upper Pleistocene (Khvalynian layer, – mQ3hv). This is spread across the Khvalynian accumulative marine terrace. Represented by mainly brownish-yellow sandy loam with dependent formations and lenses of loam and clay; salted soil has subsidence; thickness is 2.5 – 7.0 m. Lithified mining rocks of Paleozoic- Mesozoic age are distinguished as a separate complex (relics of salt-dome formations), represented by chemogenic marine formation – gray gypsum; terrigenous marine formation - sandstone on calcareous-argillaceous cement, ventilated, fractured (Mo Energy and Mineral resources et al., 2001).

3.4.3 Spatial distribution of soil features in Zone D (Southern Area, Northern Shoreline of Buzachi Peninsula)

The studied territory at the border of two geological structures of the 1st order: the Russian Platform and the Turanskaya Platform are the southern extremity of the geological structure of the 2nd order – Precaspian Syncline, the major portion occupied by the Precaspian Basin.

The geomorphologic view of the region is closely connected with the history of the geological development and is determined by a series of accumulative marine terraces formed as a result of transgressive and ingressive activities of the Caspian Sea in the Pleistocene-Holocene age (Quaternary period). Deflation and accumulative (Aeolian) processes have caused a considerable effect on the formation of the modern relief of the territory. Geomorphologic typical feature is an extreme gradation, which determines the hypsometric position of the accumulative marine terraces and deflation and accumulative forms of the relief. An accurate description is given in the study carried out by Mo Energy and Mineral resources et al., 2001.

A more detailed description of the main geomorphologic elements that determine the modern geomorphology of the territory is given below.

MODERN ACCUMULATIVE MARINE TERRACE

This terrace is located in the western, northwestern and northern parts of the region and includes the territory released from the Caspian Sea during the 30s of the twentieth century due to its unexpected level drop. The upper border of the terrace is hypsometrically determined by an absolute mark of minus 26.0m; the lower margin is the modern shoreline of the Caspian Sea currently equivalent to the absolute mark of minus 27.2 m.

The surface of the terrace is a flat valley with a slight slope towards the sea (the slope of the location is 0.00035), which does not have any vegetation and is marshed in the shoreline zone. Under the influence of the surges from the Caspian Sea and due to recent sea water level rise, the surface was flooded with sea water levels up to the absolute mark of minus 26.47 m (transgressive peak of the sea).

NOVOCASPIAN ACCUMULATIVE MARINE TERRACE

This terrace occupies the western, northern and northeastern portion of the studied territory and some sections have also been observed in the southern and western regions. The upper hypsometric border of the terrace is equivalent to the absolute mark of 22.0 m and the lowest border of the terrace to an absolute mark of minus 26.0 m. The lower portion of the terrace in the west and northwest is separated from the modern terrace by a sharply observed shoreline embankment in the form of a narrow ridge with the height from 1.5 to 3.0 m and the width from 50 m to 200 m, which determine the status of the shoreline of the Caspian Sea at different stages of the development of the Novocaspien transgression. On the remaining part of the territory the Novocaspien terrace is separated from the modern terrace with a sharply conspicuous ledge with the height from 0.5 m to 1.5 m.

The characteristic forms of the relief are range from hilly and ridgy to slopping and ridgy and ridgy, with relative overfall heights from 0.5 to 2.0 m. The lowest sections of the location are, as a rule, occupied with sors. In the northern and northeastern sections of the Novocaspien terrace's presence of relicts is a characteristic feature of the upper Khvalynian accumulative sea terrace rising above in the form of original relict islands (e.g., Baltic scerries) over the Novocaspien valley. The absolute marks of the tops of the separate Khvalynian hillocks and hills reach minus 11.32 m to minus 12.01 m.

The slopes of the island elevations, as a rule, are rather steep, sometimes abrupt, sodded with vegetation. The described forms of relief in some cases are framed with narrow shallow gally lowerings, which determine the relief zone of the fresh and saltish water accumulated in the thickness of the ridges and hills of the sandy loam deposits under the appropriate

paleoenvironmental regime. The surface of the elevations is exposed to deflation and accumulative processes.

A big valley named the Bolshoy Soris situated in the western section of the explored territory, which is a dried lagoon recently covered with sea water. It is a flat valley with absolute marks from 26.7m to minus 27.9m. The lowest sections of the lagoon are occupied with lakes with lake-salt. In the northeast and east of the lagoon there are tectonic ostanty (remainders) of half-rocks of the upper cretaceous age, which rise steeply over the location to heights from 3 m to 5 m. On the eastern shoreline of the lagoon there are embankments constituted of sand, pebble and shell *Cardium Edule*. The surface of the lagoon is hardly accessible for all types of vehicles and is inaccessible in some sections.

UPPER KHVALYNIAN ACCUMULATIVE MARINE TERRACE

This terrace is well spread throughout the central and southeastern sections of the explored territory and in the the northern and northeastern sections of the Novocaspian terrace is in the form of relict islands. The upper hypsometric border of the terrace is determined by a zero isohypse. The lower hypsometric border is equivalent to an absolute mark of minus 22.0 m, separated from the Novocaspian accumulative sea terrace with abrupt hillocks and separate cases with abrasion heights from 1.8 to 3.0 m. Typical features include flat-sloping and hilly-sloping relief forms with fluctuations of absolute marks from minus 14.0 m to minus 5.5 m on the hilltops and slopes, and from minus 17.0 to minus 18.0 m in the thalwegs of the big flat basins. The total elevation of the area is observed from the north to southern direction (Mo Energy and Mineral resources et al.,2001).

To a certain degree, the surface of the terrace has been exposed to an impact of deflation-accumulative processes, which caused the formation of weathering pits in the form of stretched cells oriented mainly in the sub meridian direction; the deepest of which are occupied with closed sors.

Within the southeastern section of the upper Khvalynian accumulative marine terrace are plentiful sand massifs of the Aeolian genesis (sands of Zhelimshik) forming of Khvalynian sea deposits. The Zhelimshik sands are divided into two separate massifs: northern and southern.

- The Northern Massif is developed within the upper Khvalynian accumulative marine terrace; negative absolute marks are typical; hillock forms of the relief are the most well-spread forms: semi-fixed sands form sloping hillocks with relative heights from 3-5 m to 10-12 m; the tops are oval, the slopes are even with angles not more than 15°; absolute marks of the location range from minus 8.1 to minus 14.6 m in the blowing basins and from minus 4.4 m to minus 0.3 m on the tops of the hillocks.

- The Southern Massif is developed within the lower Khvalynian accumulative terrace with a characteristic feature of positive absolute marks; mostly, there are hillock and ridge forms of relief with alterations of the ridges and hillocks divided by weathering pits; the length of the ridges is from 80 to 100 m to 1 km, and the width is 200 m; the slopes of the ridges are relatively flat (12°-15°) and sometimes steep (to 25°-30°); the absolute marks of the location range from plus 8.3 m to plus 11.8 m on the bottom of the blowing basins, and from plus 16.8 m to plus 28.0 m on the tops of the ridges and hillocks (Mo Energy and Mineral resources et al., 2001).

LOWER KHVALYNIAN ACCUMULATIVE MARINE TERRACE

The spread in the southeastern section of the area under the study at the lower border of the terrace is traced according to the zero isohypse, its whole surface determined by plus marks. From the upper Khvalynian terrace is divided with a relatively sharp ledge, which is approximately a height from 3 to 7 m. The steepest (western) sections of the ledge have a relatively massive net of small gullies with the depth of the erosion from 1 to 2 m. For the surface of the terrace a characteristic feature is the flat-ridgy and hilly-ridgy forms of the relief with relative heights of elevated areas over the lower from 3 to 5 m.

The absolute marks of the location contain values from plus 0.8 m to plus 9.6 m. To a certain degree, deflation and accumulative processes have affected the surface of the terrace.

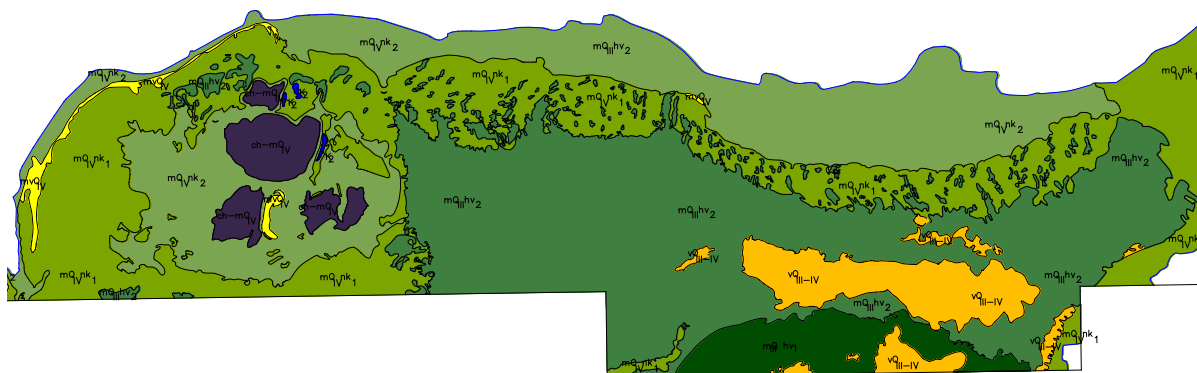


Figure 57: Map of soils distribution in the Northern shoreline of the Buzachi Peninsula, after “Mo Energy and Mineral resources et al., 2001”.

Taking into account peculiarities of the genesis and distribution, bedding conditions, and composition of non-lithified quaternary sediments within the boundary of the surveyed area, six original stratigraphic complexes with marine and continental genesis have been identified (Figure 57).

Lithified hard rocks of the Upper Mesozoic (Cretaceous period, Maastricht stage – K2) that are distributed locally have a separate stratigraphic complex. See below for a description of each of the identified stratigraphic complexes (from top to bottom):

- Complex 1: Marine halide sediments of the Upper Quaternary (Holocene) age: ch-mQ4. These are found within the boundaries of the Bolshoy Sor, at the lowest section occupied with a lake of bay salt. This section of the bay salt has a thickness up to 1.0 m and an underlying horizon of a liquid mass (mud) consisting of a mixture of black silt, organic substances, and halide salt suite with valuable medicinal properties; thickness of the horizon measures from 0.7 to 1.1 m.
- Complex 2: Non-lithified sediments of the Upper Quaternary age and marine genesis, mostly affected by the Eolithic processes mvQ4 form the bars, which are spread over the western and northwestern coast. Represented by gravelly sand with numerous whole and crushed shells *Cardium Edule*, with thin streaks (from to 2 to 3 mm) of black silt with inclusions of gravel and pebble material. Section thickness is up to 3.5 m.
- Complex 3: Non-lithified sediments of the Novocaspian (Holocene) age and marine genesis - mQ4 nk. Local name: Mangyshlak stage, are found within the development area of modern and Novocaspian accumulation marine terraces. Mainly represented by muddy, loamy sand (argillaceous sand with an admixture of silt and organic substances), with downstream lenses and single aleurite horizons. Soils of this complex consist of characteristic grey, ash grey and dark grey to black hues, hydrogen sulfide odor (which implies ongoing microbiological processes in the section), strong and excessive salinization, and high carbonate and gypsum content; in some cases, semi-decomposed and intact remains of algae are found in the aleurite section. Soils contain a distinguished weak compaction, low durability, high compressibility degree, and thyrotrophic properties. Section thickness ranges from 0.9 to 4.3 m.
- Complex 4: Non-lithified sediments of the Pleistocene and Holocene age and Eolithic genesis. Spread over Zhilimshik sand massif development area, this complex is represented by dusty, brownish grey sand, appropriately sorted, homogenous, with crushed shells of *Didacna Proetogonoides* at the base, and occasional inclusions of gravel and pebble material. Soil has weak to medium salinity and has subsidence. Penetrated section thickness is 15 m.
- Complex 5: Non-lithified sediments of the Upper Khvalynian age and marine genesis - mQ3hv2. Spread over the development area of the Upper Khvalynian accumulation marine terrace, Complex 5 is represented by muddy, yellowish brownish loamy sand

with whole and crushed shells of *Didacna Proetogonoides*, *Dresensea Polymorpha*, lenses and low thickness clay horizons at the base. Having been for a long geological period in the continental regime, the sand has undergone a loessification and acquired subsidence properties of the first category. Soil has weak to medium salinity, contains carbonates and an insignificant quantity of gypsum. Section thickness is 8 to 12 m.

- Complex 6: Non-lithified sediments of the Upper Khvalynian age and marine genesis - mQ3hv1. Spread over the development area of the Lower Khvalynian accumulation terrace and represented (from top down) by the muddy, yellowish brownish loamy sand with occasional inclusions of small pebbles; fine and dusty, brownish yellowish sand with thin streaks of clay, inclusions of small pebbles, whole and crushed shells of *Didacna Protrasta*, occasionally *Didacna Protogonoides*; gravel and pebble sediments with sand fill; *Dreissensia Polymorpha* fauna, large shells of *Didacna Protogonoides*. Soils consist of weak to medium salinity and contain carbonates and small amounts of gypsum. Having been for a long geological period in the continental regime, the sand has undergone a loessification and has acquired subsidence properties of the first category. Section thickness is from 14 to 17 m.
- Complex 7: Lithified Upper Cretaceous rocks (Maastricht stage - K2) are spread in the form of single tectonic residual hills in the northeastern section of Bolshoi Sor, and is represented by limestone and calcareous sand sections that consist of medium density.

3.5 HYDROGEOLOGICAL SETTING

From the hydrogeological point of view the Precaspian basin is a huge Artesian basin made up of thick Cainozoic, Mesozoic and Paleozoic sediments. Hydrogeological conditions of the area are complex and variable, determined by geology and climatic factors. Specific features of the basin structure are its multistage system, complex salt dome tectonics (salt plugs close to the day surface), prevailing argillaceous and marl rock. Totally flat and poorly defined relief, a lack of permanent watercourses, severe continental climate with small amount of precipitations and their high evaporating capacity lead to prevalence of saline waters in the upper part of the sediments. The lower section contains underground chloride sodium brine type water (GAS, 2007).

Falling atmospheric precipitation ensures groundwater recharge over the entire territory at the expense of infiltration through permeable sandy deposits. Besides, in the zone affected by wind-induced surges and near river systems, favourable conditions for groundwater recharge are set in. This is also promoted by geomorphological environment.

Hydrogeological section in the studied area was penetrated at depths from 1700 to 3000 m, but only the upper 300 to 500 m has been properly studied.

Deep horizons were mainly tested in the near-anticline and anticline parts of the salt domes. From the hydrogeological point of view, vast intradome zones, the most favorable for the subsurface disposal of the wastewater, have been poorly studied to date. Postsalt sequence with the reservoir bedding depth less than 2.5 km has practical value for the industrial wastewater disposal. Geological framework of the postsalt sequence includes the rocks of the Upper Permian, Triassic, Jurassic, Cretaceous, Paleogene and Neogene-Quaternary sediments. Upper Permian, Lower Triassic, as well as Upper Cretaceous (except Cenomanian) and Paleogene consist of prevailing clastic carbonate, occasionally carbonate and hemogenic sediments. Clastic rocks represent the remainder of the section, including Permian Kazansky stage, Triassic, Jurassic, Lower Cretaceous, Cenomanian stage of Cretaceous, and Quaternary-Neogene sediments. Increased shale volume and thickness of the sediments from the periphery sections towards its centre is a peculiar feature of the postsalt sequence sedimentation.

Underground waters of the postsalt sequence form artesian porous, sometimes porous and fractured aquifer systems. Main aquifer systems are predominantly confined to sand and siltstone sediments of the Cretaceous Cenomanian and Albian, Middle and Lower Jurassic, Triassic Vetluzhsky stage and Permian Tatarsky stage. Water-impermeable rocks mainly

characterize the remainder of the section. Shale rocks, except for the marginal parts of the depression, account for 60 to 80 % of the section.

Regional recharge areas of the aquifer systems comprise the edge parts of the depression, especially the northern and northeastern margin. Main movement of the underground water in the postsalt sediments is directed from the edges of the depression to its inner areas. Salt plugs penetrating the postsalt formation create natural barriers, which hamper the movement of underground water in the intradome areas. Discharge is carried out via the faults in the near-anticline parts of the salt domes, as well as in the Volga, Ural, and Emba river valleys. The above peculiarities assist in the development of the hydrodynamic zoning in the artesian basis, both vertically and areally, from periphery parts of the depression to the centre. Postsalt sequences are located in the hydrodynamic zones of the aggressive and retardant water exchange. In the deepest intradome areas the waters of the Upper Permian, and, possibly, Jurassic sediments have static drive. Aggressive water exchange zones include the aquifers and systems lying down to 300 m. 300 to 500 m depths characterize the retardant drive zone, deeper layers by static drive. As a rule, the waters in these zones have high salinity, chloride and sodium composition, with salinity from 30 to 387 g/dm³.

The important role in the retardant and static drive water exchange zones play the thick regional continuous confining beds, which isolate the aquifers and systems from the interaction with the over and underlying horizons. Four confining horizons have been identified in the Precaspian basin. Some areas have them dropped out from the section or bedding at significantly lower levels, than the ones recommended for wastewater disposal. Argillaceous carbonate salt-bearing sediments represent confining beds. The role of the beds significantly reduces in the faulting areas due to the impairment of their isolating functions (GAS, 2007).

3.5.1 Spatial distribution of hydrogeological features in Zone B (from Atyrau City to the Emba River valley)

Hydrogeological conditions of the Precaspian lowland is complicated and conditioned not only with its structural-tectonic peculiarities, lithologic-facial mutability of rocks, but climatic conditions. Two water-bearing complexes are identified in the structural-hydrogeological cross section. The first water-bearing complex is related to lithified differences of rocks of Mesozoic and represented by pressure water of high mineralization. The second water-bearing complex is related to non-lithified Pliocene-Holocene sediments. Two stages of pressure free water and low pressure water are high mineralized and low mineralized ground waters with insignificant water abundance formed within the second water-bearing complex: the first stage is confined to Early and Middle Pliocene sediments; the second stage is confined to Upper Pliocene and Holocene sediments (Mo Energy and Mineral resources et al., 2001).

Between the first and second stages is a very thick aquiclude in the form of a thick layer of clay of Khvalynian age. The major depth occurs at the second stage of the water-bearing complex. The ground waters of the second stage are subdivided into two water-bearing formations: the formation of highly mineralized ground waters and the formation of low mineralized ground waters.

3.5.1.1 Formation of High-mineralized Ground Waters

This formation is tied to marine and alluvial-marine sediments of the third, fourth and fifth stratigraphic-genetic complexes. Water containing rocks are sandy loam and sand of different rocks. The depth of deposition of groundwaters differs; therefore, the map of engineering-geological zoning has hatched sections with different depth of ground waters.

The horizontal blue shading is the area where groundwaters are at the depth of 1-3 m. The blue shading at the angle of 45° from left to the right is the area where the groundwaters are at the depth of 3-5 m. The blue shading at the angle of 45° from right to the left is the area where the ground waters are on the depth of 1-3 m (narrows between knolls) up to >5 m (knolls and ridges).

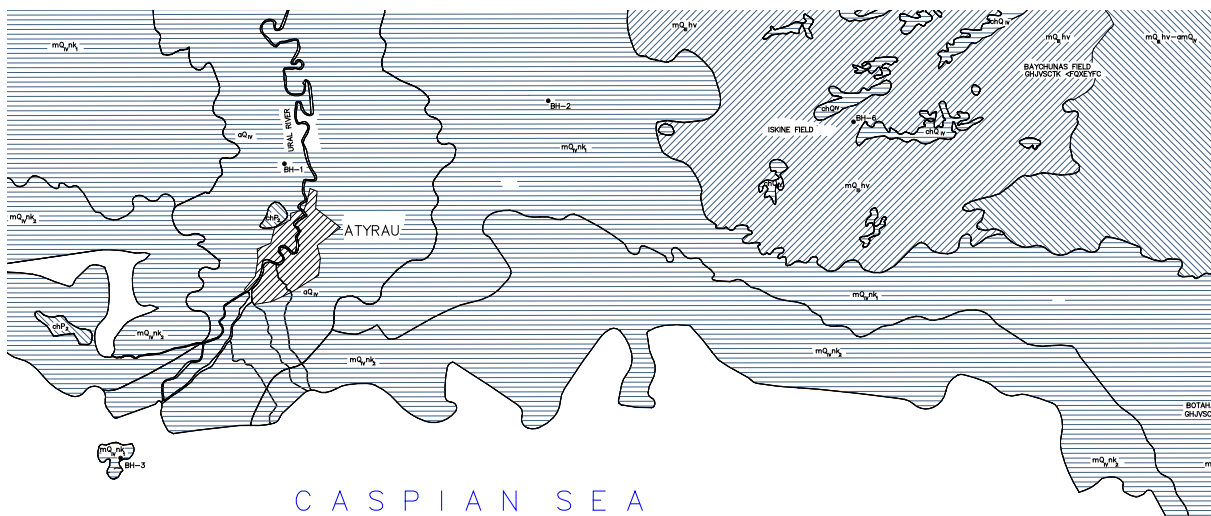


Figure 58: Groundwater depths in Zone B

The main feeder of groundwaters is atmospheric precipitation; during arid climatic conditions and high evaporation levels the feeding occurs during winter-spring periods. If the feeding process is natural the seasonal fluctuation of groundwater levels will not exceed 0.5 m.

In coastal areas subject to surge effects, an additional groundwater feeder would be the surge within the flooded area. Some desalination occurs due to the replenishment of low mineralized seawater. Taking into account that the surge occurrence is irregular, it is difficult to determine

the conditions of groundwaters. In the areas of towns, settlements, industrial zones and oil fields there is an additional feeder of ground waters, such as unregulated discharge of industrial and domestic effluents and leakage from damaged utilities. Here an artificial underflooding of the area is observed that causes the local raising of ground after levels compared to the level of groundwater around the area. In some locations the level of groundwater raises up to the day surface point causing swamping of the area. A similar situation is in locations of estuary irrigation and close to irrigation systems. Decrease of groundwater mineralization is observed in areas of artificial underflooding, which has an adverse affect on the environment and geology.

The groundwater of described formation, formed as a result of natural-historic process of area development is highly mineralized. The dry residual is 62-83 g/l, corresponding to brine group. The concentration of hydrogen ion (pH) 7.5-7.7 specifies the conditions as alkaline. Total alkalinity is 0.3-1.3 g/l (4.8-21.2 MEKV); concentration of chlorine ions 27-43 g/l (764-1218 MEKV); concentration of sulphate ions 10.1-13.6 g/l (210-277 MEKV); concentration of calcium ions 0.86-1.2 g/l (43-60 MEKV); concentration of magnesium ions 2.4-4.9 g/l (204-406 MEKV); and concentration of sodium + potassium (due to the difference) 16.7-26.3 g/l (969-1145 MEKV). The type of salinization is sulphate-magnesium-sodium-chlorine.

The parameters of filtration water properties containing complexes are as follows: filtration coefficient 0.7-1.1 m/day, impact radius 15-23 m.

3.5.1.2 Formation of Low Mineralized Ground Waters

Water containing formation is confined to alluvial sediments of the second stratigraphic-genetic complex. Water containing rocks include fine sand and sandy loam with insignificant yield of water. Water resistance and low mineralized waters come from the clays of low Khvalynian agewith a feed from atmospheric precipitation, steam condensation from the air and the rivers Ural and Emba during the freshet period (Mo Energy and Mineral resources et al., 2001).

These waters are deposited as lenses on more salty waters at a depth of 1.5-6.0 m. The lenses are either isolated from below waters by waterproof loam and clays or bedded straight on more salty waters. According to the chemical content, the water is chlorine-magnesium-sodium type with saline content 2-7.5 g/l. The salinity content and salt containment depend on the conditions of feeding from below salt waters.

3.5.2 Spatial distribution of hydrogeological features in Zone C (from the basin of the Emba River to the Mervyy Kultuk Bay)

Hydro-geological conditions of the Precaspian basin are complicated and specified not only by tectonic formation features or lithological facies change of rocks, but by climatic conditions. Two water-bearing complexes are distinguished in a hydrogeological formation cross-section. The first water-bearing complex is connected with lithified rock mass of Mezokainozoi and represented by water pressure of high mineralization. The second water-bearing complex is connected with non-lithified Pleistocene-Holocene sediments. Two layers of unconfined or poorly-confined highly mineralized groundwater with relatively small water abundance are formed within the second water-bearing complex: the first layer is tied to the sediments of Early and Middle Pleistocene, the second layer is tied to the sediments of Upper Pleistocene and Holocene.

There is a strong aquifuge in the form of a Khvalynian clay layer between the first and second layers.

Underground water from the first water-bearing complex and first layer underground water of the second water-bearing complex lie considerably deep.

The water-bearing formation for underground water of the second layer consists of sandy loam and sandy variations of upper Pleistocene and Holocene soil. The depth of underground water bedding within the studied territory differs; therefore, the locations of underground water level at certain depths are correspondingly shaded on the figure below.

The territory with underground water depositing at the depth of 0-3.0 m is horizontally shaded with blue color. The territory where underground water lies at 3.0-5.0 m depth is shown with blue shading at the angle of 45°, with the incline from the left to the right. The territory where underground water lies in more than 5.0 m depth is shown with vertical blue shading (Mo Energy and Mineral resources et al., 2001).

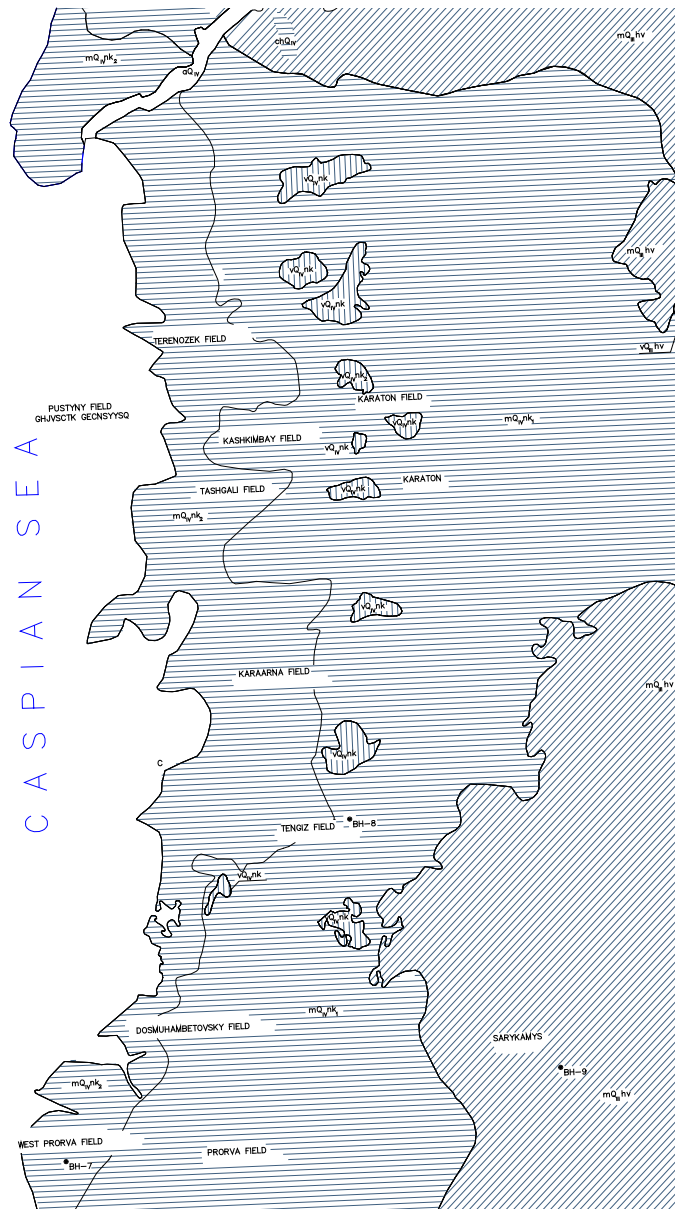


Figure 59: Groundwater depths in Zone C

The main source of underground water feeding is atmosphere precipitation. In conditions of extremely dry climate and high evaporation level this process occurs in winter-spring time. In the regime of natural feeding the seasonal change of underground water level will not be higher than 0.5 m.

In the coastal zone, which is under surge influence, the additional source of feeding is surge within the flooding zone. Desalination of underground water due to fresh seawater feeding was noted. Taking into account the irregularity of surge phenomena it is difficult to speak about underground water conditions.

An additional source of feeding in existing oil fields is domestic effluent discharge with no flood control and water leakage from various defaulted utilities.

Artificial flooding of the territory and related to that considerable rise of underground water level in comparison with surrounding area is observed here. In some places the level of underground water rises up till the points of day surface, therefore swamping of the location occurs. In the areas subject to artificial flooding decrease of underground water mineralization level was noticed. Artificial flooding of territory has an unfavorable impact on environment and geologic conditions.

Underground water of the second layer, which was formed as a result of the natural-historical process of territory formation, is characterized by a high mineralization level. Dry residue is 77.3-107.9 g/l, corresponding to a brine group. Concentration of hydrogen ion (pH) 7.4-7.6 characterizes alkaline medium. General alkalinity is 0.58- 0.76 g/l (9.6-12.4MЭKB); chlorine content is 34.2-46.9 g/l (965-1323 MECV); sulphates content is 15-24 g/l (349-498 MECV); calcium content is 0.68-0.86 g/l (34- 43 MECV); magnesium content is 5-6 g/l (410-502MECV); natrium-calcium content (per difference) is 20-29 g/l (871-1298MECV).

Parameters of filtration features of water-bearing soil complexes are the following: The filtration factor is 0.8-1.3 m/day, with an impact radius of 18-25 m (Mo Energy and Mineral resources et al., 2001).

3.5.3 Spatial distribution of hydrogeological features in Zone D (Northern Shoreline of Buzachi Peninsula)

The surveyed area has complicated hydrogeological conditions, which are defined not only by its structural and tectonic features, lithofacies variability of the rocks, but by climatic conditions as well. One should also bear in mind that the mainland zone of the surveyed area and shelf area of the Caspian Sea are the source of relief for the regional water-bearing horizons formed within Mountainous Mangyshlak. Structural hydrogeological section consists of two distinguished water-bearing complexes (from top to bottom).

First water-bearing complex is associated with the lithified differentiations of the Mesozoic-Cainozoic rocks and represented by the pressure waters with high mineralization. In the eastern part of the Kalamkas field and northeastern part of Bolshoi Sor, where the Mesozoic and Cainozoic rocks outcrop at the dayside, griffons with high water column level at the day surface at 0.5-1.0 m were observed. Underground waters of the first water-bearing complex are bedding at the relatively big depths and are not involved in the engineering facility impact area, hence their description is very brief.

Second water-bearing complex is associated with the non-lithified sediments of the Upper Pleistocene – Holocene age and marine and continental genesis. It is itself subdivided in two water-bearing horizons: fresh and saltish water and highly mineralized ground water horizon.

Fresh and saltish water horizon is associated with the sand massifs of Zhilimshik and Kyzylkum: ground water bedding depth there varies in the deflation hollows from 1 to 5 m and, under the mounds, from 10 to 15 m. Waters are fresh and saltish, with dry residue from 0.9 g/l to 4 g/l, occasionally up to 10-18 g/l. The highly mineralized ground water horizon is found everywhere within the surveyed area, except for sand massifs. Water yielding rocks include loamy sand and sandy differentiations of the Upper Pleistocene and Holocene soils of the marine genesis, highly mineralized water of brine type having dry residue from 117 g/l to 150 g/l.

Both water-bearing horizons are replenished by the atmospheric precipitation, water vapor condensation of the ambient atmosphere, as well as by the regional inflow from the south, from the Mountainous Mangyshlak side. With the natural replenishment regime, seasonal fluctuations of the ground waters will be within 0.5-0.7 m range (Mo Energy and Mineral resources et al., 2001).

Man-made sub-flooding of the areas affected by the intensive engineering and business activities associated with the industrial construction at the Kalamkas and Karazhanbas fields and the extensive infrastructure is an additional water-bearing horizon replenishment source. There are significant volumes of water leaking from the broken engineering networks of various designation with uncontrolled discharge of industrial and domestic sewage. Within the surveyed area, groundwater bedding depth varies and depends on the hypsometric position of the dayside sections of the area.

Horizontal blue strokes show the areas of the groundwater bedding from 1 to 3 m depth. Blue strokes having an angle of 45° with left to right inclination show the areas of the groundwater bedding from 3 to 5 m. Blue strokes having an angle of 45° with right to left inclination show the areas of the groundwater bedding at the depth of more than 5 m (Figure 60).

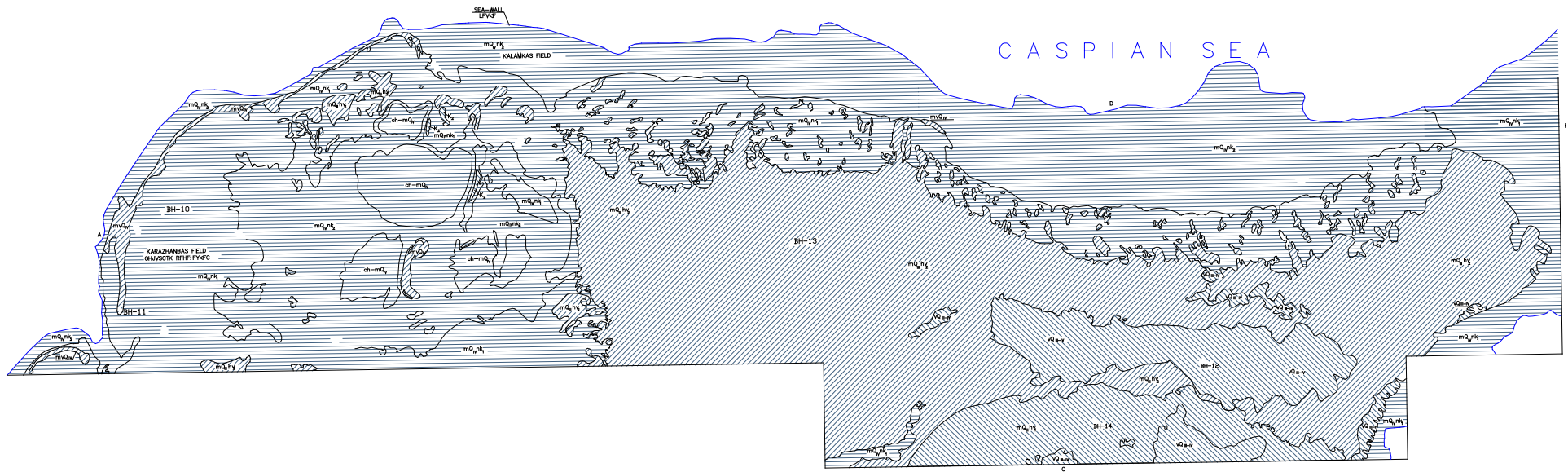


Figure 60: Groundwater depths in Zone D

3.5.4 Hydrogeology of the Tyub-Karagan Peninsula

Three aquifers are evident between the coast and the Ustyurt Plateau:

A shallow aquifer, primarily limestone (Sarmathian and Pontian strata). Groundwater depth ranges from 3 to 5 m and from 40 to 50 m. Aquifer storage and well yields are low (0.1 - 0.4 l/s), and rarely exceed 1 to 3 l/s.

At an 8 to 10 m depth, the hydraulic characteristics of the limestones vary and fracture and fissure flow increase rock permeability. Transmissivities range from 1.5 to 70 m/day, and are up to 1 - 7 m/day in marl formations. The mineral content of the water ranges from 0.5 to 15.2 g/l. Ground waters are slightly mineralised (sodium/calcium sulphate–hydrocarbonate and salty–chloride–sulphate types). The aquifer is recharged by seasonal rainfall, and discharges as springs, where the aquifer outcrops along the sea cliffs.

Deeper ground water of the Neogene–Paleogene and Cretaceous strata is associated with fracture and fissure zones, and springs occur sporadically on the north slope of the Tyub-Karagan Peninsula.

The water is often fresh, but flow rates are low, up to 1 l/s. Well drawdowns are high, about 3-10m, but occasionally the aquifer may be artesian. This water is used for local domestic or agricultural supply.

On the Tyub-Karagan spit ground water occurs sporadically but is poorly protected (Mo Energy and Mineral resources et al., 2001). The local groundwater is recharged from rainfall. A first aquifer at 1-3 m depth, fluctuates with sea level. Well yields are in the order of 0.1 - 0.5 l/s. Ground waters range from fresh to saline. No water wells exist in the Northern part of the spit but a number of wells that abstract groundwater to the south of Fort Shevchenko (near Bautino) exploit the aquifer.

3.5.5 Future Use of the Underground Waters

There are no explored fields with approved reserves of the underground waters within the area in question and adjoining areas. The underground waters are totally saline, and, therefore, cannot be used for water supply and irrigation. Thermal, mineral and industrial waters are widely spread in the area. These water resources are significant.

3.5.5.1 *Thermal and mineral waters*

In some cases, thermal waters consist of mineral content. At the total depth (3000 m) within the area the underground water temperature ranges from 75 to 80°C (Eskene field, at 2500 m

the temperature is 78°C), on the surface of the presalt sediments it is 130 to 140° C. Distribution of temperature in the aquifer systems: Upper Cretaceous horizons have the temperature 20-50°C, Lower Cretaceous 30-50°C, Permo-Triassic 68-150°C. Therefore, the following geothermal formations have been identified in the area: Cainozoic, Upper Cretaceous, Lower Cretaceous, Jurassic, Triassic-Permian, Kungurian and presalt.

Cainozoic (Quaternary-Paleogene) geothermal zone is characterized by variable geothermal stages from 22 to 55m/°C. Underground water temperature varies from 25 to 50°C depending on their bedding depth.

Upper Cretaceous geothermal formation is mainly made up of carbonate sediments (chalk, marl, limestone) having low water saturation. The formation has generally high thermal conductivity, consequently the value of a geothermal stage varies from 48 to 60 m/°C.

Lower Cretaceous geothermal formation is represented by clastic sand and clay sediments. Thickness of the Lower Cretaceous sediments decreases within the salt domes. Lower Cretaceous formations contain high salinity waters in the central part of the intradome spaces and significantly fresh waters in marginal areas. Water abundance of the sediments is high. Significant diversity of the rock geothermal properties is observed. The value of a geothermal stage varies from 37 to 83 m/°C. Such big fluctuation is determined by variable lithologic and petrographic composition of the rocks and recession of the waters with variable temperature from the adjoining aquifers to the sand reservoirs. Underground temperature in these sediments varies from 15- 25°C to 65°C.

Upper Jurassic geothermal formation is mainly represented by carbonate sediments (Mo Energy and Mineral resources et al., 2001).

Thermal conductivity of the rocks varies, sometimes it is high, geothermal stage varies from 26 to 60 m/°C. Underground water temperature varies from 25 to 75°C depending on its bedding depth.

Northern Precaspian relates top the province of the nitrogen, nitrogen and methanol and methanol mineral waters, with their major mineral components being iodine and bromine. Minimum concentration of iodine and bromine in the underground waters to be recognized as the mineral ones should be as follows, mg/dm³: iodine 5, bromine 25. Concentrations of bromine 250 mg/dm³; iodine 18 mg/dm³ are prospective for the search for industrial iodine-bromine waters (Distribution of mineral underground water in Figure 61).



Figure 61: Mineral and iodine-bromine underground waters in the study area (green circles)

3.5.5.2 *Potential wastewater disposal*

For the assessment of the condition of the area, regional (tectonic framework of the region and water exchange features, hydrogeological structure compartmentalization) and local (porosity and permeability properties of aquifers and compartmentalization of the area) factors are considered. With the low properties of permeability of an aquifer, the injectivity of certain volumes of disposed wastewater may be achieved by the increase of the number of injector wells.

Resulting from the basic environmental requirements of any aquifer, the suitability of an area for disposal first depends on compartmentalization of the hydrogeological structure and underground water exchange rate.

Robust compartmentalization of the aquifer is required not only in the area of the disposal site, but also within the area, in which a natural hydrodynamic regime is going to change due to injection of wastewater.

Three hydrodynamic zones identified in the study include the change of the hydrodynamic conditions, chemical composition, and salinity of the aquifers in the structure section:

- upper – intensive (active) water exchange and recovery,
- middle – retardant (hampered) water exchange,
- lower – strongly hampered (static) drive.

Middle and lower hydrodynamic zones may be variably suitable for wastewater disposal. In the hampered water exchange zone disposal conditions may be favourable in some areas with continuous regional confining beds. The most favourable for wastewater disposal is the static drive zone, with isolated aquifers from the impact of the surface factors and contained saline waters, which in most cases do not have any practical value.

As a consequence, aquifers potentially suitable for the disposal within the area in question are related to Neocomian, Lower and Middle Jurassic strata, found in several troughs. Boundary conditions of the aquifers are primarily determined by the presence of salt dome tectonics and hydrogeological role of the faults.

3.5.5.3 Use of low-mineralized ground water for the water supply of oil and gas industry facilities

Within the northeastern Caspian Sea region (Atyrau oblast) low mineralized underground waters with mineralization up to 3-4 g/dm³ may be of benefit to use not only for technical and agricultural water supply but also for domestic water supply (Kadyrgaliyeva et al., 2008).

The region has meagre surface waters. The river network is developed in the southwest and northeast, but most of the territory does not have any permanent watercourses. Therefore, river waters cannot always be considered as reliable sources of domestic water supply.

The longest water pipe routed in the region is Khigach (Volga)-Mangistau, which transports fresh water to Mangistau, supplying many population centres and oil-fields with water . However, due to the rise of water levels in the Caspian Sea, rundown-surge processes constantly incur this extensive water pipe with surge heights from 1.5 to 2.6m, resulting in instability of territory water supply and complications for technical operation and maintenance.

Prior to 1982 (Bali, Tugarakchan) the hydrogeological section was thoroughly examined only up to the depth of 500-520m due to little requirement and absence of required machinery

equipment. With exposed thickness of Alb-Cenomanian formations (100-220m) the effective thickness of productive strata was at 60-132 m. Underground waters were flowing, hydraulic head was at 356 m including above the ground surface from 27.0 to 29.0. Flow rates of wells measured up to 30dm/s, with level lowering - 22.2 m. Sulphate chloride sodium waters with mineralization on the Bali field area (3g/dm³), and the Tugarakchan area (3,6g/dm³). Calculated hydrogeological parameters: water transmissibility - 310 and 338 m²/day, piezoconductivity 3.5 and 1,4x10⁵ m²/day, and an effective thickness of 132 and 60 m (Kadyrgaliyeva et al., 2008).

From 1982 through 1984 the hydrogeological investigations were carried out in the South-Emba artesian basin at Zhanasu field. Water requirements exceeded the earlier approved water reserves twice throughout the basin and registered 119,000 m³/day, which caused the necessity to study the hydrogeological section in detail for fullthickness. In addition, testing of upper and lower sections was separately performed at one point using two tiered wells with a depth of 550 and 820 m. Such methodology confirmed the accuracy of the select decision. Calculated load as achieved for each water intake point represented by two wells was taken at 92 dm/s.

The new approach to the hydrogeological model of the South-Emba basin has changed the concept of calculated hydrogeological parameters of the aquifer system and Zhanasu field. The parameters are shown as follows: filtration coefficient 3,25 m/day, effective thickness 292 m, water transmissibility – 994 m²/day, piezoconductivity 1,65x10⁶ m²/day. Obtained data prove big potentialities of South-Emba artesian basin.

3.6 OIL&GAS RESOURCES

3.6.1 Description of the Precaspian basin petroleum system

3.6.1.1 *Source rocks*

Paleo-geographic conditions of sedimentation and facies architecture indicate that the principal petroleum source rocks in the North Caspian basin are basinal black-shale facies contemporaneous with upper Paleozoic carbonate platform deposits on the basin margins (Figure 62). Because of great depths, the small number of wells drilled into basinal facies, and the paucity of cores, the geochemical characteristics of the source rocks are poorly documented. Only limited analytical data are available from published sources. Lower Permian basinal facies of the west basin margin are characterized by total organic carbon (TOC) content ranging from 1.3 to 3.2 percent and hydrogen index (HI) of about 300 to 400 mg HC/g TOC (Punanova et al., 1996). Lower Permian black shale on flanks of the Karachaganak reef has TOC measurements as high as 10 percent. In Middle Carboniferous basinal black shales on the east basin margin, TOC reaches 7.8 percent (Dalyan, 1996). In the Biikzhal deep well located basinward from the southeast margin, Middle Carboniferous black shale at a depth of more than 5.5 km has TOC of 6.1 percent (Arabadzhi et al., 1993). Although data are few, high TOC and silica contents in basinal shales of all margins and characteristically high X-ray readings on gamma logs are typical of the deep-water anoxic black-shale facies. This facies contains type II kerogen and is the principal oil source rock in Paleozoic (and many Mesozoic) basins of the world (Ulmishek and Klemme, 1990).

Russian geologists believe that the Upper Devonian–Lower Carboniferous Izembet (Zilair) Formation of the east and southeast margins of the North Caspian basin contains significant petroleum source rocks (Arabadzhi et al., 1993; Tverdova et al., 1992). This coarsening-upward clastic section, especially its lower part, was partially deposited under relatively deep water conditions. Measured TOC content varies from 0.1 to 7.8 percent and averages 0.75 percent (Tverdova et al., 1992). Organic matter is of mixed terrestrial and marine sapropelic origin. On the Van Krevelen diagram, most samples are located near the boundary between kerogen types II and III. Measured HI varies from less than 100 to 450 mg HC/g rock. These data indicate that organic-rich units of the Izembet Formation could have generated gas and probably some oil. Thick Lower Permian orogenic clastics of the east and south basin margins contain only terrestrial organic matter and could have generated some gas (Arabadzhi et al., 1993).

The presence of source rocks in the suprasalt sequence has long been disputed, and some investigators believe that oil pools in salt dome-related traps were generated from these strata

(Botneva, 1987). Although some source rocks of inferior quality may be present among Triassic strata (see Figure 62), these rocks could have reached maturity only in some deepest depressions between salt domes and thus are of only local significance. Recent geologic and geochemical data show that suprasalt oils were generated from subsalt source rocks and migrated upward from depressions between domes where the salt has been completely or almost completely withdrawn.

Vitrinite reflectance and geochemical data indicate that in most fields and prospects drilled along margins of the North Caspian basin, the top of subsalt rocks occurs in the oil window or in the upper part of the gas window (Volkova, 1992). The geothermal gradient in the basin is relatively low apparently because of the cooling effect of the thick Kungurian salt sequence. The south basin margin is hotter; at the top of subsalt rocks at depths of 4–4.2 km the temperature is 100°–120°C compared to about 80°C at comparable depths on the north margin. Standard maturation modelling is difficult to apply because of differences in thermal conductivity of evaporite and clastic/carbonate rocks. Geothermal gradients in salt domes and adjacent depressions are different, and the modeling is further complicated by uncertainties in timing of salt dome formation. The difference in measured temperature at similar depths at the top of subsalt rocks under a salt dome 3.5 km thick and in an adjacent depression (in Karatobe field of the east basin margin) was 18°C (Navrotsky et al., 1982). This difference may reach 60°C under the largest salt domes of the basin. Qualitatively, it can be stated that maturation in deep parts of the basin started before deposition of the salt. Most oil generated at this stage probably was lost because of the absence of a regional seal (local seals among mostly carbonate rocks are uncommon and easily breached). This loss of early-generated hydrocarbons is demonstrated by heavy, paleo-biodegraded oils found in a number of fields at depths reaching 5.5 km (Botneva et al., 1990).

The principal stage of hydrocarbon generation and formation of fields, especially in marginal, shallower areas of the basin, probably was in Late Permian–Triassic time when the Kungurian salt seal was in place and thick orogenic molasse clastics were deposited (Borovikov, 1996; Figure 62). Significant hydrocarbon generation in later times could have occurred only locally in depressions adjacent to growing salt domes. Deposition of thick Mesozoic and Tertiary sediments in these depressions resulted in additional heating of subsalt source rocks. Triassic source rocks considered as speculative could also have reached maturity in the deepest depressions and generated some hydrocarbons.

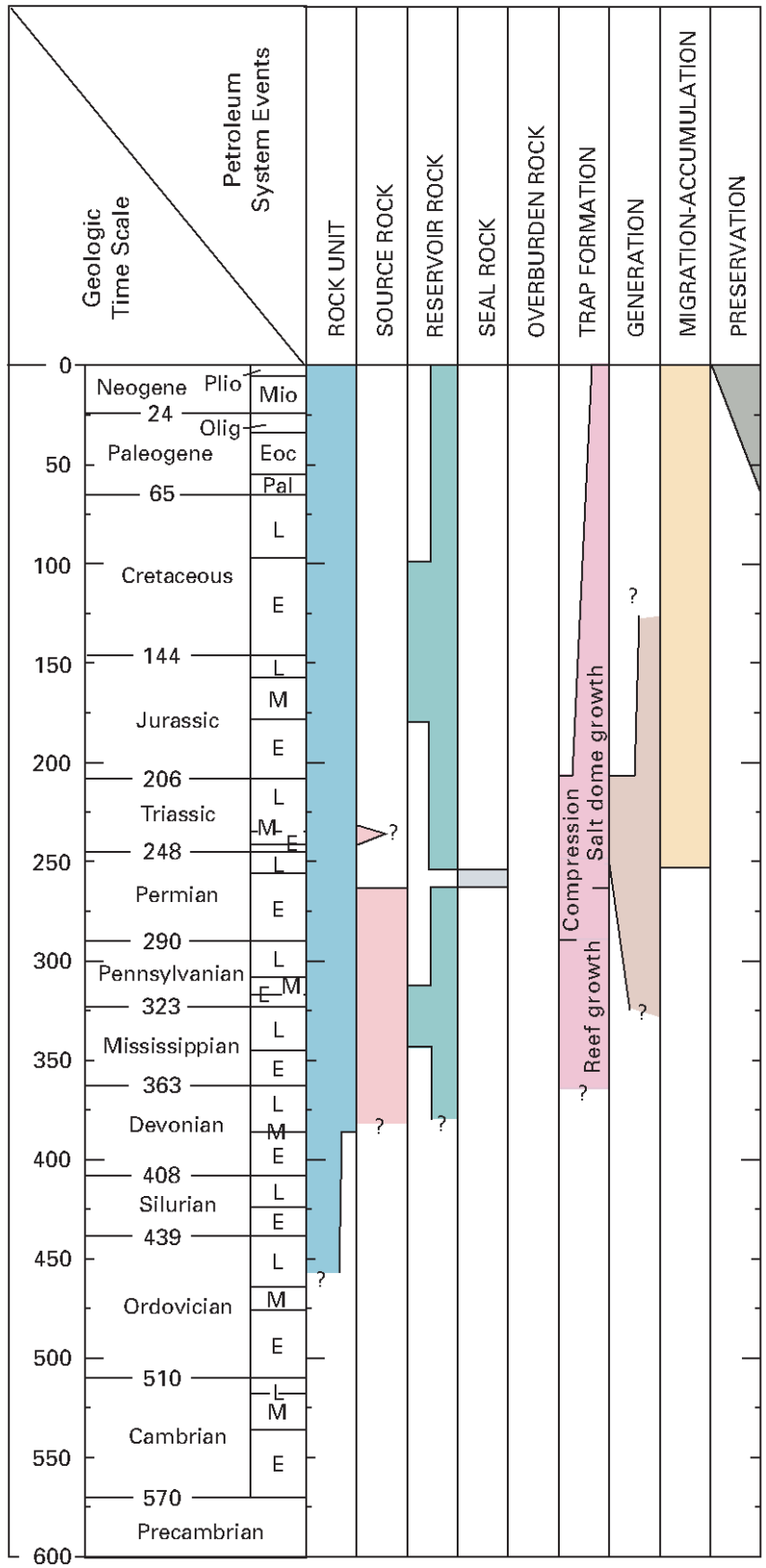


Figure 62: Events chart of North Caspian Total Petroleum System, after “Ulmishek, 2003”.
Queries indicate uncertainties in extent or identification.

3.6.1.2 *Reservoir rocks*

In the subsalt sequence, carbonate reservoirs are of better quality than clastic reservoirs. Reservoir properties of carbonate rocks strongly depend on diagenetic changes, primarily on leaching. Vuggy porosity related to leaching is better developed in reef reservoirs, especially in reef-core carbonates. For example, porosities averaging 10–14 percent are characteristic of reefal vuggy, porous limestones and dolomites in the Karachaganak field, whereas porosity of adjacent inner lagoonal facies is lower, commonly 6–10 percent or less (Shershukov, 1986).

Porosity of Upper Devonian–Middle Carboniferous carbonate reservoir rocks in the Tengiz field (Figure 35) varies from a few percent to 20 percent and averages 6 percent over this extensive atoll. Most of the porosity in this field is related to vugs, whereas the primary pore space does not exceed 2–3 percent.

Porosity exceeding 10 percent is characteristic of a ring-shape zone of the atoll's reef core (Pavlov, 1993). Porosity of carbonates deposited on slopes and in the central lagoon is significantly lower. Permeability of carbonates of the Tengiz atoll and other reefs is mainly controlled by fracturing and, in laboratory measurements, was observed to vary widely from a few to hundreds of millidarcies. In the Astrakhan field, Bashkirian detrital and oolitic limestones were deposited on a shallow bank. Porosity of the limestones averages 6 percent and is about equally divided between primary and diagenetic porosity.

Measured permeability in samples is low, commonly only 1–2 mD. However, fracturing is intensive, and most wells yield 5–10 million cubic feet of gas per day. Several small oil discoveries have been made in sandstones of the upper part of the Upper Devonian–Lower Carboniferous Izembet Formation on the east and southeast basin margins. Daily oil flows from most tested wells were low considering great depths and overpressures, and did not exceed several tens of barrels with the exception of one well that tested nearly 2,000 barrels per day. Porosity of most sandstone and gravelstone samples ranges from 10 to 20 percent; permeability is variable, in some samples reaching hundreds of millidarcies (Dalyan and Akhmetshina, 1998). The sandstones are poorly sorted, have variable but locally high content of carbonate cement, and are commonly laterally discontinuous; consequently, reservoir beds of the Izembet Formation, though locally exhibiting high porosity and permeability, are largely of moderate to poor quality. Preservation of porosity in “dirty” greywacke sandstones at great depths is probably related to high overpressure that may be twice that of hydrostatic pressure at the same depth (Dalyan and Akhmetshina, 1998).

Lower Permian (and also in places of Upper Carboniferous) orogenic molasse clastics of the east and south margins of the North Caspian basin are characterized by variable, but generally poor, reservoir properties. Exploration of this clastic play, conducted in the 1950s and 1960s, was in compressional anticlines located within the Aktyubinsk trough on the east

basin margin and farther south in the Ostansk trough. In both troughs, the orogenic molasse sequence is as much as 5 km thick. Sandstones in the more eastern anticlinal trends that were drilled are tight, probably because of deep burial and subsequent tectonic stress and unloading. The same causes resulted in poor reservoir properties of orogenic sandstones in compressional thrust-related anticlines of the Karakul-Smushkov zone in the western part of the south margin. Reservoir properties of Lower Permian sandstones outside the zones of compressional anticlines are somewhat more favourable. Several oil accumulations have been discovered in these rocks; in the largest accumulation (Kenkiyak field), at depths of 4–4.5 km, porosity varies from 5 to 11 percent and permeability does not exceed 50 mD. The main reservoir problem is the discontinuous character of sandstone beds, which probably resulted from the rapid progradational deposition of the orogenic clastic sequence. Highly variable original yields of wells that range from less than 40 to greater than 2,000 barrels/day resulted from these geologic conditions (Solovyev, 1992). Reservoir properties of Jurassic and Cretaceous sandstones that occur at shallow depths above salt domes are excellent; porosity ranges from 25 to 35 percent, and permeability is high, commonly several hundred millidarcies. Reservoir properties deteriorate somewhat in the more deeply buried Triassic and Upper Permian strata, but in a few fields where these rocks are productive, porosity remains higher than 20 percent and permeability varies from 30 to 500 mD (for example, Kenkiyak field; Figure 38).

3.6.1.3 *Seal Rocks*

The Lower Permian Kungurian evaporite sequence is the principal regional seal for subsalt reservoirs of the North Caspian basin (Figure 62, seal rock) and covers the entire basin area except for a narrow zone along the east and south margins where salt either was not deposited or was truncated by pre-Jurassic erosion. Kungurian salt is deformed into numerous domes alternating with depressions, in which the deposits are thin or absent due to lateral flowage (for example, see Figure 38). Where the otherwise impermeable seal is absent, hydrocarbons were afforded avenues to migrate from subsalt source rocks vertically into suprasalt reservoirs. Some high-amplitude carbonate build-ups are likely water bearing due to hydrocarbons leaking into suprasalt rocks (for example, Karaton build-up on the Primorsk carbonate platform, Figure 36 and Figure 38).

Nevertheless, the salt formation divides the sedimentary succession into two welldefined hydrodynamic systems. Ubiquitous overpressure and significantly higher salinity of formation waters characterize the subsalt system, whereas pressure is hydrostatic and salt content in formational water is lower in the suprasalt system. Various local and semiregional shale seals

that directly overlie hydrocarbon pools in subsalt reservoirs probably would not be effective without the Kungurian salt. Upper Jurassic and Cretaceous marine shale beds seal hydrocarbon pools in suprasalt rocks. Both subsalt and suprasalt hydrodynamic systems constitute a single total petroleum system (TPS) because they were charged by hydrocarbons from the same subsalt source rocks; however, the upper system was designated as a separate assessment unit within the TPS (Ulmishek, 2003).

3.6.1.4 *Traps*

As discussed previously, carbonate reefs are the most important traps in subsalt rocks. Various morphological types of reefs are present, but atolls and pinnacle reefs contain the largest hydrocarbon accumulations. Pools in barrier reefs are much smaller because the maximum height of the oil/gas column is defined by the back-reef slope and does not exceed 150–200 m. Several subsalt fields on the east basin margin are in structural anticlinal traps (Zhanazhol and adjacent fields). These traps are related to Hercynian compression from the Urals and were formed during Permian-Triassic time approximately contemporaneous with peak hydrocarbon generation (Figure 62). Only the giant Astrakhan gas field is apparently controlled by basement-related uplift in the crestal portion of a regional arch (Figure 39).

All hydrocarbon pools in subsalt clastic rocks (most of them non-commercial) have been discovered on anticlinal prospects. However, the discontinuous character of clastic reservoir rocks in both Lower Carboniferous and Lower Permian sections and large variability in flows from adjacent wells suggest that hydrodynamic connection between the wells is poor or absent and that many of these pools are actually in stratigraphic traps. In the suprasalt section, all productive traps are related to salt tectonics and are morphologically variable. Among them, anticlinal uplifts with a salt core and traps sealed updip by faults and by walls of salt domes are the most common types. In recent years more modern seismic equipment has improved the ability to map the structure of suprasalt rocks in depressions between salt domes, resulting in new types of structures being mapped in Upper Permian rocks (Dalyan, 1998) such as arches in depressions and semi-arches against slopes of salt domes. These structures are expressed only in Upper Permian rocks but are absent in both younger and older strata. Formation of the traps is related to non-uniform withdrawal of salt into adjacent domes.

3.6.2 **Oil&Gas Resources of the North Ustyurt Basin**

Source rocks have not been identified in the drilled sedimentary sequence of the Buzachi Arch and Surrounding Areas Composite TPS. Productive Jurassic rocks, although enriched in coaly organic material (the content of total organic carbon (TOC) is as high as 2.8 percent), were not

buried to the oil generation window. Some geologists proposed that oil accumulations in Jurassic and Cretaceous strata were formed by vertical migration of hydrocarbons from pre-Upper Permian marine rocks (Kozmodemyansky et al., 1995); however, geochemical data for these rocks are not available. Slight gas shows were recorded in pre-Upper Permian rocks during drilling, but testing was unsuccessful. Those rocks are separated from producing Jurassic strata by about 3,000 m of Upper Permian–Triassic red beds that are intensely compacted (especially the Upper Permian) and devoid of shows. Vertical migration through the red beds is unlikely. In addition, significant compaction of pre-Upper Permian rocks and the presence of numerous diabasic dikes indicate that the rocks passed through the oil window long before Jurassic time.

A more probable scenario of formation of the oil and gas fields implies migration of hydrocarbons laterally from the North Caspian basin. Source rocks for hydrocarbons in the North Caspian basin are in the deep-water basinal facies of the subsalt Paleozoic sequence. From there, oil possibly migrated vertically into post-salt rocks and then updip through continuous Mesozoic strata onto the Buzachi arch. The presence of oil and gas fields on the northern slope of the arch and their absence on the southern slope support this model. If the model is correct, the Buzachi Arch and Surrounding Areas Composite TPS is actually a part of the North Caspian Paleozoic TPS, although the Paleozoic stratigraphy and tectonic history of the area relate it to the North Ustyurt basin.

No inferences about the present state of maturity and time of maturation of source rocks can be made because the exact location of the source rocks is unknown. However, the timing of trap formation, the very shallow occurrence of pools, and partial biodegradation of oil indicate that migration of hydrocarbons and the formation of fields were recent—probably not earlier than Miocene.

All reservoir rocks of the Buzachi Arch and Surrounding Areas Composite TPS are in Middle Jurassic (principally Bathonian) and Neocomian sandstones. The fields contain a maximum of 12 pays (Kalamkas field), varying in thickness from a few to 40 m and separated by shale beds. Reservoir properties of the sandstones at shallow depths are good. Porosity ranges from 22 to 29 percent, and permeability ranges from tens to many hundreds of millidarcies.

The potential for the presence of reservoir rocks in the Triassic section is limited. On most drilled structures, Triassic rocks compose the leading edges of thrust plates (Popkov, 1991). The rocks are significantly deformed and compacted; and porosity does not exceed 4 percent. Somewhat better reservoir potential has been reported for Middle Triassic rocks on the northern slope of the Buzachi arch (Lipatova et al., 1985). In some sandstone samples from the Kalamkas field, measured porosities were as high as 22 percent. No potential reservoirs have been identified in older rocks.

All discovered fields of the Buzachi Arch and Surrounding Areas Composite TPS are in structural traps. The traps in Jurassic and Cretaceous rocks are elongated east-to-west anticlinal structures with steep northern flanks that commonly are cut by reverse faults. The southern flanks of the anticlines are much more gentle. Oblique normal faults also are present. The anticlines are arranged in several linear zones that extend offshore (Figure 33). The Jurassic-Cretaceous anticlinal zones are underlain by the leading edges of thrust sheets composed of Triassic rocks. The detachment surface probably is near the base of Upper Permian– Triassic clastics (Popkov, 1991). The Jurassic-Cretaceous anticlines were formed by mild compression and rejuvenation of movements along pre-Jurassic thrust planes. Three major compressional events took place in pre-Neocomian, pre-Tertiary, and pre-middle Miocene time.

Exploration for stratigraphic traps has not been conducted in the TPS. Many stratigraphic traps are predicted to be present in pinch-out zones of Middle Jurassic rocks that unconformably overlap the Triassic sequence on the southern slope of the Buzachi arch. Stratigraphic pinch-out traps around local Triassic uplifts were mapped in Jurassic rocks of the eastern Buzachi Peninsula (Rakhmetova et al., 1986). On the northern slope of the arch, Middle Jurassic rocks possibly contain traps that are sealed by west-trending reverse faults on the northern limbs of anticlinal folds.

4. EVALUATION OF NATURAL AND PRESENT SUBSIDENCE

4.1 ROCK COMPRESSIBILITY

4.1.1 Definitions

Compressibility is used in the Earth sciences, and particularly in geomechanics, to quantify the ability of a soil or rock to reduce in volume due to a pressure variation. The void space can be full of liquid or gas. Geologic materials reduce in volume primarily when the void spaces are reduced, yielding that the liquid or gas must be expelled from the voids. This process occurs over a certain period of time, resulting in a settlement of the ground surface.

Generally speaking, the application of a mechanical stress to a continuous medium causes deformation. The relationships between stresses and deformations in a homogeneous solid medium (e.g. steel or wood) differ substantially from those in a reservoir rock, since the latter consists of a matrix of solid grains forming a three-dimensional porous and permeable network. Reservoir rocks are subject to internal stresses, of a volumetric type, exerted by the fluids contained within the pores, and to external stresses caused by the weight of overlying rocks, and potentially by lateral stresses of tectonic nature. Karl Terzaghi formulated a principle stating that in a porous medium, the total vertical stresses induced by the weight of overlying sediments are partly supported by the pressure of the fluids saturating the pores, and in part by the stresses spread over the points of contact between grain and grain (effective stresses; Terzaghi, 1945). This principle, named after Terzaghi, can be written as follows:

$$\sigma_z = \sigma_{z_e} + P$$

Eq. 1

where σ_z is the total vertical stress, σ_{z_e} is the effective vertical stress, P is the pressure of the fluids inside the pores. If the production of fluids from a porous medium takes place at constant temperature (a good approximation in most of the reservoirs), exploiting only the energy drive of the reservoir, it follows that the variation in the distribution of stresses inside the porous medium is due exclusively to the variation of pore pressure as a consequence of the production of formation fluids. Generally speaking, each element of the subsurface, before

the extraction of the fluids saturating it, is in static and dynamic equilibrium with the stresses transmitted to it by the surrounding elements (due to tectonic forces, the movement of fluids, the confinement preventing its free expansion, etc.), in addition to its own weight. The underground fluid withdrawal causes a decrease of pore pressure at the production point that spreads over the surrounding medium according to a relation, which is a function of the permeability of the porous medium and the viscosity of the produced fluid. Following the fluid withdrawal, a decrease in volume occurs in all elements of the porous medium; regardless of the compressibility of the solid phase with respect to the decrease in pore volume, this depends on the variation in effective stresses alone. Clearly, the deformation of the depressurized elements is transmitted to all the surrounding rocks. In this context, it has been shown that there is a fundamental difference between the stresses induced in layers subject to depressurization, and those present in surrounding rocks: the former are subject mainly to vertical compression, whereas the latter may also be subject to tension and shear stresses, which may lead to horizontal movements, and sometimes fractures or creep along any faults present.

Generally speaking, compaction causes a variation in the pore volume, grain volume and total volume of the porous medium.

- The percentage variation in the total volume of the porous medium following a unit variation in stress is described as the bulk compressibility (C_b) of the porous medium.
- The percentage variation in the grain volume following a unit variation in stress is known as matrix compressibility (C_m).
- The percentage variation in pore volume following a unit variation in stress is described as pore compressibility (C_p).

Regarding bulk compressibility and pore compressibility, two types of variation in stress conditions can be defined: the one relative to the bulk volume of the rock, and that relative to the pore volume. The first is related to the variation of stresses on the outer surface of the sample (confinement pressure), while the pore pressure is kept constant. The second, on the other hand, refers to a change in pore pressure, while the pressure on the outer surface remains constant. Generally speaking, it is possible to define four different types of compressibility, keeping in mind the bulk volume (V_b) and the pore volume (V_p), as well as the

pore pressure (P_p) and the confinement pressure (P_c) of the sample, which may vary independently. Under isothermal conditions, using a notation for compressibility where the first subscript indicates the reference volume, and the second subscript the reference pressure, which can be varied, one can thus define:

$$C_{bc} = -\frac{1}{V_b} \left(\frac{\partial V_b}{\partial P_c} \right)_{P_p=const} \quad (a)$$

$$C_{bp} = -\frac{1}{V_b} \left(\frac{\partial V_b}{\partial P_p} \right)_{P_c=const} \quad (b)$$

$$C_{pc} = -\frac{1}{V_p} \left(\frac{\partial V_p}{\partial P_c} \right)_{P_p=const} \quad (c)$$

$$C_{pp} = -\frac{1}{V_p} \left(\frac{\partial V_p}{\partial P_p} \right)_{P_c=const} \quad (d)$$

Eq. 2

These definitions are valid only if it is possible to assume that both the pore pressure (P_p) and the confinement pressure (P_c) are independent variables (a hypothesis that makes physical sense only for drained tests carried out in the laboratory, during which a variation in the confinement pressure does not cause a variation in pore pressure). Under undrained conditions, this hypothesis does not hold true, and therefore lacks physical meaning. In the latter case, the undrained compressibility (C_u) may be correlated with porosity (ϵ), matrix compressibility (C_m), static bulk compressibility (C_{bc}) and the compressibility of the saturating fluid (C_f), using the following equation:

$$C_u = \frac{\varphi C_{bc} (C_f - C_m) + C_m (C_{bc} - C_m)}{\varphi (C_f - C_m) + (C_{bc} - C_m)}$$

Eq. 3

In the elasticity theory, the following equations are also valid:

$$C_m = C_{bc} - C_{bp} \quad (a)$$

$$C_m = C_{pc} - C_{pp} \quad (\text{b})$$

$$C_{bp} = \varphi C_{pc} \quad (\text{c})$$

Eq. 4

Due to the underground fluid withdrawal, the volume of porous medium subject to a pressure decrease tends to compact. The entity of compaction is mostly governed by the compressibility of the porous medium, and occurs mainly in the vertical direction. Under these conditions, one usually refers to the definition of the uniaxial compressibility or compressibility in oedometric conditions (C_m), also measured at constant temperature (Chierici, 1994):

$$C_m = -\frac{1}{h} \left(\frac{dh}{d\sigma_{bc}} \right)$$

Eq. 5

where h is the vertical dimension of the sample (or the thickness of a productive formation interval), and s_{ze} is the effective vertical stress. The laboratory measurement of the coefficient C_m is a difficult and laborious procedure; in practice, it is preferable to measure compressibility under hydrostatic conditions (indicated above as C_{bp}), which do not correspond, however, to those to which reservoir rocks are subject during production. From a theoretical point of view, the variation in volume of a porous medium depends only on the average variation in stresses. Therefore, by using an appropriate correlation coefficient, one can verify that the measurements carried out under hydrostatic conditions are equivalent to those carried out under oedometric conditions. In elasticity, the most commonly used correction factor is the following:

$$Y = \alpha \frac{1}{3} \left(\frac{1 + \nu}{1 - \nu} \right)$$

Eq. 6

where ν is the Poisson coefficient, and α is the Biot coefficient equal to:

$$\alpha = 1 - \left(\frac{C_m}{C_b} \right)$$

Eq. 7

The uniaxial compressibility from hydrostatic measurements can thus be obtained using the conversion factor Y defined above:

$$C_m = Y C_{bp}$$

Eq. 8

The bulk compressibility of the porous medium is extremely important for the study of both reservoir compaction and land subsidence, which may occur above areas subjected to the production of subsurface fluids (water, oil and gas). In particular, the mathematical models currently applied to study and predict subsidence use uniaxial compressibility as the identifying parameter for the deformability of the medium during the depressurization phase.

4.1.2 Measurements of rock compressibility

The compressibility of rocks can be determined by laboratory instruments, or through *in situ* investigations. In the laboratory, the mechanical properties of samples taken through drillings are studied, allowing one to measure deformations vs. the applied stresses. *In situ* investigations, on the other hand, aim to measure variations in the thickness of layers subject to depressurization. Laboratory measurements may be affected by significant errors, due to the disturbances caused by coring, the preparation of samples, the uncertainty regarding stress conditions in the subsurface, and the difficulties in determining the viscous component of deformation over the short time-frame of laboratory tests. Furthermore, laboratory tests are carried out on small samples, and therefore cannot provide information on the effects of the macro-heterogeneities often present in the subsurface. When the behaviour of samples in the laboratory reproduces the *in situ* conditions with sufficient accuracy, laboratory tests become precious because they provide precise information on the behaviour of the subsurface before underground fluid production. The accuracy of *in situ* measurements depends largely on the technique used, the presence of a casing, the presence and type of cementation, and the possible pre-compaction of the materials in the immediate vicinity of the borehole, provided that it had been previously used as a production well (Mancini et al., 2005).

4.1.2.1 Laboratory measurement

Laboratory measurements are carried out at constant temperature (room temperature or preferably formation temperature) on cylindrical samples whose size ranges from 2 to 10 cm in diameter, and 2 to 3 cm in length. The apparatus generally used and the stress systems applied are: a cell at uniform pressure (i.e. hydrostatic chamber), in which the sample is subjected to stresses equal in all directions ($s_x-s_y-s_z$), using a pressurized liquid; an oedometric chamber where the sample is subjected to an axial stress s_z (applied by a piston), while radial deformation is prevented by a cylindrical container, whose walls, for practical purposes, can be considered undeformable; a triaxial cell, which subjects the sample to an axial stress s_z (applied by a piston) and a radial stress s_r (applied by a pressurized liquid). The hydrostatic and triaxial cells may be used for all materials. To carry out the test one must sheath the sample in a neoprene, elastomer or copper membrane, which also generally contains a valve allowing one to vary the pore pressure. By contrast, the oedometric chamber, faster and easier to use, is suitable only for poorly cemented shales and sands, and is not recommended for cemented rocks, due to the difficulties presented in eliminating the friction between the sample and the cylindrical container, which may cause alterations in the structure of the rock matrix during the test. The hydrostatic cell enables the measurement of both the stress applied, as well as the interstitial pressure (using pressure gauges, or electrical pressure or load sensors); variations in the pore volume can also be estimated by measuring the volume of liquid expelled, and the sample volume using extensometers applied to the sample, or measuring the volume of liquid injected into the cell (obviously by adopting the appropriate corrections that take into account the compressibility of the fluid and the expansion of the cell). The oedometric cell allows one to measure both vertical stress and axial movements. Some modern oedometers also enable the calculation of the radial stress required to maintain the radial expansion at zero. With the triaxial cell, alongside interstitial pressure and variations in the sample bulk volume and pore volume, one can measure the stresses applied and the variations in the length and diameter of the sample: these parameters are calculated by measuring the movements of the piston and the variation in the diameter of rings fixed onto the sample, or by using extensometers applied to the sample itself. In the most up-to-date apparatus, the loads and the interstitial pressure are varied continuously, or in stepped load cycles. Clearly, it is possible to select the speed of stress variation or deformation. In the triaxial cell, one can keep constant the relationships between axial and radial stress, or impose predetermined deformations (e.g., one can ensure that radial deformation remains nil as the axial load varies). The loads may also be kept constant over time, so as to measure time-dependent deformation phenomena (creep). Although today a fair degree of accuracy has been reached, it is important to emphasize that all measurements are characterized by differences between the system of stresses actually applied and the theoretical system. These differences may be attributed to the use of samples with faces that

are not perfectly parallel, and to the radial expansion partially inhibited by the friction between the load plate and the piston (in the triaxial cell). Furthermore, in the oedometrical cell, if the diameter/height ratio of the sample is not small enough, the effective load applied may be reduced by the friction between sample and container.

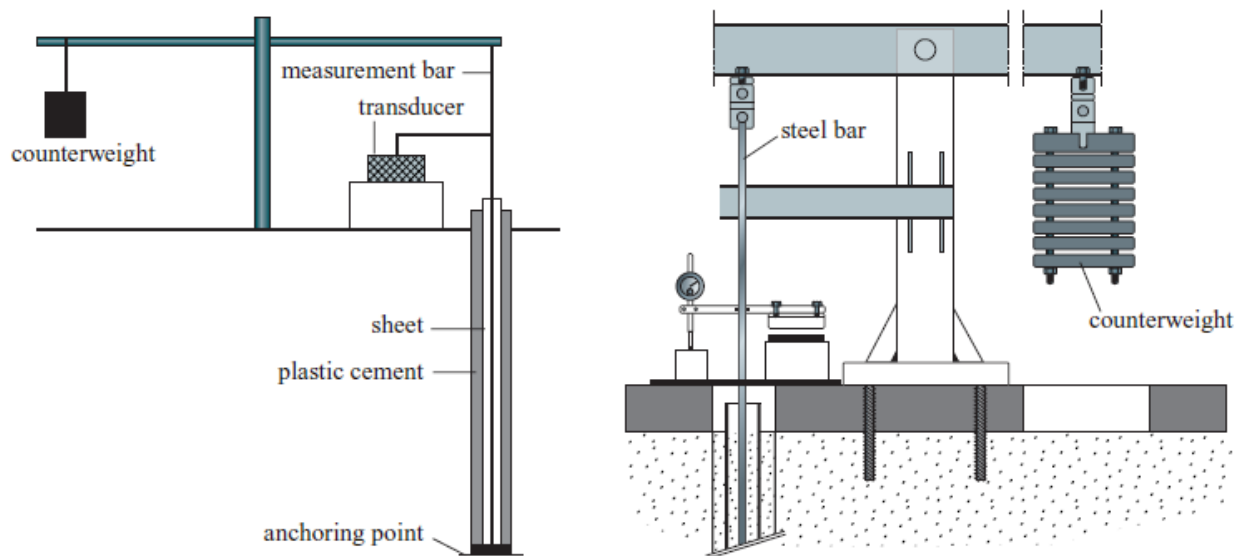


Figure 63: Sketch of an extensometric apparatus using a string of solid pipes.

4.1.2.2 *In situ* measurements

In situ measurements of subsoil compaction are essentially divided into two types. The first, better known in geotechnical engineering, measures the variations in distance between the surface and one or more bases anchored to the ground inside a borehole, using fixed equipment (extensometric apparatus or extensometer). The second determines the variations in relative distance between a series of subsurface points identified by suitable markers: the measurement is taken by running a tool into the well. This tool measures the distances between points marked using techniques deriving from geophysics, commonly applied in the oil industry, and now also widespread in civil engineering. The first type of measurement may be used up to a depth of a few hundred metres, whereas the second can be employed in wells that are several thousand metres deep.

Extensometers. According to Joseph F. Poland, the first measurements of this type were practiced almost by chance in Japan during the 1930s. It was noted that, after exploiting a superficial aquifer (at a depth of circa 60 m, and formed of gravels covered by shale beds), the casing column of some wells protruded above the ground. The compaction of the aquifer coincided with the protrusion of the casing column, which was fixed to the bottom of the

production levels (Poland, 1984). Later, it was noted that as depth increased, so did the action of the earth on the casing; therefore, the protruding length of the column no longer coincided with the compaction of the levels. To eliminate the friction between the measuring device and the subsoil, wells up to 200 m deep were drilled and cased with two concentric casing columns: the internal tube was still anchored to the bottomhole, while the outer casing, which also functioned as a true casing, was uncoupled from the bottom by means of a slip joint. In 1955, the United States Geological Service (USGS) introduced a cable extensometer, anchored in an open hole about 10 m beneath the casing shoe and counterweighted to maintain tension, used for the monitoring of subsidence to depths of around 600 m. This instrument was perfected and became widely used. In 1966, the USGS developed an extensometer in which the cable was replaced by a string of solid pipes balanced by a counterweight (Figure 63).

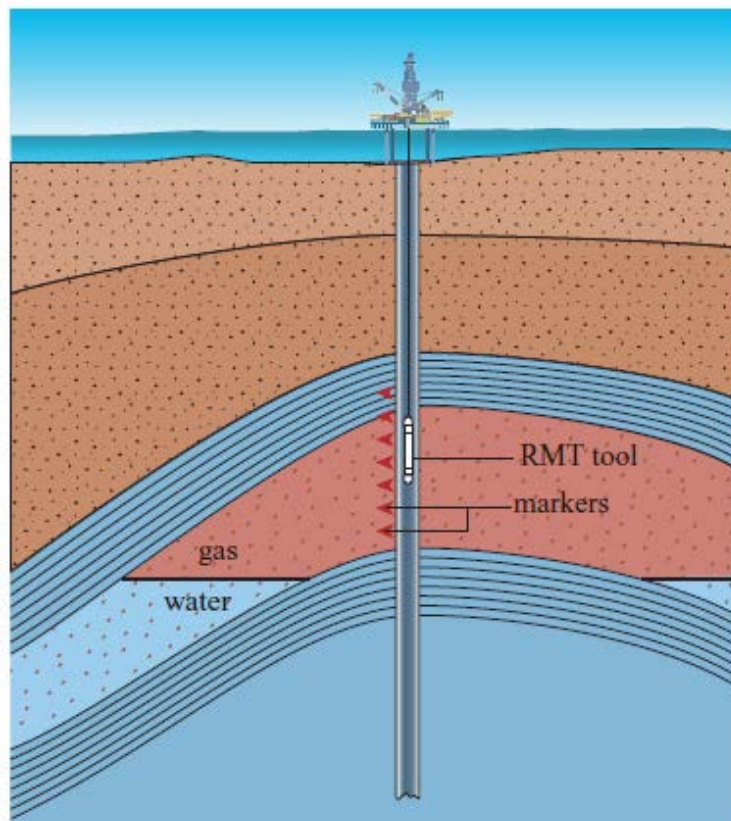


Figure 64: Radioactive marker technique for measuring the compaction of deep formations.

Radioactive markers. These methods are based on the measurement of variations in distance between markers placed along the sidewalls of the well in geologic formations subject to compaction. Among these, it is worth mentioning the casing collar locator log (CCL log), and

the radioactive bullet log. The radioactive bullet log is currently the most frequently used technique. This involves placing markers a few cm from the sidewall of the well, at depth intervals of circa 10.5 m, whose position inside the well can be located by means of a dedicated logging tool. These markers consist of a small radioactive source of ^{137}Cs (or ^{60}Co), contained within a steel tube in the form of a bullet. To avoid contaminating the formation, the radioactive matter is contained inside a hermetically sealed steel capsule, which, in turn, is sealed inside the body of hardened steel forming the actual bullet. These markers are shot into the formation by normal perforating guns with firing small explosive charges. Selecting the right amount of explosives is critical, since the marker must not penetrate too deeply into the formation (where it may not be easily detected by the measuring instrument, given the low intensity of the radiation). On the other hand, it must sufficiently penetrate the formation in order to avoid being removed by the centralizers during well casing. After placing the markers, the problem lies in monitoring their position, and, if a compaction occurs, in calculating the variation in relative distance between adjacent pairs of markers. The monitoring system is based on γ ray logging tools that use sodium iodide crystal sensors activated with thallium, coupled to a photomultiplier. To reduce errors linked both to the (absolute) precision of the measurement of the length of cable in the well, and the imperfect coincidence of the movements of the cable at the surface with respect to the movements of the tool within the hole, the current technique employed uses four sensors placed on a suitably calibrated measurement bar, whose length is approximately equal to the distance between the markers. The main causes of error associated with this measurement technique include: the stretching of the cable used to run the logging tool; the friction between the tool and the casing column; and, most of all, the difficulty of determining the exact position of the marker from the recorded γ ray profile. Another important cause of error could be the influence of a casing's presence, which could alter the deformations of the formation in the vicinity of the borehole, keeping in mind that, in order to have a reliable measurement, the marker must be fixed no deeper than, or at most equal to, the radius of the well.

4.1.3 Pore compressibility calculated by traveltime log

Different methodologies for pore compressibility calculation have been evaluated. The best approach is given in Khatchakian (1995); available data do not allow their application, so we decide to implement the methods defined by Overton and Norman (1969). Criteria explained below are referred to reservoir exploitation, but the same principles are applicable to any investigated sedimentary column.

Illustrated methodologies have been applied in collaboration with G.E.Plan consulting, private company with skills in Carbonate Sedimentology and generally in Oil&Gas sector.

Reservoirs without a water drive and without a significant change in gas-oil-ratio produced mainly by oil expansion. These are the undersaturated oil reservoirs or the heavy-oil reservoirs, where energy from gas and water is almost nil. As oil is produced the pressure drops, causing expansion of both oil and rock matrix.

Hence the overall expulsion of oil is related to volume increase of fluid and volume decrease of pore space. The pore volume shrinkage is very difficult to measure. Several investigators have tried to relate pore volume compressibility to bulk compressibility of rock, making assumptions such as constant porosity and constant stress-fluid pressure relationships. However, the reservoir porosity is generally a variable with pressure, as is rock stress; and the changes are not necessarily the same in all directions. It is expected that the maximum strains are in the vertical direction, since the restraint is less vertically. The solutions to elasticity equations yielding compressibility depend mainly upon boundary conditions. Three general types of reservoir boundary conditions can be easily recognized:

- All reservoir boundaries remain fixed, so that grain expansion intrudes pore space.
- Lateral boundaries remain fixed, with all strain occurring vertically.
- All reservoir boundaries move by varying amounts as pore pressure drops.

Case one is unrealistic, but it yields the minimum shrinkage in pore volume. Case two may occur when aquifer pressure drops simultaneously with reservoir pressure. Case three is the most general case. The theory of elasticity may be used to solve compressibility equations, whenever rock is consolidated (i.e., an elastic solid). For unconsolidated rock, expansion or contraction is not recoverable. The extreme case is that of an overpressured zone where the fluid supports most of the overburden. Reduction of pressure allows settling of grains into

more compact positions. Elasticity equations cannot be used for these cases. In the following we will deal with consolidated rocks only.

4.1.3.1 ***Solution to reservoir pore volume changes***

FIXED BOUNDARIES

An oil reservoir may be considered to have four distinguishable stresses operating on it; namely:

- a. p - Hydraulic pressure
- b. s_z - Vertical rock stress, at point contacts
- c. s_x and s_y - Lateral rock stresses

The average stress on a macroscopic section of rock may be considered to be

$$\sigma = \frac{\sigma_x + \sigma_y + \sigma_z}{3}$$

Eq. 9

so that two variables, p and s , are the important parameters causing volume changes in reservoirs.

Now if the boundaries of a reservoir are such that they cannot move as pressure drops, the grains will expand into the pore space. The bulk volume does not change, only the pore and matrix volume are rearranged; hence

$$dV_B = d(V_P + V_R) = dV_P + dV_R = 0$$

Eq. 10

Usually matrix compressibility is defined as:

$$C_R = -\frac{1}{V_R} \frac{dV_R}{dp} \quad ; \quad C_P = -\frac{1}{V_P} \frac{dV_P}{dp}$$

Eq. 11

so

$$\frac{dV_P}{V_P} = \left(\frac{1-\phi}{\phi} \right) C_R dP$$

Eq. 12

Note that for $\bar{\epsilon} = 1/3$, $C_p = -2C_r$; and for $\bar{\epsilon} = 1/10$, $C_p = -9C_r$ (upper and lower limits for sandstones). For quartz C_r is $1.865 \times 10^{-7}/\text{psi}$, so that C_p would not be expected to exceed $1.678 \times 10^{-6}/\text{psi}$ for consolidated sands. This maximum is considerably below that calculated by Fatt using bulk compressibility data. When considering unconsolidated sands where fluid is supporting overburden, greater changes can occur as fluid pressure is reduced.

FIXED LATERAL BOUNDARIES, VERTICAL STRAINS

Whenever a reservoir is constrained laterally, movement can occur vertically. This case exists whenever impermeable shales above and below a sand prevent pressure drop outside a sand vertically, and whenever aquifer pressure outside of an oil reservoir drops by similar amounts to that in the oil zone.

$$\frac{dV_P}{V_P} = \frac{dV_B}{V_P} - \frac{dV_R}{V_P} = \frac{1}{\phi} \frac{dV_B}{V_B} - \frac{1-\phi}{\phi} \frac{dV_R}{V_R} \quad (\text{a})$$

$$\frac{dV_P}{V_P} = \left(\frac{1-\phi}{\phi} \right) C_R dP + \frac{1}{\phi} \frac{dV_B}{V_B} \quad (\text{b})$$

Eq. 13

The change in V_b , is a result of DL in the z direction, with reservoir area constant

$$\frac{dV_B}{V_B} = \frac{dL}{L} = \epsilon_z$$

Eq. 14

Vertical movement occurs at contact of grains, where, for isotropic rocks (using Lamé's constant and shear modulus G)

$$\sigma_z = \lambda(\epsilon_x + \epsilon_y + \epsilon_z) + 2G\epsilon_z = (\lambda + 2G)\epsilon_z$$

Eq. 15

And since the change of stress is $+dp$ vertically, (assuming that expansion stresses cause shape distortion only.)

$$\frac{dV_P}{V_P} = \left(\frac{1-\phi}{\phi}\right) C_R dP + \frac{1}{\phi} \frac{dp}{\lambda + 2G}$$

Eq. 16

From dilatational wave study in solids, it is known that compressional velocity V_d

$$V_d = \sqrt{\frac{\lambda + 2G}{\rho}}$$

Eq. 17

When the bulk density ρ , is known

$$\frac{dV_P}{V_P} = \left(\frac{1-\phi}{\phi}\right) C_R dP + \frac{1}{\phi} \frac{dp}{\rho_B V_d^2}$$

Eq. 18

Note that the two terms in equation have opposite effects; i.e. as pressure drops, the grains expand (decreasing pore volume,) while bulk changes shrink grains.

Practically,

$$\frac{dV_P}{V_P} = \left(\frac{1-\phi}{\phi} C_R + \frac{74.4 \times 10^{-12} \Delta T^2}{\phi S.G.}\right) dp$$

Eq. 19

where S.G. is specific gravity of the rock bulk, ϕ is fractional, and ΔT is in microseconds/ft.

Although the previous equation is theoretically derived from elasticity considerations, it may be subject to considerable errors. It is based on the assumption that the strain vertically is directly related to pressure drop

For a complicated porous rock geometry, this is difficult to prove.

ALL RESERVOIR BOUNDARIES MOVE

An oil reservoir is subject to declining pressure in a tectonically stressed zone, while the surrounding aquifer maintains its original hydraulic pressure.

Assumptions:

1. Isotropy,
2. $\sigma = \frac{\sigma_x + \sigma_y + \sigma_z}{3}$
3. Overburden stress is constant,
4. Areal porosity is numerically equal to volumetric Porosity, $\varepsilon A = \varepsilon A$,
5. The rock has spherical grains of variable size.

It is not intuitive that changes in rock stress are constantly related to changes in hydraulic pressure. Rather it is more realistic that forces are radially uniform in a spherical grain as pressure changes.

Then,

$$d(\text{Force})/\text{Area of grain contact} = d(\text{Force}) / \text{Area of fluid contact}$$

$$\frac{-d\sigma}{dp} = \frac{A_p}{A_g}$$

Eq. 20

It is obvious that both contact areas involved are variables. For one spherical grain, it is clear that $A_g < 4pr^2$: and that $A_p + A_g$ is exactly $4pr^2$. Of course pores are never spherical, but a spherical configuration establishes the minimum surface area that a pore volume can realize. Also, for the spherical case,

$$\text{ratio of cross-sectional areas} = \frac{\phi_a}{1 - 2\phi_a}$$

Eq. 21

whenever one grain and one pore are identically one unit volume (this is not true for some packings).

Practically, sandstone has a lower limit of porosity of 10% hence

$$\frac{-d\sigma}{dp} > \frac{1}{8}$$

And from physical considerations,

$$\frac{-d\sigma}{dp} \leq 1$$

That is to say, no greater stress can be transmitted than the original hydraulic pressure drop. Note that for the maximum porosity observed in the field, $\phi = 1/3$, $d\sigma/dp$ has the maximum value.

Assumption 6: $\frac{d\sigma}{dp} = \frac{\phi}{1 - 2\phi}$

Eq. 22

The bulk tends to expand coincidental with a reduction in the original pore volume. This effect will tend to be propagated through the whole oil reservoir wherever dp occurs.

From the outside of the reservoir, in the aquifer, the pressure remains the same as originally. Hence a pressure $\pm dp$ acts across the reservoir boundary, resisting the tendency to expand. The net change of stress causing reservoir x,y boundaries to move is:

$$\frac{-d\sigma}{dp} = \frac{2\varphi^2}{1-2\varphi}$$

Eq. 23

whenever there is a discontinuity in pressure between oil reservoir and water aquifer. Note that at 36.6% porosity the derivative is unity.

Assuming the previous equation is a general relation and that shear stresses are insignificant, then, from definitions of the elastic constants, approximately:

$$\epsilon_z \cong \frac{dP}{\lambda + 2G} = \frac{dP}{\rho_B + V_D^2} \cong \frac{dV_B}{V_B}$$

Eq. 24

or

$$\frac{dV_P}{V_P} = \left(\frac{1-\varphi}{\varphi} C_R + \frac{\Delta T^2}{\varphi \rho_B} \left(1 - \frac{\varphi^2}{1-2\varphi} \right) \right) dp$$

Eq. 25

RESUME

The minimum shrinkage of reservoir pore space due to hydraulic pressure change in an oil reservoir is calculated to be $\frac{1-\varphi}{\varphi} C_r dp$ where C_r is a rock constant. Rock compressibility is noted to be $.94 \times 10^{-7}/\text{psi}$ for limestone and $1.865 \times 10^{-7}/\text{psi}$ for sandstone, from literature data. Hence, if the lower limits of porosity are 2% for limestone and 10% for sandstones, the minimum pore shrinkage is $1.68 \times 10^{-6}/\text{psi}$ for sandstones and $4.61 \times 10^{-6}/\text{psi}$ for limestones. Literature data calculated from bulk compressibility should not be used for reservoir pore shrinkage, since oil reservoirs do not generally expand upon reduction of pressure as do isolated core samples.

For oil reservoirs which experience a reduction of pressure, the aquifer surrounding the reservoir maintains a high pressure. This tends to keep reservoir expansion minimized. An approximate relation which shows the stress which tends to expand the reservoir is:

$$d\sigma = -\left(\frac{2\phi^2}{1-2\phi}\right)dp$$

Eq. 26

At 36.6% porosity the expansion stress is -d, while the lower limit is zero at low porosity. An approximate solution of pore volume change for this reservoir configuration is:

$$\frac{dV_P}{V_P} = \left(\frac{1-\phi}{\phi}C_R + \frac{0.893\Delta T^2}{10^{10}S.G.}\left(\frac{1}{\phi} - \frac{\phi}{1-2\phi}\right)\right)dp$$

Eq. 27

When it can be shown that reservoir boundaries do not move, except vertically, upon reduction of reservoir pressure; then:

$$\frac{dV_P}{V_P} = \left(\frac{1-\phi}{\phi}C_R + \frac{74.4 \times 10^{-12} \Delta T^2}{\phi S.G.}\right)dp$$

Eq. 28

The pore volume changes calculated from these equations require that rock be consolidated such that it acts elastically. Whenever there is unconsolidation or a significant amount of shale in a reservoir sand, change of reservoir pore volume will exceed (for a non-sealed reservoir)

$$\frac{dV_P}{V_P} \leq \frac{1-\phi}{\phi}c_r dP$$

Eq. 29

These theoretical results indicate that bulk compressibility measurements should not be used to calculate pore volume changes, since some stress and porosity configurations may exist where pore volume remains constant as pressure changes.

EMPIRICAL RELATIONSHIPS FOR CARBONATES

In general, a strength–physical property relationship for a specific rock formation is developed based on calibration through laboratory tests on rock cores from the given field. If there are no

core samples available for calibration, the next best thing would be to use empirical strength relations based on measurable physical properties. Because there are multiple choices of strength models for various rock types in different geological settings, it is necessary to understand the characteristics of the models and their range of applicability prior to utilizing them.

It is more difficult to generalize about limestones and dolomites. These relations may provide a good first approximation of the lower strength bound when no other information on rock strength is available. It is somewhat obvious, however, that calibration of empirical relations between strength and physical properties is generally required for any correlation to be used with some degree of confidence.

Thus, empirical equations relating the strength of carbonate rocks to geophysical parameters do a fairly poor job whether considering velocity, modulus or porosity data, which emphasizes the importance of being able to calibrate strength in any given case.

4.2 NATURAL SUBSIDENCE CALCULATION THROUGH NUMERICAL MODELING

4.2.1 Preliminary Analysis Of Natural Subsidence Numerical Models

Some numerical models for the assessment of long-term basin-scale subsidence have been preliminarily evaluated according to the following selection-criteria:

- i. Linkage to whole required input data encompassing the geological complexity of the area (e.g., salt diapirism, geo-dynamism), with required code for available, achievable or derivable data.
- ii. In similar contexts, ample applications for relevant projects of international value.
- iii. Availability.

Several 1D or 2D finite element models have been evaluated. Models need to reproduce present day sedimentary thickness, excess fluid pressure with respect to the hydrostatic distribution, and description of the expected geodynamics of the basin in the near future.

In general, required input data by models include:

- Thickness of stratigraphic layers;
- Age of stratigraphic boundaries;
- Lithology, with percentages attributed to different lithologies;
- Sedimentation (palaeowater) depth;
- Decompaction parameters (porosity for t_0 = initial % porosity, decompaction coefficient c , final % porosity);
- Physical properties (grain density, crustal density);
- Depth/Temperature profile;
- Paleotectonic and present-day tectonic.

Availability of required information has been checked within the Phase II, Task 2 and related GDB to identify gaps and improve data searches and gathering, and to test the applicability of the model according to existing information.

According to selection-criteria and availability of required input data, main advantages/disadvantages of first selected models are summarized in Table 4.

Table 4: Preliminary evaluation of Numerical models.

Code	Advantage	Disadvantage
BASIN (CSIC, Spain)	Complete input dataset 2D Code availability Relevant applications	Its application requires a large amount of quantitative data
GALO (Makhous and Galushkin, Moscow State University)	Code developed for areas similar to the southern Precaspian basin Complete input dataset	Code not available
DeCompactionTool (University of Wien)	Code availability Montecarlo simulation implemented	1-D finite element Few applications
NatSub (Padua University)	Code developed by experts involved in this project (Teatini and Gambolati)	1-D Montecarlo simulation not implemented
TerraMod (Terramod Ltd, UK)	Complete input dataset	Code not available

After the preliminary analysis, numerical models chosen were NATSUB and BASIN.

A brief description of the preliminary set of models evaluated follows.

4.2.2 Synthetic overview of existing models

NATSUB BY THE UNIVERSITY OF PADUA (ITALY)

NATSUB is a one-dimensional finite element model that simulates the natural compaction driven by unsteady groundwater flow in an accreting isothermal sedimentary basin. The model assumes a process of time-varying sedimentation and makes use of a 1-D model of flow where water flow obeys the relative Darcy's law in a porous medium, which undergoes a progressive compaction under the effect of an increasing load of the overburden. Soil porosity, permeability, and compressibility may vary with the effective intergranular stress according to empirically based constitutive relationship. The model correctly assumes the geometric nonlinearity that arises from the consideration of large solid grain movements.

The equations are solved using both the Eulerian and the Lagrangian approaches. With this latter approach, the model uses a dynamic mesh made of fine elements, which deforms in

time and increases in number as deposition occurs and the soil column compacts (Gambolati et al., 1998; Gambolati and Teatini, 1998).

The outcome of the model consists in the behaviour of time and of the length of the column and the velocity of its top and bottom, with the evolution over time of the pore pressure in excess of the hydrostatic value along the length of the column (Gambolati et al., 1999).

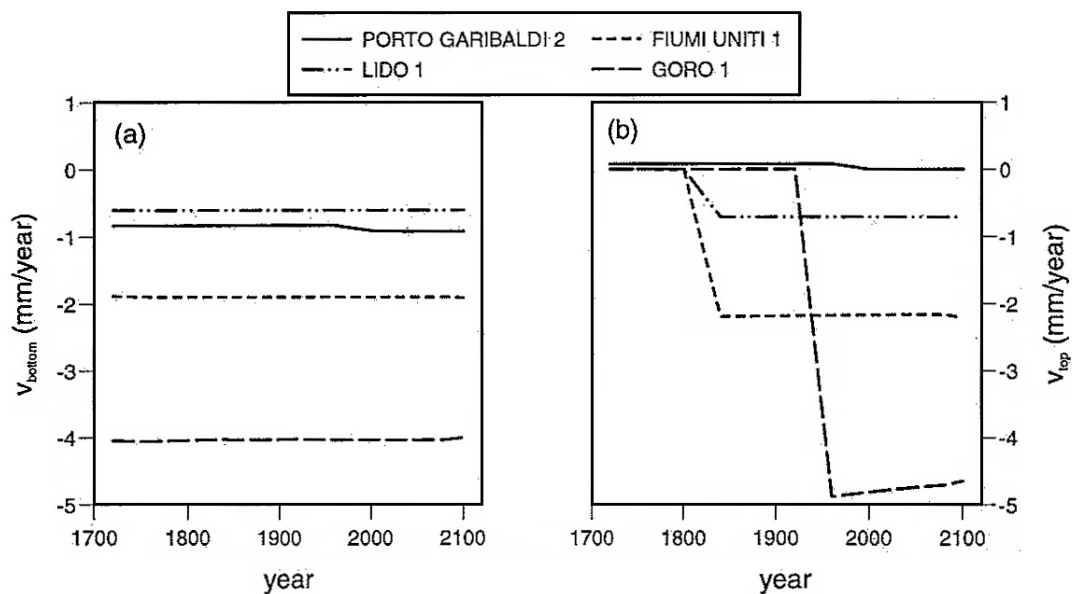


Figure 65: Evaluation of bottom velocity and land subsidence over the last three centuries, projected until 2100 in the Emilia-Romagna coast, using NATSUB, after “Gambolati et al., 1999.”

BASIN (CSIC, SPAIN)

BASIN is a 2D finite-element program that simulates the filling of a sedimentary basin and includes transport, erosion and consolidation of sediment, tectonic processes such as isostatic compensation, consolidational fluid flow, topography driven fluid flow, and heat flow including advection and solute transport. BASIN incorporates a physically consistent compaction model based on the equation of the state of porosity. A description of some underlying principles can be found in Bitzer (1996). BASINVIEW is a visualisation tool for fast analysis of simulation results. Results from experiments with BASIN may be quite numerous (in some cases exceeding 600 files) and BASINVIEW is a fast visualisation tool designed to work with GhostScript.

So far, only distensive basin configurations have been analysed by other authors. BASIN, however, is also capable of modelling compressive situations. Such situations are much more difficult to handle because of the extreme changes of basin geometry due to compression. BASIN does not provide a structural simulation. Instead, the presumed structural evolution is

used as input data in order to simulate subsidence, fluid flow, heat flow and evolution of petrophysical data like porosity, compressibility, etc. A simple molasses-like experiment showing a compressive basin with thrust sheets arriving from the right can be viewed as computer animation. The file has about 1 MB that requires Sparkle to visualize. The experiment demonstrated in the film applies only a few elements, but also contains some of the basic features of a molasse basin.

Graphics created with BASINVIEW can be printed on any printer. Another version (AIBASIN) creates Adobe Illustrator files that allow further graphic operations.

GALO MODEL (MONZER MAKHOUS, YURII GALUSHKIN, MOSCOW STATE UNIVERSITY)

The GALO program consists of three main blocks: input data for basin structure and evolution, initial parameters for basin modelling, and numerical simulation.

The first data block contains geological, geophysical and geochemical data describing basin structure and evolution, including information about the present-day sedimentary section, measured value of porosity, temperature, and vitrinite reflectance (Makhous et al, 1997).

The second block deals with preparing initial parameters for a numerical simulation of thermal history of the basin, calculating the volumes of uncompacted sediments on the surface of the basin, estimating the time and amplitude of tectonic and thermal events in the basement (thermal activation, stretching of basement, etc.), calculating the initial temperature profile, and determining temperatures at the base of the computed domain.

The third data block uses prepared parameters to carry out a one-dimensional numerical simulation of burial, thermal and geochemical evolution of the basin. The comparison of rock porosities, temperatures and vitrinite reflectance computed in this block with corresponding present-day values from the first block, as well as the calculated curves of tectonic subsidence, are used to correct the initial parameters for our basin modeling.

The third block includes the chemical-kinetic modeling package. Data of open and closed pyrolysis experiments are used here for restoring the kinetic spectrum of maturation reaction in source-rocks. This spectrum is applied to achieve a numerical estimate of hydrocarbon yield and the expulsion threshold.

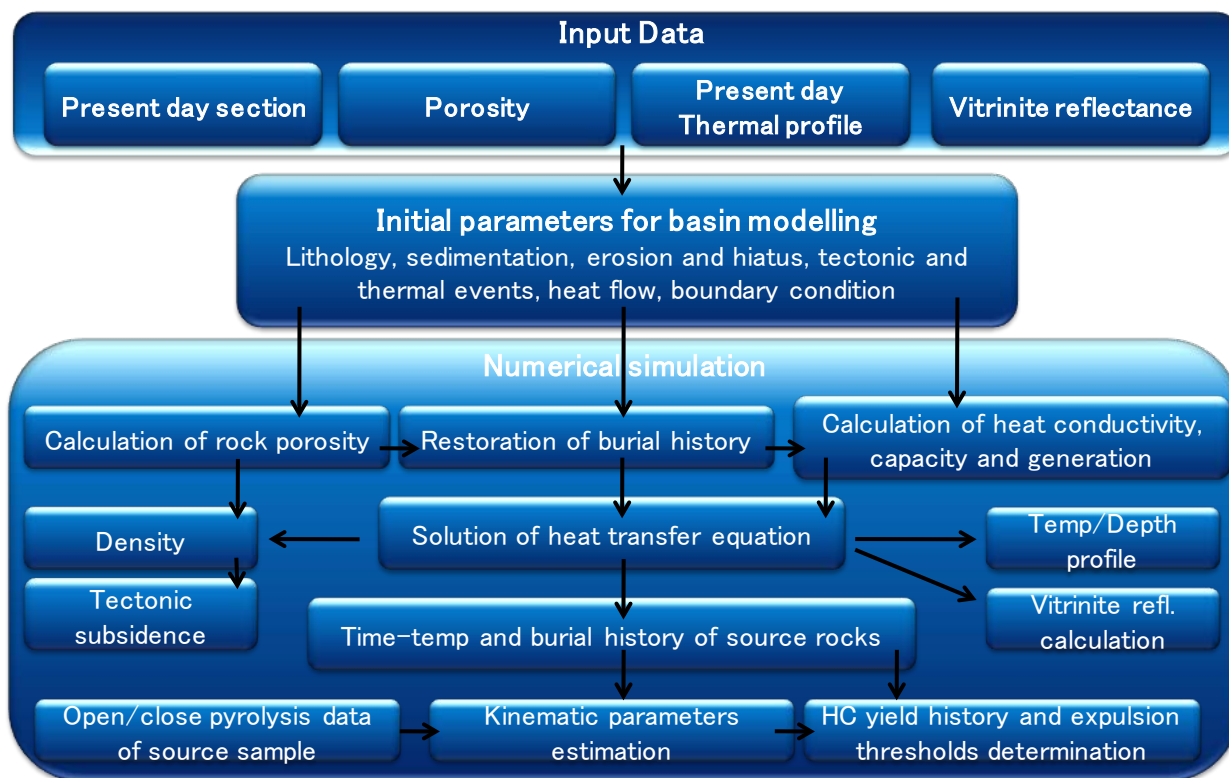


Figure 66: Three main conceptual blocks of the Galo model, after (Makhous et al, 1997).

DECOMPACTIONTOOL (UNIVERSITY OF WIEN, AUSTRIA)

This software implements error quantification on subsidence analysis, based on Monte Carlo Simulation, such that a range of possible values is assigned to each used parameter. A random function chooses input parameter values within the defined ranges and these are used to calculate the subsidence. From a number of input parameter value combinations, the average subsidence is determined. The program also incorporates for the first time the parameter “age,” as the controlling factor for the x-axis (Holzel et al., 2008).

Inputting the correct sedimentary age of backstripped layers is particularly crucial for subsidence rate calculations and thus for identifying discrete phases of subsidence. The approach used reduced errors due to ongoing uncertainties in the chronostratigraphy of the Precaspian basin.

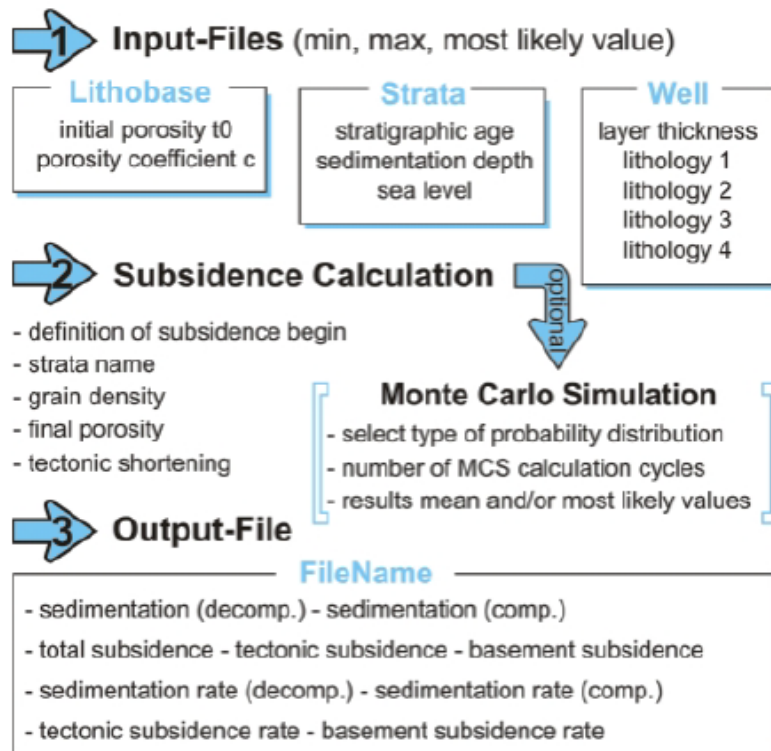


Figure 67: DeCompactionTool work flow, after “Holzel et al., 2008”.

TERRAMOD (TERRAMOD LTD)

TerraMod is a state-of-the-art basin modelling program essential for the effective evaluation of exploration of acreage and containing unique features (<http://www.terramod.com>). Providing an analysis of the history of sedimentary basins and, in particular, the evolution of its source rocks and expelled hydrocarbons, it incorporates rigorous calculation routines and automated calibration checks. A unique optimised model is created that closely fits the specific geology of an exploration area, including thrust regions.

TerraMod simulates the compaction process in iterative loops, modelling the movement of heat and fluids within the basin through geological time, taking into full account the pressure and temperature model, incorporating heating rate dependent kinetics, critical for the correct determination of generation volumes in both rapidly and slowly subsiding basins.

The program precisely simulates deposition, fluid dynamics and heat flow including the processes operating during subsidence, uplift, erosion and thrusting. It can be applied to any geological terrain and quantifies compaction through the history of a basin without relying on broad unconstrained assumptions and alerts to any elements of the model that may not be geologically correct.

The program calculates:

- geohistory and back-stripped subsidence history;

- hydrocarbon generation and expulsion through time for each of your identified kerogen types and for custom kerogen mixes using any number of independently defined source rocks;
- oil and gas volumetrics for defined source rock thicknesses and for entire kitchen areas;
- fully coupled temperature and pressure profiles indicating where under- or over-pressured layers may occur;
- oil gravity expulsion data for oils produced at any time;
- timing of active maturation and generation;
- sealing efficiency of reservoir cap rocks.

The program contains a project and well database system with files that can be configured to user preferences and retrieved as required. The models can be automatically optimised and checked against calibration data ensuring the best output solution, allowing batch simulations and batch plotting that can be run overnight saving time.

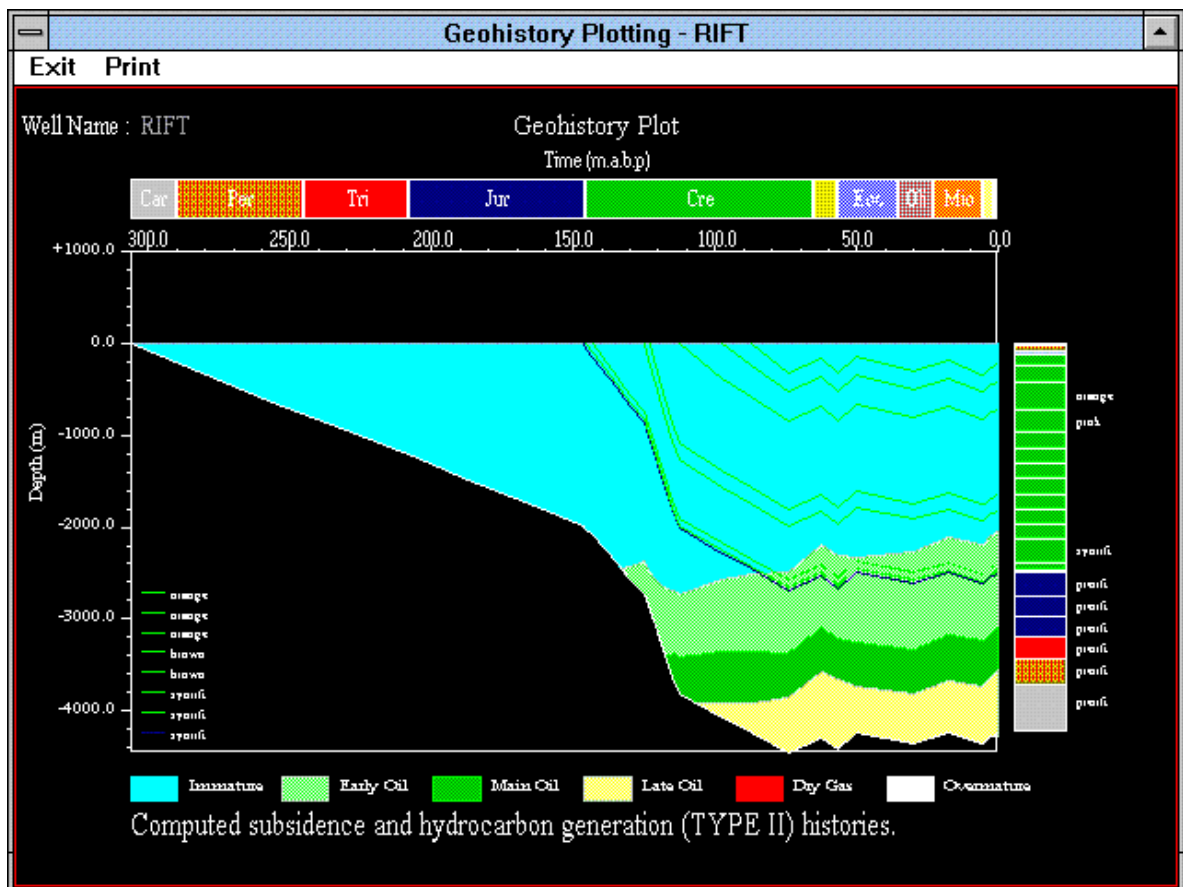


Figure 68: Print-screen of TerraMod software.

4.2.3 The Natsub code

4.2.3.1 *Introduction*

Quantitative analysis of groundwater flow due to sediment compaction in isothermal sedimentary basins can provide a useful tool to predict natural land subsidence of accreting systems in recent geological times. The first attempt to develop a mathematical model describing the evolution of pore pressure, and specifically of excess pore-pressure with respect to the hydrostatic one, was perhaps contributed in 1968 by Bredehoeft and Hanshaw who derived a linear model of flow in an accreting medium subject to a constant rate of sedimentation. The model of Bredehoeft and Hanshaw assumes constant and uniform permeability and elastic storage and does not address the natural compaction of the porous medium during the sedimentation process. It can, however, account for the development and maintenance of anomalous fluid pressure, in particular pressure in excess of the hydrostatic one, depending on the selected hydraulic conductivity (which the authors set at the order of magnitude of 10^{-10} m/s or lower) and, subordinately, the specific storage of clayey layers within the accreting system.

When describing the evolution of sedimentary basins undergoing pronounced soil compaction the vertical solid grain displacements should be taken into account and Darcy's law should be cast in terms of relative velocity. In addition soil porosity, permeability and compressibility cannot be assumed to be constant as they display a marked variation during the consolidation process. Finally, accretion and simultaneous compaction should be both accounted for in the mathematical model to obtain the correct value of the actual surface displacement.

The need for deriving the equation of groundwater flow in a deforming medium was recognized by a number of authors (Biot, 1941; Biot, 1955; Copper, 1966; Gambolati and Freeze, 1973; Smith, 1971). The contribution by Cooper (1966) is particularly important as he correctly developed the partial time derivative in the relationship linking the volume strain to the incremental effective intergranular stress. A few years later Gambolati (1973a) derived the equation of flow in a 1-D deforming porous medium by giving the appropriate consideration to soil displacement. He also elucidated and discussed the relation between the oedometer soil compressibility c_b and the classic compressibility C_b . The resulting equation is a new non linear equation defined over a time variable flow domain where both α and C_b play a primary role. The dimension of the flow domain increases with time due to accretion. However, the increase is partially offset by the concurrent medium compaction which was correctly assessed by Gambolati's model (1973) for large deformations as well. The non-linearity is further enhanced by the assumed constitutive relationship for porosity, hydraulic conductivity

and soil compressibilities which are in general highly non linear with the stress condition. The effect of non-linearity in the controlling parameters was recently included in one dimensional numerical solutions to the traditional groundwater flow equation by Bethke and Corbet (1998) while the consideration of a deforming porous medium is taken into account in the models by Bethke(1985), Keith and Rimstidt (1985), Harrison and Summa (1991) and Corbet and Bethke (1992).

In the present work we used a numerical model known as NATSUB based on the 1-D equation contributed by Gambolati (1973a). The equation correctly considers Darcy's relative velocity, the medium compaction and the dependence of the essential parameters on the effective intergranular stress. In addition, the accretion rate introduced by Bredehoeft and Hanshaw is incorporated into the model. This is solved numerically by an iterative finite element technique intended to overcome the various sources of non-linearity.

The model developed herein is intended to be used in the sedimentation and compaction analysis of the basin underlying the northeastern part of the Caspian Sea, a normally or almost normally consolidated basin where a large database of geological, hydrological and geomechanical data is at present available.

4.2.3.2 **Governing Equations**

Following Gambolati (1973a) the equation of groundwater flow in a 1-D compacting porous medium can be written as:

$$\frac{k}{\gamma_w} \frac{\partial^2 p}{\partial z^2} = \left\{ \left[\left(p \frac{d\alpha}{dp} + \alpha \right) / (1 + \alpha p) \right] + n\beta \right\} Dp - \frac{k\beta}{\gamma_w} \left(\frac{\partial p}{\partial z} \right)^2 - 2k\beta \frac{\partial p}{\partial t}$$

Eq. 30

where:

- k is the hydraulic conductivity;
- γ_w is the specific weight of water;
- α is the classical vertical soil compressibility defined as $d(\Delta z) / (\Delta z \Delta \sigma_z)$ where σ_z is the effective intergranular stress;
- n is the medium porosity;
- β is the volumetric water compressibility;
- D is the total (or Eulerian) derivative:

$$D = \frac{\partial}{\partial t} + v_g \frac{\partial}{\partial z}$$

Eq. 31

and u_g is the grain velocity;

- p is the incremental pore pressure with reference to an initial steady state condition of flow;
- z is the vertical coordinate positive upward;
- t is the time.

Eq. 30 holds under a variety of assumptions including:

- (a) $k=k^* \gamma_w / \mu$ where k^* and μ are the intrinsic permeability of medium and viscosity of water assumed to be constant;
- (b) $\gamma_w = \gamma_{w0} \exp[\beta(p_0+p)]$ where γ_{w0} and p_0 are initial reference values for γ_w and p , respectively;
- (c) $h = z + \int_0^p \frac{dp}{\gamma_w}$ is the hydraulic potential;
- (d) $n(v_w - v_g) = -k \frac{\partial h}{\partial z}$ is relative Darcy's law where v_w and v_g are the (absolute) velocity of water and solid grains, respectively;
- (e) constant total stress σ_t , i.e. $\sigma_t = p_0 + p + \sigma_{z0} + \sigma_z = \text{const}$, where σ_{z0} and σ_z are the initial and incremental effective stresses, respectively;
- (f) incompressible solid grains.

The medium compaction $u(z,t)$ and the grain velocity $u_g(z, t)$ are expressed as Gambolati, 1973a.

$$u(z, t) = - \int_0^z \frac{\alpha \sigma_z(z, t)}{1 - \alpha \sigma_z(z, t)} dz$$

Eq. 32

$$v_g(z, t) = (1 - \alpha \sigma_z) \int_0^z \frac{\left(\alpha + \sigma_z \frac{d\alpha}{d\sigma_z} \right) \frac{\partial p}{\partial t}}{(1 - \alpha \sigma_z)^2} dz$$

Eq. 33

where the incremental effective stress σ_z is taken to be positive when increasing. Note that Eq. 32 applies for large displacements $u(z,t)$ as well and represents a significant difference from Cooper's(1966) development. For a discussion, see also Cooper(1974) and Gambolati (1975).

Expanding the total derivative in

Eq. 30 and using Eq. 33 leads to an alternative expression for

Eq. 30:

$$\frac{k}{\gamma_w} \frac{\partial^2 p}{\partial z^2} = \left\{ \left(\alpha + \sigma_z \frac{d\alpha}{d\sigma_z} \right) / (1 - \alpha\sigma_z) + n\beta \right\} \left\{ \frac{\partial p}{\partial t} + (1 - \alpha\sigma_z) \frac{\partial p}{\partial z} \right. \\ \left. \cdot \int_0^z \left[\left(\alpha + \sigma_z \frac{d\alpha}{d\sigma_z} \right) \frac{\partial p}{\partial t} / (1 - \alpha\sigma_z)^2 \right] dz \right\} - \frac{k\beta}{\gamma_w} \left(\frac{\partial p}{\partial z} \right)^2 - 2k\beta \frac{\partial p}{\partial z}$$

Eq. 34

In NATSUB some of the assumptions underlying Gambolati's development are removed and the governing equations take on a different form.

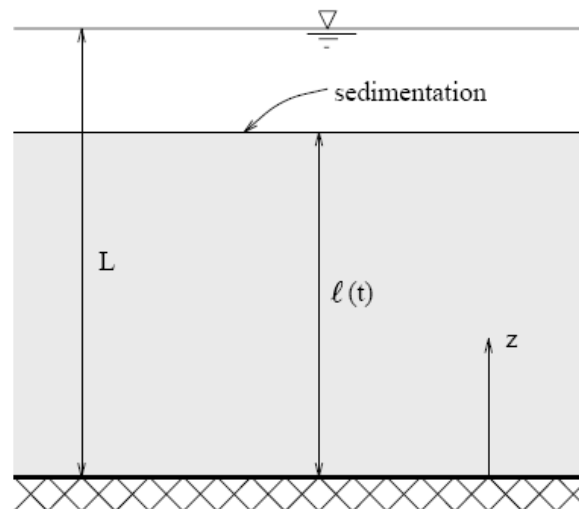


Figure 69: The sediment column has height $l(t)$ at time t after inception of the accretion process and rests on an impermeable basement at $z=0$. Seawater elevation is L .

First, the last two terms on the right-hand side of

Eq. 30 have been discarded as their contribution is negligible (Gambolati, 1973b) if the length of the sediment column is less than 10^4 m and the boundary pressure variation is less than 500 kg/cm^2 . Moreover, we assume a non zero depositional rate $\omega = \frac{dl}{dt}$ where dl is the elementary height of sediment column deposited during the time interval dt . As a major

consequence the total stress σ_t is no longer constant within the compacting column. Similarly, the porosity n and the void ratio e are dependent on σ_z , and hence on z . If we assume that the height l of the sediment column is zero at time $t=0$ (inception of the sedimentation process) and denote by L the (constant) seawater elevation (see Figure 69), and take into account the variability of both n and α with σ_z neglecting the dependance of γ_w on pore pressure,

Eq. 30 turns into Eq. 35:

$$\frac{\partial}{\partial z} \left(\frac{k}{\gamma_w} \frac{\partial p}{\partial z} \right) = \left(\frac{\sigma_z \frac{d\alpha}{d\sigma_z} + \alpha}{1 - \alpha\sigma_z} + n\beta \right) Dp - \frac{\sigma_z \frac{d\alpha}{d\sigma_z} + \alpha}{1 - \alpha\sigma_z} D\sigma_t \quad \text{a}$$

$$\sigma_t(z, t) = \int_z^{\ell(t)} [n\gamma_w + (1 - n)\gamma_s] dz - [\ell(t) - z]\gamma_w \quad \text{b}$$

$$\sigma_z = \sigma_t - p \quad \text{c}$$

$$\frac{\partial}{\partial z} \left(\frac{k}{\gamma_w} \frac{\partial p}{\partial z} \right) = \left(\frac{\sigma_z \frac{d\alpha}{d\sigma_z} + \alpha}{1 - \alpha\sigma_z} + n\beta \right) Dp - \frac{\sigma_z \frac{d\alpha}{d\sigma_z} + \alpha}{1 - \alpha\sigma_z} D\sigma_t$$

$$\sigma_t(z, t) = \int_z^{\ell(t)} [n\gamma_w + (1 - n)\gamma_s] dz - [\ell(t) - z]\gamma_w$$

$$\sigma_z = \sigma_t - p$$

$$\frac{d\ell}{dt} = \omega(t) + v_g(\ell, t)$$

d

Eq. 35

where γ_s is the specific weight of the solid grains.

In Eq. 35 γ_w , γ_s and β are constant parameters while k , α and n are to be thought of as given functions of σ_z , and p is the pore pressure in excess of the hydrostatic value related to an arbitrarily varying sea level $L(t)$. In Eq. 35b and Eq. 35c σ_t is the total stress in excess of the hydrostatic stress (equal to $(L-z)\gamma_w$). Its time derivative has a quite complex expression.

Intuitively most of the variation of the total stress in a moving soil particle is due to the weight of the sediments which are continuously accumulated on top of the column. Hence on a first approximation we can write:

$$D\sigma_t = \omega(1 - n_0)(\gamma_s - \gamma_w)$$

Eq. 36

and Eq. 35a becomes:

$$\frac{\partial}{\partial z} \left[\frac{k}{\gamma_w} \frac{\partial p}{\partial z} \right] = \left(\frac{\sigma_z \frac{d\alpha}{d\sigma_z} + \alpha}{1 - \alpha\sigma_z} + n\beta \right) Dp - \frac{\sigma_z \frac{d\alpha}{d\sigma_z} + \alpha}{1 - \alpha\sigma_z} (1 - n_0)(\gamma_s - \gamma_w)\omega$$

Eq. 37

where n_0 is the initial porosity corresponding to $\sigma_z=0$. The source term in Eq. 37 is the same as the one of Bredehoeft and Hanshaw (1968) equation. Eq. 37 forms the basis for the description of the excess pore pressure of compacting sedimentary basins subject to a burial rate $\omega = \omega(t)$. Eq. 37 is to be solved in a 1-D domain with a moving boundary $l = l(t)$ which is a priori unknown and is a part of the solution.

Note that Eq. 37 can be viewed as an extension of Bredehoeft and Hanshaw (1968) linear equation:

$$\frac{\partial^2 h'}{\partial z^2} = \frac{S_s}{k} \left(\frac{\partial h'}{\partial t} - \frac{(1-n)(\gamma_s - \gamma_w)}{\gamma_w} \omega \right)$$

Eq. 38

when medium compaction is correctly accounted for. In Eq. 38 h' is the head in excess of the sea level L (Figure 69), S_s is the classical specific elastic storage and k is the hydraulic conductivity. An equation similar to Eq. 38 was originally developed by Gibson (1958) for the analysis of consolidation of clay layers with thickness increasing with time.

Setting:

$$\ell = 0 \qquad t = 0 \qquad \text{(a)}$$

$$\left. \frac{\partial h'}{\partial z} \right|_{z=0} = 0 \qquad t > 0 \qquad \text{(b)}$$

$$h'(\ell, t) = 0 \qquad t > 0 \qquad \text{(c)}$$

$$\begin{aligned} \ell = 0 \qquad t = 0 \\ \left. \frac{\partial h'}{\partial z} \right|_{z=0} = 0 \qquad t > 0 \\ h'(\ell, t) = 0 \qquad t > 0 \\ \frac{d\ell}{dt} = \omega = \text{constant} \end{aligned} \qquad \text{(d)}$$

Eq. 39

leads to the following solution to Eq. 38:

$$\frac{h'\gamma_w}{\ell(1-n)(\gamma_s - \gamma_w)} = 1 - \left(\frac{\pi kt}{S_s \ell^2}\right)^{-\frac{1}{2}} \exp\left[-\left(\frac{z}{\ell}\right)^2 \frac{S_s \ell^2}{4kt}\right] \cdot \int_0^\infty \xi \tanh\left(\frac{\xi S_s \ell^2}{2kt}\right) \cosh\left[\left(\frac{z}{\ell}\right) \frac{\xi S_s \ell^2}{2kt}\right] \exp\left(-\frac{\xi^2 S_s \ell^2}{4kt}\right) d\xi$$

Eq. 40

Solution Eq. 40 holds under the following restrictive assumptions:

1. the porous medium increases in length due to the continuous deposition on top of the layer. However, it does not compact;
2. porosity n , elastic storage S_s and permeability k are constant;
3. the accretion rate ω is constant.

All the previous assumptions are removed in model given by Eq. 37 which will be solved numerically in the next sections. Eq. 40 will be used to test the numerical solution to Eq. 37, although only in the special case of the linear formulation, and to compare the simplified linear results with the more realistic non linear ones.

A few words must be spent on the vertical compressibility $\alpha(\sigma_z)$ which appears in eq. (8). In soil compaction analyses based on oedometer tests the compressibility c_b is usually defined as:

$$c_b = -\frac{1}{1+e} \frac{de}{d(\sigma_z - \sigma_{z0})}$$

Eq. 41

where $e=n/(1-n)$ is the void ratio. Eq. 41 is readily computed from the consolidation profile of appropriate soil samples.

In Gambolati's (1973a) analysis σ_z denotes the effective stress in excess of the in situ stress. Since we are dealing in the present analysis with a sedimentation process from the very beginning ($l=0$ for $t=0$) in Eq. 37 σ_z stands for both incremental and absolute effective stress.

It has been shown by Gambolati (1973) that the oedometer compressibility c_b is related to the classical compressibility α by Eq. 42:

$$c_b = \frac{(\sigma_z - \sigma_{z0}) \frac{d\alpha}{d\sigma_z} + \alpha}{1 - \alpha(\sigma_z - \sigma_{z0})}$$

Eq. 42

where here σ_z is the full effective stress. For a given soil c_b is computed as a function of σ_z using Eq. 41 and then Eq. 42 is solved for $\alpha = \alpha(\sigma_z, \sigma_{z0})$. The integration constant is determined by the requirement that $\alpha(\sigma_{z0}) = c_b(\sigma_{z0})$ (Gambolati, 1973). Finally integration of Eq. 41 provides $e = e(\sigma_z, \sigma_{z0})$ and the constitutive relationship for $n = n(\sigma_z, \sigma_{z0})$ is easily obtained as $n = e/(1+e)$. Both constitutive relationships $\alpha = \alpha(\sigma_z, \sigma_{z0})$ and $n = n(\sigma_z, \sigma_{z0})$ are then used in the numerical solution of Eq. 37.

Let us make an example of application of the procedure just described. Assume that the oedometer profiles point out a constant c_b value. Then integration of Eq. 41 and Eq. 42 yields:

$$e = (1 + e_0) \exp[-c_b(\sigma_z - \sigma_{z0})] - 1$$

Eq. 43

$$\alpha = \frac{1 - \exp[-c_b(\sigma_z - \sigma_{z0})]}{\sigma_z - \sigma_{z0}}$$

Eq. 44

where e_0 is the initial void ratio corresponding to the in situ stress σ_{z0} . The constitutive relationship for n is in this example:

$$n = 1 - \frac{\exp[c_b(\sigma_z - \sigma_{z0})]}{1 + e_0}$$

Eq. 45

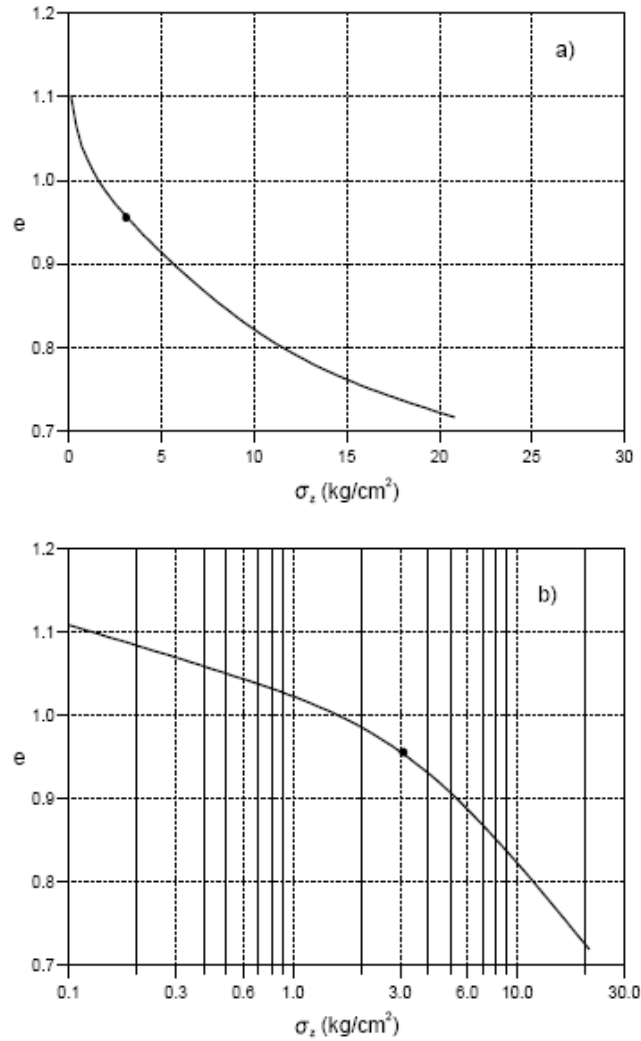


Figure 70: Typical compression profile of a cohesive soil vs. the effective intergranular stress: a) arithmetic plot and b) semilogarithmic plot.

Eq. 45 is similar to the constitutive relation derived by Sharp, Jr. (1983) and critically discussed by Bethke and Corbet (1988). It can be used for σ_z values in the neighbourhood of the in situ stress σ_{z0} only since for large σ_z deviations from σ_{z0} Eq. 45 provides unrealistic n values which can also become negative. This implies that the underlying assumption cannot be true if the range of variation of σ_z is large, i.e. c_b as defined in Eq. 41 cannot be constant for stresses which largely exceed the in situ stress.

However, several authors (Bethke, 1985; Bethke, 1988; Keith and Rimstidt, 1985; Westlake, 1968) have accounted for soil compaction using Athy's (1930) equation. Following Rubey and Hubbert (1959), Athy's constitutive relationship can be written as:

$$n = n_0 \exp[-b(\sigma_z - \sigma_{z0})]$$

Eq. 46

where b is a constant which has the same unit as a compressibility. Common values of b , as may be derived from the definition of Bethke and Corbet (1988), are in the range of 10^{-7} to 10^{-6} m^2/kg . By using Eq. 46 we can easily derive the constitutive equation for the compressibility c_b from Eq. 41. Replacing n by $e/(1+e)$, we get:

$$c_b = n_0 b \exp[-b(\sigma_z - \sigma_{z0})]$$

Eq. 47

From Eq. 47 it appears that b is the initial in situ compressibility c_{b0} divided by the initial porosity n_0 , i.e. $b=c_{b0}/n_0$.

Bethke and Corbet (1988) point out that Eq. 45 provides porosity profiles which are convex upward, indicating that the rate of porosity loss with σ_z increases as the effective stress increase. This result is not consistent with observations in sedimentary basins (Athy, 1930, Archie, 1950, Perrin and Quiblier, 1974) which indicate that the greatest compaction rates occur at shallow depths and small stresses. Porosity curves calculated from Eq. 46 are convex downward and asymptotically approach $n=0$ as σ_z becomes large. According to Bethke and Corbet (1988), p. 462, "these curves are more reasonable geologically because compaction is most rapid at small stresses and only positive values of porosity are predicted".

In NATSUB it is assumed that c_b is provided by a constitutive relationship which can be either Eq. 47 or another equation based on experimental results from the area under investigation. Using this equation for c_b we solve Eq. 42 for $\alpha(\sigma_z)$ and calculate the medium compaction at time t by Eq. 32 (Gambolati, 1973b)]. Eq. 32 will be used in the numerical solution of the consolidation equation to update the thickness of the compacting sediments while deposition occurs. By use of Eq. 42, Eq. 37 can now be written as:

$$\frac{\partial}{\partial z} \left[\frac{k(\sigma_z)}{\gamma_w} \frac{\partial p}{\partial z} \right] = [c_b(\sigma_z) + n(\sigma_z)\beta] Dp - c_b(\sigma_z)(1 - n_0)(\gamma_s - \gamma_w)\omega(t)$$

Eq. 48

Eq. 48 together with Eq. 35 (b and c) and the initial and boundary conditions Eq. 39a through Eq. 39c represents the basis for the numerical simulation of the isothermal compaction of the sedimentary basin underlying the North Caspian Sea.

4.2.3.3 Numerical solution: Lagrangian approach

Using a Lagrangian solution approach, Eq. 49 is solved on a grid where the nodes follow the grains in their compaction movement Eq. 32. This is obtained with a dynamic mesh made of finite elements which deform in time and increase in number as deposition occurs and the soil column compacts.

Over a moving node the total derivative D can be approximated by a standard difference equation as if it were a partial time derivative.

For solution by the finite element method, Eq. 48 is written in the form:

$$\frac{\partial}{\partial z} \left[k(\sigma_z) \frac{\partial p}{\partial z} \right] = \gamma_w [c_b(\sigma_z) + n(\sigma_z)\beta] Dp + f(\sigma_z, t)$$

Eq. 49

where

$$f(\sigma_z, t) = -\gamma_w c_b(\sigma_z)(1 - n_0)(\gamma_s - \gamma_w)\omega(t)$$

Eq. 50

Eq. 50 is regarded as an (unknown) source term and Dp is discretized by a time finite difference scheme with values of p taken over moving nodes. The Galerkin discretization in space with linear basis functions yields the system of non linear ordinary differential equations:

$$H(\mathbf{p})\mathbf{p} + P(\mathbf{p})\frac{d\mathbf{p}}{dt} + \mathbf{f}(\mathbf{p}) = 0$$

Eq. 51

where the vector f includes the effect of $f(\sigma_z, t)$ and the boundary condition. When an impermeable bottom is assumed, f incorporates only the forcing function.

A λ -weighted scheme is used for the time discretization (Crank-Nicolson at $\lambda = 0.5$; backward Euler at $\lambda = 1$). Denoting the time step with superscript K , Eq. 51 becomes:

$$H(P^{K+\lambda})P^{K+\lambda} + P(P^{K+\lambda})\frac{P^{K+1} - P^K}{\Delta t^{K+1}} = -f(P^{K+\lambda})$$

Eq. 52

where

$$P^{K+\lambda} = \lambda P^{K+1} + (1 - \lambda)P^K$$

with $0 \leq \lambda \leq 1$. In the schemes and simulations described in the sequel we use the 2nd order accurate Crank-Nicolson scheme ($\lambda = 1/2$).

Eq. 52 is non linear and the iterative Picard scheme (Culham and Varga, 1971) is used to overcome the non-linearity. Letting superscript (m) be an iteration counter, the Picard scheme with $\lambda = 1/2$ reads:

$$\left(\frac{1}{2} H^{K+1/2(m)} + \frac{1}{\Delta t^{K+1}} P^{K+1/2(m)} \right) P^{K+1/2(m)} = \left(\frac{1}{\Delta t^{K+1}} P^{K+1/2(m)} - \frac{1}{2} H^{K+1/2(m)} \right) P^K - \left(\frac{1}{2} f^{K+1(m)} + \frac{1}{2} f^K \right)$$

Eq. 53

where the terms of the i th row have the expression:

$$H_{i,i}^{K+1/2(m)} = \frac{k_{i-1}^{K+1/2(m)}}{\Delta z_{i-1}^{K+1/2(m)}} + \frac{k_i^{K+1/2(m)}}{\Delta z_i^{K+1/2(m)}}$$

$$H_{i,i-1}^{K+1/2(m)} = -\frac{k_{i-1}^{K+1/2(m)}}{\Delta z_{i-1}^{K+1/2(m)}}$$

$$H_{i,i+1}^{K+1/2(m)} = -\frac{k_i^{K+1/2(m)}}{\Delta z_i^{K+1/2(m)}}$$

$$P_{i,i}^{K+1/2(m)} = \frac{\gamma w}{3} \left[\left(c_b^{K+1/2(m)} + n^{K+1/2(m)} \beta \right)_{i-1} \Delta z_{i-1}^{K+1/2(m)} + \left(c_b^{K+1/2(m)} + n^{K+1/2(m)} \beta \right)_i \Delta z_i^{K+1/2(m)} \right]$$

$$P_{i,i-1}^{K+1/2(m)} = \frac{\gamma w}{6} \left(c_b^{K+1/2(m)} + n^{K+1/2(m)} \beta \right)_{i-1} \Delta z_{i-1}^{K+1/2(m)}$$

$$P_{i,i+1}^{K+1/2(m)} = \frac{\gamma w}{6} \left(c_b^{K+1/2(m)} + n^{K+1/2(m)} \beta \right)_i \Delta z_i^{K+1/2(m)}$$

Eq. 54

with Δz_i the i th element length.

Application of the iterative scheme Eq. 53 yields the symmetric tridiagonal system of equations:

$$G^{(m)}_{K+1/2} P^{(m)}_{K+1} = b^{(m)}_{K+1/2}$$

Eq. 55

where, from Eq. 53 and Eq. 54, the terms of the i th row are given by:

$$\begin{aligned} G^{(m)}_{i,i} &= \frac{1}{2} H^{(m)}_{i,i} + \frac{1}{\Delta t^{K+1}} P^{(m)}_{i,i} \\ G^{(m)}_{i,i-1} &= \frac{1}{2} H^{(m)}_{i,i-1} + \frac{1}{\Delta t^{K+1}} P^{(m)}_{i,i-1} \\ G^{(m)}_{i,i+1} &= \frac{1}{2} H^{(m)}_{i,i+1} + \frac{1}{\Delta t^{K+1}} P^{(m)}_{i,i+1} \\ b^{(m)}_{i,i} &= \left[\frac{1}{\Delta t^{K+1}} P^{(m)}_{i,i-1} - \frac{1}{2} H^{(m)}_{i,i-1} \right] P^{(m)}_{i-1} + \left[\frac{1}{\Delta t^{K+1}} P^{(m)}_{i,i} - \frac{1}{2} H^{(m)}_{i,i} \right] P^{(m)}_{i,i} \\ &\quad + \left[\frac{1}{\Delta t^{K+1}} P^{(m)}_{i,i+1} - \frac{1}{2} H^{(m)}_{i,i+1} \right] P^{(m)}_{i+1} - \left[\frac{1}{2} f^{(m)}_{i,i} + \frac{1}{2} f^{(m)}_{i,i} \right] \end{aligned}$$

Eq. 56

Eq. 55 is solved by the direct Thomas algorithm (Westlake, 1968). It is to be emphasized that the dimension of Eq. 55 is not constant but increases in time as the deposition progresses from an initial value of 2 (we start the simulation with 1 element) to a maximum of N , with N depending on the time interval spanned by the simulation, the depositional rate ω and the required accuracy of the spatial discretization.

The iterative scheme is implemented with the following procedure. Once $P^{(m)}_{K+1}$ has been computed, the approximate $\sigma_z^{(m)}$ is calculated by Eq. 35c, where σ_t is constant within each time step as we have assumed that the variation of the total stress is due only to the weight of the sediments that accumulate on top of the column. Using the constitutive relationships for the porous medium of the area under investigation, the hydrogeological parameters n , k , c_b and α are updated to iteration (m). The next step in the procedure involves the updating of the

elements' length. The compaction $\Delta u_i^{(m)}$,^(m) of the i th element (defined by nodes i and $i+1$), is computed using eq. 3 in the form:

$$\Delta u_i^{(m)} = - \int_{z_i}^{z_{i+1}} \frac{\alpha^{(m)} \sigma_z^{(m)}}{1 - \alpha^{(m)} \sigma_z^{(m)}} dz$$

the integration being performed by the trapezia formula. Consequently, the updated length $\Delta z_i^{(m)}$ is given by:

$$\Delta z_i^{(m)} = \Delta z_i^{K0} + \Delta u_i^{(m)}$$

where Δz_i^{K0} is the initial element length. Matrix G and vector b can now be recalculated and the new solution to Eq. 55 obtained. The iterations are stopped when the difference between the two last solution vectors is smaller than a prescribed tolerance; during the first iteration of each time step, the values at time t are assumed for all the non linear parameters.

At this point we are ready to start with the new time step, but first we have to bring up to date the total stress σ and to check if a new element is to be added as a result of the sedimentation process. As the new elements' length and the new elemental porosities are computed, the actual total stress at the i th node is calculated from Eq. 35b, where z is replaced by z_i , and from Eq. 36, which gives the weight of the sediment deposited during Δt^{K+1} as:

$$\omega^{K+1} (1 - n_0) (\gamma_s - \gamma_w) \Delta t^{K+1}$$

The sedimentation length $\omega^{K+1} \Delta t^{K+1}$ is cumulated with the length deposited during the time elapsed from the addition of the last new finite element. When this length exceeds the initial prescribed nodal spacing, a new element is added and the dimension of Eq. 55 grows by 1 unit. As the sedimenting material is assumed to be homogeneous, the initial hydrogeological properties of the added element are constant and coincide with the parameter values at the inception of the process.

When a new element is introduced, we have to update the dimension of p and f at the previous time step and to provide an estimate of their values in the upper new node in order to get all the components of 26 with the same size, and to calculate the known term bEq. 56. These values can be extrapolated from those of the underlying nodes. In the present analysis, we simply use the value of p and f in the node below.

4.2.3.4 Numerical solution: Eulerian approach

When the Eulerian approach is used to solve Eq. 48, a mesh with fixed nodal positions and increasing number of elements is used for the soil column discretization.

Use of Eq. 31 for the total derivative and Eq. 33 for the grain velocity leads to the following expanded form for eq. 19:

$$\frac{\partial}{\partial z} \left[k(\sigma_z) \frac{\partial p}{\partial z} \right] = \gamma_w [c_b(\sigma_z) + n(\sigma_z)\beta] \left\{ \frac{\partial p}{\partial t} + (1 - \alpha(\sigma_z)\sigma_z) \frac{\partial p}{\partial z} \right. \\ \left. \cdot \int_0^z \left[\frac{c_b(\sigma_z)}{(1 - \alpha(\sigma_z)\sigma_z)} \frac{\partial p}{\partial t} \right] dz \right\} - \gamma_w c_b(\sigma_z) (1 - n_0) (\gamma_s - \gamma_w) \omega(t)$$

Eq. 57

For solution by the finite element method, Eq. 57 is written in the form:

$$\frac{\partial}{\partial z} \left[k(\sigma_z) \frac{\partial p}{\partial z} \right] = \gamma_w [c_b(\sigma_z) + n(\sigma_z)\beta] \frac{\partial p}{\partial t} + f(\sigma_z, z, t)$$

Eq. 58

where

$$f(\sigma_z, z, t) = \gamma_w [c_b(\sigma_z) + n(\sigma_z)\beta] (1 - \alpha(\sigma_z)\sigma_z) \frac{\partial p}{\partial z} \int_0^z \left[\frac{c_b(\sigma_z)}{(1 - \alpha(\sigma_z)\sigma_z)} \frac{\partial p}{\partial t} \right] dz \\ - \gamma_w c_b(\sigma_z) (1 - n_0) (\gamma_s - \gamma_w) \omega(t)$$

Eq. 59

is again treated as an (unknown) source term.

Eq. 58 is solved by finite elements with a procedure which is formally similar to the one used in the Lagrangian approach. Consequently, Eq. 53 still holds with Eq. 54 replaced by:

$$\begin{aligned}
H_{i,i}^{(m)K+1/2} &= \frac{k_{i-1}^{(m)K+1/2}}{\Delta z_{i-1}} + \frac{k_i^{(m)K+1/2}}{\Delta z_i} \\
H_{i,i-1}^{(m)K+1/2} &= -\frac{k_{i-1}^{(m)K+1/2}}{\Delta z_{i-1}} \\
H_{i,i+1}^{(m)K+1/2} &= -\frac{k_i^{(m)K+1/2}}{\Delta z_i} \\
P_{i,i}^{(m)K+1/2} &= \frac{\gamma_w}{3} \left[\left(c_b^{(m)K+1/2} + n^{(m)K+1/2} \beta \right)_{i-1} \Delta z_{i-1} + \left(c_b^{(m)K+1/2} + n^{(m)K+1/2} \beta \right)_i \Delta z_i \right] \\
P_{i,i-1}^{(m)K+1/2} &= \frac{\gamma_w}{6} \left(c_b^{(m)K+1/2} + n^{(m)K+1/2} \beta \right)_{i-1} \Delta z_{i-1} \\
P_{i,i+1}^{(m)K+1/2} &= \frac{\gamma_w}{6} \left(c_b^{(m)K+1/2} + n^{(m)K+1/2} \beta \right)_i \Delta z_i
\end{aligned}$$

Eq. 60

As in the Lagrangian approach, the algebraic system arising from the Eulerian procedure is tridiagonal and is solved by the Thomas algorithm. The terms of the i th row are still given by Eq. 56.

The iterative procedure is implemented in a form similar to the Lagrangian formulation. Once $P^{(m)K+1}$ is computed, and hence $\sigma_z^{(m)K+1}$ (σ_z is constant within a time step), we update the hydrogeological parameters and recalculate the matrix G and the known vector b in a straightforward manner as the elements length is fixed. The computation of b requires the calculation of two partial derivatives (Eq. 59), and this is accomplished by the formulas:

$$\left(\frac{\partial p}{\partial z} \right)_i = \frac{p_{i+1} - p_{i-1}}{\Delta z_i + \Delta z_{i-1}}$$

Eq. 61

$$\left(\frac{\partial p}{\partial t} \right)^K = \frac{3p^K - 4p^{K-1} + p^{K-2}}{\Delta t^K + \Delta t^{K-1}}$$

Eq. 62

When the iterative procedure is completed and the solution P^{K+1} obtained, we have to take account of both the compaction and sedimentation that occurred in the current time step.

Since with this solution scheme the elements are fixed, only the compaction of the entire column u_ℓ^{K+1} needs to be calculated. Accordingly, Eq. 32 yields:

$$u_\ell^{K+1} = - \int_0^{\ell^{K+1}} \frac{\alpha^{K+1/2} \sigma_z^{K+1}}{1 - \alpha^{K+1/2} \sigma_z^{K+1}} dz$$

To assess the displacement of the top of the soil column during the current Δt , the actual deposition length $\omega^{K+1} \Delta t^{K+1}$ must be added to the settlement of the column top that occurred during the same time interval:

$$\omega^{K+1} \Delta t^{K+1} + \left(u_\ell^{K+1} - u_\ell^K \right)$$

Eq. 63

With a technique similar to that implemented in the Lagrangian approach, the length Eq. 63 is used to update the height of the soil column, and, after multiplication by $(1-n_0)(\gamma_s - \gamma_w)$, to update the total stress obtained from Eq. 35b. A new element is introduced when Eq. 63 reaches or exceeds the prescribed nodal spacing. The assignment of the initial hydrogeologic parameters to the new element and the updating of vector size b are performed with the procedure described in the previous section.

4.2.4 The Basin code

BASIN is inspired by an early approach to basin modelling by Harbaugh and Bonham-Carter (1970), who simulated the filling of a sedimentary basin with clastic sediments. Though simple, their conceptual model was very powerful in creating surprisingly realistic geologic system responses with fairly complex basin geometries and facies distributions. The DEPOSIM model by Bitzer and Harbaugh (1987) applied a similar algorithm for clastic sedimentation and included a simple algorithm for compaction and isostatic response. While both models were capable of creating more or less realistic basin geometries, their predictive potential was low, as both models were limited to two-dimensions and heuristic in their representation of clastic sediment transport and deposition. Other sedimentary processes were not included, most important, carbonate sedimentation was not considered. A three-dimensional model simulating clastic sedimentation proposed by Tetzlaff and Harbaugh (1989) incorporates a physically rigid approach, however, its applicability in predicting the geometry and facies distribution is constrained by the uncertainty or lack of knowledge of initial and boundary conditions during the generation of a sedimentary deposit.

In many cases, the basin geometry and facies distribution are used as the a-priori information for a basin simulation to represent the heterogeneity of the deposit. Using this representation of heterogeneity, the hydraulic and thermal evolution is calculated for a given set of initial and boundary conditions, and parameters such as fluid pressure, temperature, hydrocarbon saturation and petrophysical parameters are predicted. In such a situation, it is not necessary to apply a sedimentation simulation model, as the best outcome would be a basin geometry and facies distribution which is already assumed to be known. Thus, geometry and facies distribution will be derived from seismic sections and well data, and not be calculated with a sedimentation simulation. BASIN is basically designed for this type of situation, however, it also includes a sedimentation simulation module capable of simulating clastic and carbonate sedimentation. This module is useful to analyse the sequence stratigraphy of a basin fill in response to defined sea-level changes and subsidence. The basin fill history can either be simulated or it can be pre-defined in order to match a specific basin.

The evolving basin geometries are transformed into finite-element meshes with triangular elements as described by Bitzer (1996). Compaction or topography-driven fluid flow is calculated using these meshes. Solute transport calculation allows to trace a conservative solute in the evolving basin taking into account advection, dispersion and diffusion. Heat flow, including advective components and hydrocarbon generation employing the Lopatin method (Lopatin, 1971, Waples, 1980) are calculated as well.

The program proceeds in discrete time steps. Each module proceeds in its own time step size, imposed by the stability criteria required for the numerical solution. Space is represented

through individual layers of changing thickness defined at discrete points along the simulated cross section. The z-location (depth) and the parameters at these nodal points change during the simulation progress. However, all nodal values can be forced at any time step of the simulation to match a specific pre-defined basin situation. As the basin evolves through time, the upper boundary is moving, which requires a new mesh at each time step to be calculated and an automatic definition of boundary conditions. BASIN continuously changes the basin geometry, the finite-element meshes and the nodal and element parameters through time due to sedimentation or erosion, compaction and tectonic processes. The meshing algorithm used for BASIN is simple and may, under unfavorable situations, create meshes with extremely elongated triangles, where the numerical methods fail. Such situations may especially happen in case of several successive unconformities. Though simple, the meshing algorithm has successfully been applied to complicated basin configurations such as foreland basins with advancing nappes.

4.2.4.1 ***Sedimentation Modelling***

The basin fill may either be predefined, or the sedimentation module may be invoked to provide a sedimentation simulation at specified time steps. The simulation of deposition is mainly of interest if the stratigraphic response to sea-level change and subsidence is the main focus of the numerical experiment. BASIN considers four types of sediments, of which the first three usually are different clastic sediments and type four is carbonate sediment by default. If the sedimentation module is not invoked, all four sediment types may correspond to any sediment type, as defined in the input data set through their corresponding material properties like initial porosities, hydraulic conductivities, compressibilities, thermal capacities, thermal conductivities, densities, tortuosities, thermal and hydraulic dispersivities.

Clastic sedimentation is treated as a diffusive process similar to the model developed by Harbaugh and Bonham-Carter (1970). Sediment diffusion in BASIN is grain size dependent. In the conceptual model, a coarse sediment type diffuses more slowly into the basin than a fine grained sediment. The diffusion parameters together with the source strength of each sediment type at the model boundaries control the geometric and facial evolution of the deposit. Sediment supply can be defined at both sides of the cross section. Source strengths and maximum subaereal sedimentation rates for each sediment type are defined. Carbonate sedimentation is defined through a maximum carbonate production rate, the type of function between water-depth and carbonate production rate, and poisoning factors for each clastic sediment type. In case of high clastic sedimentation rates, carbonate production may be slowed down or completely inhibited due to the poisoning effect. On the other hand, clastic

sedimentation may reduce water-depth, providing favorable conditions for subsequent carbonate production. The interaction and feedback between the processes is represented through a system of ordinary differential equations which is solved numerically.

Sedimentation depends on available accommodation space and sediment supply. Accommodation space for subaqueous sedimentation is defined through the water-depth. In BASIN, the change of water-depth is calculated from sea-level change and change of sediment surface Eq. 64:

$$\partial W/\partial t = (\partial S - \partial L)/\partial t$$

Eq. 64

with W =water-depth, S = sea-level and L = position of the sediment during a time interval ∂t . For rising sea-level or subsiding sediment surface, water-depth and accommodation space increase. Sea-level changes are pre-defined whereas position of sediment surface and sedimentation rate along the simulation sedimentary basin are calculated as a function of sedimentation rate and subsidence.

Clastic sedimentation is calculated for each sediment type k in an iterative scheme applying different equations for subaereal and subaqueous deposition. For subaqueous deposition ($W>0$), Eq. 65 and Eq. 66 are solved:

$$\partial G_k/\partial t = (1/a_k) H_k$$

Eq. 65

$$\partial H_k/\partial t = - \partial G_k/\partial t$$

Eq. 66

with H_k = amount of clastic sediment in the water column available for sedimentation, $\partial G_k/\partial t$ = sedimentation rate and factor a_k = magnitude of sediment diffusion, subscript k indicating the sediment type. For low sediment diffusion, the sedimentation rate is high. Subaereal sedimentation ($W<0$) is calculated using Eq. 67

$$\partial G_k/\partial t = r_k/(c (s+s_0) + 1)$$

Eq. 67

with r = maximum subaereal sedimentation rate at distance s_0 from the boundary, s = distance from the model boundary and c = scaling factor. s_0 can be considered as the distance of the source area from the model boundary. The larger this distance, the lower the sedimentation rate in the subaereal parts of the basin becomes.

Carbonate sedimentation is calculated for those parts of the basin, where actual water-depth is less than the critical water-depth for carbonate deposition and more than zero Eq. 68:

$$\partial C/\partial t = b (W_{max} - W)^n - \sum f_{(k)} H$$

Eq. 68

with $\partial C/\partial t$ = carbonate production rate, W_{max} = maximum carbonate production depth, W = current water-depth (or accommodation space), b = scaling factor for carbonate production rate, n = factor that determines the relation between water-depth/carbonate production rate, and $f_{(k)}$ = the clastic sediment poisoning factor for each sediment type k . $\partial C/\partial t$ is zero under subaereal conditions or if water-depth is larger than the maximum water-depth for carbonate deposition. The equation is similar to those applied in predator-prey models in population dynamics. The first term in Eq. 68 expresses water-depth dependent carbonate production rate with scaling factor b controlling the carbonate production rate. For $n=1$, a linear relation between carbonate production and water-depth is defined. More realistic, however, are nonlinear functions with $n>1$, which give accelerated growth rates at decreasing water-depths (e.g. Scoffin, 1986). The second term in Eq. 68 describes the poisoning effect of clastic sediment types and may become large, if poisoning factors $f_{(k)}$ are large or the amount of clastic sediment in the water column is large. Factor b can be expressed using Eq. 69 as a function of maximum water-depth and maximum carbonate production rate:

$$b = (\partial C/\partial t)_{max} / (W_{max})^n$$

Eq. 69

with $(\partial C/\partial t)_{max}$ = maximum carbonate production rate. Although this conceptual model is strongly simplified, the geologic system feedback is surprisingly realistic, and complex

geometries and facies patterns can be calculated by this approach. The model can be extended to include different types of carbonate producing processes and specified interaction between them with minor changes in the code.

The position of the sediment surface changes as a result of clastic and carbonate sedimentation rate and subsidence rate $\partial R/\partial t$.

$$\partial L/\partial t = (\partial(G+C) - \partial R)/\partial t$$

Eq. 70

The sediment diffusion parameters for clastic sedimentation are heuristic. However, they can be interpreted in terms of settling velocity and energy conditions in the water column (Bitzer and Harbaugh, 1987).

4.2.4.2 ***Tectonic processes***

The basin geometry controls to a great extent the sedimentary evolution and the stratigraphic pattern (and vice versa) and may be altered by tectonic processes. The hydraulic evolution of the basin also strongly depends on the geometry. If portions of the basin are elevated above sea-level, topography driven flow regimes may evolve in parts of the basin, perturbing solute transport and heat flow. BASIN permits to calculate tectonic processes by considering defined fault block movements and isostatic response to sedimentation or erosion using the Airy model. Several fault blocks can be defined, which may act during specified time steps with individual throw rates and hydraulic conditions. Using this option, fault zones with specified hydraulic properties can be incorporated in the basin model. Faults are considered to be vertical in the model. However, as node coordinates can be altered manually, more complex fault geometries can be considered as well (Bitzer, 1997a). Additionally, a pre-defined bathymetry can be specified at individual time steps as part of the input data, if such data are available. In such cases, tectonic subsidence satisfying the assumed paleo-bathymetry is calculated.

Isostatic response is calculated applying Eq. 71 (e.g. Turcotte and Schubert, 1982):

$$\partial L/\partial t = ((\rho_s - \rho_w) / (\rho_m - \rho_s)) \partial(G + C)/\partial t$$

Eq. 71

with $\partial L/\partial t$ = basin subsidence rate, $\partial(G+C)/\partial t$ = sedimentation rate of clastic and carbonate sediment, ρ_S = sediment density (taken as weighted average of all sediment types and the corresponding porosities in the sedimentary column), ρ_W = density of water and ρ_M = mantle density. In case of pre-defined bathymetry, the tectonic subsidence along the simulated cross section is calculated, whereas the bathymetry is calculated if the tectonic subsidence is pre-defined. Bathymetry and/or tectonic subsidence can be displayed using the postprocessing program BASELINE. An interesting application of this module is to test the impact of isostatic response on resulting basin geometries and facies distribution. Generally, accommodation space is strongly increased if isostatic response is considered, and facies progradation is slowed down.

4.2.4.3 *Hydraulic Evolution*

The principal component of the program is the hydraulic simulation, which couples fluid flow and sediment consolidation. In difference to an earlier version of the code (Bitzer, 1996) BASIN includes a direct solution approach which considerably speeds up calculation and improves the quality of the numerical solution. Additionally, the current version takes advantage of the structural similarity between the equations for fluid flow, solute transport and heat flow.

The basic feature of the fluid flow calculation is the coupling of sediment consolidation and fluid expulsion incorporating the sediment compressibility as one of the controlling material properties. Hydraulic conductivity, sediment compressibility and porosity are treated as variables and are calculated in response to progressing fluid expulsion. Boundary conditions are assigned automatically. A fully implicit procedure is used, however a Crank-Nicholson solution scheme can be selected as well. In case of subaerial emersion of parts of the basin the position of the phreatic surface has to be defined as a function of topography. Topography driven flow and consolidational flow can be treated synchronously.

The consolidation equation incorporating porosity dependent sediment compressibility and hydraulic conductivity is solved (eq. 9):

$$\left(\frac{\partial}{\partial x}\right) (k_{x(\phi)} \frac{\partial p}{\partial x}) + \left(\frac{\partial}{\partial z}\right) (k_{z(\phi)} \frac{\partial p}{\partial z}) = (1-\phi) \rho g \alpha_{(\phi)} \frac{\partial p}{\partial t}$$

Eq. 72

with $k_{x(\phi)}$ = porosity dependent hydraulic conductivity in x-direction using Eq. 73, $\alpha_{(\phi)}$ = porosity dependent sediment compressibility, p = fluid pressure and ϕ = porosity. Hydraulic conductivity is calculated from porosity assuming the Kozeny-Carman relation (eq. 10),

$$k = (\rho_w g / 5 S_0^2 \mu) (\phi^3 / (1-\phi)^2)$$

Eq. 73

with S_0 = specific surface, μ = viscosity, ρ_w = density of pore fluid. Sediment compressibility is calculated using a similar function which is derived from the assumption of a constant hydraulic diffusivity (Bredehoeft and Hanshaw, 1968):

$$\alpha = c (\phi^3 / (1-\phi)^2)$$

Eq. 74

with c = constant. Further details of this approach are given in Bitzer (1996). Sediment compressibilities calculated with this approach fit very well with experimental and measured data (Bitzer, 1997b). Other functions determining porosity-hydraulic conductivity relations may be used as well.

4.2.4.4 Compaction

Fluid expulsion and mechanical compaction are coupled processes. In contrast to most other models, the nonlinear form of the equation of state of porosity is used instead of porosity/depth or porosity/effective pressure functions like Athy's law (Athy, 1930). The advantage of this approach is a physical consistent coupling of sediment consolidation and fluid flow. In BASIN, it is assumed that during sediment loading the total stress is transformed to effective stress acting between the sediment grains, and fluid pressure Eq. 75:

$$\sigma_{load} = \sigma_{effective} + P_{fluid}$$

Eq. 75

During consolidation, the ratio between effective stress and fluid pressure changes. Upon loading, the total load is initially supported by the fluid pressure. As fluids are drained, the effective stress increases and fluid pressure is released at the same rate (Eq. 76):

$$\partial\sigma_{\text{effective}} + \partial p_{\text{fluid}} = 0$$

Eq. 76

Deriving the equation of state for porosity (e.g. deMarsily 1986: p. 96), changes of porosity can be expressed as a function of the solid portion of the sediment, the fluid pressure change and porosity dependent sediment compressibility $\alpha_{(\phi)}$:

$$\partial\phi/\partial t = (1-\phi) \alpha_{(\phi)} \partial p_{\text{fluid}} / \partial t$$

Eq. 77

Rearranging Eq. 77 gives

$$\partial\phi/\partial p_{\text{fluid}} = (1-\phi) \alpha_{(\phi)}$$

Eq. 78

The equivalent form of Athy's equation to Eq. 78 can be expressed as

$$\partial\phi/\partial p_{\text{fluid}} = (b / (\rho g)) \phi$$

Eq. 79

(Bethke and Corbet, 1988) with b =constant, expressing the change of porosity as a function of the porous portion of the sediment. Constant b in Athy's equation (Eq. 79) has occasionally been interpreted as the sediment compressibility (e.g. Pedersen and Bjorlykke, 1994), which is physically not justified. Moreover, it would signify that sediment compressibility remains constant during consolidation, which is clearly not the case.

In BASIN, compaction can also be calculated independently from fluid flow, assuming that a compaction equilibrium is reached. In this case it is assumed that total stress is completely transformed to effective stress acting on a microscopic scale between sediment grains. Fluid pressures are hydrostatic in this case. The advantage of this procedure is to get a first guess on basin geometry and porosity distribution without having to solve for the whole finite-element

calculation. In cases with low or moderate sedimentation rates, overpressures are usually low, and calculated porosities are close to compaction equilibrium. Another advantage of decoupling fluid flow and compaction is, that, in case the hydraulic calculation fails because of bad elements in the finite-element mesh, equilibrium compaction can be calculated though.

4.2.4.5 *Solute Transport*

Solute transport calculation has many useful applications in basin analysis and is a prerequisite to incorporate quantitative modelling of fluid-rock interaction. For example, the compaction model used in BASIN is limited to the mechanical process of porosity reduction. More realistic, however, would be to include chemical processes as well, which may increase or decrease porosity through dissolution or cementation (and alter the fluid flow system). Thus, a more realistic approach to mechanical compaction modelling would be to include reactive transport. A comprehensive introduction to diagenetic modelling is given by Boudreau (1997). BASIN in its current state does not include such a module, however, it incorporates a module which solves the transient transport equation (Eq. 80) for a conservative tracer, accounting for diffusive, dispersive, and advective transport and adsorption:

$$D/(R_f \omega) ((\partial^2 C/\partial x^2) + (\partial^2 C/\partial z^2)) + (D_x (\partial^2 C/\partial x^2) + D_z (\partial^2 C/\partial z^2))/R_f - (v_x (\partial C/\partial x) + v_z (\partial C/\partial z))/R_f = \partial C/\partial t$$

Eq. 80

with D = coefficient of molecular diffusion, R_f = retardation factor, ω = tortuosity, C = solute concentration, D_x , D_z = coefficient of hydrodynamic dispersion in x- and z-direction, v_x , v_z = flow velocities in x- and z-direction. Tortuosities and longitudinal and transversal dispersivities are arithmetically averaged from the sediment mixtures in each element. The physical principles and the derivation of the equation are given in many hydrogeology textbooks (e.g. Domenico and Schwartz, 1990). Numerical solutions of the equation require several stability conditions to be satisfied. One of these conditions is imposed by the grid-Peclet number Pe , which defines the ratio between advective and dispersive/diffusive flux (Eq. 81):

$$Pe_x = v_x dx/D$$

Eq. 81

with v_x = flow velocity in x-direction and dx = grid point distance. For $Pe > 1$ advective transport dominates. In this case, discretisation of the model requires nodal distances to be lower than dispersivities to avoid numerical dispersion (Kinzelbach, 1986). Definition of dispersivities is a crucial point as it sets limits in the spatial discretisation of the model. Dispersivity is a scale dependent quantity. Dispersive transport in a large scale problem such as a sedimentary basin involves large scale inhomogeneities (e.g. channels, reefs) which cannot be observed in a small scale. Thus, dispersivities should be chosen in function of the scale of the problem domain. If discretisation involves grid-Peclet numbers > 1 the numerical solution may exhibit numerical dispersion and dispersivities in the order of maximum nodal distances should be chosen. Calculating solute transport with BASIN, the finite-element discretisation is usually not known in advance. Therefore, calculated solute concentrations should be carefully checked for oscillations or other artefacts, indicating discretisation problems.

Discretisation of time is restricted by the Courant-criterion. The length of a time step must be chosen such that the maximum distance a virtual particle may travel during a time step is less than the distance between adjacent nodes. BASIN applies an automatic time stepping scheme that checks velocities and nodal distances in the model and calculates maximum time step sizes that satisfy the Courant-criterion. In case of high flow velocities as for example during topography driven fluid flow, transport modeling over geologic time may involve a large number of time steps, requiring extensive computing time. In such cases, a maximum of time steps can be defined, overriding the Courant-criterion. The numerical result, however, may then exhibit numerical errors.

4.2.4.6 **Heat Flow And Hydrocarbon Generation**

BASIN calculates conductive, dispersive and advective heat transport. Heat flow is controlled by the thermal conductivity κ and specific heat c . As heat is transported through the rock matrix and water, thermal conductivities and specific heat of both are involved. The heat flow equation has a similar structure as the transport equation (Domenico and Schwartz, 1990):

$$\lambda \left(\frac{\partial^2 T}{\partial x^2} + \frac{\partial^2 T}{\partial y^2} \right) - r (v_x \frac{\partial T}{\partial x} + v_y \frac{\partial T}{\partial y}) = \frac{\partial T}{\partial t}$$

Eq. 82

with

$$r = (\phi \rho_w c_w) / (\rho_r c_r)$$

Eq. 83

$$\lambda = \kappa_r / \rho_r c_r + r \alpha |v|$$

Eq. 84

with κ_r = thermal conductivity of rocks, c_r = specific heat of rocks, ρ_r =averaged rock density, T =temperature, ρ_w =density of water, c_w =specific heat of water, ϕ = porosity and v =flow velocity. λ is the thermal dispersion coefficient, which is in the absence of advective transport equal to the thermal diffusion coefficient. α is the thermal dispersivity. Thermal conductivities and heat capacity of rocks are averaged according to Horai (1971) and Domenico and Schwartz (1990):

$$\kappa_r = \kappa_m (1-\phi) + \kappa_w \phi$$

Eq. 85

$$\rho_r c_r = \phi \rho_w c_w + (1-\phi) \rho_m c_m$$

Eq. 86

with index m indicating properties of the rock matrix, which is averaged from all sediment types. Thermal conductivity is a function of temperature. In BASIN, the following functions are used:

$$\kappa_{m,T} = \kappa_{m,20} (293 / (273 + T))$$

Eq. 87

with $\kappa_{m,20}$ =thermal conductivity of the rock matrix at 20°C,

$$\kappa_{w,T} = 0.56 + 0.003 T^{0.0827} \quad (\text{Temperatures between 0 and 50}^\circ \text{C})$$

Eq. 88

$$\kappa_{w,T} = 0.442 + 0.0519 \ln T \text{ (Temperatures greater } 50^\circ \text{ C)}$$

Eq. 89

4.2.5 Models application and results

4.2.5.1 Calculation of rock compressibility from wireline logs

DATASET

The dataset utilized to make compressibility calculations was provided by O&G companies and it is referred to five wells drilled in the offshore zone of the study area.

Only few of these data were complete and in digital LAS (Log Ascii Standard) format. For the other wells, the wireline logs data were digitized from original masterlogs in pdf format by Neuralog software.

The data provided is shown in the table below. There are the type of wireline logs used, the abbreviation of channel with measurement units and a brief description. In the table is not shown the bit size, used to check the quality of sonic log data.

Table 5: Main logs used for this study.

TYPE OF LOG	CHANNEL ABB.	DESCRIPTION
CALIPER	CAL	Borehole Diameter
DENSITY	RHOB (g/cm ³)	Bulk Density
POROSITY	NPHI	Neutron Porosity
SONIC	DT (μs/ft)	Compressional Slowness

APPROACH

The approach used for all wells was as first step the data quality check to be sure all data are reliable and useable. For some wells we digitized the wireline log curves starting from the pdf files using Neuralog software. The second step was to calculate bulk rock compressibility for all the wells.

We tested also the possibility to calculate the pore compressibility for two wells, but the uncertainties in estimating the matrix compressibility using the Overton and Norman (1969) method made these calculations useless. The third step was to evaluate for some wells the

overburden pressure and then lithostatic pressure versus depth. The fourth and last step was the propagation in three dimensions of the compressibility values across the entire area.

DATA CLEANING AND QUALITY CHECK

The caliper log data was used to evaluate the data quality during the acquisition of the logs and especially of the sonic log. These data were compared with bit size data to see where the hole is engaged or caved. In rough hole in fact it is not possible to ensure that the sonic probe is always centred in the borehole. The result is the severe attenuation of the acoustic signal. Energy is also lost by diffraction at angles in the rough hole. The transmitter receiver distance is effectively much longer in rough hole than in smooth hole. Since hole rough is often a result of alteration of the formation by drilling mud. This approach was used only for two wells, because for the other wells the caliper data was not available.

All the logs data was then checked to filter negative and null data. Density logs were compared with the lithological column and other wireline logs provided to be sure the density data were realistic. All density data below 1.95 g/cm^3 was considered as non valid due to incorrect measurements/readings or malfunction of the sonic tool. The wireline log data coverage is different from well to well and usually they cover the range from seabed to bottom hole. In this interval the data was not always complete because of tool problems or other technical issues.

BULK ROCK COMPRESSIBILITY CALCULATION

The calculation of rock and pore compressibility are fundamental to understanding the behaviour of the reservoir, especially for evaluating the reservoir performance and compaction. The theory of rock compressibility is given in 4. However, main definitions of properties involved in the calculation of compressibility are given.

Three kinds of compressibility can be distinguished in rocks: rock matrix compressibility, rock bulk compressibility and pore compressibility. Bulk rock compressibility is the fractional change in volume of the bulk rock volume with unit change in pressure. In the other hand rock matrix compressibility is the fractional change in volume of the solid rock material (grains) with unit change in pressure. Pore compressibility is the fractional change in pore volume of the rock with a unit change in pressure.

Compressional velocity is related to the rock density and the bulk modulus of the rock. The bulk compressibility is calculated as the inverse of bulk modulus. So the bulk rock compressibility can be written as below (Eq. 90):

$$\text{Compressibility} = \frac{1}{\rho * V_p^2}$$

Eq. 90

where ρ is the rock density (kg/m^3) and V_p the velocity of P wave (compressional slowness logged by sonic log) measured in m/sec. The compressibility is measured in pascal (Pa).

We tried also to evaluate the pore compressibility was calculated by using Overton and Norman method (1969). This method take into account formation porosity (obtained from data of neutron log), travel time (from data of sonic log) and density (from data of density log). The formula by authors is the following (Eq. 91):

$$\text{Compressibility} = \frac{1 - \emptyset}{\emptyset} * C_r + 0.744 * \frac{\Delta T^2}{\emptyset * \rho * 10^{10}}$$

Eq. 91

where \emptyset is the porosity, ΔT is the travel time ($\mu\text{s/ft}$), ρ is the density of the rock (g/cm^3), 0.744 is a constant derived from empirical calculations to obtain the formula. The compressibility unit measurement is psi^{-1} . In the formula there is a constant C_r called compressibility of matrix and it is an adimensional number (Eq. 92). This compressibility is calculated using a shale factor for carbonate or clastic units. For evaporites this value is constant. In fact in evaporites porosity is equal zero or very low so the lower term of the formula is only constant divided by one.

$$C_r = \left(\left(\sum_{i=1}^n [v_i(i) C_i(r_i)] + v_{sh} C_{sh} \right) \right) / (1 - \emptyset)$$

Eq. 92

In our calculations we used C_r for calcite. v_i , C_{ri} , v_{sh} , C_{sh} are shale factors for carbonates or clastic units. The authors to obtain the formula Eq. 91 assumed that all reservoir boundaries move by varying amounts as pore pressure drops. This formula is valid only for consolidated rock and it is not applicable for unconsolidated rocks according to the authors.

We tried to calculate the pore compressibility for two wells, but the strong uncertainties in evaluating C_r led to unrealistic results. The compressibility of rock frame can be calculated also using logs using the approach of Khatchikian (1995), but only in case of the availability of the shear sonic logs. It is important to highlight both methods, also that we used for our

calculations, are applied according to the authors, originally for laboratory conditions and not for wellbore conditions.

LITHOSTATIC PRESSURE CALCULATION

Lithostatic (or overburden) pressure is a term to denote the pressure imposed on a stratigraphic layer by the weight of overlying layers of material. This pressure is exerted in all direction like a hydrostatic pressure. In fact it doesn't produce deformations, but only compaction and rock volume reductions. The normal value in the earth crust is 2.7×10^6 Pa/km.

Lithostatic pressure induces a stress in rocks. Rocks can respond to that stress in two ways: with the lithostatic stress causes a reduction of the volume of the rock, thus an increase in its density or with a non lithostatic (or directed stress) causes a change in the rock change (or strain). When the elastic limit of the rock is reached, it will change shape in non reversible way. At depth, the pressure will be so high that no more pore spaces exist in rocks, preventing water to flow. Sediment porosity decreases under the effect of burial (compaction) and it is proportional to the increase in overburden pressure. In the case of clays, this reduction is essentially dependent on the weight of the sediments. If clay porosity and depth are represented in arithmetical scales, the relationship between these two parameters is an exponential function. In sandstones and carbonates, this relationship is a function of many parameters other than compaction, such as diagenetic effects, sorting, original composition and so on. A decrease in porosity is necessarily accompanied by an increase in density. This pressure can be seen also as sum of fluid pressure in the pore space and the stress between the rock grains of the matrix. At the given depth the overburden pressure remains constant so that with production of the reservoir fluid, the fluid pressure decreases, creating an increase in the grain to grain stress. This may result in the grains of rock crushing closer together, providing a small amount of drive energy (compaction drive) to production. In extreme cases of pressure depletion in poorly compacted rocks this can give rise to reduction in the thickness of reservoir, leading ultimately to surface subsidence. For lithostatic pressure calculations we used the following formula from literature (Hantschel and Kauerauf 2009) (Eq. 93):

$$P_l = 9.81 \times \rho \times z + p_0$$

Eq. 93

The lithostatic pressure P_l in the formula (Eq. 93) is measured in Pa, 9.81 m/s^2 is the gravity acceleration constant, ρ is the rock density (kg/m^3), p_0 is the datum pressure and dz is the

depth interval. In other mathematical form the formula (Eq. 93) can be written considering the interval from surface (z) to n -depth (z_n) so we can calculate the lithostatic pressure:

$$PI = \sum_{i=0}^n \rho \times 9.81 \times z_n$$

Eq. 94

The integral for each depth interval from surface to n -depth, z_n represents the depth increment with assumed constant density ρ (kg/m^3), 9.81 m/s^2 is gravitation acceleration constant. The lithostatic pressure is measured in Pascal. For the density values in the intervals of all wells where there aren't availability of the data for some reasons (tool problems or other issues) we used an average of the rock density of the previous interval checking the lithology to be sure to assign a correct value to missing density interval. For our purposes we used always a column with raw density data and the other with filtered (or interpreted) density data.

RESULTS

Compressibility results are briefly discussed for each well.

A graphic with depth in horizontal axis and bulk rock compressibility values in vertical axis is provided. It was used a logarithmic scale instead of linear scale for vertical axis to visualize better the bulk rock compressibility variations (beside background noise) also at small details. The depth scale was adjusted according the availability of log data (in most cases the range is between 0 and 4,500 – 5,000 meters. The vertical logarithmic scale was kept always the same from 1 to 10^{-8} psi^{-1} (except for one well where the scale is from 0.1 to 10^{-8} psi^{-1}).

- Well "Test 1"

For the Test 1 the bulk rock compressibility was calculated as explained above.

Calculations showed that at 806.2 meters there is an area where the bulk rock compressibility decreases due to change in lithology; from 1,708.7 to 3,592.7 meters interval bulk rock compressibility is pretty stable due to evaporites sequence. The values are between 10^{-6} and 10^{-7} psi^{-1} . The bulk rock compressibility decreases with depth as expected because on the top

there are more unconsolidated formation than deeper where the rocks are more compacted for the overlying sediments.

- Well “Test 2”

At 241.9 meters there is a decrease in the bulk rock compressibility due to presence of claystone intercalations in limestones. Bulk rock compressibility decreases with an increasing of density of claystone. We can observe also at 1,226.8 meters there is an another area of decreasing of bulk rock compressibility due to massive limestone (Upper Jurassic Carbonate sequence) with an increasing of density the bulk rock compressibility decreases obviously. The bulk rock compressibility values are included between 10^{-6} and 10^{-7} psi^{-1} and they are decreasing with depth.

- Well “Test 3”

At 449.9, 513.8 and 581.6 meters there is a decrease in the bulk rock compressibility due to presence of argillaceous limestone moderately consolidated (Upper Cretaceous Carbonate sequence). We can observe also that at, 1,352.7 meters, there is an another zone of decreasing of bulk rock compressibility; it's due to presence of argillaceous limestone in first half of Upper Jurassic limestone sequence and also after 2,258.9 meters till the end of data due to presence of shale silicified in part and massive limestone. The bulk rock compressibility values are included between 10^{-6} and 10^{-7} psi^{-1} and the general trend is decreasing with depth.

- Well “Test 4”

It was possible to notice that at 1,422.9 meters there is depletion in the bulk rock compressibility due to presence of dolomite/dolomitic limestone facies inside limestone (Upper Jurassic Carbonate sequence). We can observe also at 2,667.4 and 2,900.2 – 2,940.7 meters interval there is an another zone of suddenly decreasing of bulk rock compressibility due to presence of claystone and transition to anhydrite (Permian Kungurian Evaporite sequence). Also from 2,985.7 meters till the end of data we can watch a flat area due to halite and anhydrite (Kungurian Halite and Basal Anhydrite). Bulk rock compressibility values are included between 10^{-6} and 10^{-7} psi^{-1} and the general trend is decreasing with depth.

We tried also to evaluate the pore compressibility using Norman and Overton method (1969). In fact in the interval 1,326.3 – 1,434.7 meters there is a suddenly increase in the pore compressibility due to Upper Jurassic Carbonate sequence (massive limestone). At 2,843 m the pore compressibility values are out of scale due to evaporites sequence and its very low

porosity. So the compressibility is very high value (about 1 psi^{-1}) for elastic behaviour of them. The pore compressibility is higher than bulk compressibility values as expected and they increase with depth. The values are included between 10^{-6} and 10^{-5} psi^{-1} . In this case we used a matrix compressibility of a quartzitic rock: this is the cause of the abnormal values of pore compressibility in the evaporites.

- Well “Test 5”

We can notice that at 1,695.9 meters there is a decrease in the bulk rock compressibility followed by an increase due to lithology change; from 2,649.3 to 4,001.6 meters there is a flat area due to evaporites sequence. After 4,001.6 meters there is a suddenly decreasing to the end of data due to presence of shale. The bulk rock compressibility values are included between 10^{-6} and 10^{-7} psi^{-1} and the general trend is decreasing with depth.

Also for this well, we tried to evaluate the pore compressibility. At 1,191.5 meters, there is a decreasing of pore compressibility due to presence of claystone interbeds in the limestone. At 1,331.7 meters, there is an increasing of pore compressibility due to argillaceous limestone. In the interval 1,647 – 1,749 meters there is an increasing followed by decreasing in the pore compressibility due to Upper Jurassic carbonate sequence (massive limestone). The pore compressibility trend is increasing with depth and the pore compressibility values are included between 10^{-6} and 10^{-5} psi^{-1} . After 3,955 meters, there is not availability of porosity log data so we cannot calculate further the pore compressibility.

4.2.5.2 *Natsub*

The mechanical properties of the sedimentary sequence in the Precaspian basin are of primary importance for the simulation and prediction of soil compaction during the basin formation. Available relevant data are:

1. Sonic logs, referred to wells drilled in the Northeastern Caspian Sea. These data, processed as described in 4.2.5.1, provide information about rock compressibility (only for two wells) and bulk compressibility (every well).
2. Geotechnical report, carried out both onshore and offshore.

It has to be underlined that the definition of these compressibilities is not given in these documents. Terms as “Modulus of deformation” or “Compaction factor” are used without a detailed description. They are representative of the bulk compressibility but cannot allow the distinction among different types of compressibility (volumetric, oedometric, etc). Anyway,

these data have been assumed comparable to the other available information (i.e., they are assumed as oedometric values) and plotted versus depth to provide the order of magnitude of the soil compressibility at shallow depths.

Due to the large uncertainty on the values of this fundamental parameter, we have preferred to perform the numerical simulations described below by using three basin-scale C_b vs z constitutive relationships obtained by regressing the data with straight-lines in the double log-log plot. The regression passing through the barycentre of the data provides the expected law, i.e., the relationship characterized by the highest probability to occur, the other two the upper and the lower limit of the range of variability of the parameter.

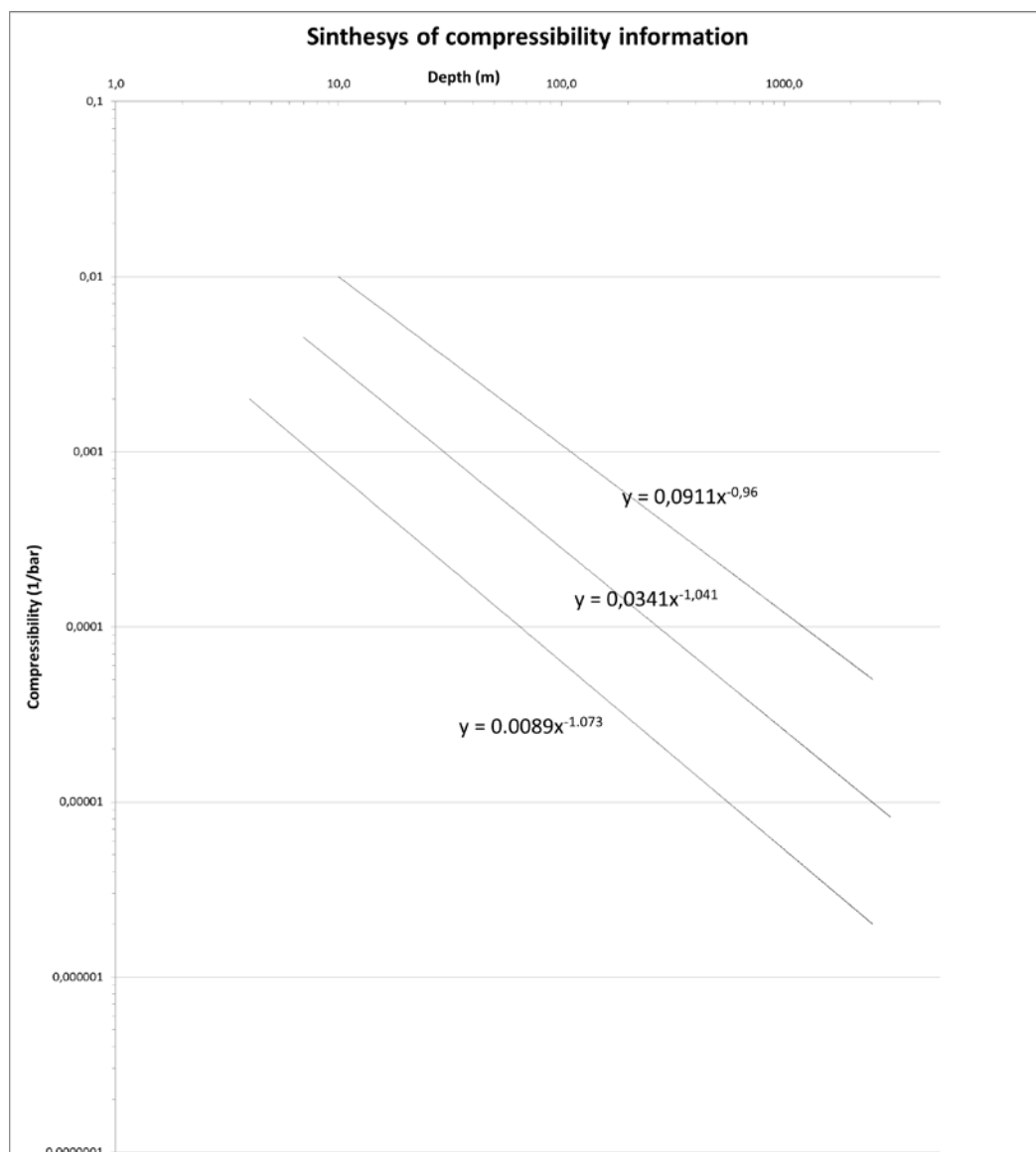


Figure 71: Log-log graphic of the whole compressibility dataset.

Eq. 95 - Eq. 97 provide the explicit form of the three equations obtained through data integrations described above.

$C_b = 0.0911z^{-0.96}$ Highest C_b /depth trend

Eq. 95

$C_b = 0.0341z^{-1.041}$ Mean/expected C_b /depth trend

Eq. 96

$C_b = 0.0089z^{-1.073}$ Lowest C_b /depth trend

Eq. 97

To apply the theory developed by Gambolati et al. (1997) we need, however, the relation between C_b and the effective intergranular stress σ_z . The basin can be preliminary assumed normally consolidated and normally pressured at least down to the depth of interest for the present study.

Therefore the pore pressure p is assumed to vary hydrostatically with z :

$p = \gamma_w \cdot z$

Eq. 98

where γ_w is the specific weight of water. The oedometer compressibility C_b is defined as:

$$c_b = -\frac{1}{1+e} \frac{de}{d\sigma_z}$$

Eq. 99

where $e = n/(1-n)$ is the void ratio and n is the medium porosity. The total stress s_t in a column with length z is given by the integral:

$$\sigma_z = \int_0^z [n\gamma_w + (1-n)\gamma_s] dz$$

Eq. 100

where γ_s is the specific weight of grains which are assumed to be individually incompressible in the present analysis. Differentiating Eq. 98 and using Terzaghi's principle of effective intergranular stress:

$$d\sigma_z = d\sigma_z + p$$

Eq. 101

leads to:

$$d\sigma_z = d\sigma_z + \gamma_w dz$$

Eq. 102

where d stands for infinitesimal increment. Differentiation of Eq. 100 yields:

$$d\sigma_z = [\gamma_s + n(\gamma_w - \gamma_s)] dz$$

Eq. 103

Combining Eq. 102 and Eq. 103 provides:

$$d\sigma_z = \frac{1}{1+e} (\gamma_s - \gamma_w) dz$$

Eq. 104

Replacing Eq. 104 into Eq. 99 gives the relationship between C_b and the soil depth z :

$$C_b = - \frac{1}{\gamma_s - \gamma_w} \frac{de}{dz}$$

Eq. 105

Equating Eq. 95, Eq. 96 and Eq. 97, written in the general form as $C_b = a z^b$, with Eq. 105 leads to:

$$az^b = -\frac{1}{\gamma_s - \gamma_w} \frac{de}{dz}$$

Eq. 106

Integration of Eq. 106 between z_0 and z (with $z > z_0$) provides the constitutive equation of e (and hence n) vs. z :

$$e = e_0 - \frac{a}{b+1} (\gamma_s - \gamma_w) (z^{b+1} - z_0^{b+1})$$

Eq. 107

The values of the parameters a and b are provided by Eq. 95, Eq. 96 and Eq. 97 for high, medium and low trends, respectively.

To activate Eq. 107 an initial e_0 -value corresponding to an arbitrary depth z_0 is needed. Typically z_0 should be related to a shallow sample in the range 10-50 m (for a smaller z_0 the sediments are very young, were deposited during historical or pre-historical times and might have been remoulded recently). From the extensive analysis of shallow soils analysed in O&G companies reports listed above, we take as representative data those presented in Table 6.

Table 6: Mean values of e_0 vs. z_0 founded in geotechnical reports and values assumed during the model application for $z_0=20$ m.

z_0	e_0	n_0
10	0.399429	0.665081
15	0.373143	0.59526
20	0.349714	0.537786
25	0.339429	0.513841
29	0.336143	0.506348

According to the e_0 selection of Table 6, Eq. 107 provides the porosity-depth profiles, and considering three compressional trends results are given for each well (Figure 72, Figure 73, Figure 74, Figure 75 and Figure 76). For the ensuing calculations we take the average curve which correspond to $n_0=0.538$ at $z_0=20$ m (Table 6).

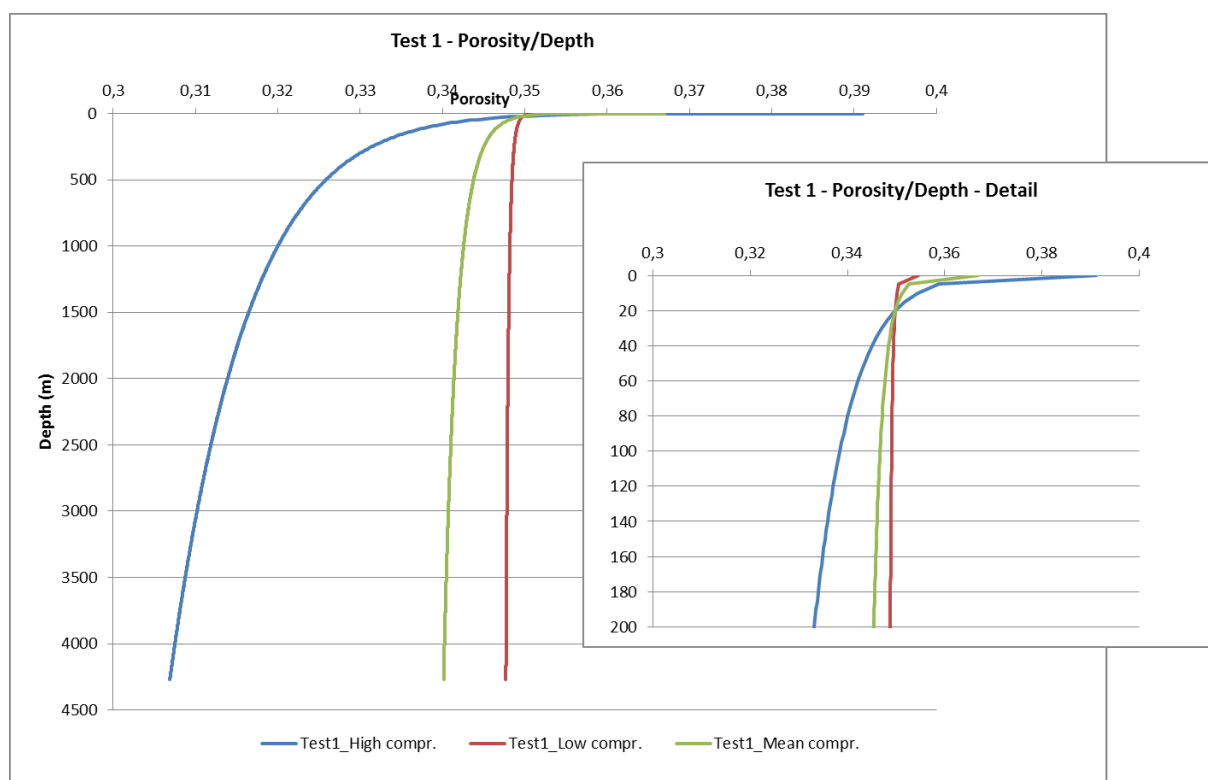


Figure 72: Porosity n vs. depth z at Test 1 well, for different compressional trends.

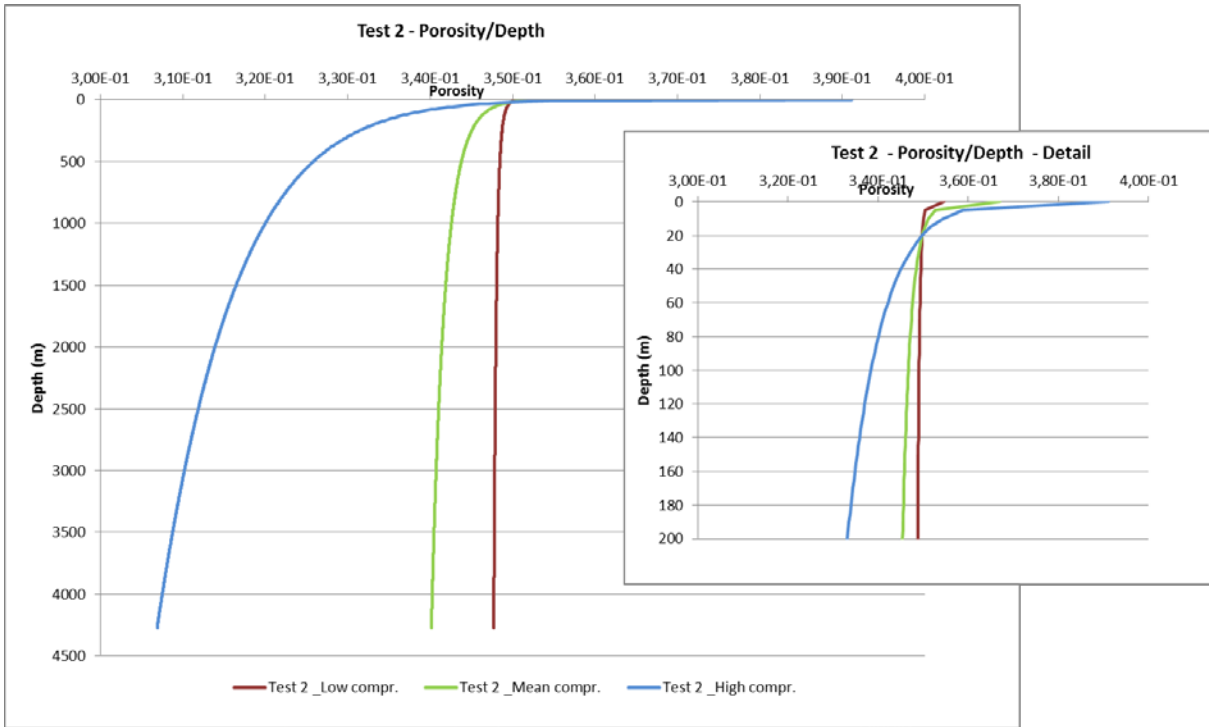


Figure 73: Porosity n vs. depth z at Test 2 well, for different compressional trends.

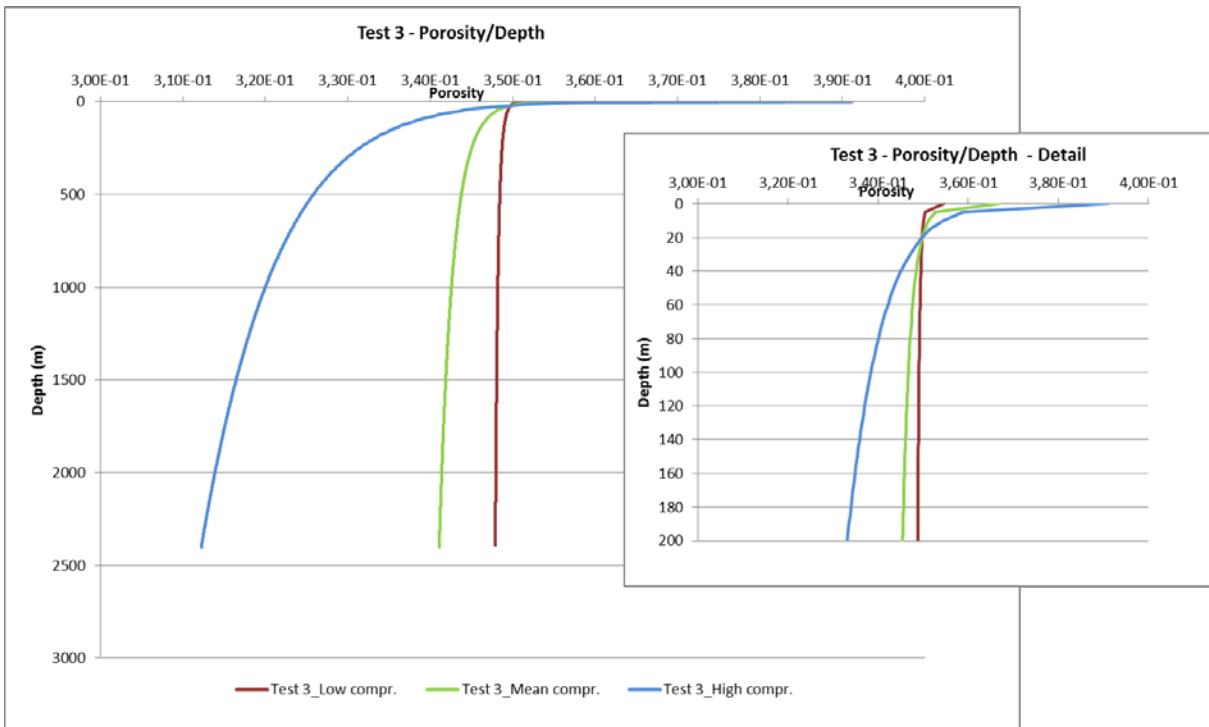


Figure 74: Porosity n vs. depth z at Test 3 well, for different compressional trends.

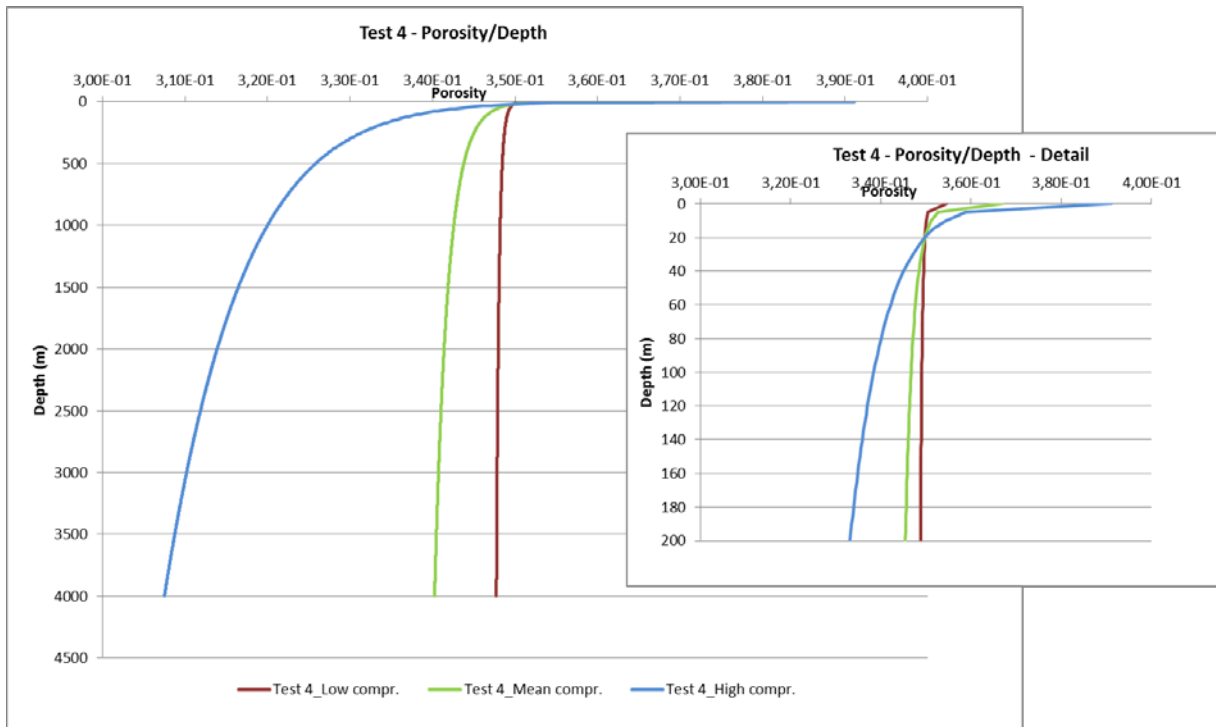


Figure 75: Porosity n vs. depth z at Test 4 well, for different compressional trends.

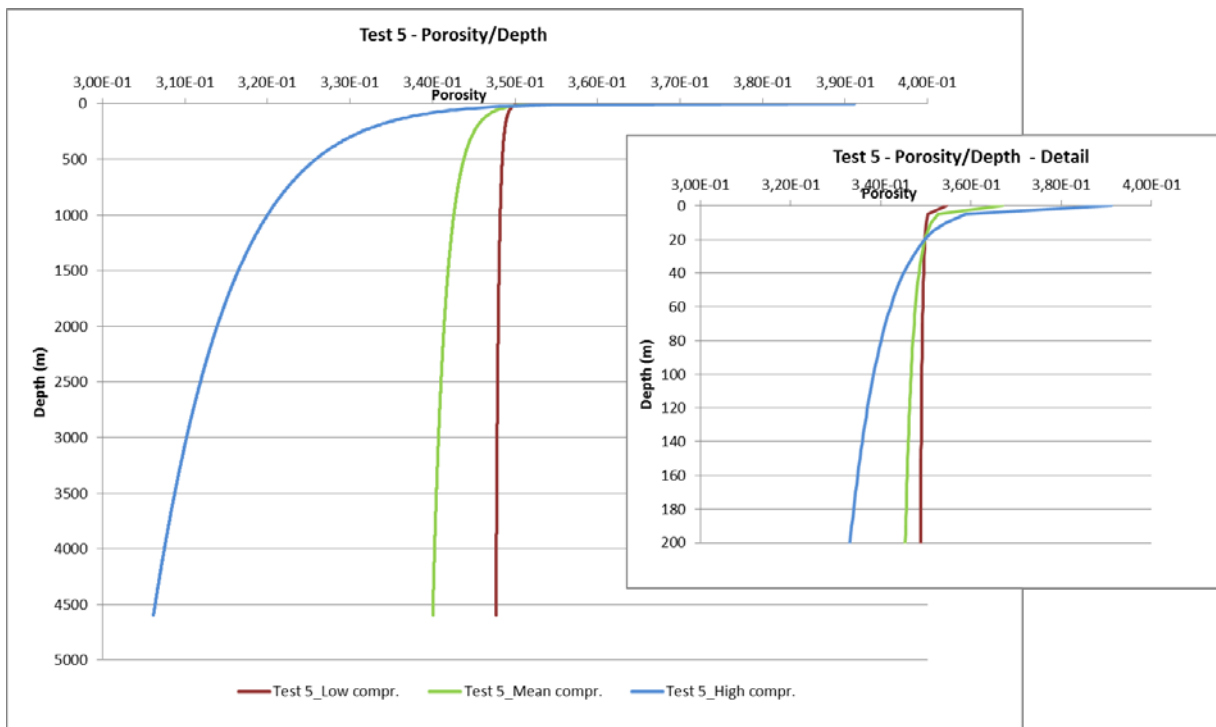


Figure 76: Porosity n vs. depth z at Test 5 well, for different compressional trends.

As is shown by Gambolati et al. (1997) the shortening $u(z^*, t)$ of a soil column, whose height is z^* (measured from the column bottom) at time t , is calculated by the integral:

$$u(z^*, t) = - \int_0^{z^*} \frac{\alpha \sigma_z(z, t)}{1 - \alpha \sigma_z(z, t)} dz$$

Eq. 108

where α is the classical soil compressibility and is related to C_b by Eq. 109:

$$c_b = \frac{(\sigma_z - \sigma_{z0}) \frac{d\alpha}{d\sigma_z} + \alpha}{1 - \alpha(\sigma_z - \sigma_{z0})}$$

Eq. 109

with σ_{z0} the initial effective stress, i.e. the effective stress at the initial conditions prior to the inception of the deformation. If we consider the deformation of an accreting column whose initial length is zero, we set $\sigma_{z0}=0$.

Eq. 109 can be rewritten as:

$$(\sigma_z - \sigma_{z0}) \frac{d\alpha}{d\sigma_z} + [1 + (\sigma_z - \sigma_{z0})c_b]\alpha - c_b = 0$$

Eq. 110

From the known relationships of C_b , σ_t and σ_z vs z we can compute C_b vs σ_z , and consequently Eq. 110 can be numerically integrated to yield $\alpha=\alpha(\sigma_z)$ for any initial σ_{z0} -value subject to the condition $\alpha(\sigma_{z0})=b(\sigma_{z0})$ (see Gambolati, 1973b).

The above soil constitutive model is also useful to assess the sedimentary rate occurred during the time interval T if we know the present thickness of the sediments laid down during the time T . Denote by Δz_0 the initial (unconsolidated) height of a soil column whose present length is Δz . Let e_0 and e be the corresponding void ratios. Since the grains are assumed to be incompressible, we can write the equation:

$$\frac{\Delta z_0}{1 + e_0} = \frac{\Delta z}{1 + e} = \frac{\Delta z_0 + \delta(\Delta z_0)}{1 + e}$$

Eq. 111

namely:

$$\frac{\delta(\Delta z_0)}{\Delta z_0} = \frac{e - e_0}{1 + e_0}$$

Eq. 112

Replacing $\delta(\Delta z_0) = \Delta z - \Delta z_0$ into Eq. 112 yields:

$$\Delta z_0 = \frac{1 + e_0}{1 + e} \Delta z$$

Eq. 113

Eq. 113 is the initial thickness of an elementary soil layer which has the present length Δz . If the layer exhibits a finite thickness from the depth z_1 down to z_2 , Eq. 113 must be replaced by the integral:

$$b_i = (1 + e_0) \int_{z_1}^{z_2} \frac{dz}{1 + e}$$

Eq. 114

where b_i is the layer initial thickness and e is supplied by Eq. 107. Eq. 107 and Eq. 114 are the basis for the estimate of the uncompacted thickness of the various layers composing the Precaspian basin and deposited during recognized time intervals. Each uncompacted thickness allows for the calculation of the related average depositional rate.

After defining the constitutive models for the stratigraphic column, we estimate the average sedimentation rates ω for the whole sedimentary column at five defined locations.

Detailed information about stratigraphy and chronostratigraphy comes from sonic logs and related end of well reports of wells drilled in the study area. The depth of investigation changes from one well to another: Table 7 shows the investigation depth for each well.

Table 7: Depth of available sonic logs.

Well	Depth (top, m)	Depth (bottom, m)
Test 1	71	4.267
Test 2	70	3.850
Test 3	100	2.300.9
Test 4	1014	5137.3
Test 5	852	4.580

The average sedimentation rates ω have been assessed by dividing the unconsolidated sediment thickness by the respective depositional time. The unconsolidated thickness b_i of the sedimentary layer located from depth z_1 down to z_2 is computed by Eq. 114 with e given by Eq. 107. Table 7, Table 8, table 9, Table 10 and Table 11 show the results of such a calculation for the layering sequence of the available wells.

Information is extrapolated from detailed strip logs; every layer's thickness is calculated by using TDVss values, rectified with values of rotary table elevation and depth of sea bed. Values are rounded off for model's requirement.

Note the low variation between consolidated and unconsolidated thickness indicating the low compressibility of the Precaspian basin's sediments, as highlighted during the calculation or rock compressibility (Table 13).

Table 8: Present thickness of the layering sequence at Test 1 as compared to the uncompacted thickness b_i .

Age (m.y.)	From (formation)	To (formation)	Dt (m.y.)	Present Bottom Depth (m, TVDss)	Present Thickness (m, round off)	Uncompacted thickness (low compressibility)	Sedimentation rate (low compressibility)	Uncompacted thickness (mean compressibility)	Sedimentation rate (mean compressibility (m/y))	Uncompacted thickness (high compressibility)	Sedimentation rate (high compressibility)
1.5	Sea Bottom	Top Tertiary	1.5	-70	40	40.00851	2.67E-05	40.03626	2.67E-05	40.12704	2.68E-05
66.4	Top Tertiary	Top Upper Cretaceous	42.7	-169.7	100	100.1128	1.54E-06	100.4893	1.55E-06	101.8006	1.57E-06
97.5	Top Upper Cretaceous	Top Lower Cretaceous	31.1	-521.7	350	350.6824	1.13E-05	353.0242	1.14E-05	361.8079	1.16E-05
119	Top Lower Cretaceous	Top Neocomian	6	-1079.3	560	561.4162	2.61E-05	566.3739	2.63E-05	586.0357	2.73E-05
144	Top Neocomian	Top Upper Jurassic	25	-1473	400	401.1317	1.6E-05	405.1364	1.62E-05	421.5167	1.69E-05
163	Top Upper Jurassic	Top Middle Jurassic	19	-1646.5	170	170.5017	8.97E-06	172.2849	9.07E-06	179.6746	9.46E-06
183	Top Middle Jurassic	Top Aaelenian	20	-2069.7	430	431.3125	2.16E-05	435.9959	2.18E-05	455.6219	2.28E-05
187	Top Aaelenian	Top Lower Jurassic	4	-2381.4	310	310.9788	7.77E-05	314.4852	7.86E-05	329.351	8.23E-05
208	Top Lower Jurassic	Top Upper Triassic	21	-2705.8	320	320.9038	1.53E-05	324.1504	1.54E-05	338.0245	1.61E-05
258	Top Upper Triassic	Top Of Kungurian Evaporite	13	-2779.2	70	70.32689	1.41E-06	71.50298	1.43E-06	76.55233	1.53E-06
263	Top Of Kungurian	Top Artinskian	5	-3716.5	950	953.1986	0.000191	964.7502	0.000193	1014.912	0.000203
308	Top Artinskian	Top Lower Bashkirian	45	-3772.9	60	60.2069	1.34E-06	60.95648	1.35E-06	64.24199	1.43E-06
320	Top Lower Bashkirian	Top Serpukhovian	12	-3875.8	100	100.346	8.36E-06	101.6	8.47E-06	107.104	8.93E-06
333	Top Serpukhovian	Top Upper Viséan	13	-3927.5	50	50.17352	3.86E-06	50.80271	3.91E-06	53.56765	4.12E-06
340	Top Upper Viséan	Top Middle Viséan	7	-4227.6	300	301.0482	4.3E-05	304.8526	4.36E-05	321.6176	4.59E-05
346	Top Middle Viséan	Top Lower Viséan	6	-4248.8	20	20.0703	3.35E-06	20.32566	3.39E-06	21.45372	3.58E-06
352	Top Lower Viséan	Top Upper Tournaisian	6	-4267	20	20.07033	3.35E-06	20.32579	3.39E-06	21.45448	3.58E-06

Table 9: Present thickness of the layering sequence at Test 2 as compared to the uncompacted thickness b_i.

Age (m.y.)	From (formation)	To (formation)	Dt (m.y.)	Present Bottom Depth (m, TVDss)	Present Thickness (m, round off)	Uncompacted thickness (low compressibility)	Sedimentation rate (low compressibility)	Uncompacted thickness (mean compressibility)	Sedimentation rate (mean compressibility (m/y))	Uncompacted thickness (high compressibility)	Sedimentation rate (high compressibility)
23.7	Sea Bottom	Top Paleogene	23.7	5	10	10	4.22E-07	10	4.22E-07	10	4.22E-07
66.4	Top Paleogene	Top Upper Cretaceous	42.7	-95.2	60	70.03334	1.64E-06	70.14314	1.64E-06	70.51124	1.65E-06
97.5	Top Upper Cretaceous	Top Lower Cretaceous	31.1	-388.2	290	290.4875	9.34E-06	292.1467	9.39E-06	298.2283	9.59E-06
119	Top Lower Cretaceous	Top Neocomian	21.5	-890	500	501.1913	2.33E-05	505.3401	2.35E-05	521.5548	2.43E-05
144	Top Neocomian	Top Upper Jurassic	25	-1235.3	350	350.9512	1.4E-05	354.3034	1.42E-05	367.8528	1.47E-05
163	Top Upper Jurassic	Top Middle Jurassic	19	-1410.3	180	180.5138	9.5E-06	182.3336	9.6E-06	189.7959	9.99E-06
183	Top Middle Jurassic	Top Aaelenian	20	-1767.7	360	361.0667	1.81E-05	364.8601	1.82E-05	380.6011	1.9E-05
187	Top Aaelenian	Top Lower Jurassic	4	-1918.2	150	150.4576	3.76E-05	152.0902	3.8E-05	158.9297	3.97E-05
208	Top Lower Jurassic	Top Upper Triassic	21	-2138.3	220	220.6825	1.05E-05	223.1225	1.06E-05	233.4038	1.11E-05
258	Top Upper Triassic	Top Of Kungurian Evaporite	50	-2423.1	280	280.888	5.62E-06	284.0707	5.68E-06	297.5856	5.95E-06
263	Top Of Kungurian	Top Artinskian	5	-3721.8	1290	1294.3	0.000259	1309.808	0.000262	1376.897	0.000275
308	Top Artinskian	Top Lower Bashkirian	45	-3783.4	60	60.20682	1.34E-06	60.95604	1.35E-06	64.23941	1.43E-06
320	Top Lower Bashkirian	Top Serpukhovian	12	-3850	70	70.24194	5.85E-06	71.11874	5.93E-06	74.96541	6.25E-06

Table 10: Present thickness of the layering sequence at Test 3 as compared to the uncompacted thickness b_i .

Age (m.y.)	From (formation)	To (formation)	Dt (m.y.)	Present Bottom Depth (m, TVDss)	Present Thickness (m, round off)	Uncompacted thickness (low compressibility)	Sedimentation rate (low compressibility)	Uncompacted thickness (mean compressibility)	Sedimentation rate (mean compressibility (m/y))	Uncompacted thickness (high compressibility)	Sedimentation rate (high compressibility)
23.7	Sea Bottom	Top Paleogene	23.7	-100	100	100.067067	4.22E-06	100.289315	4.23E-06	101.047175	4.26E-06
36.6	Top Paleogene	Top Late Eocene	12.9	-155.5	60	60.0843007	4.66E-06	60.3680532	4.68E-06	61.3768379	4.76E-06
43.6	Top Late Eocene	Top Middle Eocene	7	-221.5	70	70.1172252	1E-05	70.5153774	1.01E-05	71.9661582	1.03E-05
66.4	Top Middle Eocene	Top Upper Cretaceous	22.8	-283.5	60	60.1118152	2.64E-06	60.4940413	2.65E-06	61.9116565	2.72E-06
97.5	Top Upper Cretaceous	Top Lower Cretaceous	31.1	-688.5	400	400.89888	1.29E-05	404.014362	1.3E-05	416.026077	1.34E-05
113	Top Lower Cretaceous	Top Aptian	15.5	-1035.9	350	350.913274	2.26E-05	354.119122	2.28E-05	366.931249	2.37E-05
119	Top Aptian	Top Neocomian	6	-1149.9	110	110.302923	1.84E-05	111.371841	1.86E-05	115.708193	1.93E-05
144	Top Neocomian	Top Upper Jurassic	25	-1343.9	190	190.53751	7.62E-06	192.439498	7.7E-06	200.217823	8.01E-06
163	Top Upper Jurassic	Top Middle Jurassic	19	-1554.5	210	210.612327	1.11E-05	212.786074	1.12E-05	221.759535	1.17E-05
169	Top Middle Jurassic	Top Bathonian	6	-1610.4	60	60.1780777	1E-05	60.811479	1.01E-05	63.4410466	1.06E-05
187	Top Aalenian	Top Lower Jurassic	18	-2140.9	530	531.623919	2.95E-05	537.421111	2.99E-05	561.746766	3.12E-05
208	Top Lower Jurassic	Top Upper Triassic	21	-2202.9	60	60.1889274	2.87E-06	60.8655263	2.9E-06	63.7312258	3.03E-06
274	Top Upper Triassic	Top Asselian	66	-2241.9	40	40.1264652	6.08E-07	40.5795919	6.15E-07	42.5015509	6.44E-07
305	Top Asselian	Top Bashkirian	31	-2300.9	60	60.1904487	1.94E-06	60.8731546	1.96E-06	63.7729611	2.06E-06

Table 11: Present thickness of the layering sequence at Test 4 as compared to the uncompacted thickness b_i .

Age (m.y.)	From (formation)	To (formation)	Dt (m.y.)	Present Bottom Depth (m, TVDss)	Present Thickness (m, round off)	Uncompacted thickness (low compressibility)	Sedimentation rate (low compressibility)	Uncompacted thickness (mean compressibility)	Sedimentation rate (mean compressibility (m/y))	Uncompacted thickness (high compressibility)	Sedimentation rate (high compressibility)
23.7	Sea Bottom	Top Paleogene	23.7	-18.2	20.0	20	8.43882E-07	20	8.43882E-07	20	8.43882E-07
66.4	Top Paleogene	Top Upper Cretaceous	42.7	-78	60.0	60.04378	1.40618E-06	60.18826	1.40956E-06	60.67571444	1.42098E-06
97.5	Top Upper Cretaceous	Top Lower Cretaceous	31.1	-484	410.0	410.7599	1.32077E-05	413.3615	1.32914E-05	423.0598703	1.36032E-05
113	Top Lower Cretaceous	Top Aptian	15.5	-838	350.0	350.8565	2.26359E-05	353.8454	2.28287E-05	365.5945432	2.35867E-05
119	Top Aptian	Top Neocomian	6	-1015	180.0	180.4781	3.00797E-05	182.1592	3.03599E-05	188.9089866	3.14848E-05
144	Top Neocomian	Top Upper Jurassic	25	-1385	370.0	371.039	1.48416E-05	374.7126	1.49885E-05	389.7039672	1.55882E-05
163	Top Upper Jurassic	Top Middle Jurassic	19	-1620	240.0	240.7059	1.26687E-05	243.2142	1.28007E-05	253.597242	1.33472E-05
183	Top Middle Jurassic	Top Aalenian	20	-2033	410.0	411.2515	2.05626E-05	415.7173	2.07859E-05	434.4313968	2.17216E-05
187	Top Aalenian	Top Lower Jurassic	4	-2322	290.0	290.9142	7.27285E-05	294.1884	7.35471E-05	308.0621378	7.70155E-05
208	Top Lower Jurassic	Top Upper Triassic	21	-2480	160.0	160.5132	7.64349E-06	162.3553	7.73121E-06	170.2092584	8.1052E-06
245	Top Upper Triassic	Permian-Triassic	37	-2560	80.0	80.25879	2.16916E-06	81.18862	2.19429E-06	85.16526667	2.30176E-06
258	Permian-Triassic	Top Of Kungurian Evaporite	13	-2900	340.0	341.1148	2.62396E-05	345.1271	2.65482E-05	362.3730897	2.78749E-05
263	Top Of Kungurian	Top Artinskian	5	-3953.3	1050.0	1053.571	0.000210714	1066.486	0.000213297	1122.792306	0.000224558
308	Top Artinskian	Top Lower Bashkirian	45	-4029	80.0	80.2789	1.78398E-06	81.29079	1.80646E-06	85.7457686	1.90546E-06
320	Top Lower Bashkirian	Top Serpukhovian	12	-4134.4	110.0	110.3849	9.19874E-06	111.782	9.31516E-06	117.9420133	9.8285E-06
333	Top Serpukhovian	Top Upper Viséan	13	-4167.3	30.0	30.10524	2.31579E-06	30.4874	2.34518E-06	32.1742213	2.47494E-06
340	Top Upper Viséan	Top Middle Viséan	7	-4450.8	280.0	280.9877	4.01411E-05	284.5772	4.06539E-05	300.4574099	4.29225E-05
346	Top Middle Viséan	Top Lower Viséan	6	-4549.3	100.0	100.3551	1.67258E-05	101.6466	1.69411E-05	107.3762342	1.7896E-05
352	Top Lower Viséan	Top Upper Tournaisan	6	-4609.8	60.0	60.21361	1.00356E-05	60.99088	1.01651E-05	64.44289399	1.07405E-05
360	Top Upper Tournaisan	Top Devonian	8	-4832.3	220.0	220.7868	2.75983E-05	223.6514	2.79564E-05	236.3979169	2.95497E-05
374	Top Devonian	Middle/Late Devonian	14	-5137.3	300.0	311.1176	2.22227E-05	315.1915	2.25137E-05	333.3817	2.3813E-05

Table 12: Present thickness of the layering sequence at Test 5 as compared to the uncompacted thickness b_i .

Age (m.y.)	From (formation)	To (formation)	Dt (m.y.)	Present Bottom Depth (m, TVDss)	Present Thickness (m, round off)	Uncompacted thickness (low compressibility)	Sedimentation rate (low compressibility)	Uncompacted thickness (mean compressibility)	Sedimentation rate (mean compressibility (m/y))	Uncompacted thickness (high compressibility)	Sedimentation rate (high compressibility)
66.4	Sea Bottom	Top Upper Cretaceous	66.4	-104	100	100.0671	2.3435E-06	100.2893	2.3487E-06	101.0472	2.3664E-06
97.5	Top Upper Cretaceous	Top Lower Cretaceous	31.1	-550	450	450.8748	1.4498E-05	453.8784	1.4594E-05	465.1637	1.4957E-05
113	Top Lower Cretaceous	Top Aptian	15.5	-920	370	370.9282	2.3931E-05	374.1746	2.414E-05	387.0162	2.4969E-05
119	Top Aptian	Top Neocomian	6	-1116	200	200.5422	3.3424E-05	202.4525	3.3742E-05	210.1676	3.5028E-05
144	Top Neocomian	Top Upper Jurassic	25	-1525.9	410	411.174	1.6447E-05	415.3338	1.6613E-05	432.4108	1.7296E-05
163	Top Upper Jurassic	Top Middle Jurassic	19	-1774.9	250	250.7485	1.3197E-05	253.4136	1.3338E-05	264.5096	1.3922E-05
183	Top Middle Jurassic	Top Aaelenian	20	-2071.8	300	300.9246	1.5046E-05	304.2273	1.5211E-05	318.1122	1.5906E-05
187	Top Aaelenian	Top Lower Jurassic	4	-2442.9	370	371.1737	9.2793E-05	375.381	9.3845E-05	393.2482	9.8312E-05
258	Top Lower Jurassic	Top Of Kungurian Evaporite	71	-2514.8	70	70.22574	9.8909E-07	71.03651	1.0005E-06	74.50005	1.0493E-06
263	Top Of Kungurian	Top Artinskian	5	-3943.9	1430	1434.813	0.00028696	1452.196	0.00029044	1527.682	0.00030554
308	Top Artinskian	Top Lower Bashkirian	45	-4010.7	60	60.20901	1.338E-06	60.96726	1.3548E-06	64.30449	1.429E-06
320	Top Lower Bashkirian	Top Serpukhovian	12	-4088.5	80	80.27943	6.69E-06	81.29354	6.7745E-06	85.76178	7.1468E-06
333	Top Serpukhovian	Top Upper Viséan	13	-4138.3	50	50.17508	3.8596E-06	50.81067	3.9085E-06	53.61395	4.1242E-06
340	Top Upper Viséan	Top Middle Viséan	7	-4426.5	290	291.0217	4.1575E-05	294.7341	4.2105E-05	311.1498	4.445E-05
346	Top Middle Viséan	Top Lower Viséan	6	-4435.5	10	10.03542	1.6726E-06	10.1642	1.694E-06	10.73491	1.7892E-06
352	Top Lower Viséan	Top Upper Tournaisian	6	-4580.8	140	140.4971	2.3416E-05	142.3053	2.3718E-05	150.3267	2.5054E-05

Table 13: Comparison between present total thicknesses and uncompacted ones.

Well	Present thickness (m)	Uncompacted thickness (low compressibility) (m) and variation (%)		Uncompacted thickness (mean compressibility) (m) and variation (%)		Uncompacted thickness (high compressibility) (m) and variation (%)	
Test 1	4250	4262.489	+0.3	4307.093	1.4	4494.863	+5.7
Test 2	3820	3841.02	+0.6	3880.293	+1.6	4044.565	+5.9
Test 3	2300	2305.95316	+0.3	2326.94855	+1.2	2412.13826	+4.9
Test 4	5140.0	5165.737	+0.5	5222.162	+1,6	5462.492	+6.3
Test 5	4580	4593.69	+0.3	4642.658	+1.4	4849.749	+5.9

Using the finite element model developed by Gambolati et al. (1997) and the data shown above, the evolution of a representative sedimentary column has been predicted at the five selected locations in the offshore portion of the study area. The first step of simulations depends on the elder strata drilled and the last is completed in 3000 AD. Model application foresees no sedimentation during future projection. In following graphics, time zero is referred to the first step of simulation and the last the future projection.

Time value assigned for future projection follows the concept of the “geologic time scale” and not the “life cycle time scale”; notwithstanding, simulated geomechanical characteristics permit to highlight that any significant rock/sediment compaction will happen in the future.

As illustrated, the model has been applied in correspondence to wells considered. Consistent with the available information, the model has been run so as to reproduce along the compacting column negligible pore pressure in excess of the hydrostatic value. This has allowed for the estimate of representative hydraulic conductivities k_z which have turned out to be quite similar in the four locations.

In order to test the influence of hydraulic conductivity within the numerical simulation, a sensitivity analysis has been done for well Test 1 (higher compressibility trend). Simulations shown that for obtain by means of the model the measured thickness of the sedimentary column the appropriate value of K is 10^{-10} m/s. However, sensitivity analysis showed that numerical simulations’ results are not strongly affected by variation of hydraulic conductivity.

Output results are shown through specific sheet, structured as illustrated below (Table 14).

Table 14: Results sheet description.

<i>Field 1: NAME WELL</i>		
<i>Field 2: Sedimentation rate (Sed.rate) and settling velocity (Bott.vel.) vs. geological time (High trend)</i>	<i>Field 3: Sedimentation rate (Sed.rate) and settling velocity (Bott.vel.) vs. geological time (Mean trend)</i>	<i>Field 4: Sedimentation rate (Sed.rate) and settling velocity (Bott.vel.) vs. geological time (Low trend)</i>
<i>Field 5: Sedimentary column depths comparison, at selected time steps (high, mean and low trends)</i>	<i>Field 6: Sedimentary column compaction vs. time (high, mean and low trends)</i>	
	<i>Field 7: Pore pressure vs. depth (high, mean and low trends)</i>	<i>Field 8: Pore pressure vs. time (high, mean and low trends)</i>

NATSUB RESULTS FOR WELL TEST 1

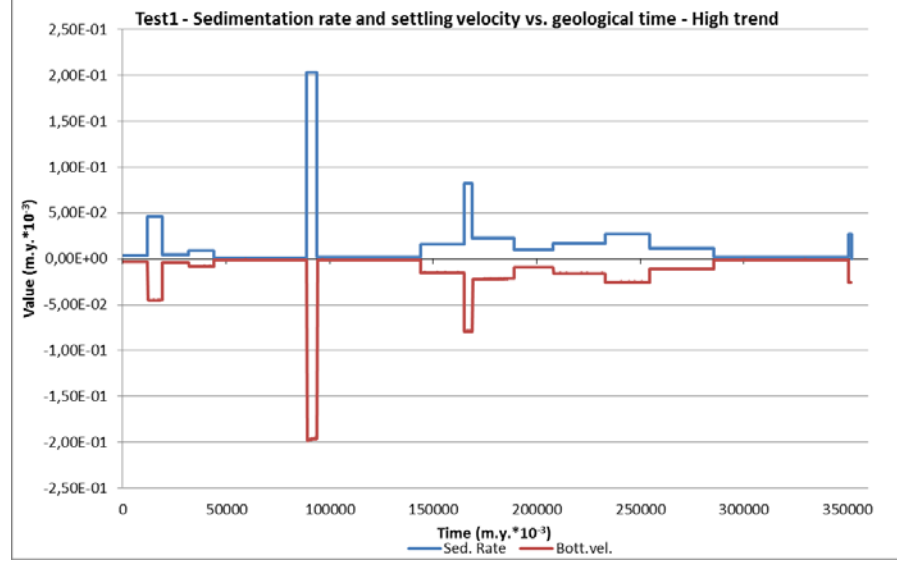


Figure 77: Sedimentation rate (Sed.rate) and settling velocity (Bott.vel.) vs. geological time (high trend).

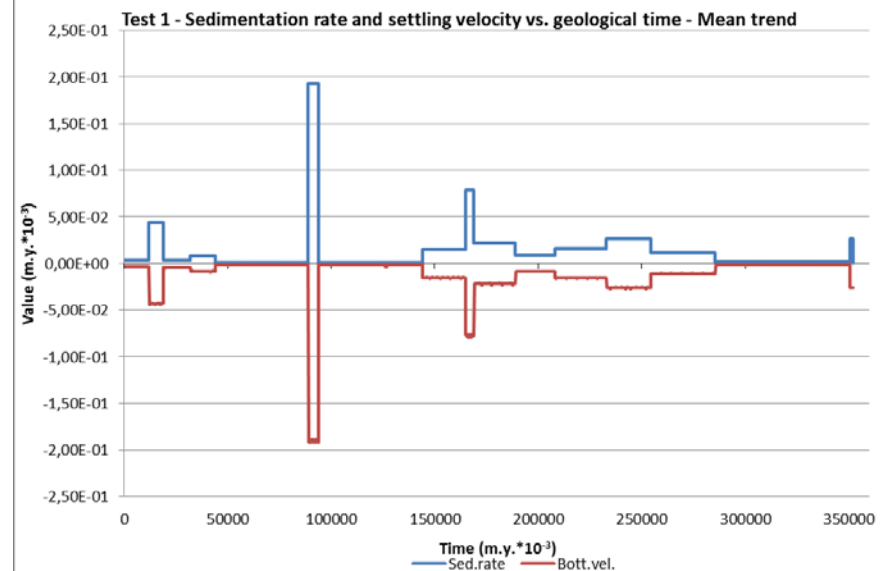


Figure 78: Sedimentation rate (Sed.rate) and settling velocity (Bott.vel.) vs. geological time (mean trend).

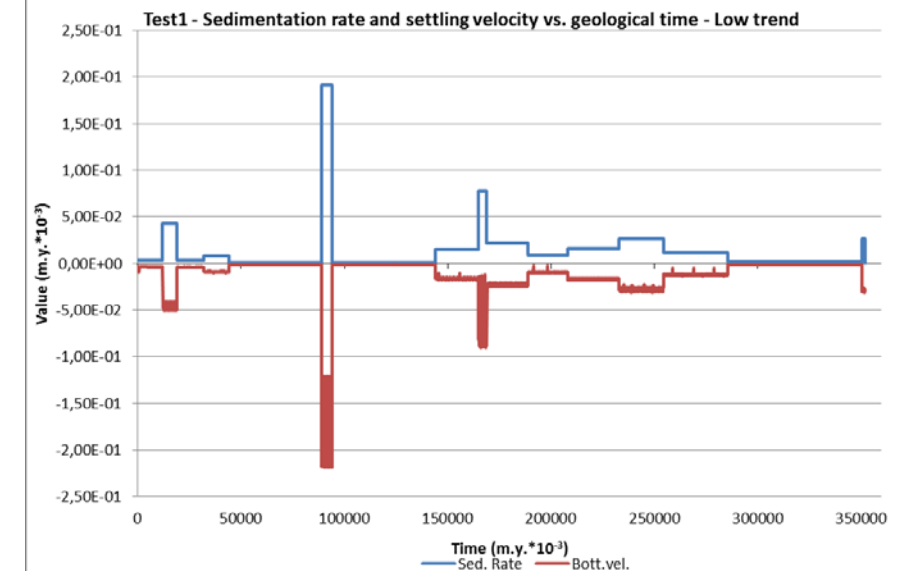


Figure 79: Sedimentation rate (Sed.rate) and settling velocity (Bott.vel.) vs. geological time (low trend)

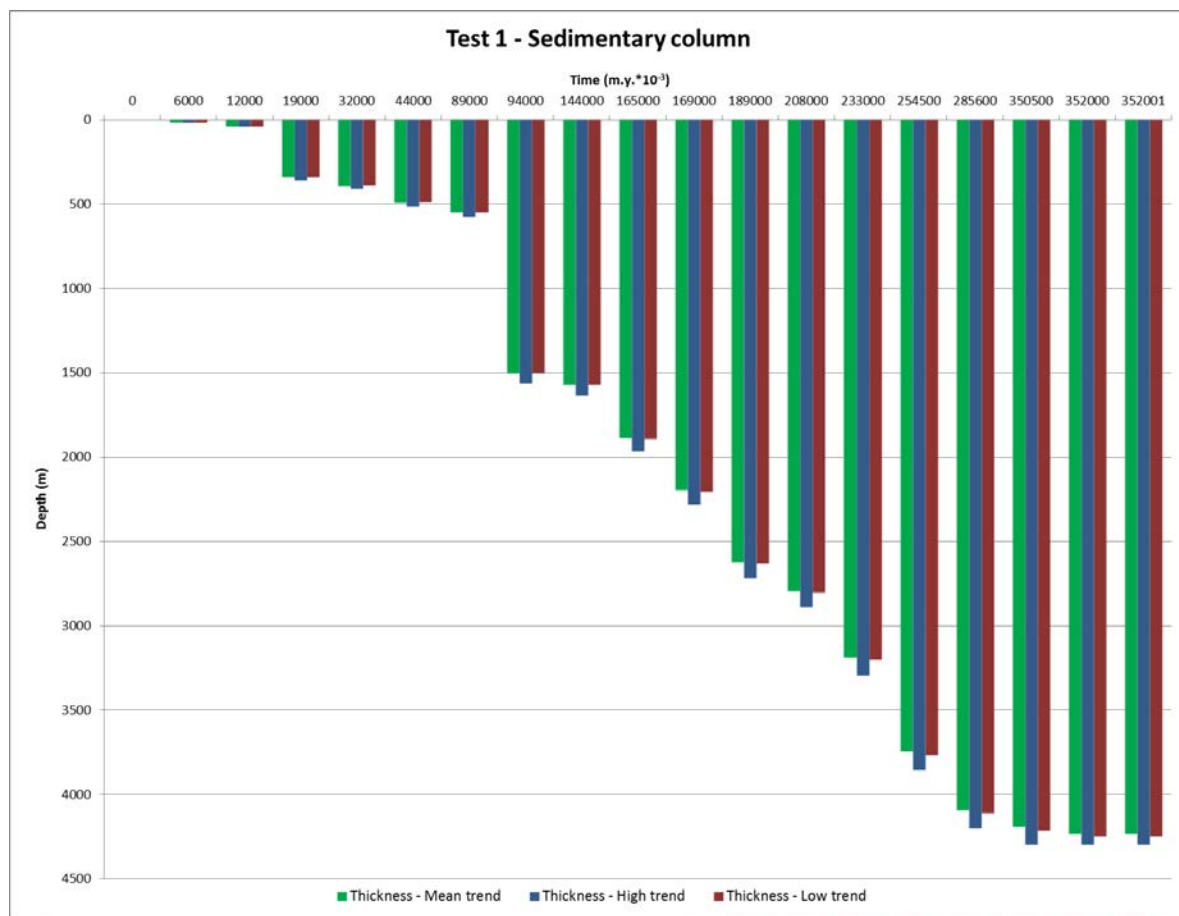


Figure 80: AK1 Sedimentary column depths comparison, at selected time steps (high, mean and low trends).

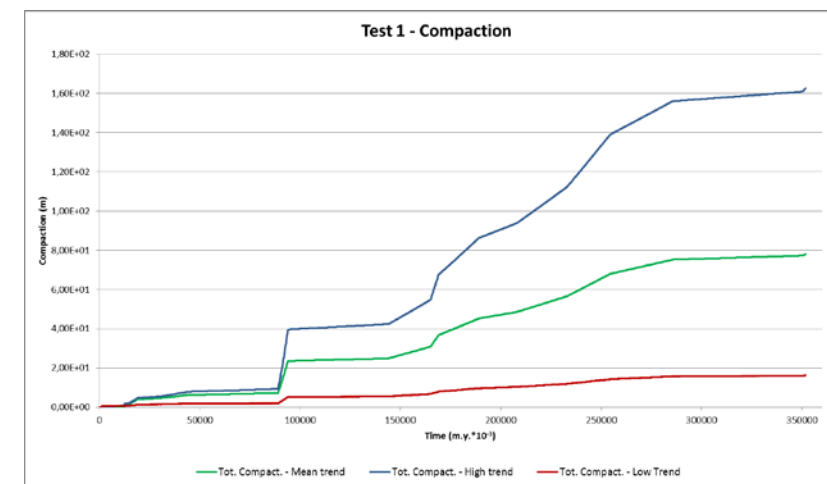


Figure 81: Sedimentary column compaction vs. time.

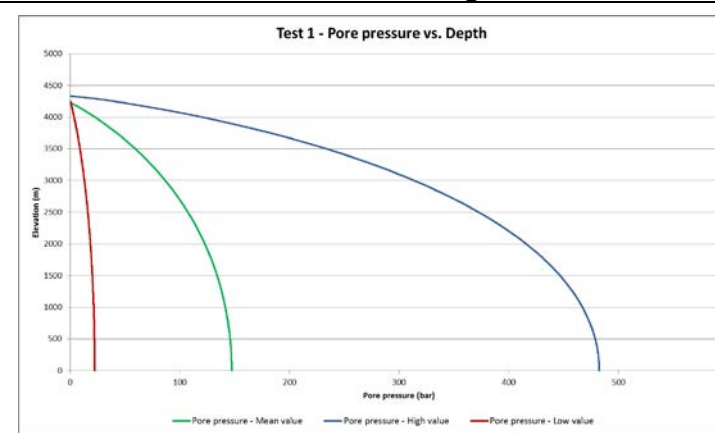


Figure 82: Pore pressure vs. depth.

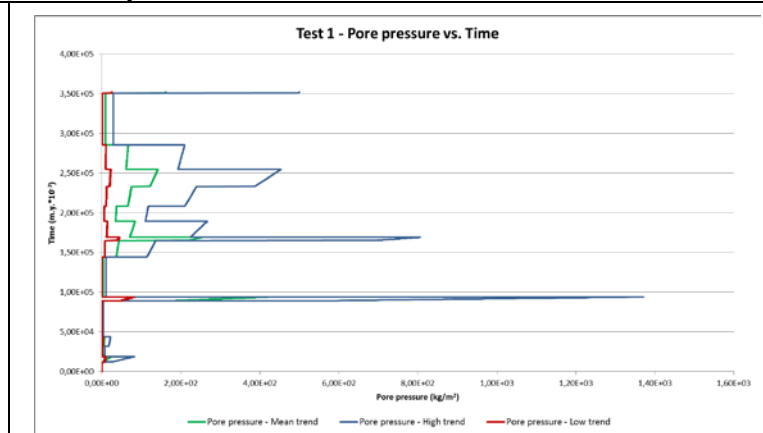


Figure 83: Pore pressure vs. time.

NATSUB RESULTS FOR WELL TEST 2

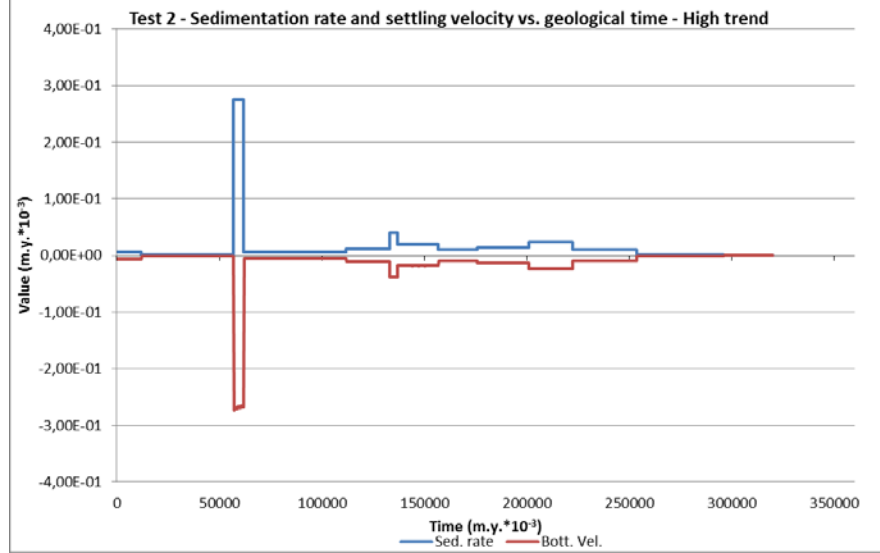


Figure 84: Sedimentation rate (Sed. rate) and settling velocity (Bott.vel.) vs. geological time (high trend).

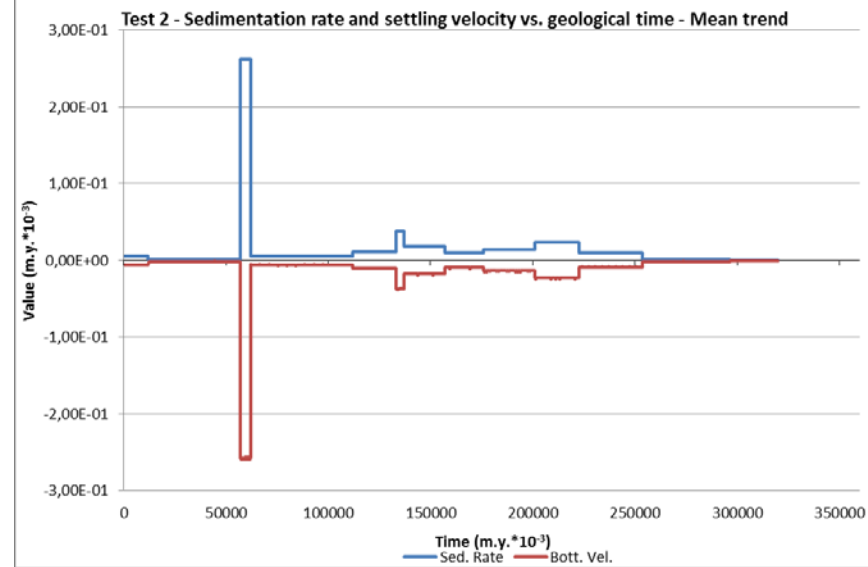


Figure 85: Sedimentation rate (Sed. rate) and settling velocity (Bott.vel.) vs. geological time (mean trend).

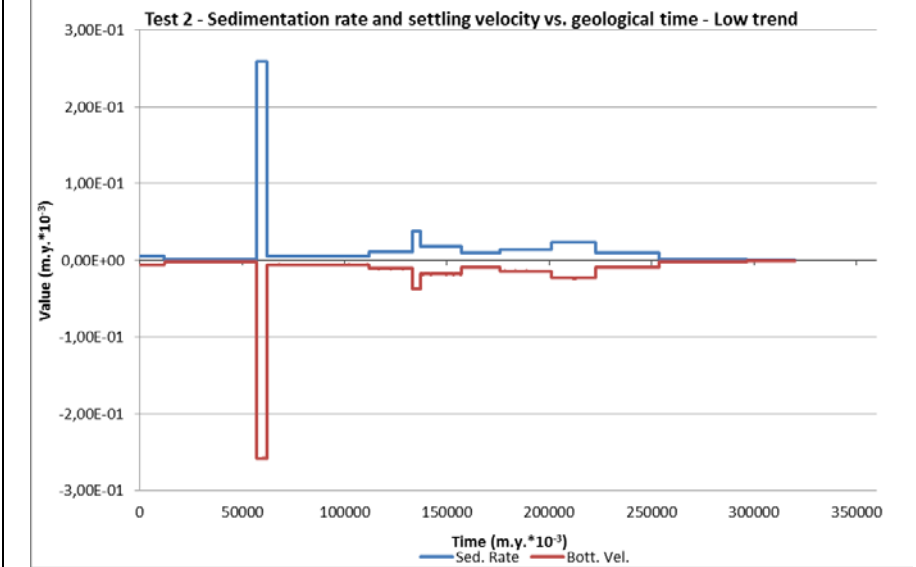


Figure 86: Sedimentation rate (Sed. rate) and settling velocity (Bott.vel.) vs. geological time (low trend).

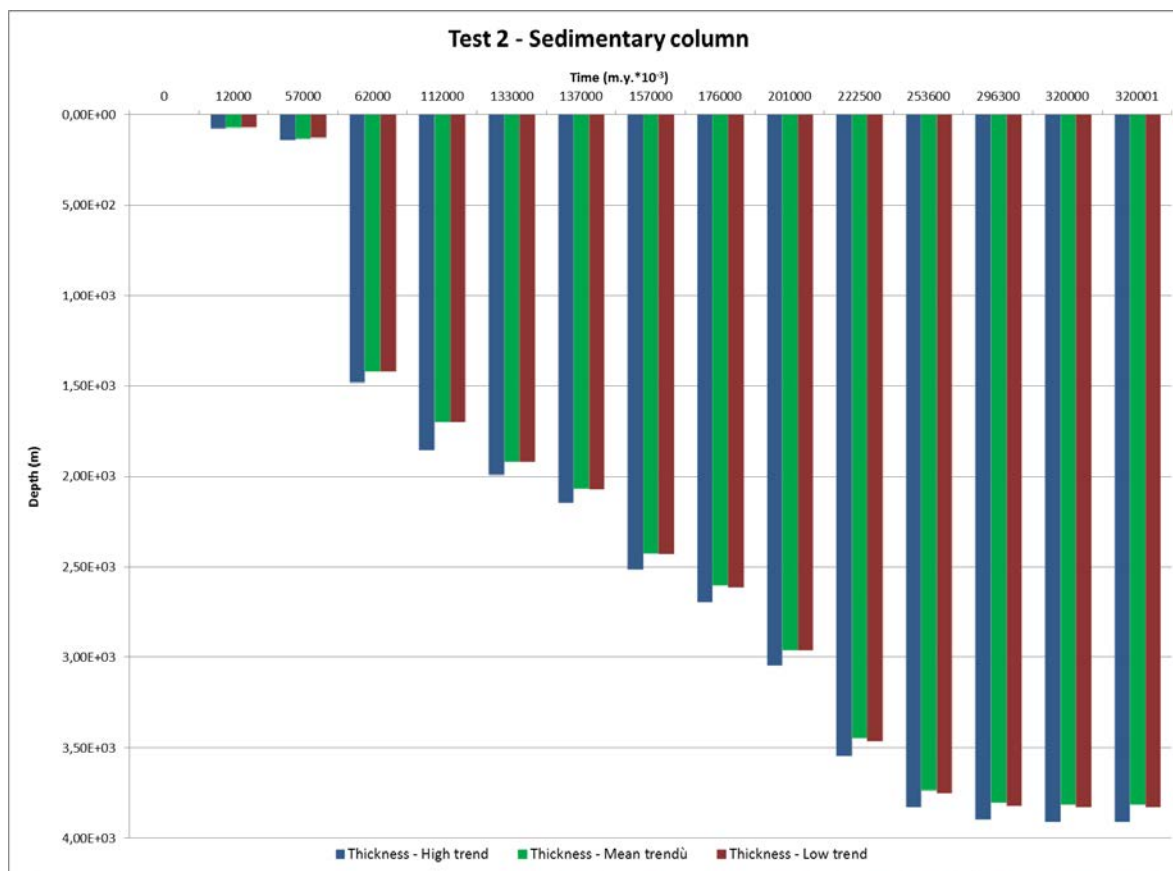


Figure 87: Sedimentary column depths comparison, at selected time steps.

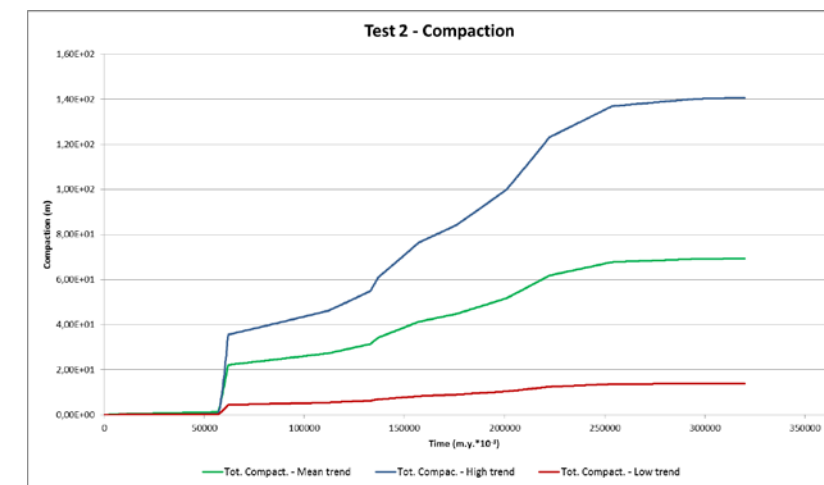


Figure 88: Sedimentary column compaction vs. time.

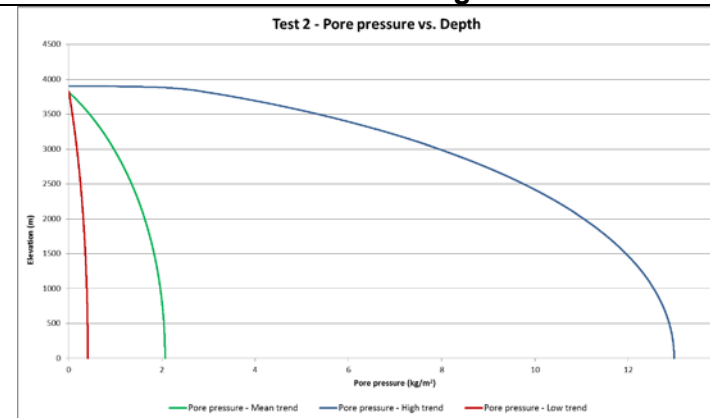


Figure 89: Pore pressure vs. depth.

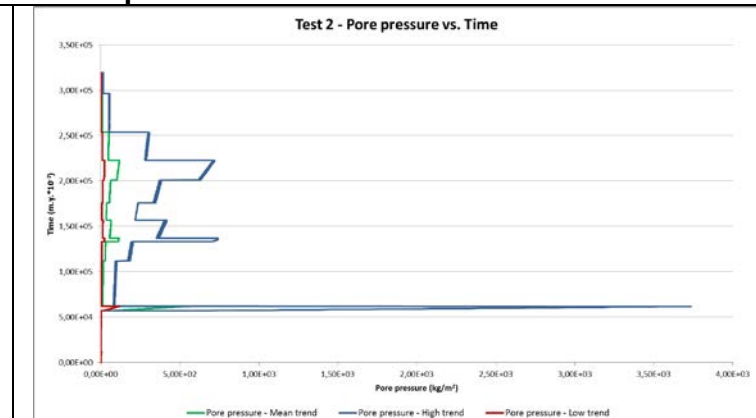


Figure 90: Pore pressure vs. time

NATSUB RESULTS FOR WELL TEST 3

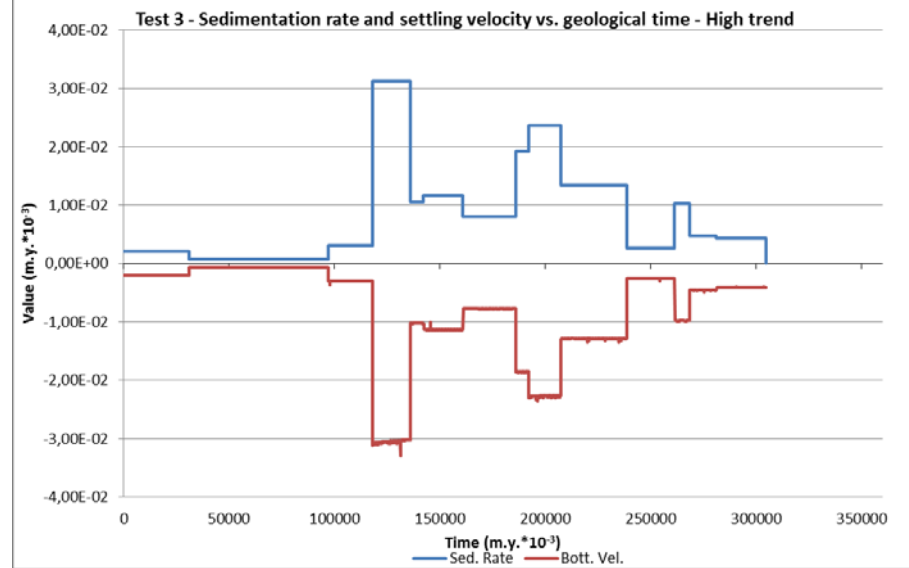


Figure 91: Sedimentation rate (Sed.rate) and settling velocity (Bott.vel.) vs. geological time (high trend).

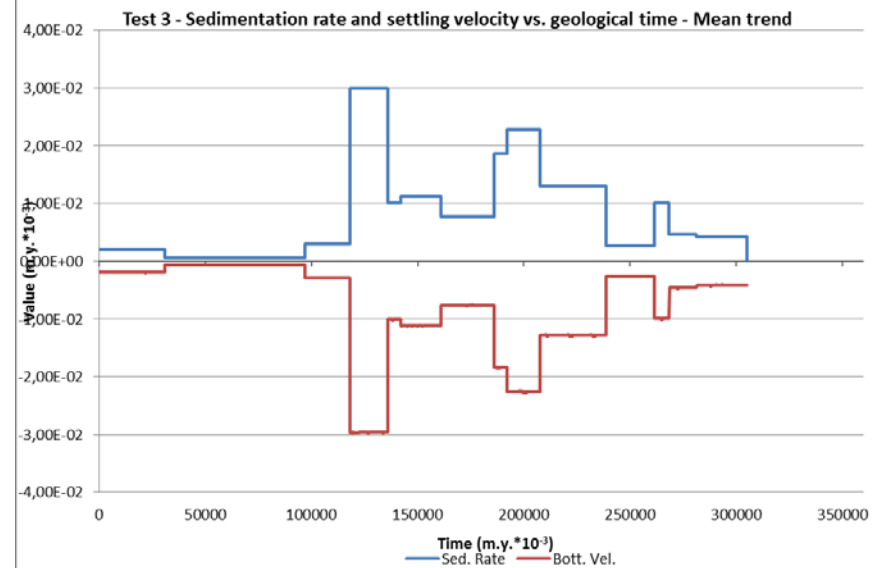


Figure 92: Sedimentation rate (Sed.rate) and settling velocity (Bott.vel.) vs. geological time (mean trend).

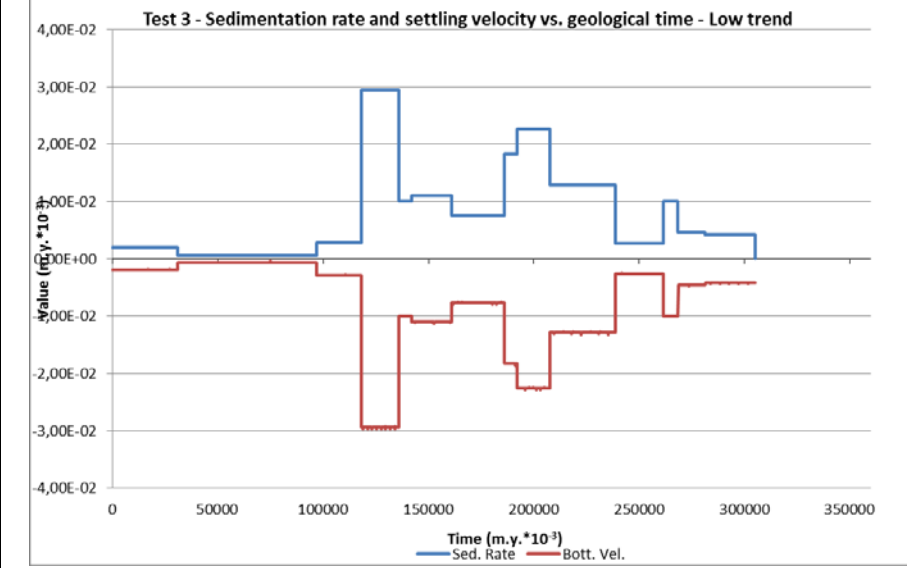


Figure 93: Sedimentation rate (Sed.rate) and settling velocity (Bott.vel.) vs. geological time (low trend).

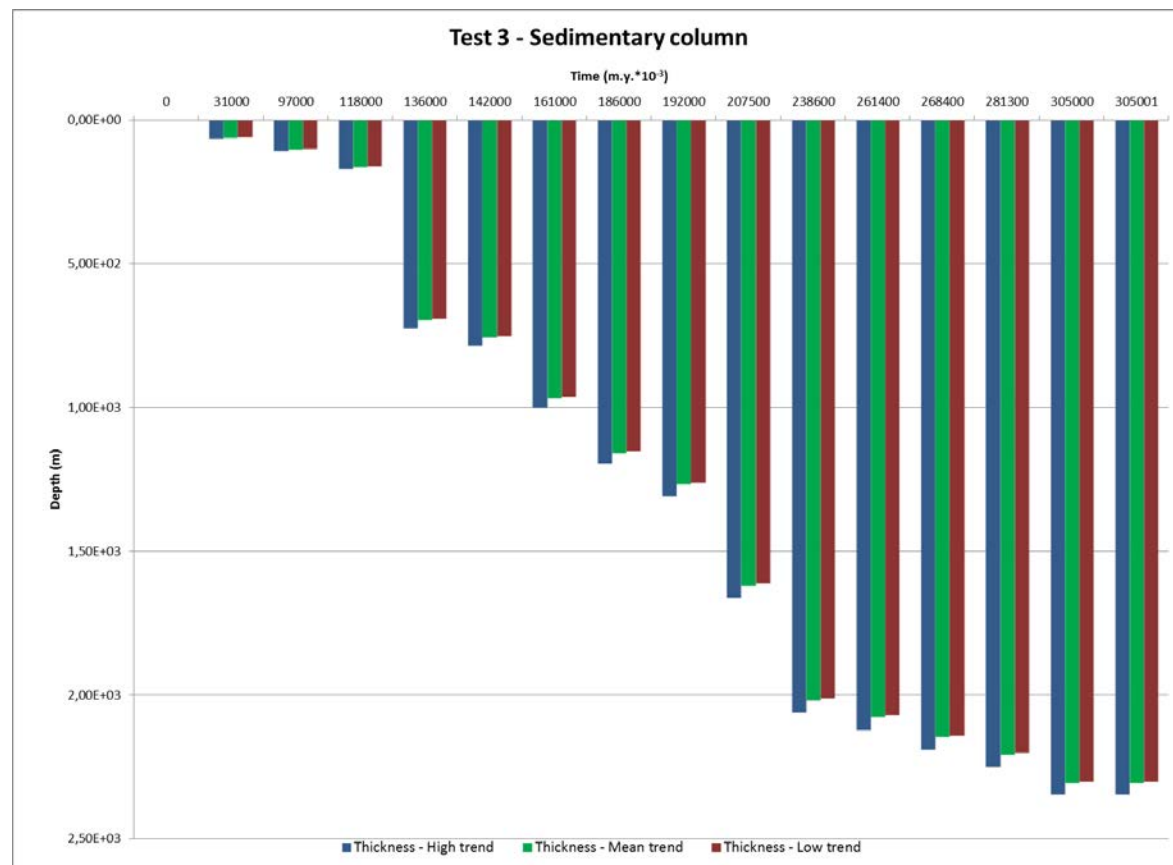


Figure 94: Sedimentary column depths comparison, at selected time steps.

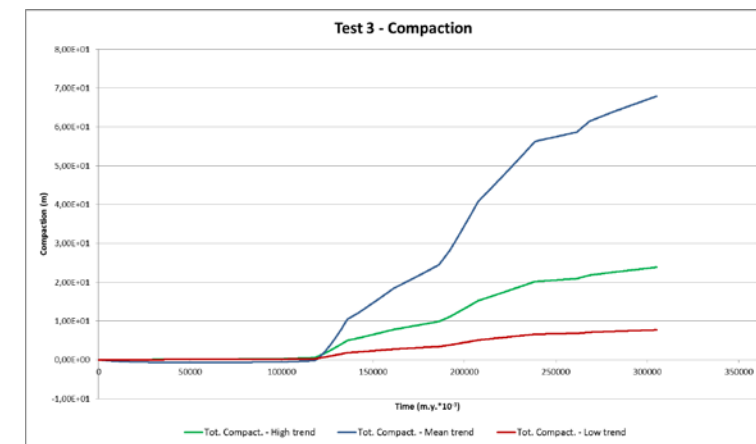


Figure 95: Sedimentary column compaction vs. time

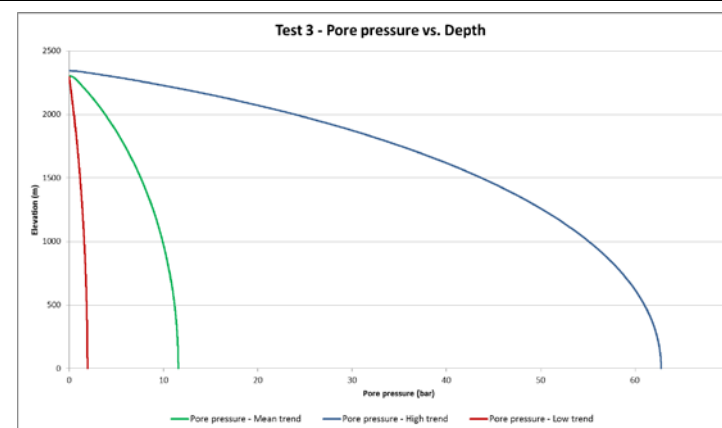


Figure 96: Pore pressure vs. depth.

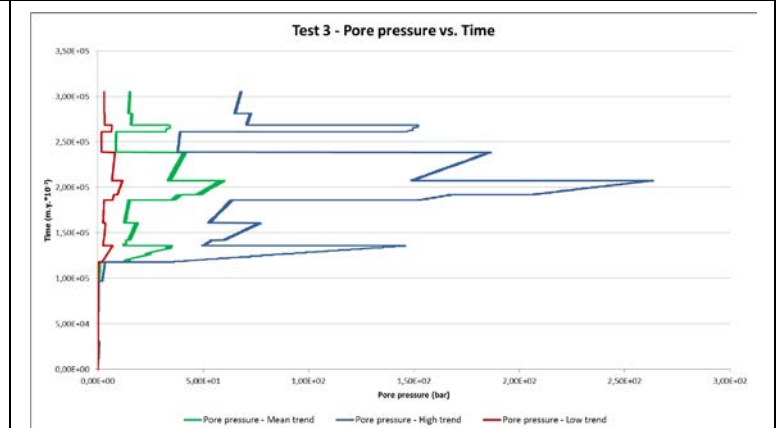


Figure 97: Pore pressure vs. time.

NATSUB RESULTS FOR WELL TEST 4

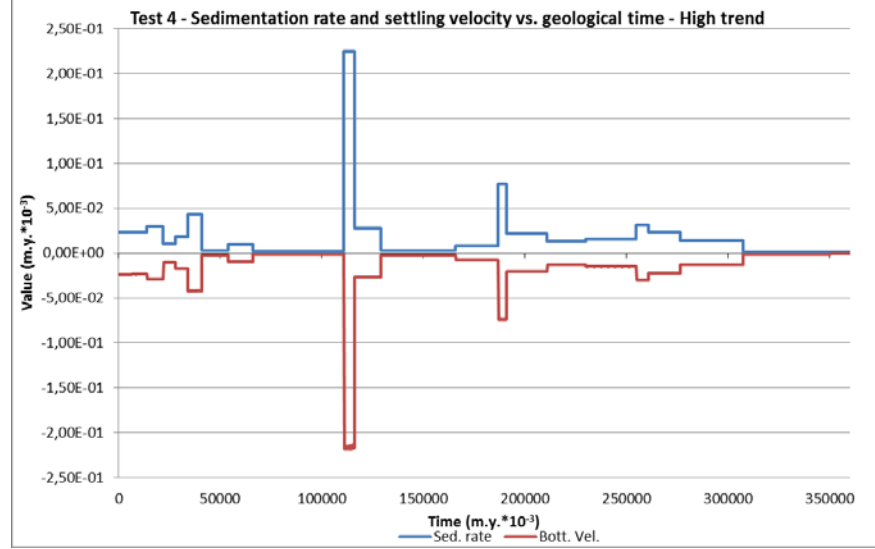


Figure 98: Sedimentation rate (Sed.rate) and settling velocity (Bott.vel.) vs. geological time (high trend).

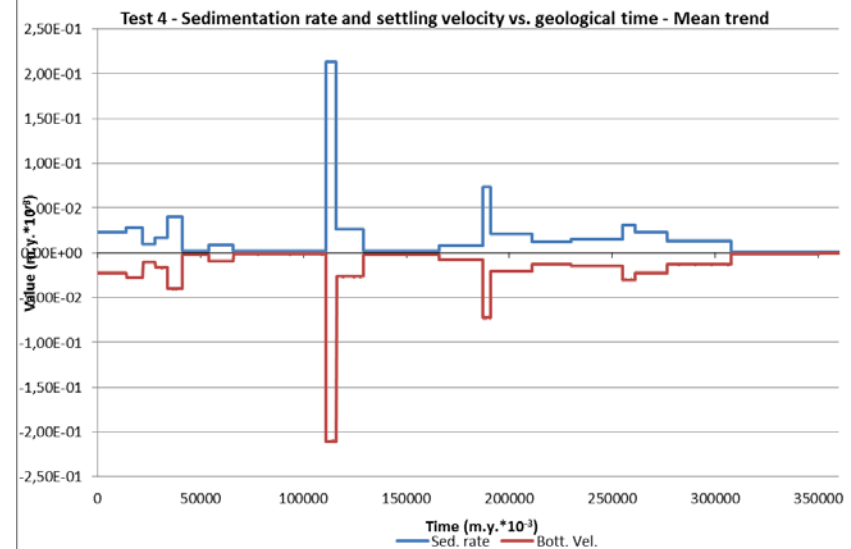


Figure 99: Sedimentation rate (Sed.rate) and settling velocity (Bott.vel.) vs. geological time (mean trend).

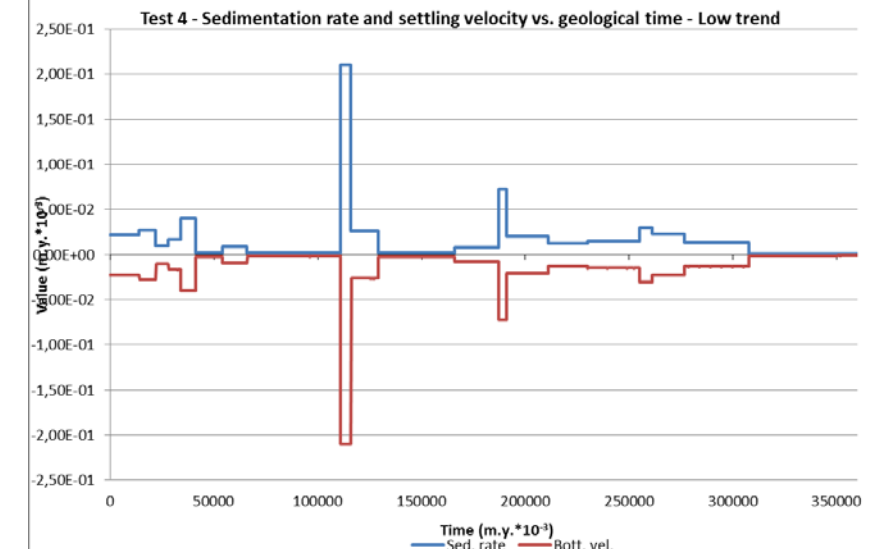


Figure 100: Sedimentation rate (Sed.rate) and settling velocity (Bott.vel.) vs. geological time (low trend).

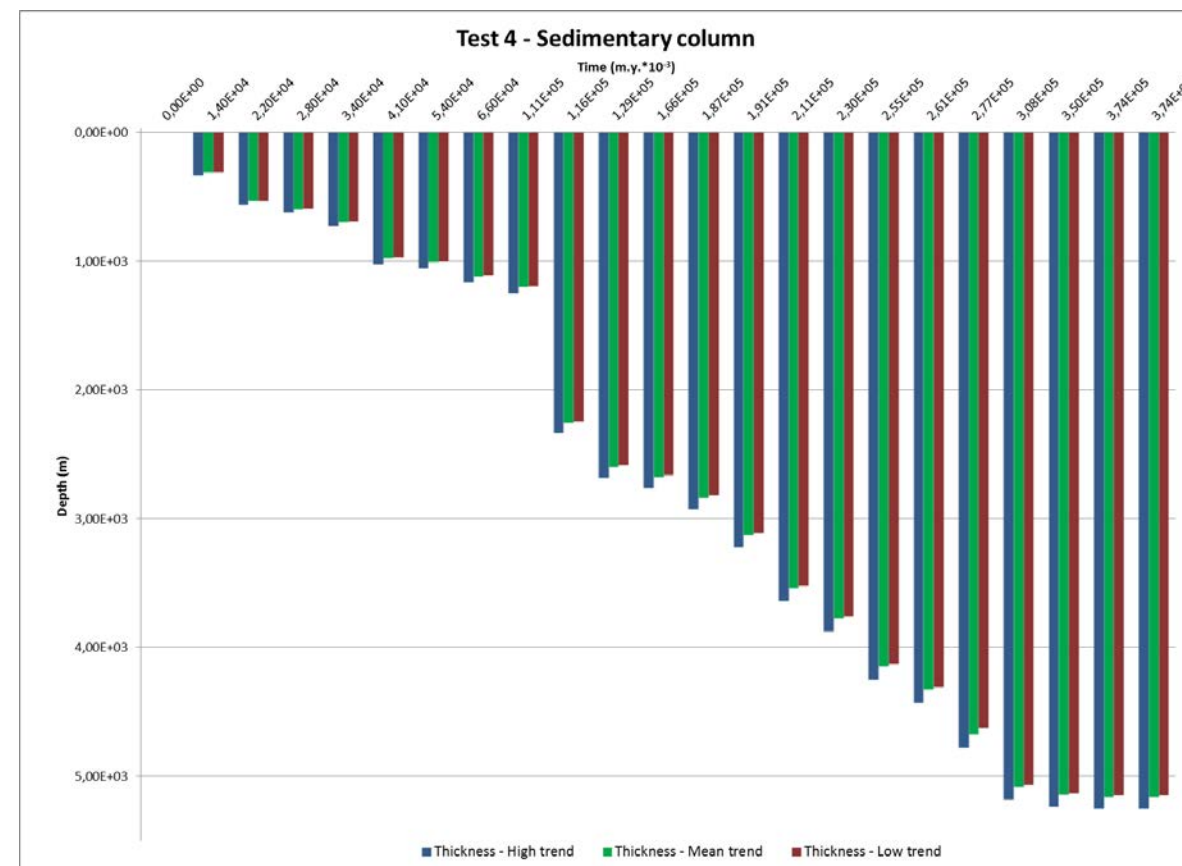


Figure 101: Sedimentary column depths comparison, at selected time steps.

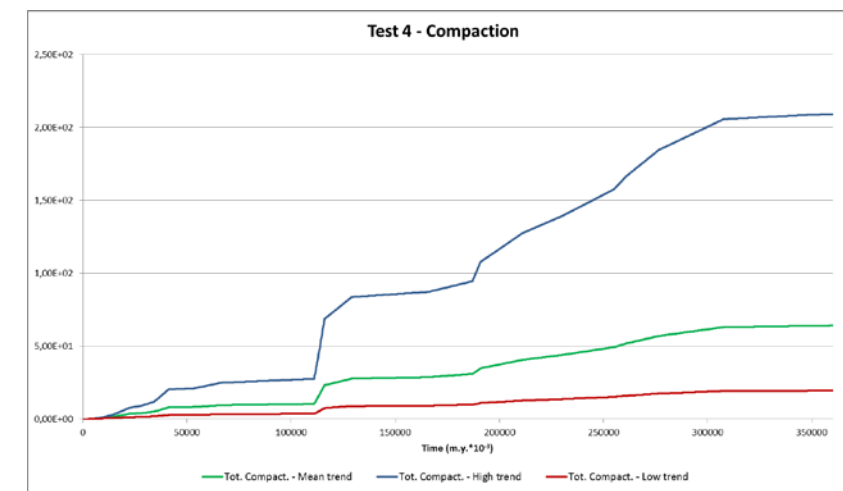


Figure 102: Sedimentary column compaction vs. time

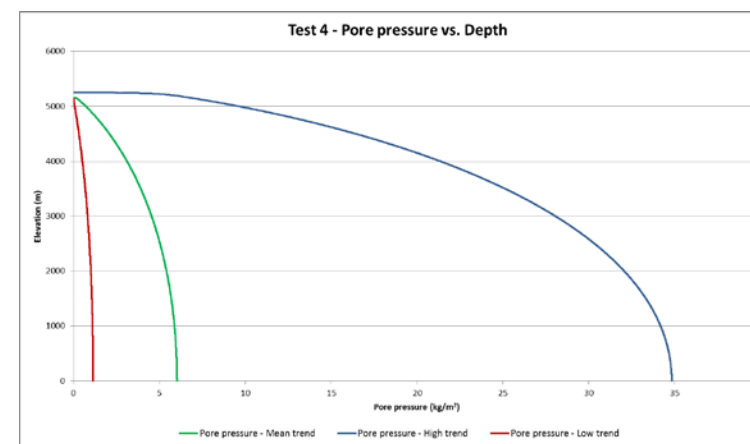


Figure 103: Pore pressure vs. depth.

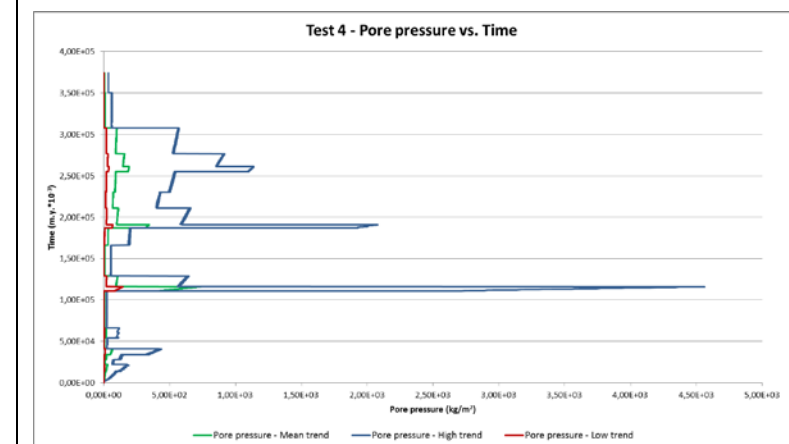


Figure 104: Pore pressure vs. time.

NATSUB RESULTS FOR WELL TEST 5

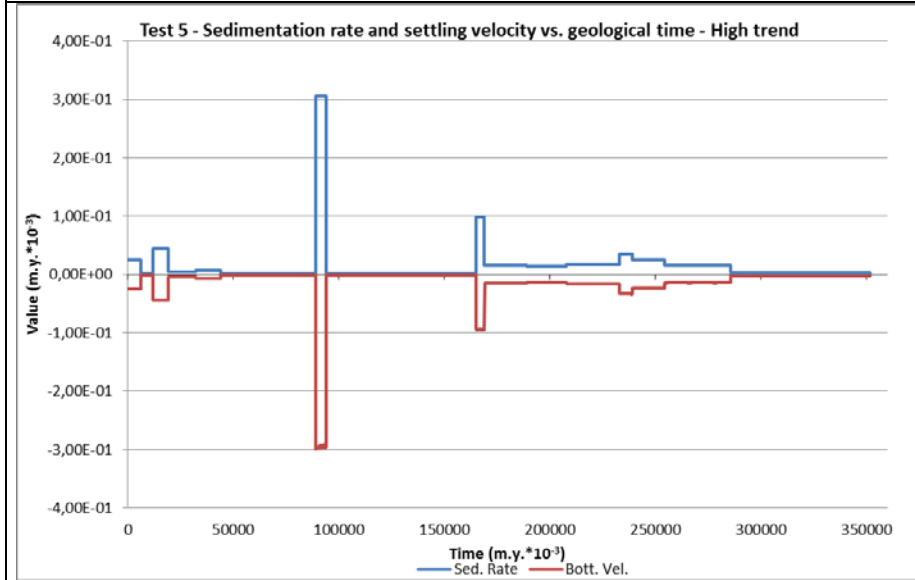


Figure 105: Sedimentation rate (Sed.rate) and settling velocity (Bott.vel.) vs. geological time (high trend).

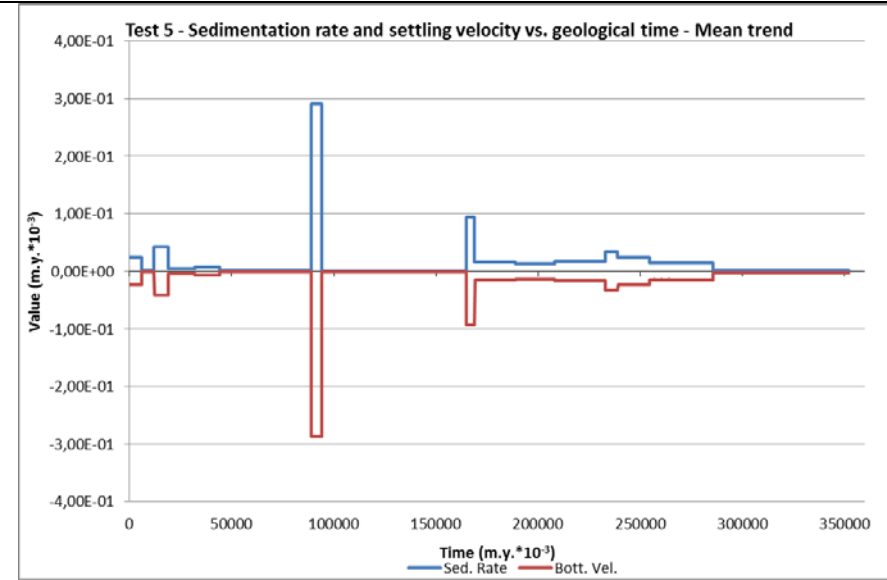


Figure 106: Sedimentation rate (Sed.rate) and settling velocity (Bott.vel.) vs. geological time (mean trend).

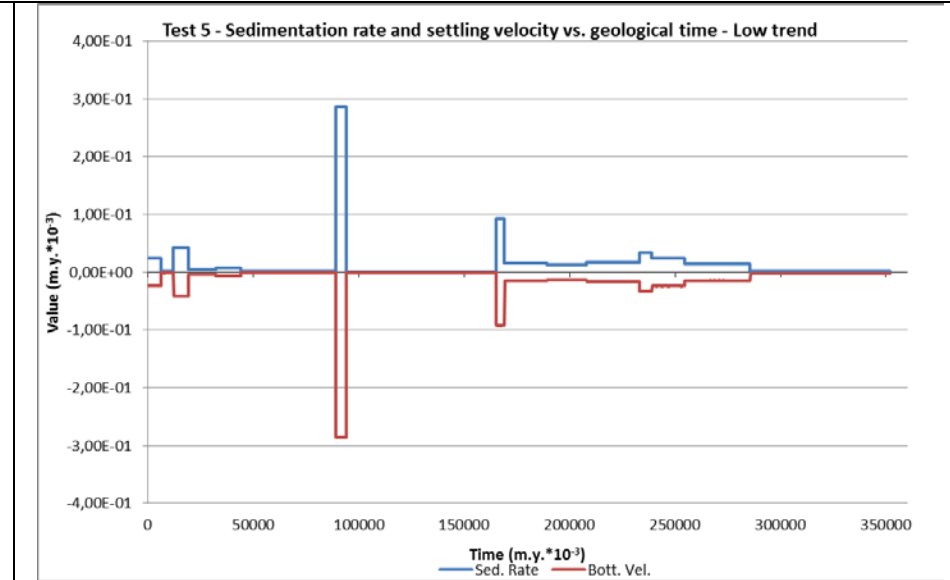


Figure 107: Sedimentation rate (Sed.rate) and settling velocity (Bott.vel.) vs. geological time (low trend).

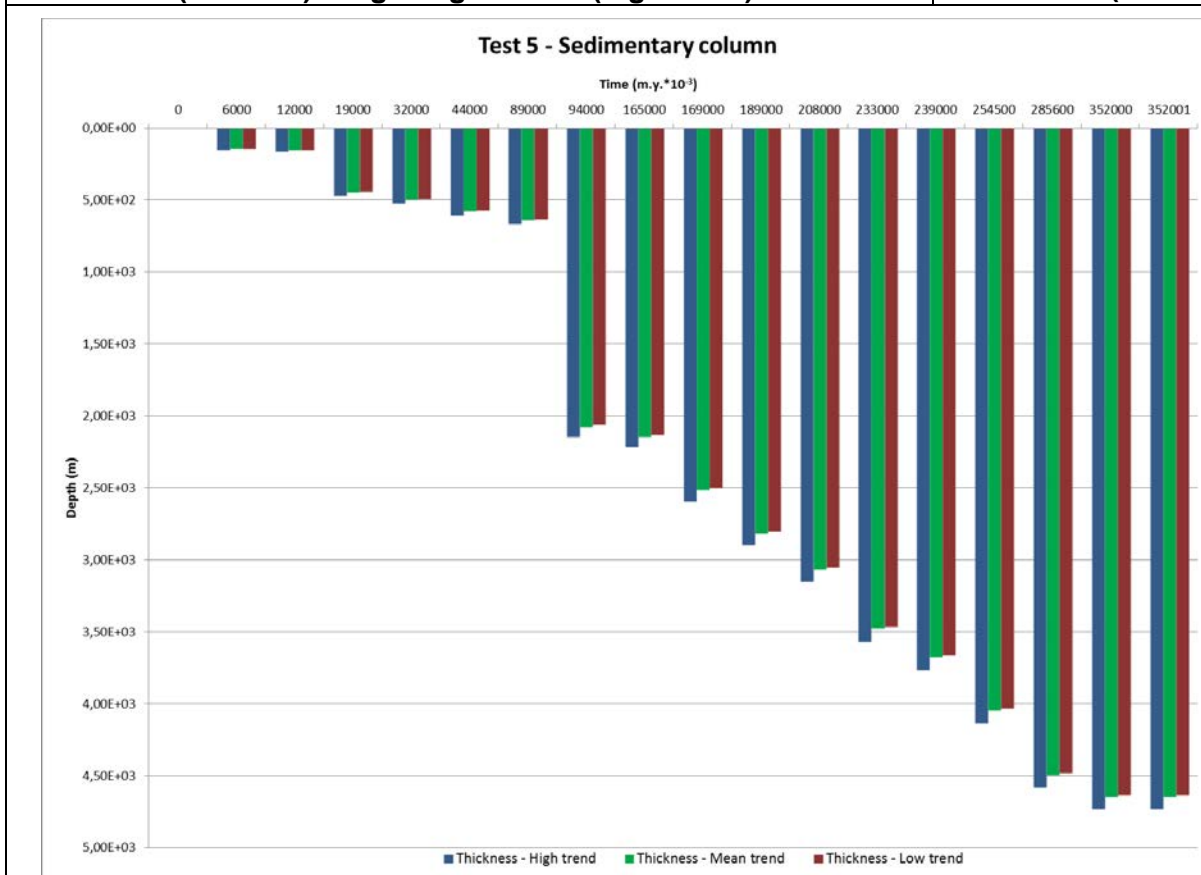


Figure 108: Sedimentary column depths comparison, at selected time steps.

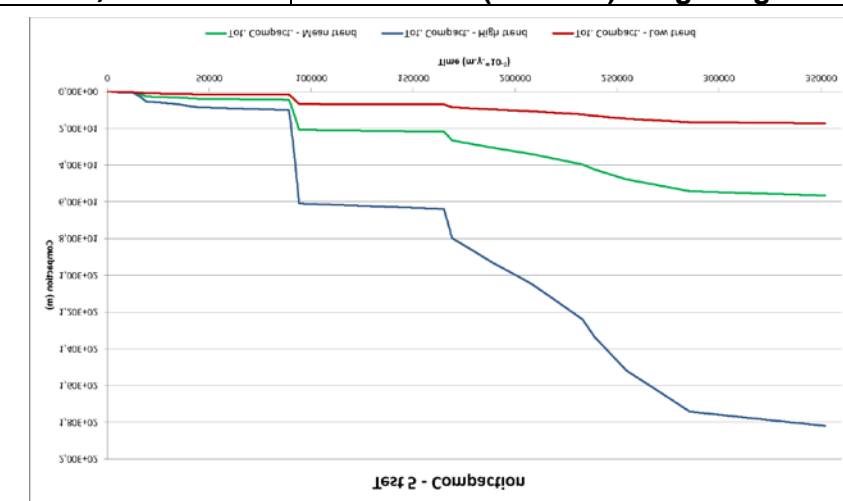


Figure 109: Sedimentary column compaction vs. time

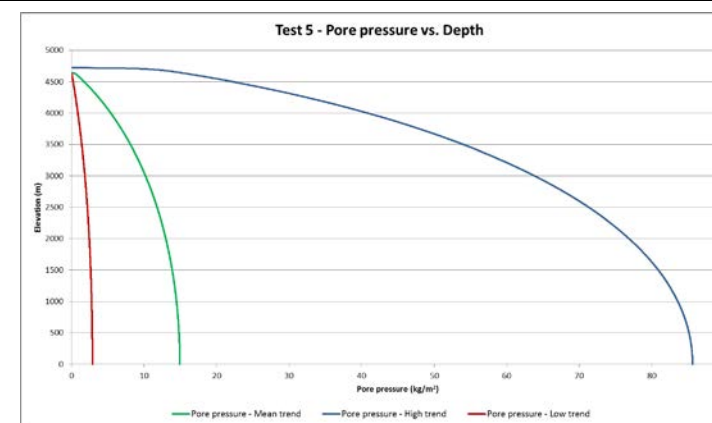


Figure 110: Pore pressure vs. depth.

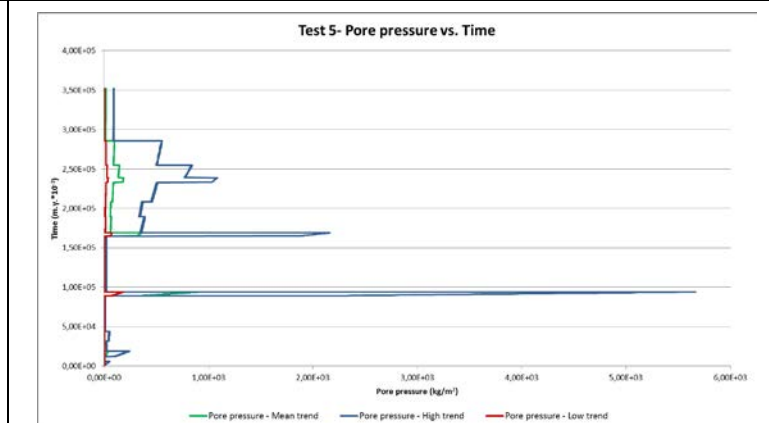


Figure 111: Pore pressure vs. time.

4.2.5.3 **Basin**

INPUT DATA

BASIN requires the parameters for an experiment to be defined in several input data files. Obligatory input data files include basic definitions of the sedimentary basin to be simulated such as number of layers, initial and boundary conditions and physical sediment properties. Additional (or optional) data files include data to alter boundaries or physical sediment properties at specified nodal points and time steps in order to match a specific basin evolution.

Two applications of BASIN are provided: the first (Simulation 1) calculates the properties variation considering a simplified stratigraphical asset (that foresees only one sediment's type), the second (Simulation 2) includes three different type of sediments (pre-salt, salt, post-salt) (respectively type 4, type 3 and type 1 of Figure 113) and related properties are approximates in function of their nature and geological history.

File "global" contains the dimensions of an experiment, numerical parameters, tolerance values, defines the processes to be simulated, the time steps for which result files are to be stored, the wells and elements to be observed, and most of the physical sediment parameters like initial porosities, hydraulic conductivities, specific storage, tortuosities, densities, thermal conductivities and heat capacities.

Key input data for the present simulation:

- Mesh: 40 column x 21 time steps (that correspond to 625 km of distance and 374 my);
- Initial porosity: for the first simulation, as defined in NATSUB application value for porosity at 20 m is 0.538 and decrease with depth, following the trend shown in Figure 72 - Figure 76; for the latter, minimum porosity value is assigned to salt layers, mean value for pre-salt layers (0.2) and 0.538 for the post-salt sequence.
- Specific storage: 0.0005; similar values have been adopted for the three type of sediments, in order to confirm values of compressibility calculated by wireline logs;
- Density of sediment, water and mantle: respectively 2700, 1150, 3300;
- Hydraulic conductivity: as defined in NATSUB application, value for shallow hydraulic conductivity is 10^{-10} m/s and decrease with depth; for the second simulation, minimum allowed (by the code) value is attributed to salt formation, mean value to pre-salt sequence and higher value to post-salt layers.
- Depth of main stratigraphic horizons (Figure 24).

File "geom" contains the initial geometry of the basin with x- and z-coordinates and a definition of the faults considered in a simulation experiment, including the duration of fault activity, throw rates and hydraulic conditions of the fault zone. The simulation domain extends over a 625 km long 2D section. Faults are not implemented within the simulation; available cross-sections confirm that faults involve the basement of the Precaspian basin and the filling sediments are not clearly influenced by tectonic movements (Figure 113).

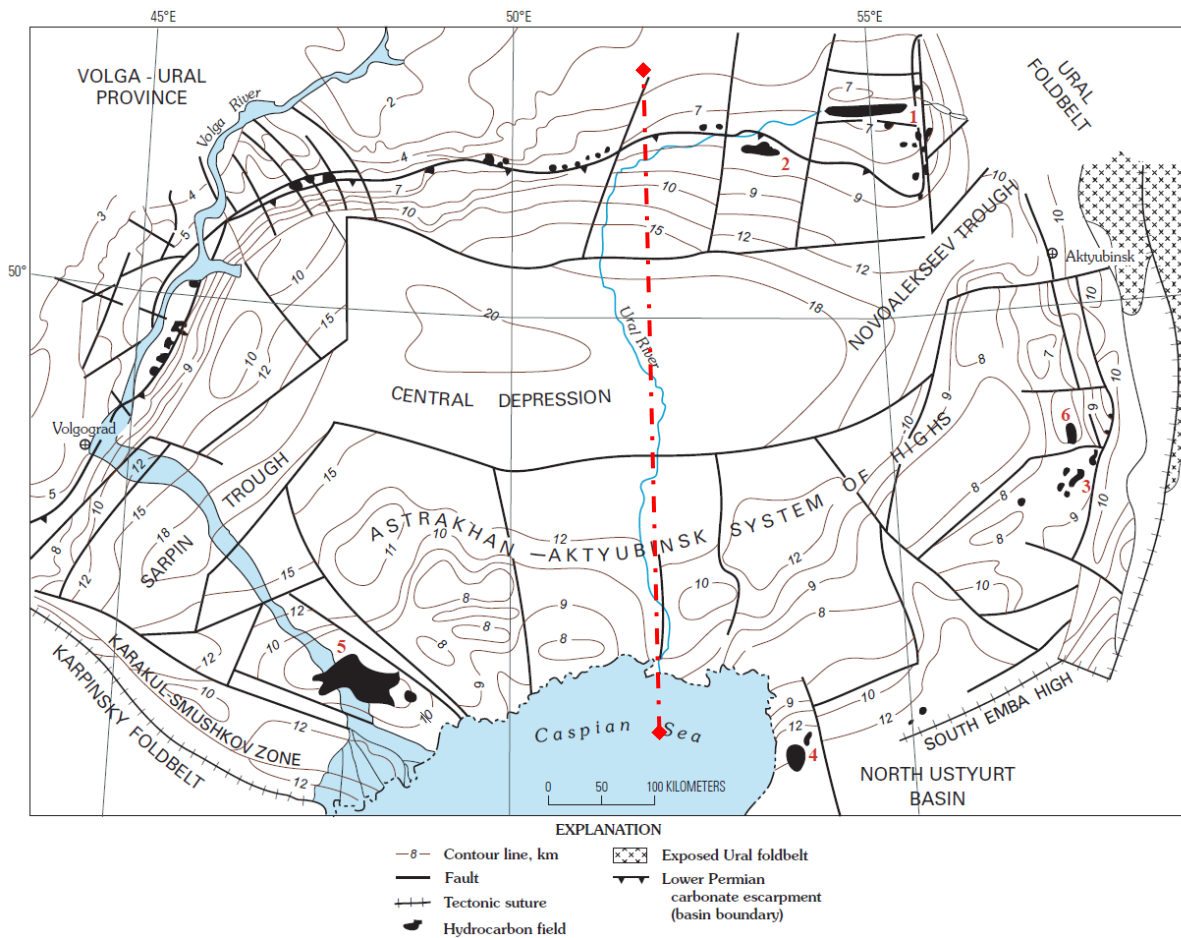


Figure 112: Position of numerical simulation 2D section.

File "sedim" contains the definition of the sediment fill in a layer (or time step) and base heat flow rates. Within a time step, either a sedimentation simulation or a pre-defined sediment fill can be specified. According to the specified option, file "sedim" contains sedimentation parameters like maximum carbonate production depth, poisoning factors, maximum subaerial clastic sedimentation rates, distance from sediment source and subaqueous clastic sedimentation rates, or it contains a defined sediment mixture of the layer. Thus, "sedim" has a strongly variable data format depending on what and when it is intended to be simulated. For the time, sedimentation rate in the present study is set for simulate 14 m/My in section's

margins (in accord to data extrapolated from well logs description); in the centre of the Precaspian basin sedimentation rate is defined on the basis of depth information (Volozh et al., 2003; Volozh et al., 2009; Brunet et al, 1999).

File "hydro" mainly contains information on hydraulic parameters such as anisotropy of hydraulic conductivity, longitudinal and transversal dispersivities for solute transport and heat flow, and the diffusion coefficient. It also includes free surface boundary definition of phreatic aquifers which might occur during emersion of parts of the sedimentary basin. Considering the aim of the present simulation some of these options are not activated (e.g., solute transport or heat flow).. Most important, it contains a "switch board" to call for specific optional input data files at specified time steps. If for example at a certain time step boundary conditions such as a pre-defined topography or physical parameters at one or several points of the finite-element-mesh are to be redefined, file "hydro" contains a mark that forces BASIN to read these data from a specified optional input data file.

File "time" contains data on time step size and the sea-level change at each time step. Time intervals follow the criteria considered during the NATSUB implementation, sea level changes are set according to Volozh et al. (2003).

These five files have to be prepared for each experiment. Care must be taken, that input data are consistent and the number of defined layers coincides with the sedimentation data in "sedim" and the number of time steps in "time". In order to trace inconsistencies in these files, an echo file which helps to detect errors is created after reading the input data.

Optional input data files have a three-digit extension which relates to the time step, when they are called for. For example, file "topo023" contains a predefined basin topography at time step 23. In this case, BASIN will assume a topography as defined in this file, and calculates subsidence due to tectonic processes to account for this topography. As a result, to the "topo023" file corresponds a "subside023"-output file containing the tectonic subsidence along the simulated cross section calculated at that time step. Additionally, if calculation of isostatic compensation has been defined, the "iso023" file contains the subsidence due to isostatic compensation at the corresponding time step. Changes of mesh coordinates and physical parameters at defined time steps for specified nodal points are defined in the "bcmeshXXX" file (with XXX identifying the time step). Changes in boundary conditions for the hydraulic calculation are defined in file "bchydXXX", for solute transport in file "bctransXXX" and heat flow in file "bctempXXX". This feature allows to match specific basin situations and to perform experiments incorporating complex and varying boundary conditions. Care must be taken, that the files are available during the experiment. A typical error in experiments with BASIN is, that in file "hydro" change of boundary conditions is defined, but the corresponding data file has not

been supplied. In order to facilitate input data creation, each data block starts with a comment line which gives a short indication of the parameters to be defined.

OUTPUT DATA

Result files from the simulated cross section have a three-digit extension, which defines the corresponding time step. Some result files have an element-wise storage scheme, however the majority of files store nodal values. Result files related to observation wells or elements have a four-digit extension. The data format is designed to work with the post processing programs distributed with BASIN. The following cross-sectional result files are created:

- concXXX concentration of a conservative solute;
- densityXXX rock density (kg/m^3);
- direcXXX flow direction;
- faciesXXX sediment mixture ("facies") distribution;
- headXXX distribution of hydraulic head (or overpressure, if defined in "global.dat" (m));
- heatXXX temperature distribution ($^{\circ}\text{C}$);
- hydconXXX hydraulic conductivity (in log m/s);
- isoXXX isostatic compensation along the cross section (m);
- kumulXXX cumulative fluid flow (m);
- lambdaXXX distribution of the relation between fluid pressure and total stress (-);
- settleXXX consolidational settling rate (m/myr);
- storXXX specific storage ($\log \text{m}^{-1}$);
- stratiXXX stratigraphic data (necessary, as the mesh geometry does not coincide with stratigraphy, if erosional events occur) (m);
- thermcondXXX thermal conductivity ($\text{cal (m sec } ^{\circ}\text{C)}^{-1}$);
- tmissiXXX transmissivity (m^2);
- ttiXXX time temperature index (TTI) (-)
- vel3eckXXX flow velocity (log m/kyr);
- wdepthwater-depth at deposition (only stored at the end of experiment) (m).

Additionally, the distribution of all parameters along a vertical section ("well") is stored in "wellXXXX" files with "XXXX" indicating the location of the well. The temporal evolution of all

parameters in a specified element of the simulated cross section is stored in "elementXXXX" files with "XXXX" indicating the element number. The number of output files varies with the processes to be calculated and the definition of time steps, when results are to be stored. A maximum of 730 result files are created if all time steps are conserved.

POST-PROCESSING

The large number of result files requires some post-processing supporting programs. In order to visualize BASIN results on any computer system, post-processing of result files is based on the ghostview software, which is public domain and available for UNIX, Linux, Windows and Macintosh computer systems. BASINVIEW creates ghostview-readable files from the output files described before. AIBASIN creates Adobe Illustrator-readable files using different layers, facilitating subsequent graphic manipulation. BASELINE is used to create plots of well- or element data either for ghostview or Adobe Illustrator. The post processing programs are written in Fortran77. The visualization options are defined in file "ps-parameter", containing scaling parameters, definitions of line widths, figure captions, colour fill definitions and parameters and time steps to be visualized. Different graphics can be combined, for example arrow plots with hydraulic head, porosity with finite elements mesh, stratigraphy with layers etc. Graphic files for visualization with ghostview have a prefix "gst" and an extension "XXX" defining the corresponding time step. Graphic files for Adobe Illustrator have a prefix "ai" instead of "gst". Well and element files have a prefix "ai" and an extension "XXXX" defining the well number or the element number. Due to the large number of parameters, well and element plots come in three separated files. Well plots include an automatically generated coloured stratigraphic and lithologic column. The present simulation is set for the modelling of some selected phenomena :

- Simulated stratigraphy (main geological horizons are identified);
- Simulation's mesh;
- Porosity;
- Specific storage ($\log m^{-1}$);
- Hydraulic conductivity ($\log m/s$);
- Consolidational settling rate (m/myr).

Output referred to the simplified simulation are shown in Figure 114 - Figure 118; results given by the more realistic simulation are shown in Figure 119 - Figure 123. For both the simulations, results are shown for time steps of simulation n° 5, 10, 15, 21. Following image (Figure 113) shows the chronostratigraphy simulated through BASIN model and comparison with schematic cross-section elaborated by Max Petroleum (2008) covering the same S-N alignment of investigation.

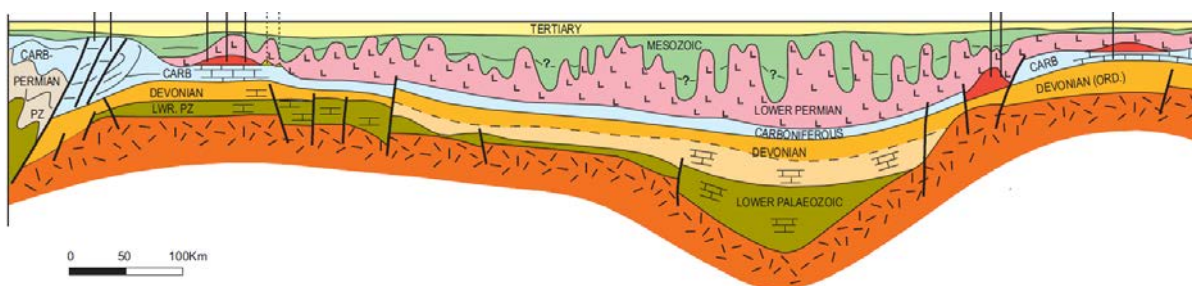
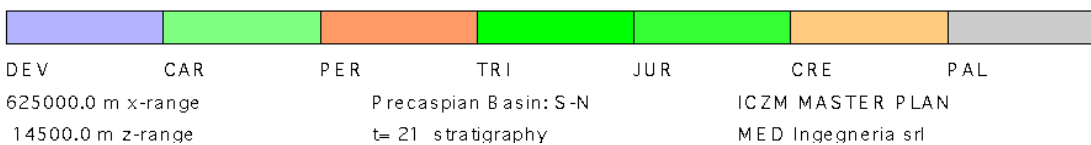
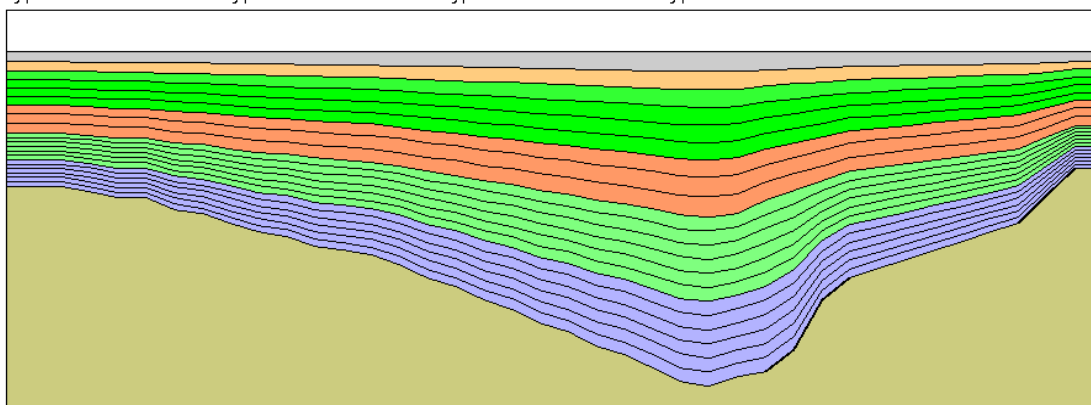
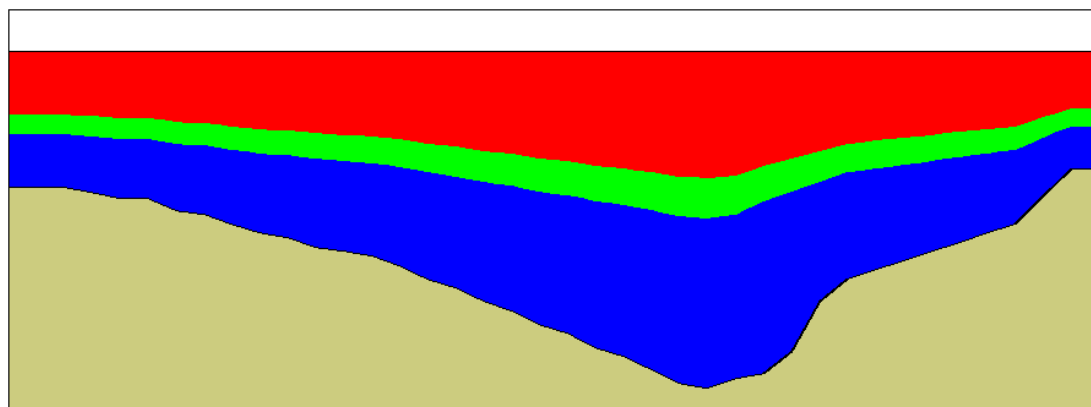


Figure 113: Chronostratigraphy simulated through BASIN model (Simulation 1) and comparison with schematic cross-section elaborated by Max Petroleum (2008).

SIMULATION 1

- Mesh

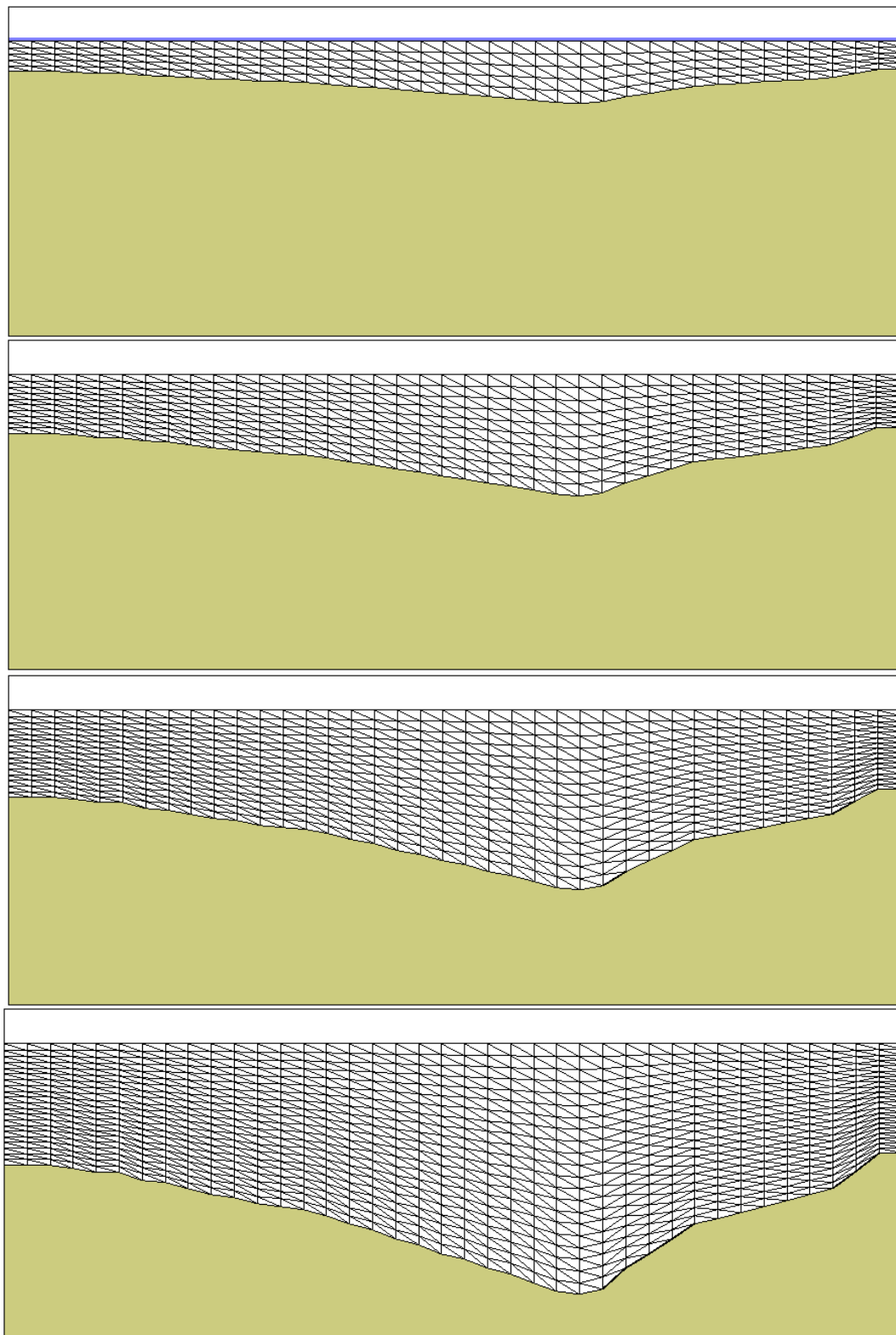


Figure 114: Simulation's mesh at different time steps (Late Devonian, Serpukhovian-Bashkirian boundary, Triassic-Jurassic boundary, Early Cretaceous) (Simulation 1).

- Porosity

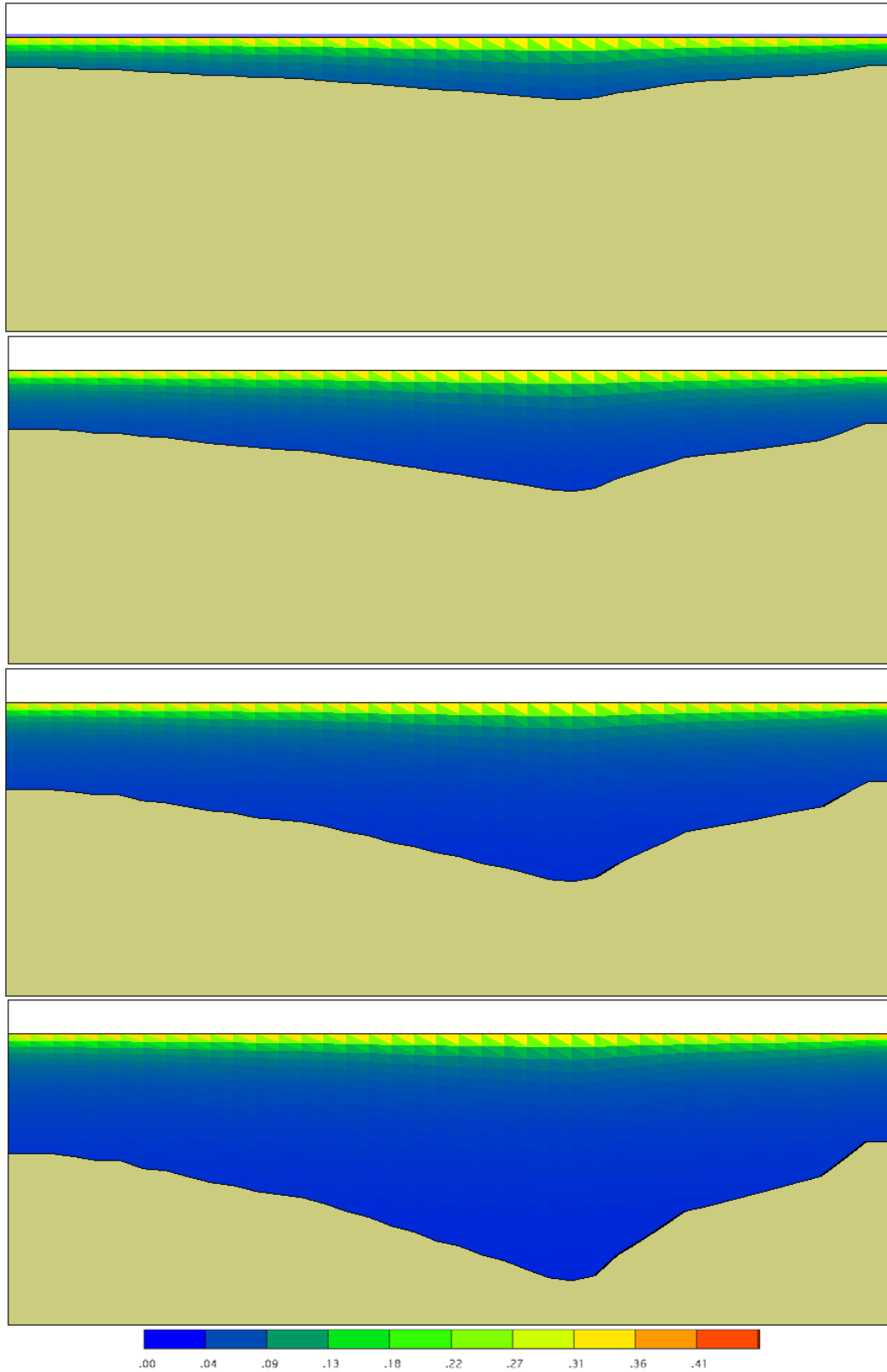


Figure 115: Porosity at different time steps (Late Devonian, Serpukhovian-Bashkirian boundary, Triassic-Jurassic boundary, Early Cretaceous) (Simulation 1).

- Specific storage ($\log m^{-1}$);

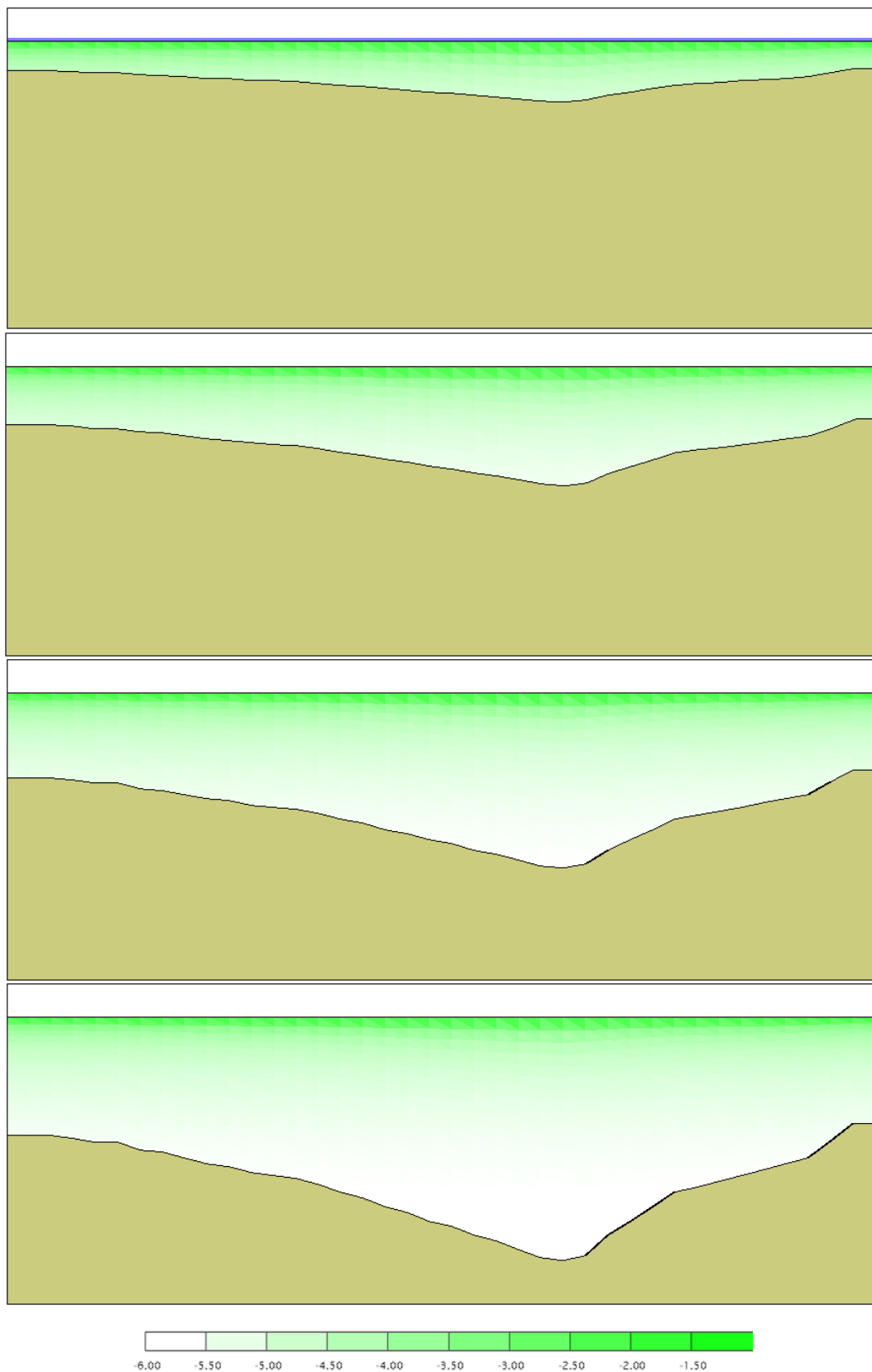


Figure 116: Specific storage at different time steps (Late Devonian, Serpukhovian-Bashkirian boundary, Triassic-Jurassic boundary, Early Cretaceous) (Simulation 1).

- Hydraulic conductivity (log m/s);

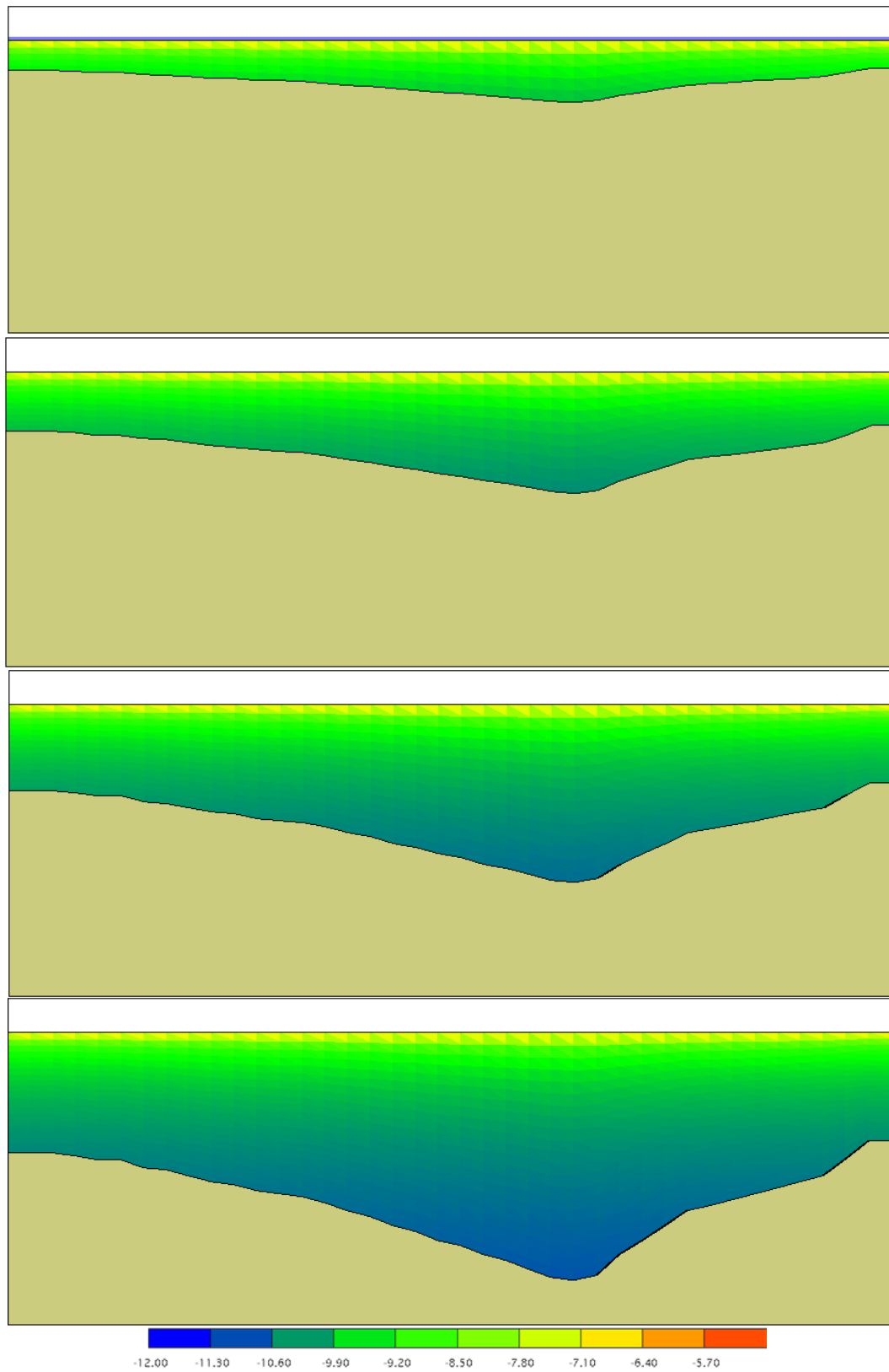


Figure 117: Hydraulic conductivity at different time steps (Late Devonian, Serpukhovian-Bashkirian boundary, Triassic-Jurassic boundary, Early Cretaceous) (Simulation 1).

- Consolidational settling rate (m/myr)

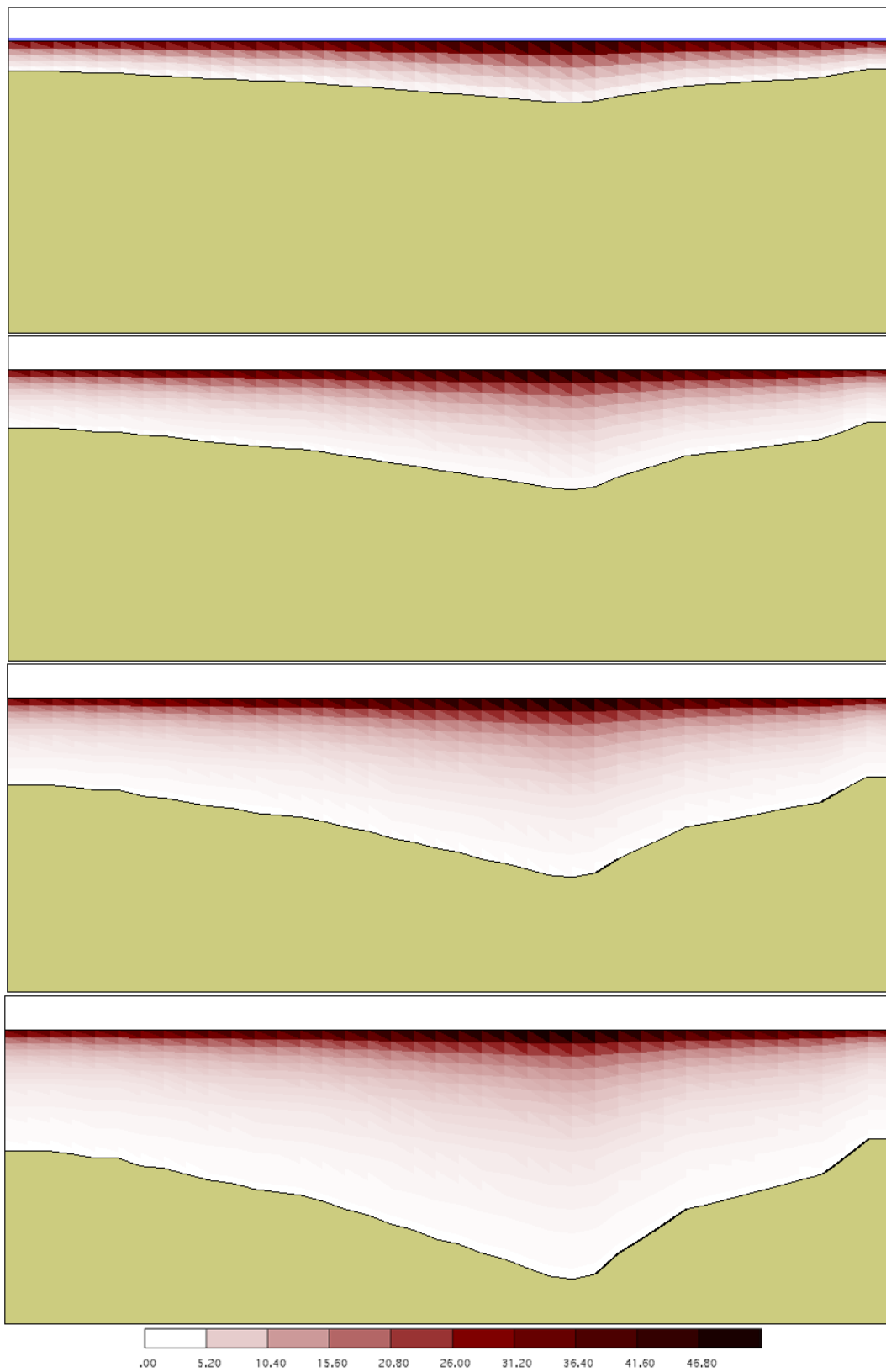


Figure 118: Consolidational settling rate at different time steps (Late Devonian, Serpukhovian-Bashkirian boundary, Triassic-Jurassic boundary, Early Cretaceous) (Simulation 1).

SIMULATION 2

- Mesh

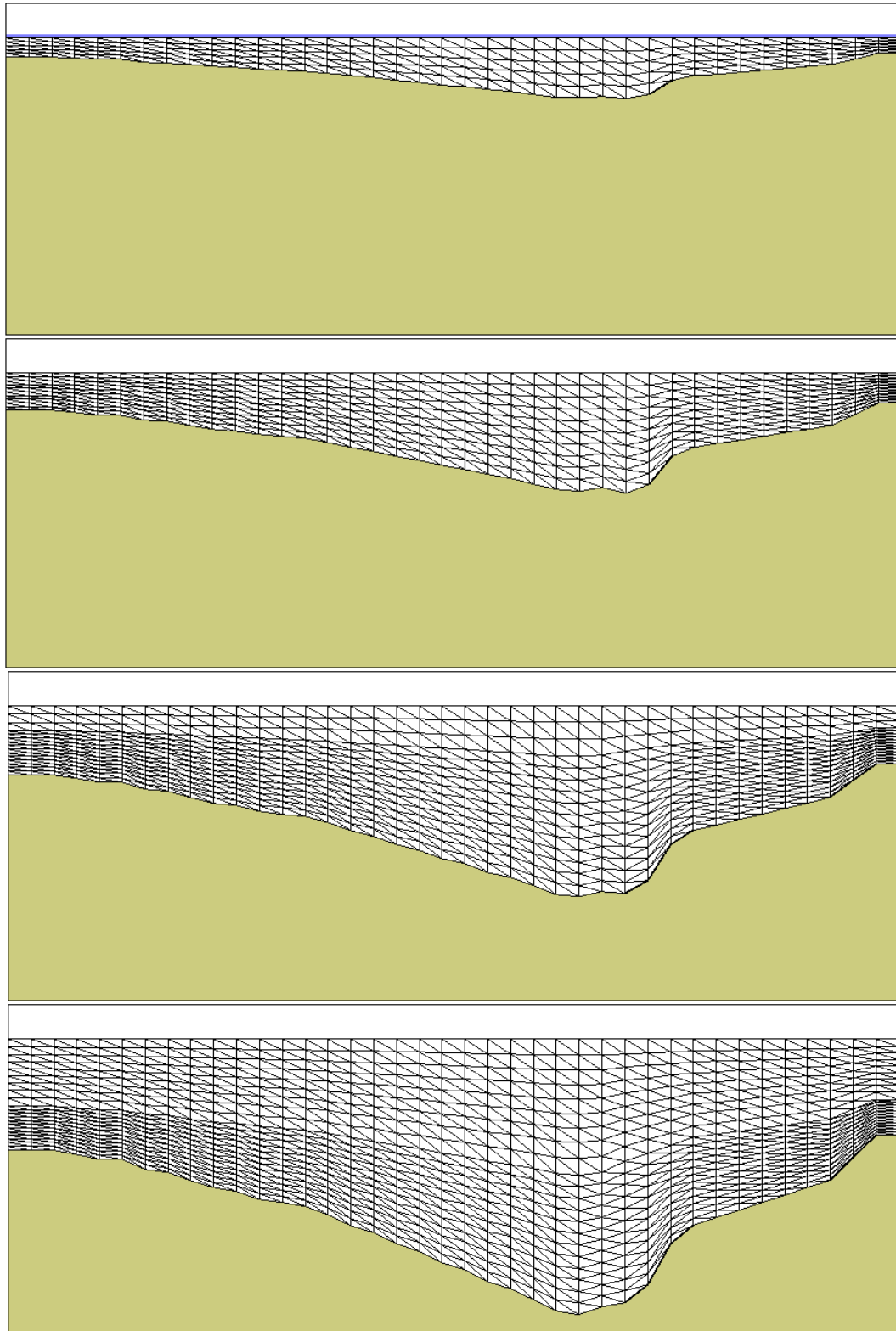


Figure 119: Simulation's mesh at different time steps (Late Devonian, Serpukhovian-Bashkirian boundary, Triassic-Jurassic boundary, Early Cretaceous) (Simulation 2).

- Porosity

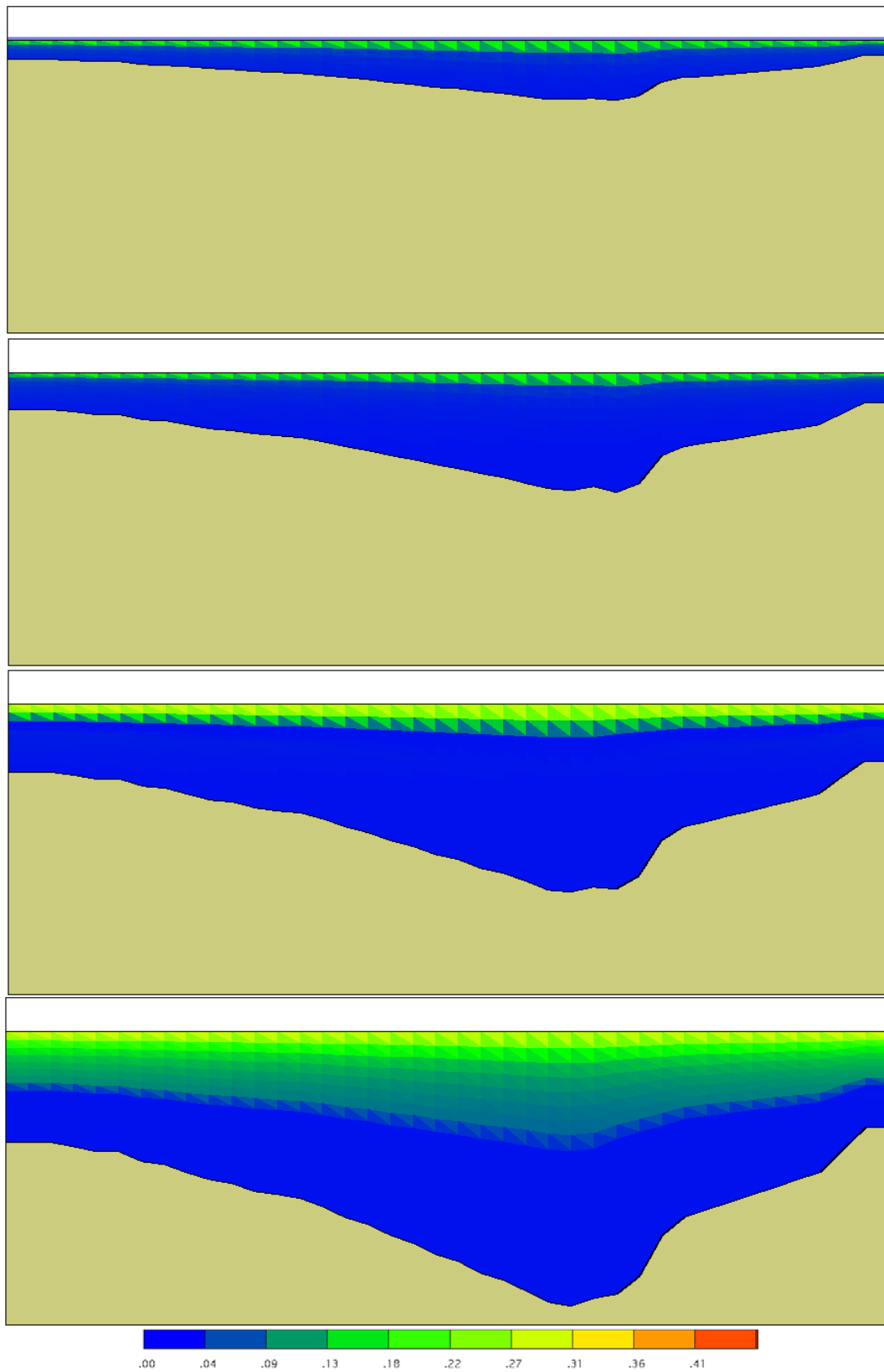


Figure 120: Porosity at different time steps (Late Devonian, Serpukhovian-Bashkirian boundary, Triassic-Jurassic boundary, Early Cretaceous) (Simulation 2).

- Specific storage ($\log m^{-1}$);

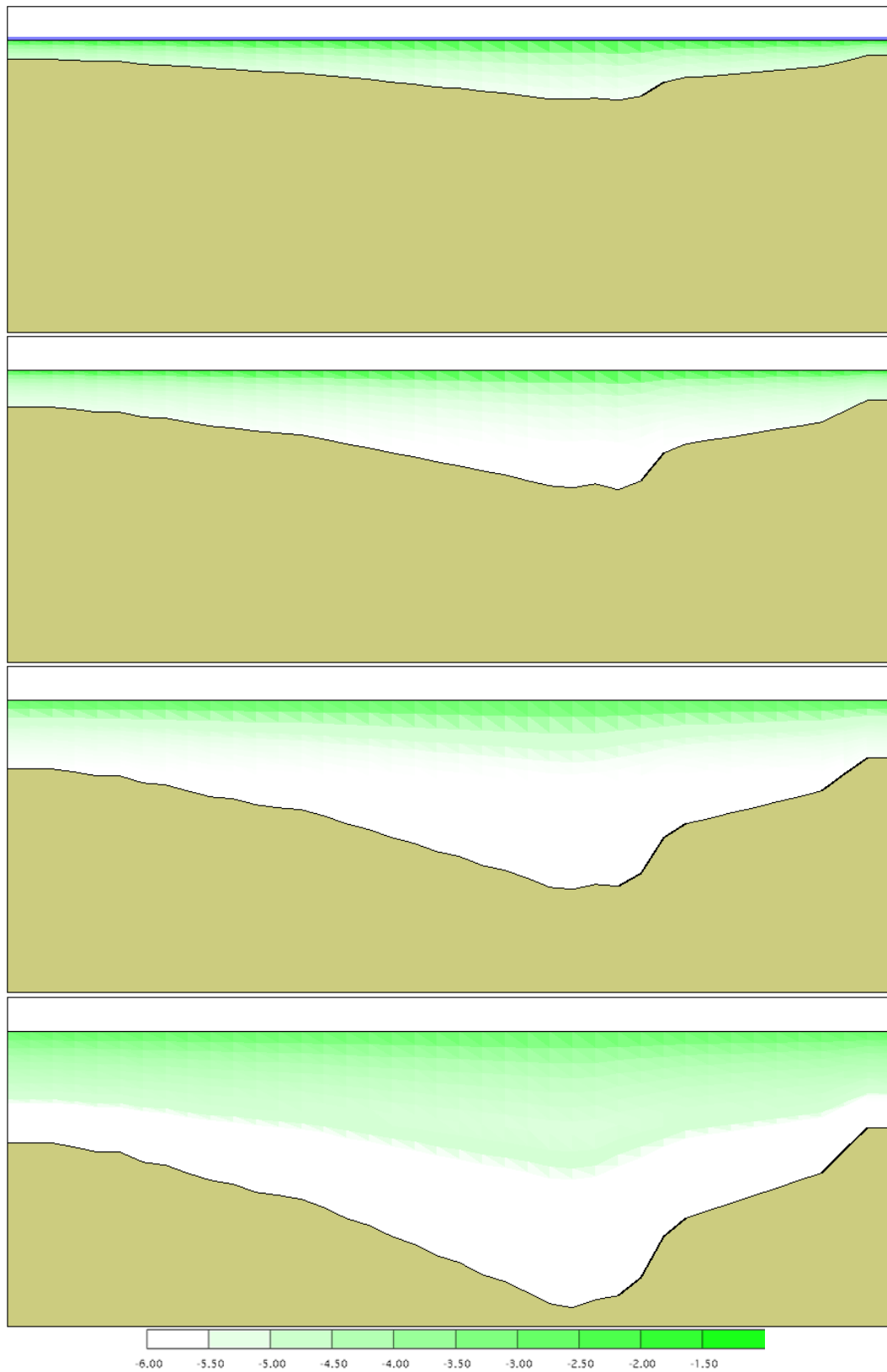


Figure 121: Specific storage at different time steps (Late Devonian, Serpukhovian-Bashkirian boundary, Triassic-Jurassic boundary, Early Cretaceous) (Simulation 2).

- Hydraulic conductivity (log m/s);

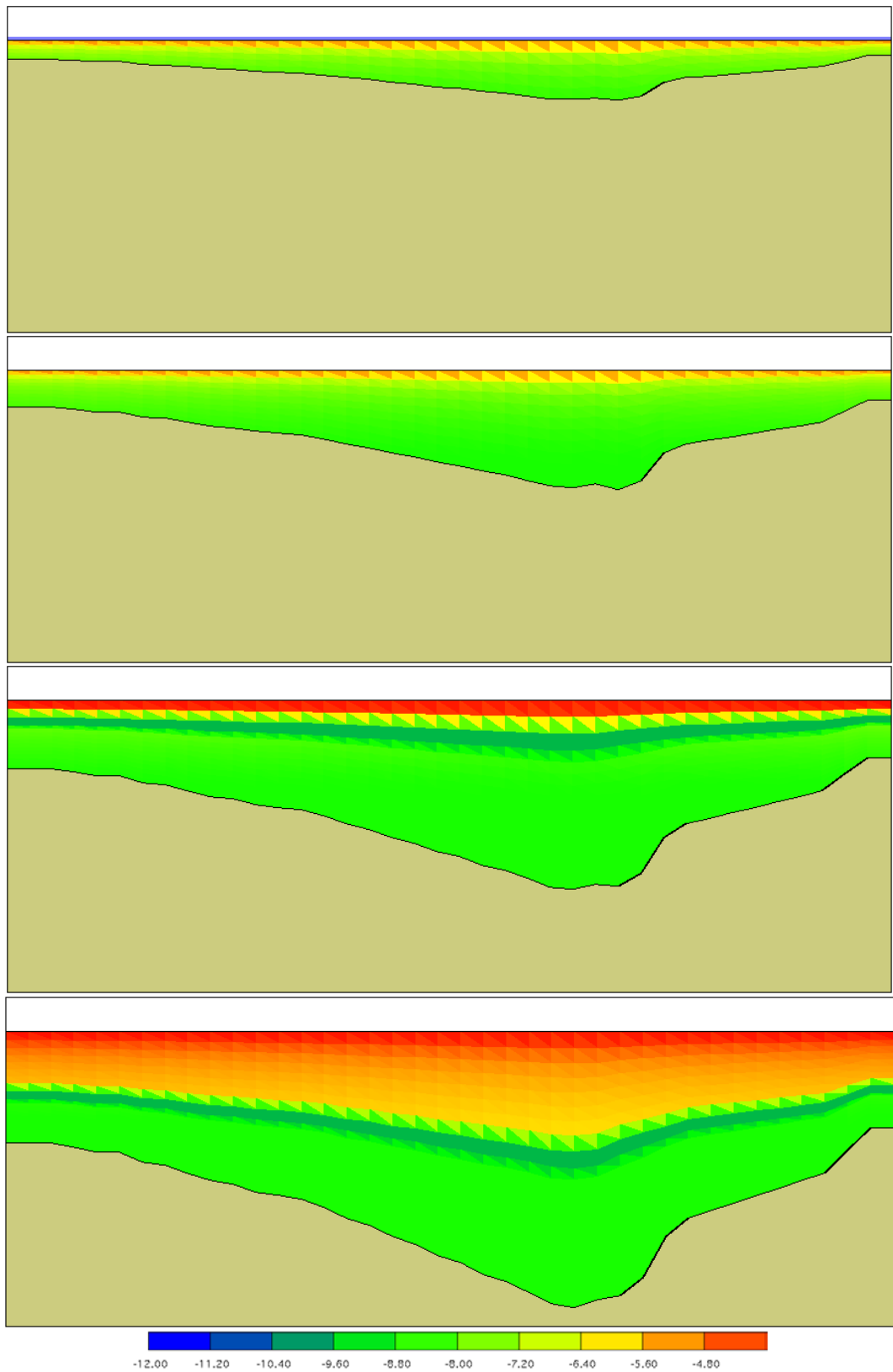


Figure 122: Hydraulic conductivity at different time steps (Late Devonian, Serpukhovian-Bashkirian boundary, Triassic-Jurassic boundary, Early Cretaceous) (Simulation 2).

- Consolidational settling rate (m/myr)

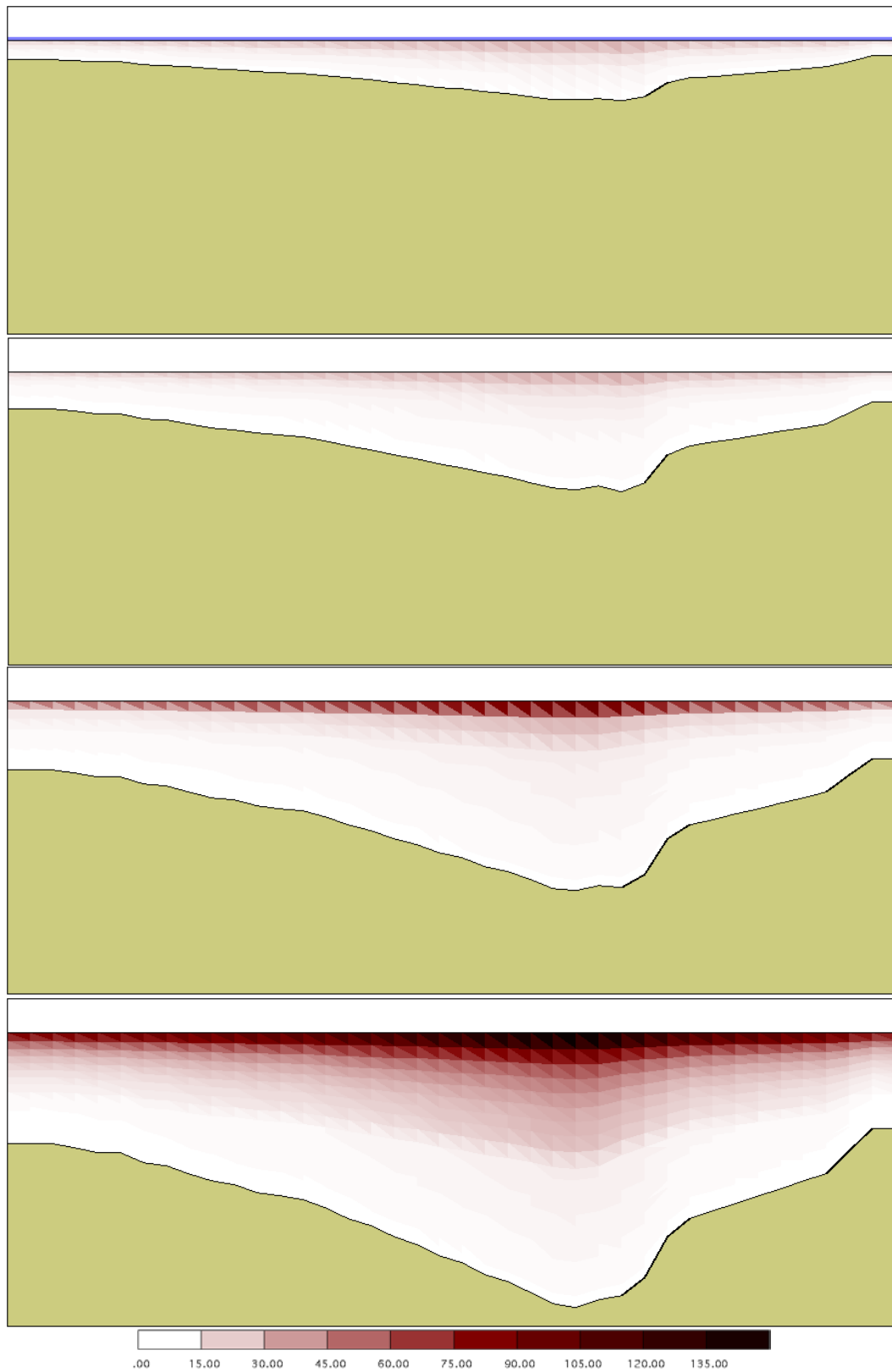


Figure 123: Consolidational settling rate at different time steps (Late Devonian, Serpukhovian-Bashkirian boundary, Triassic-Jurassic boundary, Early Cretaceous) (Simulation 2).

4.2.6 Discussion of NATSUB and BASIN results

Applied models provided results with different level of detail.

NATSUB application has been based on well log data (wireline logs and chronostratigraphies) and results are detailed but localised in the offshore part of the study area. On the contrary, available data allows a qualitative application of BASIN along a S-N section that cross the whole Precaspian basin; lacks of information concerning the central and northern parts of the basin affects the precision of results, that can be considered as an indication of parameters variation along the S-N cross section. However, some comparison between the two models applied have been done.

One dimensional results show that very low value of calculated compressibilities and sedimentation rates affect the whole set of results.

- Porosity values show clear reduction from the top to the bottom, in particular for simulations with high compressibility trend; however variation range is limited in every considered well, and in every used compressional trend. Maximum porosity variation has been obtained at well Test 5 (top minus bottom values of 0.0849 – High trend) while minimum porosity variation has been obtained at well Test 3 (top minus bottom values of 0.0066 – Low trend).
- Sedimentation rates, calculated for each well, are very low. Generally speaking, in this portion of the Precaspian basin the elder (and deeper) strata drilled correspond to Devonian carbonates and reach a depth of about 4 km. In every well, except for Test 3, it is clearly visible the salt layer deposited during Kungurian age and in general it is recognisable every depositional event during the whole geological history.
Low rates of sedimentation influence the velocity of the bottom, that is the mirror image of the represented sedimentation rates. To understand the meaning of these results we have to recall the assumption we made that subsidence is in equilibrium with sedimentation during the time interval with zero variation in sea bathymetry: if sea bathymetry remains constant in time, the column basement must subside to fully compensate the depositional rate.
- Thickness of the sedimentary column shows, for different compactional trends, the depth of the bottom. Differences among three simulations/wells have limited extent; this behaviour is consequence of compaction trends.
- Pore pressure is small even at largest depths for each well. The phenomena is due to the low sedimentation rates, that permit overpressure dispersion. By contrast, the behaviour of pore pressure has not always been so small during the basin history and has displayed an increase during intensively depositional periods. However, their

magnitude does not reach high values (excluding the depositional event occurred in Kungurian age, pore pressure maximum values reach 200 bar).

BASIN application confirms the results founded in the offshore area of the Caspian Sea and agree with NATSUB results; values of different parameters record their maximum variation in the most shallow sedimentary layers, and values decrease with depth.

BASIN results show that sedimentary column properties are strongly dependant by the geometry of the basin and the basement depth. Values magnitude increase toward the deepest part of the Precaspian basin; however, these portions of sedimentary basin are not included in the study area and values cannot be confirmed.

Magnitude of subsidence is quite different in the two simulations carried out. In case of simulation 1 values reach a maximum value of about 0.05 mm/y in correspondence of the deepest part of the basin and value decreases toward the basin's margins. In the same simulation, subsidence values decrease quickly with depth, more quickly at the basin's margins than the centre of Precaspian basin. Calculated values are probably underestimated because of the uniformity assumed for the whole sedimentary column.

Simulation 2, more similar to the real geological asset of the area, confirms decreasing trends from the centre to the margins of the basin and from the surface to the bottom. However, gradients are lower than simulation 1 and the contrast between the post-salt sequence and the evaporitic formation is clear.

Natural subsidence values, as expected, highlight negligible lowerings and the general stability of this ancient and mature sedimentary basin, even if magnitude is higher than the simulation 1.

4.3 EVALUATION OF PRESENT SUBSIDENCE BY SAR INTERFEROMETRY

4.3.1 Principles of Interferometric SAR technique

Synthetic Aperture Radar (SAR) is a microwave imaging system. It has cloud-penetrating capabilities because it uses microwaves. It has day and night operational capabilities because it is an active system. Finally, its 'interferometric configuration', Interferometric SAR or InSAR, allows accurate measurements of the radiation travel path because it is coherent. In the following description of the technique two satellites are considered (Ferretti et al., 2007).

- ENVISAT

Launched in 2002, ENVISAT is the largest Earth Observation spacecraft ever built. It carries ten sophisticated optical and radar instruments to provide continuous observation and monitoring of the Earth's land, atmosphere, oceans and ice caps. ENVISAT data collectively provide a wealth of information on the workings of the Earth system, including insights into factors contributing to climate change.

Furthermore, the data returned by its suite of instruments are also facilitating the development of a number of operational and commercial applications. ENVISAT's largest single instrument is the Advanced Synthetic Aperture Radar (ASAR), operating at C-band. This ensures continuity of data after ERS-2, despite a small (31 MHz) central frequency shift. It features enhanced capability in terms of coverage, range of incidence angles, polarisation, and modes of operation. The improvements allow radar beam elevation steering and the selection of different swaths, 100 or 400 km wide. ENVISAT is in a 98.54° sun-synchronous circular orbit at 800 km altitude, with a 35-day repeat and the same ground track as ERS-2.

Its primary objectives are:

- To provide continuity of the observations started with the ERS satellites, including those obtained from radar-based observations;
- To enhance the ERS mission, notably the ocean and ice mission;
- To extend the range of parameters observed, to meet the need for increasing knowledge of the factors affecting the environment;
- To make a significant contribution to environmental studies, notably in the area of atmospheric chemistry and ocean studies (including marine biology).

- RADARSAT

RADARSAT-2 was launched in 2007 by the Canadian Space Agency following the launch of RADARSAT-1. It carries a Synthetic Aperture Radar (SAR) sensor, which is

a powerful microwave instrument that can transmit and receive signals to obtain detailed images of the Earth.

SAR sensors are a form of active remote sensing where, instead of recording the amount of sunlight reflected from a surface or radiation emitted from a surface (e.g., thermal imaging), radar pulses are emitted from the sensor and then the reflected responses are recorded. Radar sensors operate in the microwave region of the electromagnetic spectrum. RADARSAT-1 and RADARSAT-2 operate in the C-band frequency range of the electromagnetic spectrum at a wavelength of 5.6 cm (MacDonald, Dettwiler and associates Ltd, 2009).

- ERS

The European Remote Sensing satellite, ERS-1, was ESA's first Earth Observation satellite; it carried a comprehensive payload including an imaging Synthetic Aperture Radar (SAR). With its launch in July 1991 and the validation of its interferometric capability in September of the same year, an ever-growing set of interferometric data became available to many research groups. ERS-2, which was identical to ERS-1 apart from having an extra instrument, was launched in 1995. Shortly after the launch of ERS-2, ESA decided to link the two spacecraft in the first ever 'tandem' mission, which lasted for nine months, from 16 August 1995 until mid-May 1996. During this time the orbits of the two spacecraft were phased to orbit the Earth only 24 hours apart, thus providing a 24-hour revisit interval.

The huge collection of image pairs from the ERS tandem mission remains uniquely useful even today, because the brief 24-hour revisit time between acquisitions results in much greater interferogram coherence. The increased frequency and level of data available to scientists offered a unique opportunity to generate detailed elevation maps (DEMs) and to observe changes over a very short space of time. Even after the tandem mission ended, the high orbital stability and careful operational control allowed acquisition of more SAR pairs for the remainder of the time that both spacecraft were in orbit, although without the same stringent mission constraints.

The near-polar orbit of ERS in combination with the Earth's rotation (E-W) enables two acquisitions of the same area to be made from two different look angles on each satellite cycle. If just one acquisition geometry is used, the accuracy of the final DEM in geographic coordinates strongly depends on the local terrain slope, and this may not be acceptable for the final user. Combining DEMs obtained from ascending (S-N) and descending (N-S) orbits can mitigate the problems due to the acquisition geometry and

the uneven sampling of the area of interest, especially on areas of hilly terrain. The ERS antenna looks to the right, so for example a slope that is mainly oriented to the West would be foreshortened on an ascending orbit, hence a descending orbit should be used instead. In March 2000 the ERS-1 satellite finally ended its operations. ERS-2 is expected to continue operating for some time, although with a lower accuracy of attitude control since a gyro failure that occurred in January 2001.

4.3.1.1 *What is a strip-map SAR imaging system?*

A SAR imaging system (Curlander, 1991) from a satellite (such as ERS, ENVISAT or RADARSAT) is sketched in Figure 124. A satellite carries a radar with the antenna pointed to the Earth's surface in the plane perpendicular to the orbit (in practice this is not strictly true, because it is necessary to compensate for the Earth's rotation). The inclination of the antenna with respect to the nadir is called the off-nadir angle and in contemporary systems is usually in the range between 20° and 50° . Due to the curvature of the Earth's surface, the incidence angle of the radiation on a flat horizontal terrain is larger than the off-nadir. However, for the sake of simplicity it is assumed here that the Earth is flat, and hence that the incidence angle is equal to the off-nadir angle, as shown in the figure.

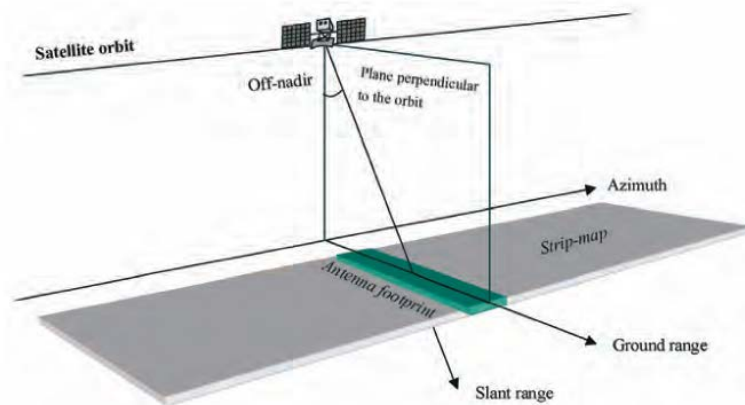


Figure 124: SAR system from a satellite (Ferretti et al., 2007).

Currently, operational satellite SAR systems work in one of the following microwave bands:

- C band – 5.3 GHz (ESA's ERS and ENVISAT, the Canadian RADARSAT, and the US shuttle missions);

- L band – 1.2 GHz (the Japanese J-ERS and ALOS);
- X band – 10 GHz (the German-Italian X-SAR on the shuttle missions).

In the case of ENVISAT, the illuminated area on the ground (the antenna footprint) is about 5 km in the along-track direction (also called the azimuth direction) and about 100 km in the across-track direction (also called the ground range direction).

The direction along the Line of Sight (LOS) is usually called the slant-range direction. The antenna footprint moves at the satellite speed along its orbit. For ENVISAT, the satellite speed is about 7430 m/s in a quasi-polar orbit that crosses the equator at an angle of 9° and an elevation of about 800 km. The footprint traces a swath 100 km wide in ground range on the Earth's surface, with the capability of imaging a strip 445 km long every minute (strip map mode).

A digital SAR image can be seen as a mosaic (i.e. a two-dimensional array formed by columns and rows) of small picture elements (pixels). Each pixel is associated with a small area of the Earth's surface (called a resolution cell). Each pixel gives a complex number that carries amplitude and phase information about the microwave field backscattered by all the scatterers (rocks, vegetation, buildings etc.) within the corresponding resolution cell projected on the ground. Different rows of the image are associated with different azimuth locations, whereas different columns indicate different slant range locations. The location and dimension of the resolution cell in azimuth and slant-range coordinates depend only on the SAR system characteristics. In the ENVISAT case, the SAR resolution cell dimension is about 5 metres in azimuth and about 9.5 metres in slant-range. The distance between adjacent cells is about 4 metres in azimuth and about 8 metres in slant range. The SAR resolution cells are thus slightly overlapped both in azimuth and in slant-range.

4.3.1.2 ***The detected SAR image***

The detected SAR image contains a measurement of the amplitude of the radiation backscattered toward the radar by the objects (scatterers) contained in each SAR resolution cell. This amplitude depends more on the roughness than on the chemical composition of the scatterers on the terrain. Typically, exposed rocks and urban areas show strong amplitudes, whereas smooth flat surfaces (like quiet water basins) show low amplitudes, since the radiation is mainly mirrored away from the radar.

The detected SAR image is generally visualised by means of grey scale levels: bright pixels correspond to areas of strong backscattered radiation (e.g. urban areas), whereas dark pixels correspond to low backscattered radiation (e.g. a quiet water basin).

4.3.1.3 *The phase SAR image*

The radiation transmitted from the radar has to reach the scatterers on the ground and then come back to the radar in order to form the SAR image (two-way travel).

Scatterers at different distances from the radar (different slant ranges) introduce different delays between transmission and reception of the radiation.

Due to the almost purely sinusoidal nature of the transmitted signal, this delay t is equivalent to a phase change ϕ between transmitted and received signals.

The phase change is thus proportional to the two-way travel distance $2R$ of the radiation divided by the transmitted wavelength λ .

This concept is illustrated in Figure 125.

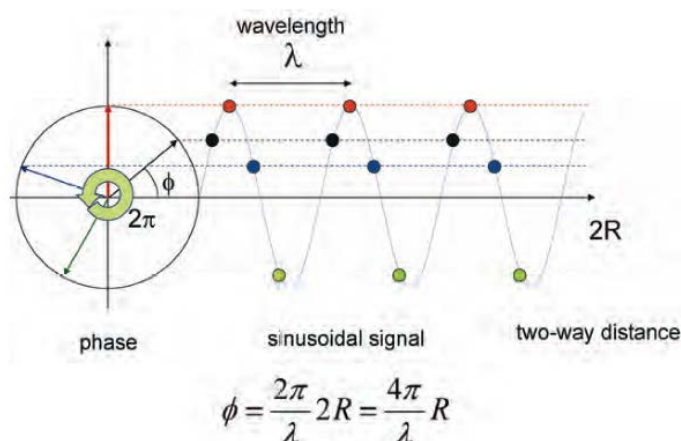


Figure 125: Sinusoidal function $\sin \phi$ is periodic with a 2π radian period.

In the case of a relative narrow-band SAR (i.e. ENVISAT and ERS), the transmitted signal can be assimilated, as first approximation, to a pure sinusoid whose angle or phase ϕ has the following linear dependence on the slant range coordinate r : $\phi = 2\pi r / \lambda$ (where λ is the SAR wavelength). Thus, assuming that the phase of the transmitted signal is zero, the received signal that covers the distance $2R$ travelling from the satellite to the target and back, shows a phase $\phi = 4\pi R / \lambda$ radians (Ferretti et al., 2007).

However, due to the periodic nature of the signal, travel distances that differ by an integer multiple of the wavelength introduce exactly the same phase change. In other words the phase

of the SAR signal is a measure of just the last fraction of the two-way travel distance that is smaller than the transmitted wavelength.

In practice, due to the huge ratio between the resolution cell dimension (of the order of a few metres) and wavelength (~5.6 cm for ENVISAT), the phase change passing from one pixel to another within a single SAR image looks random and is of no practical utility.

4.3.1.4 *Speckle*

The presence of several scatterers within each SAR resolution cell generates the so-called 'speckle' effect that is common to all coherent imaging systems. Speckle is present in SAR, but not in optical images. Homogeneous areas of terrain that extend across many SAR resolution cells (imagine, for example, a large agricultural field covered by one type of cultivation) are imaged with different amplitudes in different resolution cells. The visual effect is a sort of 'salt and pepper' screen superimposed on a uniform amplitude image.

This speckle effect is a direct consequence of the superposition of the signals reflected by many small elementary scatterers (those with a dimension comparable to the radar wavelength) within the resolution cell. These signals, which have random phase because of multiple reflections between scatterers, add to the directly reflected radiation. From an intuitive point of view, the resulting amplitude will depend on the imbalance between signals with positive and negative sign.

Speckle has an impact on the quality and usefulness of detected SAR images. Typically, image segmentation suffers severely from speckle. However, by taking more images of the same area at different times or from slightly different look angles, speckle can be greatly reduced: averaging several images tends to cancel out the random amplitude variability and leave the uniform amplitude level unchanged (Ferretti et al., 2007).

4.3.2 **SAR resolution: cell projection on the ground**

The terrain area imaged in each SAR resolution cell (called the ground resolution cell) depends on the local topography. It strongly depends on the terrain slope in the plane perpendicular to the orbit (ground range direction), and on the terrain slope in the azimuth direction. The dimension of the ground resolution cell in azimuth is related to that of the SAR resolution cell by the usual perspective deformation we experience every day looking at surfaces from different angles (e.g. a postcard seen at 90 degrees is a line).

The dimension of the ground resolution cell in range is related to that of the SAR resolution cell by an unusual perspective deformation. Figure 126 shows how slant-range is projected

onto the ground. Here five identical slant-range resolution cells are shown. The first two cells correspond to flat terrain and they contain three triangles each. The third cell contains seven of these triangles due to the positive slope of the terrain. Finally the fourth and fifth cells contain less than three triangles due to the negative slope of the terrain.

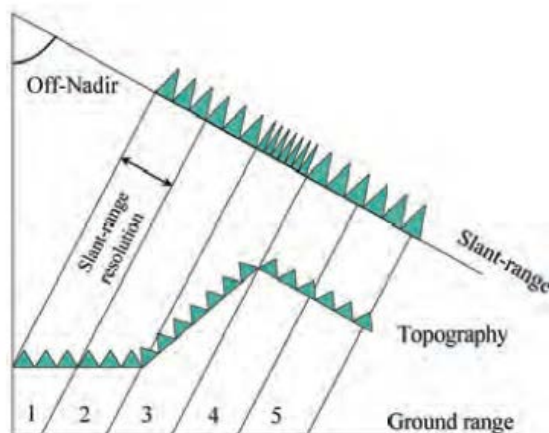


Figure 126: Effect of terrain on the SAR image.

For SAR resolution cells in the plane perpendicular to the orbit, the part of the terrain imaged in each resolution cell clearly depends on the topography (Ferretti et al., 2007).

As the terrain slope increases with respect to a flat horizontal surface (i.e. as the normal to the terrain moves toward the line of sight (LOS)), the ground resolution cell dimension in range increases. This effect is called foreshortening. When the terrain slope is close to the radar off-nadir angle, the cell dimension becomes very large and all the details are lost. Moreover, when the terrain slope exceeds the radar off-nadir angle the scatterers are imaged in reverse order and superimposed on the contribution coming from other areas. This effect is called layover, and is sketched in Figure 127.

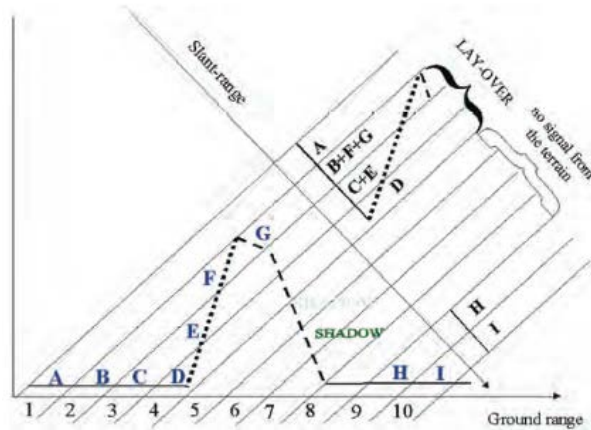


Figure 127: Layover and shadow effects.

Depending on the terrain slope, scatterers that are located at increasing ground range positions can be imaged in reverse order by the SAR system (points D, E, F and G). Moreover they are imaged in the same SAR resolution cells as scatterers B and C, which belong to a different area on the ground (layover). On the other side of the elevation profile, scatterers located between points G and H cannot be illuminated by the radar since they are in shadow. As a consequence, SAR resolution cells from 5 to 8 do not contain any signal from the ground and they generate a dark gap on the detected image (Ferretti et al., 2007).

On the other hand, when the terrain slope decreases with respect to the flat horizontal reference surface the resolution cell dimension decreases. The minimum resolution cell dimension (i.e. equal to the slant range resolution) is reached when the terrain is parallel to the LOS. This is also the lower slope limit that can be imaged at all by a SAR system, since beyond this angle the terrain is in shadow. As an example, in the case of ENVISAT systems, the resolution cell dimension as a function of the terrain slope is shown in Figure 128.

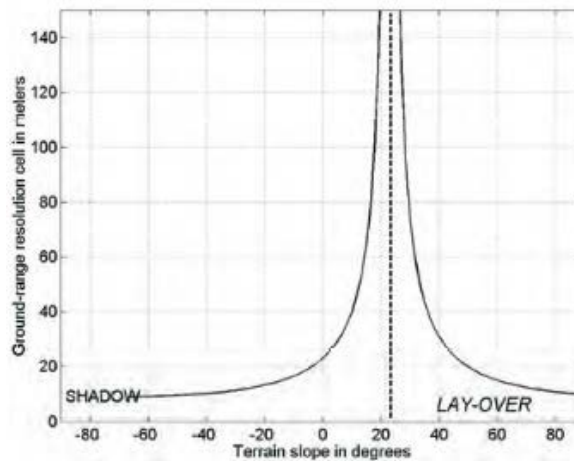


Figure 128: ENVISAT resolution cell dimension in ground range as a function of the terrain slope. The vertical dotted line indicates the incidence angle relative to a flat horizontal terrain (23°) (Ferretti et al., 2007).

It should be pointed out that foreshortening has a strong impact on the amplitude of the detected SAR image. Foreshortened areas are brighter on the image because the resolution cell is larger (hence more power is backscattered towards the satellite) and the incidence angle is steeper.

4.3.3 Applications and limits

A satellite SAR can observe the same area from slightly different look angles. This can be done either simultaneously (with two radars mounted on the same platform) or at different times by exploiting repeated orbits of the same satellite. The latter is the case for ERS-1, ERS-2 and ENVISAT. For these satellites, time intervals between observations of 1, 35, or a multiple of 35 days are available.

The distance between the two satellites (or orbits) in the plane perpendicular to the orbit is called the interferometer baseline (see Figure 129) and its projection perpendicular to the slant range is the perpendicular baseline.

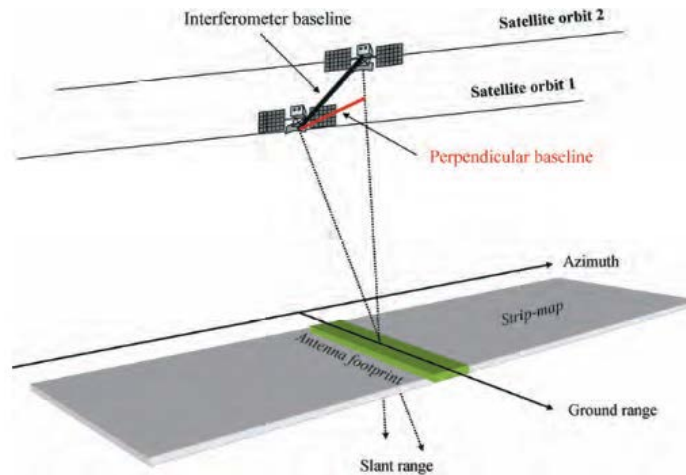


Figure 129: Geometry of a satellite interferometric SAR system.
The orbit separation is called the interferometer baseline, and its projection perpendicular to the slant range direction is one of the key parameters of SAR interferometry (Ferretti et al., 2007).

The SAR interferogram is generated by cross-multiplying, pixel by pixel, the first SAR image with the complex conjugate of the second (Bamler et al., 1998, Massonnet et al., 1998, Franceschetti et al., 1999, Rosen et al., 2000).

Thus, the interferogram amplitude is the amplitude of the first image multiplied by that of the second one, whereas its phase (the interferometric phase) is the phase difference between the images.

4.3.3.1 ***Terrain altitude measurement through the interferometric phase***

Let us suppose we have only one dominant point scatterer in each ground resolution cell that does not change over time.

These point scatterers are observed by two SARs from slightly different look angles as shown in Figure 129. In this case the interferometric phase of each SAR image pixel would depend only on the difference in the travel paths from each of the two SARs to the considered resolution cell. Any possible phase contribution introduced by the point scatterers does not affect the interferometric phase since it is cancelled out by the difference.

Once a ground reference point has been identified, the variation of the travel path difference Δr that results in passing from the reference resolution cell to another can be given by a simple expression (an approximation that holds for small baselines and resolution cells that are not too far apart) that depends on a few geometric parameters shown in Figure 130.

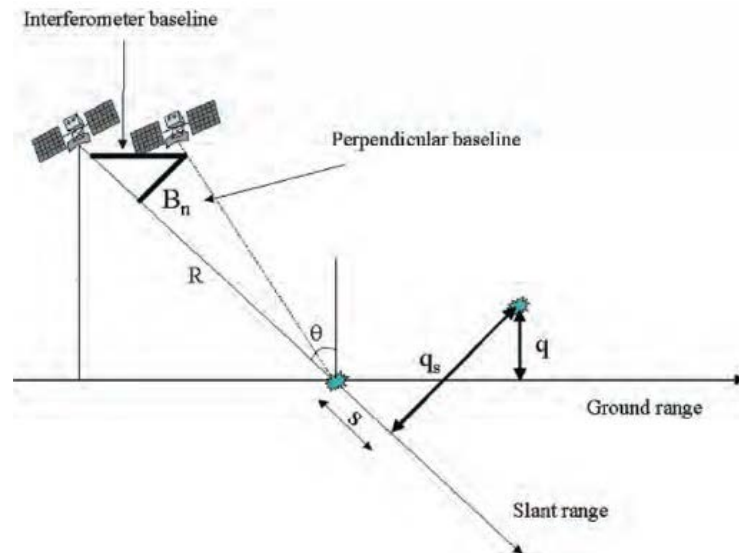


Figure 130: Geometric parameters of a satellite interferometric SAR system (Ferretti et al., 2007).

The parameters are:

1. The perpendicular baseline B_n ;
2. The radar-target distance R ;
3. The displacement between the resolution cells along the perpendicular to the slant range, q_s .

The following approximated expression of Δr holds:

$$\Delta r = -2 \frac{B_n q_s}{R}$$

The interferometric phase variation $\Delta\phi$ is then proportional to Δr divided by the transmitted wavelength λ :

$$\Delta\phi = \frac{2\pi\Delta r}{\lambda} = \frac{4\pi}{\lambda} \frac{B_n q_s}{R}$$

INTERFEROGRAM FLATTENING

The interferometric phase variation can be split into two contributions:

1. A phase variation proportional to the altitude difference q between the point targets, referred to a horizontal reference plane;
2. A phase variation proportional to the slant range displacement s of the point targets.

$$\Delta\phi = -\frac{4\pi}{\lambda} \frac{B_n q}{R \sin \theta} - \frac{4\pi}{\lambda} \frac{B_n s}{R \tan \theta}$$

where θ is the radiation incidence angle with respect to the reference.

It should be noted that the perpendicular baseline is known from precise orbital data, and the second phase term can be computed and subtracted from the interferometric phase. This operation is called interferogram flattening and, as a result, it generates a phase map proportional to the relative terrain altitude (Ferretti et al., 2007).

ALTITUDE OF AMBIGUITY

The altitude of ambiguity h_a is defined as the altitude difference that generates an interferometric phase change of 2π after interferogram flattening. The altitude of ambiguity is inversely proportional to the perpendicular baseline:

$$h_a = \frac{\lambda R \sin \theta}{2B_n}$$

In the ENVISAT case with $\lambda = 5.6$ cm, $\theta = 23^\circ$, and $R = 850$ km, the following expression holds (in metres):

$$h_a \approx \frac{9300}{B_n}$$

As an example, if a 100 metre perpendicular baseline is used, a 2π change of the interferometric phase corresponds to an altitude difference of about 93 metres. In principle, the higher the baseline the more accurate the altitude measurement, since the phase noise (see next section) is equivalent to a smaller altitude noise. However, there is an upper limit to the perpendicular baseline, over which the interferometric signals decorrelate and no fringes can be generated. In conclusion there is an optimum perpendicular baseline that maximises the signal to noise power ratio (where the signal is terrain altitude).

PHASE UNWRAPPING

The flattened interferogram provides an ambiguous measurement of the relative terrain altitude due to the 2π cyclic nature of the interferometric phase. The phase variation between two points on the flattened interferogram provides a measurement of the actual altitude variation, after deleting any integer number of altitudes of ambiguity (equivalent to an integer number of 2π phase cycles). The process of adding the correct integer multiple of 2π to the interferometric fringes is called phase unwrapping.

There are several well-known phase unwrapping techniques; however it should be noted that usually phase unwrapping does not have a unique solution, and a priori information should be exploited to get the right solution (Ferretti et al., 2007).

4.3.3.2 *Terrain motion measurement: Differential Interferometry*

Suppose that some of the point scatterers on the ground slightly change their relative position in the time interval between two SAR observations (as, for example, in the event of subsidence, landslide, earthquake, etc.). In such cases the following additive phase term, independent of the baseline, appears in the interferometric phase:

$$\Delta\phi_s = \frac{4\pi}{\lambda} d$$

where d is the relative scatterer displacement projected on the slant range direction.

This means that after interferogram flattening, the interferometric phase contains both altitude and motion contributions:

$$\Delta\phi = -\frac{4\pi}{\lambda} \frac{B_n q}{R \sin \theta} + \frac{4\pi}{\lambda} d$$

Moreover, if a digital elevation model (DEM) is available, the altitude contribution can be subtracted from the interferometric phase (generating the so-called differential interferogram) and the terrain motion component can be measured (Ferretti et al., 2007).

4.3.3.3 *The atmospheric contribution to the interferometric phase*

When two interferometric SAR images are not simultaneous, the radiation travel path for each can be affected differently by the atmosphere. In particular, different atmospheric humidity,

temperature and pressure between the two takes will have a visible consequence on the interferometric phase.

This effect is usually confined within a 2π peak-to-peak interferometric phase change along the image with a smooth spatial variability (from a few hundred metres to a few kilometres). The effect of such a contribution impacts on both altitude (especially in the case of small baselines) and terrain deformation measurements.

4.3.3.4 ***Other phase noise sources***

In the previous sections it has been hypothesised that only one dominant stable scatterer is present in each resolution cell. This is seldom the case in reality. We should analyse the situation where many elementary scatterers are present in each resolution cell (distributed scatterers), each of which may change in the time interval between two SAR acquisitions. The main effect of the presence of many scatterers per resolution cell and their changes in time is the introduction of phase noise (Ferretti et al., 2007).

Three main contributions to the phase noise should be taken into consideration:

1. Phase noise due to temporal change of the scatterers In the case of a water basin or densely vegetated areas, the scatterers change totally after a few milliseconds, whereas exposed rocks or urban areas remain stable even after years. The coastland of the northern Caspian sea appears in an intermediated situation: it is mainly a rural territory with reduced vegetation. Therefore the SAR applicability is a challenge
2. Phase noise due to different look angle Speckle will change due to the different combination of elementary echoes even if the scatterers do not change in time. The most important consequence of this effect is that there exists a critical baseline over which the interferometric phase is pure noise. The critical baseline depends on the dimension of the ground range resolution cell (and thus also on the terrain slope), on the radar frequency, and on the sensor-target distance. This phase noise term, however, can be removed from the interferogram by means of a pre-processing step of the two SAR images known as spectral shift or common band filtering.
3. Phase noise due to volume scattering The critical baseline reduces in the case of volume scattering when the elementary scatterers are not disposed on a plane surface but occupy a volume (e.g. the branches of a tree). In this case the speckle change depends also on the depth of the volume occupied by the elementary scatterers.

4.3.3.5 *Coherence maps*

The phase noise can be estimated from the interferometric SAR pair by means of the local coherence γ . The local coherence is the cross-correlation coefficient of the SAR image pair estimated over a small window (a few pixels in range and azimuth), once all the deterministic phase components (mainly due to the terrain elevation) are compensated for.

The deterministic phase components in such a small window are, as a first approximation, linear both in azimuth and slant-range. Thus, they can be estimated from the interferogram itself by means of well-known methods of frequency detection of complex sinusoids in noise (e.g. 2-D Fast Fourier Transform (FFT)).

The coherence map of the scene is then formed by computing the absolute value of γ on a moving window that covers the whole SAR image. The coherence value ranges from 0 (the interferometric phase is just noise) to 1 (complete absence of phase noise). The exact relation between the interferometric phase dispersion and coherence can be found through complicated mathematical computation (Lee et al., 1994). However, if the number of looks (NL) is greater than four, then independent pixels with the same coherence are averaged after topography compensation (multi-look interferogram) and the following simple approximation holds (Rosen et al., 2000):

$$\sigma_{\phi} = \frac{1}{\sqrt{2NL}} \frac{\sqrt{1-\gamma^2}}{\gamma}$$

From a mathematical point of view, this formula is a good approximation of the exact phase dispersion shown in Figure 131 when $\sigma_{\phi} < 12^{\circ}$. That is, when NL is large and γ close to one. However, for most practical applications of SAR interferometry, the approximated formula can be suitably exploited for coherence values higher than 0.2 and $NL > 4$. A comparison between the exact and approximated curves is shown in Figure 132.

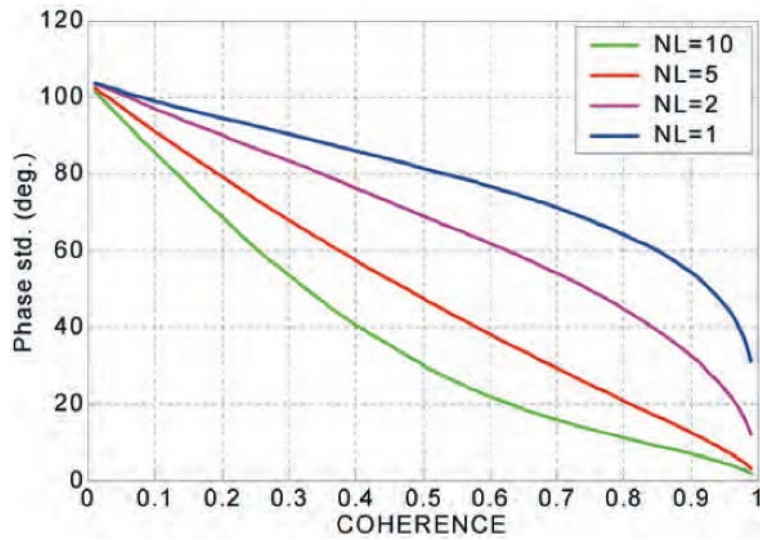


Figure 131: Interferometric phase dispersion (degrees) as a function of the coherence for varying numbers of looks (NL) (Ferretti et al., 2007).

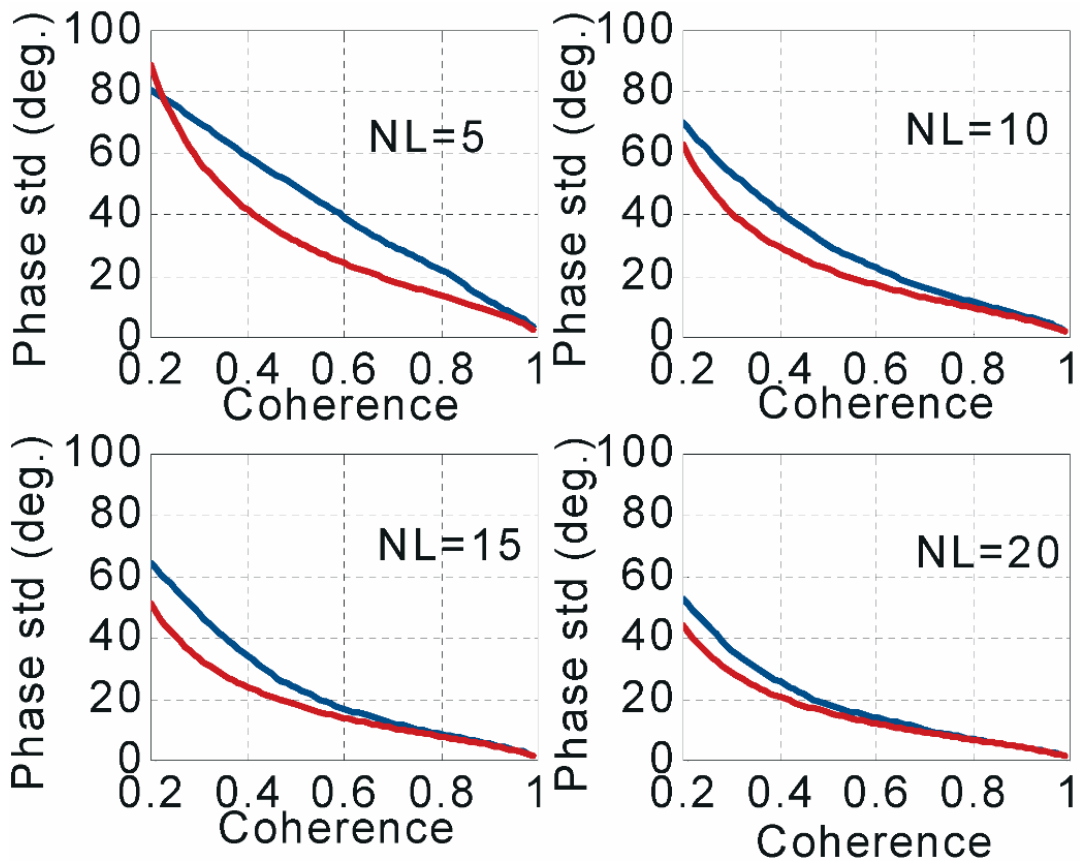


Figure 132: Interferometric phase dispersion exact values (blue curves) and approximated ones (red curves) (Ferretti et al., 2007).

4.3.3.6 **Multiple Short Baseline Analysis (SBAS)**

The Small BAseline Subset technique is a DInSAR approach that relies on the use of a large number of SAR acquisitions and implements an easy combination of a properly chosen set of multilook DInSAR interferograms computed from these data, finally leading to the generation of mean deformation velocity maps and displacement time series.

A detailed discussion on the basic SBAS approach is clearly outside the scope of this work; accordingly, we highlight in this section what are the key issues of the algorithm and refer to Berardino et al. (2002) for a more detailed analysis.

Let us start our discussion by considering a set of $N+1$ SAR images relative to the same area, acquired at the ordered times (t_0, \dots, t_N) ; it is also assumed that they are co-registered with respect to an image referred to as master. This allows us to identify a common (reference) spatial grid. The starting point of the SBAS technique is represented by the generation of a number, say M , of multilook DInSAR interferograms that involve the previously mentioned set of $N+1$ SAR acquisitions. Note also that each of these interferograms is calibrated with respect to a single pixel located in an area that can be assumed stable or, at least, with a known deformation behaviour; this point is often referred to as reference SAR pixel (Casu et al., 2006).

Consider a generic pixel of azimuth and range coordinates (x, r) ; the expression of the generic j -th interferogram computed from the SAR acquisitions at times t_B and t_A , according to Berardino et al. (2002), will be the following:

$$\begin{aligned} \delta\phi_j(x, r) &= \phi(t_B, x, r) - \phi(t_A, x, r) \\ &\approx \frac{4\pi}{\lambda} [d(t_B, x, r) - d(t_A, x, r)] + \Delta\phi_j^{\text{topo}}(x, r) \\ &\quad + \Delta\phi_j^{\text{atm}}(t_B, t_A, x, r) + \Delta n_j(x, r) \end{aligned}$$

wherein j ranges between 1 and M , λ is the transmitted signal central wavelength, $\phi(t_B, x, r)$ and $\phi(t_A, x, r)$ represent the phases of the two images involved in the interferogram generation and $d(t_B, x, r)$ and $d(t_A, x, r)$ are the radar line of sight (LOS) projections of the cumulative deformations at times t_B and t_A , with respect to the instant t_0 assumed as a reference and implying $\phi(t_0, x, r) = 0$ for each (x, r) . Moreover, for what concerns the right hand side of the last identity in equation, the second term $\Delta\phi_j^{\text{topo}}(x, r)$ accounts for possible topographic artifacts that can be present in the Digital Elevation Model (DEM) used for the interferogram generation. Finally, the term $\Delta\phi_j^{\text{atm}}(t_B, t_A, x, r)$ accomplishes for possible inhomogeneities

between the two acquisitions, usually referred to as atmospheric phase artifacts (Goldstein, 1995), while the last factor $\Delta n_j(x, r)$ accounts for the noise effects referred to as decorrelation phenomena (Zebker et al., 1992).

The main tasks of the SBAS procedure can be synthesized as follows: first of all, the coherent pixels of the interferograms, i.e., those pixels characterized by small values of the factor $\Delta n_j(x, r)$, $j=1, \dots, M$ must be identified. Subsequently, the algorithm must provide an estimate of the deformation time series $d(t_i, x, r)$, for t_i ranging between t_0 and t_N , and for each coherent pixel. In order to achieve this task, the information relevant to all the interferograms have to properly combine to detect and cancel out the topographic and atmospheric signal components highlighted in the previous equation.

Therefore, the key steps involved in the displacement time series retrieval, implemented via the SBAS algorithm, are the following:

- The data pairs used to generate the multilook DInSAR interferograms are properly chosen with the key objective to mitigate the decorrelation phenomena (Zebker et al., 1992). In particular, this data pairs selection involves the introduction of constraints on the allowed maximum spatial and temporal separation (baseline) between the orbits relevant to the interferometric SAR image couples and has a main goal of maximizing the number of coherent pixels in the multilook interferograms;
- A retrieval step (usually referred to as phase unwrapping operation) of the original (unwrapped) phase $\delta\Phi_j(x, r)$ from the modulus- 2π restricted (wrapped) signal directly computed from the generated multilook interferograms, is carried out. This operation is implemented via the procedure described by Costantini et al. (1999). It allows one to process data available on a sparse grid that in this case is relevant to the pixels remaining coherent in the investigated interferograms. The basic algorithm of Costantini et al. (1999) is also integrated with a region growing procedure allowing one to improve the algorithm performances in areas with relatively low coherence;
- The Singular Value Decomposition (SVD) method is applied to “combine” the unwrapped DInSAR interferograms. In particular, the SBAS approach implies the solution, on a (coherent) pixel by pixel basis, of the linear system of equations in order to get an estimate of the deformation time series. However, the previously mentioned baseline constraints in the data pair selection may have as a consequence that the SAR data involved in the interferograms generation belong to “independent subset”, thus causing the system of equations to have infinite solutions. Accordingly, the application of the SVD method within the SBAS technique allows one to regularize the problem and to generate the minimum norm Least Square (LS) solution of the system of equations that, as shown by Lanari et al.

(2004), generally guarantees a physically sound solution; in any case, the tendency is to minimize the number of data subsets;

- As a final step of the SBAS procedure, a space–time filtering operation is carried out in order to estimate and subsequently remove possible artifacts due to atmospheric inhomogeneities between the acquisition pairs. This operation is based on the observation that the atmospheric signal phase component is highly correlated in space but poorly in time, see Ferretti et al. (2000). Accordingly, the undesired atmospheric phase signal is estimated from the time series computed via the SVD technique through the cascade of a lowpass filtering step in the two-dimensional spatial domain followed by a temporal highpass filtering operation. Moreover, this operation also allows one to detect possible orbital fringes caused by inaccuracies in the SAR sensors orbit information (Lanari et al., 2004). Indeed, such errors are also typically not correlated in time but strongly correlated in space and they are often well approximated by spatial ramps usually referred to as orbital ramps. Based on these considerations, an estimate of these orbital patterns is performed in the approach by searching for the best-fit ramp to the temporal high-pass / spatially low-pass time series signal component; following this step, the detected ramps are removed from each differential interferograms. Accordingly, we do not use additional information obtained from a set of ground control points to get rid of these orbital errors. The removal of the estimated atmospheric artifacts and orbital ramps finally leads to the generation of the required deformation time series.

In summary the SBAS technique, whose block diagram is sketched in Figure 133, allows one to satisfy two key requirements: to follow the temporal evolution of the detected displacements by using nearly all the available SAR acquisitions and to preserve the capabilities of the system to provide spatially dense deformation maps, which is a key issue of conventional DInSAR interferometry.

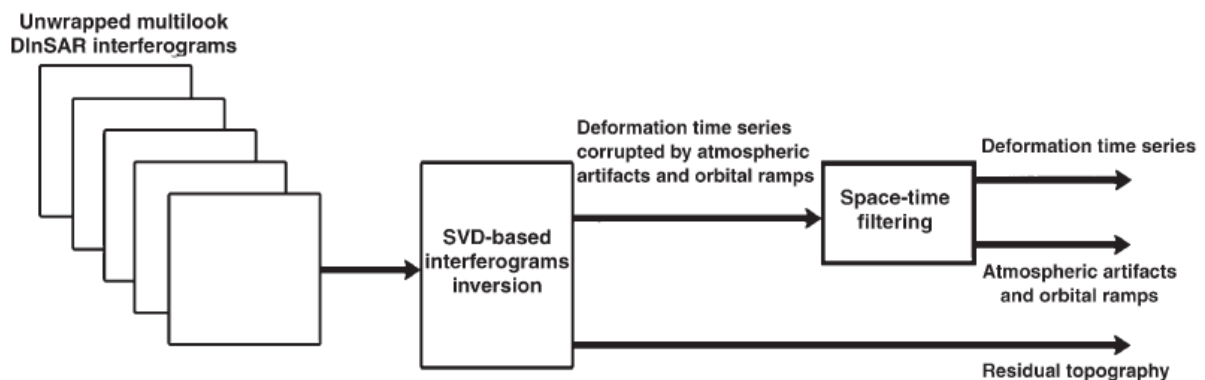


Figure 133: SBAS algorithm block diagram (Casu et al., 2006).

4.3.3.7 *Interferometric Point Target Analysis (IPTA)*

Interferometric Point Target Analysis, or Persistent (also known as permanent) Scatterer Interferometry, (PSI) uses a different approach than SBAS for processing SAR imagery. PSI (Ferretti et al. 2000, 2001) involves the processing of numerous, typically more than 30, interferograms to identify a network of persistent, temporally stable, highly reflective ground features-permanent scatterers. These scatterers typically are cultural features of the developed landscape such as buildings, utility poles, roadways, etc. or natural stable reflectors as exposed rocks.

The phase history of each scatterer is extracted by estimating a predefined displacement model (typically a linear, constant-rate model) to provide interpolated maps of average annual displacements, or the displacement history, up to the length of a SAR data archive, of each individual scatterer, thus providing a “virtual” GPS network with “instant” history. By focusing on temporally stable targets in the image, temporal decorrelation is avoided or strongly reduced. Furthermore, most of the strong and stable reflectors identified represent small individual scattering elements. For this type of scatterer though, a larger fraction of the reflected energy remains coherent for larger interferometric baselines, allowing a larger set of SAR scenes to be used in the analysis (Galloway et al., 2007).

Finally, the large number of observations available in a typical SAR data set used in a PSI analysis supports a statistical analysis of the observed phase histories in space and time, and depending on the characteristics of the displacements, it is often possible to separate the phase differences caused by atmospheric variations and uncompensated topography from those due to surface displacements.

IPTA has been applied primarily in urban environments, where the density of stable scatterers (e.g. buildings, roadways, poles, etc.) typically is quite high (as many as a few hundred per square kilometre). Over natural terrain, the paucity of stable targets severely limits PSI’s successful application. A small number of investigations have demonstrated a successful application of PSI in “rural” terrain (Usai 2001; Kircher 2004, Teatini et al., 2007). However, the investigations in the Netherlands and western Germany, used stable targets such as houses and other man-made features that were present in sufficient numbers. Hooper et al. (2004) have proposed a modified algorithm for natural terrain, but this has been demonstrated for relatively dry conditions and it is questionable whether their approach will work over agricultural areas prone to temporal decorrelation owing to variable moisture and crop conditions.

The PSI technique is a relatively recent development that can reduce the principal errors inherent in InSAR processing methods, errors caused by temporal and geometrical decorrelation and atmospheric artifacts. A potentially severe limitation of PSI, particularly

where scatterer density is small and displacement magnitudes are large, is the necessity to determine a motion model a priori, which is used in resolving phase ambiguities.

Another limitation of PSI is the difficulty of identifying stable targets in rural and agricultural areas. The majority of PSI applications have focused on urban areas, e.g. Paris, France (Fruneau et al., 2000); San Francisco Bay Area, USA (Ferretti et al. 2004); Bangkok, Thailand (Worawattanamateekul et al. 2004); Phoenix, USA (Beaver et al. 2005); Arno River Basin-Florence, Italy; (Canuti et al. 2005); Berlin, Germany and Las Vegas, USA (Kampes, 2005); London (NPA, 2006). Some applications in rural (Teatini et al., 2007) as well as desert areas (Vasco et al., 2010) have been recently performed.

4.3.4 Innovative aspects of InSAR application to the study area

On the north-east Caspian sea relatively large series of satellite SAR data exist for the archives of the ENVISAT ASAR and RADARSAT-1 sensors. Considering the experimental application of the technique in this area we decided to perform our study with ENVISAT ASAR data; the cost of ENVISAT ASAR data is one order of magnitude lower than that of RADARSAT-1 while temporal sampling of acquisitions, ground spatial resolution and frequency of the SAR sensors are in our case similar. Because the area of interest is predominantly desert, there are not many urban areas, the topography is flat, and subsidence maps are required at regional scale, we decided to follow a processing approach based on multiple short baseline interferometry (SBAS). The process has been carried out in collaboration with GAMMA Remote Sensing; they have extensive experience in active and passive microwave remote sensing techniques, theoretical and empirical modelling, and applications. This experience has been gained during their work at universities and laboratories in Switzerland, UK, Sweden, Germany and USA, and in the frame of GAMMA's research projects.

The interferometric processing can be divided in several logical steps (for each step engineering tests are applied):

- 1) Data acquisition;
- 2) SAR pre-processing;
- 3) SAR processing;
- 4) Preparation of topographic reference;
- 5) Image registration;
- 6) Differential INSAR processing;
- 7) Phase unwrapping;

- 8) Multi-baseline interferometry;
- 9) Phase to deformation rate transformation;
- 10) Geocoding and consistency testing;
- 11) Finalization of the product.

Several aspects of the interferometric application make this case study scientifically innovative: first of all, this work represent the first successfull DInSAR application in the Kazakh coastal zone.

In addition, the characteristics of the study area do not allow a standard application. Among the factors of uncertainty it has to be underlined the following ones:

- The area presents a low degree of urbanisation and the absence of man-made structures for the majority of the investigated areas did not ensure the signal coherence;
- The land-sea transitional area is widely affected by storm surges, introducing errors in signal coherence;
- The type of soils in the frames of study did not guarantee a coherent response to radar signal;
- The presence of snow in several radar images made them useless.

These characteristics led to an innovative DInSAR application, characterised by several specific solutions described in detail the chapters below.

The evaluation of existing land subsidence have been performed excluding areas covered by on-shore extraction activities of Oil&Gas companies.

4.3.4.1 ***Data acquisition***

Data acquisition was performed from the SARCOM consortium. Three frames, labelled, from north to south, as Z1, Z2 and Z3 were considered.

- Number 1 is from ENVISAT ASAR Track 464, Frame 2653, Swath I2 in descending orbit.
- Number 2 is from ENVISAT ASAR Track 421, Frame 2673, Swath I2 in descending orbit.
- Number 3 is from ENVISAT ASAR Track 464, Frame 2697, Swath I2 in descending orbit.

In Table 15 dates and orbits of the ordered ENVISAT ASAR data are listed. Quick-looks are shown in Figure 134.

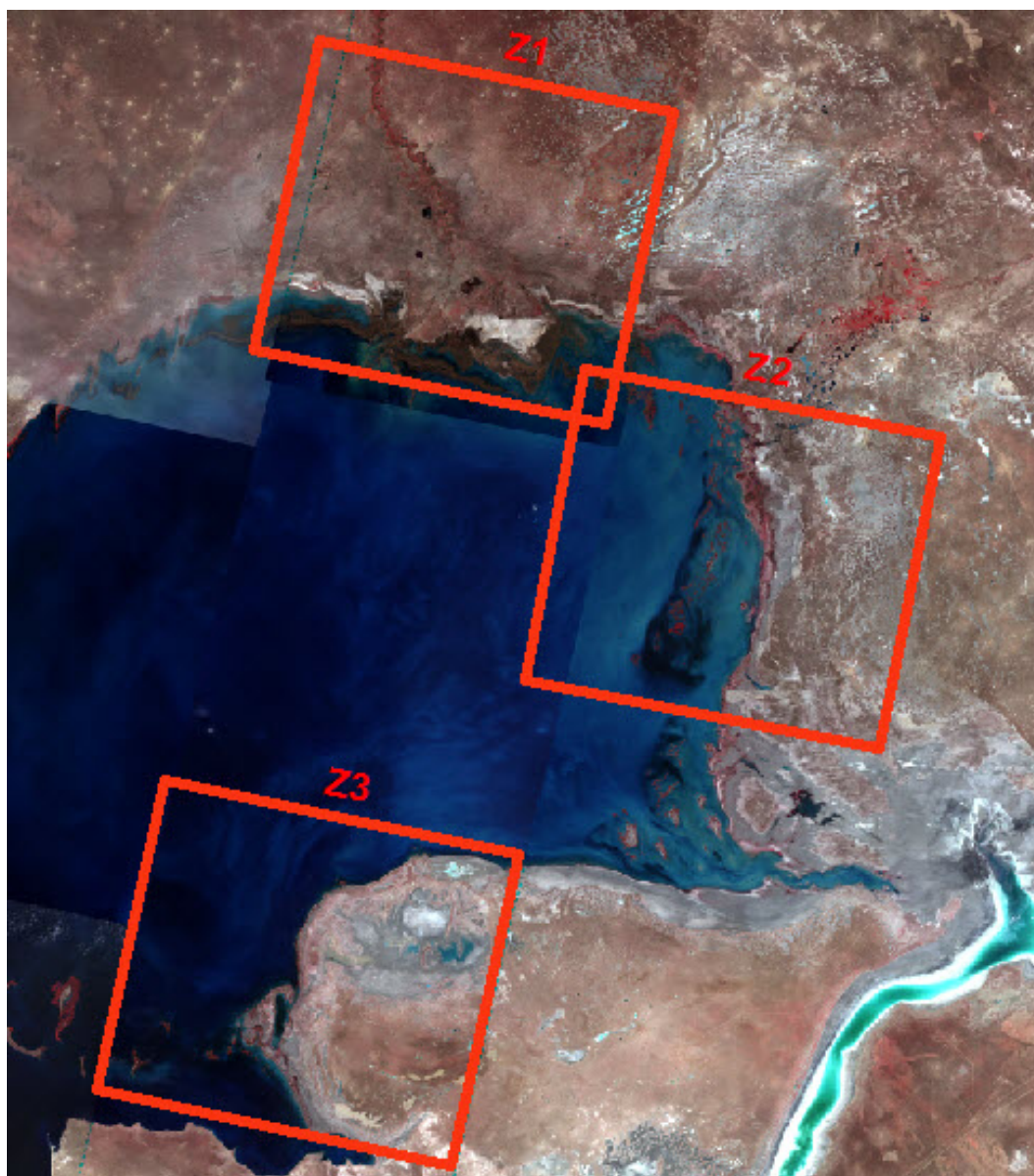


Figure 134: Frames of SBAS application in the area of interest.

Table 15: Dates and orbits of acquisition.

Frame Z1		Frame Z2		Frame Z3	
Date	Orbit	Date	Orbit	Date	Orbit
8/9/2003	7532	7/21/2004	12499	8/9/2003	7532
11/22/2003	9035	1/12/2005	15004	11/22/2003	9035

Frame Z1		Frame Z2		Frame Z3	
Date	Orbit	Date	Orbit	Date	Orbit
4/10/2004	11039	2/16/2005	15505	4/10/2004	11039
6/19/2004	12041	3/23/2005	16006	6/19/2004	12041
7/24/2004	12542	4/27/2005	16507	7/24/2004	12542
1/15/2005	15047	6/1/2005	17008	1/15/2005	15047
2/19/2005	15548	7/6/2005	17509	2/19/2005	15548
3/26/2005	16049	8/10/2005	18010	3/26/2005	16049
4/30/2005	16550	9/14/2005	18511	4/30/2005	16550
6/4/2005	17051	10/19/2005	19012	6/4/2005	17051
7/9/2005	17552	11/23/2005	19513	7/9/2005	17552
8/13/2005	18053	4/12/2006	21517	8/13/2005	18053
9/17/2005	18554	5/17/2006	22018	9/17/2005	18554
10/22/2005	19055	6/21/2006	22519	10/22/2005	19055
11/26/2005	19556	7/26/2006	23020	11/26/2005	19556
4/15/2006	21560	8/30/2006	23521	4/15/2006	21560
5/20/2006	22061	10/4/2006	24022	5/20/2006	22061
6/24/2006	22562	11/8/2006	24523	6/24/2006	22562
7/29/2006	23063	1/17/2007	25525	7/29/2006	23063
9/2/2006	23564	2/21/2007	26026	9/2/2006	23564
10/7/2006	24065	3/28/2007	26527	10/7/2006	24065
11/11/2006	24566	5/2/2007	27028	11/11/2006	24566
12/16/2006	25067	6/6/2007	27529	12/16/2006	25067
1/20/2007	25568	7/11/2007	28030	1/20/2007	25568
3/31/2007	26570	8/15/2007	28531	3/31/2007	26570
5/5/2007	27071	9/19/2007	29032	5/5/2007	27071
6/9/2007	27572	10/24/2007	29533	6/9/2007	27572

Frame Z1		Frame Z2		Frame Z3	
Date	Orbit	Date	Orbit	Date	Orbit
7/14/2007	28073	11/28/2007	30034	7/14/2007	28073
8/18/2007	28574	10/8/2008	34543	8/18/2007	28574
9/22/2007	29075	11/12/2008	35044	9/22/2007	29075
10/27/2007	29576	12/17/2008	35545	10/27/2007	29576
12/1/2007	30077	1/21/2009	36046	12/1/2007	30077
10/11/2008	34586	2/25/2009	36547	10/11/2008	34586
12/20/2008	35588			12/20/2008	35588
1/24/2009	36089			1/24/2009	36089
2/28/2009	36590			2/28/2009	36590

4.3.4.2 *Pre-processing*

The pre-processing steps include data download, check of ENVISAT raw data for missing lines, and the addition of the precision orbits from DELFT state vectors. The raw data quality control has been done using the GAMMA MSP software. For frames 1 and 3 one acquisition, i.e. those of 2004.07.24 and 2006.04.15, respectively, had not be further analysed because of a large number of missing lines.

4.3.4.3 *SAR processing*

The SAR processing has been done using the GAMMA MSP software. This SAR processing step includes:

- Doppler centroid estimation and optimization, checked by the first two components of the Doppler polynomial,
- Autofocus, assured by the SNR (signal to noise ratio) and the Doppler ambiguity error estimate,
- Radiometric calibration by the average backscattering coefficient..

The radiometric calibration is checked for frames Z1, Z2 and Z3. A total of 35, 33 and 35 images have been well focused (Figure 135, Figure 136 and Figure 137).

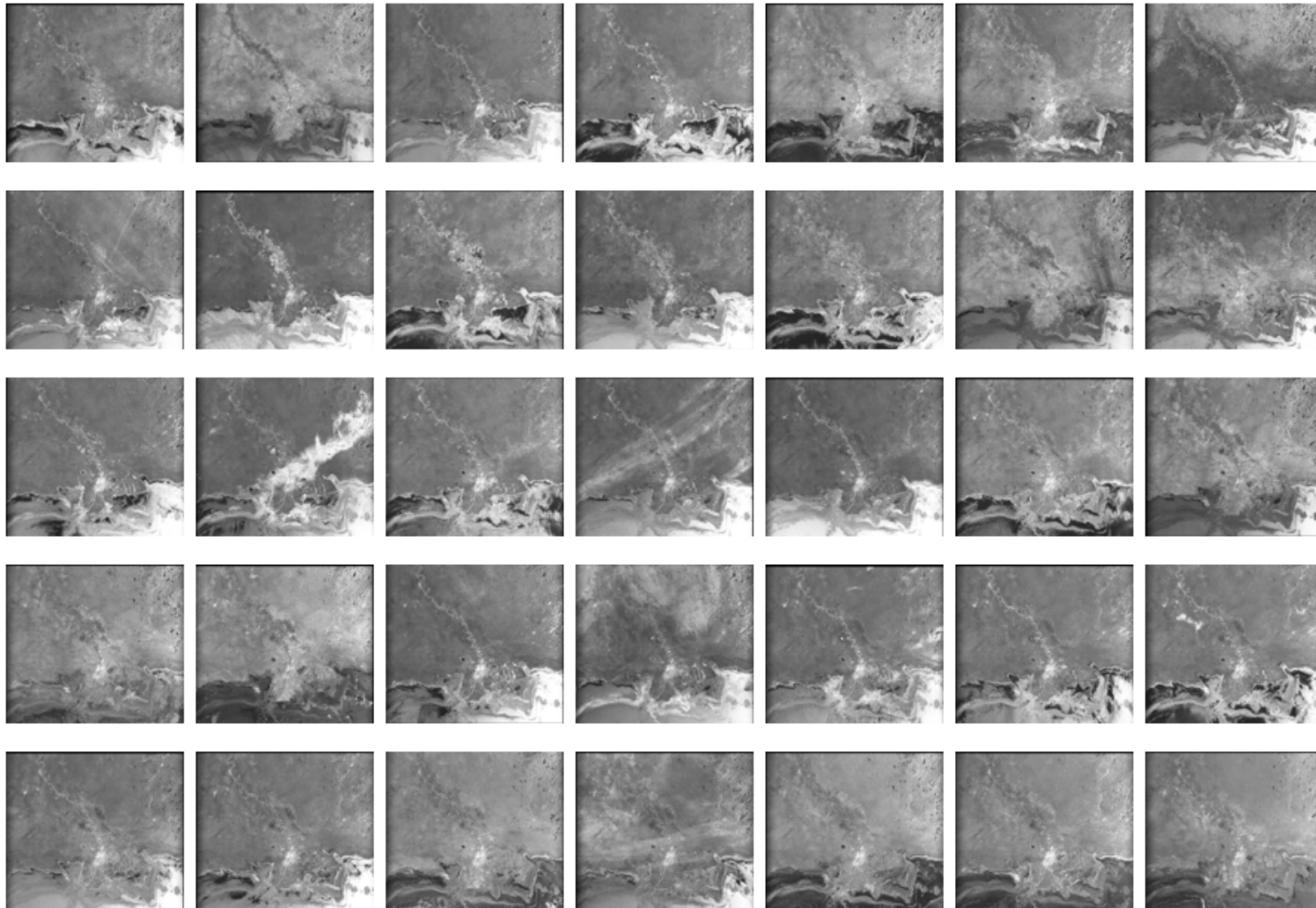


Figure 135: Images focused on Frame Z1.

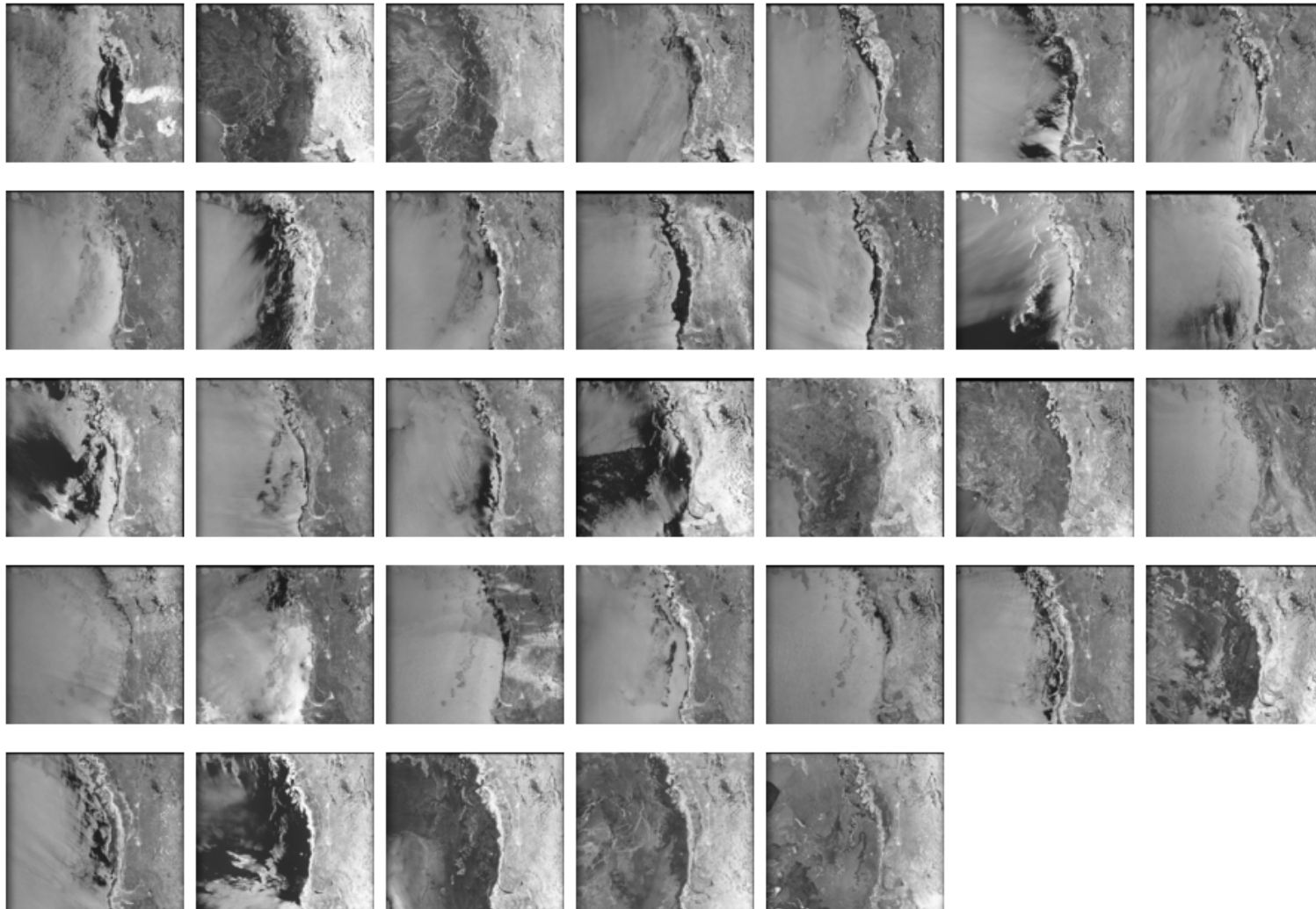


Figure 136: Images focused on Frame Z2.

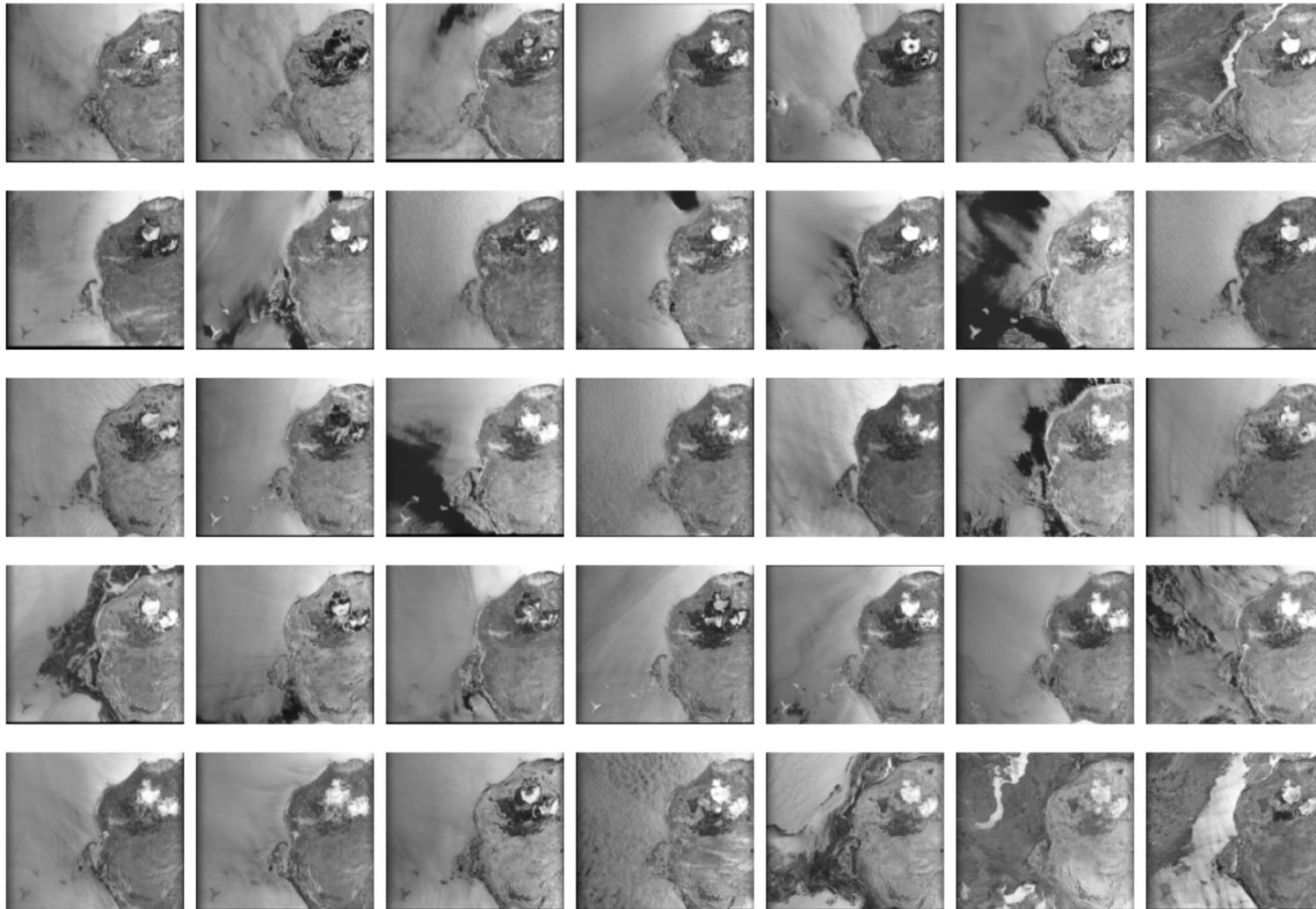


Figure 137: Images focused on Frame Z3.

4.3.4.4 *Preparation of topographic reference*

The topographic reference is used for SAR image co-registration, topographic phase removal in differential SAR interferometry, and terrain corrected geocoding. The topographic reference is based on the SRTM Digital Elevation Model version 4 (Figure 138). Standard deviation values from a “real” SAR intensity image and one simulated from the DEM are used to test the success of the topographic reference preparation.

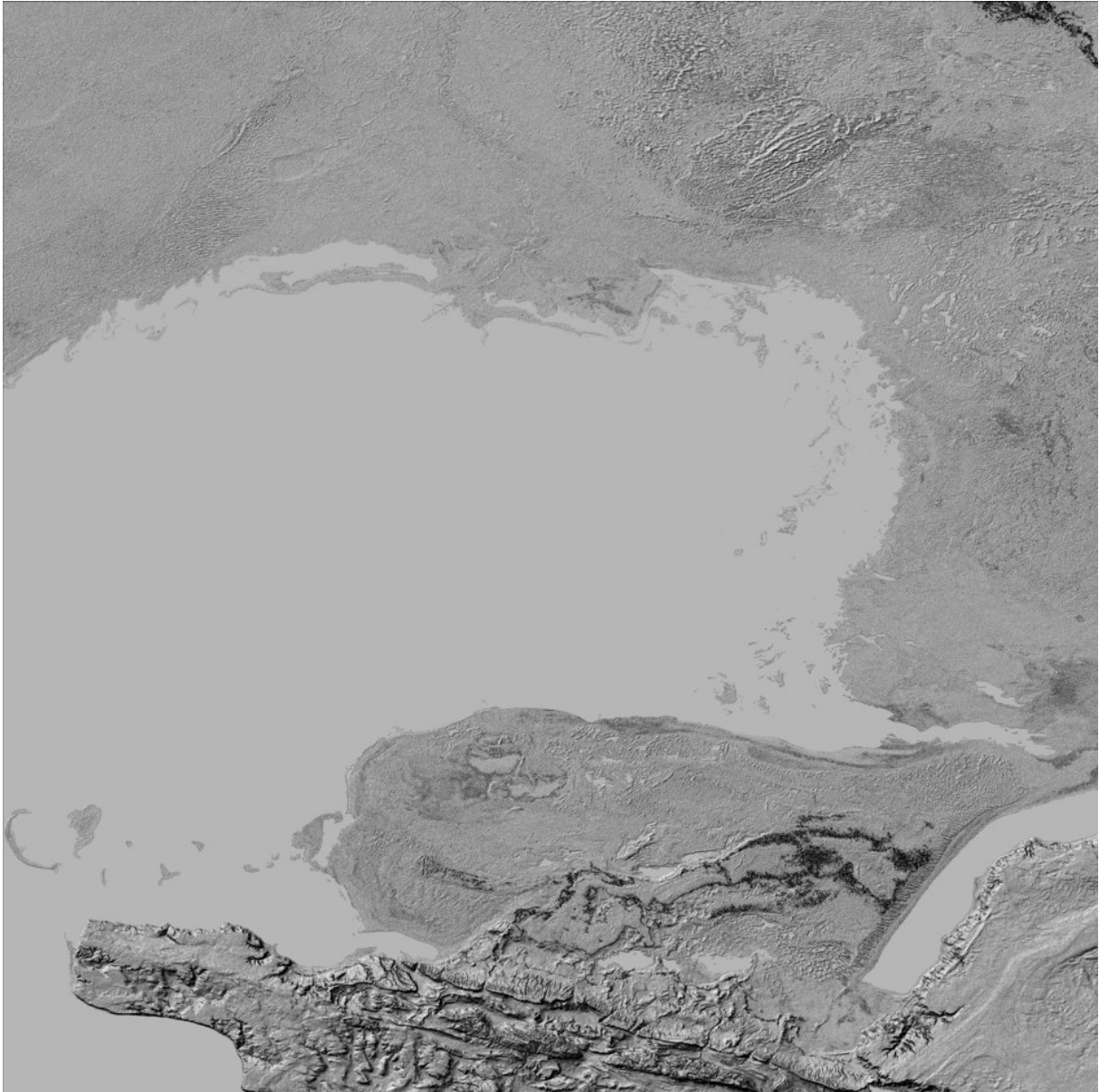


Figure 138: Topographic reference of the study area based on SRTM.

4.3.4.5 Co-registration of SAR images

In preparation of the interferogram generation, the SLC images have been co-registered to a common geometry at sub-pixel accuracy with consideration of the topography. The quality of the co-registration is determined during the derivation of the range and azimuth offset polynomials. As quality measures the standard deviation of the individual offset, estimates from the polynomial fits for the range and azimuth offsets were used. These standard deviations were in the sub-pixel domain (e.g. < 0.5 pixel).

As common reference a summer acquisition at a central temporal interval and spatial baseline has been selected. For frames 1 and 3 the central common reference was on 2007.08.18, for frame 2 this was on 2007.07.11. The following plots (Figure 139, Figure 140 and Figure 141) illustrate the temporal and spatial baselines of all the other acquisitions with respect to the central one.

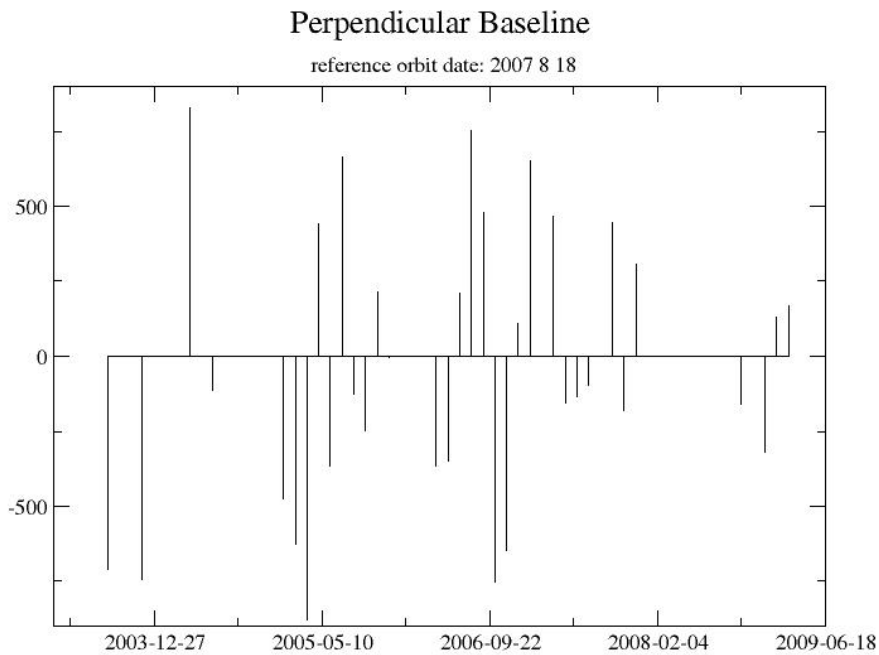


Figure 139: Temporal and spatial baseline of frame Z1.

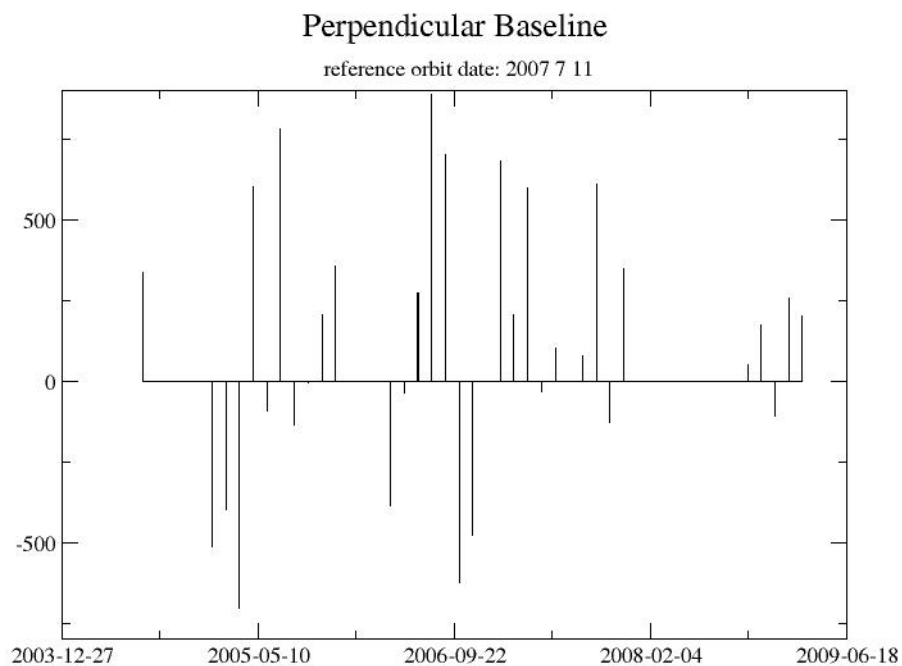


Figure 140: Temporal and spatial baseline of frame Z2.

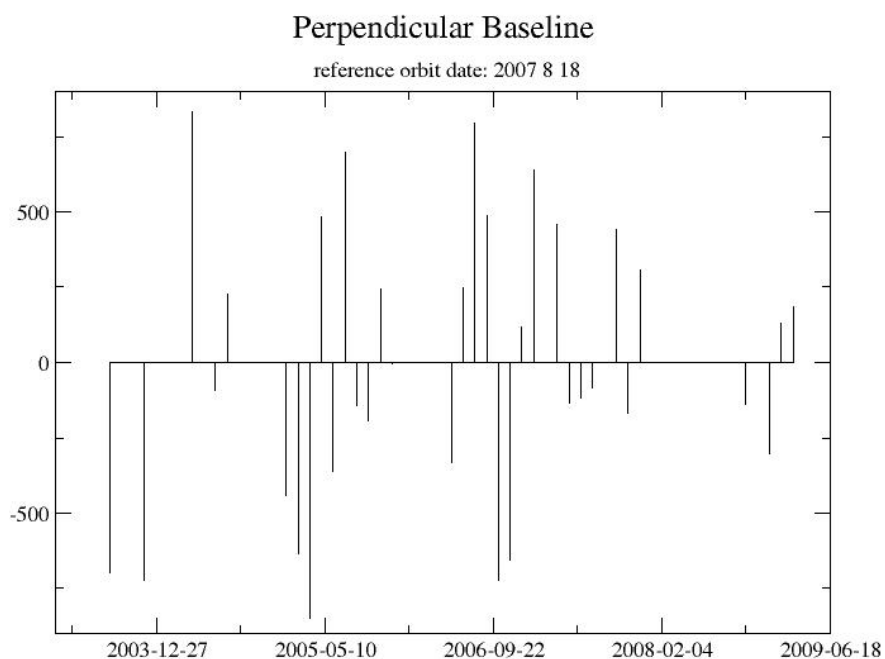


Figure 141: Temporal and spatial baseline of frame Z3.

4.3.4.6 *Interferometric processing*

The interferometric processing, including baseline estimation and interferogram flattening (i.e. the removal of the orbital phase trend), has been carried out using the GAMMA ISP software with 2 looks in range and 10 looks in azimuth. For the three frames all possible interferograms

with baselines shorter than 200 m independently of the acquisition time interval and the season have been computed (Figure 142, Figure 143 and Figure 144). Differential interferometric processing, i.e. the removal of the topographic related phase, has been done using the GAMMA DIFF&GEO software.

The quality of the interferograms was visually checked. Some of the interferograms, in particular for the southern frame, have shown a coherence lower than most of all the others. We attribute the loss of coherence in particular to the presence of wet snow cover. The interferograms with reduced coherence have been removed from further processing.

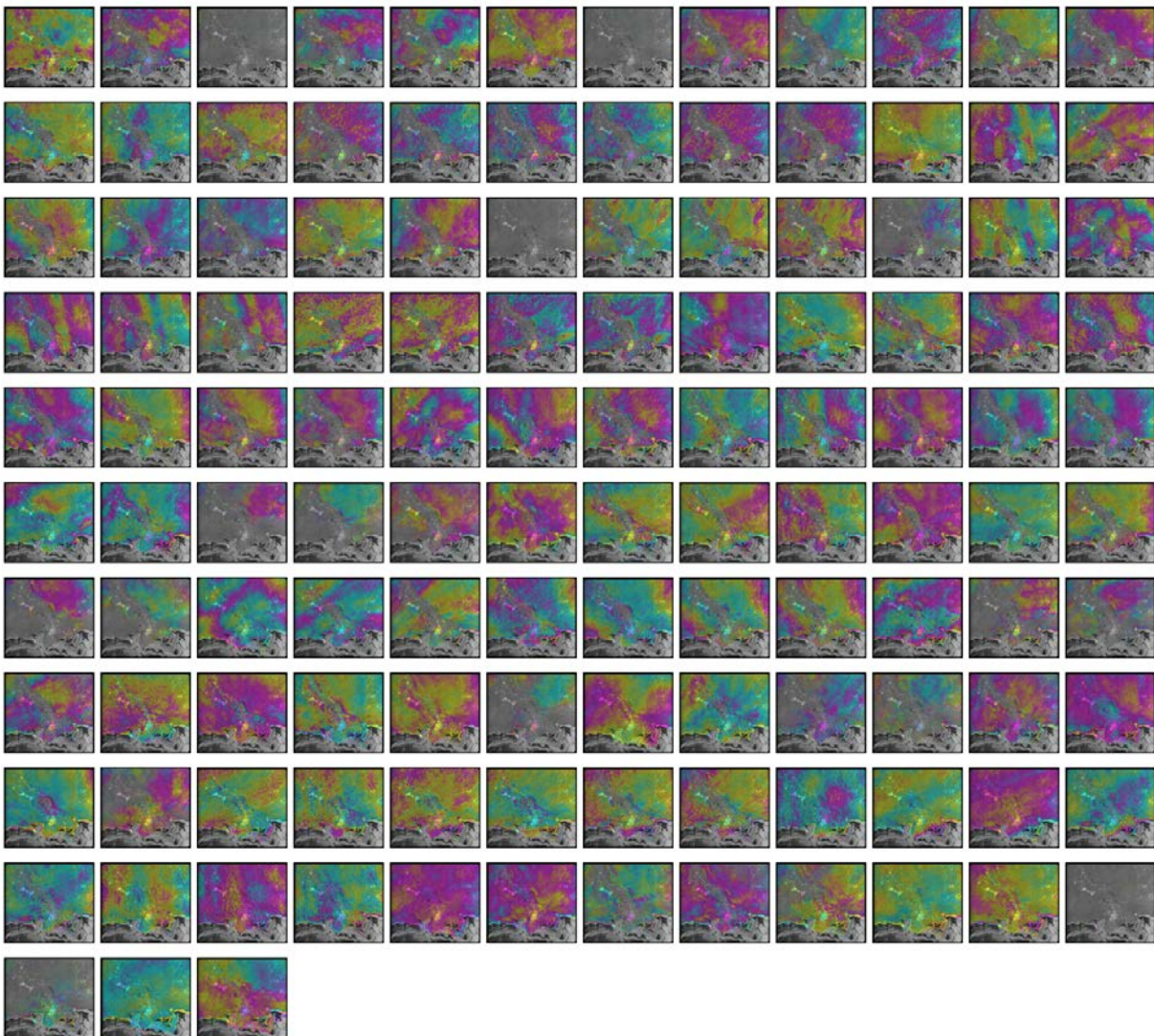


Figure 142: Possible interferograms with baselines shorter than 200 m in frame Z1.

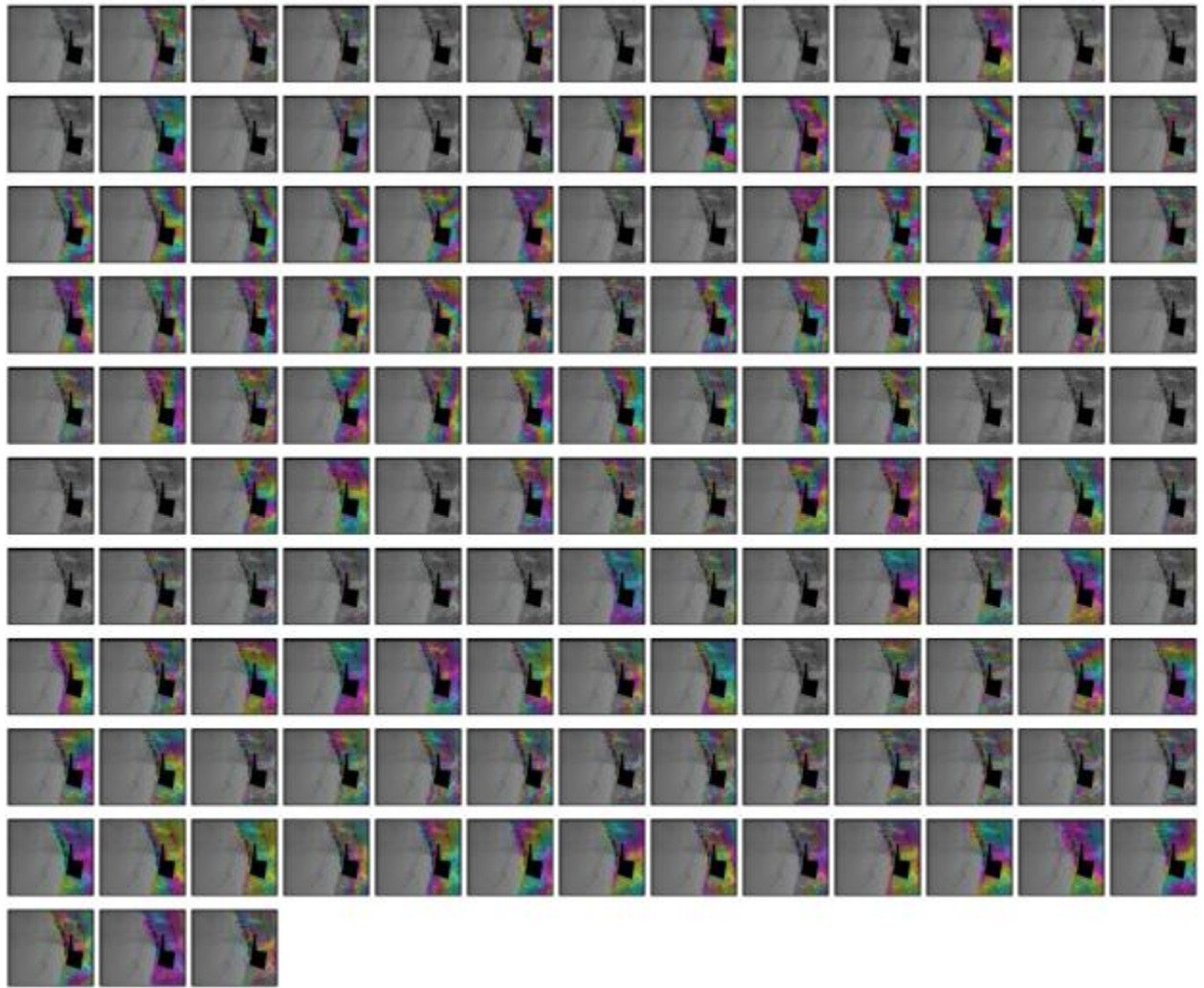


Figure 143: Possible interferograms with baselines shorter than 200 m in frame Z2.



Figure 144: Possible interferograms with baselines shorter than 200 m in frame Z3.

4.3.4.7 *Phase unwrapping*

Phase unwrapping is performed after filtering with a minimum-cost flow algorithm for sparse data. For frames Z1 and Z2 a coherence mask is computed as average of all the considered interferograms. For frame Z3 only 60 interferograms, the most coherent ones, have been considered to compute the coherence mask. This means that in some of the remaining interferograms phase noise is larger, reducing the accuracy of the measurements. An adaptive coherence estimator has been found suitable to identify also small built-up areas.

Especially for differential interferograms with large areas of low coherence phase unwrapping is not an easy and straightforward task. Once unwrapped, the differential interferograms are therefore critically investigated for errors and, if necessary, phase unwrapping has been repeated with modified parameters regarding flow costs or multi-looking. In some cases, it has

been necessary to remove some of the interferograms which could not be successfully unwrapped.

Another critical element of the processing chain is the selection of a reference point. Within every frame, the reference point was chosen in a potentially stable area; green triangles in Figure 145 show their position.



Figure 145: Location of the reference point (green triangle) in each frame.

With the availability of the unwrapped interferograms the estimation of the baselines is improved with a least-square approach using the SRTM terrain heights.

The final list of the interferograms considered for further processing excluding thus those with reduced coherence and with phase unwrapping errors, is provided in Table 16.

Table 16: List of interferograms considered after phase unwrapping.

Frame 1				Frame 2				Frame 3			
Date 1 (yyyymmdd)	Date 2 (yyyymmdd)	Baseline (m)	Interval (days)	Date 1 (yyyymmdd)	Date 2 (yyyymmdd)	Baseline (m)	Interval (days)	Date 1 (yyyymmdd)	Date 2 (yyyymmdd)	Baseline (m)	Interval (days)
20030809	20031122	-33.387	105	20040721	20051123	19.3468	490	20030809	20050219	61.2893	560
20030809	20050219	87.325	560	20040721	20060621	-63.2765	700	20031122	20050219	88.2919	455
20030809	20061007	-39.6027	1155	20050112	20050216	112.8121	35	20031122	20050326	-126.6686	490
20030809	20061111	62.68	1190	20050112	20061004	-110.3108	630	20031122	20061007	1.9213	1050
20031122	20061007	-6.2157	1050	20050323	20061004	82.6894	560	20031122	20061111	68.0094	1085
20040410	20050709	-167.1165	455	20050427	20070919	6.2305	875	20040619	20050813	-50.5425	420
20040619	20050813	-13.2524	420	20050601	20050810	-43.4687	70	20040619	20050917	-101.8805	455
20040619	20050917	-137.5002	455	20050601	20050914	84.2604	105	20040619	20051126	86.1817	525
20040619	20051126	107.4047	525	20050601	20060517	55.4755	350	20040619	20070714	7.8316	1120
20040619	20070609	-23.4471	1085	20050601	20070502	60.2911	700	20040619	20070818	90.6421	1155
20040619	20070714	16.6563	1120	20050601	20070606	194.0689	735	20040619	20071027	-79.2979	1225
20040619	20070818	111.8635	1155	20050601	20070711	91.7012	770	20040724	20051022	14.6095	455
20040619	20071027	-67.9991	1225	20050601	20070815	169.7308	805	20040724	20060624	20.781	700

Frame 1				Frame 2				Frame 3			
Date 1 (yyyymmdd)	Date 2 (yyyymmdd)	Baseline (m)	Interval (days)	Date 1 (yyyymmdd)	Date 2 (yyyymmdd)	Baseline (m)	Interval (days)	Date 1 (yyyymmdd)	Date 2 (yyyymmdd)	Baseline (m)	Interval (days)
20040619	20081011	-48.7328	1575	20050601	20071024	-37.7717	875	20040724	20061216	-112.5317	875
20050115	20050219	-147.8255	35	20050601	20081008	139.7806	1225	20050115	20060520	111.6353	490
20050115	20050604	109.2973	140	20050601	20081217	-17.5667	1295	20050326	20061111	194.678	595
20050115	20060415	112.8272	455	20050706	20060726	109.132	385	20050604	20050917	168.606	105
20050115	20060520	129.6438	490	20050706	20060830	-76.9256	420	20050604	20060520	29.499	350
20050115	20061111	-172.4705	665	20050706	20070919	-169.3766	805	20050813	20050917	-51.338	35
20050115	20081220	155.6738	1435	20050810	20050914	127.7291	35	20050813	20051126	136.7242	105
20050219	20061007	-126.9277	595	20050810	20060517	98.9442	280	20050813	20060520	-190.445	280
20050219	20061111	-24.645	630	20050810	20070502	103.7598	630	20050813	20070505	8.3705	630
20050430	20060902	40.5207	490	20050810	20070711	135.1699	700	20050813	20070609	21.6833	665
20050430	20070331	25.2712	700	20050810	20071024	5.697	805	20050813	20070714	58.3741	700
20050430	20070922	6.6864	875	20050810	20081008	183.2493	1155	20050813	20070818	141.1846	735
20050604	20050917	117.9775	105	20050810	20081217	25.902	1225	20050813	20071027	-28.7554	805
20050604	20060415	3.5299	315	20050914	20060517	-28.7849	245	20050813	20081011	3.9641	1155

Frame 1				Frame 2				Frame 3			
Date 1 (yyyymmdd)	Date 2 (yyyymmdd)	Baseline (m)	Interval (days)	Date 1 (yyyymmdd)	Date 2 (yyyymmdd)	Baseline (m)	Interval (days)	Date 1 (yyyymmdd)	Date 2 (yyyymmdd)	Baseline (m)	Interval (days)
20050604	20060520	20.3465	350	20050914	20070502	-23.9693	595	20050813	20081220	-160.6309	1225
20050604	20081220	46.3765	1295	20050914	20070606	109.8085	630	20050917	20051126	188.0622	70
20050709	20060729	87.9249	385	20050914	20070711	7.4408	665	20050917	20060520	-139.107	245
20050709	20060902	-181.9449	420	20050914	20070815	85.4704	700	20050917	20070505	59.7085	595
20050709	20070120	-11.0586	560	20050914	20071024	-122.0321	770	20050917	20070609	73.0213	630
20050709	20070331	-197.1944	630	20050914	20081008	55.5202	1120	20050917	20070714	109.7121	665
20050813	20050917	-124.2478	35	20050914	20081112	181.4798	1155	20050917	20070818	192.5226	700
20050813	20051126	120.6571	105	20050914	20081217	-101.8271	1190	20050917	20081011	55.3021	1120
20050813	20070505	-30.0472	630	20051019	20060621	69.7278	245	20051022	20060624	6.1715	245
20050813	20070609	-10.1947	665	20051019	20070221	1.7217	490	20051022	20061216	-127.1412	420
20050813	20070714	29.9087	700	20051019	20070606	-101.64	595	20051022	20070922	197.8067	700
20050813	20070818	125.1159	735	20051019	20070815	-125.9781	665	20051022	20071201	61.442	770
20050813	20071027	-54.7467	805	20051019	20071128	143.3924	770	20051022	20090228	-59.1889	1225
20050813	20081011	-35.4804	1155	20051019	20081008	-155.9283	1085	20051126	20061216	120.8299	385

Frame 1				Frame 2				Frame 3			
Date 1 (yyyymmdd)	Date 2 (yyyymmdd)	Baseline (m)	Interval (days)	Date 1 (yyyymmdd)	Date 2 (yyyymmdd)	Baseline (m)	Interval (days)	Date 1 (yyyymmdd)	Date 2 (yyyymmdd)	Baseline (m)	Interval (days)
20050917	20060415	-114.4476	210	20051019	20081112	-29.9687	1120	20051126	20070505	-128.3537	525
20050917	20060520	-97.631	245	20051019	20090225	-2.7032	1225	20051126	20070609	-115.0409	560
20050917	20070505	94.2006	595	20051123	20060621	-82.6233	210	20051126	20070714	-78.3501	595
20050917	20070609	114.0531	630	20060412	20061108	-90.7519	210	20051126	20070818	4.4604	630
20050917	20070714	154.1565	665	20060517	20070502	4.8156	350	20051126	20071027	-165.4796	700
20050917	20071027	69.5011	770	20060517	20070606	138.5934	385	20051126	20081011	-132.7601	1050
20050917	20081011	88.7674	1120	20060517	20070711	36.2257	420	20051126	20090228	188.7822	1190
20050917	20081220	-71.601	1190	20060517	20070815	114.2553	455	20060520	20070505	198.8155	350
20051022	20060624	-2.6142	245	20060517	20071024	-93.2472	525	20060624	20061216	-133.3127	175
20051022	20061216	-101.288	420	20060517	20081008	84.3051	875	20060624	20071201	55.2705	525
20051126	20061216	115.7028	385	20060517	20081217	-73.0422	945	20060624	20090228	-65.3604	980
20051126	20070505	-150.7043	525	20060726	20060830	-186.0576	35	20060902	20070331	-28.9004	210
20051126	20070609	-130.8518	560	20060830	20070919	-92.451	385	20060902	20070922	-46.8706	385
20051126	20071027	-175.4038	700	20061004	20061108	145.7334	35	20060902	20071201	-183.2353	455

Frame 1				Frame 2				Frame 3			
Date 1 (yyyymmdd)	Date 2 (yyyymmdd)	Baseline (m)	Interval (days)	Date 1 (yyyymmdd)	Date 2 (yyyymmdd)	Baseline (m)	Interval (days)	Date 1 (yyyymmdd)	Date 2 (yyyymmdd)	Baseline (m)	Interval (days)
20051126	20081011	-156.1375	1050	20070117	20070328	-84.4394	70	20061007	20061111	66.0881	35
20060415	20060520	16.8166	35	20070221	20070606	-103.3617	105	20061216	20070714	-199.18	210
20060415	20071027	183.9487	560	20070221	20070815	-127.6998	175	20061216	20070818	-116.3695	245
20060415	20081220	42.8466	980	20070221	20071128	141.6707	280	20061216	20071201	188.5832	350
20060520	20070505	191.8316	350	20070221	20081008	-157.65	595	20061216	20090228	67.9523	805
20060520	20071027	167.1321	525	20070221	20081112	-31.6904	630	20070120	20070331	-179.5032	70
20060520	20081011	186.3984	875	20070221	20090225	-4.4249	735	20070331	20070922	-17.9702	175
20060520	20081220	26.03	945	20070502	20070606	133.7778	35	20070331	20071201	-154.3349	245
20060624	20061216	-98.6738	175	20070502	20070711	31.4101	70	20070505	20070609	13.3128	35
20060624	20090228	-41.9918	980	20070502	20070815	109.4397	105	20070505	20070818	132.8141	105
20060729	20070120	-98.9835	175	20070502	20071024	-98.0628	175	20070505	20071027	-37.1259	175
20060902	20070120	170.8863	140	20070502	20081008	79.4895	525	20070505	20081011	-4.4064	525
20060902	20070331	-15.2495	210	20070502	20081217	-77.8578	595	20070505	20081220	-169.0014	595
20060902	20070922	-33.8343	385	20070606	20070711	-102.3677	35	20070609	20070714	36.6908	35

Frame 1				Frame 2				Frame 3			
Date 1 (yyyymmdd)	Date 2 (yyyymmdd)	Baseline (m)	Interval (days)	Date 1 (yyyymmdd)	Date 2 (yyyymmdd)	Baseline (m)	Interval (days)	Date 1 (yyyymmdd)	Date 2 (yyyymmdd)	Baseline (m)	Interval (days)
20061007	20061111	102.2827	35	20070606	20070815	-24.3381	70	20070609	20070818	119.5013	70
20061216	20070818	-111.244	245	20070606	20081008	-54.2883	490	20070609	20071027	-50.4387	140
20061216	20090228	56.682	805	20070606	20081112	71.6713	525	20070609	20081011	-17.7192	490
20070120	20070331	-186.1358	70	20070606	20090225	98.9368	630	20070714	20070818	82.8105	35
20070331	20070922	-18.5848	175	20070711	20070815	78.0296	35	20070714	20071027	-87.1295	105
20070505	20070609	19.8525	35	20070711	20071024	-129.4729	105	20070818	20071027	-169.94	70
20070505	20070818	155.1631	105	20070711	20081008	48.0794	455	20070818	20081011	-137.2205	420
20070505	20071027	-24.6995	175	20070711	20081112	174.039	490	20070818	20090228	184.3218	560
20070505	20081011	-5.4332	525	20070711	20081217	-109.2679	525	20070922	20071201	-136.3647	70
20070505	20081220	-165.8016	595	20070815	20081008	-29.9502	420	20071027	20081011	32.7195	350
20070609	20070714	40.1034	35	20070815	20081112	96.0094	455	20071027	20081220	-131.8755	420
20070609	20070818	135.3106	70	20070815	20081217	-187.2975	490	20071201	20090228	-120.6309	455
20070609	20071027	-44.552	140	20070815	20090225	123.2749	560	20081011	20081220	-164.595	70
20070609	20081011	-25.2857	490	20071024	20081008	177.5523	350	20060729	20060902	-306.2842	35

Frame 1				Frame 2				Frame 3			
Date 1 (yyyymmdd)	Date 2 (yyyymmdd)	Baseline (m)	Interval (days)	Date 1 (yyyymmdd)	Date 2 (yyyymmdd)	Baseline (m)	Interval (days)	Date 1 (yyyymmdd)	Date 2 (yyyymmdd)	Baseline (m)	Interval (days)
20070609	20081220	-185.6541	560	20071024	20081217	20.205	420				
20070714	20070818	95.2072	35	20071128	20081112	-173.3611	350				
20070714	20071027	-84.6554	105	20071128	20090225	-146.0956	455				
20070714	20081011	-65.3891	455	20081008	20081112	125.9596	35				
20070818	20071027	-179.8626	70	20081008	20081217	-157.3473	70				
20070818	20081011	-160.5963	420	20081008	20090225	153.2251	140				
20070818	20090228	167.926	560	20081112	20090121	81.1653	70				
20070922	20071201	-140.0655	70	20081112	20090225	27.2655	105				
20071027	20081011	19.2663	350	20090121	20090225	-53.8998	35				
20071027	20081220	-141.1021	420	20060412	20060517	349.7084	35				
20081011	20081220	-160.3684	70	20070221	20070328	389.5526	35				

For frame Z1 out of a total of 123 interferograms with baselines shorter than 200 m, 94 have been considered for further processing. In that way two winter images (2005.03.26 and 2009.01.24), which were always decorrelated, were discarded from further processing (Figure 146).

For frame Z2 out of a total of 131 interferograms with baselines shorter than 200 m 92 have been considered for further processing. However, in order to have all acquisition dates connected to each other it was necessary to compute also two interferograms with baselines larger than 200 m showing good coherence (Figure 147).

For frame Z3 out of a total of 129 interferograms with baselines shorter than 200 m 82 have been used for further processing. In order to have the acquisition of 2006.07.29 connected with the others it was necessary to compute also one interferogram with a baseline larger than 200 m showing good coherence. However, in that way three winter images (2004.04.10, 2005.04.30 and 2009.01.24), always decorrelated, and one summer image (2005.07.09), which could not be connected with the others, have been discarded from further processing (Figure 148).



Figure 146: Interferograms considered after phase unwrapping in frame Z1.

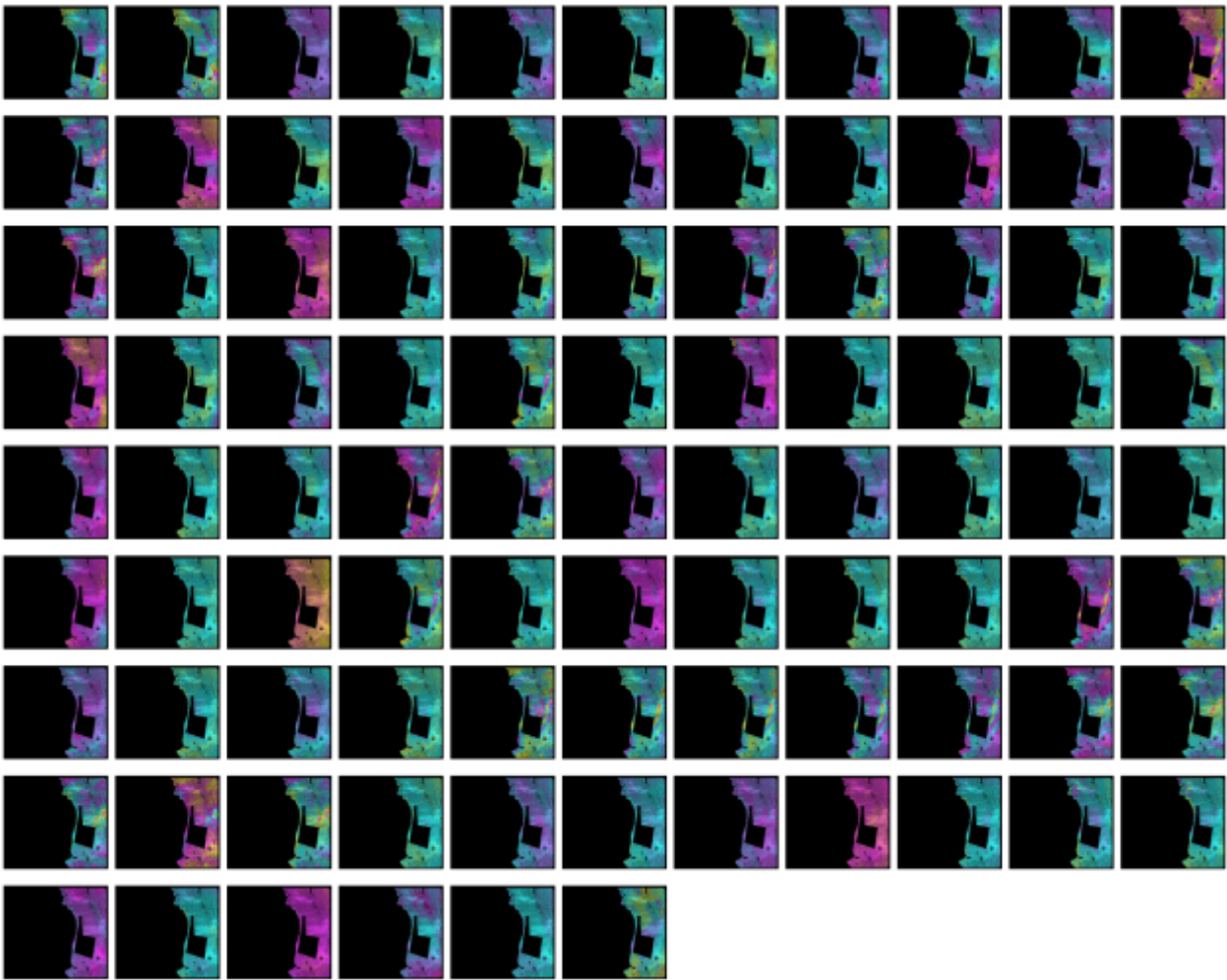


Figure 147: Interferograms considered after phase unwrapping in frame Z2.



Figure 148: Interferograms considered after phase unwrapping in frame Z3.

4.3.4.8 *Multi-baseline interferometry*

A phase time series is computed from the set of multi-reference continuous unwrapped interferograms using a least-square solution. The resulting 33, 33 and 31 phase images for frames Z1, Z2 and Z3, respectively, are shown in Figure 149, Figure 150 and Figure 151.

Atmospheric artifacts are visible in some of the images, in particular during summer time. In winter, on the other hand, phase signals are sometimes visible over glaciated or snow-covered surfaces. An error model is used to calculate the expected accuracy for the combined result and checks are conducted by the operator to control the consistency of the multiple results. We found in particular that for frame 2 the first acquisition of July 2004 was contaminated by strong atmospheric artifacts and the reference date of that time series was changed to image number 20 (21.02.2007).

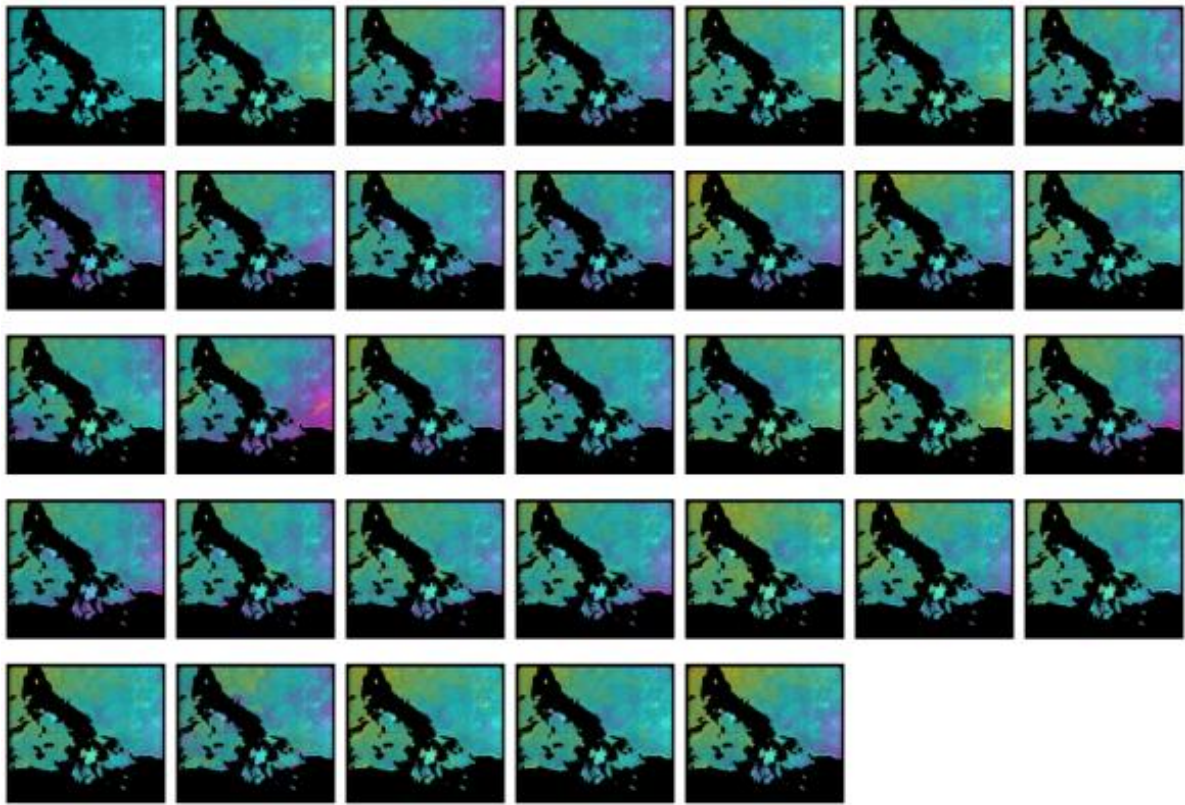


Figure 149: Interferograms considered after multi-baseline interferometry analysis in frame Z1.

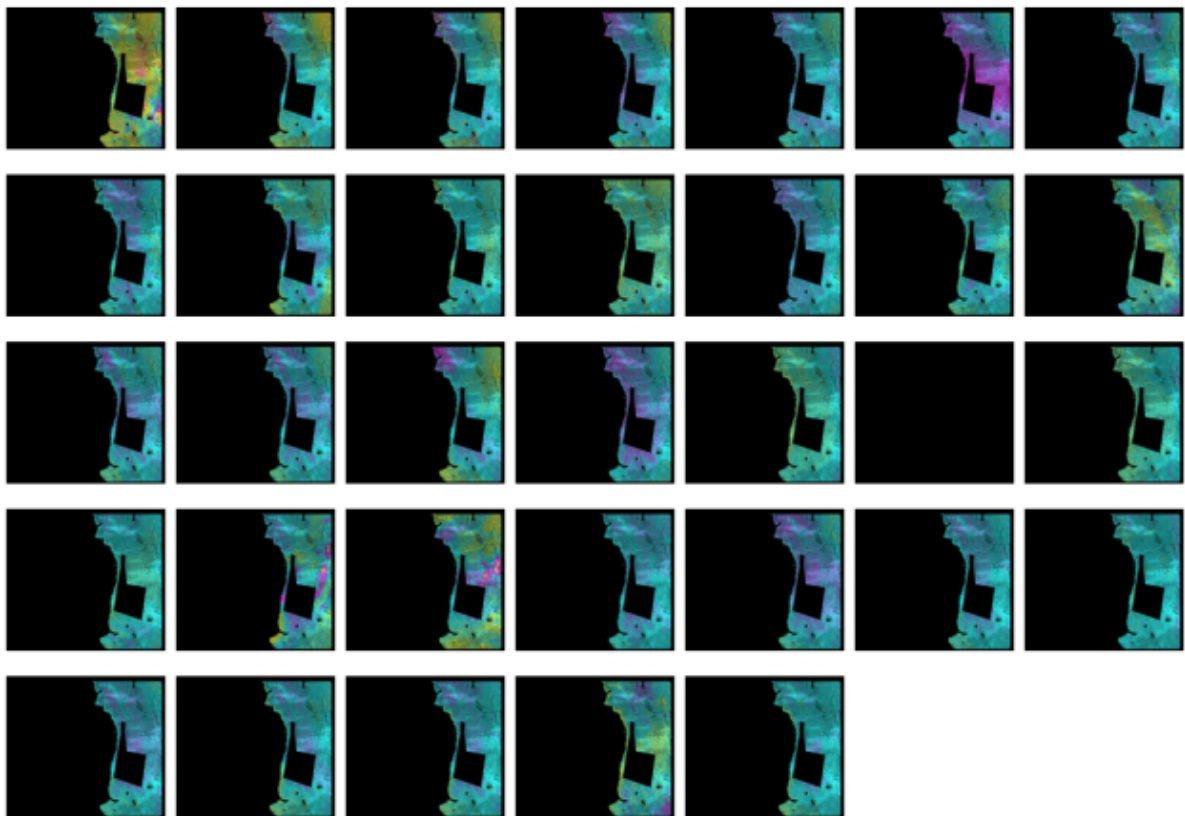


Figure 150: Interferograms considered after multi-baseline interferometry analysis in frame Z2.

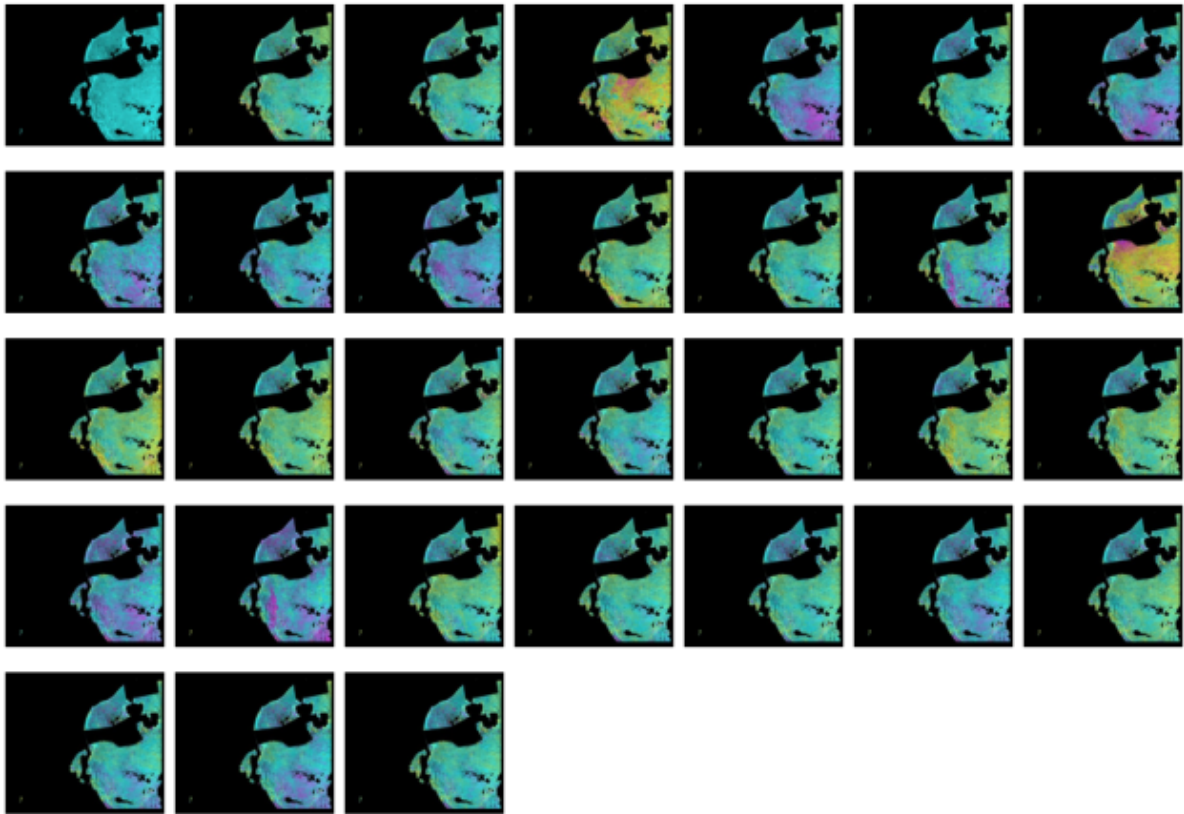


Figure 151: Interferograms considered after multi-baseline interferometry analysis in frame Z3.

4.3.4.9 *Estimation of linear deformation rate and time series of displacement*

From the phase time series a linear deformation rate and time series of displacement have been calculated. Movements are computed in the satellite line-of-sight direction. Temporal filtering on a 180 days' time span is applied to the time series. Temporal filtering reduces some of the atmospheric disturbances but also creates artefacts at the beginning and at the end of the series and when a single acquisition is contaminated by strong atmosphere. Time series of displacement are therefore delivered with and without temporal filtering.

Because the first acquisition of July 2004 of frame Z2 has particularly strong atmospheric effects, this layer was not considered in the computation of the mean deformation rate.

For frame Z1 we noticed by the computation of the mean deformation rate an apparent uplift of about 2 mm/yr for large areas. The movement value of the reference point chosen during phase unwrapping was therefore lowered by 2 mm/yr. Of course, proper calibration with respect to stable points is still required in the interpretation of the results.

4.3.4.10 ***Geocoding and consistency testing;***

SAR terrain corrected geocoding is the geometric transformation from slant range into the product geometry. This step has been done using the GAMMA DIFF&GEO software by use of topographic reference.

4.3.4.11 ***Product finalizing***

The mean subsidence values derived from SAR interferometry are delivered as ASCII files together with geographical coordinates in order to facilitate the transfer to any GIS software. Time series of displacement are delivered with and without temporal filtering.

4.3.5 Analysis and interpretation of SBAS results

The spatial coverage with valid information is large, because the coherence mask has been calculated from all filtered interferograms. Interferograms with winter image pairs are coherent also over water surfaces (frozen in winter) and areas vegetated during summer. Care is thus required for the interpretation of signals close to water and vegetated surfaces

The combination of strong summer atmospheric artefacts, presence of frozen water surfaces and snow-cover in winter and absence of large numbers of anthropogenic structures makes the accuracy of our measurements lower than that determined with persistent scatterers interferometry over European urban areas and quantified by Crosetto et al. (2010) as 1.3-1.8 mm/yr for ENVISAT. Even if the mm/yr cannot be interpreted, the generally high coherence over this semi-desertic landscape ensures a good quality of the results.

It has also to be highlighted that SAR-based techniques without absolute GPS calibrations do not provide absolute displacements; within every frame, the movements are referred to a defined point that potentially could be affected by a vertical movement. For this reason, the displacements discussed below cannot be considered as absolute values, but must be considered as an indication of relative movement compared to another area in the same frame of study. It's obvious that the reference points have been selected in potentially stable areas.

InSAR results are analysed at different level of detail. Firstly, a general "frame scale" view is given; in addition the study focuses on zones of interest, as urban areas or zones where the vertical movements detected are marked. Analysis of trends for specific spots was carried out: figures showing the movement (mm) versus time (years) were plotted. As highlighted in the following paragraphs, these points are distributed both in stable areas and on specific sites of interest.

For every frame, a brief discussion on the observed displacements is provided.

4.3.5.1 *Frame Z1*

Multiple short baseline interferometry (SBAS) analysis in this frame is affected by strong disturbs and not fully cover the area. As shown in Figure 152 there is no data along the fluvial belt near the Ural River. Missing data are probably linked to vegetational cycles, which cause the loss of signal coherence between different couples of acquired signals.

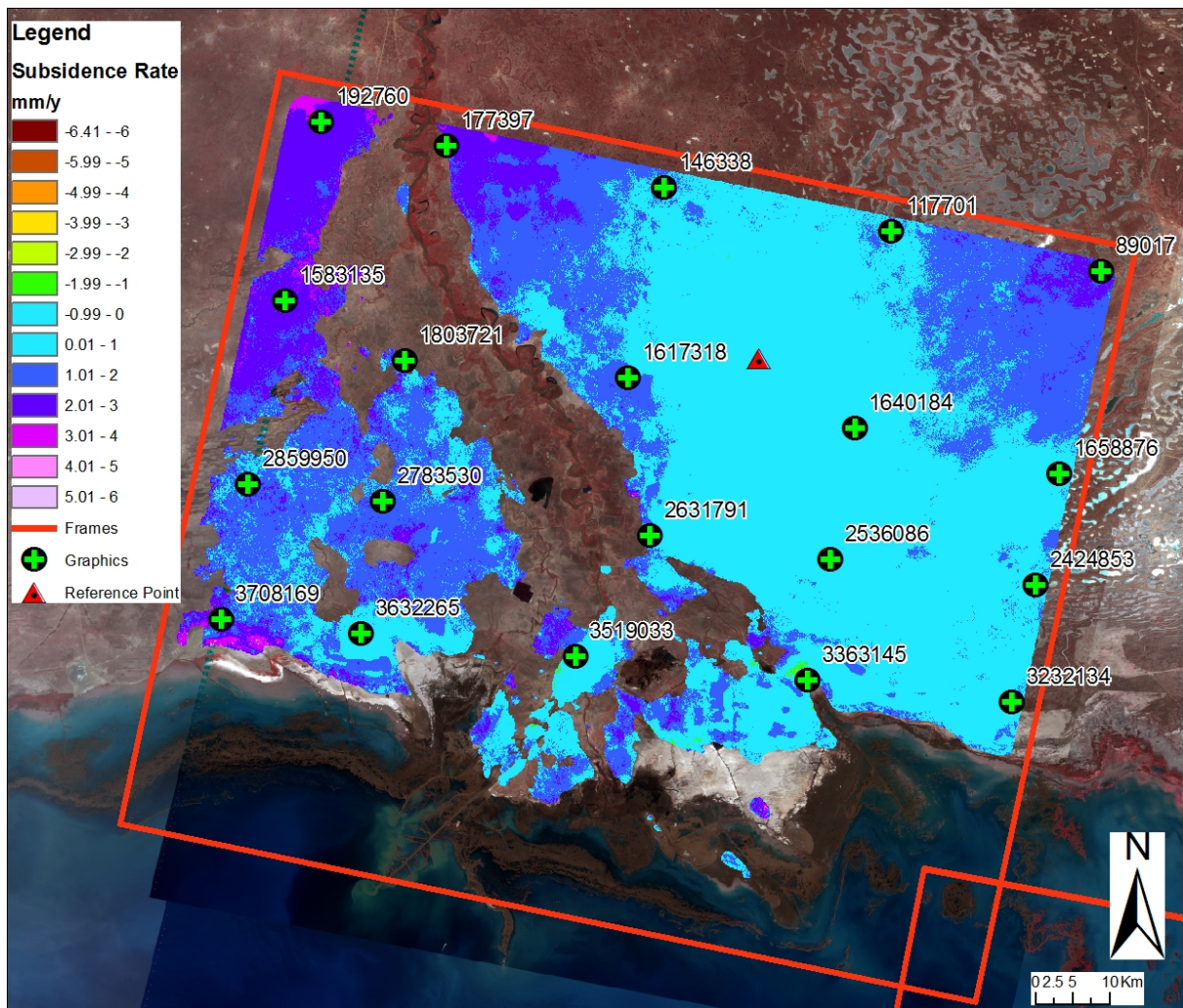


Figure 152: Results of SBAS analysis in frame Z1.

For frame 1 no clear signals, i.e. with magnitudes larger than ± 4 mm/y, were detected. Excluding movements comprise between ± 1 mm/y (light blue), that substantially define stable zones, some features with detected movements among ± 2 and ± 4 mm/y are visible, but interpretation has to be performed with care.

Within these areas, localised in the western side and N-E corners of the frame, movements comprise between +2 and +4 mm/y could be due to atmospheric artefacts (stronger than others filtered) or to movements of wide diapirs of salt. This second hypothesis cannot be verified because of the lack of a detailed map of salt domes, and in any case appears more unrealistic than the atmospheric influence (in the area of study uplifts due to diapirism reach 1 mm/y according with Volozh et al. (2003). InSAR technique has been proved to provide good results by Shimoni et al. (2002) to study the influence of salt diapirs on superficial movements in Lisan Peninsula (Dead Sea Rift) where the movements of the ground surface have been quantified in more than 50 mm/y.

Two areas of interest are shown in Figure 153.

The first one is referred to the urban area of Atyrau; a detail in this area is needed to evaluate potential sedimentary compaction caused by the weight of the buildings. The second area concerns the coastal zone 20 km E of Atyrau, in which displacements are particularly marked. In both of them, the measured lowering of the ground is up to -3 mm/y.

Multiple short baseline interferometry is a technique suitable for wide areas and their results, as visible in Figure 153, cannot detect movements at "building scale" (IPTA technique, applied only for frame Z1, for the same area reveals more localised movements). For further details see section 4.3.6.

The coastal area involved in subsidential processes has a surface of about 9 km²; the movement can be caused by human activities (e.g. agriculture) or by natural processes of focused coastal erosion or deflation.

The time behaviour of the displacement measured for some sites of interest (pt. 3519033 for Atyrau and pt. 3363145 for coastal zone), and in other sites distributed within the whole frame Z1 are plotted in Table 17; their location is shown in Figure 152.

For each of them both the filtered (TPF: Temporal Phase Filtered, brown line) and unfiltered signals (ATM: ATMospheric, orange dots) from atmospheric disturb are plotted. The regression lines and their low values of coefficient of determination R² confirm that there isn't a specific trend for the majority of the surface detected; only in areas where relative movements recorded exceed values of ±2 mm/y a trend is quite clear, with value of R² up to 0.8.

For frame Z1 complete results are shown in drawings Map.II.3.1 (Quick-looks after inversion and trend analysis) and Map.II.3.2 (INSAR-SBAS Analysis).

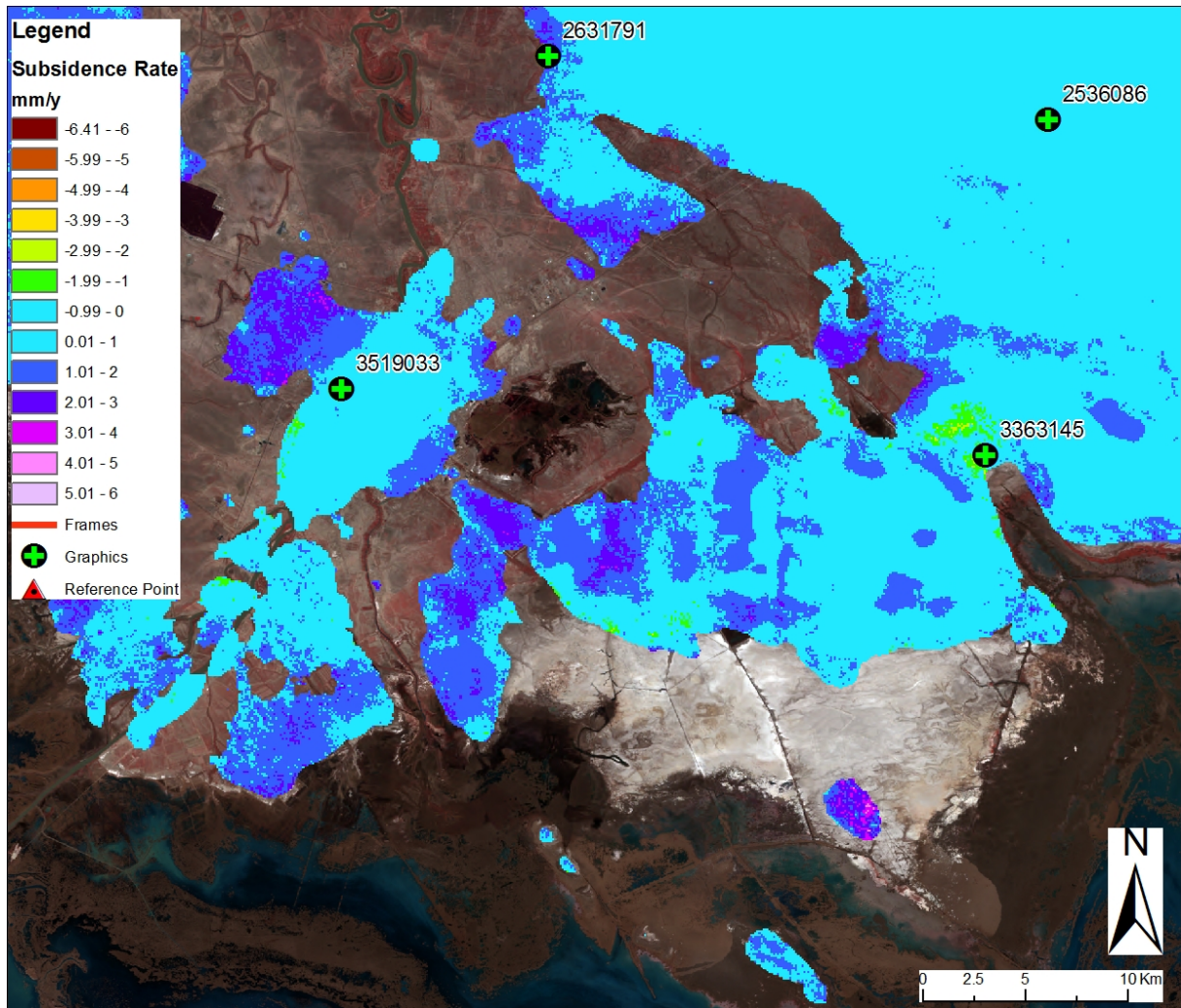
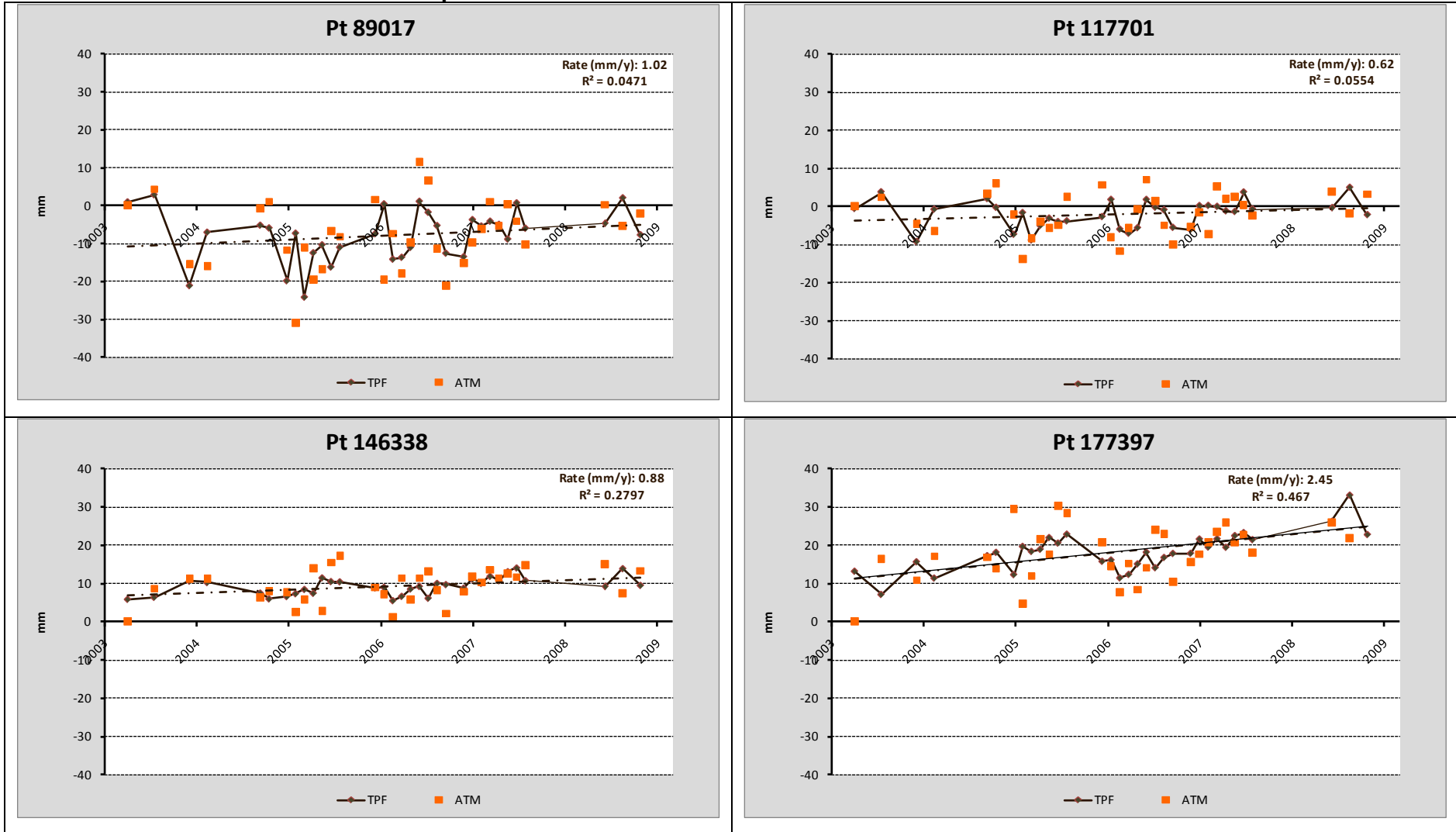
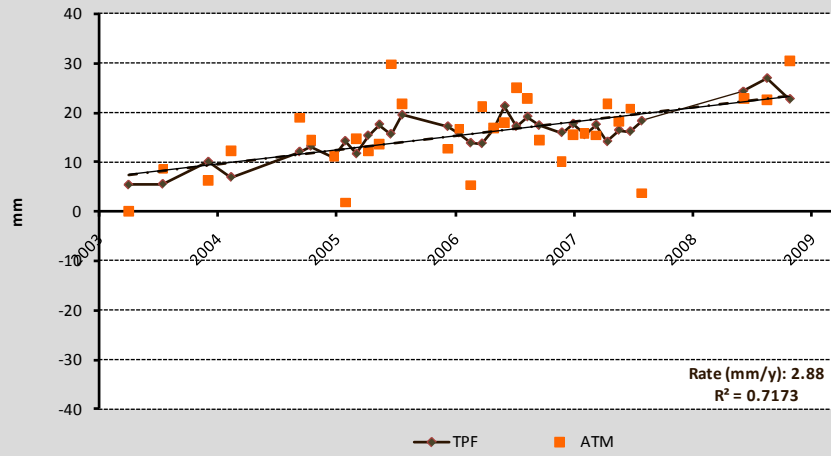


Figure 153: Detail of SBAS analysis within frame Z1.

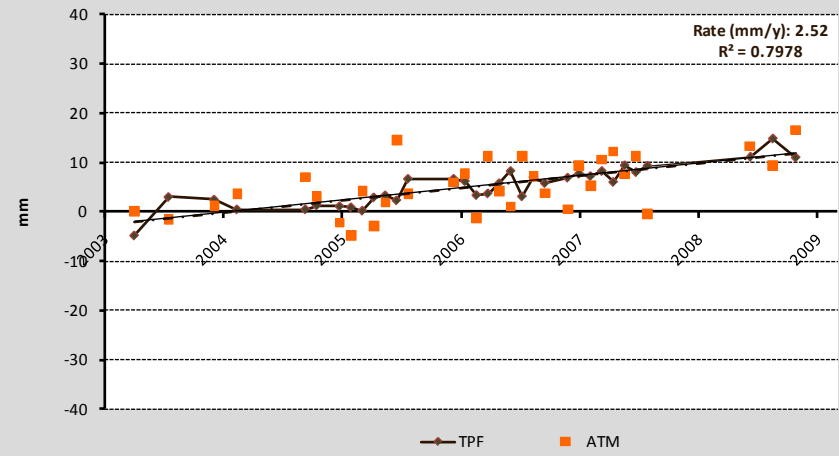
Table 17: Displacements versus time for a few sites selected within the Z1 frame.



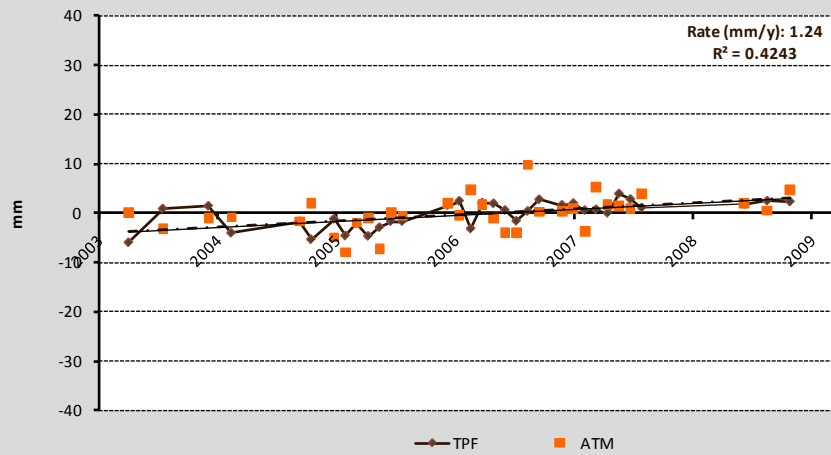
Pt 192760



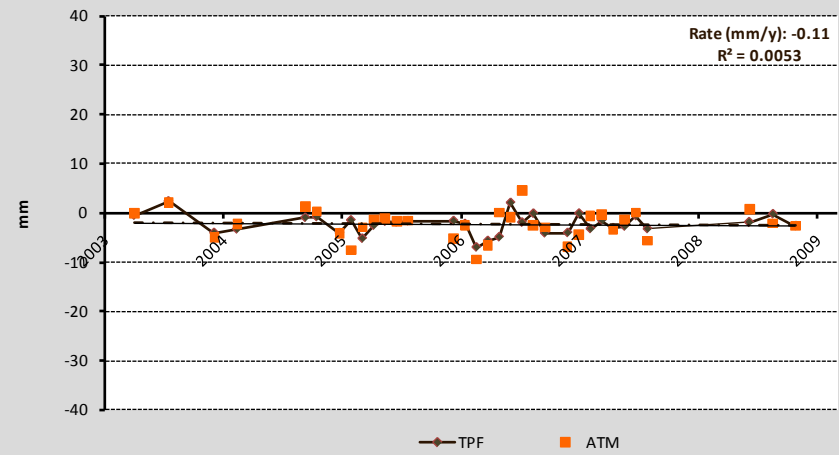
Pt 1583135



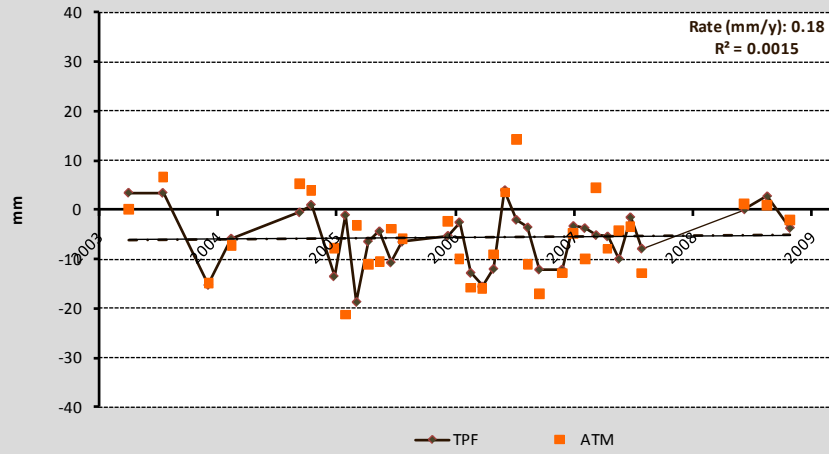
Pt 1617318



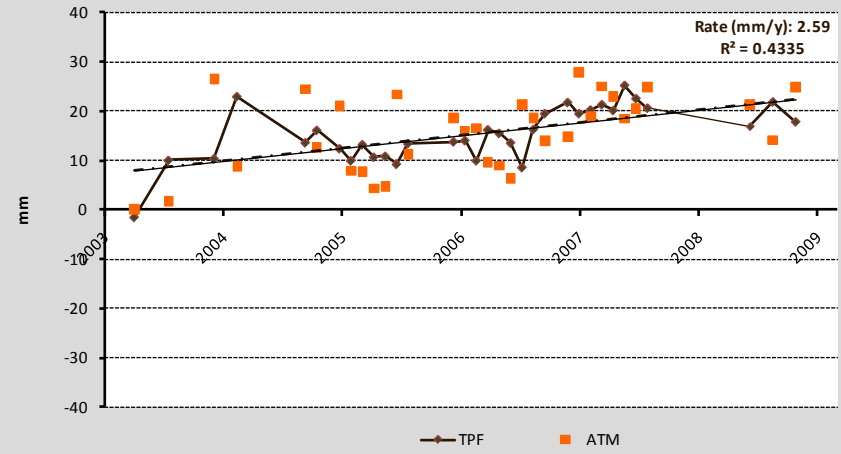
Pt 1640184



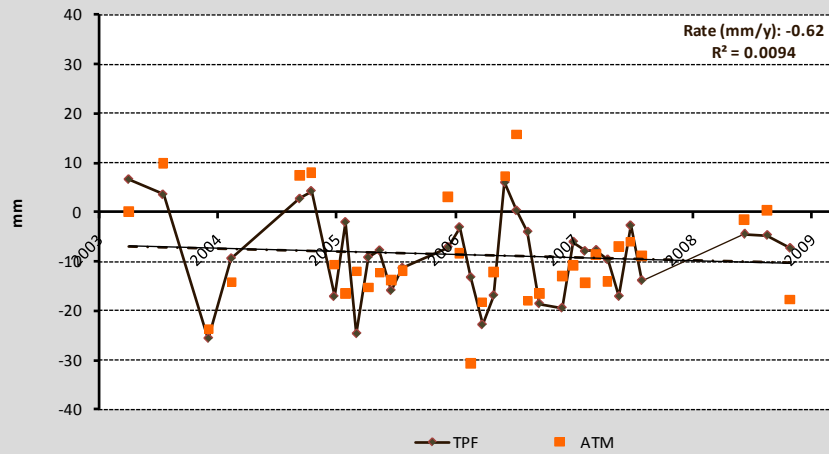
Pt 1658876



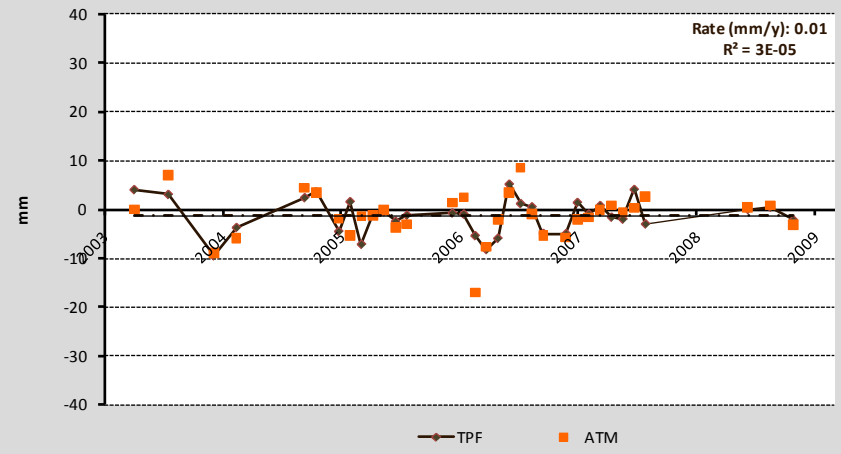
Pt 1803721



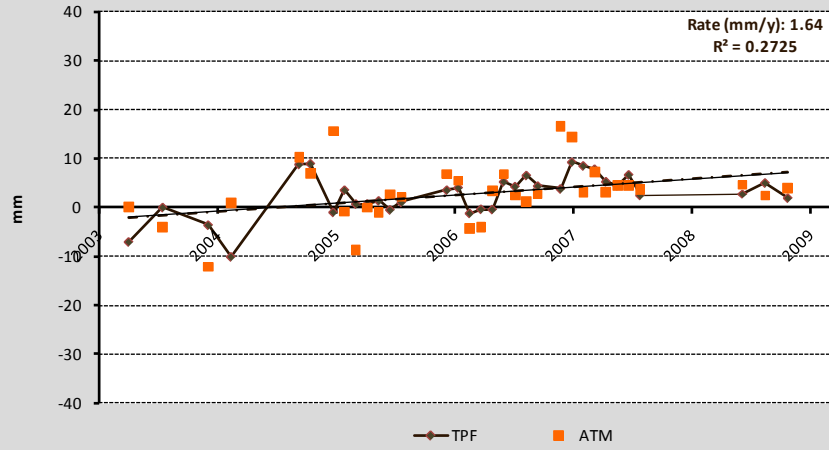
Pt 2424853



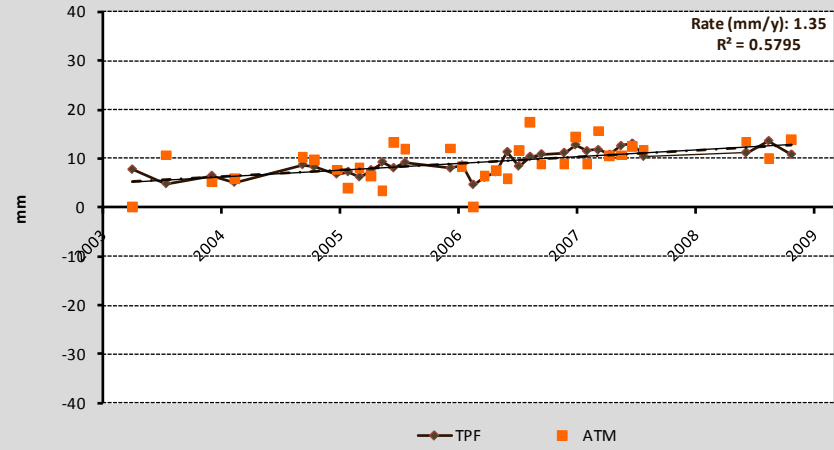
Pt 2536086



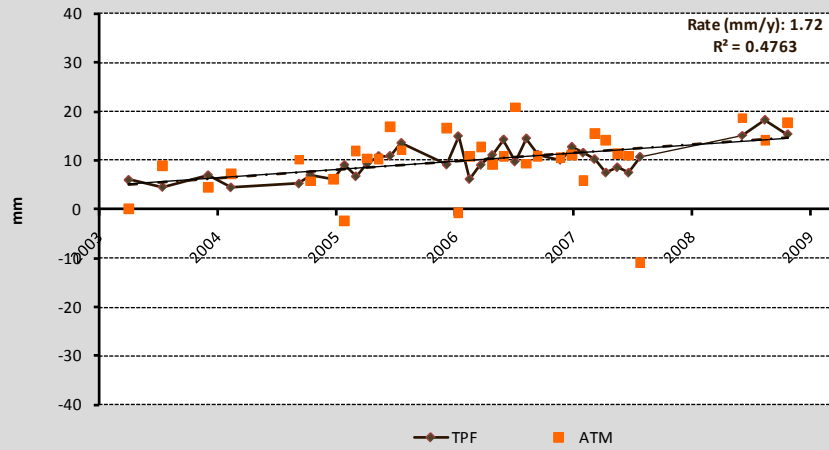
Pt 2631791



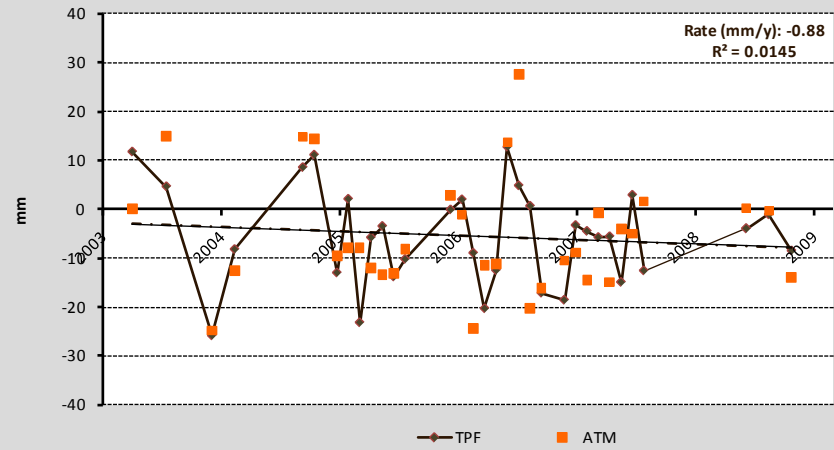
Pt 2783530



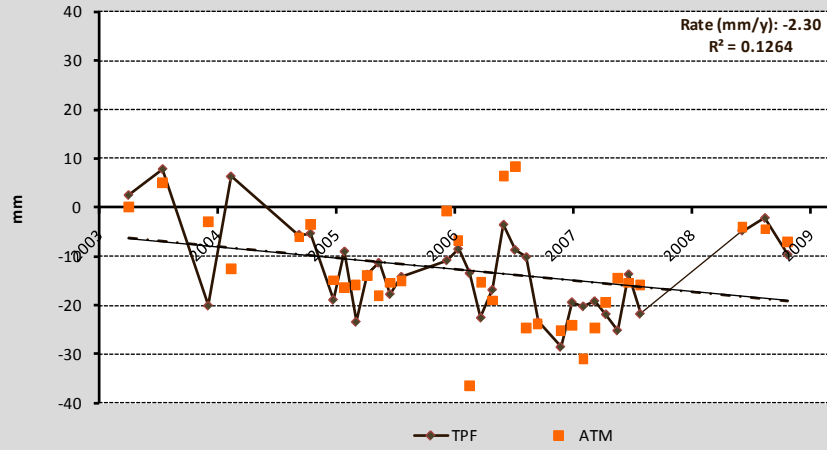
Pt 2859950



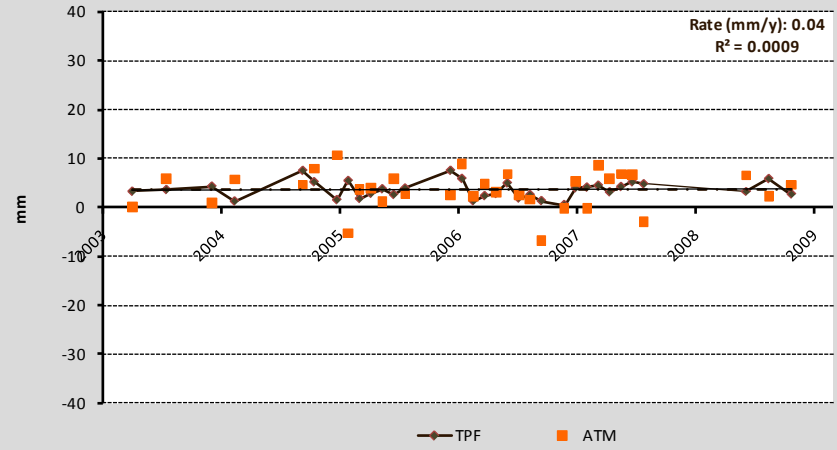
Pt 3232134



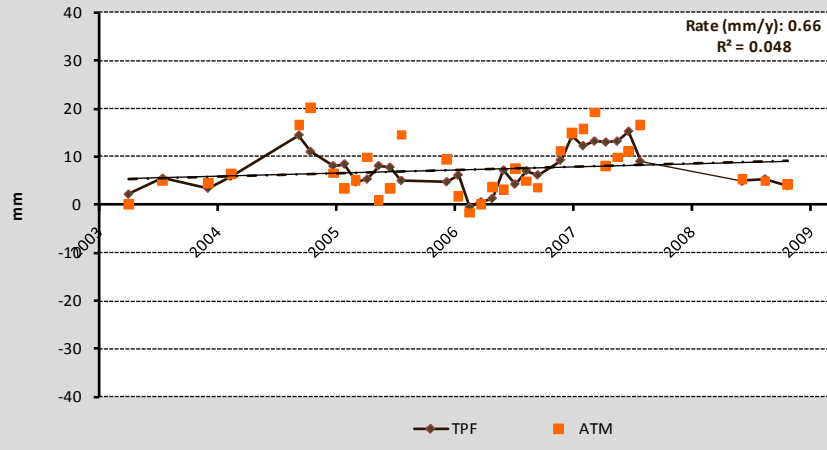
Pt 3363145



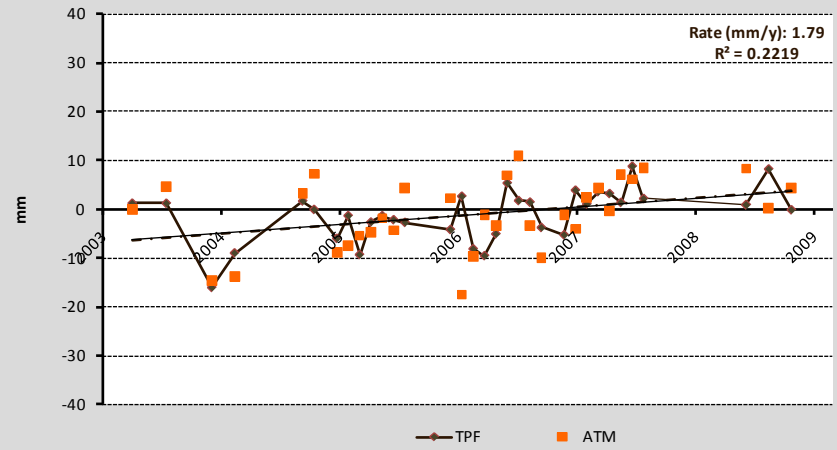
Pt 3519033



Pt 3632265



Pt 3708169



4.3.5.2 Frame Z2

Multiple short baseline interferometry (SBAS) analysis in this frame is not affected by strong disturbs, the area of study is fully covered and results are clear.

For the most of the investigated area, results of frame Z2 coincide to Z1 ones; light blue areas, that represent relative movements comprises between ± 1 mm/y (stable zones) cover the majority of the frame (Figure 154).

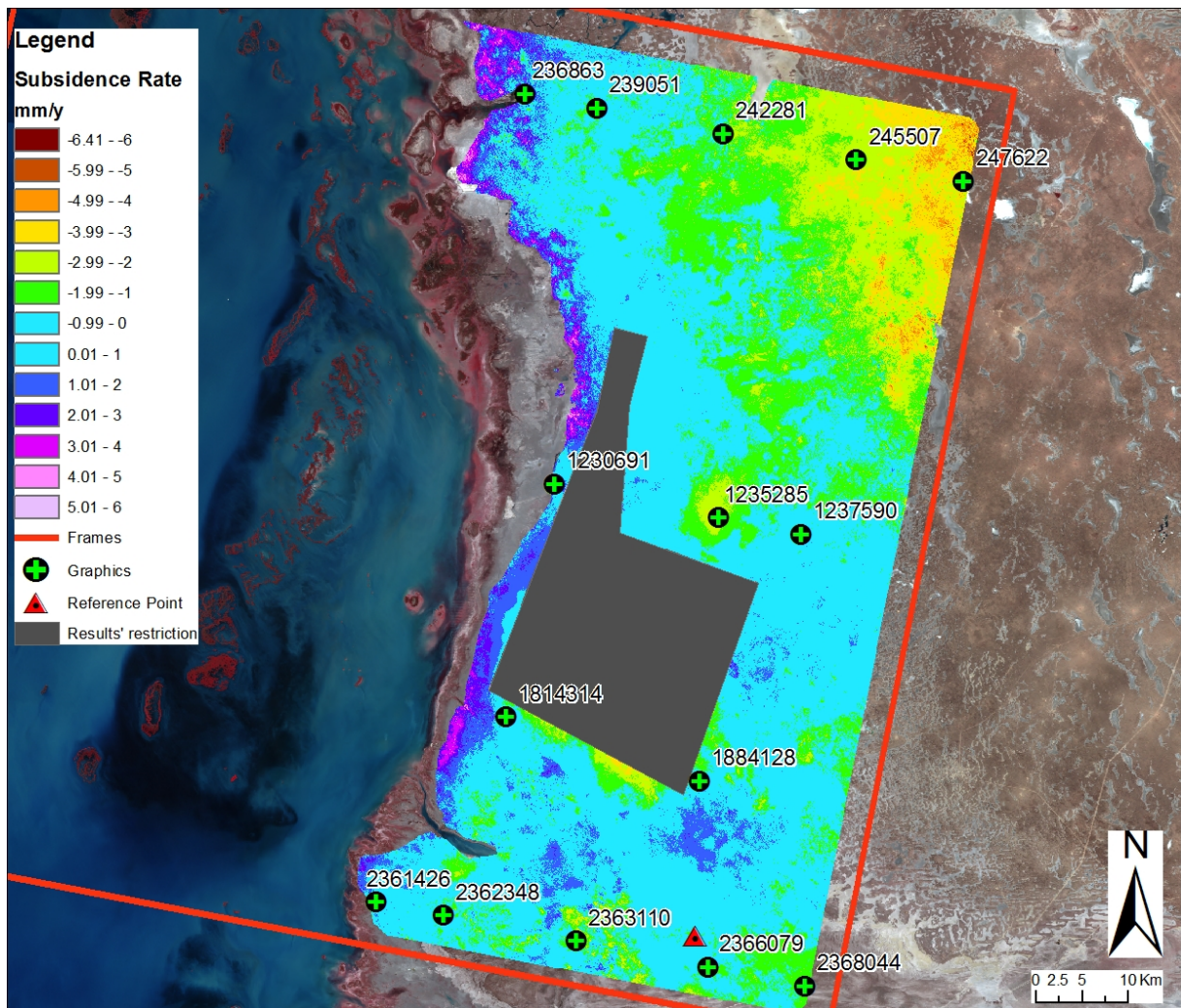


Figure 154: Results of SBAS analysis in frame Z2.

Areas with detected movements among ± 1 and ± 4 mm/y are visible. In the north-eastern corner of the frame InSAR technique detects a wide area of around 480 km² where the relative lowering rate reaches values comprises between -1 and -5 mm/y (availability of images since 2004). Reasons are unknown, probably linked to the geological complexity of the area and the interactions of big salt diapirs to the sedimentary cover.

An opposite trends are detected along the coastal area: uplift rates comprise between +1 and +4 mm/y, as shown in Figure 154 are identified along a thin zone along the whole coastal area. It's possible to identify similar features in the previous frame Z1, but coastal area is not fully covered and uplifts are fragmented. Interpretations have to be performed with care, but on the whole movements could be related to coastal processes and to the effect of ice-deice cycles on sediments. Considering that images used for the analysis were taken exclusively in summer-autumn periods, the most reasonable hypothesis supposes that these uplifts are caused by the scarcely cemented sediments' reaction of a decompression due to the melting of ice coverage. Other hypothesis could be an accretion due to wind-transported sediments trapped by coastal vegetation, the increasing of water table levels within unconsolidated sediments during storm surge events combined with a general depositional trend.

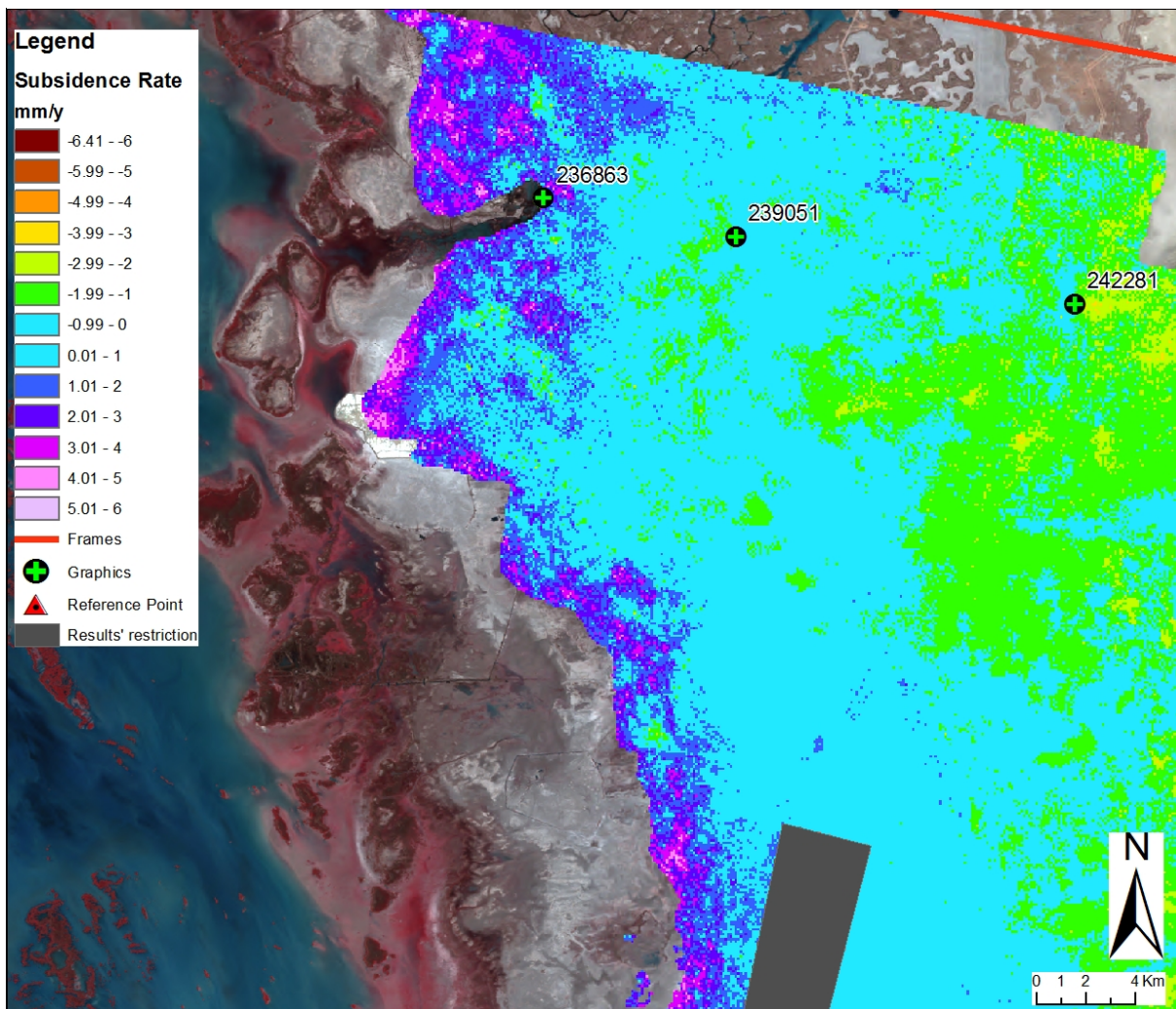


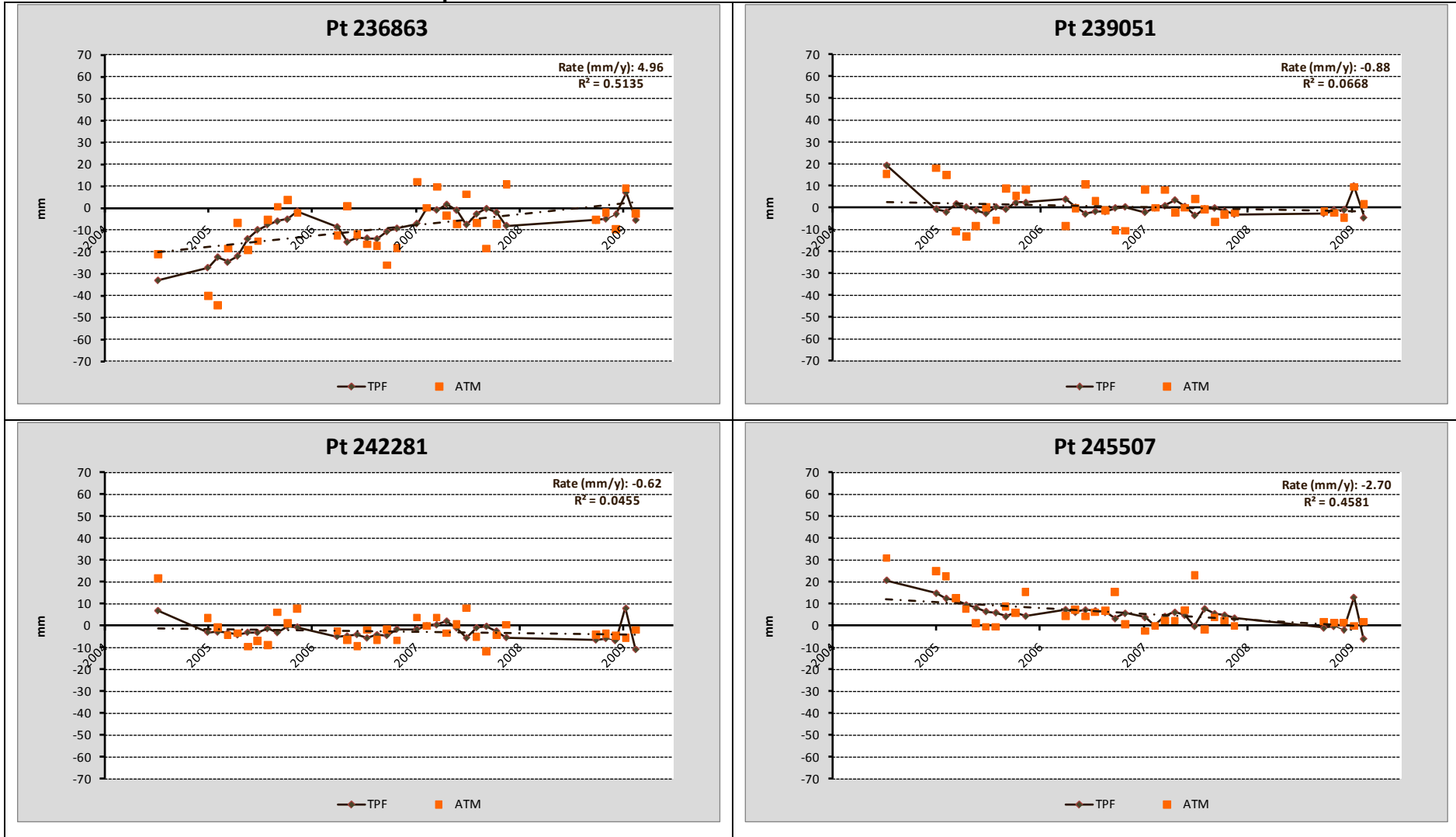
Figure 155: Uplifts along the coastal area.

The time behaviour of the displacement measured for some zones of interest within the whole frame Z2 are shown in Table 18; their location is provided in Figure 154.

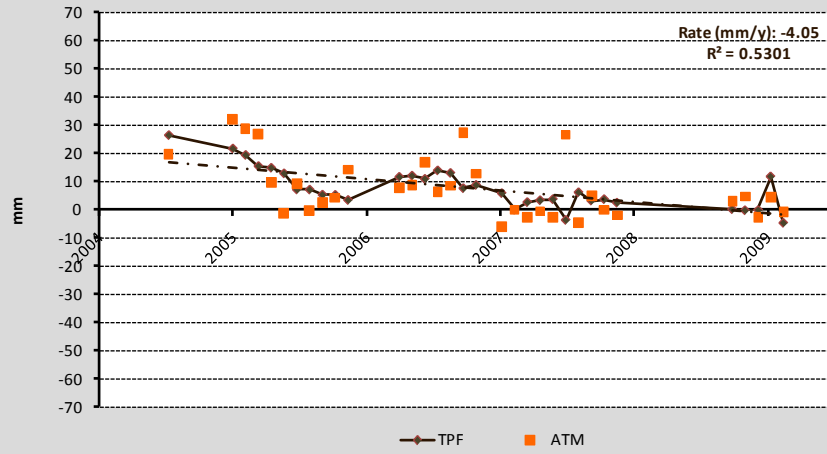
The regression lines and their low values of coefficient of determination R^2 confirm that there isn't a specific trend for the majority of the stable surface detected; only in areas where movements recorded exceed values of ± 1 mm/y trends are quite clear, with value of R^2 up to 0.5.

For frame Z2 complete results are shown in drawings Map.II.3.3 (Quick-looks after inversion and trend analysis) and Map.II.3.4 (INSAR-SBAS Analysis).

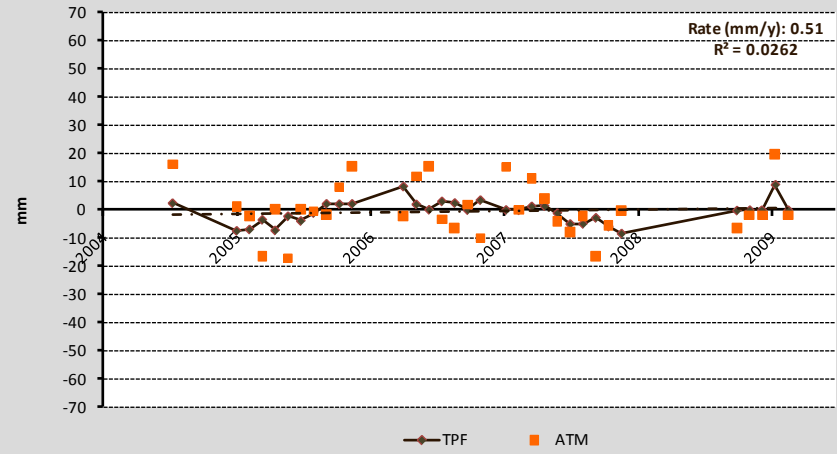
Table 18: Displacements versus time for a few sites selected within the frame Z2.



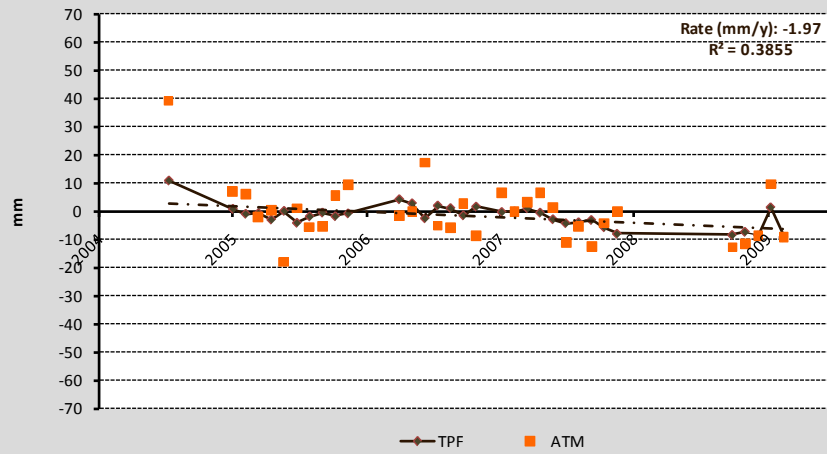
Pt 247622



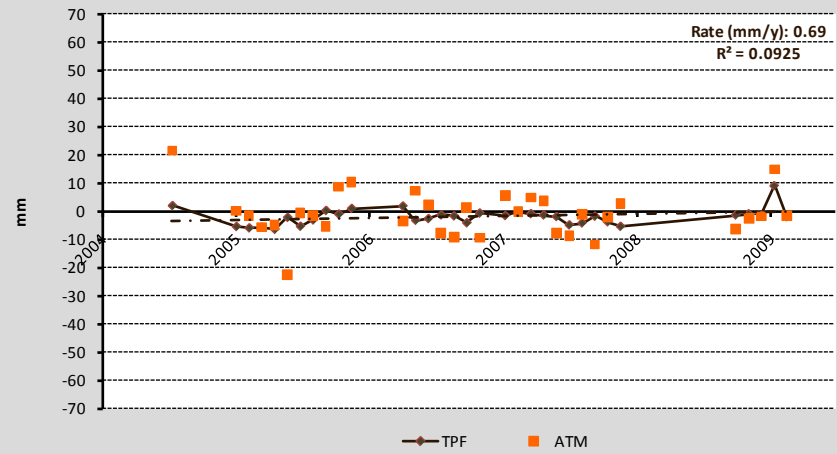
Pt 1230691



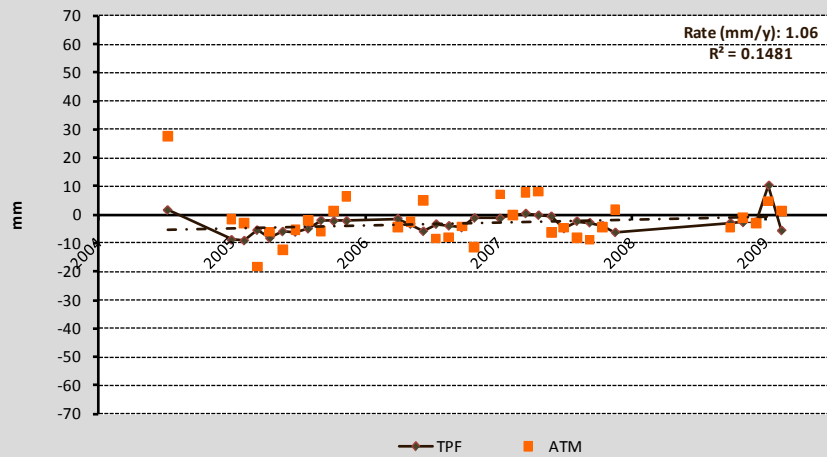
Pt 1235285



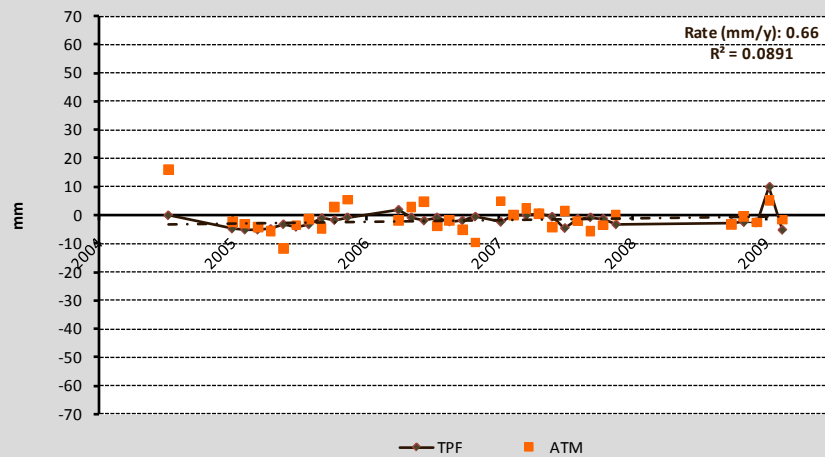
Pt 1237590



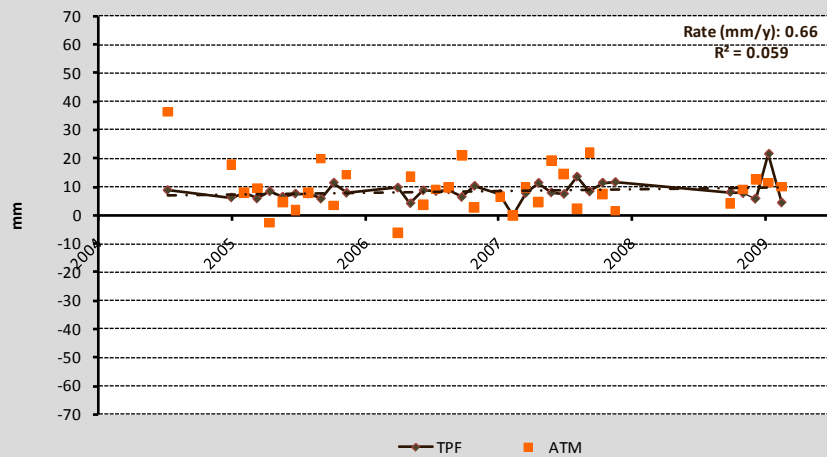
Pt 1814314



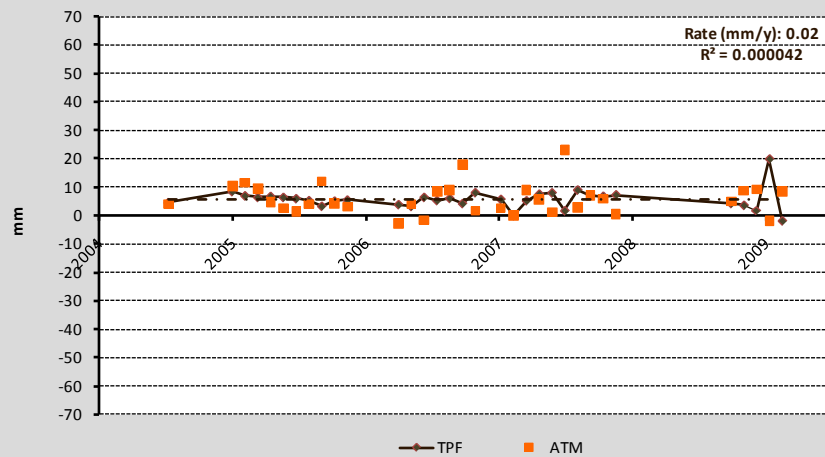
Pt 1884128



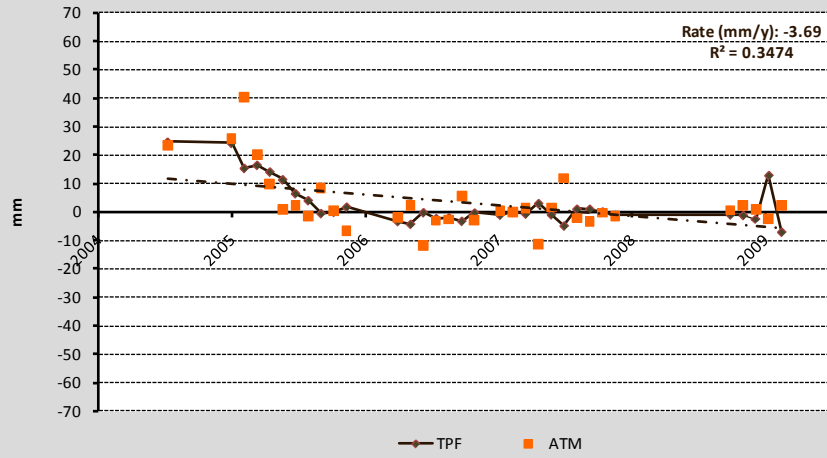
Pt 2361426



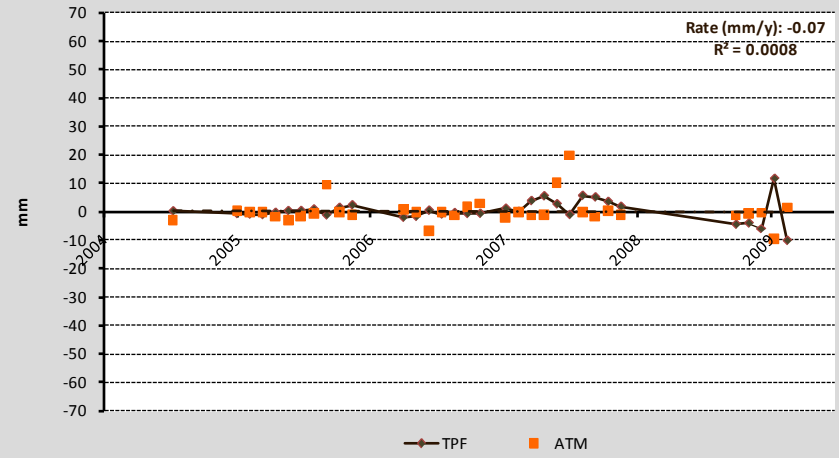
Pt 2362348



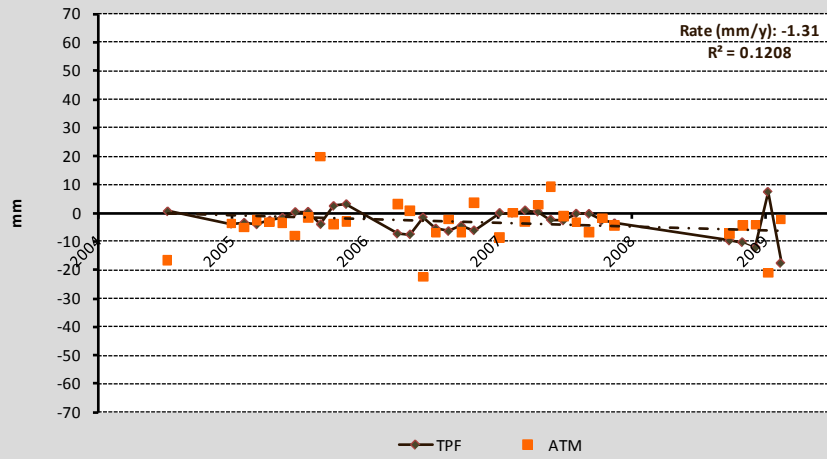
Pt 2363110



Pt 2366079



Pt 2368044



4.3.5.3 Frame Z3

InSAR analysis in the third frame of the study area (Figure 156) is affected by strong disturbs only in central portion, probably because of the physical characteristics of the Buzachi Peninsula; low areas, sometimes flooded, cause the loss of signal coherence among the set of available images. Despite these areas, the SBAS capability to resolve land movement is adequate within this frame.

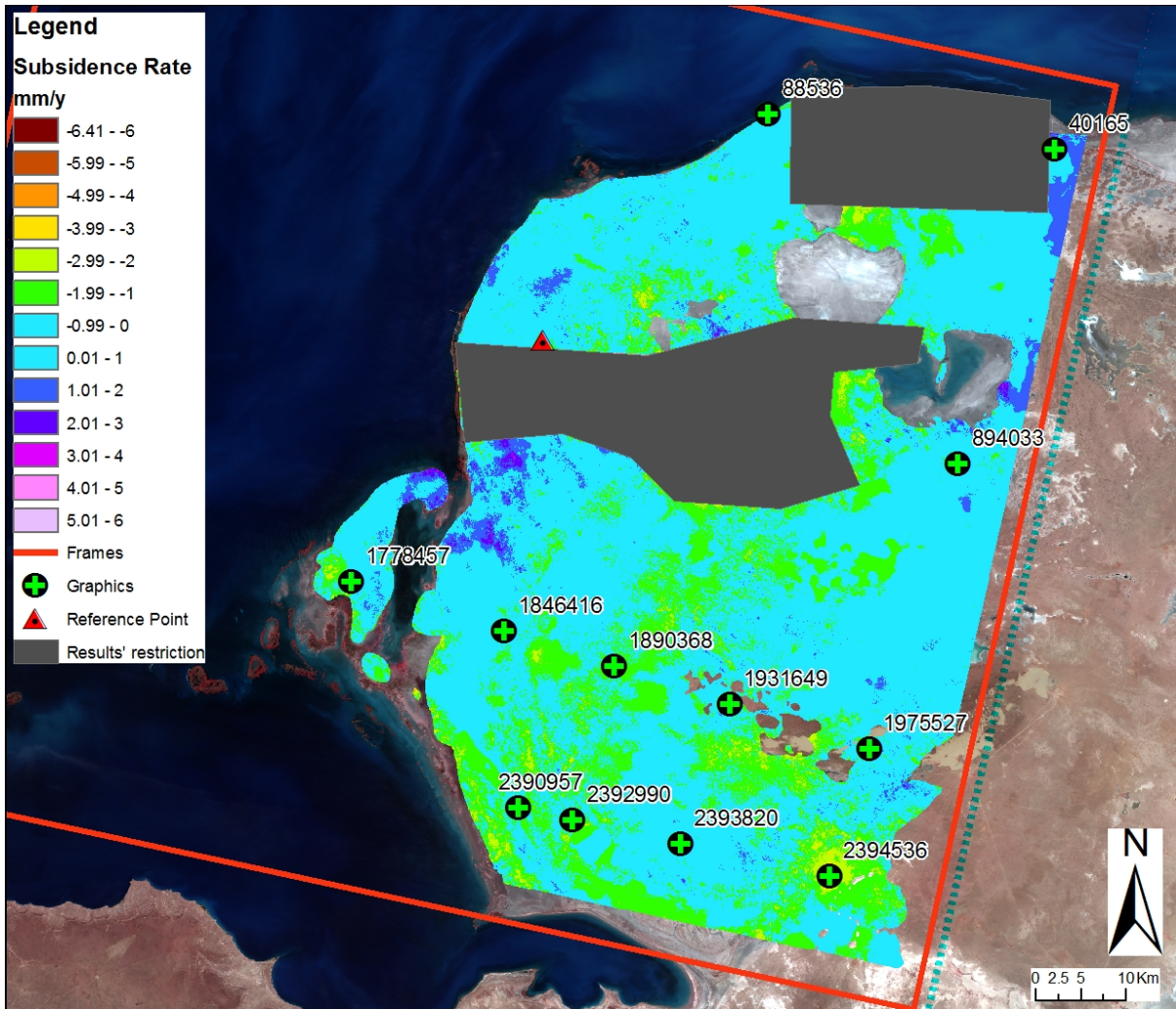


Figure 156: Results of SBAS analysis in frame Z3.

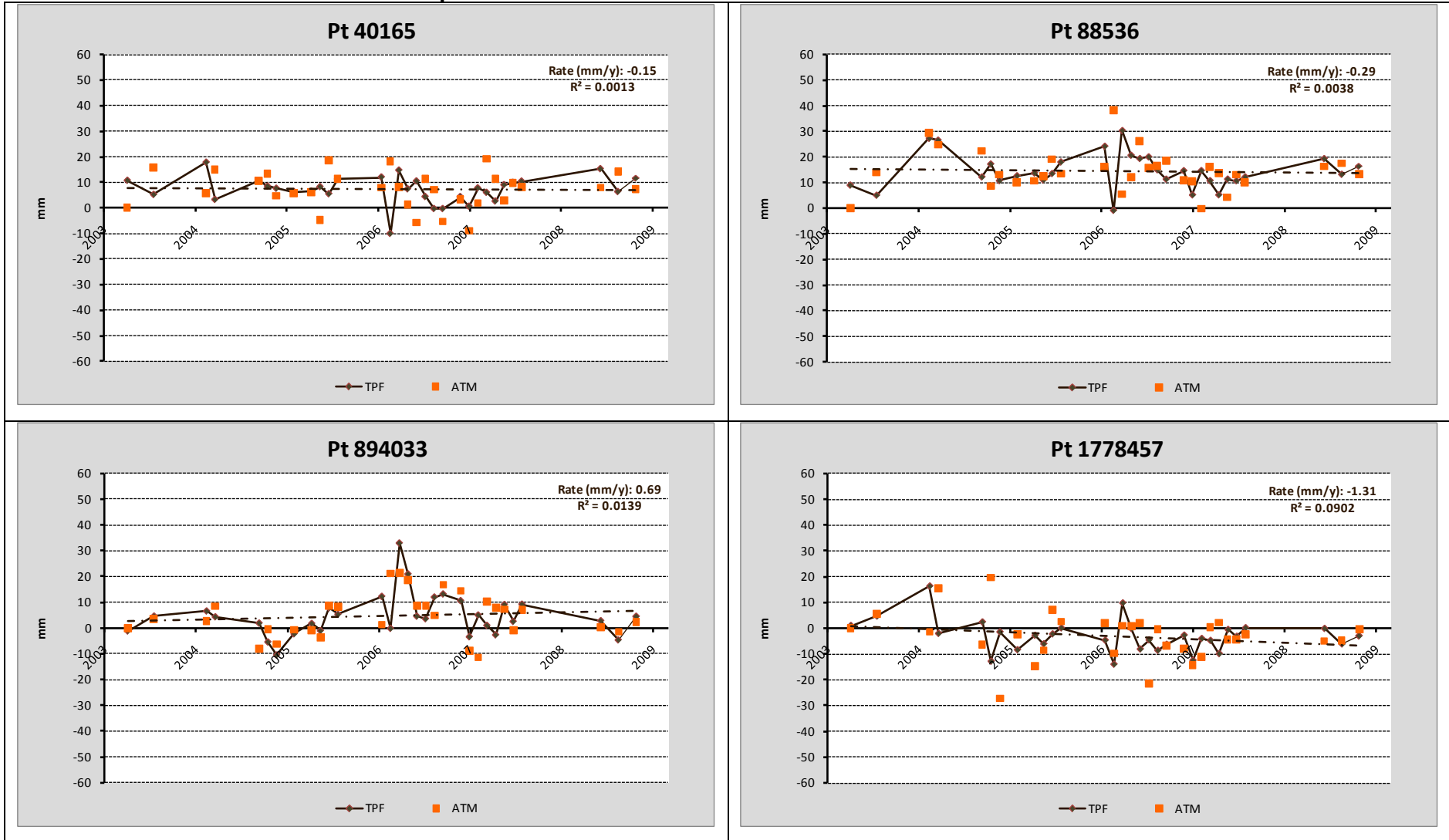
Considering the natural development of the area, Buzachi Peninsula is characterised by stable behaviour, with relative displacements comprise between ± 1 mm/y for the most of the area. In some limited areas movements reach values up to -3 mm/y.

The time behaviour of the displacement measured for some zones of interest distributed within the whole frame Z3 are shown in Table 19; their location is shown in Figure 156.

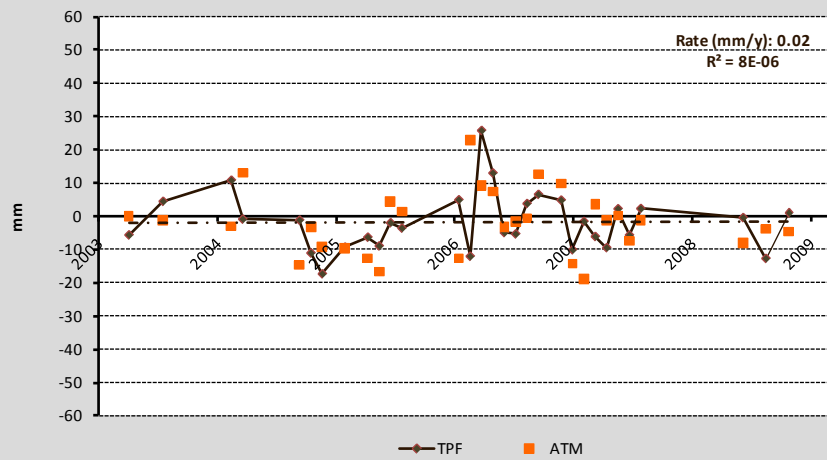
The regression lines and their low values of coefficient of determination R^2 confirm that there isn't a specific trend for the majority of the stable surface detected; only in areas where movements recorded exceed values of ± 2 mm/y trends are quite clear.

For frame Z3 complete results are shown in drawings Map.II.3.5 (Quick-looks after inversion and trend analysis) and Map.II.3.6 (INSAR-SBAS Analysis).

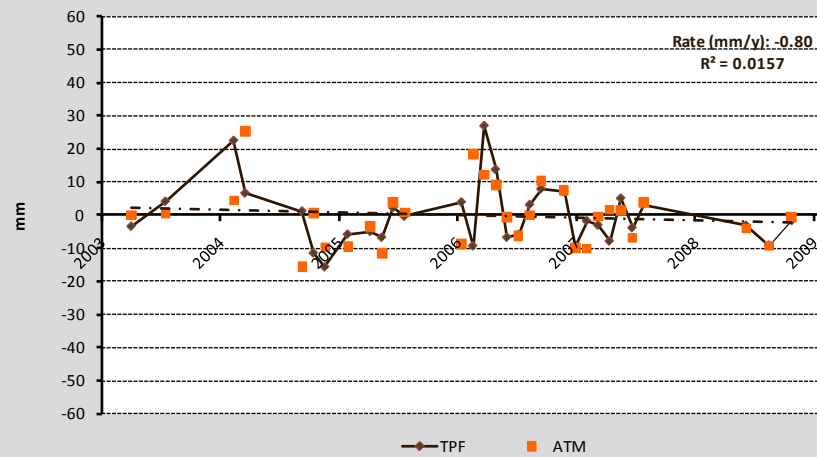
Table 19: Displacements versus time for a few sites selected within the frame Z3.



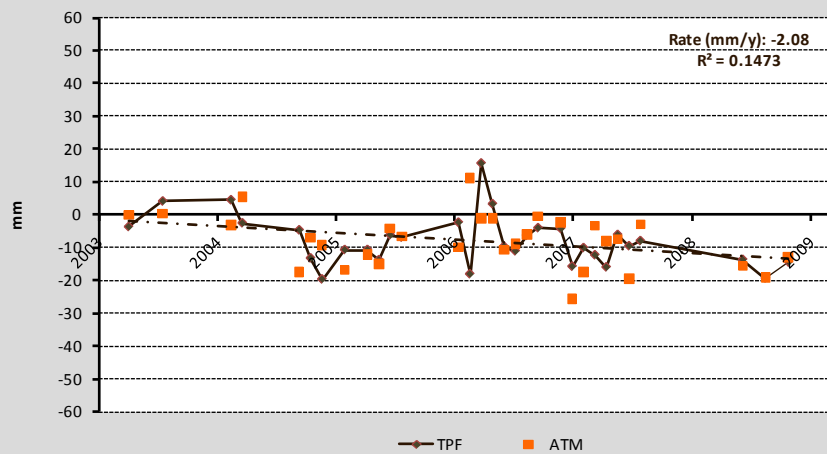
Pt 1846416



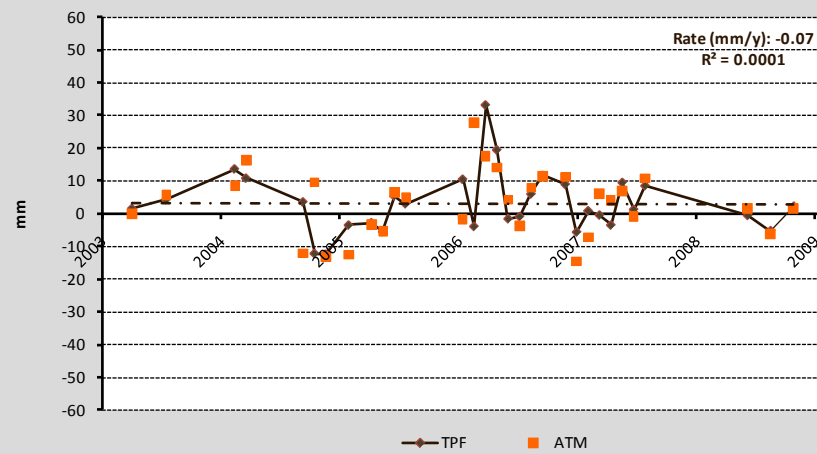
Pt 1890368



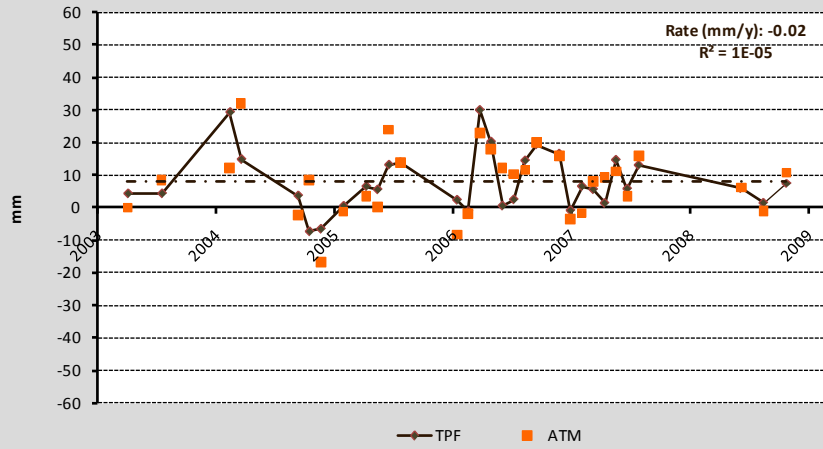
Pt 1931649



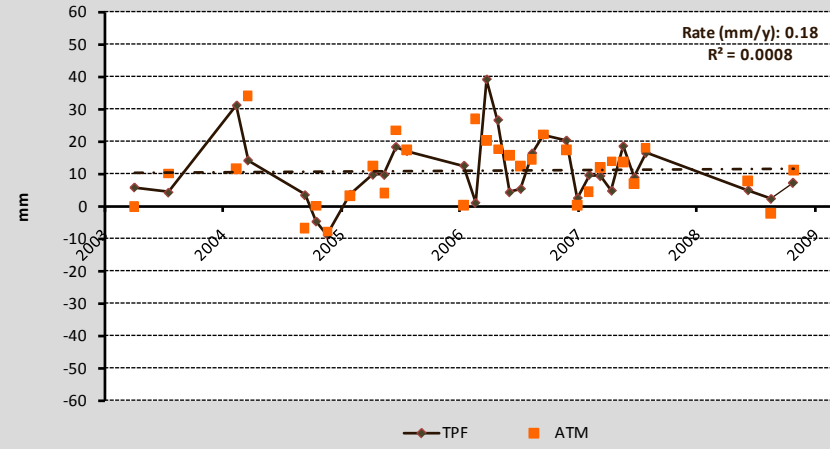
Pt 1975527



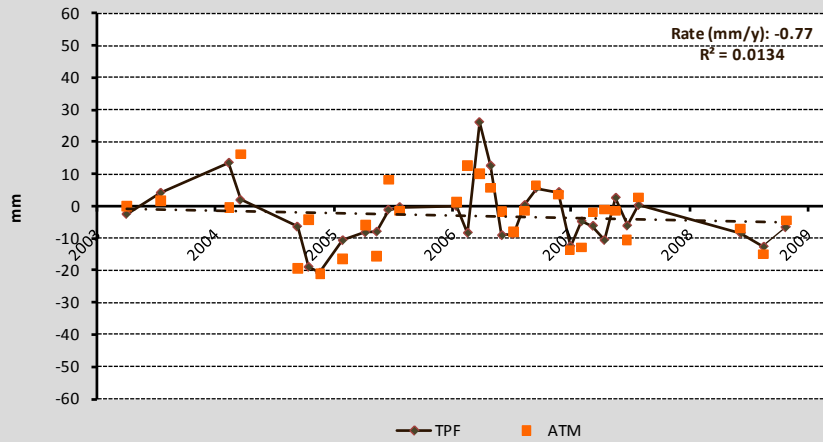
Pt 2390957



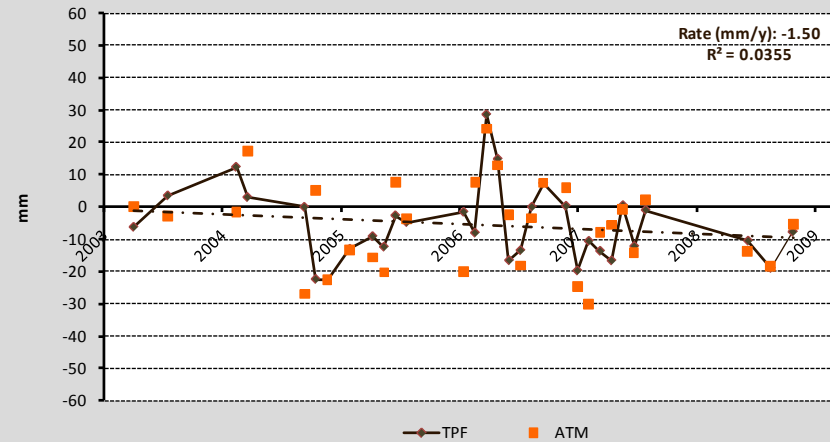
Pt 2392990



Pt 2393820



Pt 2394536



4.3.6 Preliminary application of IPTA

We have tried to investigate the capability of IPTA to detect land displacements in the study area. The PSI technique is a relatively recent development that can reduce the principal errors inherent in InSAR processing methods, errors caused by temporal and geometrical decorrelation and atmospheric artifacts.

Moreover, this technique is suitable for monitoring activities. Further details 8.

The IPTA application has been carried out with two steps. First, the distribution of candidate point targets has been obtained for the three selected frames. Second, the interferometric procedure has been completely developed only for frame Z1, in which the number of PT is appropriate.

In order to test the possibility of applying this methodology to area of investigation using the available ENVISAT data set, candidate point targets have been identified for the three frames based on the intensity variability of the co-registered single-look complex images and the spectral characteristics averaged over the stack of single-look complex images. The quality of the candidate point-targets has been further examined on point-target interferograms calculated with respect to the central reference used in image co-registration and flattened with use precision Delft orbits. The standard deviation of a two-dimensional linear regression to solve for both the height corrections with respect to the SRTM height and the deformation rate computed for neighbouring points gives a more robust indication of candidate point targets.

As indicated in Figure 157, Figure 158 and Figure 159, the number of candidate point targets is sufficiently high only for all the three frames and, in particular, in frame Z1. There are large areas where any persistent reflectors have been detected. A possible explanation for this is the presence of snow-cover on a large number of acquisitions. Taking also into account that the number of available scenes is just sufficient to perform a persistent scatterer investigation, the results obtained through this preliminary investigation confirm that traditional multi-baseline interferometry is a more robust general approach for the analysis of the subsidence of the north-east part of the Caspian Sea with ENVISAT ASAR data.

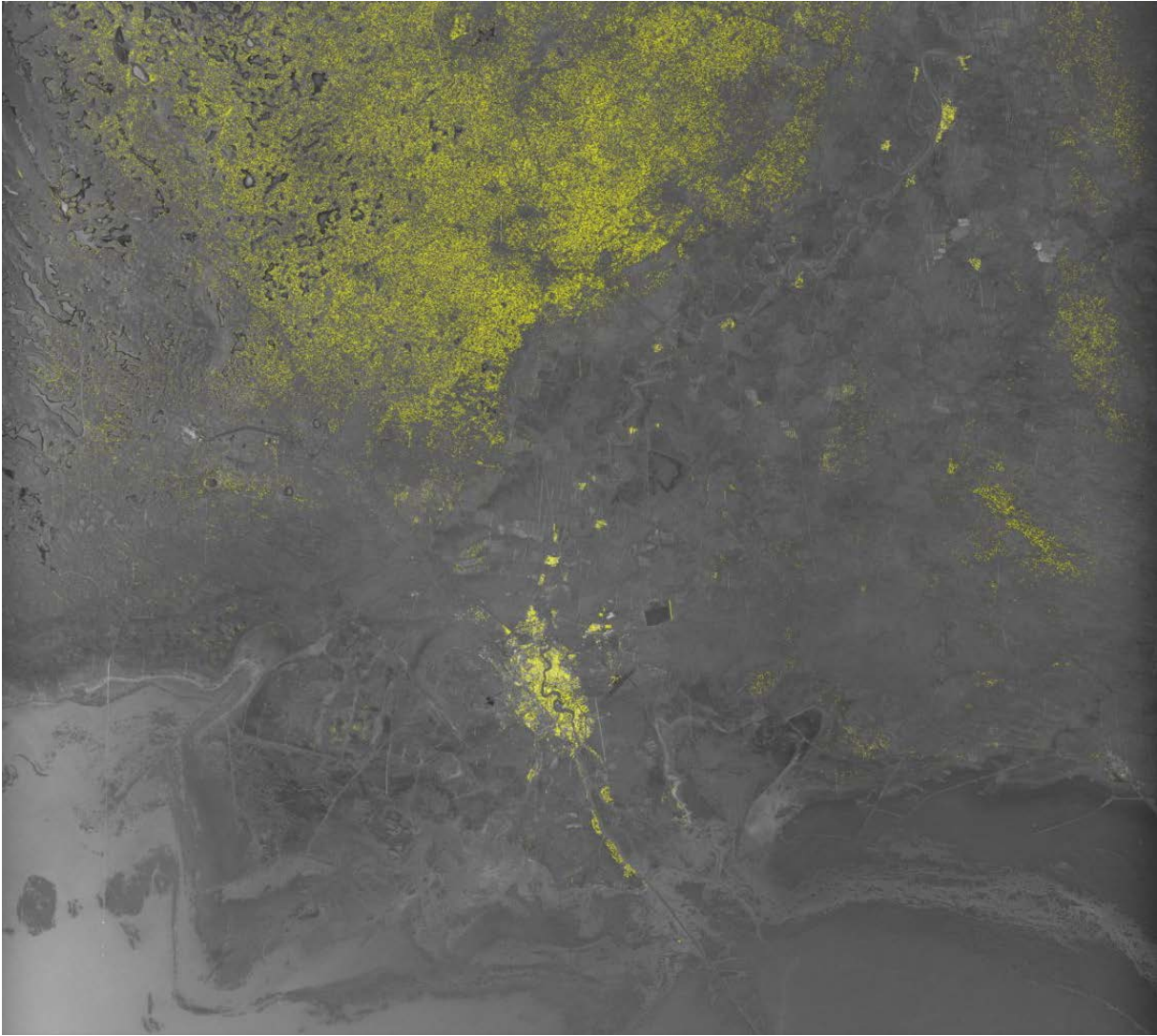


Figure 157: Identification of candidate persistent scatterers in frame Z1.

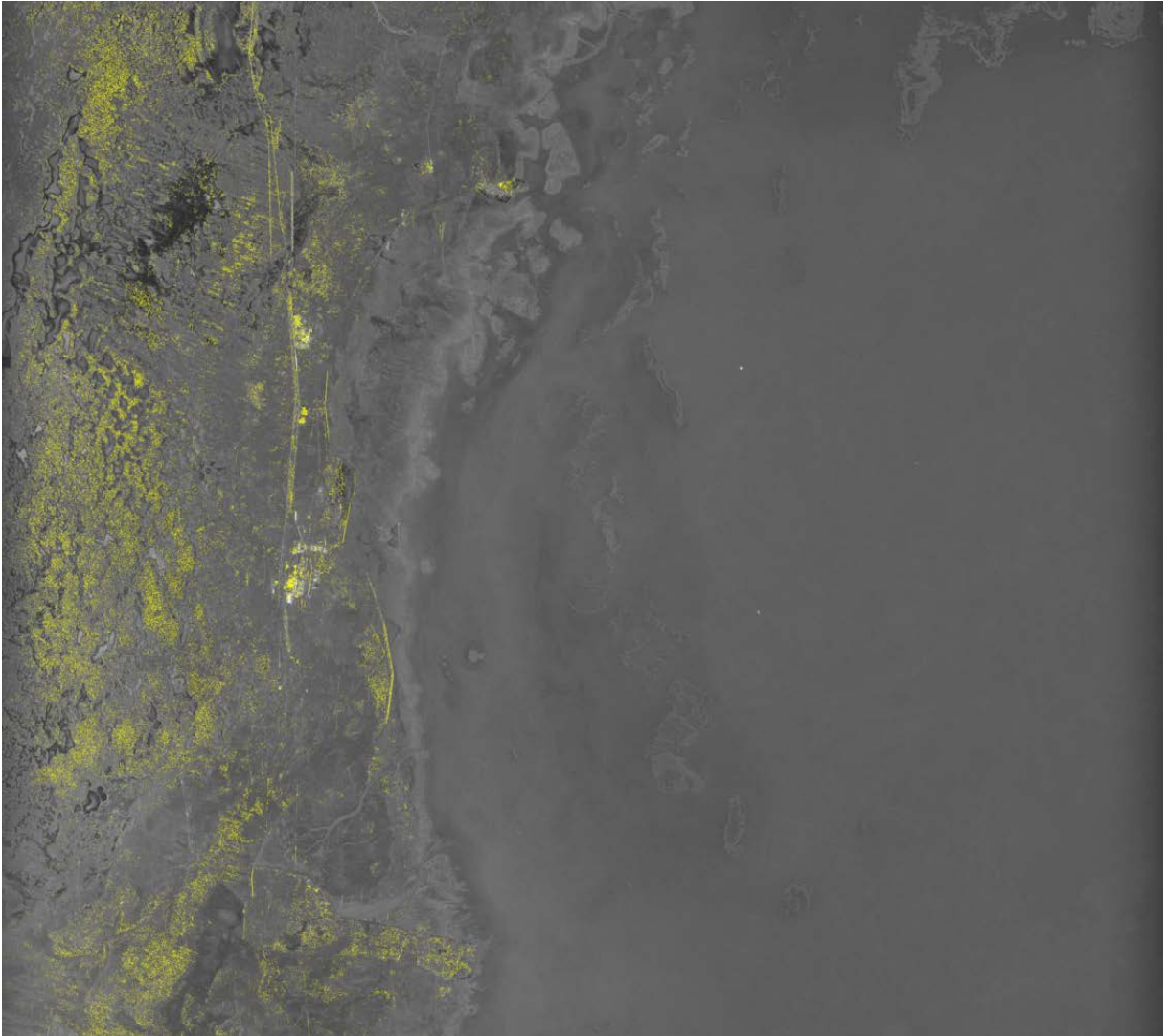


Figure 158: Identification of candidate persistent scatterers in frame Z2.

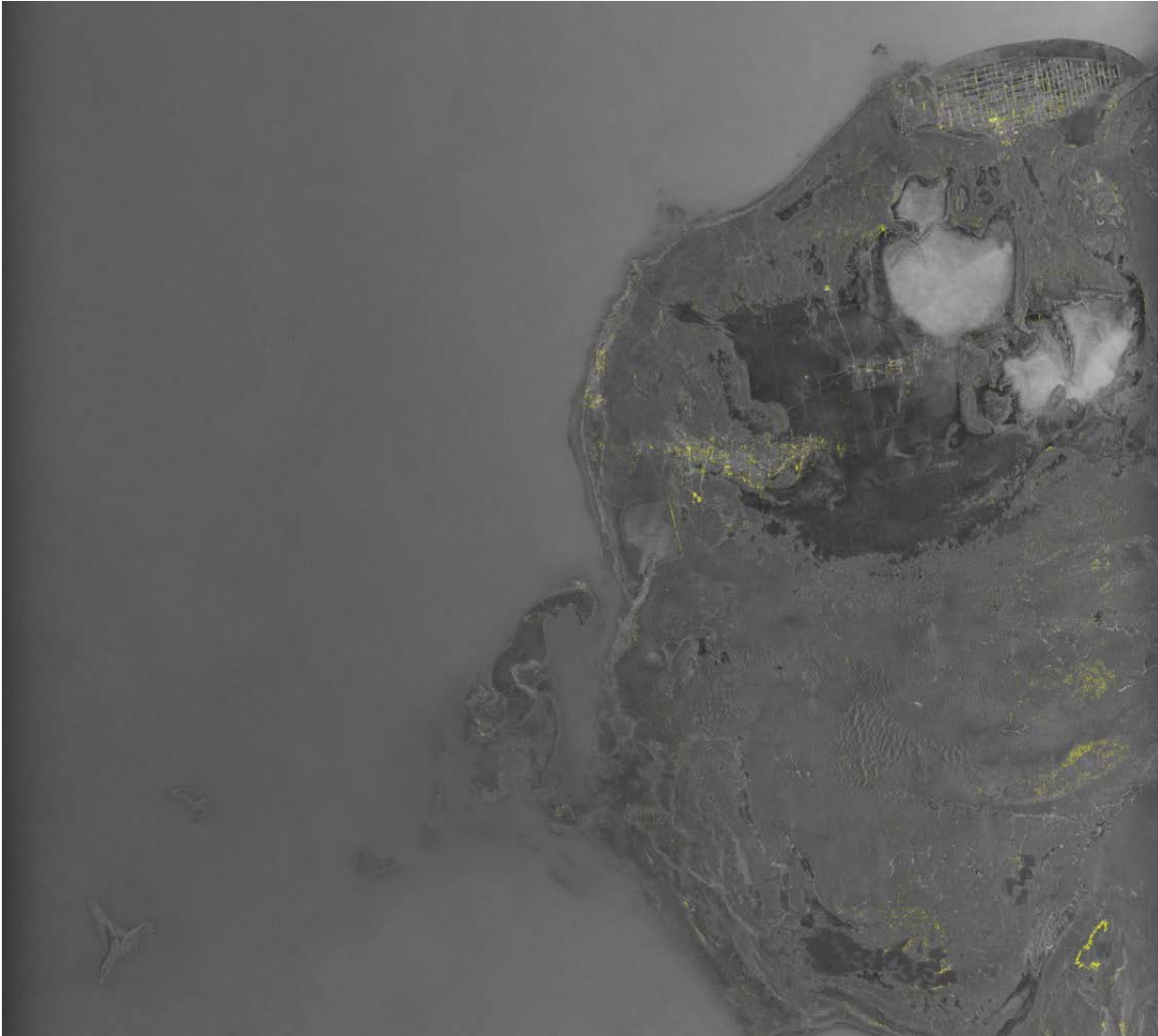


Figure 159: Identification of candidate persistent scatterers in frame Z3.

IPTA has been performed for the frame Z1 with use of GAMMA IPTA software. In order keep the number of data used in the regression, all acquisitions were considered. As a consequence of snow-cover and frozen surfaces in winter we expect a larger noise over the rural, semi-desertic areas than over the urban areas. The IPTA results are shown in Figure 160.

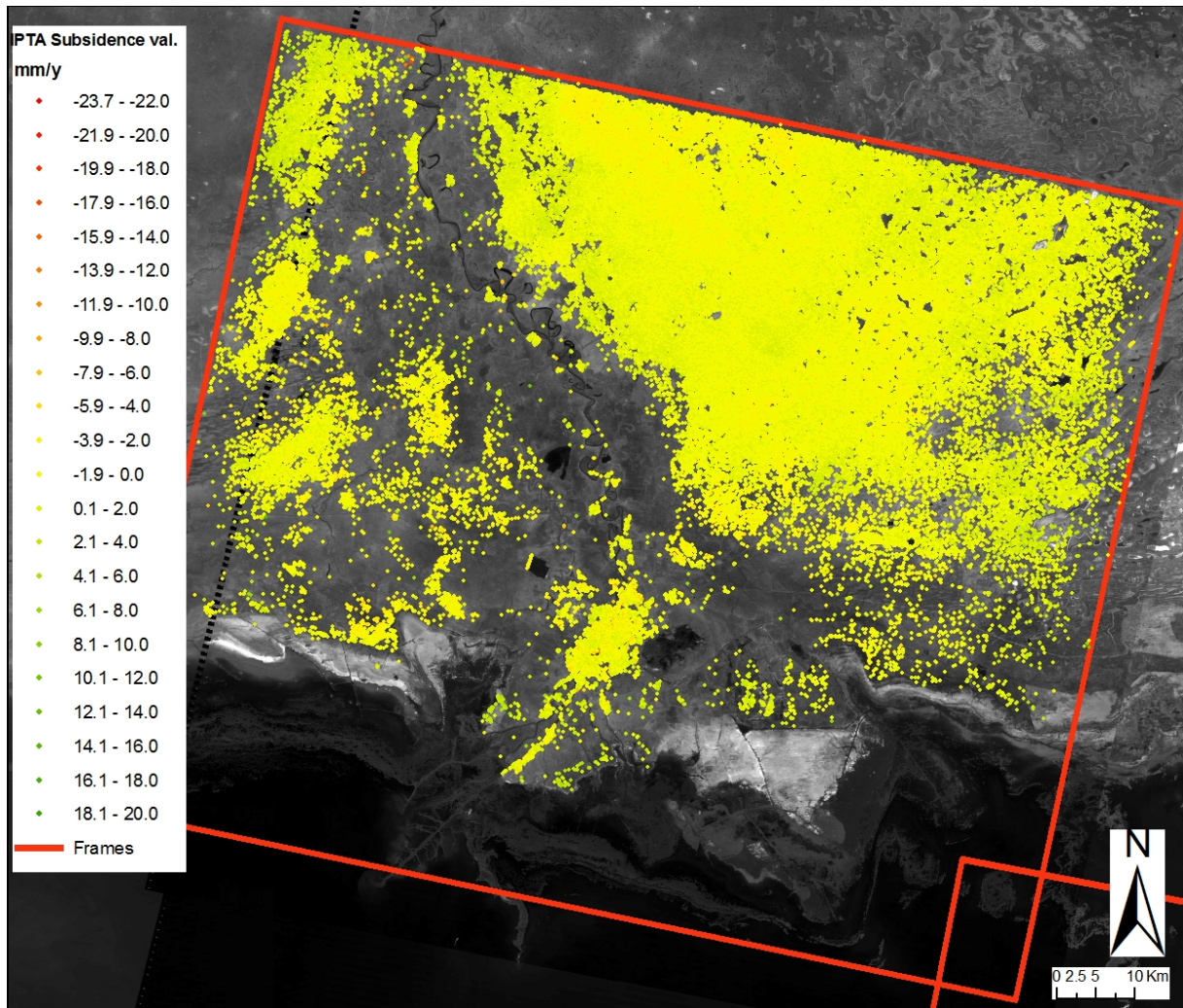


Figure 160: Results of IPTA before outliers filtering.

It is well known from the scientific literature that SAR analyses on persistent scatterers produce displacement rates that are characterized by a certain variability. This is due to the fact that, conversely to SBAS, which computes the average movement of each pixel of the SAR images, IPTA detects the displacement of single point-wise reflectors. By IPTA we are able to measure the movement of single engineered structures that can differ significantly for close structures also due to, for instance, the foundation typology, the structure load, the subsoil properties, the date of construction of the buildings. An example is shown in Figure 161, where a detail of the displacements measured at a zone of Atyrau is presented. The figure clearly shows that adjacent buildings move with different velocity.



Figure 161: Example of local displacements in a zone of Atyrau (light blue dots: rates value between ± 2 mm/y; yellow dots: rates value between -2 and -8 mm/y).

Because the main interest of the study is to provide the "average" subsidence that characterizes the coastland of the northern Caspian, it is preferably to remove some of the scatterers with a movement significantly different from those of the nearby points. These scatterers can be viewed as outliers and have to be filter out. An automatic procedure has been implemented for this purpose. The area of frame Z1 has been divided in a regular grid of dimension 250mx250m and for each cell the mean displacement value and the related standard deviation are calculated. Then the scattarer characterized by a movement exceeding the average \pm twice the standard deviation have been deleted.

Figure 162 shows the location of the removed PT. Their number amounts to 2134, out of the original 186850, i.e. about 1,14%. The final map thus obtained is shown in Figure 163.

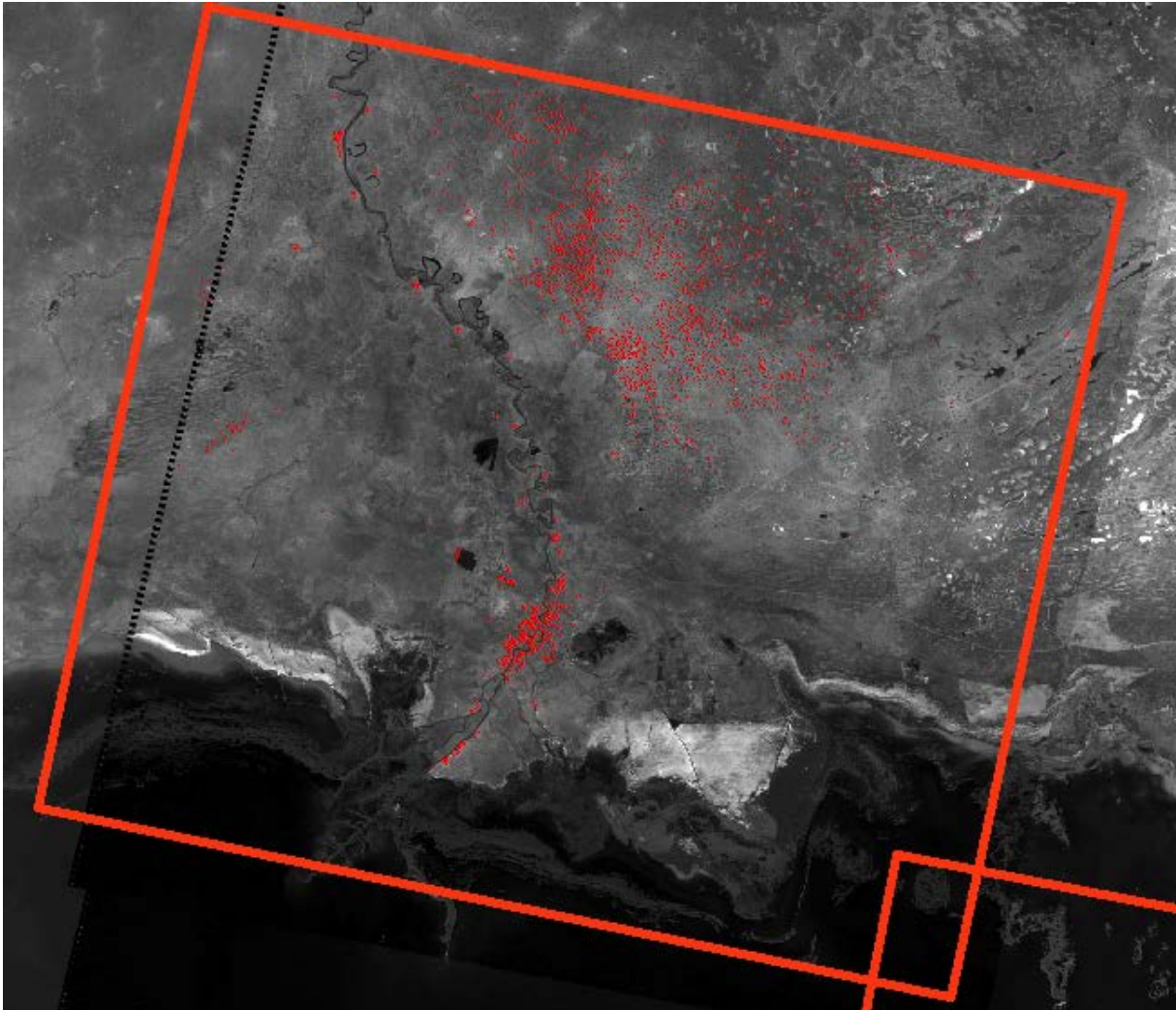


Figure 162: Location of the persistent scatterers removed from the regional investigation.

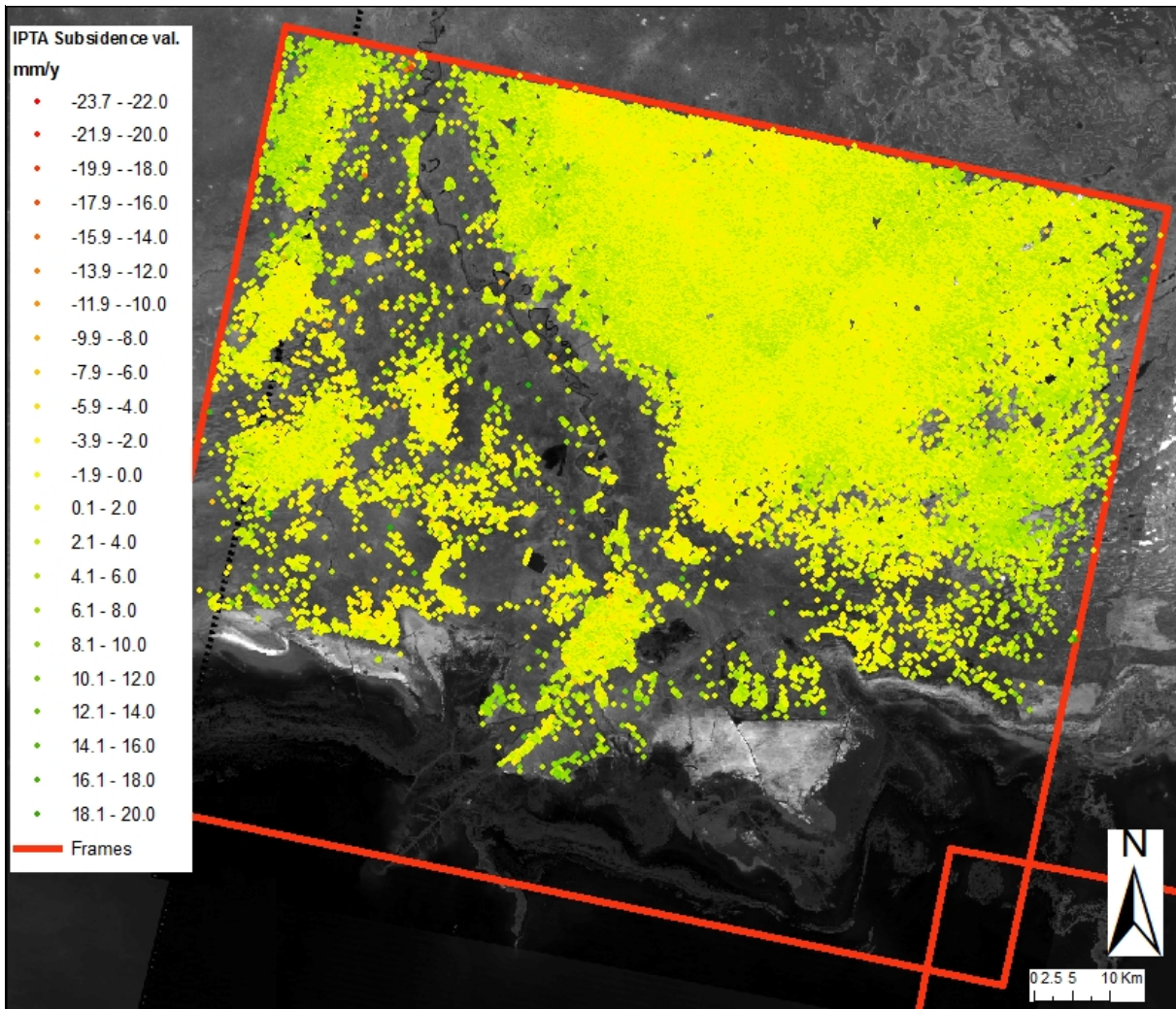


Figure 163: Displacement map for the frame Z1 obtained by IPTA after filtering out the measurements affected by a site-specific displacement trend.

Over the city the quality of IPTA is in general similar to that obtained with multi-baseline interferometry. The behaviour of certain isolated points not following the general trend is typical of persistent scatterer interferometry. This effect is removed in multi-baseline interferometry by the spatial phase filtering (Figure 164).

On the other hand, where anthropogenic structures are not present we observe larger disturbances and there is a difference of up to a few mm/year between IPTA and multi-baseline interferometry (Figure 165).

Phase signals related to snow-cover and frozen areas in addition to those related to atmospheric disturbances are the cause of phase-unwrapping errors in some of the layers. In IPTA, this effect is even larger than in multi-baseline interferometry because of the reduced number of points and decorrelation over some of the winter acquisitions. In addition, for multi-baseline interferometry more care was dedicated to phase unwrapping with eventually the removal before least-squares inversion of certain image pairs.

Even if performed with a rather general approach without care of the specific conditions of the area under investigation, IPTA do not indicate the presence of important movements covering large zone over frame Z1.

IPTA preliminary application results are shown in drawing Map.II.3.7_Frame 1_INSAR-IPTA_Analysis.

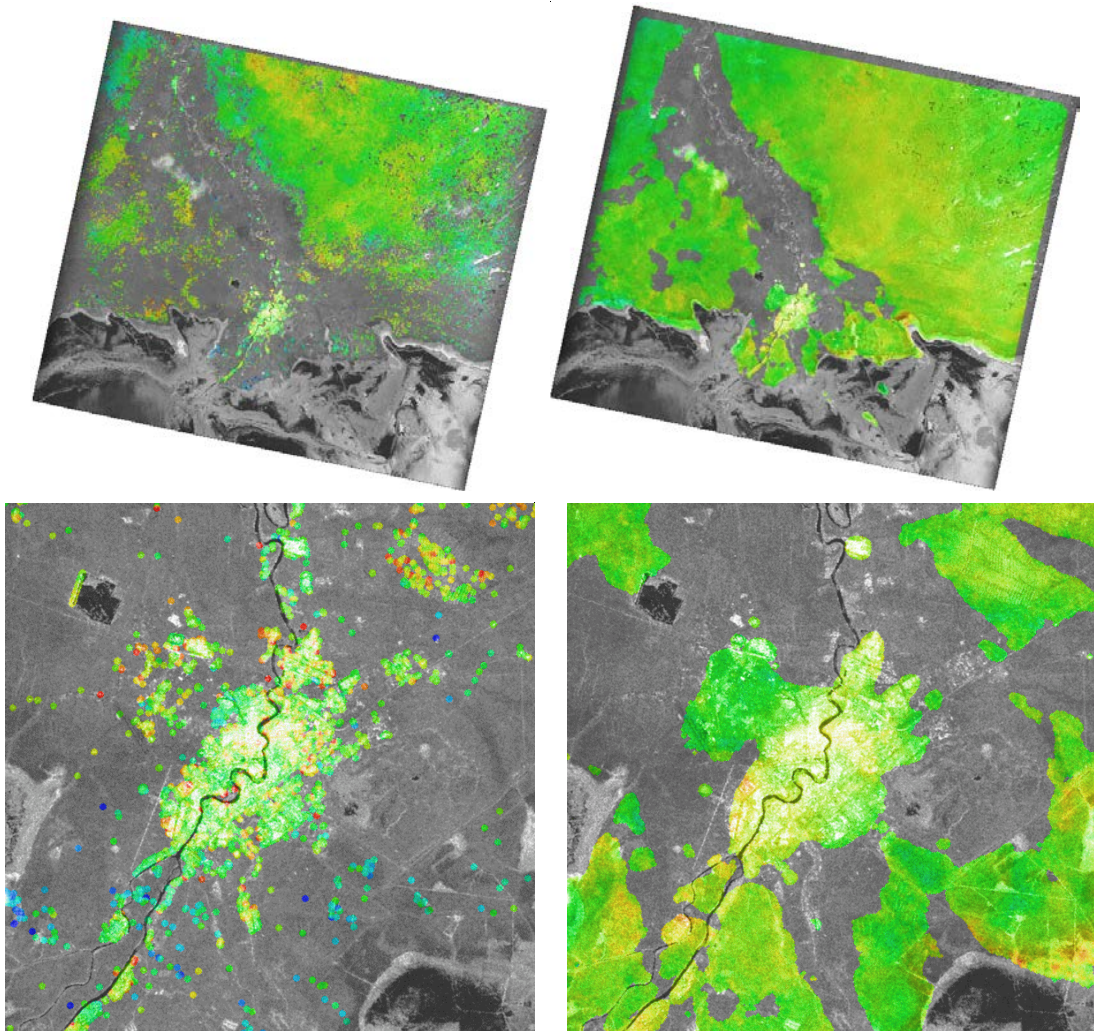


Figure 164: Comparison between IPTA (left) and SBAS (right) on the whole frame Z1 and in correspondence to Atyrau.

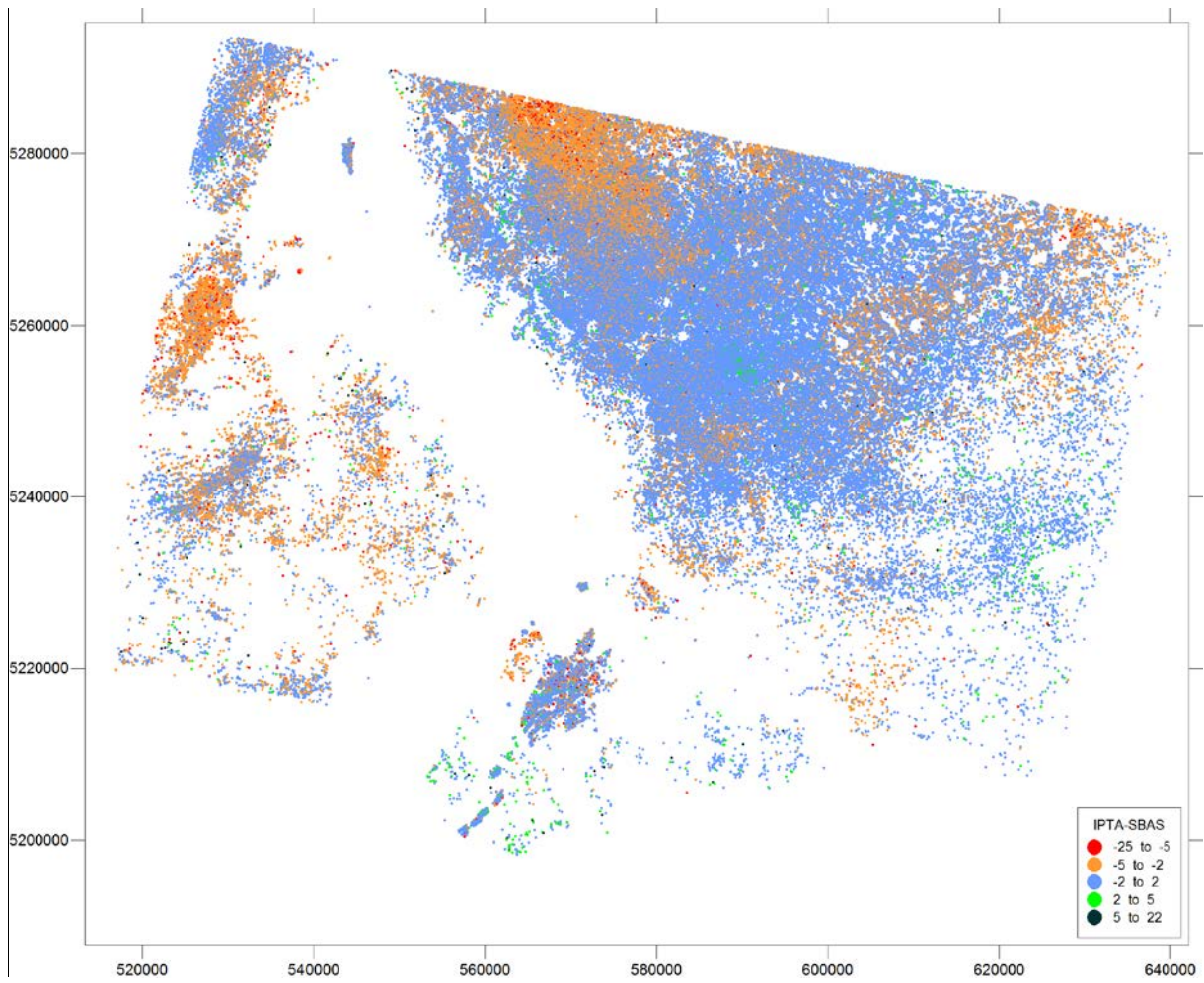


Figure 165: Differences between IPTA and SBAS analysis.

4.3.7 Comparison of achieved results with the northern Adriatic coastland case study

A brief comparison of the result achieved during the study with ones obtained in similar projects is given.

For this purpose, different studies carried out by specialists in the last years (Teatini et al., 2011; Teatini et al., 2007; Teatini et al., 2005; Strozzi et al., 2009; Tosi et al., 2010; Tosi et al., 2009) in the northwestern coast of the Adriatic Sea (Venice lagoon and Po river delta) have been considered.

Relative sea level rise (RSLR), i.e., the interaction between sea eustatic rise and land subsidence, represents one of the geologic hazards threatening the low-lying coastal areas worldwide. The coast of the northern Adriatic Sea characterized by the presence of lagoons, i.e., Grado, Marano, Venice and those in the Po River delta, from the north to the south, marshes and reclaimed farmlands generally lying below the mean sea level, is the Italian area at greatest risk (Figure 166). The combined effect of land subsidence and eustasy (Figure 167) has produced ground settlements ranging from centimeters to meters, and created a significant ecological and environmental impact. The entire area has experienced permanent changes in coastal morphology and morphodynamics, which in turn have caused temporary, sometimes very destructive, effects such as erosion, wave setup, flooding and sea encroachment (e.g., Gatto and Carbognin 1981; Gambolati 1998; Gambolati et al. 1999). In this wide and complex area, land subsidence is characterized by a highly non-uniform distribution with several natural and anthropogenic factors controlling land motion. They act individually or together, on different depth-, area- and timescales (from millions to thousands of years and hundred to tens of years, respectively), thus reflecting the geological history and the human development of the territory. Natural causes (Figure 168) refer to substratum deformation due to tectonics and geostatic load, together with natural consolidation of the Quaternary poorly consolidated sedimentary sequence, primarily the shallow transgressive Holocene deposits. Anthropogenic factors are mainly related to subsurface fluid removal and more locally to oxidation of recently reclaimed marshes and consolidation due to surface loads.

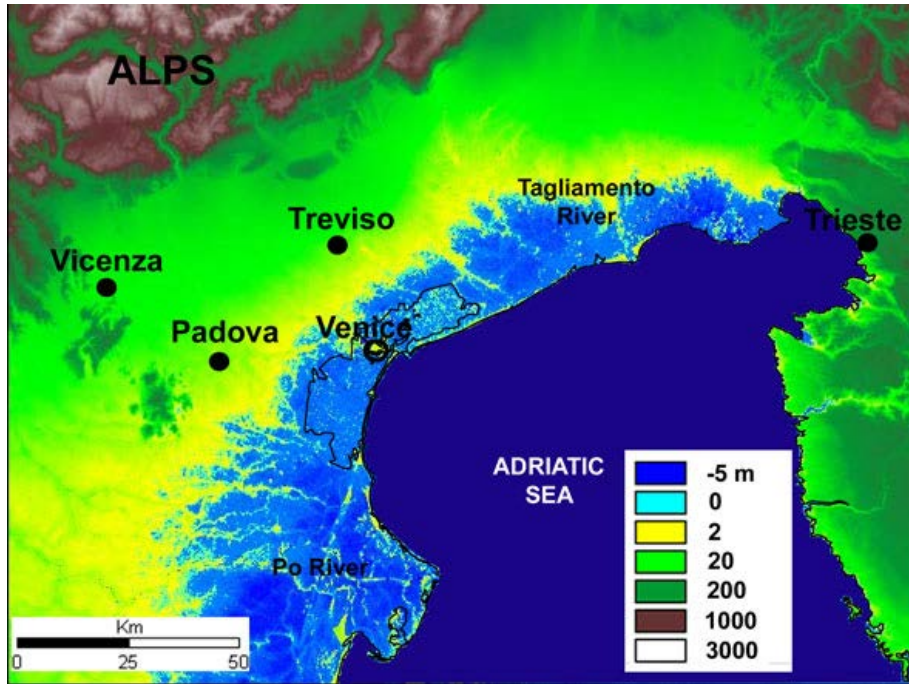


Figure 166: Digital elevation model (DEM) of the northern Adriatic region obtained from SRTM data.

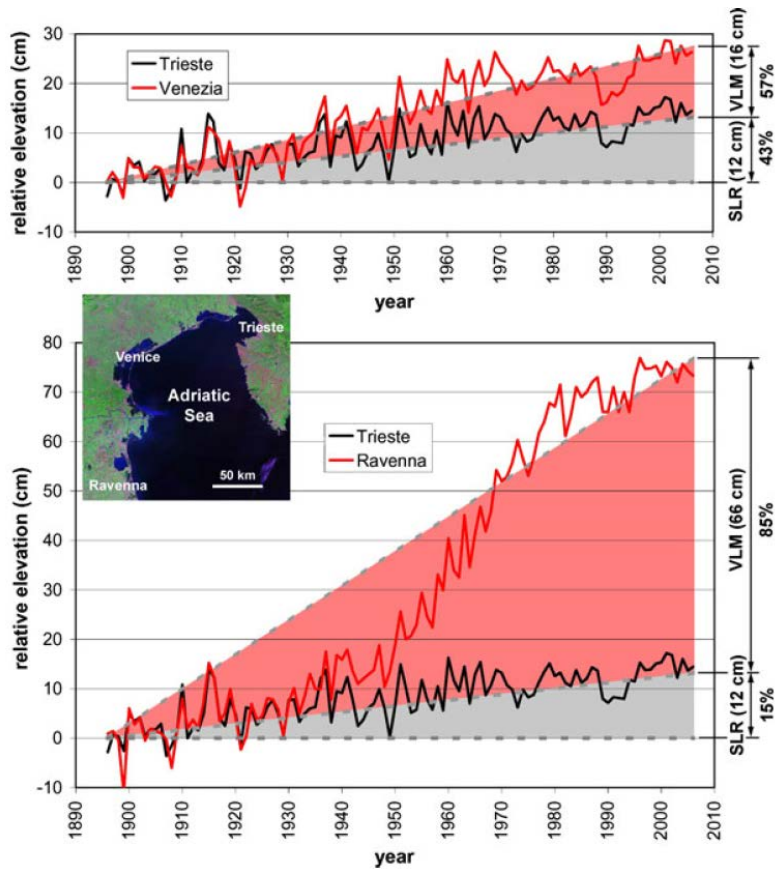


Figure 167: Relative sea level rise (RSLR) at Venice and Ravenna over the period 1896–2007.

Short-term anthropogenic causes became a key problem for the land stability of the whole northern Adriatic coastland during the twentieth century, especially from the World War II to the end of the 1960s when the civil, industrial, agricultural and tourist developments required huge amounts of water and an increasing energy supply. The only difference was the nature of the withdrawn fluids: artesian water in the Venice area (Carbognin et al. 1977), gas-bearing water in the Po Delta (Caputo et al. 1970), and both groundwater and gas (inshore and offshore) in the Ravenna region (Carbognin et al. 1978). Since the end of the 1970s, countermeasures have been taken and subsidence has been greatly reduced all over the study area (Carbognin et al. 1977; Carbognin et al. 2000).

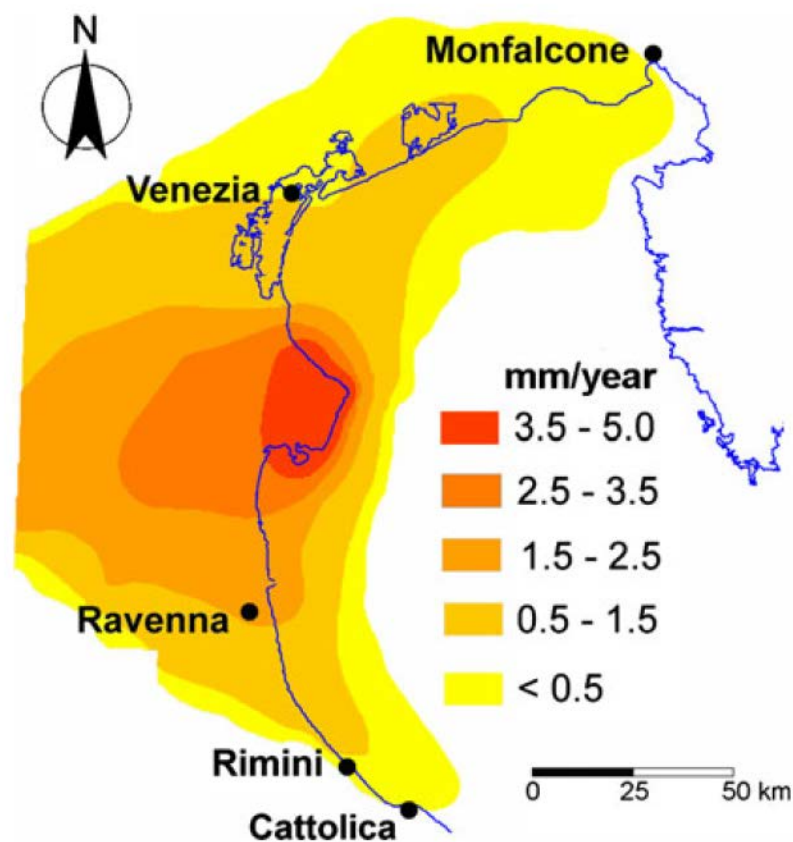


Figure 168: Recent natural land subsidence in the northern Adriatic coastal area (after Gambolati and Teatini 1998).

Nevertheless, RSLR has produced permanent loss in land elevation that has significantly increased the flood frequency and the impact of marine storms, causing severe damages to urban heritages and lagoon and coastal morphologies, especially in the most susceptible areas. In Venice, for example, the 25 cm of relative land elevation loss over the twentieth century has created a major concern despite this small value.

Geodetic measurements by high-precision leveling have been periodically carried out in the Venice coastal area since the end of the nineteenth century. Monitoring of land subsidence has been significantly improved over the last decade by space-borne observation techniques based on synthetic aperture radar (SAR) interferometry. Differential interferometric SAR (DInSAR) has been initially used to complement the ground-based methods (Tosi et al. 2002; Teatini et al. 2005). More recently, interferometric point target analysis (IPTA) has been applied (Teatini et al. 2007, 2009; Strozzi et al. 2009) in combination with leveling and GPS measurements with the main purpose of calibrating the SAR surveys as detailed in the methods section.

The analysis describes the present ground vertical movements in the Veneto coastland both at the “regional” (100 X 100 km²) and “local” (few square kilometers) scales.

4.3.7.1 *Ground vertical movements of the Veneto coastland: methods*

Geodetic surveys, though not made on a regular basis, have been periodically carried out in the eastern Po Plain since the end of the nineteenth century. The networks of leveling lines generally connected to inland “stable” reference benchmarks and running along the coast, were gradually improved over the decades. Leveling represented the only monitoring technique up to the 1970s.

Starting from the 1980s, space-based geodetic techniques such as the global positioning system (GPS) have been adopted to monitor vertical movements, mostly from the late 1990s. Differential and continuous global positioning system (DGPS and CGPS, respectively) surveys have been extensively used in the Venice area since then. The analysis of long CGPS time series of acquisition over many years allows estimating the velocity of movement with the level of accuracy of 1 mm/year.

Since 2000, SAR-based techniques have also been used to improve the qualitative and quantitative analysis of the vertical displacements in the Venice region. The measurements were initially carried out by the DInSAR approach, which has been used in geophysical sciences since the late 1980s (Gabriel et al. 1989), and more recently by IPTA, a refined approach developed about 10 years later and included within the so-called persistent scatterer interferometry (PSI) approach (Usai and Klees 1999; Ferretti et al. 2001; Werner et al. 2003).

Various satellite images have been used for different purposes:

- A total of 80 ERS-1/2 scenes (35 days repeat cycle) have been processed to map the movements occurring from 1992 to 2002, within the 100 X 100 km² area including the whole coastland and the inland of Vicenza, Padova, Treviso, and Venice (Tosi et al.

2002, Teatini et al. 2005). The first 59 ERS-1/2 scenes acquired before March 2000 were processed to a common Doppler centroid value of 250 Hz and were first used to estimate the average displacement rate. After March 2000, authors only considered ERS-2 scenes with Doppler centroid values between -89 and 1,144 Hz to extend the time series of displacement. These scenes, processed to their own Doppler centroid value, were in particular useful for continuity with ENVISAT.

- As much as 40 ENVISAT scenes (35 days repeat cycle) have been analyzed to monitor the recent coastland displacements from the northern portion of the Po River delta to the Tagliamento Rivers starting from 2003 (Teatini et al. 2007, 2009).
- A total of 30 TerraSAR-X stripmap images (11 days repeat cycle) acquired from 2008 have been used to detect the effect of the man-made intervention on the present ground movements in areas near the inlets of the Venice Lagoon (Strozzi et al. 2009).

4.3.7.2 ***Detected Veneto coastland vertical movements of the***

The ground vertical movements in the study area have been mapped over the three periods, 1992–2002, 2003–2007 and 2008–2009, using images acquired by the ERS-1/2 and ENVISAT satellites of the European Space Agency (ESA) and the new TerraSAR-X satellite launched by the German Space Agency, respectively.

The regional analysis performed for the first period has been of particular significance.

This has been carried out by developing an innovative “subsidence integrated monitoring system” (SIMS) that efficiently merges the different displacement measurements obtained by spirit leveling, DGPS, CGPS and SAR-based interferometry (Teatini et al. 2005). The SIMS has provided a high-resolution map of the land displacement rates from 1992 to 2002 of the entire Venice territory, which was never previously obtained at this scale (Figure 169). The map has pointed out the significant spatial variability of the ground vertical movements, both at the regional and local scales, with velocities ranging from a slight (1–2 mm/year) uplift to a significant subsidence of more than 10 mm/year.

The recent vertical movements of the Venice coastland between the northern portion of the Po River delta and the Tagliamento River is detected by ENVISAT (Figure 170) allowing continuing characterization of the vertical movements also in small areas scattered along the coastland, e.g., the islands located within the Venice Lagoon (Teatini et al. 2009). With respect to the previous decade, the main difference of the 2003–2007 displacement rates has been detected in the northern sector where a certain increase of the subsidence rates has been observed in the San Donà di Piave, Portogruaro and Caorle areas.

Figure 171 shows the map of the total displacements 1992–2007 as obtained by integrating the IPTA outcome based on ERS 1/2 and ENVISAT acquisitions. The map has been obtained by interpolating the two dataset values on the same 250 X 250 m grid using the kriging technique.

The result highlights a stable sector between Treviso and Venice, an uplift zone in the vicinity of Piove di Sacco-Lova (i.e., the western margin of the southern lagoon basin) and two major subsiding areas, i.e., eastward of the Piave River and between the Adige and the Po Rivers, where up to 8 and 10 cm settlements, respectively, have been measured over the 17-year period. The validation of the SAR data using high-precision spirit leveling has verified the high accuracy of the SAR-based interferometric analysis (Figure 172). The last generation of satellite-borne radar, i.e., TerraSAR-X, opens new perspectives in measuring ground displacements at very high spatial and temporal resolutions (Strozzi et al. 2009). We have applied SAR interferometry on a stack of 30 TerraSAR-X images acquired between 5 March 2008 and 29 January 2009 covering large parts of the Venice Lagoon.

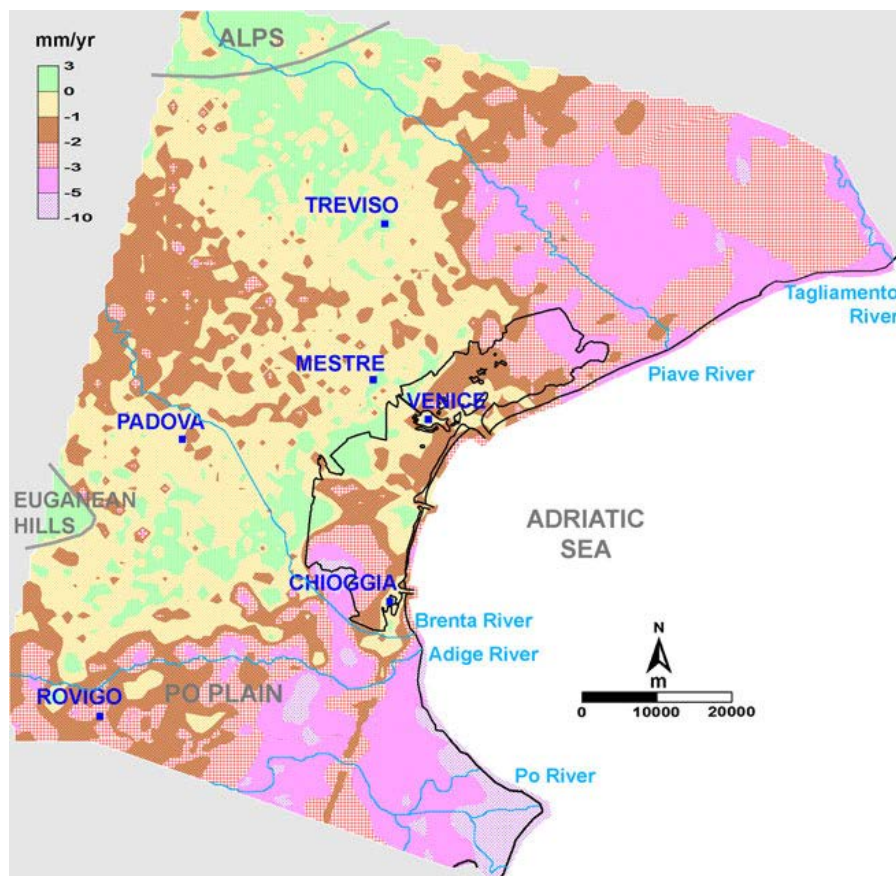


Figure 169: Vertical displacement rates (mm/year) in the Venetian region obtained by the SIMS over the decade 1992–2002.

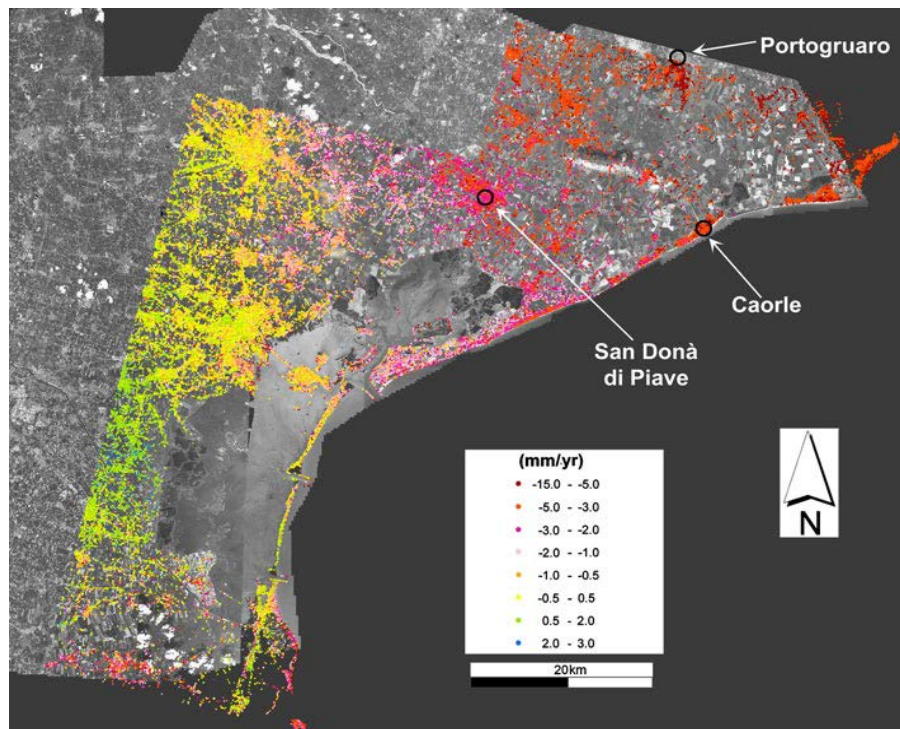


Figure 170: Vertical displacement rates (mm/year) in the Venetian coastland obtained by IPTA of ENVISAT scenes acquired between 2003 and 2007.

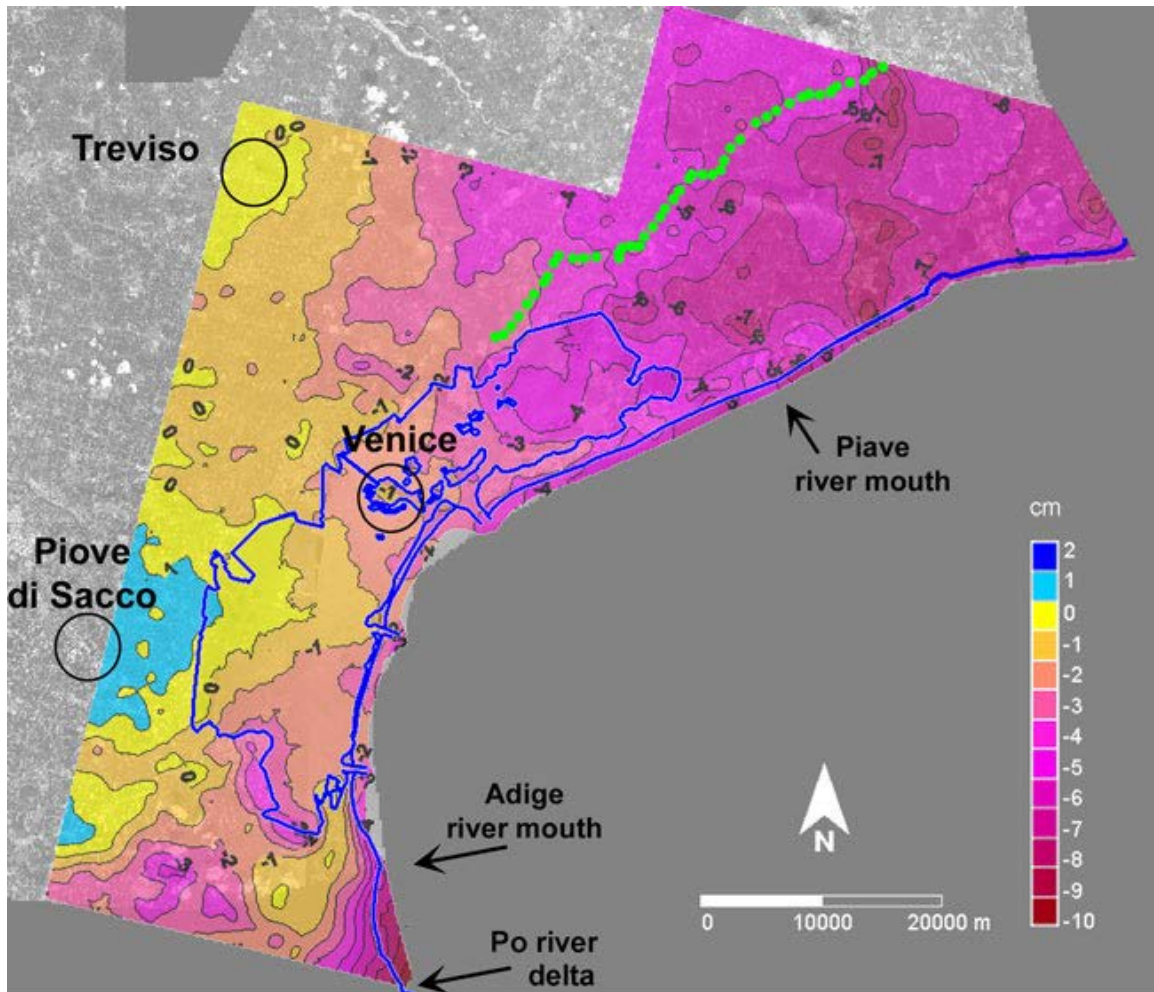


Figure 171: Map of the cumulative displacements (cm) occurring from 1992 to 2007 in the Venetian coastland as obtained by the integration of ERS-1/2 and ENVISAT IPTA results. Green dots position of the IGM34 (IRMA54) leveling benchmarks used for the validation of the IPTA outcomes.

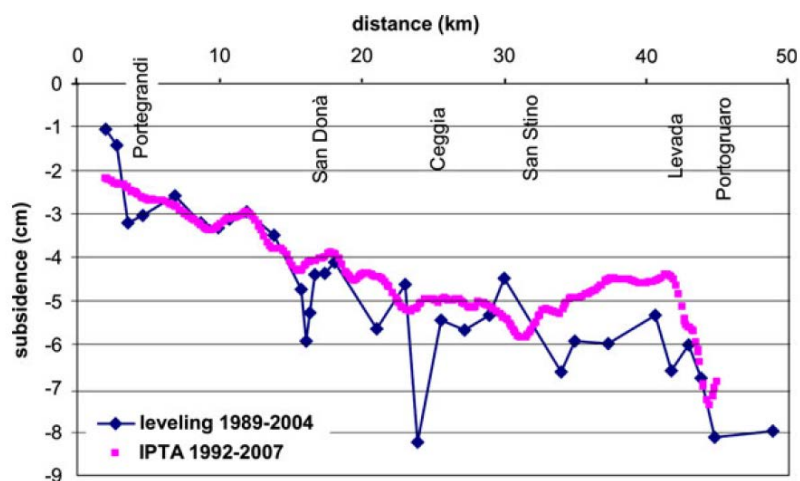


Figure 172: Comparison between leveling and IPTA results along the IGM34 (IRMA54) line.

4.3.7.3 **Summary of Veneto case study results**

The mapping of the recent (1992–2002) and present (2003–2009) vertical movements highlights a significant spatial variability with displacement rates ranging from a 1–2 mm/ year uplift to more than 10 mm/year subsidence.

In general, tectonics, differential consolidation of the Pleistocene and Holocene deposits and human activities, such as subsurface fluid withdrawals, land reclamation of marshes and swamp areas and farmland conversion into urban areas, combine to produce the observed displacements. According to Tosi et al. (2009), the displacement components have been distinguished on the basis of the depth of their occurrence. Deep causes, acting at a depth generally greater than 400–600 m below m.s.l., refer to downward movements of the pre-Quaternary basement and land uplift (up to 2 mm/year) most likely related to neo-tectonic activity connected with the Alpine thrust belts and a NW–SE fault system.

The displacement factors located in the medium depth interval, i.e., between 50 and 400 m below m.s.l., are of both natural and anthropogenic origin. The former refers to the Medium-Late Pleistocene deposits that exhibit a larger cumulative thickness of clayey compressible layers at the lagoon extremities with respect to the central lagoon area where stiffer sandy formations prevail. Land subsidence due to aquifer exploitation mainly occurs in the northeastern sector of the coastland where thousands of active wells are located.

In a 10–15 km wide coastal strip, the thickness, texture and depositional environment of the Holocene deposits (Tosi et al. 2009; Rizzetto et al. 2009) play a significant role in controlling shallow causes of land subsidence. Other factors that contribute to increasing land subsidence at a smaller areal extent are the salinization of clay deposits due to saltwater intrusion and the biochemical oxidation of outcropping peat soils (Gambolati et al. 2005; Carbognin et al. 2006). Even the load of buildings and structures after the conversion of farmland into urbanized areas causes local shallow compaction.

4.3.7.4 **Kazakh and Veneto case studies comparison**

For different aspects, the Kazakh coast involved in the present work is quite similar to the Italian one. Below are listed some parallelisms between the two considered areas (Figure 173):

- Similar latitude;
- Similar habitats and species;
- Presence of endemic & protected species;

- Flyway of migratory species;
- Face off- shore O&G extractive area;
- Potential subsidence hazard;
- Sustain fishery sector;
- International harbour activities.

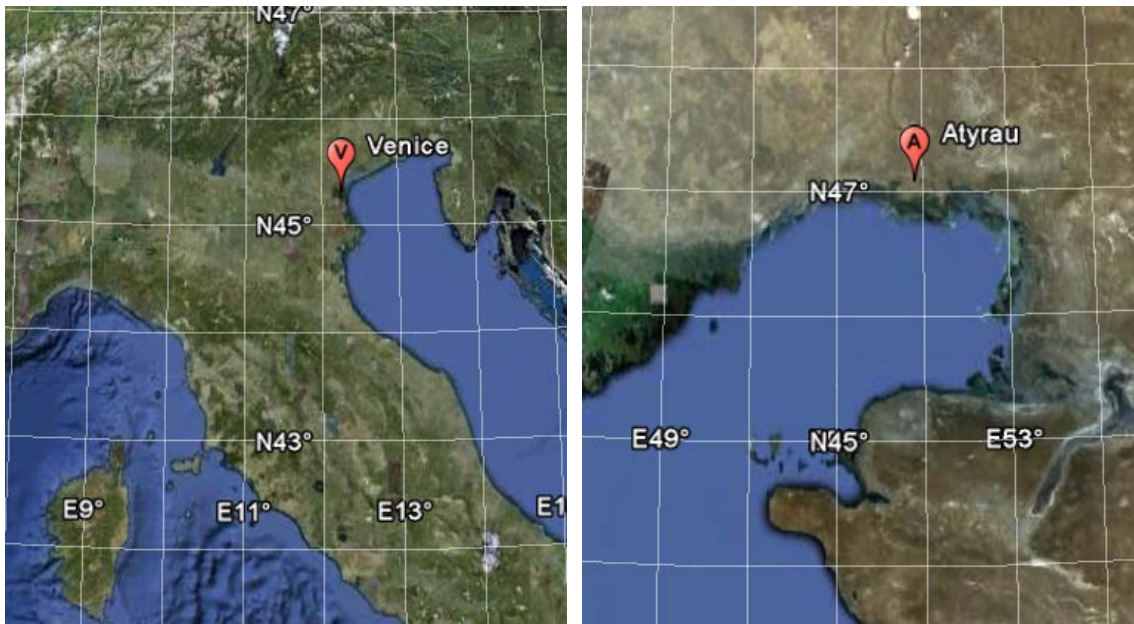


Figure 173: Parallelisms between two different study areas.

In the Adriatic Sea coast differential InSAR (DInSAR), first, and interferometric point target analysis (IPTA), at a later stage, have been applied to measure and map displacements occurring since 1992 when SAR data first became available.

The accuracy of measurements in the two areas is different: the capability of SAR interferometry to measure ground vertical movements in Italian areas at millimetric accuracy has significantly improved the knowledge of the phenomenon. The integration of DInSAR techniques with values coming from direct surveys (both spirit levelling and global positioning system methods) allows to reach an accuracy higher than the Kazak study area. In addition, the high urbanization of the Adriatic Sea coast (i.e. the high presence of point targets) allows a wide application of IPTA technique. Here following (Figure 174) an example of the precision reached by the SAR based techniques in city of Venice.

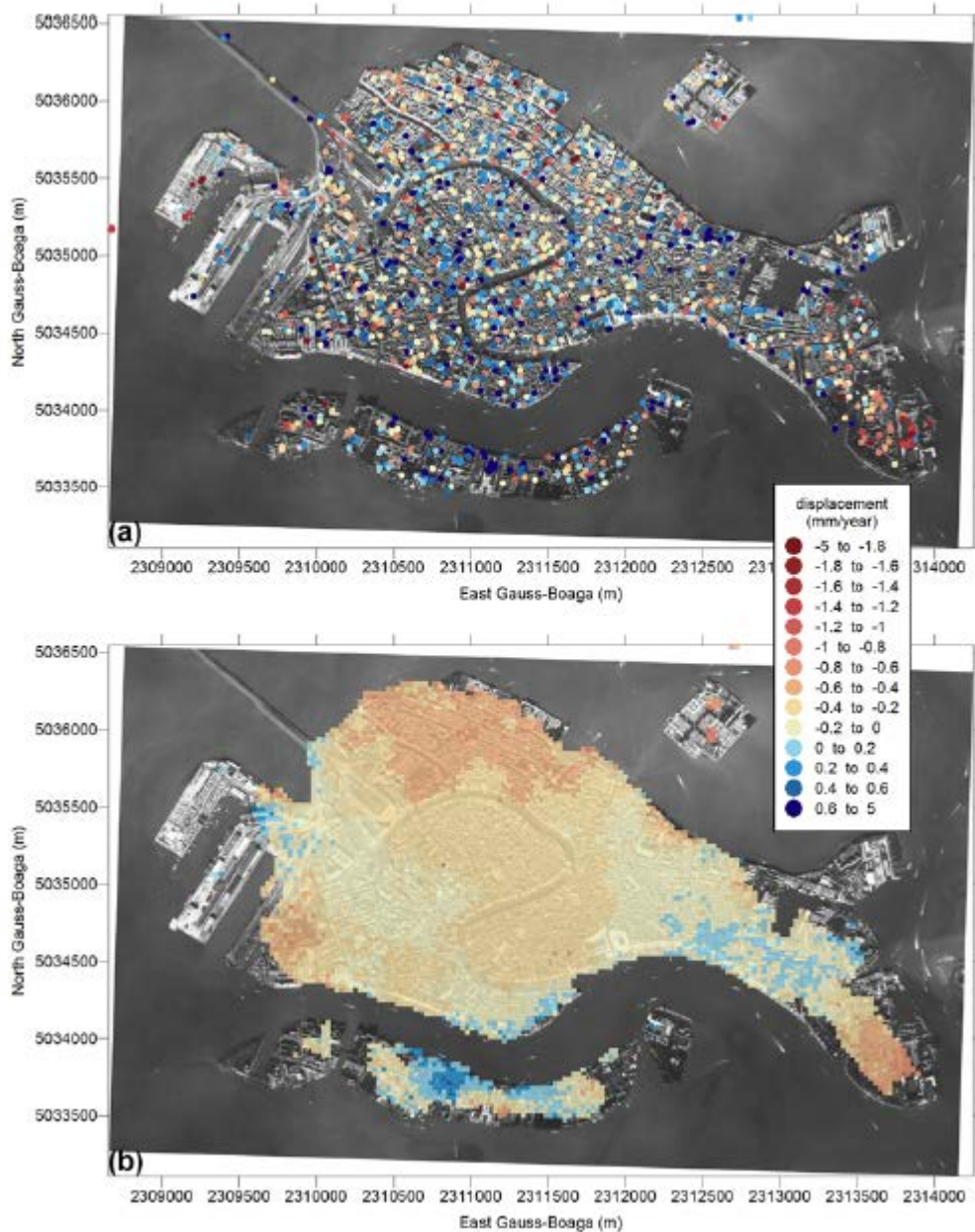


Figure 174: Reached detail of SAR based measured at Venice (Teatini et al., 2007).

Comprehensive maps of the vertical displacements have revealed the high spatial variability characterizing the ground movements in the Venice region. A general land stability has been detected in the central part of the study area, including the major cities of Venice, Padova and Treviso, with scattered local bowls of subsidence of up to 2–3 mm/year. Low values fit with ones measured in most of the Caspian Sea coastal area. However, some typical characteristics founded in the present study differ to the Italian one: the uplifts localized along the Kazak coast and local displacement, probably linked to the geological asset of the area and salt diapirism, are not identified in the Adriatic coastal zone.

5. CALCULATED AND MEASURED RESULTS COMPARISON AND CONCLUSION

Considering both the applied methodologies, results' comparison is briefly discussed.

The two approaches, as widely discussed above, are completely different and they investigate different aspects of subsidence. Applied numerical models (especially NATSUB model) have been implemented to calculate the compaction of a typical sedimentary column and its effects on porosity, hydraulic conductivity etc., while SAR-based analysis focuses on present lowerings (or uplifts) occurred in the last decade. The latter, due to its remote sensing nature, cannot distinguish movements caused by sediments' compaction from other sources of subsidence (e.g., terrain compaction due to the weight of buildings. fluid withdrawal).

The wireline logs availability allowed a numerical application only in the offshore part of the study area, while DInSAR works exclusively in onshore environment; the two methodologies seem to be incomparable, however:

- it's reasonable to think that the behaviour of the stratigraphic sequence could be similar in the whole coastal area investigated (depths of main stratigraphic horizons are quite similar);
- human activities are very localized and, for the most of the investigated areas, results are referable to the natural evolution of the sedimentary basin.

For these reasons, a qualitative comparison has been done.

NATSUB quantitative results and BASIN outputs underline the stable behaviour of the area and the absence of clear subsidential phenomena. In the southern margin of the Precaspian basin, the limited depth of elder drilled strata (carbonates of Devonian period) reveals that the basin was filled with very low rates of sedimentation and NATSUB shows that consolidational processes were coeval with sedimentational ones. Therefore, subsidential processes do not affect the deep and ancient rocks, and BASIN application shows that the consolidation involves only shallow sedimentary layers.

DInSAR analysis confirms the calculated trend. Recorded movements for the most of the area investigated are negligible, with values comprise between ± 1 mm/y. This technique identified areas of particular interest (with values up to -6 and +5), in which movements are probably linked to salt diapirs (uplifts in correspondence to the top of the salt domes, and lowerings more marked within intra-domes areas) or coastal processes. Lack of data (detailed

compressibility and chronostratigraphy available only at offshore wells, and not sufficient knowledge of salt domes distribution) does not allow the application of the model in areas of particular interest highlighted by InSAR.

In conclusion, results coming from two different methodologies confirm that the study area considered in present study is a stable one, with very low values of subsidence caused by sediments' compaction.

6. SWOT ANALYSIS

Table 20: Natural and present SWOT analysis

	STRENGTHS (S)	WEAKNESSES (W)	OPPORTUNITIES (O)	THREATS (T)
Natural subsidence <i>(Numerical models application)</i>	Availability of different numerical models suitable for application in the study area; Very low values of compressibility of the whole sedimentary column.	Lack of data related to salt domes distribution: it does not permit to define areas not involved in salt diapirism, or intra-domes areas; in these areas the thickness (and consequently the compressibility) of the sediments is higher; Non homogenous data distribution: information is localized in the offshore area; no wells are available in the onshore portion of the study area.	To profit of more existing available different data useful for rock compressibility calculation and/or to gather more wireline logs in onshore area, in order to obtain more accurate (and better distributed) values of compressibility.	To not quantify properly the natural component of subsidence, and consequently to not compare accurately natural subsidence with present one.

	STRENGTHS (S)	WEAKNESSES (W)	OPPORTUNITIES (O)	THREATS (T)
Present subsidence <i>(Differential Synthetic Aperture Radar Interferometry application - DInSAR)</i>	<p>Availability of advanced technologies that permit the detection of ground movements with high accuracy.</p> <p>Low degree of urbanization of the study area permits to consider, in most of the cases, present subsidence as natural one, i.e. measured values can be referred exclusively to sediment compaction.</p>	<p>Discontinuous analysis could not consider the phenomenon in its totality: the experimental SAR application has not been done in the whole coastal area, excluding areas involved in Oil&Gas activities;</p> <p>Inadequate knowledge of all anthropic activities in studied areas;</p> <p>Absence of historical and recent measures of displacements;</p> <p>Absence of GPS measurements in the study area.</p>	<p>To expand the DInSAR analysis to the whole study area;</p> <p>To correlate DInSAR results with human activities;</p> <p>To foresee future lowerings/uplifts in function of planned Oil&Gas activities.</p>	<p>An increase values of present subsidence because of anthropic activities.</p>

7. FUTURE SCENARIO ESTIMATION

Considerations about subsidence future scenario have been done considering both the calculated (through numerical models) and detected (through DInSAR) subsidence values.

In NATSUB approach, the beginning of simulations depends on the elder strata drilled and they have been completed in 3000 AD. The portions of simulations related to future scenarios foresee no sedimentation: Figure 175, detail of one simulation, shows in detail that between the present time (2000) and the future (3500) in absence of sedimentational processes the thickness of the sedimentary does not change (Figure 176).

Time value assigned for future projection follows the concept of the “geologic time scale” and not the “life cycle time scale”; notwithstanding, simulated geomechanical characteristics allow to highlight that any significant rock/sediment compaction will happen in the future (Figure 175).

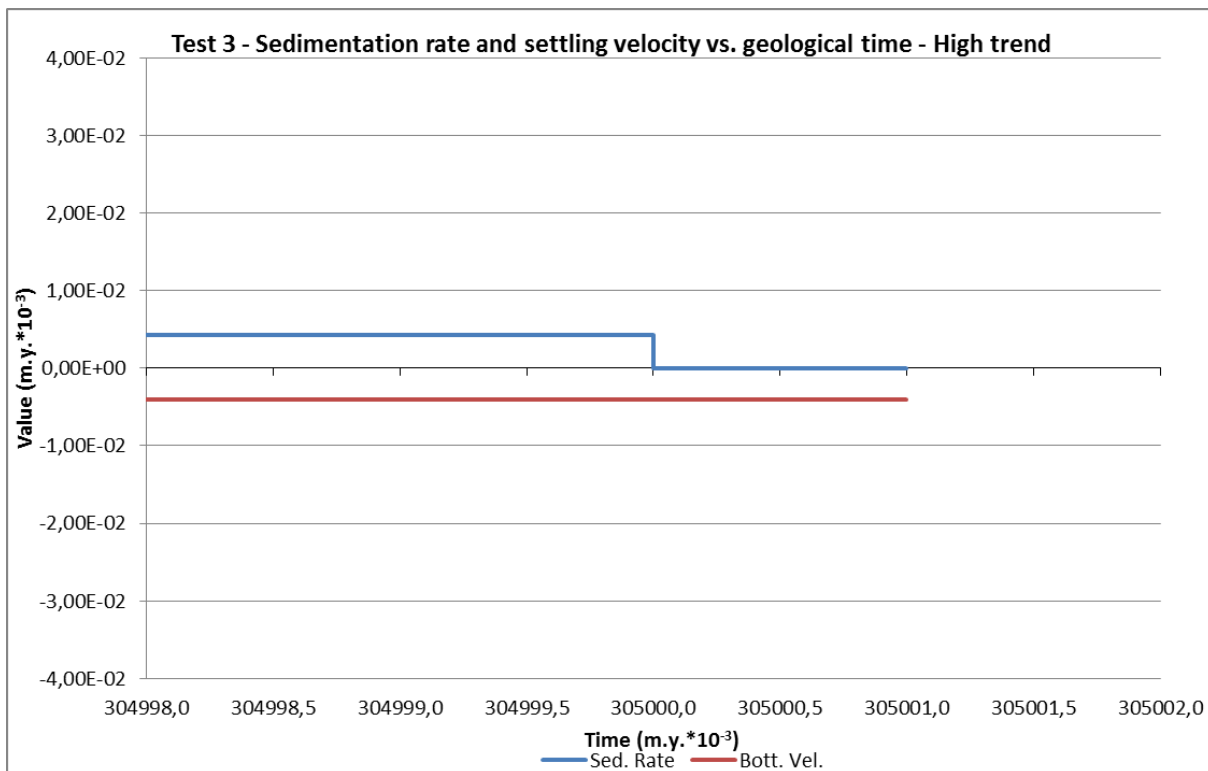


Figure 175: Example of sedimentation rate and settling velocity during future scenario, well Test 3.

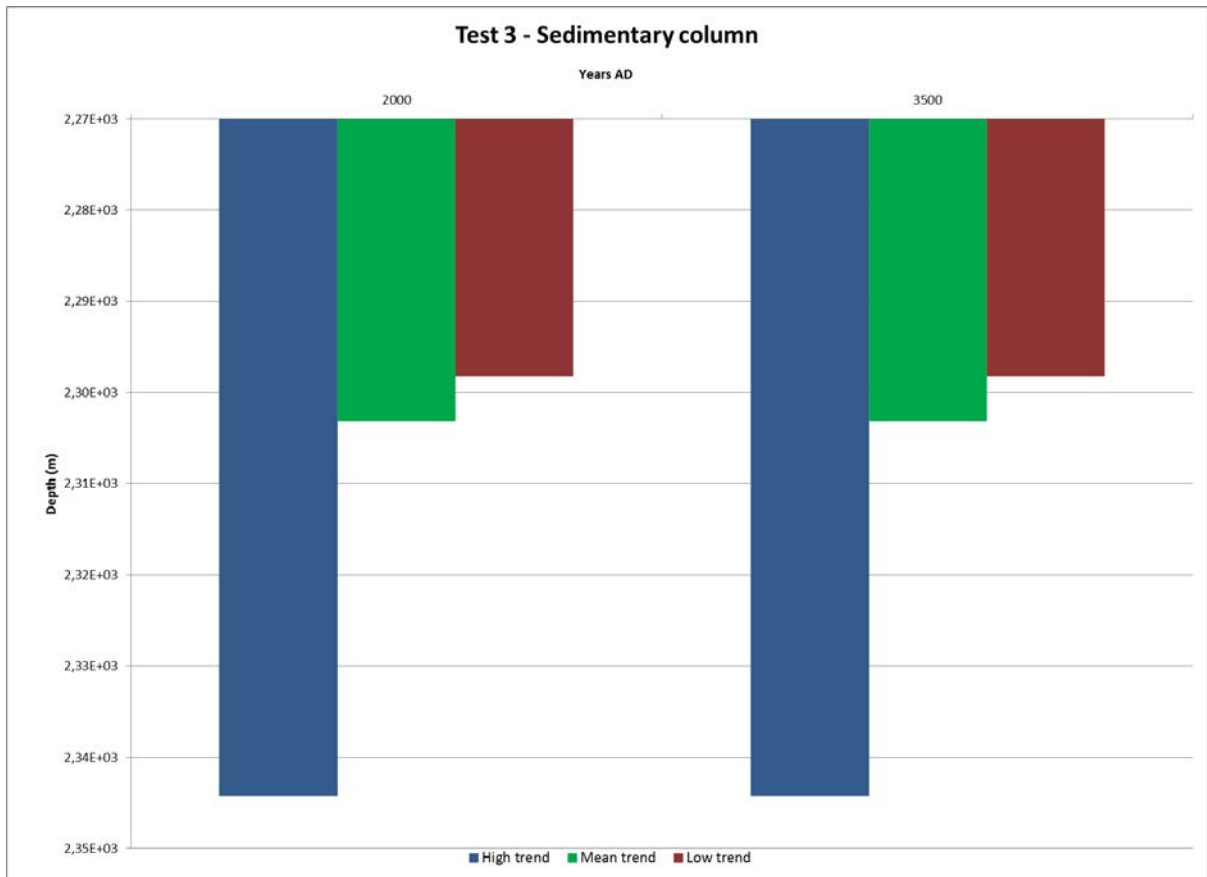


Figure 176: Example of depth (or thickness) of the sedimentary column during future scenario, well Test 3

Results of undertaken DInSAR analysis show that the three frames investigated are characterised by stable behaviour, with relative displacements comprise between ± 1 mm/y for the most of the area covered by the analysis. In some limited areas movements reach negative values up to -6 mm/y and positive values up to +4 mm/y (northeastern corner and near shore belt of frame Z2).

In absence of information related to planned human activities, subsidence rates cannot be modified and future trends have to be assumed similar to detected ones.

8. MONITORING PLAN

8.1 SPATIAL AND TEMPORAL DISTRIBUTION OF RADAR IMAGES ACQUISITION FOR SBAS MONITORING ANALYSIS WITHIN FRAMES Z1, Z2 AND Z3

The application of DInSAR SBAS technique in the study area has revealed that this methodology is adequate to the monitoring of subsidence. For this reason, future monitoring activities through SAR-based technique can (and should) be planned.

Areas of investigation could be the same involved in the study, maybe modified depending on the orbit of selected satellites. Monitoring plan could be set for a yearly acquisition and elaboration of radar images (acquisition of necessary available images every October).

ENVISAT products, used for the study of present subsidence, cannot be used for monitoring activities; related satellites were dismissed in October 2010. Radar images could be acquired by other satellites, as RADARSAT-2, TerraSAR-X or COSMO-SkyMed. Cost of monitoring activities depends on selected images (type, number) and varies from 2000 to 3000 €/image.

8.2 INTEGRATION OF MONITORING PLAN WITH ARTIFICIAL PERSISTENT SCATTERERS AND FIX GPS STATIONS

Attempt of DInSAR IPTA technique has revealed that only within frame Z1 there are sufficient Persistent Scatterers; however, the capability of IPTA to detect localised land displacements makes the technique suitable for monitoring activities.

Following figures shows the distribution of natural PTs used for IPTA analysis in frame Z1 (Figure 177) and natural PTs identified within frames Z2 and Z3 (Figure 178 and Figure 179); as discussed, PTs availability in Z2 and Z3 does not permit the IPTA application, but present PTs eventually rounded out with artificial PTs, represent a good chance to carry out very detailed monitoring activities.

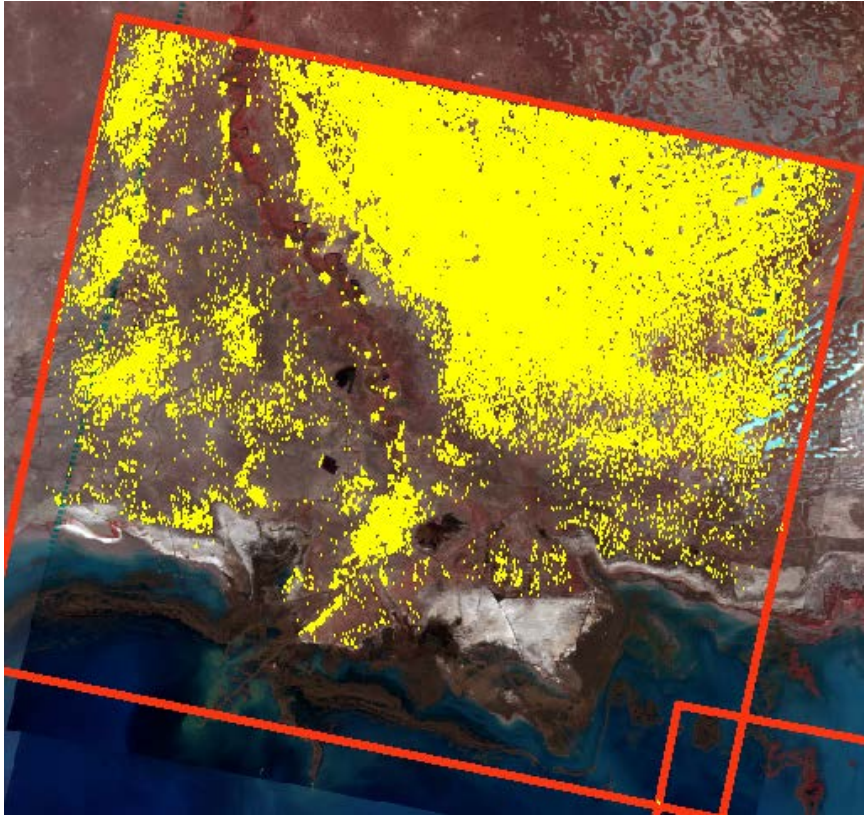


Figure 177: Identified PT in frame Z1

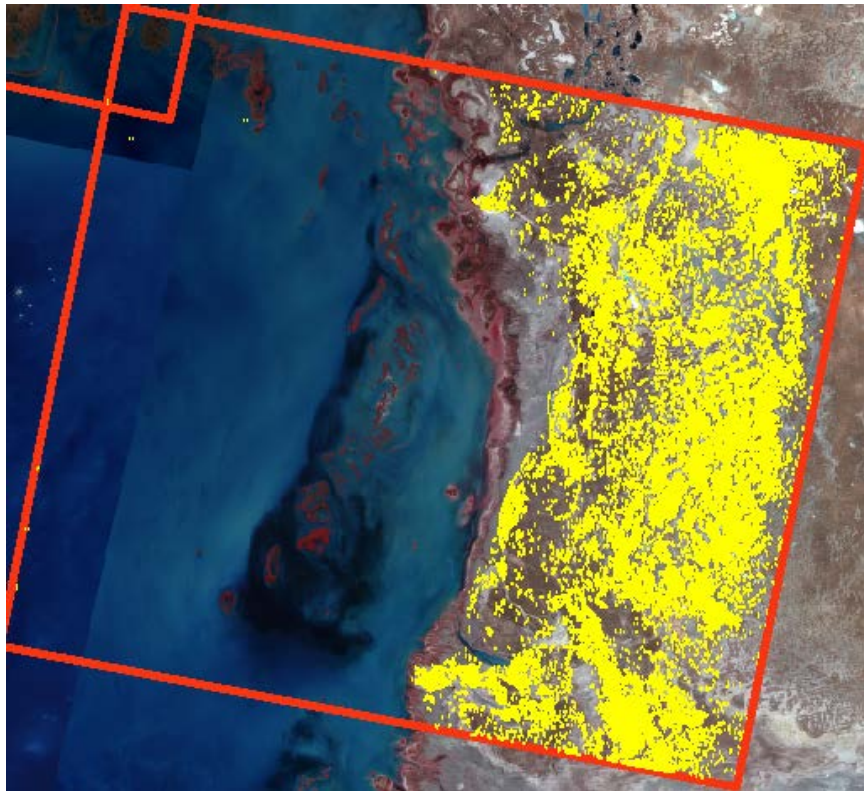


Figure 178: Identified PT in frame Z2

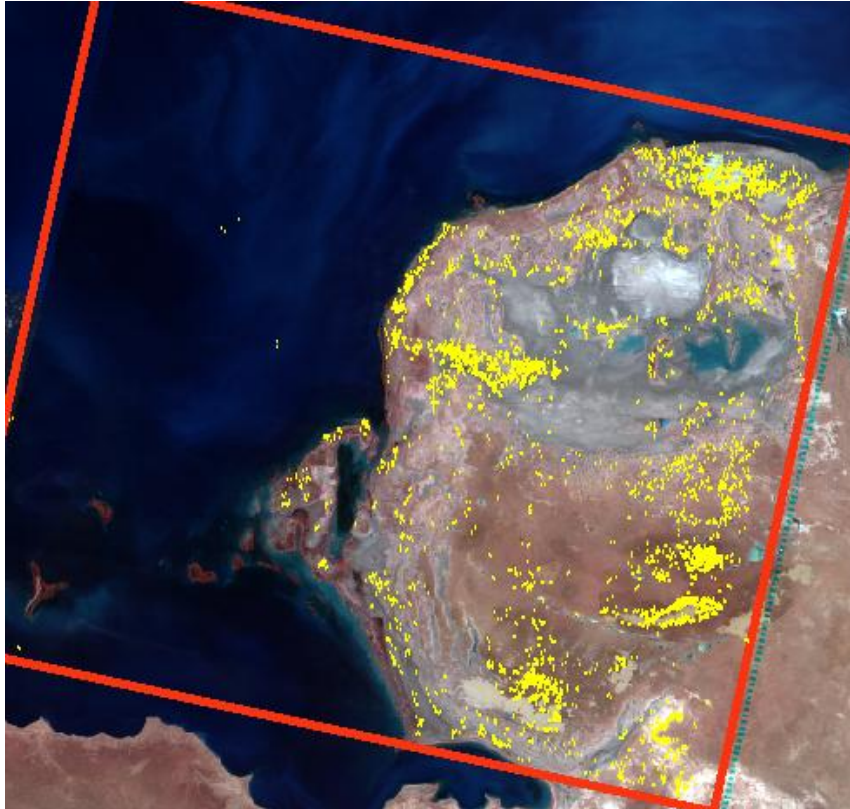


Figure 179: Identified PT in frame Z3

Installation of artificial PTs should be done in areas not sufficiently covered by natural PT reflectors: their distribution must be planned considering that the distance between two PTs should be less than 2 km.

Monitoring activities planned through IPTA technique should be implemented at specific location within the frame (a frame scale monitoring is covered by SBAS analysis), in area of specific interest (e.g., areas characterized by lowerings or uplifts, near Oil&Gas facilities or in the Ural delta).

Proposed technique, already applied in similar environment, assures very high resolution of measurements with limited costs: construction and installation of these metallic structures is quite easy and every PT costs 200-300 €, depending on the type and dimensions of the structure. Technique's constrain could be relate to PTs stability in areas where onshore ice movements generally occurred.

An example of integration between natural and artificial PTs is shown in Figure 180.

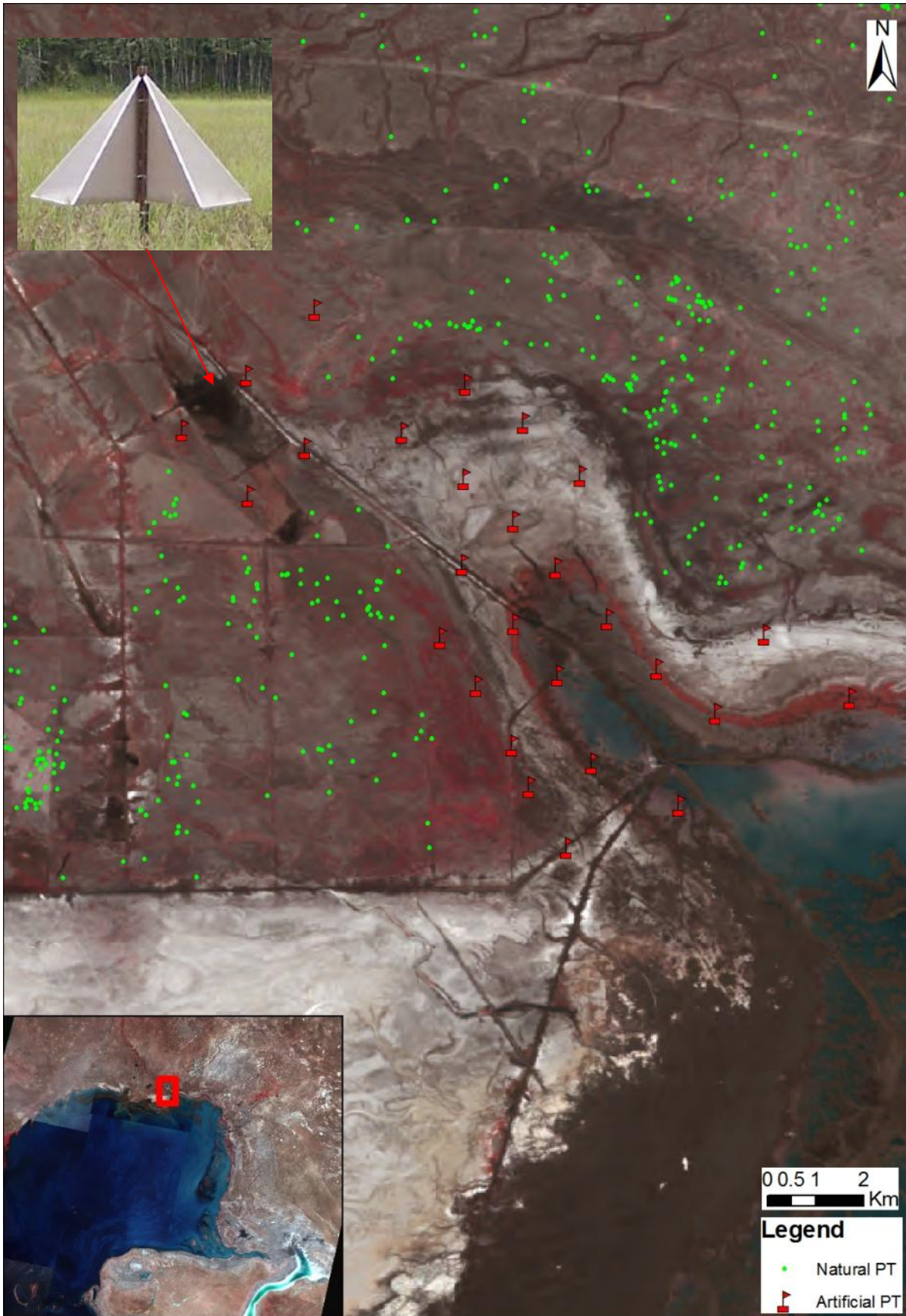


Figure 180: Integration between natural and artificial PTs

8.3 BEST SOLUTION FOR FIX GPS INSTALLATION

Similar to levelling, SAR-based data are differential measurements, i.e. the measured displacements are relative to the movement of a reference (e.g., Teatini et al., 2010). Therefore, the movement of the reference has to be known e.g., from previous levelling or GPS surveys, to calibrate the SAR results and obtain “absolute” displacements. The establishment of a few GPS permanent stations is therefore of paramount importance.

Also looking within international GPS networks (e.g., the network managed by the Scripps Orbit and Permanent Array Centre – SOPAC, see Figure 181), no station have been detected in the study area.

If no geodetic data will be available, already gathered and new displacements measured by DInSAR will be referred to a point chosen according with the available geologic information and, in any case, as far as possible from the coastland.

Proposed solution’s constrain could be relate to the achievement of required authorizations.

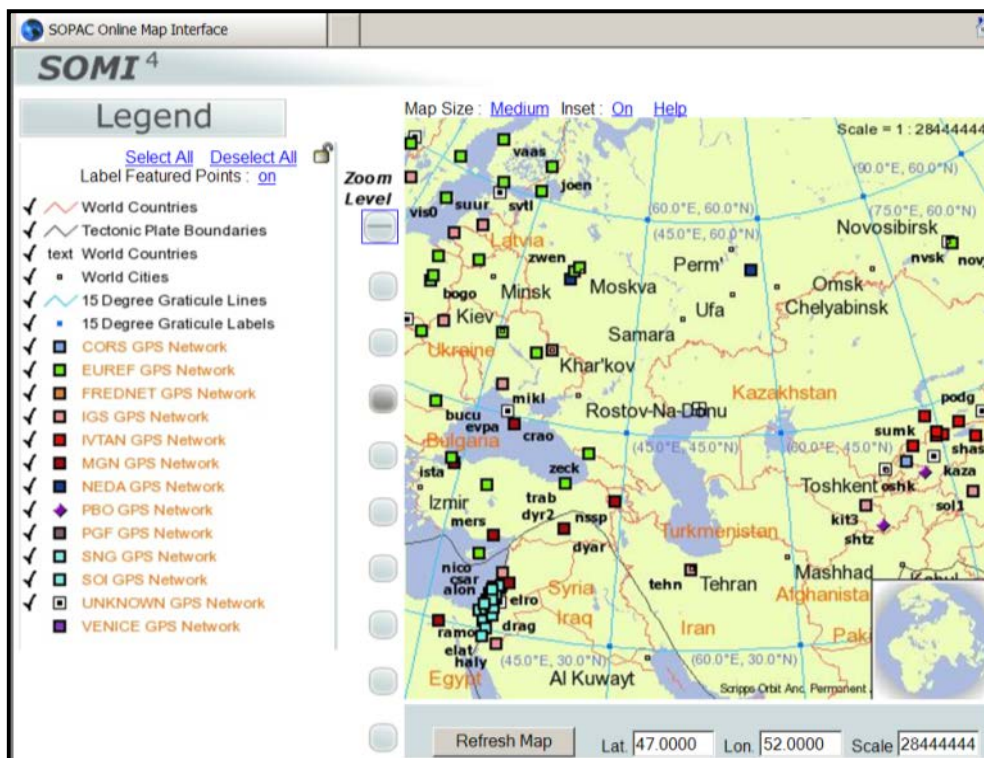


Figure 181: Location of the GPS stations in international GPS networks around the Caspian Sea (after SOPAC archives, <http://sopac.ucsd.edu/sites/>)

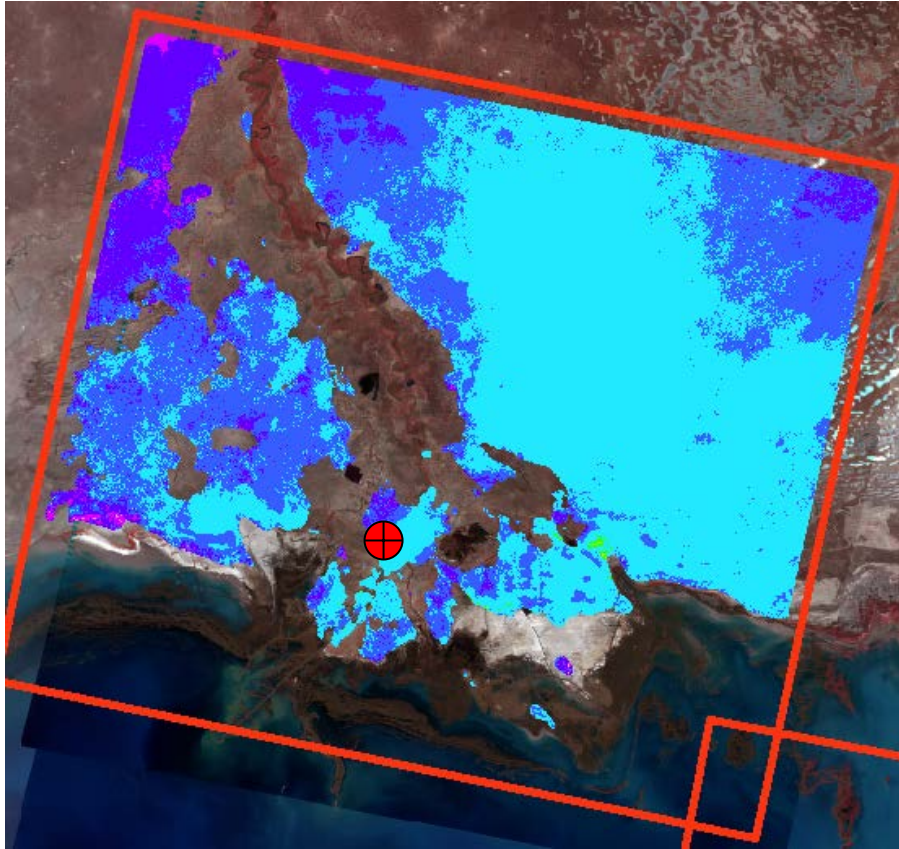


Figure 182: Possible GPS location (red circle) within frame Z1

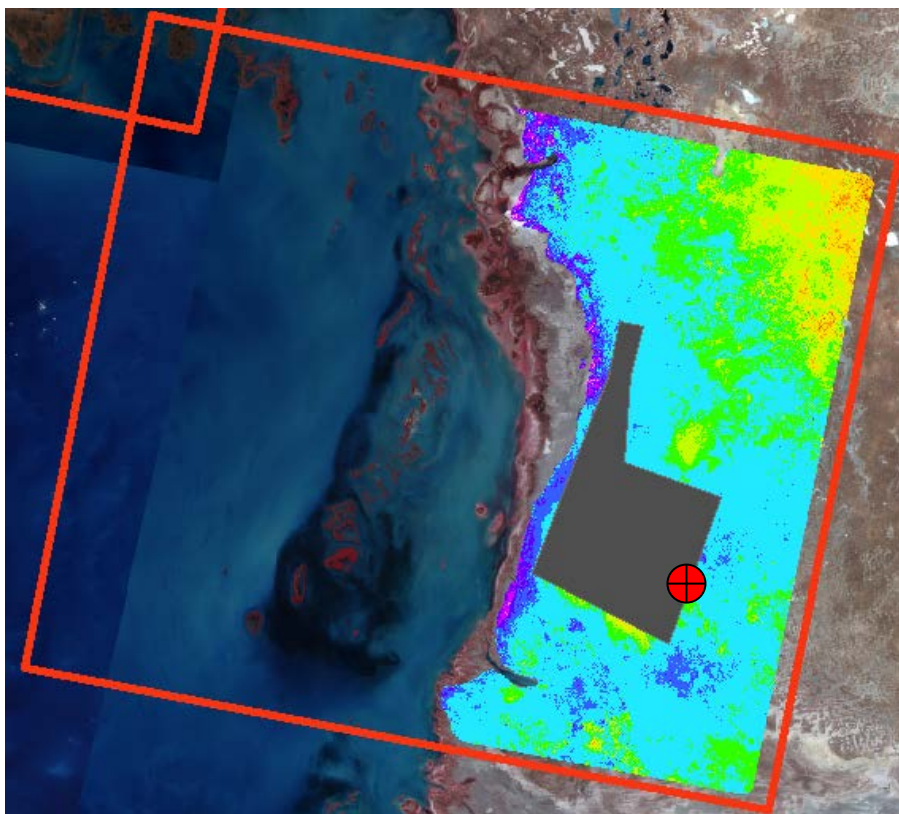


Figure 183: Possible GPS location (red circle) within frame Z2

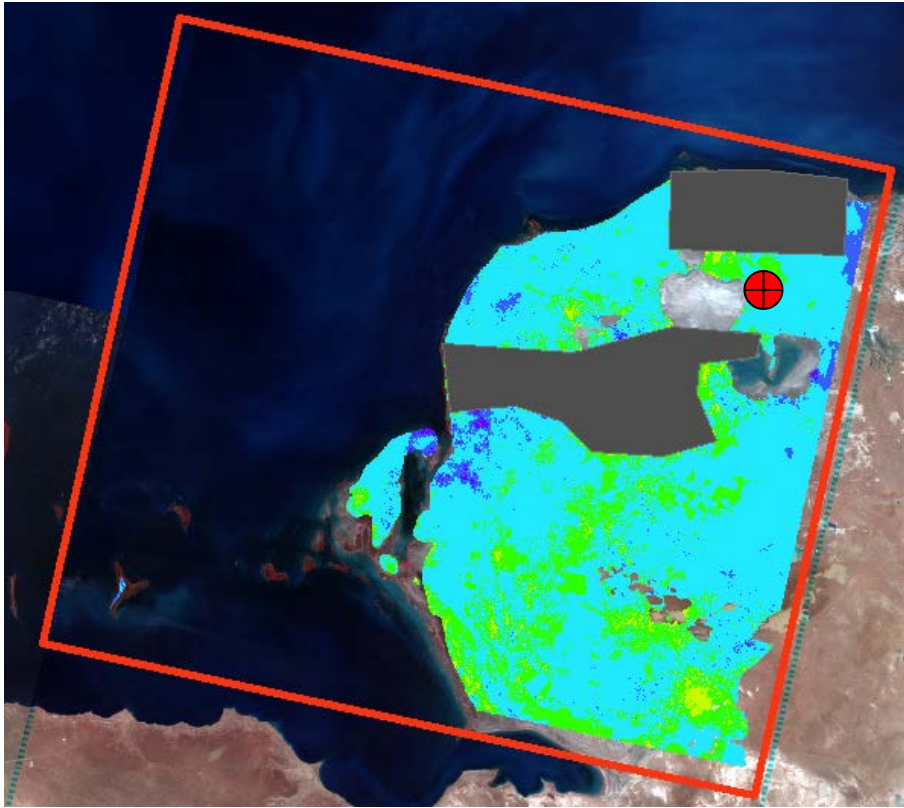


Figure 184: Possible GPS location (red circle) within frame Z3

9. PROPOSED NEXT ACTIVITIES

9.1 PRESENT SUBSIDENCE MONITORING ALONG THE WHOLE KAZAKH COASTAL AREA

InSAR application could be a suitable technique to monitor the whole coastland of the northern Caspian Sea area.

A check of ENVISAT (for images till 2010) and RADARSAT availability along the whole coastal area (Figure 185) highlight that SAR images are available for the entire Kazakh coastal area. Suitable satellites for the proposed activities are the same identified in 8.1.

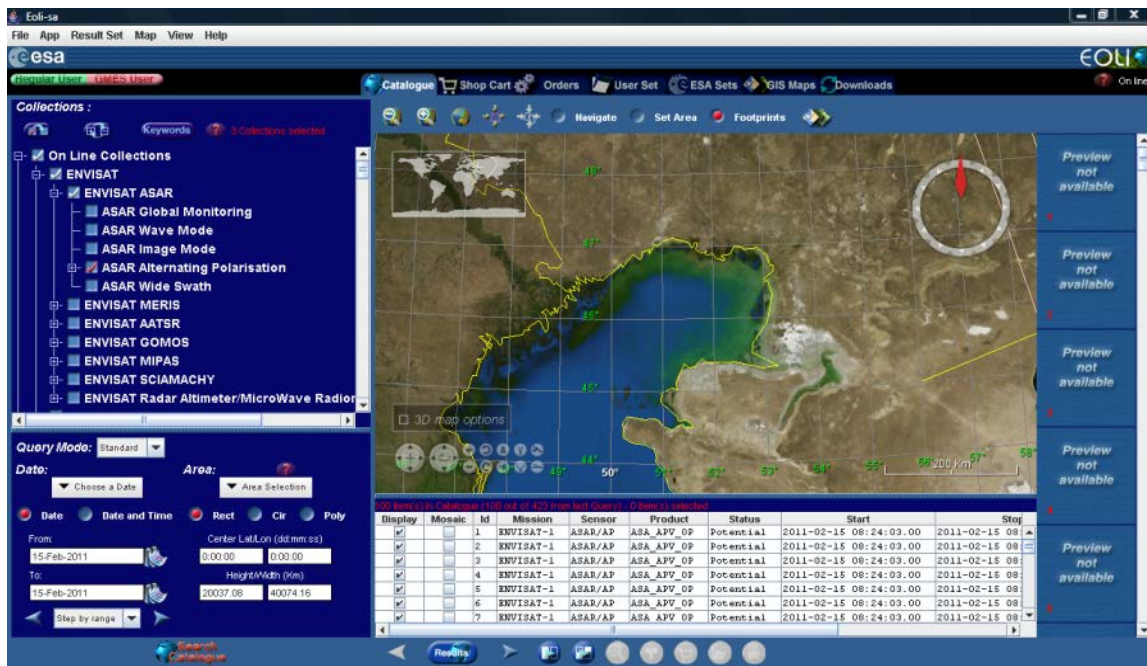


Figure 185: Snapshot of ESA imagery catalogue

Four RADARSAT tracks in descending mode cover both the study area and other portions of Kazakh coastal area (Figure 186). For Tracks 1-3 more than 60 acquisitions are available between 2004 and 2009. Unfortunately, only 4 acquisitions are available on Track 4, i.e. a insufficient number for the interferometric. Similar to ENVISAT-ASAR, three frames could be initially used for the DInSAR investigation, one in each inland part detected by the geological zoning. A preliminary selection of the 100 km x 100 km frames of interest are shown in Figure 187.

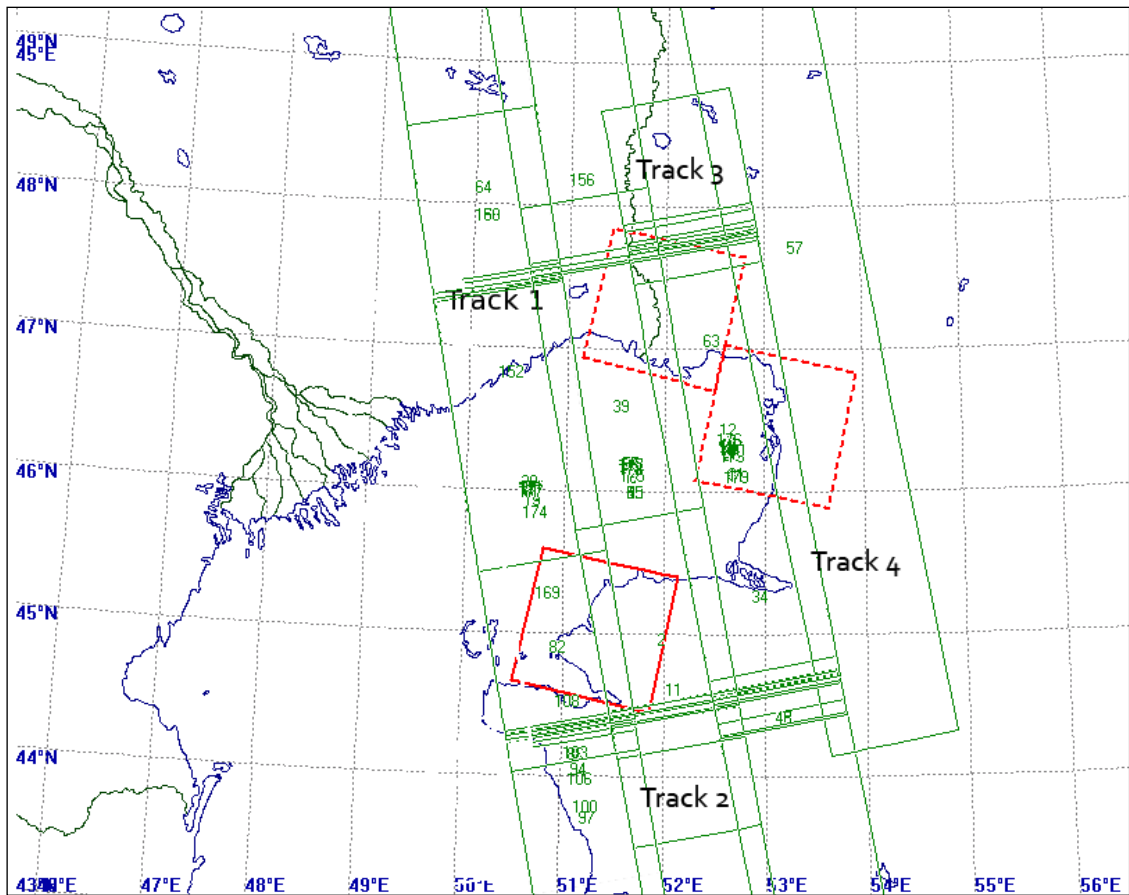


Figure 186: RADARSAT-1 tracks covering the north-eastern Caspian. The red "squares" represent the three frames selected from the ENVISAT-ASAR archive.

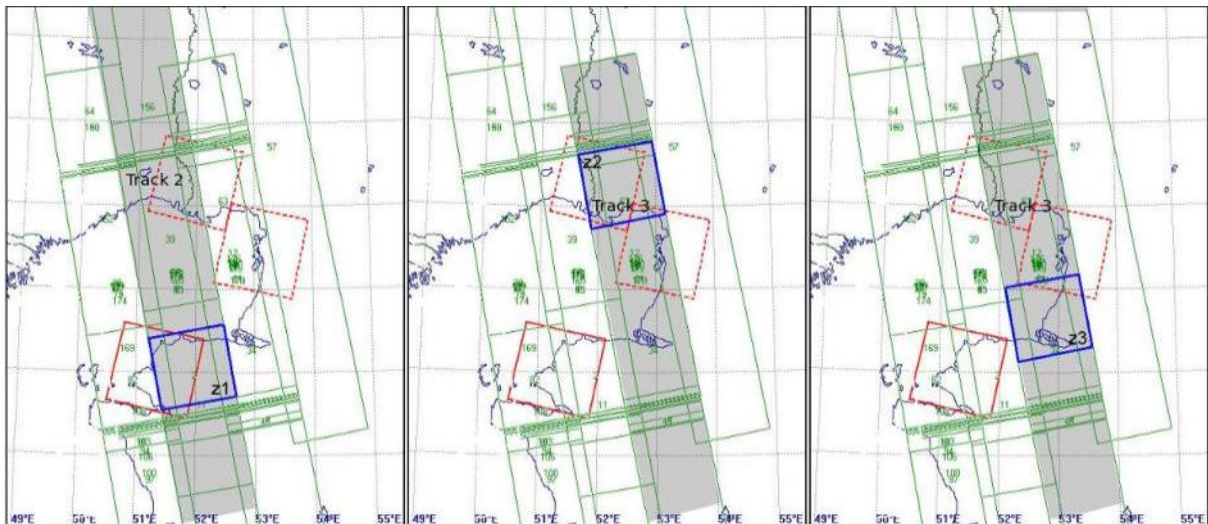


Figure 187: Preliminary selection of RADARSAT-1 frames (in blue) for the DInSAR analysis.

9.2 CREATION OF A DIGITAL ELEVATION MODEL

Space-borne SAR interferometry is one possible method for the generation of digital elevation models (DEMs). The sensitivity of this technique depends strongly on system parameters as the time interval between the observations used and the spatial baseline. Longer time intervals are less suited because of temporal decorrelation of the signal. Longer spatial baselines result in an increased height sensitivity. ERS-2 and ENVISAT ASAR operate in identical orbits at slightly different sensor frequencies with ASAR preceding ERS-2 by 28 min. This configuration offers a unique opportunity to study and apply ERS–ENVISAT interferometry. ERS-2–ENVISAT ASAR IS2 VV-polarization interferograms are characterized by a short 28 min repeat-pass interval and a long 1.5–2.5 km baseline. Given the long baseline and short time interval ERS–ENVISAT interferometry has a good potential for the generation of precise DEMs in relatively flat areas. The idea to use ERS–ENVISAT interferometry for DEM generation is not new, nevertheless, very few adequate data sets were identified and analyzed in the past. Now, thanks to a recent dedicated ERS-2–ENVISAT Tandem mission of ESA many well suited data sets became available.

From the literature, the accuracy of DEM of InSAR is of the order of 5 - 10 meters depending on the frequency, base line, terrain slope, decorrelation of the signal etc.

At the moment, available Digital Elevation Models (DEM) are

- **SHUTTLE RADAR TOPOGRAPHY MISSION (SRTM)**, for the whole project area: **(SRTM)** obtained elevation data on a near-global scale to generate the most complete high-resolution digital topographic database of the Earth. SRTM consists of a specially modified radar system that flew onboard the Space Shuttle Endeavour during an 11-day mission in February of 2000. The SRTM absolute and relative errors are listed in Table 21.

Table 21: Summary of SRTM performance. All quantities represent 90% errors in meters.

	Africa	Australia	Eurasia	N. America
Absolute Geolocation error	11.9	7.2	8.8	12.6
Absolute Height error	5.6	6.0	6.2	9.0
Relative Height error	9.8	4.7	8.7	7.0
Long wave length error	3.1	6.0	2.6	4.0

- **LIGHT DETECTION AND RANGING (LIDAR)**, only for a strict zone of project area, specifically, south to Bolashak facilities. This raster dataset contains LIDAR data acquired in July 2009 from an aerial survey performed by KazGeoCosmos (KGC).

The LIDAR data has the following characteristics:

Coordinate system	Gauss Kruger Zone 9
Spatial resolution	5 m
Horizontal accuracy	RMSE 0.049 m using 5 control points
Vertical accuracy	Mean error 0.02 m using 7 control points
Format	IMG

- **DEM GENERATED FROM RUSSIAN TOPOGRAPHIC MAPS (SCALE 1:100.000)**, covering the whole project area. Points have been digitalized considering a buffer of about 50 km landward from actual shoreline.

This proposed activity represents an opportunity considering that the resolution of Digital Elevation Models available in the northeastern coast of the Caspian Sea affects different kinds of studies (e.g. inundation maps, future scenarios etc.)

Within the work supported by ESA under contract 19366/05/I-EC-CCN5 and the project “ERS-ENVISAT Tandem Cross-InSAR Campaigns: Case Studies” an experimental application of DEM generation is under elaboration in correspondence to the eastern part of the Volga Delta. Figure 188 shows a step of elaboration: in the differential interferogram is recognisable loss of coherence on offshore ice, topographic variations linked to dunes along coastline and residual atmospheric artefacts toward the onshore part of the area investigated.

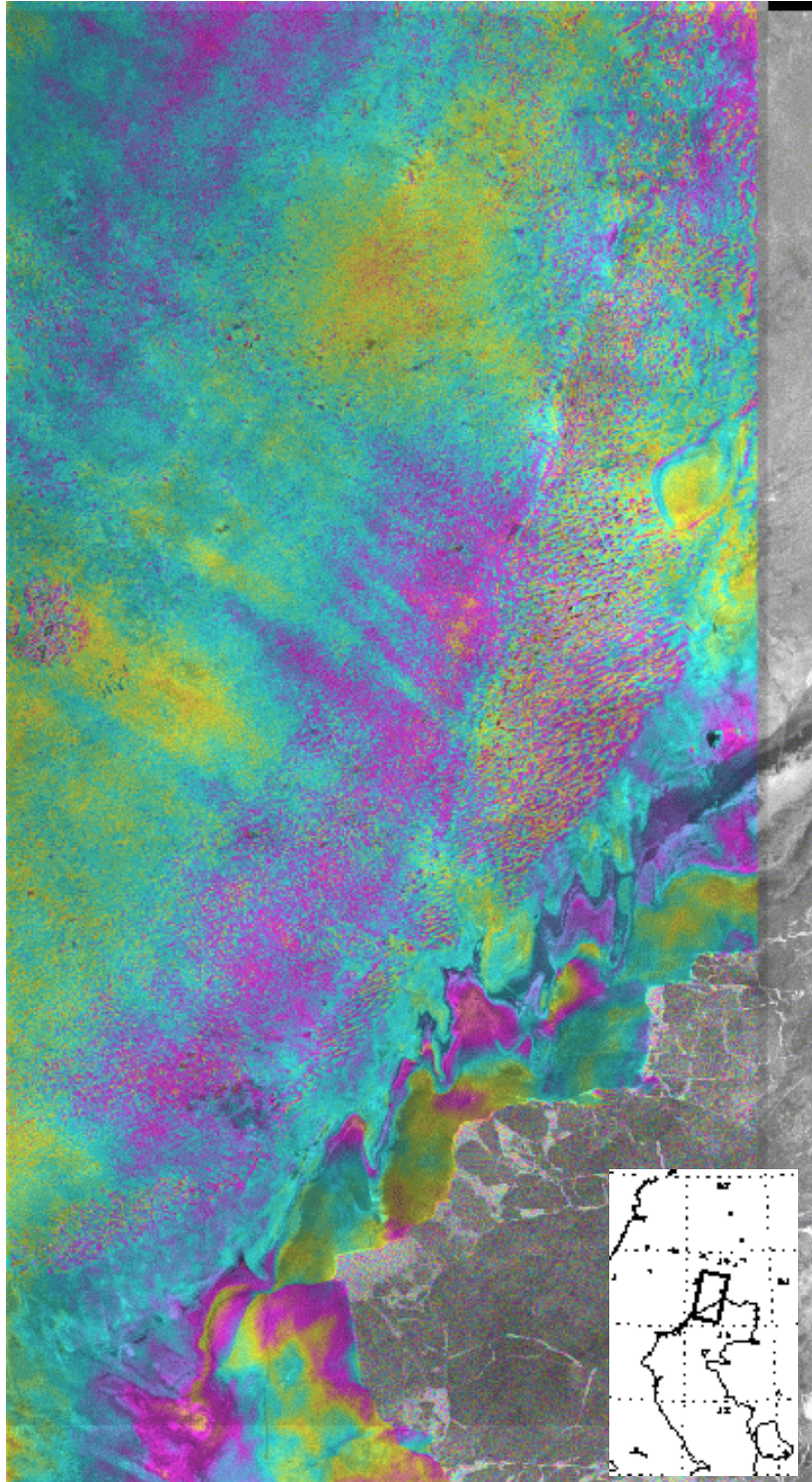


Figure 188: DEM generation in the eastern part of the Volga Delta: step of elaboration.

9.3 InSAR ANALYSIS ON PRODUCTION ISLANDS

DInSAR IPTA technique could be suitable for the detection of movements of a structure, or more than one structure, if the distance between them is less than 2 km. The anthropic nature of these structures guarantees the presence of PTs and no further installations should be required. Considering present structures, the distance between islands sometimes is low enough to allow to measure displacements between two (or more) artificial islands.

InSAR technique has been already applied on artificial islands monitoring (e.g., Palm Jumeirah, Dubai).

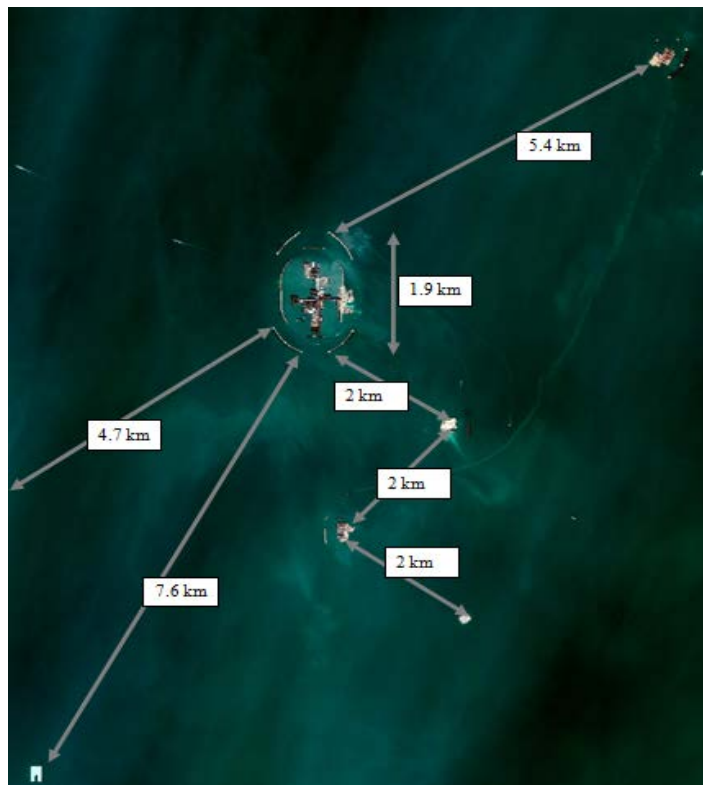


Figure 189: Distances between artificial islands at Kashagan area



Figure 190: InSAR technique applied to the artificial Island of Palm Jumeirah, Dubai

10. REFERENCES

- Abdulin A.A., (1981), "Geology of Kazakhstan", Nauka, 312;
- Afanasenkov A.P., Skvortsov M. B., Nikishin A. M., Murzin Sh. M., and Polyakov A. A. (2008), "Geological Evolution and Petroleum Systems in the North Caspian Region", *Moscow University Geology Bulletin*, Vol. 63, No. 3, 131–139;
- Alexander, A. C., E. Iwaniw, S. C. Otto, O. S. Turkov, H. K. Kerr, and C. Darlington, (2000), "Tectonic model for the evolution of the Greater Caspian area", *AAPG International Conference and Exhibition*, Istanbul, Turkey, July 9–12, 11–14.
- Akhmetshina, L.Z., Bulekbaev, Z.E., Gibshman, N.V., (1993), "Devonian of the east flank of the Precaspian syncline", *Otecestv. Geol.* 2, 42– 48;
- Antipov, M. P., Yu. A. Volozh, Yu. A. Lavrushin, Yu. G. Leonov, (1996), "Geological events and sea level change in the Caspian Sea", *Geoecology*, 3, 38–50;
- Arabadzhi, M.S., Bezborodov, R.S., Bukharov, A.V., (1993), "Prediction of petroleum potential of the southeastern North Caspian basin", *Moscow, Nedra*, 160 p.;
- Archie, G. E., (1942), "The electrical resistivity log as an aid in determining some reservoir characteristics", *American Institute of Mining, Metallurgical and Petroleum Engineers transactions*, 146, 54-62;
- Archie, G. E. (1950), "Introduction to petrophysics of reservoir rocks", *Am. Assoc. Pet. Geol. Bull.*, 34(5), 943-961;
- Aristarkhova L.B., Varushchenko A.N., Lukyanova S.A. et al., (1970), "Structural geomorphological investigation in North Ustyurt region in connection with oil and gas prospecting" *Geomorphology*, 2, 48-53;
- Artyushkov E.V. (2007), Formation of the superdeep South Caspian basin: subsidence driven by phase change in continental crust, *Russian Geology and Geophysics* 48, 1002–1014;
- Athy, L. F. (1930), "Density, porosity, and compaction of sedimentary rocks", *Am. Assoc. Pet. Geol. Bull.*, 14(1), 1-24;
- Bakirov, K.Kh., Daumov, S.G., and Zhuykov, O.A., (1991), "Petroleum potential and regionalization of the Zilair Formation of the eastern North Caspian basin", *Sovetskaya Geologiya*, 2, 11–19;
- Bamler, R., and P. Hartl (1998), Synthetic aperture radar interferometry, *Inverse Probl.*, 14, R1– R54;
- Beaver, J., Tatlow, M., Cohen, D., Marra, M., (2005), "Monitoring subsidence trends in Phoenix with SAR interferometry", *EOS TransAGU Fall Meet Suppl* 86(52), abstract G51C-0852;
- Berardino, P., Fornaro, G., Lanari, R., & Sansosti, E. (2002), "A new algorithm for surface deformation monitoring based on small baseline differential SAR interferograms", *IEEE Transactions on Geoscience and Remote Sensing*, 40 (11), 2375–2383;
- Bethke, C. M. (1985), "A numerical model of compaction-driven groundwater flow and heat transfer and its application to the paleohydrology of intracratonic sedimentary basins", *J. Geophys. Res.*, 90(B8), 6817-6828;
- Bethke, C. M. and Corbet, T. F. (1988), "Linear and nonlinear solutions of onedimensional compaction flow in sedimentary basins", *Water Resour. Res.*, 24(3), 461-467;

- Biot, M. A., (1941), "General theory of three-dimensional consolidation", *J. Appl. Phys.*, 12(2), 155-164;
- Biot, M. A. (1955), "Theory of elasticity and consolidation for a porous anisotropic solid", *J. Appl. Phys.*, 26(2), 182-185."
- Bitzer, K. and Harbaugh, J. W. (1987), "DEPOSIM: A Macintosh computer model for two-dimensional simulation of transport, deposition, erosion and compaction of clastic sediments", *Computers & Geosciences*, 13(6), 611-637.
- Bitzer K. (1996), "Modeling consolidation and fluid flow in sedimentary basins", *Comput. Geosci.*, 22(5), 467-478;
- Bitzer, K. (1997a), "BASIN: a finite-element model for simulation of consolidation, fluid flow, solute transport and heat flow in sedimentary basins", *Proceedings IAMG '97*, ed. V. Pawlovsky-Glahn, pp. 444-449, CIMNE, UPC, Barcelona;
- Bitzer, K. (1997b), "Pressure evolution and heat flow in a rift basin: a case study of the Barcelona Half-Graben", *Proceedings IAMG '97*, ed. V. Pawlovsky-Glahn, pp. 579-584, CIMNE, UPC, Barcelona;
- Bitzer, K., (1999), "Two-dimensional simulation of clastic and carbonate sedimentation, consolidation, subsidence, fluid flow, heat flow and solute transport during the formation of sedimentary basins", *Computer&Geoscience* 25, 431-447;
- Botneva, T.A., (1987), "Genetic principles of classification of oils", *Moscow, Nedra*, 197 p Brunet, M.-F., (1995), "Geodynamic evolution of the pre-Caspian basin after subsidence analysis", *ILP, 6th Origin of sedimentary basin Workshop*, Barcelona, 129;
- Brunet M. F., Volozh Yuri A., Antipov Mikhail P. and Leopold I. Lobkovskyc (1999), "The geodynamic evolution of the Precaspian Basin (Kazakhstan) along a north-south section", *Tectonophysics*, 313, 85-106;
- Boudreau, B. P. (1997), "Diagenetic models and their implementation", *Springer*, Berlin, 414 pp.;
- Bredehoeft, J. D. and Hanshaw, B. B. (1968), "On the maintenance of anomalous fluid pressure, Thick sedimentary sequences". *Geol. Soc. American Bull.*, 79, 1097-1106;
- Brunet, M.-F., (1995), "Geodynamic evolution of the pre-Caspian basin after subsidence analysis", *ILP, 6th Origin of sedimentary basin Workshop*, Barcelona, 129;
- Brunet M. F., Volozh Yuri A., Antipov Mikhail P. and Leopold I. Lobkovskyc (1999), "The geodynamic evolution of the Precaspian Basin (Kazakhstan) along a north-south section", *Tectonophysics*, 313, 85-106;
- Burtman, V.S., Gurarii, G.Z., Dvorova, A.V., Kuznetsov, N.B., Shipunov, S.V., (2000), "The Uralian Paleoocean in the Devonian (as inferred from Paleomagnetic data)", *Geotectonics* 34, 397- 406;
- Canuti, P., Casagli, N., Farina, P., Marks, F., Ferretti, A., Menduni, G., (2005), "Land subsidence in the Arno River Basin studied through SAR interferometry", *Proceedings of the 7th International Symposium on Land Subsidence*, vol 1, Shanghai, 23-28 Oct 2005, Shanghai Scientific and Technical Publishers, pp 407-416;
- Caputo M, Pieri L, Unguendoli M (1970) Geometric investigation of the subsidence in the Po Delta. *Bollettino di Geofisica Teorica e Applicata* 47:187-207
- Carbognin L, Gatto P, Mozzi G, Gambolati G, Ricceri G (1977) New trend in the subsidence of Venice. In: *Land subsidence*. IAHS Publ. no. 121, Wallingford, pp 65-81
- Carbognin L, Gatto P, Mozzi G, Gambolati G (1978) Land subsidence of Ravenna and its similarities with the Venice case. In: Saxena SK (ed) *Evaluation and prediction of subsidence*. Proc. Int. Conf. on Ev. and Pred. of Sub. ASCE, New York, pp 254-266
- Carbognin L, Gambolati G, Putti M, Rizzetto F, Teatini P, Tosi L (2006) Soil contamination and land subsidence raise concern in the Venice watershed, Italy. In: *Brebbia CA, Conti M, Tiezzi E (eds) Management of natural*

resources, sustainable development and ecological hazards. WIT transactions on ecology and the environment, vol 99. WIT Press, Southampton, UK, pp 691–700, doi: 10.2495/RAV060671

- Carbognin L, Frankenfield Zanin J, Marabini F (2000) River delta region, Italy. An overview of environmental evolution and land subsidence. CNR (ed) La Garagola, 42 pp
- Casu, F., Manzo, M., Lanari, R., (2006), “A quantitative assessment of the SBAS algorithm performance for surface deformation retrieval from DInSAR data”, *Remote Sensing of Environment* 102, 195–210;
- Chang, C., Zoback, M. D., Khaksar, A., (2006), “Empirical relations between rock strength and physical properties in sedimentary rocks”, *Journal of Petroleum Science and Engineering*, 51, 223-237;
- Chierici, G. L., (1994), “Principles of petroleum reservoir engineering”, *Berlin, Springer*;
- ConocoPhillips (2008), “Kashagan fault stress analysis”;
- Cooper, H. H., Jr. (1966), “The equation of groundwater flow in fixed and deforming coordinates”, *J. Geophys. Res.*, 71(20), 4785-4790;
- Cooper, H. H., Jr. (1974), “Comment on Equation for one-dimensional vertical flow of groundwater”, *Water Resour. Res.*, 10(6), 1261.
- Corbet, T. F. and Bethke, C. M. (1992), “Disequilibrium fluid pressures and groundwater flow in the western Canada sedimentary basin”, *J. Geophys. Res.*, 97(B5), 7203-7217;
- Costantini, M., Rosen, P. A. (1999), “A generalized phase unwrapping approach for sparse data”, *IGARSS'99 Proc., Hamburg (Germany)* 267–269;
- Crosetto, M., Monserrat, O., Cuevas, M., Crippa, B., (2010), “Persistent Scatterer Interferometry based on TerraSAR-X Imagery: The Barcelona Test Area”, *Wagner W., Székely, B. (eds.): ISPRS TC VII Symposium*;
- Culham, W. E. and Varga, R. S. (1971), “Numerical methods for time-dependent, nonlinear boundary value problems”, *Soc. Pet. Eng. J.*, 11, 374-388;
- Curlander J C and R N McDonough, (1991), “Synthetic aperture radar: systems and signal processing”, *John Wiley & Sons, Inc*;
- Dalyan, I.B., (1998), “New data on uplifts and semi-arch structures in Upper Permian rocks in the eastern North Caspian basin”, *Geologiya Nefti i Gaza*, 9, 22–26;
- Dalyan, I.B., and Akhmetshina, L.Z., (1998), “Lower Carboniferous clastic rocks of the eastern North Caspian basin and their petroleum productivity”, *Geologiya Nefti i Gaza*, 3, 31–34;
- deMarsily, G. (1986), “Quantitative hydrogeology”, *Academic Press*, New York, 440 pp.;
- Deutsch C.V., (2002), “Geostatistical Reservoir Modeling”, *Oxford University Press*, New York;
- Devlin, W. J., J. M. Cogswell, G. M. Gaskins, G. H. Isaksen, D. M. Pitcher, D. P. Puls, K. O. Stanley, and G. R. T. Wall, (1999), “South Caspian basin: young, cool, and full of promise”, *GSA Today*, 9, 1– 9;
- Domenico, P. A., and Schwartz, F. W. (1990), “Physical and chemical hydrogeology”, *Wiley and Sons, New York*, 824 pp.;
- Fatt, I., “Pore Volume Compressibilities of Sandstone Reservoir Rocks”, *March JPT*, p. 362;
- Ferretti, A., Prati, C., & Rocca, F. (2000), “Non-linear subsidence rate estimation using permanent scatterers in differential SAR interferometry”, *IEEE Transaction on Geoscience and Remote Sensing*, 38, 5;

- Ferretti A, Prati C, Rocca F., (2001), "Permanent scatterers in SAR interferometry", *IEEE Trans Geosci Remote Sens* 39(1), 8–20;
- Ferretti, A., Novali, R., Bürgmann, R., Hilley, G., Prati, C., (2004), "InSAR permanent scatterer analysis reveals ups and downs in the San Francisco Bay Area", *EOS* 85(34):317–324;
- Ferretti, A., Monti-Guarnieri, A., Prati, C., Rocca, F., (2007), "InSAR Principles: Guidelines for SAR Interferometry Processing and Interpretation", *ESA Publications*;
- Franceschetti, G. and Lanari R., (1999), "Synthetic Aperture Radar Processing", *CRC Press*;
- Fruneau, B., Sarti, F., (2000), "Detection of ground subsidence in the city of Paris using radar interferometry: isolation of deformation from atmospheric artifacts using correlation", *Geophys. Res. Lett.* 27;
- Gambolati, G. and Freeze, R. A. (1973), "Mathematical simulation of the subsidence of Venice", *Water Resour. Res.*, 9(3), 721-733;
- Gambolati, G. (1973a), "Equation for one-dimensional vertical flow of groundwater", *Water Resour. Res.*, 9(4), 1022-1028;
- Gambolati G., Giunta G. and Teatini P. (1998), "Numerical modeling of natural land subsidence over sedimentary basins undergoing large compaction". In: *CENAS, Coastline Evolution of the Upper Adriatic Sea due to Sea Level Rise and Natural and Anthropogenic Land Subsidence*, Kluwer Academic Publ., G. Gambolati ed., Water Science & Technology Library, n.28, 77–102;
- Gambolati G. and Teatini P. (1998), "Numerical analysis of land subsidence due to natural compaction of the Upper Adriatic Sea basin". In: *CENAS, Coastline Evolution of the Upper Adriatic Sea due to Sea Level Rise and Natural and Anthropogenic Land Subsidence*, G. Gambolati ed., Kluwer Academic Publ., Water Science and Technology Library NO. 28, 103-132;
- Gambolati G., Teatini P., Tomasi L. and Gonella M. (1999), "Coastline regression of the Romagna region, Italy, due to natural and anthropogenic land subsidence and sea level rise", *Water Resources Research*, 35(1), 163–184;
- Gambolati G, Putti M, Teatini P, Camporese M, Ferraris S, Gasparetto-Stori G, Nicoletti V, Rizzetto F, Silvestri S, Tosi L (2005) Peatland oxidation enhances subsidence in the Venice watershed. *EOS Trans AGU* 6(23):217–224;
- Garagash, I.A., Lobkovsky, L.L., Volozh, Y.A., Brunet, M.-F., (1997), "Numerical modelling of Precaspian Basin subsidence as a result of eclogite penetration beneath earth crust during Vendian collision", *Peri-Tethys Programme*, 3rd Moscow Workshop, May 12–15, Moscow, Russia, pp. 12–13
- Gatto P, Carbognin L (1981) The Lagoon of Venice: natural environmental trend and man-induced modification. *Hydrol Sci Bull* 26(4/12):379–391
- Gibson, R. E. (1958), "The progress of consolidation in a clay layer increasing in thickness with time", *Geotechnique*, 8, 171-182;
- Giese, U., Glasmacher, U., Kozlov, V.I., Matenaar, I., Puchkov, V.N., Stroink, L., Bauer, W., Ladage, S., Walter, R., (1999), "Structural framework of the Bashkirian anticlinorium, SW Urals", *Geol. Rundsch.* 87, 526– 544;
- Goldstein, R. M. (1995), "Atmospheric limitations to repeat-track radar interferometry", *Geophysical Research Letters*, 22, 2517–2520;
- Grachevsky, M.M., Berlin, Yu.M., Dubovskoy, I.T., and Ulmishek, G.F., (1976), "Correlation of formations composed of different facies in oil and gas exploration", *Nedra*, 296 p;
- Granherne (2006), "Geotechnical interpretative report";

- Harbaugh, J. W. and Bonham Carter, G. (1970), "Computer simulation in geology", *Wiley and Sons, New York*, 574 pp.;
- Hantschel T., A.I. Kauereauf A.I.,(2009), "Fundamentals of Basin and Petroleum Systems Modelling", *Springer*
- Harrison, W. J. and Summa, L. L. (1991), "Paleohydrology of the gulf of Mexico basin", *Amer. J. Science*, 291, 109-176;
- Holzel, M., Wagreich, M., Faber, R., Strauss, P., (2008), "Regional subsidence analysis in the Vienna Basin (Austria)", *Austrian Journal of Earth Sciences*, 101, 88-89;
- Hooper A, Zebker HA, Segall P, Kampes B., (2004), "A new method for measuring deformation on volcanoes and other natural terrains using InSAR persistent scatterers", *Geophys. Res. Lett.* 31;
- Horai, K. (1971), "Thermal conductivity of rock-forming minerals", *Journal of Geophysical Research*, 76, 1278-1308;
- Ismail-Zadeh A. T., Talbot C. J. and Volozh Y. A. (2001), Dynamic restoration of profiles across diapiric salt structures: numerical approach and its applications, *Tectonophysics* 337, 23-38;
- Kalinko, M.K. (1970), "Fluid-Confining Barriers and Their Influence on the Distribution of Petroleum Fields", *State and Objectives of Soviet Lithology*, 77–81.
- Kampes, D., (2005), "Displacement parameter estimation using permanent scatterer interferometry", *DLR-Forschungsberichte* 16;
- Karazhanbasunai, (2008), "KBM in Kazakhstan: Promise + Potential", *Subsidiary of Nations Energy Company, Alberta, Canada*;
- KDPC (2002), "Seismic Hazard Assessment For Kashagan Field Development Project"
- Keith, L. A. and Rimstidt, J. D. (1985), "A numerical compaction model of overpressuring in shales", *Math. Geol.*, 17(2), 115-135;
- Khain, V.E., (1977), "Regional geotectonics—Extra-Alpine Europe and western Asia", *Nedra*, 360 p;
- Khatchakian A, (1995), "Deriving reservoir pore volume compressibility from well logs", *Society of Petroleum Engineering (SPE)*, 26963;
- Kinzelbach, W. (1986), "Groundwater modeling", *Elsevier, Amsterdam*, 331 pp.;
- Kircher M., (2004), "Analysis of extensive subsidence in sedimentary areas with the new techniques of radar remote sensing using the example of the lower Rhine basin", *PhD Thesis, Universität Bonn, Germany*;
- Kleshchev, K.A., Petrov, A.I., and Shein, V.S. (1995), Geodynamics and new types of oil and gas reservoirs in nature (Geodinamika i novye tipy prirodnykh rezervuarov nefti i gaza): Moscow, *Nedra*, 284;
- Kostyuchenko, S.L., Egorkin, A.V., Solodilov, L.N., (1999), "Structure and genetic mechanisms of the Precambrian rifts of the East-European platform in Russia by integrated study of seismic, gravity, and magnetic data", *Tectonophysics* 313, 9– 28;
- Lanari, R., Mora, O., Manunta, M., Mallorquí, J. J., Berardino, P., & Sansosti, E. (2004), "A small baseline approach for investigating deformations on full resolution differential SAR interferograms", *IEEE Transactions on Geoscience and Remote Sensing*, 42, 7;
- Lee J.S., Hoppel K.W., Mango S.A., and Miller (1994), "Intensity and phase statistics of multilook polarimetric and interferometric sar imagery", *IEEE Trans. GARS*, 30:1017;
- Letavin, A.I., (1980), "Basement of the young platform of the southern USSR", *Nauka*, 152 p.;

- Lobkovsky L. I., S. Cloetingh, Nikishin A. M., Volozh Y. A., Lankreijer A. C., Belyakov S. L., Groshev V. G., Fokin R. A., Milanovsky E. E., Pevzner L.A., Gorbachev V.I., Korneev M.A. (1996), Extensional basins of the former Soviet Union -- structure, basin formation mechanisms and subsidence history, *Tectonophysics* 266, 251-285
- Lopatin, N. V. (1971), "Temperature and time as factors in coalification (in Russian)", *Akad. Nauk SSSR Izvestya, Seriya Geolicheskaya*, 3, 96-106.
- MacDonald, Dettwiler and associates Ltd, (2009), "RADARSAT-2 product description", *RN-SP-52-1238*;
- Mancini, P., Mesini, E., (2005), "Petrophysical characteristics of reservoir rock", *Departement of mining engineering, University of Bologna*;
- Makhous, M., Galushkin, Yu., Lopatin, N., (1997), "Burial history and kinematic modelling for hydrocarbon potential generation, part I: The Galo Model", *AAPG Bulletin*, 10, 1660-1699;
- Massonnet, D. and Feigl, K.L., "Radar interferometry and its application to changes in the earth's surface", *Reviews of Geophysics*, 36(4):441-500;
- Milanovsky, E.E., (1987), "Geology of the USSR", *Volume 1: Moscow University*, 414 p.;
- Mo Energy and Mineral Resources, Committee for Geology and Subsoil Use, CaspiMunayGas Research Institute LTD, Kazakh Oil and Gas Institute, West Kazakhstan Territorial Geology and Subsoil Use Department (2007), "Geological report on selection of subsoil area for the treated industrial wastewater injection";
- Mo Energy and Mineral resources, Caspimunaigas, CGM (2001), "Geotechnical data on the northern caspian coast feasibility study survey materials";
- Murzagaliev, D.M., (1994), "Goals of petroleum exploration in the Emba-Uil area", *Geologiya Nefti i Gaza*, 4, 16–19;
- Murzagaliev, D.M., (1995), "Subsalt carbonate reservoirs on the northern Caspian shelf and their petroleum potential", *Geologiya Nefti i Gaza*, 5, 22–25;
- Nevolin, N.V., (1978), "Deep structure of the Precaspian depression", *Geotectonics* 12, 192– 199;
- NPA, (2006), "Ground stability (InSAR): applications and case studies", *London, UK*;
- Orlov, V.P., and Voronin, N.I., (1999), "Petroleum productivity of the Devonian-Lower Carboniferous sequence of the Astrakhan arch", *Geologiya Nefti i Gaza*, 1–2, p. 2–6;
- Overton, L. H., Norman, C., (1969), "Reservoir pore volume compressibility calculated by traveltime log", *University of Boston*;
- Ovcharenko A. V., Ermakov B. V., Myatchin K. M., and Shlezinger A. E. (2007), Caprocks in Hydrocarbon Fields, *Lithology and Mineral Resources* Vol. 42, No. 2, 180–191;
- Pavlov, N.D., (1993), "Areal distribution of seismic and petrophysical characteristics and productivity of the reservoir in the Tengiz field and problems of optimization of its development", *Geologiya Nefti i Gaza*, 9, 30–35;
- Pedersen, T. and Bjorlykke, K. (1994), "Fluid flow in sedimentary basins: a model of pore water in a vertical fracture", *Basin Research*, 6, 1-16;
- Perrier, R. and Quiblier, J. (1974), "Thickness changes in sedimentary layers during compaction history", *Am. Assoc. Pet. Geol. Bull.*, 58(3), 507-520;
- Pilipenko, A.I., (1990), "Upper Paleozoic rocks of the southwestern Aral Lake on seismic data", *Geologiya Nefti i Gaza*, 4, 23–26;
- Puchkov, V.N., (2000), "Paleogeodynamics of South and Middle Urals", *Ufa*;

- Rizzetto F, Tosi L, Zecchin M, Brancolini G, Baradello L, Tang C (2009) Ancient geomorphological features in shallows of the Venice Lagoon (Italy). *J Coast Res* 56:752–756
- Ronchi P.,Ortenzi A.,Borromeo O.,Claps M.,Zempolich W.G., (2010), “Depositional setting and diagenetic processes and their impact on the reservoir quality in Visean-Bashkirian Kashagan carbonate platform (Precaspian Basin,Kazakhstan)”, *AAPG Bulletin* v.94 No.9, pp. 1313-1348;
- Rosen, P., Hensley, S., Joughin, I., Li, F., Madsen, S., Rodriguez, E., Goldstein, R., (2000), “Synthetic Aperture Radar Interferometry”, *Proc. IEEE*, pp. 333 – 379;
- Rubey, W. W. and Hubbert, M. K. (1959), “Role of fluid pressure in mechanics of overthrust faulting”, *Geol. Soc. Am. Bull.*, 70(2), 167-205;
- Sanders, C.W., (1939), “Emba salt-dome region, U.R.S.S., and some comparison with other salt-dome region”, *Bulletin of American Association of Petroleum Geologist*, 23, 492-518;
- Sapozhnikov, R.B., Shlezinger, A.B., and Yanshin, A.I., (1986), “Pre-Late Permian development of the eastern and southeastern North Caspian basin”, *Sovetskaya Geologiya*, 4, 90–100;
- Scoffin, T. (1986), “An introduction to carbonate sediments and rocks”, *Chapman and Hall, New York*, 274 pp.;
- Segalovich V. I., Volozh Yu. A., Antipov M. P., and Vasil'ev O. A. (2007), Nature of the North Caspian Gravity Anomaly, *Geotectonics* Vol. 41, No. 3, 195–209;
- Sharp, Jr., J. M. (1983), “Permeability controls on aquathermal pressuring”, *Am. Assoc. Pet. Geol. Bull.*, 67(11), 2057-2061;
- Shershukov, I.V., (1986), “Dependence of reservoir properties of porous carbonate rocks on depositional facies in the Karachaganak field”, *Sovetskaya Geologiya*, 12, 39–41;
- Shimoni, M., Hanssen, R.F., van de Meer, F., Kampes, B.M., Ben-Dor, E., (2002), “Salt diapir movements using SAR Interferometry in the Lisan Peninsula, Dead Sea Rift”, *Proc. SPIE vol. 4345, SAR Image Analysis, Modelling and Techniques IV*, pp. 151-160;
- Smith, J. E. (1971), “The dynamics of shale compaction and evolution of pore-fluid pressure”, *Math. Geol.*, 3(3), 239-263;
- Snyder, W.S., Spinosa, C., Davydov, V.I., Belasky, P., (1994), “Petroleum Geology of the southern Pre-Uralian Foredeep with reference to the Northeastern Pre-Caspian Basin”, *Int. Geol. Rev.* 36, 452– 472;
- Solovyev, B.A., (1992), “Stages of evolution and petroleum productivity of the sedimentary cover of the North Caspian basin”, *Geologiya Nefti i Gaza*, 8, 13–18.
- Strozzi T., Wegmüller U., Tosi L., Bitelli G., and Spreckels V. (2001), “Land subsidence monitoring with Differential SAR Interferometry”, *Photogramm. Eng. Remote Sens.*, 67(11), 1261–1270;
- Strozzi, T., Teatini, P., Tosi, L., (2009), “TerraSAR-X reveals the impact of the mobile barrier works on Venice coastland stability”, *Remote Sensing of Environment* 113, 2682–2688;
- Talbot, C. J., (1998), “Extrusion of Hormuz salt in Iran”, *The past is the key to the present*, Geological Society (London) Special Publication 143, 315– 334.
- Teatini P., Tosi L., Strozzi S., Carbognin L., Wegmüller U., and Rizzetto F. (2005), “Mapping regional land displacements in the Venice coastland by an integrated monitoring system”, *Remote Sens. Environ.*, 98(4), 403–413;
- Teatini, P., Strozzi, T., Tosi, L., Wegmüller, U., Werner, C., and Carbognin, L., (2007), “Assessing short- and long-time displacements in the Venice coastland by synthetic aperture radar interferometric point target analysis”, *Journal Of Geophysical Research*, Vol. 112;

- Teatini P, Tosi L, Strozzi T, Carbognin L, Cecconi G, Rosselli R, Libardo S (2009) Resolving land subsidence within the Venice Lagoon by persistent scatterer SAR interferometry. *Phys Chem Earth*. doi:10.1016/j.pce.2010.01.002
- Teatini, P., Gambolati, G., Ferronato, M., Settari, A., Walters, D., (2011), "Land uplift due to subsurface fluid injection", *Journal of Geodynamics* 51, 1–16;
- Terzaghi K., (1942),"Theoretical soil mechanics", N.-Y. 1942, 510 p
- Tetzlaff, D. and Harbaugh, J. W. (1989) "Simulating clastic sedimentation", *Van Nostrand Reinhold, New York*, 202 pp.;
- Tosi L, Carbognin L, Teatini P, Strozzi T, Wegmu"ller U (2002) Evidences of the present relative land stability of Venice, Italy, from land, sea, and space observations. *Geophys Res Lett* 29(12):1562. doi: 10.1029/2001GL013211
- Tosi L., Teatini P., Carbognin L., Brancolini., (2009), "Using high resolution data to reveal depth-dependent mechanisms that drive land subsidence: The Venice coast, Italy", *Tectonophysics* 474, 271–284;
- Tosi L., Teatini P., Strozzi S., Carbognin L., Brancolini., G., Rizzetto, F., (2010), "Ground surface dynamics in the northern Adriatic coastland over the last two decades", *Rend. Fis. Acc. Lincei*, 21;
- Turcotte, D. L., and Schubert, G. (1982), "Geodynamics: applications of continuum physics to geological problems", *Wiley and Sons*, 450 pp.;
- Ulmishek, G.F., and Klemme, H.D., (1990), "Depositional controls, distribution, and effectiveness of world's petroleum source rocks", *U.S. Geological Survey Bulletin* 1931, 59 p.;
- Ulmishek, G.F., Bogino, V.A., Keller, M.B., and Poznyakevich, Z.L. (1994), "Structure, stratigraphy, and petroleum geology of the Pripyat and Dnieper-Donets basins, Belarus and Ukraine, *Interior rift basins: American Association of Petroleum Geologists Memoir* 59, 125–156.
- Ulmishek F. Gregory (2003), Petroleum Geology and Resources of the Middle Caspian Basin, Kazakhstan and Uzbekistan, *U.S. Geological Survey Bulletin* 2201-D;
- Ulmishek F. Gregory (2003), "Petroleum Geology and resource of the North Caspian Basin", *U.S. Geological Survey Bulletin* 2201-B;
- Ulmishek F. Gregory (2003), "Petroleum Geology and Resources of the North Ustyurt Basin, Kazakhstan and Uzbekistan", *U.S. Geological Survey Bulletin* 2201-D;
- Usai S., (2001), "A new approach for long term monitoring of deformations by differential SAR interferometry", *PhD Thesis, Technische Universiteit Delft, The Netherlands*;
- Vasco, D.W., Rucci, A., Ferretti, A., Novali, F., Bissel, R., Ringrose, P., Mathieson, A., Wright, I., (2010), "Satellite-based measurements of surface deformation reveal fluid flow associated with the geological storage of carbon dioxide", *Geophysical Research Letters*;
- Volchegursky, L.F., Vladimirova, T.V., Kapustin, I.N., and Natapov, L.M., (1995), "Evolution of the North Caspian basin in middle-late Paleozoic time, *Otechestvennaya Geologiya*, 2, 44–49.
- Volkova, T.P., (1992), "Paleogeothermal conditions and catagenesis of organic mater in subsalt rocks", *Prognosis of petroleum productivity of subsalt Paleozoic rocks of the eastern and southeastern North Caspian basin, Moscow, Nauka*, 71–88.
- Volozh, Yu. A., V. G. Groshev, and A. V. Sinelnikov, (1994), "The overhangs of the Southern Pre-Caspian Basin (Kazakhstan): proposals for a genetic classification", *Bulletin of the Center for Research Exploration Elf Aquitaine*, 18, 19– 32;

- Volozh Yu.A., Antipov M.P., Brunet M.F., Garagash I.A, Lobkovskii L.I., Cadet J.P. (2003), Pre-Mesozoic geodynamics of the Precaspian Basin (Kazakhstan), *Sedimentary Geology* 156, 35-58;
- Volozh, Yu.A, Talbot, C. and Ismail-Zadeh, A., (2003), "Salt structures and hydrocarbon in the Precaspian Basin", *AAPG Bulletin*, 87-2, 313–334;
- Volozh, Yu.A., Parasyina, V.S., (2008), "Astrakhan Carbonate Massif: Geological Structure and Petroleum Potential", *Nauchnyi Mir*, Moscow;
- Yakhimovich, N.N., (1996), "Geodynamics of the Sol-Iletska tectonic uplift on the southeastern Russian platform", *Otechestvennaya Geologiya*, 7, 24–32;
- Waples, D. W. (1980), "Time and temperature in petroleum formation: application of Lopatin's method to petroleum exploration" *American Association of Petroleum Geologists Bulletin*, 64(8), 916-926;
- Werner, C., Wegmuller, U., Strozzi, T., Wiesmann, A., (2003), "Interferometric point target analysis for deformation mapping". In *Proceeding of IEEE Geoscience and Remote Sensing Symposium (IGARSS'03)*, Toulouse, France, 2003, volume 7, pp. 4362-4364, (Piscataway, NJ:IEEE).
- Westlake, J. R. (1968), "Numerical Matrix Inversion and Solution of Linear Equations", John Wiley, New York.
- Worawattanamateekul, J., Hoffmann, J., Adam, N., Kampers, B., Altermann, W., (2004), "Radar interferometry technique for urban subsidence monitoring: a case study in Bangkok and its vicinity", *ENVISAT Symposium*, Salzburg, Austria, 6–10 Sept;
- Zebker, H. A., & Villasenor, J. (1992), "Decorrelation in interferometric radar echoes", *IEEE Transactions on Geoscience and Remote Sensing*, 30, 950–959;
- Zonenshain, L.P., Kuzmin, M.I., Natapov, L.M., (1990), "Geology of the USSR: a plate-tectonic synthesis" *Geophys. Union, Geodyn. Ser.* 21. 242.

11.ACKNOWLEDGEMENT

This work was performed in the framework of the project “North Caspian coastal zone Bio&Geodiversity Management Masterplan” (MED Ingegneria srl). For confidentiality agreement some data is not fully presented in this document.